University of Glasgow | School of Chemistry

Rational Design of Nanostructured Electrodes for Li-ion Batteries

Josefa Vidal Laveda

Submitted in fulfilment of the requirements for the degree of Doctor of Philosophy

School of Chemistry
College of Science and Engineering
University of Glasgow

Supervisor: Dr. Serena A. Corr

February 2017

Acknowledgements

Firstly, I would like to acknowledge the School of Chemistry at Glasgow University for giving me the opportunity to carry out this Doctorate of Philosophy in the area of materials chemistry and electrochemistry. In particular, I would like to give my deepest gratitude to my supervisor Dr. Serena A. Corr for all her enthusiasm, expertise, encouragement and guidance over the past three years and a half. I am very grateful for the opportunities of numerous beamtimes, conferences and research visits in which I have met excellent research scientists. Furthermore, I want to thank all the Corr group members for their support and interesting discussions that have made challenges endurable and enjoyable. Moreover, I also would like to thank Mr. Michael Beglan for his constant help in the lab, without his help this work would have never been possible. It has been a great pleasure to work as a part of this exellent research group.

I would like to thank Mr. Jim Gallagher in the School of Chemistry and Mr. Peter Chung in the School of Geographical and Earth Sciences at the University of Glasgow for their advice in the scanning electron microscopy analysis. Also, thank Dr. Gary Paterson and Dr. Donald MacLaren in the School of Physics and Astronomy at the University of Glasgow for their assistance on conducting the transmission electron microscopy measurements. Furthermore, I would also like to thank Dr. Claire Wilson for her contribution in the single crystal diffraction studies of the metal alkoxide precursors and Dr. Stephen Sproules and Dr. David Adam for their support on the NMR experiments.

I would like to highly acknowledge Dr. Matt Tucker and Dr. Helen Playford at ISIS pulsed Neutron and Muon source for their assistance in the high resolution neutron powder diffraction and neutron pair distribution function experiments of $LiFe_{1-x}Mn_xPO_4$ nanostructures and subsequent data analysis. Your support has been fantastic and very fruitful. Moreover, thank you very much for getting me started on the Reverse Monte Carlo modeling. Furthermore, thank Dr. Peter Baker at ISIS for his cooperation in the muon spin resonance studies of the $LiFe_{1-x}Mn_xPO_4$ phases. Also, thank you very much to Dr. Claire Murray at Diamond Light Source for conducting high resolution X-ray diffraction measurements on some of our olivine nanostructures.

On the other hand, I would like to personally thank Prof. Simon Billinge and Prof. Kirsten Jensen for giving me the great opportunity of visiting Columbia University in order to learn pair distribution function (PDF) analysis with the world-leading experts in this technique. It has been a privilege to work with you. Your help, support and discussions have been invaluable. Also, thank Maxwell Terban in Prof. Billinge's group for his guidance on X-ray PDF data analysis.

Finally, I would like to save my biggest gratitude for my family and all my friends for their constant support in the long distance and for always encouraging me over the time of this

PhD. Particularly my parents, whose support have been pivotal through this PhD and I would not have been able to do it whithout them.

This work was supported by funding from the EPSRC (EP/K026290/1 and EP/ N001982/1). I also gratefully acknowledge the Kelvin Nanocharacterisation Centre for use of their facilities and the STFC for beamtime allocations at the Polaris, EMU and I11 beamlines at the ISIS Neutron and Muon Source and Diamond Light Source. Also thank National Synchrotron Light Source (NSLS) and the NSLS-II at Brookhaven National Laboratory for use of their facilities.

Abstract

This thesis focuses on the rational design of fast and low temperature synthetic routes for the preparation of energy storage nanostructures with potential applications as electrode materials for Li-ion batteries. The materials synthesised in this work have been fully investigated by powder X-ray diffraction, electron microscopy and potentiodynamic measurements. Where possible, high resolution powder X-ray and neutron diffraction, X-ray and neutron pair distribution function (PDF) analysis and muon spin relaxation (μ^+SR) studies have been conducted in order to have a better understanding of the structure-property relationship and have a complete and detailed characterisation of these battery materials.

Chapter 1 includes a general introduction about Li-ion batteries and a brief analysis of the most promising electrode materials used in Li-ion batteries. Furthermore, a short description about different synthetic methodologies such as solid state, microwave-assisted and solvothermal syntheses is included. In particular, the benefits of single source precursor processes are highlighted. Finally, the main aims of this thesis are also discussed.

The objective of **Chapter 2** is to provide detailed experimental procedures of all materials synthesis and also to briefly describe the main characterisation techniques employed during this research, exploring in more detail those not commonly used, such as pair distribution function analysis and muon spin relaxation.

In **Chapter 3**, a microwave-assisted solvothermal approach for the preparation of a family of $LiFe_{1-x}Mn_xPO_4$ (x=0, 0.25, 0.5, 0.75 and 1) olivines using commercial starting materials is presented. To fully characterise and have a deeper insight of the structure-property relationship of these nanocrystalline phases, high resolution powder neutron diffraction and neutron PDF analyses of these phases are conducted, allowing the examination of the local structure, cation distribution, presence of defects and Li content. Moreover, muon spin relaxation is used for the first time to investigate the lithium diffusion in this series of olivine mixed metal phosphate phases. By understanding how this double transition metal system operates, it may be possible to synthesise high performing electrode nanomaterials with higher energy density than $LiFePO_4$ with no significant increase in cost and exhibiting charge/discharge rates acceptable for commercial applications.

Chapter 4 covers a fast and energy-efficient synthetic route to olivine nanostructured $LiFe_{1-x}Mn_xPO_4$ cathodes and Mn_3O_4 hausmannite conversion anodes for Li-ion batteries using a new class of metal alkoxides containing one or two transition metals. The main advantage of metal alkoxides over commercially available inorganic salt mixtures is that the different metals of the final product are already present in a single precursor, which significantly reduces the energy required for reaction of a multicomponent precursor

mixture employed in conventional synthesis. Furthermore, thermal decomposition of these metal alkoxide compounds can be performed at relatively low temperatures, allowing decreased temperatures during synthesis and making the process more energy efficient. This work intends to emphasise the versatility of metal alkoxide precursors in the preparation of nanostructured Li-ion battery materials for both positive and negative electrodes through relatively fast and low temperature microwave and ultrasound-assisted methods.

In **Chapter 5**, having confirmed the suitability of employing transition metal alkoxide precursors for the preparation of nanostructured electrodes *via* microwave or ultrasound assisted methods, efforts have been directed to develop the synthesis of a series of heterometallic alkoxide complexes containing both Li and a transition metal (Fe, Mn). These heterometallic alkoxide precursors are then used for the generation of highly crystalline $LiFe_{1-x}Mn_xPO_4$ olivine nanostructures exhibiting an outstanding electrochemical performance. Co-location of all the required metals in these metallorganic precursors could bypass the need of diffusional mixing and allow the reactions to proceed faster and at lower temperatures generating better crystallised materials. X-ray PDF analyses of these $LiFe_{1-x}Mn_xPO_4$ olivine nanophases are conducted in an effort to examine the local structure, defect chemistry and show that microwave processes produce highly crystalline materials even after short reaction times. Finally, a ionothermal microwave-assisted synthesis of $LiFePO_4$ nanoparticles using heterometallic alkoxide precursors has been examined in order to study the influence of the solvent in the resulting electrochemical performance.

Chapter 6 explores the preparation of olivine $LiFe_{1-x}Mn_xPO_4$ nanostructures through conventional solvothermal processes using the same single source heterometallic alkoxide precursors. A reduction in particle size and an enhancement in the electrochemical behaviour are achieved when using single source precursor metallorganic compexes compared to commonly used commercial starting materials. Moreover, the fabrication of Fe_3O_4 magnetite nanoparticles by the room temperature hydrolysis of the $[FeLi_2Br(O^tBu)_4(THF)_2]_n$ heterometallic alkoxide precursor and its application as anode material for Li-ion batteries is presented.

Chapter 7 further develops this family of heterometallic precursors by examining the preparation of olivine nanostructured Ni-doped $LiFePO_4$ cathodes *via* microwave processes. The effect of the addition of polyvinylpyrrolidone (PVP) in the reaction mixture, which could act as a capping and dispersing agent to prevent particle growth and agglomeration as well as a possible carbon source for all-in-one carbon coating procedures, is investigated. The preparation of a Li and Ni containing metal alkoxide and its utilisation as a Ni precursor for the preparation of nanostructured $LiFe_{1-x}Ni_xPO_4$ olivine cathodes and

NiO conversion anodes is presented, demonstrating again the versatility of single source precursor synthesis using heterometallic alkoxides in the preparation of both Li-ion battery cathode and anode materials.

Finally, **Chapter 8** includes some general conclusions and an outlook for future work including some preliminary investigations on microwave syntheses of non-olivine β-$LiFe_{1-x}M_xPO_4$ (*M*=Fe, Co, Ni) and maricite $NaFe_{1-x}Mn_xPO_4$ nanostructures for Li and Na-ion battery applications.

Table of Contents

List of Tables

List of Figures

Abbreviations

LIBs	Lithium-ion batteries
PXRD	Powder X-Ray Diffraction
SCXRD	Single crystal X-Ray Diffraction
HR SEM	High Resolution Scanning Electron Microscopy
HR TEM	High Resolution Transmission Electron Microscopy
PND	Powder Neutron Diffraction
μ^+SR	Muon Spin Relaxation
PDF	Pair Distribution Function
BET	Brunauer-Emmet-Teller
NMR	Nuclear Magnetic Resonance
FT IR	Fourier Transform Infrared Spectroscopy
GCPL	Galvanostatic Cycling with Potential Limitation
CV	Cyclic Voltammetry
AAS	Atomic Absorption Spectroscopy
$Fe(acac)_3$	Iron(III) acetylacetonate
$Mn(acac)_3$	Manganese (III) acetylacetonate
^{t}Bu	*tert*-butyl
EG	Ethylene glycol
EC	Ethylene carbonate
DMC	Dimethyl carbonate
PTFE	Polytetrafluoroethylene
PVP	Polyvinylpyrrolidone
THF	Tetrahydrofuran
EMI-TFMS	1-ethyl-3 methyl imidazolium trifluoromethanesulfonate
μλ	Microwaves
GHz	Gigahertz
RT	Room temperature
ZF	Zero field
LF	Longitudinal field
TF	Transverse field
TOF	Time-of-flight
SAED	Selected Area Electron Diffraction
EDS	Energy Dispersive X-ray Spectroscopy
SEI	Solid electrolyte interface
ILs	Ionic liquids
SSP	Single Source Precursor
ICSD	Inorganic Crystal Structure Database
FWHM	Full Width at Half Maximum

1 Introduction

1.1 Basic aspects of Li-ion batteries

Nowadays, owing to the urgent need of making a more efficient use of our scarce and finite natural resources, there is a growing interest in the development of high efficiency energy storage systems. In particular, electrochemical systems such as Li-ion batteries (LIBs), which can work as an energy storage device by converting electric energy into electrochemical energy, have revolutionised the portable electronics industry, propelling the study of high performance electrodes to the forefront of modern research. LIBs reversibly convert between electrical and chemical energy *via* redox reactions, thus storing the energy as chemical potential in their electrodes.[1] LIBs have evolved as the major power source since their commercialisation by Sony in 1991[2] and represent one of the major successes of materials electrochemistry. In view of the growing day-to-day demand for Li-ion batteries, intensive research is being pursued globally to develop new high performing, cost effective electrode materials without compromising on environmental issues and safety. LIBs are currently under intense investigation to meet the performance specifications required by consumers in portable electronic devices (cell phones, notebook computers, iPads, etc.), (hybrid) electric vehicles and stationary storage as a back-up for intermittent renewable energy generation technologies. LIB cells generally offer high energy density, flexible and lightweight design, and longer lifespan compared to other battery technologies. The energy storage properties for most of the common rechargeable batteries are shown in Figure 1.1. Li-ion batteries outperform (energy densities of approximately 210 $Wh \cdot kg^{-1}$, 650 $Wh \cdot l^{-1}$), by at least a factor of 2.5, compared with competing technologies (nickel (Ni)-metal hydride, Ni-cadmium (Cd), and lead (Pb)-acid) in terms of delivered energy while providing high specific power.[3] The overwhelming appeal of Li-electrochemistry lies in the low molecular weight of lithium, its small ionic radius (which facilitates diffusion) and low redox potential (E^0 (Li^+/Li^0)=-3.04 V *vs.* standard hydrogen electrode (SHE)), which enables high-output voltages and therefore high-energy densities.[4] LIBs have an operating voltage of ~3.6 V with capacities ranging from 700 to 2400 mA·h. LIBs are usually charged and discharged at current rates between 0.2 C and 1 C, meaning that the full capacity of the cell is stored or used in five or one hour, respectively, with typical operating temperature ranges of 15 to 60 °C. At lower temperatures the capacity generally decreases, whereas at higher temperatures slow degradation of the electrode and/or electrolyte can take place. The 2010 annual worldwide production of LIBs was worth about US $ 11.8 billion[5] and, with the expected use of large-scale LIBs for vehicles and stationary off-peak energy storage systems and other applications, the industry projected demands and growth is estimated to

dramatically increase to a market value up to US $ 53.7 billion in 2020.[5] This has lead to an exponential growth in the investigation of LIB materials.

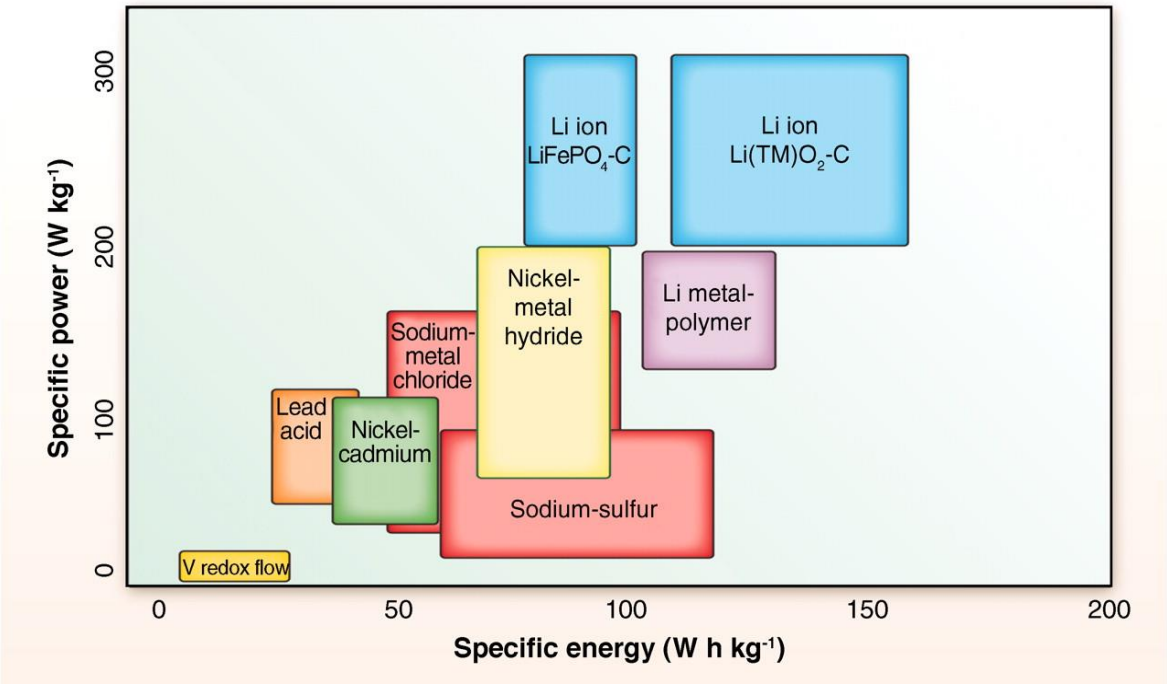

Figure 1.1. Gravimetric power and energy densities for different rechargeable batteries.[4]

1.2 Configuration and working principles of Li-ion batteries

A Li-ion cell consists of a positive and a negative electrode separated by an electrolyte solution containing dissociated salts, which enables ion transport between the two electrodes. The electrode reactions taking place in these electrochemical systems are based on the reversible insertion and extraction of Li^+ ions into the host electrode materials with a concomitant addition/removal of electrons into the host. Li^+ ions are extracted from the cathode and inserted into the anode during the charge process, and the reverse reaction occurs during discharge. The electrodes are then connected externally, enabling the current to be tapped by the user. A LIB schematic diagram is shown in Figure 1.2. In its most conventional structure, a LIB contains a graphite anode, a cathode formed by a lithium metal oxide and an electrolyte consisting of a solution of a lithium salt in a mixed organic solvent imbedded in a separator.[6]

1.3 Key challenges in Li-ion batteries

A high level of safety, low environmental impact, good cycle life, low cost, large power generation and wide temperature operational range are the main requirements for the development of the most advanced LIB energy storage systems. Nowadays, scaling up the chemistry of common LIBs in view of their application for sustainable vehicles and renewable energy plants is still challenging. For example, an increase by a factor of 15 in the energy density delivered by a battery (180 $Wh \cdot kg^{-1}$) is still needed in order to match

1 L of gasoline (3000 $Wh \cdot l^{-1}$).[7] Barriers of various nature including safety, cost, energy density, cyclability and materials availability present challenges to achieving this important step. Considerations on battery performance such as cell potential, capacity and energy density are strongly related to the intrinsic properties of the materials that form the positive and negative electrodes. This is a major driver for the development of green and energy-efficient synthesis of novel energy storage materials. The chances of drastically improving today's Li-ion cells energy density are mainly rooted in identifying better electrode materials that could either display greater redox potentials or larger capacity (materials capable of reversibly inserting more than one electron per 3*d* transition metal).[8] Current approaches to achieving better performance include: the replacement of the graphite anode and lithium cobalt oxide cathodes with alternative, higher power and lower cost electrode materials, and the substitution of the organic liquid electrolyte solutions with safer, more reliable and wider working voltage window electrolyte systems such as solid electrolytes.[6, 9]

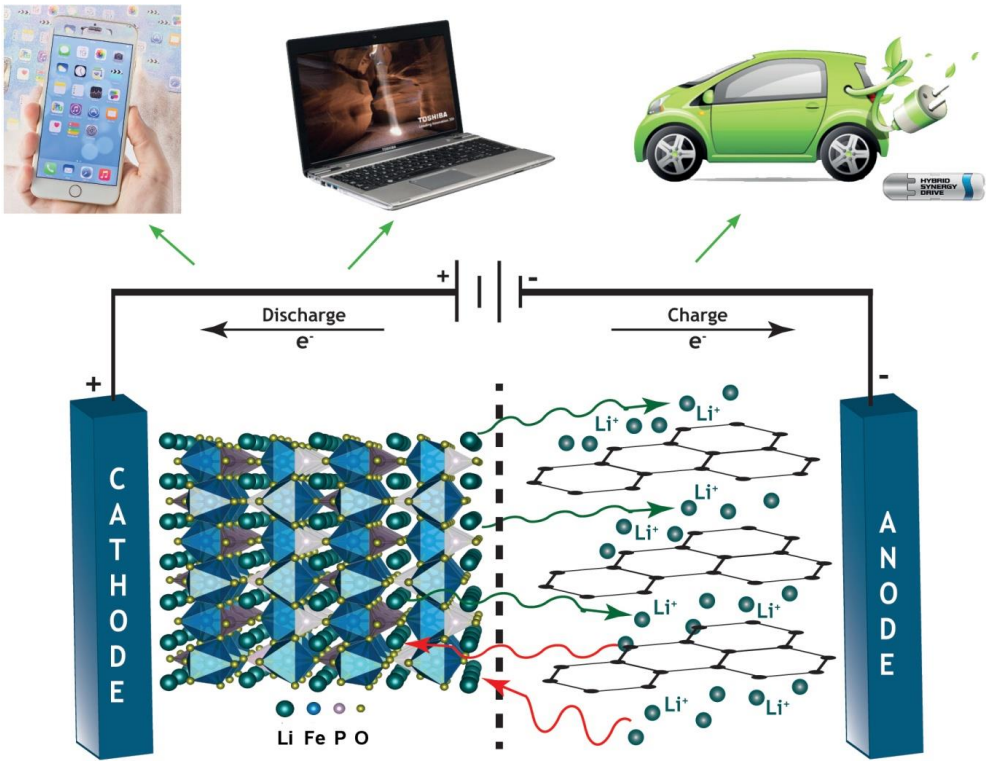

Figure 1.2. Li-ion battery schematic diagram.

1.4 Cell voltage

The cell voltage of a battery is determined by the compatibility of the entire system, including the anode, cathode and electrolyte. The choice of electrode material depends mainly on the electrochemical potential (μ_A for the anode and μ_C for the cathode) as well as their positions relative to the energy gap (E_g) of the electrolyte. As shown in Figure 1.3, for a stable cell, μ_A should be lower in energy than the LUMO (lowest unoccupied

molecular orbital) of the electrolyte, otherwise the electrolyte will be reduced. On the other hand, μ_C should be higher in energy than the HOMO (highest occupied molecular orbital) of the electrolyte to inhibit the oxidation of the electrolyte. High energy storage density can be achieved in a cell with the maximum electrochemical potential difference between the anode and the cathode as well as their high lithium intercalation ability. The stability of the electrolyte must not be overlooked. The difference in chemical potential between the anode (μ_A) and the cathode (μ_C) is the working voltage (also known as the open voltage circuit) and can be calculated according to the following equation 1.1:

$$V_{OC} = \frac{\mu_A - \mu_C}{e} \quad (1.1)$$

where *e* is the magnitude of the electric charge.[1]

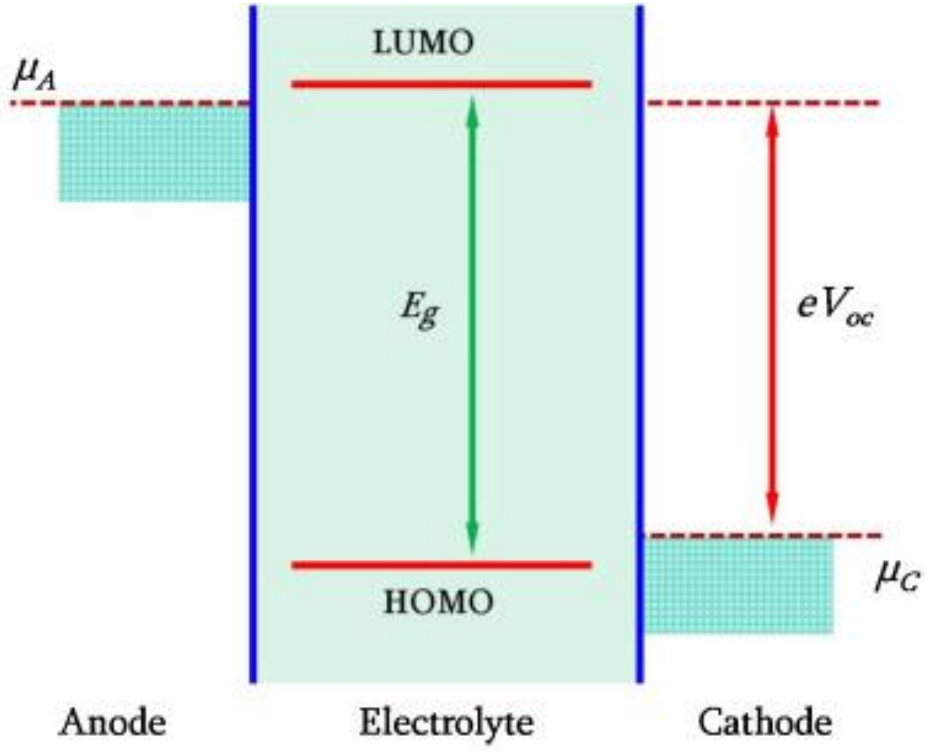

Figure 1.3. Relative energy diagram of electrode potentials and electrolyte energy gap, E_g, in LIBs.[1]

1.5 Electrode materials for Li-ion batteries

1.5.1 Intercalation cathode materials

An intercalation cathode is a solid host framework capable of storing guest ions that can be reversibly inserted into and extracted from the host network. In a Li-ion reachargeable battery, Li^+ are the guest ions that can diffuse along the host network lattice, which are typically metal chalcogenides, transition metal oxides and polyanionic compounds. Robust crystal structures with sufficient Li^+ storing sites are required to generate a material with stable cyclability and high specific capacity.[10] The key factors

determining the Li^+ storage capacity through intercalation are: (1) the electrode capability to change valence states; (2) the available space to accommodate Li^+ ions; and (3) the reversibility of the intercalation reactions. Typical intercalation materials include layered oxides, spinels and olivines.

1.5.1.1 Layered transition metal oxides Li*M*O_2 (*M*=Co, Mn, Ni)

$LiCoO_2$ first introduced by Goodenough as cathode material,[11] is the most commercially successful layered transition metal oxide cathode. The first LIB system using $LiCoO_2$ as cathode and graphite as anode was commercialised in 1991 by Sony and is still used in the majority of commercial LIBs. The electrochemical reaction at the graphite anode can be described as:

$$C_6 + x\,Li^+ + x\,e^- \leftrightarrow Li_xC_6$$

while at the $LiCoO_2$ cathode the following reaction is taking place:

$$LiCoO_2 \leftrightarrow Li_{1-x}CoO_2 + x\,Li^+ + x\,e^-$$

$LiCoO_2$ is a very attractive cathode material due to its relatively high theoretical capacity of 274 mAh·g^{-1}, low self-discharge and good cycling performance. The $LiCoO_2$ structure consists of a close-packed network of oxygen ions in which the Li^+ ions lie between slabs of [CoO_6] octahedra that form CoO_2 sheets, allowing Li^+ to diffuse in two-dimension between the CoO_2 sheets.[12, 13] Nevertheless, the main limitations are the high cost and toxicity of Co, low thermal stability and rapid capacity fade at high current rates or during deep cycling. Low thermal stability often leads to the exothermic release of oxygen when this cathode is heated above certain temperature, resulting in a runaway reaction in which the cell can overheat and burst into flames. The strong oxidising behaviour of this layered oxide cathode in an overcharged state when in contact with common organic electrolytes could lead to combustion or even explosion, with this effect even more pronounced for nanosized materials with high surface area. Furthermore, deep cycling (delithiation above 4.2 V) can induce a lattice distortion from hexagonal to monoclinic symmetry and the resulting volume change can deteriorate the cycling performance leading to a significant reduction in the capacity retention. Several reasons including lattice defects, oxygen loss, transition metal dissolution and structural degradation, which are associated with intensified electrolyte decomposition and electrode–electrolyte side reactions, are believed to account for the poor performance of $LiCoO_2$ at high voltages. As a result, in practical $Li_{1-x}CoO_2$ lithium ion cells only a reversible insertion/extraction of 0.5 lithium is possible delivering approximately 140 mAh·g^{-1} around 4 V *vs.* Li^+/Li^0. Although this limitation was originally associated with structural transitions around $(1-x)=0.5$,[14] several chemical delithiation investigations suggest that the limitation may be attributed primarily to chemical instability for $(1-x)<0.5$, arising from a significant overlap of the redox active $Co^{3+/4+}$:t_{2g} band with the top of the O^{2-}:2*p* band as depicted in Figure 1.4.[15] When compared to other transition

metals, the redox active $Ni^{3+/4+}$:e_g band only barely touches the top of the O^{2-}:2*p* band in $Li_{1-x}NiO_2$, while the redox active $Mn^{3+/4+}$:e_g band lies well above the top of the O^{2-}:2*p* band in $Li_{1-x}MnO_2$. As a result, both the $Ni^{3+/4+}$ and $Mn^{3+/4+}$ couples generally exhibit better chemical stability than the $Co^{3+/4+}$ couple in $Li_{1-x}MO_2$.[16] $LiNiO_2$ exhibits the same crystal structure than $LiCoO_2$ and has a similar specific theoretical capacity of 275 mAh·g^{-1}. Its relatively high energy density and lower cost in comparison to Co based materials are the main advantages. However, pure $LiNiO_2$ is not a suitable cathode because Ni^{2+} ions have a tendency to substitute Li^+ sites during synthesis and delithiation, blocking the Li^+ diffusion pathways.[17] Furthermore, $LiNiO_2$ is even more thermally unstable than $LiCoO_2$ because Ni^{3+} is more readily reduced than Co^{3+}.[18] On the other hand, $Li_{1-x}MnO_2$ suffers from a layered to spinel structural transition during the charge-discharge process.[19, 20] In an effort to further improve the electrochemical properties of layered transition metal oxides, different $LiNi_xMn_yCo_zO_2$ compositions have been investigated.[21] Among the different layered lithium mixed transition metal oxides, $LiNi_{1/3}Mn_{1/3}Co_{1/3}O_2$ (NMC) consisting of Co^{3+}, Ni^{2+}, and Mn^{4+} has been shown to have high rate capability, excellent cyclability and high capacity due to unique electronic structure combined with a small change in lattice volume in the range of $0 < x < 2/3$ in $Li_{1-x}Ni_{1/3}Mn_{1/3}Co_{1/3}O_2$.[22] $LiNi_{1/3}Mn_{1/3}Co_{1/3}O_2$ exhibits a synergistic effect in which Ni could raise the charge/discharge capacity, Co could decrease the cation mixing improving the rate capabilities and Mn could enhance the thermal stability and reduce production costs, thus enhancing its applicability and safety.[10, 23] Some recent efforts, such as formation of macroporous NMC, showed reversible specific capacity as high as 234 mAh·g^{-1} and good cycle stability even at 50 ºC.[24]

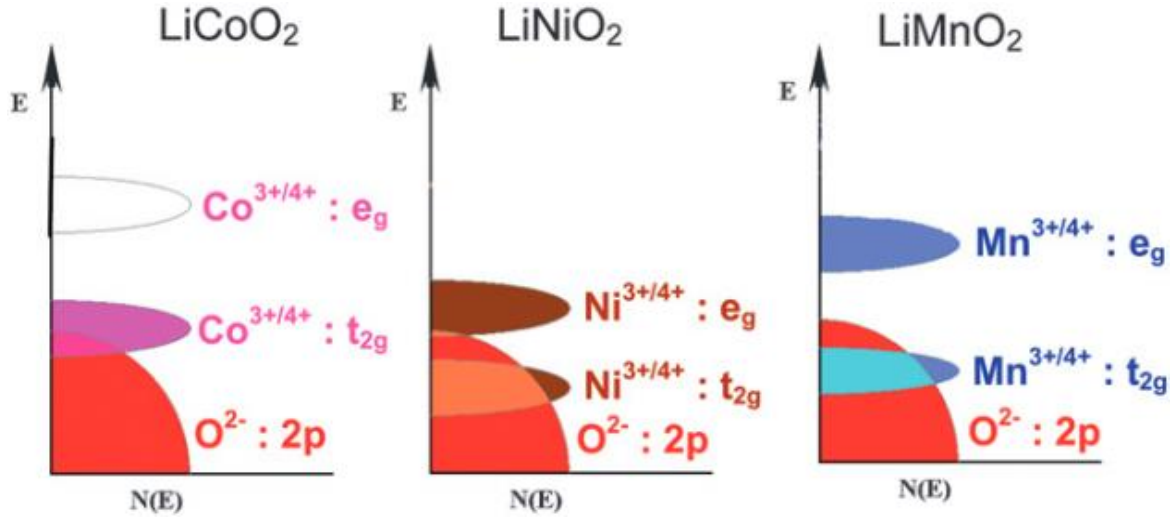

Figure 1.4. Comparative energy diagrams of layered $LiCoO_2$, $LiNiO_2$ and $LiMnO_2$.[16]

1.5.1.2 Spinel LiM_2O_4

An alternative cathode material based on layered oxides is spinel $LiMn_2O_4$. This insertion electrode exhibits a three-dimensional Li^+ ion pathway, features high power

capability and excellent safety. Furthermore, it has the advantage of being cheap, environmentally friendly and non-toxic. Nevertheless, spinel $LiMn_2O_4$ displays a slightly lower reversible capacity of ~120 $mAh \cdot g^{-1}$ at a working potential of ~3.8 V *vs.* Li^+/Li^0 and its application as cathode material in LIBs has been mainly hampered by the phase transition observed from cubic to tetragonal symmetry related to Jahn-Teller distortion of Mn^{3+} ions, resulting in a huge volume change contributing to a severe capacity fading over cycling. $LiMn_2O_4$ adopts a spinel structure belonging to the $Fd\overline{3}m$ space group in which the Li and Mn occupy the tetrahedral and octahedral sites of the cubic close-packed oxygen ions, respectively. The edge-sharing Mn_2O_4 octahedra in this structure are highly stable and exhibit a series of intersecting tunnels formed by face-sharing tetrahedral lithium sites and empty octahedral sites facilitating the three-dimensional diffusion of lithium.[25] The capacity of spinel $LiMn_2O_4$ is generally limited to < 120 $mAh \cdot g^{-1}$ around 4 V *vs.* Li^+/Li^0, which corresponds to a reversible insertion/extraction of ~0.8 lithiums per $LiMn_2O_4$ formula unit. Although an additional lithium could be inserted into the empty octahedral sites of the Mn_2O_4 framework at a lower voltage of ~3 V *vs.* Li^+/Li^0, this is accompanied by the aforementioned phase transformation from cubic to tetragonal symmetry due to the associated Jahn–Teller distortion. Therefore, the capacity in the 3 V region could not be used in practical cells.[26] Stabilisation of the cubic spinel structure has been possible by controlled formation of cationic defects,[27] by lithium[28] or 3*d* metal substitution[29] into spinel lattice as well as by isoelectronic sulfur substitution.[30, 31] Finally, it should be noted that the instability of the high oxidation state of this transition metal in the charged state can lead to oxygen evolution (similarly to the layered oxide cathodes) and consequent side reactions with the electrolyte.[32] Figure 1.5 illustrates the crystal structures of layered $LiCoO_2$ and spinel $LiMn_2O_4$.

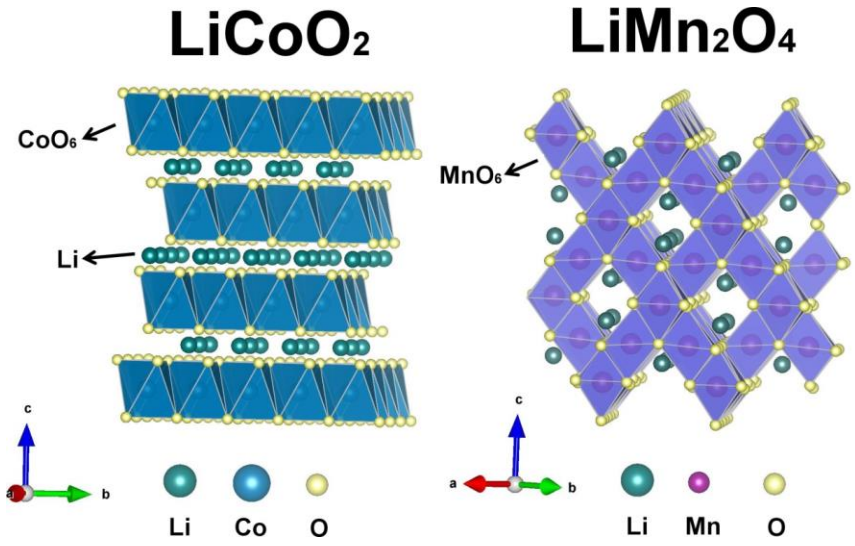

Figure 1.5. Crystal structures of layered $LiCoO_2$ and spinel $LiMn_2O_4$.[33]

1.5.1.3 Polyanionic compounds

An interesting and promising group of insertion cathode materials are polyoxoanionic Li*MX*O_4 (*M*=3*d* metal, *X*=S, P, As, Mo, W) type compounds. Large XO_4^{3-} polyanions occupy lattice positions and increase redox potential while also stabilising its structure.[33] Compared to layered oxide compounds, the strong *X*-O bonding in polyanionic compounds can introduce ionicity in the *M*-O bond and the weaker *M*-O bond leads to high redox potentials. This is called the "inductive effect" in polyanion type electrode materials, where the strength of the *X*-O bond in the *M*-O-*X*-O-*M* linkage can influence the *M*-O covalency and thereby the relative position of the M^{3+}/M^{2+} redox potential. The stronger the *X*-O bonding, the weaker the *M*-O bonding and consequently the lower the M^{3+}/M^{2+} redox potential, which results in a higher cell voltage.[34] Furthermore, such special framework compounds have been known to undergo topotactic insertion/extraction of Li^+ ions, resulting in minimal structural rearrangements during cycling. Thanks to their structural diversity and stability, combined with the strong inductive effect of polyanions, such electrode materials generally have suitable operating potential and outstanding cycling performance.[35] In particular, over the last decades phospho-olivine type (Li*M*PO_4, *M*=Mn, Fe, Co, Ni) electrode materials, pioneerd by Padhi and Goodenough,[34] have been identified as serious contenders for high power electrode materials, with $LiFePO_4$ being one of the most promising among them.

1.5.1.3.1 $LiFePO_4$ cathode material

Olivine-structured $LiFePO_4$ has emerged as an attractive positive insertion material for LIBs substituting current toxic, unsafe and expensive cathode materials such as $LiCoO_2$. The main advantages of $LiFePO_4$ include its relatively high theoretical capacity of 170 $mAh \cdot g^{-1}$, suitable flat voltage region of 3.45 V, safety, non-toxicity, environment friendliness, low production costs, rich source of raw materials and high thermal/electrochemical stability provided by the strong covalent P-O bonds. Moreover, this positive insertion electrode exhibits good cyclability and is complementary to most conventional polymer electrolytes.[36] Nevertheless, the main drawbacks of this material are that it suffers from poor electronic conductivity (10^{-9} $S \cdot cm^{-1}$ at RT) and low ionic diffusivity (which often requires application of carbon coatings and composite formulation) and the fact that its olivine crystal structure only tolerates 1D Li-diffusion. Furthermore, the processing costs of $LiFePO_4$ are generally high because carbon coating or small particle size are required in order to obtain the appropriate cycling performance at high current rates.[37]

$LiFePO_4$ crystallises in an olivine structure with an orthorhombic unit cell (*Pnma* space group), where oxygen atoms constitute a slightly distorted hexagonal close packing arrangement, and Fe and Li atoms are located in oxygen octahedral centers forming FeO_6 and LiO_6 octahedra. Phosphorus atoms in the center of four oxygen atoms form an edge-

shared PO_4 tetrahedral network which provides structural stability.[34] A three dimensional framework is formed by FeO_6 octahedra sharing common O-corners with PO_4 tetrahedra while LiO_6 groups form a linear chain of edge-shared octahedral parallel to the *b* axis. The delithiated phase $FePO_4$ has essentially the same structure as $LiFePO_4$. This structural similarity not only avoids capacity degradation resulting from severe volumetric changes during the charge-discharge process, but it also effectively compensates the volume changes during the delithiation and lithiation process. This could explain the excellent electrochemical cyclability of this olivine system to some extent.[38] Finally, it should be highlighted that $LiFePO_4$ exhibiting a phase pure olivine structure can be easily fabricated through conventional synthetic approaches such as solid-state ceramic routes,[39] sol-gel methods[40], solvothermal routes[41-44] and fast and low temperature microwave-assisted reactions.[45-48]

A polymorph of $LiFePO_4$ (ß-$LiFePO_4$) with the same orthorhombic symmetry but belonging to a *Cmcm* space group has also been reported.[49] The main structural differences between the two polymorphs concern the coordination and the alignment of the cations. In this structure, a FeO_6 octahedron shares two opposite edges with neighboring FeO_6 octahedra and two apical oxygen atoms with two LiO_4 and two phosphate groups. A PO_4 group shares two oxygen atoms with two different MO_6 polyhedra and one edge with a LiO_4 tetrahedron.[50] Figure 1.6 illustrates the crystal structures of both α and ß-$LiFePO_4$ polymorphs. Non-olivine ß-$LiFePO_4$ is almost electrochemically inactive with no capacity for LIBs because the Li^+ ions are stored in the tetrahedral LiO_4 groups with a very high activation barrier for migration. The one-dimensional migration channels of Li^+ ions typically observed in the olivine α-$LiFePO_4$ phase disappear in ß-$LiFePO_4$ polymorph.[51] Previous experimental investigations have revealed that ß-$LiFePO_4$ exhibits almost no electrochemical activation with very low capacity (10-20 $mAh \cdot g^{-1}$).[50] Nevertheless, it has recently been demonstrated that the ß-$LiFePO_4$ polymorph can be activated through creation of effective paths of Li-ion migration by inducing optimised disordering such as $Fe_{Li}Li_{Fe}$ antisite defects, crystal distortion and amorphous domains. Guo *et al*. mixed the as-made ß-$LiFePO_4$ nanocrystals with acetylene black carbon and ball milled the mixture for different times as a treatment for controlled disorder. They demonstrated that the 8 hr ball milled ß-$LiFePO_4$ sample achieved a capacity of 128 $mAh \cdot g^{-1}$ at a 0.1 C rate with a extraordinary cycling performance in which 94.5 % of the initial capacity is retained after 1000 cycles at 1 C.[52]

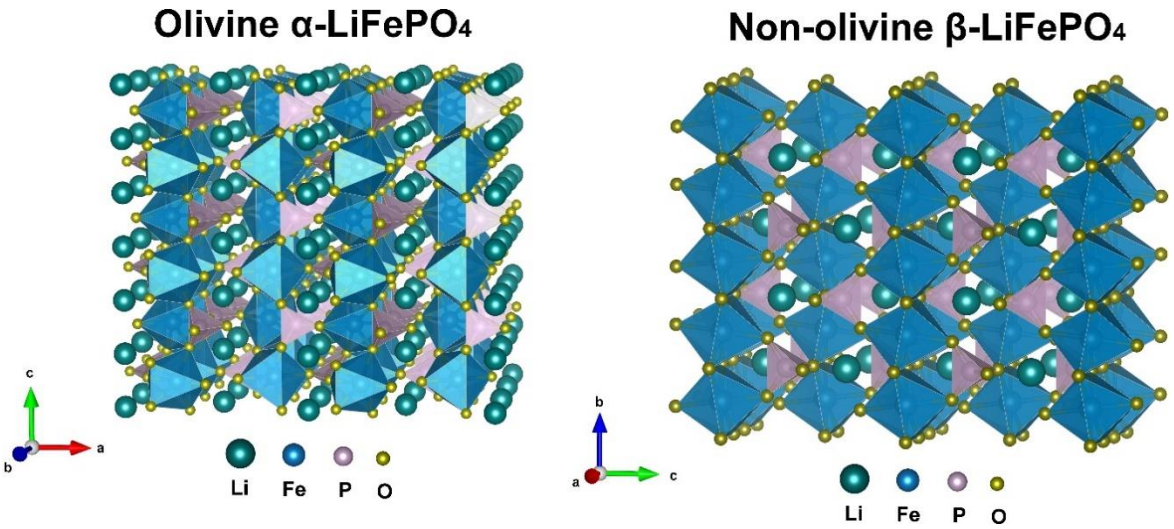

Figure 1.6. Crystal structures of α and β-$LiFePO_4$ polymorphs.

1.5.1.3.2 Li^+ diffusion mechanisms in olivine $LiFePO_4$

The underlying Li^+ transport properties and defect chemistry in $LiFePO_4$ are complex on the atomic scale. Atomistic modeling studies have revealed that the lowest energy Li^+ migration pathway takes place along the [010] channel, following a nonlinear, "wavelike" trajectory between adjacent Li positions (see Figure 1.7 (a)). Furthermore, it has also been found that the most favourable intrinsic defect is a Li-Fe antisite pair consisting of a Li^+ ion (on the M1 site) and an Fe^{2+} ion (on the M2 site) being interchanged. Antisite cation exchange is a typical lattice defect frequently observed in crystalline solids. Antisite defects can be particularly apparent in many lithium intercalation compounds in which lithium and transition metal cations of similar size usually maintain a well-ordered framework. Consequently, as the overall mobility of Li^+ ions can be greatly affected by cation exchange, control of both the concentration and the distribution of antisite exchange defects is critical for improving lithium migration and reaching high rate (de)intercalation reactions.[53] Knowing that, it is highly probable that the Li-Fe antisite defects in olivine $LiFePO_4$ could block the diffusion path through [010] channels leading to an inhibition of the long-range Li^+ migration.[54] Islam *et al.* also investigated the defect and transport properties of olivine mixed-metal phosphate $LiFe_{0.5}Mn_{0.5}PO_4$ by atomistic modeling methods and found that the Li^+ diffusion in this mixed-metal system also occurs down the *b* axis channel following a curved path (see Figure 1.7 (b)). They also reported that the intrinsic defect type with the lowest energy is the cation antisite defect, in which Li and Fe/Mn ions exchange positions. Furthermore, migration energies for Fe and Mn antisite cations on Li sites suggested that Mn defects would impede bulk Li^+ mobility in $LiFe_{0.5}Mn_{0.5}PO_4$ to a greater extent than Fe antisite defects in $LiFePO_4$.[55] Yamada *et al.* provided experimental evidence for a curved one-dimensional chain for lithium motion by combining high-temperature neutron diffraction analysis and the

maximum entropy method visualising the lithium distribution along the [010] direction in Li_xFePO_4 ($0<x>1$).[56]

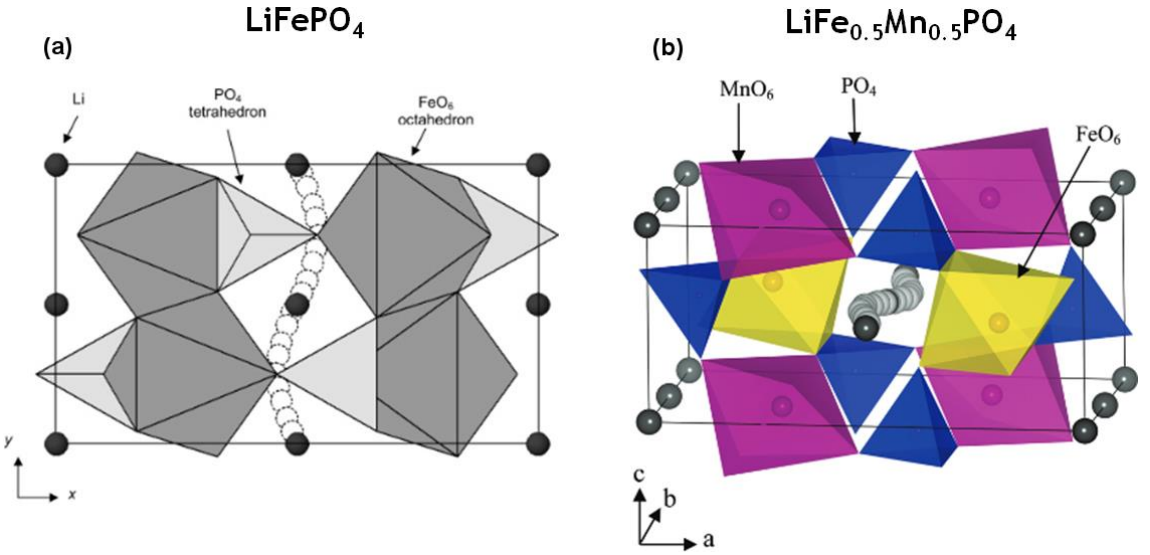

Figure 1.7. Curved trajectories for Li^+ migration in **(a)** $LiFePO_4$[54] and **(b)** $LiFe_{0.5}Mn_{0.5}PO_4$[55] between sites in the [010] direction.

Understanding the phase transformation mechanism as well as the lithium intercalation pathaway in Li-ion electrode materials during the charge/discharge process is of crucial importance for battery performance, limiting high rate capabilities and life cycle. In the particular case of olivine $LiFePO_4$, the Li^+ deintercalation/intercalation process is generally believed to proceed through a two phase reaction between compositions very close to $LiFePO_4$ and $FePO_4$. As both endmembers are very poor ionic and electronic conductors, it is challenging to completely understand the intercalation mechanism at the microscopic scale.[57, 58] In the interpretation of the Li^+ insertion/extraction mechanism in $LiFePO_4$, several models have been proposed. Newmann *et al.* developed a mathematical model to describe the Li^+ intercalation process and phase transformation in a $LiFePO_4$ electrode. The juxtaposition of the two phases is assumed to follow the form of a shrinking core where a shell of one phase covers a core of the second phase. They report a "radial migration model" in which Li^+ is out and in of $LiFePO_4$ assuming a core shrinking movement ot the $FePO_4/LiFePO_4$ interface (Figure 1.8 (a)).[59] An alternative model proposed by Andersson *et al.* envisages that Li^+ extraction/insertion can take place at many sites within a given particle (mosaic model). During charge, separate lithium-extracted regions ($FePO_4$) are formed and they impinge on one another. On discharge, lithium re-enters the major part of these $FePO_4$ regions, leaving only the cores as unconverted $FePO_4$ (Figure 1.8 (b). At the same time, some inactive $LiFePO_4$ regions may be left entrapped by a thin coating of some amorphous material.[60] Andersson *et al.* also examined the extraction and insertion of Li^+ in solid state synthesised $LiFePO_4$ by *in situ* X-ray diffraction and Mössbauer spectroscopy. They concluded that the structural rearrangement on the Li^+ extraction/insertion is small, given that the change in the Fe-O

bond distance is minimal: the mean Fe-O distances are 2.17 Å and 2.04 Å for $LiFePO_4$ and $FePO_4$, respectively. This could explain to a large extent the excellent electrochemical cycling properties of the system.[57] On the other hand, Delmas *et al.* investigated a family of deintercalated $LiFePO_4$ nanomaterials by X-ray diffraction and electron microscopy and demonstrated the co-existence of fully intercalated and fully deintercalated individual particles. They argued that the peculiar olivine structure with edge sharing between each FeO_6 octahedron and each PO_4 tetrahedron potentially limits the structural flexibility required to allow the formation of a solid solution. As a result, during the charge/discharge process, all compositional and structural modifications are mainly localised within the interfacial zone between the two endmembers. With this in mind, they proposed a "domino-cascade model" described by a fast anisotropic lithium insertion/deinsertion process coupled to the $LiFePO_4$-$FePO_4$ interface movement through a Li^+ hopping mechanism in nanocrystallites (Figure 1.8 (c)). They reported that the very high concentration of Li^+/vacancies and Fe^{2+}/Fe^{3+} polarons localised in the interfacial zone enables a very fast Li^+ transport.[58]

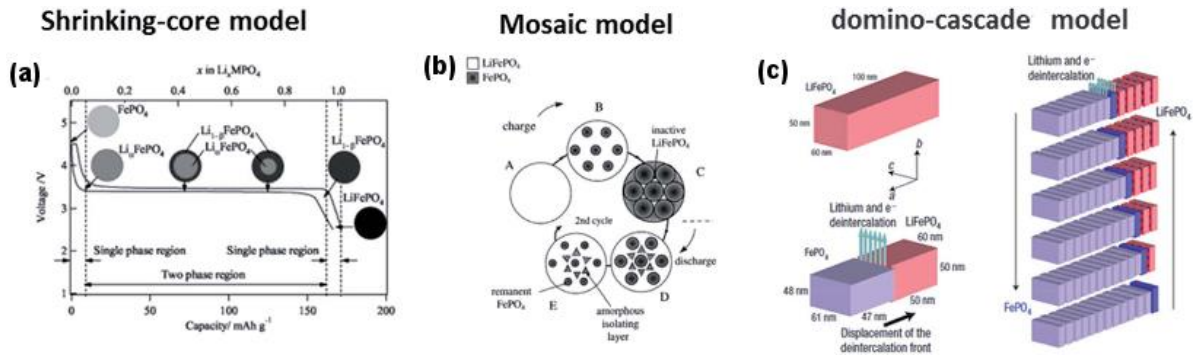

Figure 1.8. Different classic two-phase models for olivine $LiFePO_4$. **(a)** Shrinking-core model,[59] **(b)** Mosaic model[60] and **(c)** Domino-cascade model.[58]

However, it must be taken into consideration that the two-phase coexistence mechanism may change with particle size, morphology and the electrochemical testing conditions (fast or slow charging rate).[61] On the other hand, although the two-phase mechanism has been widely accepted, the contradiction between the theoretically low ion diffusion capability of $LiFePO_4$ and its practically high rate capability has lead to the consideration of solid solution mechanisms in which the phase transformation between $LiFePO_4$ and $FePO_4$ may undergo a single-phase and not a two-phase mechanism. Orikasa *et al.* used *in operando* synchrotron XRD techniques to track the phase transformation in olivine $LiFePO_4$ and reported a metastable crystal phase in fast charging microsized $LiFePO_4$, in addition to the thermodynamically stable $LiFePO_4$ and $FePO_4$ phases. Also, they found that this metastable phase exhibits a short life time (a couple of minutes), as it diminishes under open circuit conditions. Moreover, this metastable Li_xFePO_4 (x=0.6–0.75) phase only

appears at high charging rates and is absent at slow charging rates. Therefore, it is suggested that at high rates, the phase transformation in $LiFePO_4$ may take place through the metastable phase, which decreases the nucleation energy leading to a higher rate performance.[62] Another of the latest *in situ* XRD studies by Grey *et al*. captured the metastable solid solution phase in fast-charging nanosized $LiFePO_4$. Different from the intermediate Li_xFePO_4 (x=0.6–0.75) phase at high rates in the microsized samples, the studies with nanosized $LiFePO_4$ demonstrated that the continuous solid solution phase can display a wider composition, Li_xFePO_4 ($0 < x < 1$), which is composed of the entire range between the two end members of $LiFePO_4$ and $FePO_4$ at high rates. This suggests that nanosized $LiFePO_4$ may undergo continuous structural change without the phase boundary movement and nucleation step, which can also explain the high rate performance of $LiFePO_4$.[63]

1.5.1.4 High voltage olivine Li*M*PO_4 (*M*=Mn, Co, Ni) cathodes

Nowadays high energy density for the next generation of energy storage devices is in growing demand and, therefore, the development of high voltage cathode materials is required. The fairly low reaction voltage of $LiFePO_4$ (3.45 V *vs.* Li^+/Li^0) has encouraged the investigation of isostructural olivine-type Li*M*PO_4 (*M*=Mn, Co, Ni) with higher operating voltages. Transition metal ions such as Mn^{2+}, Co^{2+} and Ni^{2+} are good candidates for substitution because they are able to occupy the same crystallographic position as Fe^{2+} due to their similar crystal-chemistry properties. In particular, $LiMnPO_4$ reacts at 4.1 V *vs.* Li^+/Li^0 providing a ~20% higher energy density than $LiFePO_4$. The higher redox potential of $LiMnPO_4$ compared to $LiFePO_4$ could be explained by the *d*-orbital splitting of the Mn^{2+} cations in octahedral coordination. The pairing energy of the sixth electron in the t_{2g} orbital in the Fe olivine lowers the voltage *vs* Li^+/Li^0 compared to the Mn compound (Figure 1.9).[64] The electronic and ionic conductivity of $LiMnPO_4$ is also insufficient for good electrochemical performance ($<10^{-10}$ $S \cdot cm^{-1}$ and 1.8×10^{-9} $S \cdot cm^{-1}$ for $LiMnPO_4$ and $LiFePO_4$, respectively).[65, 66] $LiMnPO_4$ also shows structural instability over cycling mainly originating the large volume changes between the lithiated and delithiated phases of the electrochemical couple $LiMnPO_4$ and $MnPO_4$ due to the Jahn-Teller distortion induced by Mn^{3+} ions.[67] For example, it has been reported that the lattice misfit between the equilibrium coexisting phases in the $LiFePO_4/FePO_4$ system is 6.6 vol %,[68] while for its Mn counterpart $LiMnPO_4/MnPO_4$ the misfit is larger at ~11.7 %.[69] Poper *et al*. also investigated the nature of the Jahn-Teller distortions in Li_xMnPO_4 using a combination of density functional theory with soft and hard X-ray spectroscopy analysis and results suggested that the distorstion of the MnO_6 octahedra in the Mn^{3+} state is not a strict Jahn-Teller distortion but is instead a preferential elongation of the two equatorial Mn-O bonds (edge-sharing PO_4). They claim that the elongation of the equatorial bonds in the Mn^{3+} charge

state is responsible for increasing the activation energy for the Li^+ diffusion, thereby accounting for the sluggish intrinsic kinetics of the Mn olivine compare to the Fe olivine.[70]

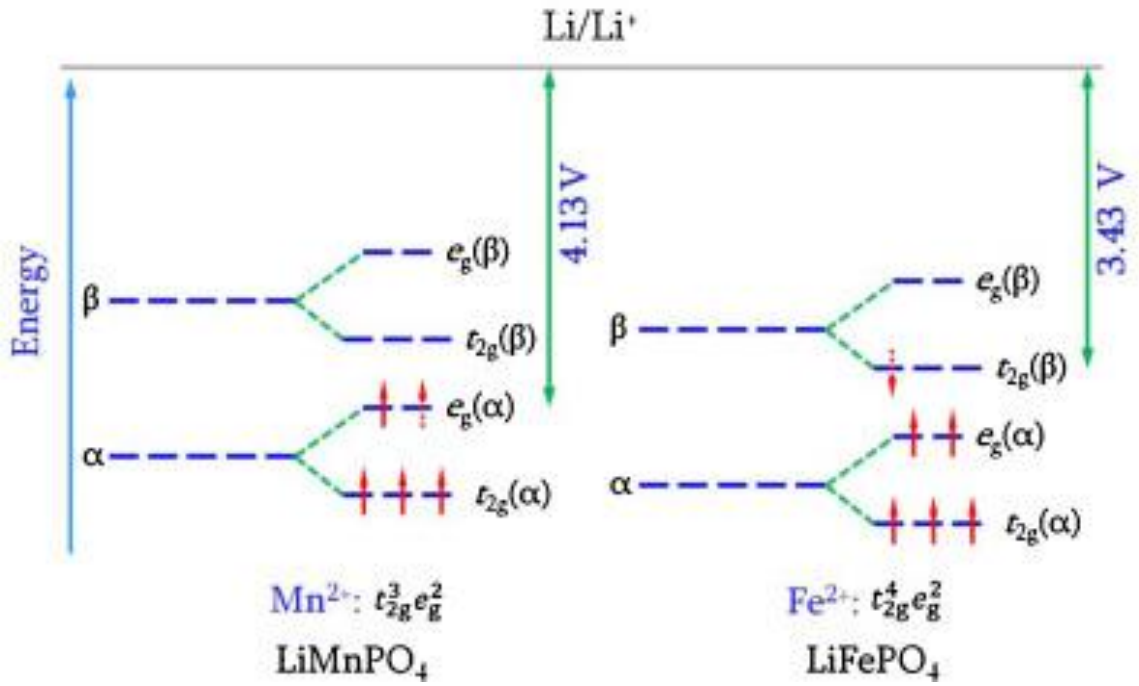

Figure 1.9. Crystal field splitting of the M^{2+} cations in octahedral coordination. The Fe comound delivers a lower voltage vs. Li^+/Li^0 compared to the Mn compound because of the shift in the $Fe^{3+/2+}$ redox energy due to the pairing energy of the sixth electron in the t_{2g} orbital.[64, 71]

$LiCoPO_4$ and $LiNiPO_4$ exhibit higher reaction voltage at 4.8 V and 5.1 V, respectively, and high theoretical capacities of 167 $mAh{\cdot}g^{-1}$. However, although this results in higher theoretical energy densities, those high operating potentials put at risk the stability of most conventional electrolyte solutions, as there is still a serious need of stable electrolytes at potential values of over 5 V *vs.* Li^+/Li^0. Efforts to utilise $LiCoPO_4$ have demonstrated limited capacity and fast fading of the capacity upon repetitive cycles.[72, 73] Furthermore, the synthesis of olivine $LiCoPO_4$ has been shown to be quite challenging since many of the available Co precursors can be easily reduced to form impurities such as Co metal, Co_3O_4 and Li_3PO_4 phases. A $CoHPO_4{\cdot}xH_2O$ nanoplate precursor has been used to simplify the synthesis process and minimise impurities, yielding $LiCoPO_4$/C cathode materials that delivered a specific capacity of 125 $mAh{\cdot}g^{-1}$ at C/10 rate, but maintaining only 80 $mAh{\cdot}g^{-1}$ after 50 cycles.[74] The fast capacity fading in $LiPF_6$ containing electrolyte solutions can be due to the nucleophilic attack of the HF present in these electrolytes on the P atoms of the olivine compound in the delithiated state resulting in the formation of soluble PO_3F^{2-}, $PO_2F_2^-$, POF_3 and H_2O. Here, the H_2O produced can react with PF_6^-, POF_3 and $PO_2F_2^-$ to generate more HF.[73] Olivine C/Li*M*PO_4 (*M*=Co and Ni) nanocomposites have also been fabricated by a polyvinylpyrrolidone (PVP) assisted polyol method using acrylic acid to carbon coat the surface of the nanoparticles. Electrochemical testing showed intial discharge capacities of 180 and 97 $mAh{\cdot}g^{-1}$ at 0.1 C rate for the C/$LiCoPO_4$ and

C/$LiNiPO_4$ cathodes, respectively, with a noticeable capacity fading over cycling due to the instability of the electrolyte at higher potentials.[75] A C/$LiNiPO_4$ nanocomposite has also been successfully synthesised by a solvothermal microwave-assisted technique demonstrating excellent stable discharge capacities of 150.2 $mAh \cdot g^{-1}$ at a 0.1 C rate with a good capacity retention (92%) after 100 cycles.[76]

1.5.1.4.1 Olivine mixed metal phosphates $LiFe_{1-x}Mn_xPO_4$

Olivine mixed transition metal phosphate systems have recently attracted considerable interest since such composite materials facilitate fine-tuning of the inherent properties of the pure analogues, such as the voltage and the stability of the cathode upon delithiation. Amongst these materials, $LiFe_{1-x}Mn_xPO_4$ has drawn much attention as it exhibits higher energy density and enhanced redox kinetics due to the improved electronic conductivity in comparison to the pure olivines.[77] These mixed-metal phosphate phases are isostructural with the end-members $LiFePO_4$ and $LiMnPO_4$. Partial substitution of Fe by Mn in these olivine structures leads to electrode materials with increased voltage due to the higher $Mn^{3+/2+}$ redox potential compared to the pair $Fe^{2+/3+}$.[66] Nevertheless, it should be highlighted that the existence of Mn^{3+} ions in delithiated $MnPO_4$ triggers a Jahn-Teller distortion and interfacial strain, detrimental to ion and electron hopping during the charge/discharge process. The Jahn-Teller effect induces volume and cell distortion of the electrode, leading to a rapid mechanical degradation of the electrode and consequently, poor electrochemical performance. Padhi *et al*. investigated the electrochemical performance of a series of $LiFe_{1-x}Mn_xPO_4$ (x=0.25, 0.50, 0.75, 1.0) materials and found that the specific capacity notably decreases when $x > 0.75$.[34] Yamada *et al*. reported that Mn-rich $LiFe_{1-x}Mn_xPO_4$ ($x > 0.8$) phases are not the best performing mixed metal phosphates due to the large anisotropic distortion of Mn^{3+} during cycling.[78, 79] They also reported a phase diagram of $Li_{1-x}Fe_{1-y}Mn_yPO_4$ as a function of both lithium and manganese concentration, obtained by a chemical extraction of lithium from materials with compositions $0 \leq y \leq 1$.[67, 78, 80] They stated that the best starting compositions of $LiFe_{1-y}Mn_yPO_4$ in terms of possible application in LIBs are those containing similar amounts of manganese and iron ions.[81] Wu *et al*. have investigated a series of solvothermally synthesised $LiFe_{1-x}Mn_xPO_4$ by synchrotron radiation X-ray absorption spectroscopy combined with first-principles calculations and energy-dispersive X-ray spectroscopy measurements. Results demonstrated the coexistence of $LiFePO_4$ and $LiMnPO_4$ phases randomly stacked and characterised by a pronounced structural distortion of the MO_6 (M=Fe, Mn) octahedra. Furthermore, it was also observed that increasing the Mn doping concentration leads to an increased distortion of the MO_6 octahedra. Among different Fe/Mn compositions, electrochemical examination revealed that the $LiFe_{0.75}Mn_{0.25}PO_4$ material exhibits the best electrochemical performance.[82] Previous experimental findings have also demonstrated that after a typical carbon coating process with heat treaments under reducing

atmosphere, $LiFe_{0.5}Mn_{0.5}PO_4$ nanophases usually undergo a rearrangement of their cations into Mn-rich and Fe-rich domains and it is only after such cation rearrangement *via* segregation that the redox processes evolve at two distinct potentials corresponding to the Fe^{3+}/Fe^{2+} and Mn^{3+}/Mn^{2+} redox pairs. On the contrary, $LiFe_{0.5}Mn_{0.5}PO_4$ nanoplatelets (~10 nm thick) with Fe and Mn cations rather homogeneously distributed in the lattice displayed a single broad peak in the CV analysis, which could be explained by the synergistic effect on the redox potentials. Therefore, these results suggested that the degree of cation mixing in this olivine mixed metal olivine lattice directly influences the redox potentials, which in turn determines the charge/discharge characteristics.[83]

The phase stability of $Li_{1-y}Fe_{1-x}Mn_xPO_4$ ($0 \leq x, y \leq 1$) materials during the delithiation and lithiation process has been investigated as a function of temperature, Li composition and Fe/Mn content using temperature-controlled *in situ* XRD. Fully lithiated $LiFe_{1-x}Mn_xPO_4$ remained stable up to high temperatures (>700 ºC). On the other hand, the thermal stability of delithiated $Li_{1-y}Fe_{1-x}Mn_xPO_4$ ($0 \leq x, y \leq 1$) was significantly influenced by the Fe/Mn content in the structure. Furthermore, the delithiation mechanism (one phase *vs.* two phase reaction) was dependent on the Fe/Mn ratio. It was generally observed that higher Mn containing binary olivine materials exhibited inferior thermal stabilities in the charged states and a stronger preference for two-phase behavior.[84] In order to gain a deeper insight of the lithiation/delithiation mechanism in olivine mixed metal phosphates, *in situ* XAS in conjuction with ^{57}Fe Mössbauer and ^{7}Li NMR spectroscopy have been used to examine the evolution of the local structure and the oxidation states of the transition metals in a $LiFe_{0.4}Mn_{0.6}PO_4$ sample during cycling. Results suggested a high reversibility of the reactions in this electrode material. Overall, a two-phase reaction mechanism with an intermediate, partially delithiated phase was observed. It was also found that while the oxidation/reduction of Fe^{3+}/Fe^{2+} is complete, Mn is only partially oxidised/reduced.[65] On the other hand, recent mechanistic studies of the (de)lithiation process that occur in Co doped $LiFe_xCo_{1-x}PO_4$ olivine using *in situ* XRD and supporting *ex situ* ^{31}P NMR suggested that two intermediate phases are formed during the first charge: $Li_{1-x}(Fe^{3+})(Co^{2+})_{1-x}PO_4$ for $0 < x < 1$ (after oxidation of Fe^{2+} to Fe^{3+}) and $Li_{2/3}Fe_xCo_{1-x}PO_4$ for $0 \leq x \leq 0.5$ (Co-majority materials). These investigations demonstrated that in Fe-rich materials a single-phase mechanism occurred while in Co-majority materials a two phase mechanism is observed.[85]

1.5.2 Anode materials

1.5.2.1. Li metal

The most elementary anode material for LIBs is metallic lithium, which has been used for primary, non-rechargeable batteries since the early 1960s. Metallic lithium possesses a extremely high theoretical specific capacity (3860 $mAh \cdot g^{-1}$), the lowest standard potential (–3.05 V *vs.* a standard hydrogen electrode (SHE)) and the lowest atomic weight (6.94 $g \cdot mol^{-1}$; specific gravity: $\rho = 0.53\ g \cdot cm^{-3}$) among all metals, allowing

high energy densities.[86] However, a severe limitation is the inhomogeneous lithium plating which occurs thereby hindering their commercial development. Furthermore, this inhomogeneous deposition of lithium onto the anode surface upon charge/discharge cycling leads to the formation of dendrites. These dendrites consist of highly branched lithium metal structures with high surface areas, which continuously grow and generate the risk of penetrating the separator and electrically connecting the anode and cathode to short circuit the cell. This spontaneous and uncontrolled event results in local heat evolution and in unfortunate cases the thermal runaway of the cell. In order to overcome this severe safety issue, the concept of lithium ion host structures was developed, thus significantly avoiding the risk of superficial (dendritic) lithium growth.[87, 88]

1.5.2.2 Carbon

Carbonaceous materials were the primary choice and have been the commercially most successful anode material as lithium-ion host framework in LIBs. They could be categorised in different forms: graphite, non-graphitised carbon, soft carbon and hard carbon. Highly crystalline graphitic carbon can take in one Li atom per six C atoms in a completely reversible process with a theoretical capacity of 372 $mAh \cdot g^{-1}$. However, several factors, such as SEI formation and solvated lithium insertion in the graphene layers, affects the reversibility of the intercalation reaction, increase cell resistance and thereby decreases the power density over cycling. Lithium diffusion entirely depends upon the crystal structure of the carbonaceous material and this fact drives the use of bulk carbonaceous materials to nano-carbon materials in different dimensions such as carbon nanotubes and carbon nanofibers for 1 D, graphene nanosheets for 2D and porous carbon with pore sizes in the nanometer range.[89, 90]

1.5.2.3 Transition metal oxides as conversion anodes

Transition metal oxides have been widely recognised as the next generation anode materials for LIBs due to their high energy and power density. Therefore, a variety of transition metal oxides (e.g. CoO, Co_3O_4, FeO, Fe_2O_3, Fe_3O_4, NiO, Mn_3O_4 and CuO) have been explored as alternatives to the commercial carbonaceous anodes.[91] Since transition metal oxides can react with more than one Li^+ per transition metal atom, exceptionally high specific capacities are theoretically possible.[92] However, the low electronic conductivity and large volume expansion associated with these materials often leads to poor cycling performance. Drastic volume variations during charging/discharging can cause a progressive desintegration of the electrode and significantly decreases the capacity retention over cycling. Tarascon's group first reported studies on *M*O (*M*=Fe, Co, Ni and Cu) as anode materials *via* the "conversion/displacement reaction" and demonstrated electrochemical capacities of ~ 700 $mAh \cdot g^{-1}$, with 100% capacity retention for up to 100 cycles at high charging rates.[93] The mechanism of Li reactivity differs from the classical Li insertion/extraction or Li-alloying processes. Generally, these metal

oxides are converted to metallic clusters embedded in a Li_2O matrix during the lithiation process, and converted back to metal oxides at the subsequent delithiation, which involves reversible reduction and oxidation of metal oxides, accompanied by the formation and decomposition of Li_2O. The conversion reaction mechanism of metal oxides can be described by the following reaction:

$$M_xO_y + 2yLi^+ + 2ye^- \leftrightarrow yLi_2O + xM$$

where *M* represents a transition metal. Furthermore, it must be remarked that the phase structures of conversion reaction anode materials are usually changed after the lithiation process. It has been demonstrated that the reaction pathway for lithiation/delithiation of conversion reaction anode materials is affected by the discharge/charge rate and the texture of the active material (for example, crystallite size and specific surface area). In electrochemical conversion processes, usually large structural reorganisation and volumetric changes cause particle isolation and cracking. Disconnection of Li_2O and the metal particles results in a significant electrochemical capacity fading during cycling. Therefore, the main challenge for the implementation of high capacity conversion anode materials is control over the large volume expansion/contraction and severe particle agglomeration. To overcome this problem, several synthetic strategies have been proposed to circumvent the large volume variations issue. In comparison to bulk materials, nanostructured anode materials can efficiently accommodate the mechanical strains caused by the large volume change and particle crack, and promote electrochemical reactivity. In particular, the electrochemical lithium storage properties of conversion reaction anodes are strongly affected by their particle size and morphology. For example, Luo *et al*. demonstrated that a carbon nanotube-Mn_3O_4 composite displayed a reversible capacity of 701 and 561 $mAh \cdot g^{-1}$ for 4 and 9 nm particles, respectively, compared to 367 $mAh \cdot g^{-1}$ for 165 nm Mn_3O_4 particles.[94] These results also showed that decreasing the particle size markedly reduces the polarisation displayed by the electrodes and improves the reversibility of the cycling process and the rate capability. Moreover, Li^+ ions could be stored at the interface, surface and in nanopores of the conversion reaction materials. Various nanostructures including nanoparticles, nanowires, nanorods, nanotubes, 3D porous particles and different nano-architectures have been employed to improve the electrochemical properties of conversion-type anode materials.[95] On the other hand, multiphase composites with active materials and matrices have been designed to accommodate and buffer the large volume changes of active materials during the lithium insertion/extraction process. The main purpose of using matrices is to reduce the aggregation of active particles during cycling. Carbon-based materials are the main active matrices used in conversion anodes. The enhanced electrochemical performances of carbon-based nanocomposites are attributed to the low volume changes, good electronic and ionic conductivity, and the buffering effect from carbon. Also, compared to powder

materials, thin films can display commonly higher reversible capacities and improved cycling stability.[96-99] The enhancement in the electrochemical properties such as capacity retention, cycling stability and rate capability are due to the strong adhesion of nanostructured films onto the substrate, which allows the active material and substrate to maintain a good electrical contact. Furthermore, the higher capacity delivered by thin films can also be attributed to the absence of inert additives such as polymer binder and the high contact of active materials. Finally, the electrochemical properties of thin films strongly depend on the thickness of the film, roughness of substrate-surface, substrate component, deposition conditions and heat treatment. For example, porous Fe_3O_4 thin films served as a high-performance binder-free anode for LIBs delivering specific capacities of 1100, 880 and 660 mAh·g^{-1} at 0.1, 0.2 and 0.5 C rate, respectively.[100]

1.5.2.3.1 Fe_3O_4 magnetite

Among the different transition metal oxides, iron oxides have received increased attention as anode materials for LIBs because of its very high theoretical capacity (for example, 1007 mAh·g^{-1} for Fe_2O_3 hematite and 924 mAh g^{-1} for Fe_3O_4 magnetite) as iron oxides can generally store 6~8 Li ions per formula unit *via* electrochemical conversion reactions. Futhermore, the main advantages of iron oxides are their low cost, low toxicity, natural abundance of raw materials, environmental benignity and high corrosion resistance.[101] Nevertheless, in spite of these highly appealing features, the electrochemical reversibility of these electrodes was particularly much lower than the theoretical expectation, mainly due to severe volume expansion, low electrical conductivity, excessive SEI formation, fast capacity fading due to severe aggregation of iron oxide nanoparticles and low coulombic efficiency.[102, 103] The hybridisation of Fe_3O_4 nanoparticles with conductive matrices such as carbon and the fabrication of hollow structures have been adopted to overcome these problems. The very large capacities (above 900 mAh·g^{-1}) sustained for even up to 50-100 cycles that have been reported to date hold the promise of the applicability of these compounds.[104-107] For example, Fe_3O_4 nanoparticles homogeneously dispersed into carbon nanotubes demonstrated negligible capacity loss up to 100 cycles and high discharge capacity of 930 mAh·g^{-1} after 20 cycles at 100 mA·g^{-1} current density. This composite also exhibited excellent rate capability where up to the 78.8 % of the original capacity was retained even at high current discharge rates of 1000 mA·g^{-1}. The outstanding electrochemical behaviour was attributed to the unique porous architecture based on homogeneous dispersion of Fe_3O_4 nanoparticles into carbon nanotubes networks, which leads to shorter Li^+ diffusion parthways, high electric conductivity and buffering space to accommodate large volume changes of Fe_3O_4 during the charge-discharge process.[108] Also, Fe_3O_4 microspheres encapsulated in hollow graphene shells have recently delivered reversible specific capacities of 1480, 1270, 1100, 920, 760, and 533 mAh·g^{-1} at the cycling rates of 0.1, 0.2, 0.5, 1, 2, and 5 mA·g^{-1},

respectively,[95] confirming the promising applicability of iron oxides as conversion anodes for LIBs. Even more sophisticaded and complex composite formation such as a sandwich-like mesoporous graphene@Fe_3O_4@carbon nanosheets with a 2D nanoarchitecture has been successfully fabricated by a one-step solvothermal process, which displayed a very high discharge capacity of 913 mAh·g^{-1} after 100 cycles at a current density of 200 mA·g^{-1}. This composite even exhibited a stable discharge capacity of 483 mAh·g^{-1} at a rate of 1600 mA·g^{-1}.[109] Particle downsizing has also shown to play a key role in reaching enhanced electrochemical performances. For example, graphene nanosheets decorated with ultra small Fe_3O_4 nanoparticles were synthesised *via* a facile hydrothermal method demonstrating superior cyclic ability, delivering 1177, 1096, 833, 488, 242, and 146 mAh·g^{-1} at current densities of 90, 180, 900, 1800, 3600, and 7200 mA·g^{-1}, respectively. In this case, the excellent rate capability can be ascribed to the ultra-small size of active lithium storage sites of Fe_3O_4 with an average diameter less than 5 nm.[110]

1.5.2.3.2 Mn_3O_4 hausmannite

Manganese oxides have also been investigated because of their high theoretical specific capacity, low reaction potential (0.2–0.5 V during the initial discharge)[111] and low voltage hysteresis (<0.8 V) compared with other transition metal oxides.[112] Manganese oxides exhibit a variety of crystallographic structures, which include cubic rock salt (MnO, 756 mAh·g^{-1}), inverse spinel (Mn_3O_4, 937 mAh·g^{-1}), hexagonal corundum (Mn_2O_3, 1019 mAh·g^{-1}), and a manganese dioxide structure (MnO_2, 1223 mAh·g^{-1}).[5] They are also attractive candidates for use as anode material in LIBs due to the high abundance of Mn, its environmental-friendliness and low cost.[113] However, full utilisation of manganese oxide is difficult due to the extremely low electrical conductivity (≈10^{-7}–10^{-8} S·cm^{-1} for Mn_3O_4).[113] Increased capacities can also be realised through the use of conductive coatings such as reduced graphene oxide and the growth of porous or hollow morphologies.[113-116] A composite fabricated by combining 2D graphene nanosheets and 1D Mn_3O_4 nanowires manifested excellent electrochemical properties delivering 802 mAh·g^{-1} at 100 mA·g^{-1} and a high rate capacity of 308 mAh·g^{-1} with good cycling stability at a current density of 2000 mA·g^{-1}.[117] Also, 3-dimensional porous Mn_3O_4 nanosheet arrays reached reversible capacities of 1166.3 mAh·g^{-1} and remained 667.9 mAh·g^{-1} after 1000 cycles at 1000 mA·g^{-1}.[118]

1.5.2.3.3 NiO

Nickel monoxide has also been exploited as an LIBs anode materials due to its high theoretical capacity of 718 mAh g^{-1} (in which NiO is reversibly decomposed and converted into metallic Ni nanoclusters and Li_2O) together with its relatively low price, abundance and acceptable toxicity.[119] Recently, 3D NiO microspheres assembled from porous nanosheets exhibited an excellent electrochemical performance with reversible discharge

capacities up to 820 mAh·g^{-1} after 100 cycles at a current density of 100 mA·g^{-1} and even 634 mAh·g^{-1} at 1000 mA·g^{-1}. The 3D microsphere architecture can contribute to enhanced electrochemical performance by improving the Li^+ transfer with sufficient electrode/electrolyte contact areas and more efficiently accommodating the volume change occurring during the (de)lithiation process. [120] Also, vertically aligned NiO nanowalls fabricated on nickel foils using a plasma-assisted oxidation method displayed capacities of ~638 mAh·g^{-1} at 895 mA·g^{-1} rate with excellent capacity retention up to 85 cycles. The superior electrochemical performance of NiO nanowalls can be ascribed to the large surface area and shorter diffusion path lengths for mass and charge transport.[121] To summarise, Figure 1.10 illustrates the approximate range of discharge potentials and specific capacities for some of the most common cathode and anode materials for the next generation of rechargeable Li-based batteries.

1.6 Synthesis of electrode materials

New materials hold the key to fundamental advances in energy conversion and storage technologies, as the performance of energy devices depends intimately on the properties of their constituent materials.[122] The properties of functional materials are directly linked to the material characteristics such as crystal structure, structural defects, crystallite and particle size, all of which strongly depend on the preparation method employed. One of the major goals in modern materials chemistry is thus to develop synthetic routes that allow for the precise control of the material characteristics, while ensuring that the synthesis is still cheap, environmentally-friendly and ideally capable of fast large scale production.

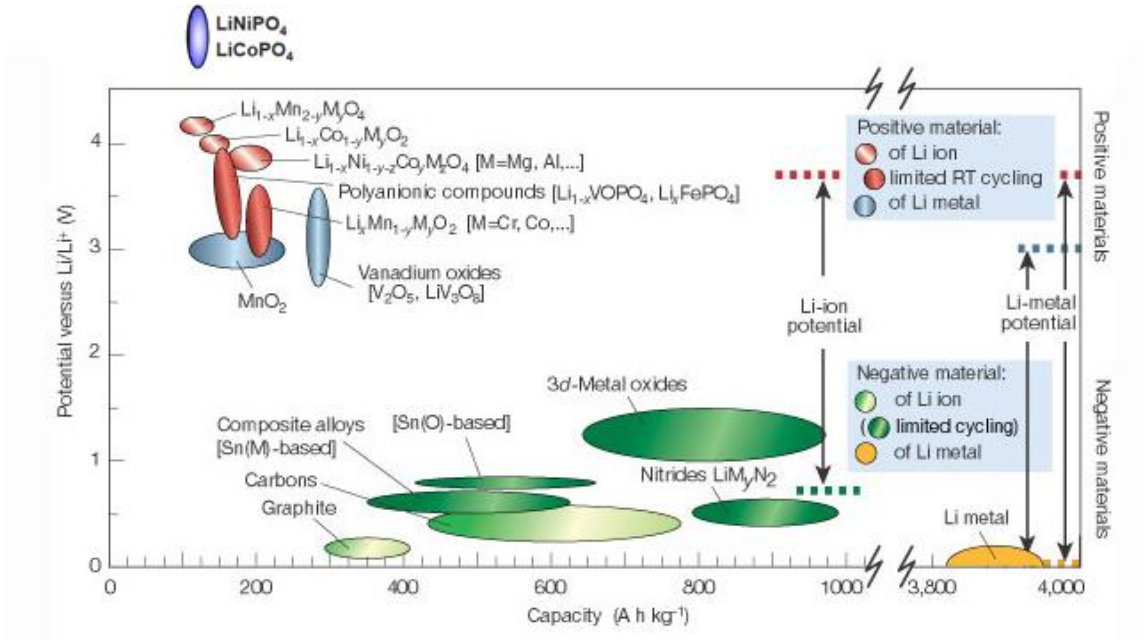

Figure 1.10. Voltage *vs.* capacity for positive and negative electrode materials used or under consideration for the next generation of rechargeable Li-based batteries.[3]

1.6.2 Solid state synthesis

Conventional solid state state synthesis is the simplest and most traditional synthetic approach mainly because of its easy procedure and scalability. It generally involves intimate grinding of the reactants and their subsequent heating in air, oxidative, reducing or inert atmosphere, depending on the targeted material. However, the great disadvantages of this method are the requirement of high calcination temperatures (generally from 700 to 1500 ºC) and long reaction times (up to several days) in order to overcome diffusion barriers and achieve homogeneous products. Moreover, high temperatures and long reaction times usually provoke the growth and sintering of the crystals, leading to micrometer-sized particles. Unfortunately, the macroscopic dimensions of as-synthesised particles in LIB electrode materials may lead to limited kinetics of Li^+ insertion/extraction process during cycling.[123] In the particular case of olivine $LiFePO_4$, the starting mixture often consists of a stoichiometric amount of iron salt (Fe(II) acetate, Fe(II) oxalate),a lithium compound (lithium carbonate or lithium hydroxide), and most commonly ammonium phosphates as a phosphorous source.[124-126] The starting mixture initially decomposes at a temperature range of 300–400 ºC to expel the gases, and, after being reground, it is calcined at temperatures from 400 to 800 ºC for 10–24 hr. Before the second grinding step, some carbon containing compounds, for example carboxylic acid or sucrose,[127] can be added to the precursor as a carbon source in the $LiFePO_4$/C composite formation. The purity of the material often depends on the growth parameters, such as the temperature of calcination and exposure time.[128, 129] During calcination, due to the Fe oxidation state (2+), the use of inert (usually nitrogen or argon) or slightly reductive atmosphere (argon or nitrogen with a small addition of hydrogen) is necessary. However, the presence of residual Fe^{3+} phases such as Fe_2O_3 and $Li_3Fe_2(PO_4)_3$ are still possible and often reported.[130] A family of $LiFe_{1-x}Mn_xPO_4$/C (x=0, 0.2, 0.5, 0.8 and 1) phases have been successfully fabricated by solid state reactions using the appropriate quantity of citric acid and sugar.[131] Electrochemical tests revealed that the energy density and rate capability of $LiFe_{1-x}Mn_xPO_4$/C decreased with higher Mn contents, but the nanoporous $LiFe_{0.2}Mn_{0.8}PO_4$/C phase still displayed capacities of 138.3 mAh g^{-1} at a rate of C/10.[132] Uncontrollable particle growth and agglomeration associated with solid state synthesis has lead to the development of alternative solution chemistry methods that significantly reduce energy consumption, cost and processing times. In particular, solution-based routes generally result in smaller and more uniform particle sizes, higher purity, more homogeneous carbon coating and higher electrochemical capacities.[133]

1.6.3 Solvothermal synthesis

A solvothermal process can be defined as a chemical reaction in a closed system in the presence of a solvent (aqueous or non-aqueous) at a temperature higher than that of the boiling point of such a solvent and at pressures above 1 bar. In general, synthesis

techniques that involve the dissolution of all reactants often promote greater homogeneity in the final product. Moreover, mass transport in the liquid phase is more favoured than in solids, and syntheses require much lower temperatures (generally lower than 200 ºC). This can result in a better kinetic control of the products formed, and it is much easier to prepare metastable phases using this synthetic approach than it is using traditional solid state methods. Furthermore, by easily changing very simple synthesis parameters such as temeperature, pressure, precursor concentration or using different solvent/cosolvent/surfactant systems, the particle characteristics can be tailored. In general, solvothermal synthesis is an effective method to afford well-crystallised materials with well defined morphologies, where no additional high post-heat treatment is needed. Moreover, solvothermal processes facilitate a wide range of reactions, such as multicomponent reactions, heat treatment reactions to modify or change the composition, phase transformation reactions, decomposition reactions, extraction, precipitation, disproportionation reactions, crystallisation and solidification.[133] The most common method of accomplishing solvothermal synthesis is to seal the reactants mixture inside Teflon-lined autoclaves so that there is also significant autogenous solvothermal pressure produced, often up to 15 bar (Figure 1.11). Usually, for solvothermal reactions the precursors are either in solution, slurry or gel form.[134]

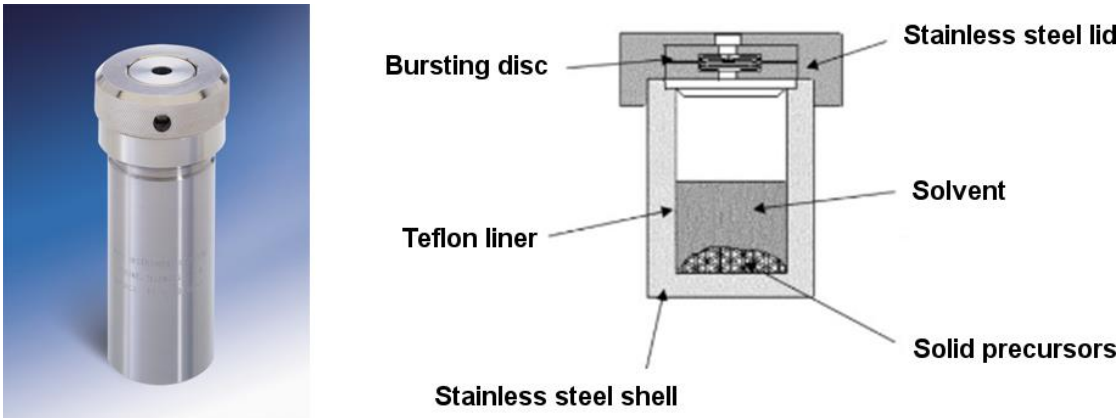

Figure 1.11. Schematic drawing of an autoclave for solvothermal synthesis.

Solvothermal processes have been widely used for the preparation of promising electrode materials such as olivine $LiFePO_4$ with the possibility of easily tailoring particle sizes and morphology. For example, $LiFePO_4$ nanoparticles (~50 nm in size), nanoplates (100 nm thick and 800 nm wide) and microplates (300 nm thick and 3 μm wide) have been selectively synthesised by a solvothermal method in a water–polyethylene glycol (PEG) binary solvent using H_3PO_4, $LiOH{\cdot}H_2O$ and $FeSO_4{\cdot}7H_2O$ as precursors. The morphology and size of the $LiFePO_4$ particles were strongly dependent on synthetic parameters such as volume ratio of PEG to water, temperature, concentration and feeding sequence.[135] A microspherical, hollow and monodispersed $LiFePO_4$ olivine material has also been

successfully synthesised by a solvothermal method using a spherical Li_3PO_4 template and $FeCl_2 \cdot 4H_2O$ as the Fe^{2+} source. The electrochemical measurements demonstrated that the carbon coated $LiFePO_4$ materials could exhibit outstanding high charge/discharge capacities of 158, 144, 125, 101, and even 72 mAh g^{-1} at 0.1 C, C, 5C, 20 C, and 50 C, respectively.[136]

The solvothermal technique is thus a promising method for the production of energy storage materials. Nevertheless, the mechanisms controlling the fundamental particle formation taking place during the solvothermal process are often poorly understood, and extensive trial-and-error experiments are usually required in order to design the synthesis of a certain material with tailor-made properties. As a deeper knowledge of these processes is crucial, *in situ* studies of solvothermal processes, which consist of investigations of the chemical reactions in real time, have become important in the understanding of material formation. The use of *in situ* techniques allow the observation of intermediate phases, which are generally difficult to isolate during an *ex situ* synthesis.[137] For example, an *in situ* synchrotron XRD investigation of a one pot hydrothermal synthesis of olivine $LiFePO_4$ demonstrated that $LiFePO_4$ can be formed at temperatures as low as 105 ºC. It was shown that the formation of $LiFePO_4$ occurs by a straightforward dissolution-reprecipitation process. Moreover, no obvious intermediate phases were formed during the synthesis, which fosters the rapid formation of olivine $LiFePO_4$ under hydrothermal conditions at low temperatures. They also examined the concentration of iron on lithium sites and the evolution of the lattice parameters by Rietveld analysis of the PXRD data as a function of the reaction temperature. Results revealed a competition between thermal expansion of the cell volume and cation ordering, which results in a contraction of the unit cell, as the cell volume decreases due to the elimination of antisite defects. At temperatures from 180 to 210 ºC, less than 0.5% iron disorder was observed and nearly defect free material was obtained when the sample reached ~195 ºC.[138]

1.6.4 Ultrasound synthesis

The utilisation of high intensity ultrasound irradiation (20 kHz-10 MHz) offers a facile, versatile synthetic technique for nanostructured materials that are not often available by traditional synthetic methods. The primary physical phenomena associated with ultrasound irradiation are cavitation and nebulisation. Acoustic cavitation, defined as the formation, growth and implosive collapse of bubbles in a liquid, creates extreme conditions inside the collapsing bubble. When liquids are irradiated with ultrasound, the alternating expansive and compressive acoustic waves creates bubbles and makes them oscillate. These oscillating bubbles can accumulate ultrasonic energy effectively while growing to a certain size (typically tens of mm). Under the right conditions, a bubble can overgrow and subsequently collapse, releasing the concentrated energy stored in the

bubble within a very short time (with a heating and cooling rate of $>10^{10}$ K s^{-1}). This cavitational implosion is generally very localised and transient with a temperature of ~5000 K and a pressure of ~1000 bar. The sudden collapse results in an oxidative environment due to the generation of highly reactive species, including hydroxyl radicals ($^{\cdot}OH$) and $^{\cdot}H$.[139] Cavitation-induced sonochemistry provides a unique interaction between energy and matter under exceptional conditions that gives access to a range of chemical reactions normally not accessible allowing the generation of a wide variety of nanostructured materials.[140] Compared to traditional energy sources, ultrasonic irradiation provides rather unusual reaction conditions such as a short duration of extremely high temperatures and pressures in liquids that cannot be created by other methods.[140] The use of the sonochemical method for synthesis of different nanomaterials has become an important technique in recent years due to its simplicity, the low price of equipment and to the fact that in many cases crystallline materials are obtained at lower temperatures. The effects of ultrasound irradiation are particularly relevant in those cases where mass transport is highly hindered and in those procedures that require the rupture of nanoparticle aggregates to obtain a homogeneous dispersion.[141] In particular, high intensity ultrasound can be used for the production of novel nanomaterials, including transition metal oxides.[142] A myriad of metal oxides have been prepared by a sonochemical approach. Gedanken and co-workers have reported various nanostructured metal oxide syntheses including TiO_2,[143] Fe_3O_4,[144] a-Ni$(OH)_2$,[145] GaO(OH),[146] In$(OH)_3$,[147] and $BaFe_{12}O_{19}$.[148] In their syntheses, sonication of an aqueous metal salt solution is carried out under ambient conditions to prepare various forms of nanostructured metal oxides.[140] Highly crystalline metal oxide nanoparticles such as TiO_2, WO_3 and V_2O_5 have also been synthesised in just few minutes *via* a sonochemical process by reacting transition metal chlorides with a non-aqueous solvent such as benzyl alcohol.[149] Even a wet chemical co-precipitation process promoted by ultrasonic irradiation in aqueous solutions has also provided a simple and economic route to nanosized $LiFePO_4$/C composites exhibiting good cycling performance in which discharge capacities of 159, 147 and 135 mA·hg^{-1} at 0.1 C, 0.5 C and 2 C rates, respectively, were reached.[150]

1.6.5 Microwave synthesis

In the past decade, microwave-assisted solvothermal synthesis has shown to be a fast and low temperature route to prepare high quality functional nanomaterials by combining the strong interaction between polar/ionic solvents and microwave radiation. In traditional heating methods, energy is delivered to the material through conduction, convection and radiation processes. Nevertheless, in microwave dielectric heating the electromagnetic energy is volumetrically and instantaneously absorbed by all the parts of the mixture so that uniform and rapid increase of temperature can be achieved within a short period of time. In particular, the synthesis of nanoparticles, whose growth is

extremely sensitive to the reaction conditions, could benefit from the efficient and controlled heating provided by microwave irradiation. Furthermore, microwave processes can also suppress side reactions, improving the yield and reproducibility of the synthetic procedure. In general, microwave heating can offer the following advantages in comparison to conventional heating for chemical synthesis: high heating rates, excellent control of the reaction parameters (which is not only important with respect to the quality of the product, but also addresses a serious safety issue), selective heating in the case where the reaction mixture contains compounds with different microwave absorbing properties, higher yields, better selectivity due to reduced side reactions, improved reproducibility, possibility of automatisation and high throughput synthesis, and no direct contact between the heating source and the reactants and/or solvents. Finally, it is worth mentioning the simplicity of microwave-assisted methods in which a precursor mixture in an adequate solvent is taken inside a microwave vessel and irradiated.[151] Modern commercially available dedicated microwave reactors feature built-in magnetic stirrers and direct temperature and pressure monitoring by various probes and sensors, contributing to a better understanding of the microwave process and increased safety. However, some of the major drawbacks of microwave chemistry are the high costs of dedicated microwave reactors and the size limitation of the reactors due to the short penetration depth of microwave irradiation, which could be a serious problem for scaling-up.

The microwave dielectric heating effect uses the ability of some liquids and solids to convert electromagnetic energy into heat and thereby drive reactions in which some control of the material's properties and reaction selectivity can be achieved. In many instances, the use of microwaves has been demonstrated to significantly reduce processing times, increase product yields and enhance product purities compared to other conventional synthetic routes.[152] The origin of the heating effect produced by high frequency electromagnetic waves (2.45 GHz in industrial microwave heaters) arises from the ability of an electric field to exert a force on charged particles. When the particles contained in a substance can move freely through it, a current is induced. However, if the charge carriers are bound to certain regions, they will move until a counter force balances them resulting in a dielectric polarisation. Both conduction and dielectric polarisation are sources of microwave heating. Microwave dielectric heating relies on the ability of an electric field to polarise charges in a material and the inability of this polarisation to follow fast reversals of an electric field. In dipolar polarisation, individual dipoles rotate due to the moment applied by the electric field (Figure 1.12 (a)) and heating occurs because of frictional losses as the molecule attempts to realign with the electric field, and these frictional losses can be considered to be analogous to the bulk viscosity of the liquid. At higher temperatures the molecular friction decreases because

the molecules can more easily follow the alternating electric field and consequently, less energy is dissipated as heat. In the case of ionic conduction the dissolved charged particles oscillate back and forth under the influence of the microwave irradiation, colliding with neighbouring molecules, and thus creating heat (Figure 1.12 (b)). The extent to which a material interacts with an electric field can be characterised by its dielectric properties, so elucidation of the dielectric properties of each component and the bulk reaction mixture is essential in understanding the interaction of electromagnetic waves with a material. The dielectric constant, ε' is the ability of a material to store electromagnetic energy through polarisation and the dielectric loss factor, ε'' is the ability to convert the stored energy into heat. The ratio ε'/ε'' is generally used to assess the heating ability of a material under microwave irradiation and this quantity is known as the loss tangent, tan δ = ε''/ε'. In general, media exhibiting high tanδ values are characterised by high absorption ability and, respectively, efficiency of heating.[153] In Table 1.1 the dielectric loss tangent of different solvents are listed.[154] This information suggests that the high tanδ of glycols and alcohols makes them ideal solvents for an effective microwave heating.

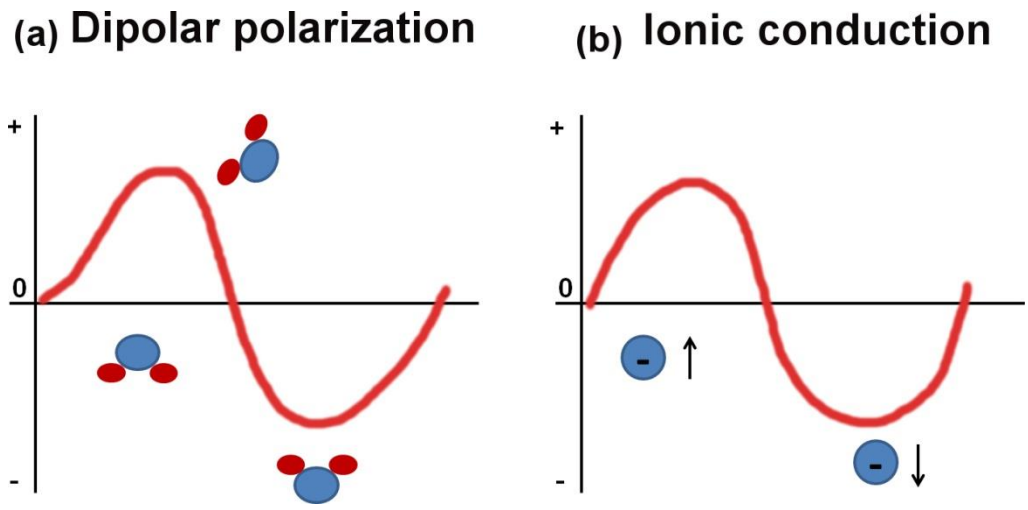

Figure 1.12. (a) Dipolar polarisation: dipolar molecules which try to align with an oscillating electric feld. **(b)** Ionic conduction: charged particles in solution will follow the applied electric field.

Table 1.1. Dielectric loss tangent tanδ (2.45 GHz, 20 ºC) for common pure solvents

Solvent	tanδ	Solvent	tanδ
Ethylene glycol	1.350	DMF	0.161
Ethanol	0.941	Acetonitrile	0.062
DMSO	0.825	Acetone	0.054
Water	0.123	Chloroform	0.091
Methanol	0.659	Dichlorometane	0.042

Solvothermal microwave-assisted have shown to yield high performing electrode materials for Li-ion batteries. For example, 3 min microwave-assisted liquid phase synthesis of highly crystalline $LiFePO_4$, $LiMnPO_4$ and mixed $LiMn_{0.65}Fe_{0.35}O_4$ olivines in benzyl alcohol has been reported by Niederberger *et al.* The $LiFePO_4$ electrode demonstrated an excellent initial discharge capacity of 150 $mAh \cdot g^{-1}$ and very stable cycling performance, allowing a capacity retention with a decline of only 5–10% after 160 cycles. The initial specific charge of $LiMnPO_4$ was ~125 $mAh \cdot g^{-1}$, however with a gradual capacity fade over cycling.[45] In general, it has been found that microwave processed $LiFePO_4$ powders generally exhibit smaller particle size, more uniform size distribution, smoother surface morphology and higher discharge capacity. On the other hand, microwave processes allow access to kinetically driven reactions, which opens up the possibility of obtaining low-temperature metastable phases and polymorphs that could not be synthesised with conventional techniques.[155-157] In particular, microwave synthesis has also been a facile approach to directly tailor two $LiFePO_4$ polymorphs in a controlled way under mild conditions. Employing a microwave-assisted non-aqueous route, highly crystalline olivine α-$LiFePO_4$ (*Pnma* space group) or non-olivine β-phase $LiFePO_4$ (*Cmcm* space group) have been efficiently synthesised by simply tuning the ratio of the solvents benzyl alcohol and 2-pyrrolidone.[50] Also, orthorhombic but non-olivine polymorphs $LiMPO_4$ (*M*=Mn, Fe, Co and Ni) described by a *Cmcm* space group have been fabricated by a rapid microwave-assisted solvothermal synthesis using dry tetraethylene glycol.[158] Our group also reported the formation of a mixture of α-and β-$LiFePO_4$ polymorphs through a solvothermal microwave–assisted approach using $FeC_2O_4 \cdot 2H_2O$ and LiH_2PO_4 in ethylene glycol.[51]

1.6.6 Ionothermal synthesis

Ionic liquids (ILs) are a class of organic solvents with high polarity and a preorganised solvent structure. They are defined as room temperature molten salts that differ from inorganic salts such as NaCl (T_f=801°C) because their melting temperature is lower than 100°C. They are made of organic cations and anions, the choice and combination of which will mainly affect their melting point and their solvating properties. In recent years, ILs have received increased attention as novel green media in inorganic materials synthesis due to their excellent properties such as high thermal stability, low vapor pressure, wide temperature range for liquid state, low interfacial tension, and high ionic conductivity. Owing to the high thermal stability of ILs, reactions can be conducted at temperatures well beyond 100 ºC in non-pressurised vessels. Moreover, the low interfacial tension provides good stabilisation or solvation of molecular species, resulting in high nucleation rates.[159] It also has to be noted that ILs present, as solvents, great opportunities to purposely direct nucleation due to the flexible nature of the cationic/anionic pairs. Over the past decades, ionothermal synthesis has developed into

an advantageous synthetic technique for the preparation of zeotypes[160] and other porous materials such as metal organic framework compounds (MOFs).[161] However, there has been a very limited use of this synthetic approach in the generation of inorganic compounds. Tarascon *et al*. explored the ionothermal synthesis of electrode materials and they assessed the effect of various ionic liquid architectures on the resulting morphology and electrochemical performances of olivines $LiFePO_4$ and $LiMnPO_4$ powders, addressing also the possibility of easily recovering and reusing the expensive ILs.[162, 163] They also demonstrated the effectiveness of ionothermal synthesis in the preparation of nanometric Li-based fluorophosphates $LiFePO_4F$ and $LiTiPO_4F$ electrodes with structures isotopic to tavorite $LiFePO_4(OH)$ at temperatures of only 260 °C, while temperatures of 600−700 °C are required to obtain coarse powders *via* traditional ceramic methods.[164] Various structures and morphologies of $Li_3V_2(PO_4)_3$ cathode materials have also been synthesised by a novel ionothermal method using three kinds of imidazolium-based ILs as both reaction media and structure-directing agents at ambient pressure. These materials presented excellent electrochemical performance with high rate capabilities and cycle stability.[165] On the other hand, ionic liquids are highly susceptible to microwave irradiation because of their ionic character and high polarisability, making them excellent microwave adsorbers. The combination of microwave heating and ILs can provide superior benefits for the fast synthesis of high performing functional materials over the conventional heating methods, especially in terms of rapidness, energy-efficiency and increased crystallinity.[166] Our group has successfully synthesised nanoparticulate olivine $LiFePO_4$ through a microwave route using $FeC_2O_4{\cdot}2H_2O$ and LiH_2PO_4 precursors in 1-ethyl-3-methyl imidazolium trifluoromethanesulfonate (EMI-TFMS).[51]

1.6.7 Synthetic strategies to electrochemical performance enhancement

Innovative materials chemistry lies at the heart of the main advances made in energy conversion and storage. Further breakthroughs in materials processing hold the key to new high performing energy storage and conversion devices. In particular, the poor electrical and ionic conductivity of some electrode materials are generally the main causes of poor rate performance during battery cycling. Therefore, exploring new synthetic strategies able to overcome these drawbacks has become an essential factor in the development of novel high performing electrode materials. Novel and creative approaches that can be used to improve LIB performance include:

(i) selective cationic doping can allow higher cell voltages, a faster ionic and electronic transport and even some enhancement in the chemical/thermal stability.[167] For example, Li-sites in olivine $LiFePO_4$ have been substituted for ions with small ionic radius such as Na,[168-170] Nb,[171, 172] and Al[173] leading to an enhancement of the electrochemical performance. Li-site doping can increase the electronic conductivity and decrease the charge transfer resistance. However, the origin of the enhanced conductivity is under

debate. Controversy has centered on whether the ions are actually doped into the lattice or whether a conductive nanonetwork of metal-rich phosphides is responsible for the enhanced conductivity.[174, 175] First principle calculations have also demonstrated that Fe-site doping may facilitate the diffusion of lithium along the 1D channels and increase both the electronic and ionic conductivity of $LiFePO_4$ cathodes. The enhanced electronic and ionic conductivity may be ascribed to the weakening of the Li-O bond in $LiFePO_4$. Certain doping elements such as Ni and Zn can remarkably enhance the electrochemical performance of $LiFePO_4$ cathodes. Ornek *et al.* demonstrated that Ni doped $LiNi_xFe_{1-x}PO_4/C$ cathodes can exhibit a noticeable improvement in electrical conductivity and diffusion coefficient of lithium ions. Their $LiFe_{0.95}Ni_{0.05}PO_4/C$ sample synthesised by sol-gel-assisted carbothermal reduction method displayed discharge capacities of 155 $mAh \cdot g^{-1}$ in comparison to 122 $mAh \cdot g^{-1}$ from the undoped $LiFePO_4/C$.[176] Shenouda *et al.* investigated Zi-doped $LiFePO_4$ materials and reported that the un-doped $LiFePO_4$ showed a decrease from 135 to 125 $mAh \cdot g^{-1}$ after 150 cycles, while 2.5% ZnO-doped $LiFePO_4$ exhibited an initial capacity of 177 $mAh \cdot g^{-1}$ and maintained 167 $mAh \cdot g^{-1}$ after 150 cycles.[177] Attempts to dope $LiFePO_4$ with more than one different transition metal have also been pursued.[178, 179] Recently, a grape-like $LiFe_{0.97}M_{0.03}PO_4/C$ (M=Ni, Co, Mn) composite prepared by a wet-milling assisted carbothermal reduction method delivered an excellent rate capability with discharge capacities of 167.5 (0.2 C), 161.2 (0.5 C), 151.1 (C), 146.7 (2 C), 135.5 (5 C) and 124.9 $mAh \cdot g^{-1}$ (10 C). The synergistic effect of Ni-Co-Mn doping, carbon coating and well-defined morphology are believed to be the reasons of the outstanding cycling behaviour.[180]

(ii) Decreasing the particle size could be another way to obtain a greater capacities and rate capabilities, as smaller partice sizes allow shorter pathlengths for the Li^+ ions to diffuse while the increased surface areas improve the electrode-electrolyte interactions.[10] For example, Lee *et al.* fabricated $LiFePO_4$ samples with and without surfactant by vibratory milling followed by thermal heat treatment. The addition of a surfactant led to uniform-sized smaller particles with less agglomerates and higher specific surface area. Electrochemical impedance spectroscopy measurements showed a low charge transfer resistance in these electrodes, which led to a significantly enhanced cycling performance.[181] Furthermore, particle minimisation can also relieve stress and improve the mechanical stability facilitating structural transformations. Therefore, nanostructured electrodes are proven to be effective in improving the kinetics of phase transformation and minimising undesirable consequences such as degraded flexibility for the insertion or extraction of Li^+ ions and thus diminished capacity retention. For instance, when ultrathin $LiMn_2O_4$ nanowires with diameters less than 10 nm were used as cathodes, a more facile structural transformation was observed in a large composition range with high reversibility and good capacity retention.[182] On the other hand, nanostructured

materials can also lead to new Li-storage mechanisms, enabling higher capacities than conventional intercalation mechanisms. It has been demonstrated that Li^+ ions can be stored on the surface,[183] interface[184, 185] and in nanopores[186, 187] without causing any mechanical crumbling in the electrode, thus leading to excess lithium storage. Nevertheless, nanomaterials may incur high fabrication cost due to complex synthetic processes, low volumetric energy density due to reduced packing density of nanoparticles, and undesired side reactions between the electrode and the electrolyte due to large surface areas. Furthermore, nanomaterials tend to form agglomerates during the electrode fabrication process, making it difficult to uniformly disperse them in the electrodes.[188]

(iii) Another alternative includes customising particle morphologies taking into account that the synthetic method followed and the solvent chosen are detrimental factors in the resulting morphology and particle size. Designing unique shapes and morphologies of electrode materials is important to enhance the electrochemical peroformance, as different morphologies can enlarge the electrode/electrolyte interface and shorten the transport path for lithium ions and electrons.[189] Most conventional morphological control is based on a variety of nanostructures such as nanowires, nanoparticles, nanosheets and core–shell structures. In particular, the core–shell structured $LiFePO_4$/carbon composite allows fast lithium ion and electron transportation, enabling high rate performance. Zhou *et al.* designed a $LiFePO_4$/carbon nanocomposite with a core–shell structure and the obtained $LiFePO_4$ showed a high rate capability and long life cycle (168 $mAh \cdot g^{-1}$ at 0.6 C and 90 $mAh \cdot g^{-1}$ at 60 C, and less than 5% discharge capacity loss over 1100 cycles).[190] On the other hand, Peng *et al.* demonstrated that self-assembled single-crystalline $LiFePO_4$ nanowires exhibited reversible capacities of 110 $mAh \cdot g^{-1}$ at a 30 C rate, showing the strong potential of 1D nanostructured electrode materials for LIBs.[191] The nanowires morphology may enhance the contact with the electrolyte, improve permeation and mitigate the problem of slow Li^+ transport.[189]

(iv) Also, all-in-one carbon coating procedures using low cost and environmentally-friendly carbon sources have shown to increase the electronic conductivity of electrode materials and consequently enhance the electrochemical performance. Conductive coatings can stabilise surface reactions protecting the active materials from the electrolyte and potentially suppressing side reactions due to electrolyte decomposition.[192] A variety of carbon sources with different chemical and physical properties have been applied to the carbon coating process for electrode materials. Some classic carbon sources include some organics (glucose, citric acid and lactose) and some inorganic sources (acetylene black, carbon nanotubes and graphene).Organic carbon sources are advantageous in forming a homogeneous carbon-coating layer and allow for good control of the carbon layer structure (thickness, homogeneity, full coverage) during the pyrolysis

process at high temperatures, but the carbon quality (conductivity, graphitised degree) is hard to control. On the other side, inorganic carbon provides the opposite advantages and disadvantages.[61] For example, a carbon coated $LiFePO_4$-porous carbon composite (C-$LiFePO_4$–PC) exhibited a much better rate capability compared to bare $LiFePO_4$-porous carbon ($LiFePO_4$–PC), displaying discharge capacities of 152 $mAh \cdot g^{-1}$ and 140 $mAh \cdot g^{-1}$ at 0.1 C rate, respectively. In addition, the C-$LiFePO_4$–PC electrodes exhibit a much better rate capability compared to the $LiFePO_4$–PC electrode operated at various rates between 0.2 C and 5 C. The carbon coating may enhance the structural stability and improve the lithium storage kinetics.[193] Ramesh *et al*. studied the effect of carbon coating on the surface of $LiMnPO_4$ nanorods and also observed an improvement in battery performance compared to the bare sample (75 $mAh \cdot g^{-1}$ for bare $LiMnPO_4$ *vs*. 110 $mAh \cdot g^{-1}$ for C/$LiMnPO_4$).[194]

(v) Finally, high specific surface areas may improve the accessibility of the active electrode materials to the electrolyte, which could effectively enhance Li^+ transport and rate capability.[95, 105] Hollow nanostructured materials generally can offer higher capacity and rate capability compared to their bulk counterparts due to larger surface area, shorter path length for Li^+ migration and more freedom to accommodate volume changes, which can reduce the overpotential and allow faster reaction kinetic at the electrode surface. In particular, encapsulation of electrochemically active particles in a graphene hollow shell to form a core-void-shell composite is a promising way to improve the electrochemical performance of some battery materials such as transition metal oxides.[195] It has been demonstrated that the continuous graphene shell may enhance the electrical conductivity of the electrodes and thus facilitate current collection and charge transfer associated with lithium storage. The unique shell structure may suppress particle aggregation of the core active particles while the void space between the core and shell may accommodate the large volume changes of the core material during the Li^+ insertion and extraction process.[95] Figure 1.13 summarises the general strategies for performance enhacement of electrode materials.[33]

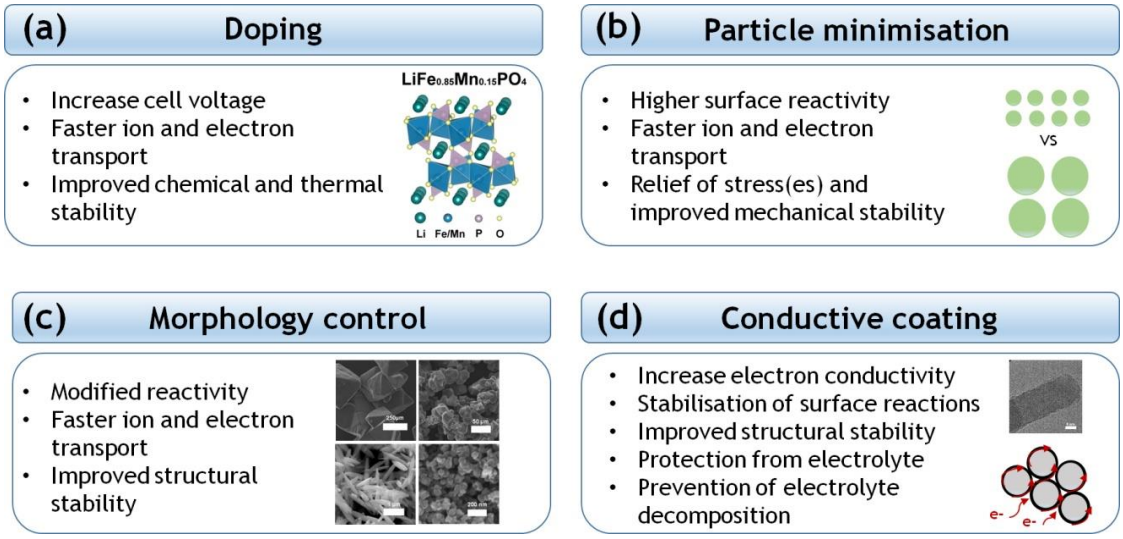

Figure 1.13. General strategies for electrochemical performance enhancement and their rationale: **(a)** doping, **(b)** reducing dimensions of active material, **(c)** tuning particle morphology and **(d)** formation of conductive coatings around the active material.

1.6.8 Single source precursor (SSP) synthesis

Nowadays, intensive research is focused towards the development of novel synthetic methodologies that allow generalisable, large-scale, energy-efficient and low cost routes to high quality nanomaterials with targeted properties. The synthesis of inorganic nanocrystals with control over shape, size, composition, crystal structure and surface chemistry is crucial for the fundamental understanding of their structure-property relationship. However, the design of suitable synthetic processes for the growth of well-shaped, monodispersed crystalline nanoparticles still remains a challange. A new direction for nanomaterials preparation being pursued is the use of single source precursors (SSP) which possess all the desired elements in a unique molecular precursor. Co-location of these desired elements in a single starting material can potentially shorten reaction times and temperatures due to a decrease in diffusional energy requirements usually needed for reactions to proceed. Furthermore, intimate mixing at the molecular level generally ensures product homogeneity. Therefore, the preparation of nanocomposite materials from single source precursors represents a highly promising approach towards tailor-made phase compositions, morphologies, microstructures and, consequently, specific properties. The fabrication of inorganic materials from metallorganic precursors often has advantages over “traditional routes” which include lower reaction temperatures and better compositional uniformity. Furthermore, the bridging or chelating organic ligands in the precursor molecules can help prevent molecular segregation and the loss of the volatile organic moiety in the course of decomposition may impart unusual and/or desirable structural features in the final product such as high surface area, low density, connected channels or the formation of metastable phases. In addition, the binding strength of the ligands on the single source

metal precursor can be tailored to tune the decomposition kinetics of the complex.[196, 197] For example, metal alkoxides constitute an important class of metallorganic compounds characterised by the metal-oxygen-carbon bond system. Therefore, metal alkoxides $M(OR)_n$ are ideal metallorganic precursors for the formation of metal oxides due to the fact that they already have the metal-oxygen bond templated in a single molecular precursor. The properties of metal alkoxides are dependent on numerous interrelated factors. The ratio of metal atoms to alkoxide residues (the number of OR groups per metal atom) and how closely that number approaches to the maximum coordination number possible for the metal atom, is very important and influences whether monomers $M(OR)_x$, oligomers $[M(OR)_x]_{2,3 \text{ or } 4}$ or extended lattices $[M(OR)_x]_n$ are likely, whatever the polarity of the M-O bond. The size and shape of the alkyl group also play a prominent role in determining the properties of the alkoxides. Another attractive feature of metal alkoxides is their solubility in a large variety of solvents and their ability to form heterometallic species, especially by mixing alkoxides of different metals. The formation of double metal alkoxides can be considered to be partially due to the tendency of the metal to form coordination complexes in order to achieve its maximum coordination number.[198]

Recently, single source precursor approaches have been successfully applied for the preparation of several metal oxide nanoparticles. In previous reports, novel aqueous-based, single source precursor methods for the synthesis of pure, room temperature-stable, nanocrystalline ß-$NiMoO_4$ with controlled composition has been reported. The soft–chemical nature of this synthetic approach and the crystal structure features of the bimetallic hydroxyisobutyrate precursor were found to play an essential role in the fabrication of this metastable oxide under mild reaction conditions.[199] Transition metal doped titanium glycolates have been directly used as single source precursors for the preparation of porous metal-doped titania (TiO_2) through a simple thermal treatment process. The obtained product demonstrated high crystallinity, a large surface area and appropriate transition metal doping, all of which were beneficial to the enhancement of the photocatalytic performance of the doped TiO_2 material.[200] Deng *et al.* have also reported a controllable synthesis of spinel $ZnMn_2O_4$ nanoparticles prepared *via* a single source precursor route by calcination of a Zn-Mn citrate complex precursor. This potential conversion anode for LIBs exhibited attractive rate capabilities delivering 330 $mAh \cdot g^{-1}$ after more than 35 cycles at 600 $mA \cdot g^{-1}$.[201] A new single source precursor approach to synthesise graphene-like MoS_2 flakes with tunable layers (from mono- to multi layer) by thermal decomposition of a single source $Mo(Et_2NCS_2)_4$ precursor has also been reported. This graphene-like MoS_2 retained high storage capacity of 330 $mAh \cdot g^{-1}$ after 100 cycles at a current density of 500 $mA \cdot g^{-1}$. This synthetic route opens up a new method to controlled and large-scale synthesis of graphene-like transition metal sulphides for energy storage applications.[202] In this thesis, single source precursor synthetic strategy using metal

alkoxides has been applied to the fabrication of olivine nanostructured $LiFe_{1-x}Mn_xPO_4$ cathodes and transition metal oxide anodes for LIBs.

1.7 Aims

This PhD aims to develop environmentally-friendly and energy-efficient synthetic routes to high performing nanostructured electrodes for LIB applications. Generating high quality functional nanomaterials *via* fast, low temperature and inexpensive approaches offers a tremendous potential for developing high performance LIBs required to meet our growing energy storage needs. Principally, this research focuses on the design, synthesis, structure determination and electrochemical evaluation of LIB electrodes. In particular, olivine $LiFe_{1-x}Mn_xPO_4$ nanostructures and transition metal oxide nanoparticles are the main objective of this thesis due to their potential applications as electrode materials in LIBs. The aim is centred on examining the local structure of these electrode nanomaterials in order to gain further insights into their electrochemical behaviour. These investigations mainly concentrate on the fabrication of a series of tailored metal alkoxide precursors containing all the required metals in a single compound, which are then used for the preparation of nanostructured transition metal phosphate insertion cathodes and metal oxides conversion anodes *via* fast and low temperature microwave and ultrasound-assisted processes. This project aims to demonstrate that the use of single source heterometallic alkoxide precursors in conjuction with microwave heating yields non-defective and highly cyrstalline nanomaterials exhibiting excellent electrochemical performances. The structure, particle size and morphology, and electrochemical performance of the materials synthesised here is fully investigated by powder X-ray/neutron diffraction, electron microscopy and potentiostatic measurements. When possible, X-ray/neutron total scattering methods with pair distribution function analysis have been conducted to obtain a detailed characterisation of the local structure and a complete examination of atomic disorder in these olivine structured nanocrystallites. Elucidation of the local structure of these nanocrystalline phases strongly contributes to understand the cycling behavior of these electrodes and, consequently, provides essential information for the future development of high performing battery materials. Finally, the microscopic Li^+ diffusion properties in olivine $LiFe_{1-x}Mn_xPO_4$ phases are evaluated for the first time using muon spin relaxation (μ^+SR) technique.

2 Materials and Characterisation Methods

2.1 Materials

The following chemicals and solvents were purchased and used without further purification: $Fe(acac)_3$ (Sigma Aldrich), $FeSO_4 \cdot 7H_2O$ (Sigma Aldrich), $FeC_2O_4 \cdot 2H_2O$ (Alfa Aesar), $MnC_2O_4 \cdot 2H_2O$ (Alfa Aesar), $Mn(acac)_3$ (Alfa Aesar), $MnCO_3$ (Sigma Aldrich), $MnSO_4 \cdot H_2O$ (Sigma Aldrich), $NiC_2O_4 \cdot H_2O$ (Alfa Aesar), $CoC_2O_4 \cdot H_2O$ (Sigma Aldrich), LiH_2PO_4 (Alfa Aesar), NaO^tBu (Sigma Aldrich), LiO^tBu (Alfa Aesar), $FeBr_2$ anhydrous (Sigma Aldrich), $MnBr_2$ anhydrous (Alfa Aesar). $FeCl_2$ anhydrous (Sigma Adrich), $NiCl_2$ anhydrous (98%, Alfa Aesar), $LiOH \cdot H_2O$ (Sigma Aldrich), $^7LiOH \cdot H_2O$ (Sigma Aldrich, 97 atom % ^7Li), Li_2CO_3 (Sigma Aldrich), H_3PO_4 (Sigma Aldrich, 85 wt. % in H_2O), H_3PO_4 crystalline (Sigma Aldrich), sucrose (Sigma Aldrich), glucose (Sigma Aldrich), polyvinylpyrrolidone (average mol wt 10000, Sigma Aldrich), benzyl alcohol (Sigma Aldrich), ethylene glycol (Alfa Aesar), tetraethylene glycol (Alfa Aesar), 1-ethyl-3-methylimidazolium trifluoromethanesulfonate (Sigma Aldrich), acetic acid (Sigma Aldrich), ethanol (VWR Chemicals), acetone (VWR Chemicals) and Benzene-d_6 (Alfa Aesar). Dry THF was obtained from an in house Solvent Purification System. For battery preparation, the following were obtained: Whatman glass microfiber filter as separator (Fischer Scientific), 1 M lithium hexafluorophosphate ($LiPF_6$) in ethylene carbonate (EC) and dimethyl carbonate (DMC) 1:1 v/v as electrolyte (Solvionic) and Li metal (Sigma Aldrich, ribbon, thickness x W 0.75 mm x 45 mm 99.9% trace metal basis), Na metal (Sigma Aldrich), polytetrafluoroethylene powder (Fisher Scientific), carbon black KET JENBACK EC-600JD (AkzoNobel) and conductive carbon black EQ-Libs-Super C45.

2.2 Experimental procedure

2.2.1 Synthesis of LiH_2PO_4

$LiOH \cdot H_2O$ or $^7LiOH \cdot H_2O$ (9.00 g, 0.214 mol) were weighed and dissolved in 15 mL distilled H_2O. 16.7 mL H_3PO_4 (85 wt. % in H_2O) was added dropwise with a Pasteur pipette while thoroughly stirring. Some white precipitate was immediately formed and the mixture was heated until complete evaporation of the solvent. The precipitate was then cooled to room temperature and washed with few mL of acetone. Finally, the LiH_2PO_4 powders were dried overnight in a vacuum oven at 80 ºC and thoroughly ground prior to use in the subsequent syntheses. Enriched $^7LiOH \cdot H_2O$ was employed to prepare $^7LiH_2PO_4$, used for preparation of samples for high resolution powder neutron diffraction and neutron PDF experiments.

2.2.2 Microwave synthesis of $C/LiFe_{1-x}Mn_xPO_4$ olivines from commercial starting materials

$LiFe_{1-x}Mn_xPO_4$ (x=0, 0.25, 0.5, 0.75 and 1) powders were prepared by weighing and grinding in an Ar filled glovebox the stoichimetric amounts of LiH_2PO_4 (0.208 g, 2 mmol),

$Fe(acac)_3$ and $MnC_2O_4 \cdot 2H_2O$ (2 mmol transition metal precursors) ($Mn(acac)_3$ for tbe $LiMnPO_4$ sample) in an agate pestle and mortar. The powders were transferred into 35 mL glass reaction vessels and 10 mL of ethylene glycol was added. The mixtures were stirred for 20 minutes before irradiation with microwaves in a CEM Discover SP microwave synthesiser (operating frequency of 2.45 GHz) for 3 hr at 220 ºC. A pre-stirring step of two minutes was also used prior to microwave irradiation to ensure complete mixing. After the microwave-assisted synthesis, the obtained powders were washed with distilled H_2O (2 x 35 mL), ethanol (2 x 35 mL) and acetone (2 x 35 mL). Finally, the product was dried in a vacuum oven at 80 ºC overnight and ground.

The product was annealed under an Ar atmosphere at 500 ºC for 1 hr in a tube furnace to increase crystallinity and also to decrease possible Li_3PO_4 impurities remaining in the sample. Any remaining Li_3PO_4 could be removed with a weak acid such as acetic acid. The washing is carried out by adding 10 mL of acetic acid 0.01 M to the impure sample (around 0.20-0.25 g) and then stirring the mixture for 4 min. The mixture was centrifuged for 1 min at 4000 rpm and the pH was checked (should be around 3). Next, the sample was washed with distilled water (2 x 20 mL) and with acetone (1 x 20 mL). Finally, the product was dried overnight in the vacuum oven at 80 ºC. In order to obtain the sufficient amount of sample for neutron diffraction experiments, multiple syntheses were conducted under identical conditions using the same starting materials, and the powders obtained were combined.

2.2.2.1 Carbon coating of C/$LiFe_{1-x}Mn_xPO_4$ olivines

For the battery cycling experiments, a carbon coating of the $LiFe_{1-x}Mn_xPO_4$ phases was conducted using sucrose in order to increase the conductivity of the electrode materials. $LiFe_{1-x}Mn_xPO_4$ powders were mixed with sucrose (based on 15% wt. carbon coming from sucrose) and a 1:1 mixture in v/v of distilled H_2O:ethanol was added. The resulting suspension was sonicated for 20 min and the solvent was evaporated by heating at 100 ºC and stirring. Finally, the dried powder was transferred to a tube furnace equipped with flowing Ar gas and heat treated at 700 ºC for 3 hr. During the heat treatment the sucrose carbonises forming a carbon layer coating the particles.

2.2.3 Synthesis of "$[Fe_{1-x}Mn_x(O^tBu)_2(THF)]_2$" ($x$=0, 0.5 and 1) metal alkoxide precursors

Synthesis of $[Fe(O^tBu)_2(THF)]_2$ (I)

NaO^tBu (5.667 g, 60 mmol) and $FeBr_2$ (6.470 g, 30 mmol) were weighed in an Ar-filled glovebox and transferred into a Schlenk flask. Dry THF (90 mL) was added and the mixture was stirred at room temperature for 24 hr. A grey precipitate of NaBr was formed

and the liquid phase was transferred into a separate flask using a glass syringe. The solvent was evaporated under vacuum to yield extremely air sensitive grey-greenish crystals of $[Fe(O^tBu)_2(THF)]_2$ (I). All the manipulations were performed using a Schlenk line.

Synthesis of "$[Mn(O^tBu)_2(THF)]_2$" (II)

The same preparation method was followed using $MnBr_2$ (6.443 g, 30 mmol) and NaO^tBu (5.766 g, 60 mmol) in 90 mL of THF in order to synthesise the equivalent Mn-containing alkoxide with expected formula "$[Mn(O^tBu)_2(THF)]_2$" (II).

Synthesis of "$[Fe_{0.5}Mn_{0.5}(O^tBu)_2(THF)]_2$" (III)

A similar salt elimination reaction was conducted to prepare the bimetallic alkoxide with suggested formula "$[Fe_{0.5}Mn_{0.5}(O^tBu)_2(THF)]_2$" (III). $FeBr_2$ (3.235 g, 15 mmol), $MnBr_2$ (3.221 g, 15 mmol) and NaO^tBu (5.766 g, 60 mmol) in 90 mL of THF were used in the preparation of "$[Fe_{0.5}Mn_{0.5}(O^tBu)_2(THF)]_2$" (III).

2.2.4 Microwave synthesis of $LiFe_{1-x}Mn_xPO_4$ nanostructures from "$[Fe_{1-x}Mn_x(O^tBu)_2(THF)]_2$" (x=0, 0.5 and 1) metal alkoxide precursors

The metal alkoxide precursors $[Fe(O^tBu)_2(THF)]_2$ (I), "$[Mn(O^tBu)_2(THF)]_2$" (II) and "$[Fe_{0.5}Mn_{0.5}(O^tBu)_2(THF)]_2$" (III) (0.030 g, 0.07 mmol) were each independently mixed with $LiOH{\cdot}H_2O$ (0.007 g, 0.14 mmol) and H_3PO_4 (0.015 g, 0.14 mmol) in 4 mL benzyl alcohol. The mixtures were irradiated with microwaves for 15 min at 80 ºC then for 10 min at 240 ºC using a CEM Discover SP microwave synthesiser (2.45 GHz). The resulting products were washed thoroughly with ethanol (30 mL × 3) and acetone (30 mL × 3) and then dried overnight in a vacuum oven at 80 ºC to obtain the $LiFePO_4$_I, $LiMnPO_4$_II, $LiFe_{0.5}Mn_{0.5}PO_4$_III and $LiFe_{0.5}Mn_{0.5}PO_4$_I-II powders.

The $LiFePO_4$_I, $LiMnPO_4$_II and $LiFe_{0.5}Mn_{0.5}PO_4$_III samples were carbon coated as previously described in section 2.2.2.1 using 15% wt. C from sucrose (heat treatment for 1 hr at 700 ºC under Ar flow).

2.2.5 Ultrasonic-assisted synthesis of C/Mn_3O_4 hausmannite from "$[Mn(O^tBu)_2(THF)]_2$" metal alkoxide precursor

As previously reported by Gun´ko *et al.*,[203, 204] the careful hydrolysis and ultrasonic treatment of $[Fe(O^tBu)_2(THF)]_2$ affords nanoparticles of magnetite (Fe_3O_4). Knowing this, the remaining "$[Mn(O^tBu)_2(THF)]_2$" (II) and NaBr precipitate obtained after syringing out the "$[Mn(O^tBu)_2(THF)]_2$" (II) liquid phase was hydrolysed with 60 mL of degassed H_2O and kept in the ultrasonic bath for 1 hr to afford nanostructured Mn_3O_4 hausmannite. The addition of degassed H_2O and the ultrasonic treatment were repeated 6 times. After that, the obtained precipitate was washed again 4 times with 30 mL of distilled H_2O to completely remove the remaining NaBr. Mn_3O_4 powders were carbon coated using sucrose as previously described in section 2.2.2.1 by heating for 1 hr at 500 ºC under air.

2.2.6 Synthesis of "[*M*Li$_2$*X*(O^{t}Bu)$_4$(THF)$_2$]$_n$" (*M*=Fe, Mn, Ni; *X*=Br, Cl) heterometallic alkoxide precursors

Synthesis of [FeLi$_2$Br(O^{t}Bu)$_4$(THF)$_2$]$_n$ (IV)

$FeBr_2$ (1.078 g, 5 mmol) and LiO^{t}Bu (1.201 g, 15 mmol) were weighed out in a glovebox and transferred into a Schlenk flask. The flask was then connected to a Schlenk line and cooled with an ice bath. 40 mL of dry THF were carefully added *via* glass syringe to the Schlenk flask. The resulting dark brownish mixture was stirred at room temperature for 24 hr, after which the mixture was filtered through Celite 535 to remove greyish LiBr precipitate formed. A small aliquot of solution (~3 mL) was transferred into a small Schlenk flask in order to grow suitable crystals for single crystal diffraction experiments. The aliquot was kept in the fridge to allow the recrystallisation and dark-brownish crystals of enough quality for single crystal measurements were obtained after three days. For the remaining sample, the solvent was slowly evaporated under vacuum and the obtained powder was thoroughly ground and used as a precursor for the preparation of $LiFePO_4$ nanostructures.

Synthesis of "[FeLi$_2$Cl(O^{t}Bu)$_4$(THF)$_2$]$_n$" (V)

The same synthetic procedure was followed using $FeCl_2$ (0.634 g, 5 mmol) and LiO^{t}Bu (1.201 g, 15 mmol) in 40 mL of THF in order to obtain the structural analogue "[FeLi$_2$Cl(O^{t}Bu)$_4$(THF)$_2$]$_n$" (V) heterometallic alkoxide precursor.

Synthesis of "[MnLi$_2$Br(O^{t}Bu)$_4$(THF)$_2$]$_n$" (VI)

A similar preparation method was also employed to perform the reaction of $MnBr_2$ (1.074 g, 5 mmol) and LiO^{t}Bu (1.201 g, 15 mmol) in 40 mL of THF to yield pinkish powders of "[MnLi$_2$Br(O^{t}Bu)$_4$(THF)$_2$]$_n$" (VI) heterometallic alkoxide precursor.

Synthesis of "[Fe$_{0.5}$Mn$_{0.5}$Li$_2$Br(O^{t}Bu)$_4$(THF)$_2$]$_n$" (VII)

The same synthetic approach was used to prepare the trimetallic alkoxide precursor "[Fe$_{0.5}$Mn$_{0.5}$Li$_2$Br(O^{t}Bu)$_4$(THF)$_2$]$_n$" (VII) by reaction of $FeBr_2$ (0.539 g, 2.5 mmol), $MnBr_2$ (0.537 g, 2.5 mmol) and LiO^{t}Bu (1.201 g, 15 mmol) in 40 mL of THF.

Synthesis of "[NiLi$_2$Cl(O^{t}Bu)$_4$(THF)$_2$]$_n$" (VIII)

A similar synthetic procedure was followed to perform the reaction between $NiCl_2$ (0.635 g, 5 mmol) and three molar equivalents of LiO^{t}Bu (1.201 g, 15 mmol) in 40 mL of THF to yield greysh-purplish powders of "[NiLi$_2$Cl(O^{t}Bu)$_4$(THF)$_2$]$_n$" (VIII) heterometallic alkoxide precursor.

2.2.7 Microwave synthesis of LiFe$_{1-x}$Mn$_x$PO$_4$ nanostructures from "[Fe$_{1-x}$Mn$_x$Li$_2$Br(O^{t}Bu)$_4$(THF)$_2$]$_n$" (*x*=0, 0.5 and 1) and "[FeLi$_2$Cl(O^{t}Bu)$_4$(THF)$_2$]$_n$" heterometallic alkoxide precursors

The different heterometallic alkoxide precursors [FeLi$_2$Br(O^{t}Bu)$_4$(THF)$_2$]$_n$ (IV), "[FeLi$_2$Cl(O^{t}Bu)$_4$(THF)$_2$]$_n$" (V), "[MnLi$_2$Br(O^{t}Bu)$_4$(THF)$_2$]$_n$" (VI) and

"$[Fe_{0.5}Mn_{0.5}Li_2Br(O^tBu)_4(THF)_2]_n$" (VII) (0.200 g, 0.340 mmol) were individually mixed with H_3PO_4 (0.033 g, 0.340 mmol) in 10 mL of ethylene glycol and then irradiated with microwaves for 15 min at 80 ºC and 10 min at 240 ºC using a CEM Discover SP microwave synthesiser (2.45 GHz). The resulting products were washed thoroughly with ethanol (30 mL × 2), acetic acid glacial 0.01 M in order to dissolve and remove the Li_3PO_4 formed during the microwave synthesis (10 mL × 1), distilled H_2O (10 mL × 3) and acetone (40 mL × 3). The products were then dried overnight in a vacuum oven at 80 ºC to yield the β-$LiFePO_4$_IV, α-$LiFePO_4$_V, $LiMnPO_4$_VI, $LiFe_{0.5}Mn_{0.5}PO_4$_VII, $LiFe_{0.5}Mn_{0.5}PO_4$_IV-VI and $LiFe_{0.5}Mn_{0.5}PO_4$_V-VI powders.

The β-$LiFePO_4$_IV, α-$LiFePO_4$_V, $LiMnPO_4$_VI, $LiFe_{0.5}Mn_{0.5}PO_4$_VII, $LiFe_{0.5}Mn_{0.5}PO_4$_IV-VI and $LiFe_{0.5}Mn_{0.5}PO_4$_V-VI samples were carbon coated as previously described in section 2.2.2.1 using 15% wt. C from sucrose (heat treatment for 1 hr at 700 ºC under Ar flow).

2.2.8 Ionothermal microwave synthesis of $LiFePO_4$ nanostructures using "$[FeLi_2Cl(O^tBu)_4(THF)_2]_n$" heterometallic alkoxide precursor

The heterometallic alkoxide precursor "$[FeLi_2Cl(O^tBu)_4(THF)_2]_n$" (V) (0.150 g, 0.280 mmol) was mixed with H_3PO_4 (0.027 g, 0.280 mmol) in 5 mL of ionic liquid 1-ethyl-3-methylimidazolium trifluoromethanesulfonate (EMI-TFMS) and then irradiated with microwaves for 10 min or 1 hr at 240 ºC using a CEM Discover SP microwave synthesiser (2.45 GHz). The resulting products were washed thoroughly with ethanol (30 mL × 2), acetic acid glacial 0.01 M in order to dissolve and remove excess Li_3PO_4 (5 mL × 1), distilled H_2O (10 mL × 3) and acetone (30 mL × 3). The products were then dried overnight in a vacuum oven at 80 ºC to yield the $LiFePO_4$_V_IL_10 min or $LiFePO_4$_V_IL_1 hr powders.

The $LiFePO_4$_V_IL_10 min sample was carbon coated as previously described in section 2.2.2.1 using 15% wt. C from sucrose (heat treatment for 1 hr at 700 ºC under Ar flow).

2.2.9 Solvothermal synthesis of $LiFe_{1-x}Mn_xPO_4$ nanostructures from "$[Fe_{1-x}Mn_xLi_2Br(O^tBu)_4(THF)_2]_n$" ($x$=0, 0.5 and 1) heterometallic alkoxide precursors

The heterometallic alkoxide precursors $FeLi_2Br(O^tBu)_4(THF)_2]_n$ (IV), "$[MnLi_2Br(O^tBu)_4(THF)_2]_n$" (VI) and "$[Fe_{0.5}Mn_{0.5}Li_2Br(O^tBu)_4(THF)_2]_n$" (VII) (0.400 g. 0.680 mmol) were individually weighed and mixed with H_3PO_4 (0.067 g, 0.680 mmol) in an Ar-filled glovebox and transferred into a Teflon lined stainless-steel autoclave with a capacity of 50 mL. After that, 30 mL of ethylene glycol were added. The mixture was stirred approximately for 30 min and then heated for 12 hr at 220 ºC in a Carbolite oven with a heating rate of 10 ºC/min. The resulting products were washed thoroughly with ethanol (30 mL × 2) and acetone (30 mL × 3). After that, the products were dried overnight in a vacuum oven at 80 ºC to yield the $LiFePO_4$_S_IV_12 hr, $LiMnPO_4$_S_VI_12 hr and $LiFe_{0.5}Mn_{0.5}PO_4$_S_VII_12 hr powders.

The $LiFePO_4$_S_IV_12 hr, $LiMnPO_4$_S_VI_12hr and $LiFe_{0.5}Mn_{0.5}PO_4$_S_VII_12 hr samples were carbon coated as previously described in section 2.2.2.1 using 15% wt. C from sucrose (heat treatment for 1 hr at 700 ºC under Ar flow).

In an effort to decrease the reaction time for the preparation of $LiFePO_4$ nanostructures, similar solvothermal reactions using a Teflon lined reactor were conducted at 1, 4, 8 and 10 hr at 220 ºC to yield the $LiFePO_4$_S_IV_1 hr, $LiFePO_4$_S_IV_4 hr, $LiFePO_4$_S_IV_8 hr and $LiFePO_4$_S_IV_10 hr products.

2.2.10 Solvothermal synthesis of $LiFePO_4$ nanostructures from commercial starting materials

$FeSO_4 \cdot 7H_2O$ (2 mmol, 0.556 g), $LiOH \cdot H_2O$ (4 mmol, 0.168 g) and H_3PO_4 (2 mmol, 0.196 g) were weighed and transferred into a Teflon lined reactor. After that, 30 mL of ethylene glycol were added. The mixture was stirred approximately for 30 min and then heated for 8, 10 or 12 hr at 220 ºC in a Carbolite oven with a heating rate of 10 ºC/min. The resulting products were washed thoroughly with ethanol (30 mL × 2) and acetone (30 mL × 3). The products were dried overnight in a vacuum oven at 80 ºC to yield the $LiFePO_4$_S_Com._8 hr, $LiFePO_4$_S_Com._10 hr and $LiFePO_4$_S_Com._12 hr powders.

The $LiFePO_4$_S_Com._12 hr phase was carbon coated as previously described in section 2.2.2.1 using 15% wt. C from sucrose (heat treatment for 1 hr at 700 ºC under Ar flow).

2.2.11 Ultrasonic-assisted synthesis of Fe_3O_4 magnetite from $[FeLi_2Br(O^tBu)_4(THF)_2]_n$ heterometallic alkoxide precursor

The remaining $[FeLi_2Br(O^tBu)_4(THF)_2]_n$ (IV) and LiBr precipitate was hydrolysed with 60 mL of degassed H_2O and kept in the ultrasonic bath for 1 hr at room temperature to afford nanostructured Fe_3O_4 magnetite. The addition of degassed H_2O and the ultrasonic treatment were repeated 4 times. After that, the obtained precipitate was washed again 4 times with 30 mL of distilled H_2O to completely remove the remaining LiBr.

The Fe_3O_4 nanoparticles were mixed with 15% wt. C from sucrose and thoroughly ground. The mixture was heat treated in a tube furnace for 3 hr at 500 ºC under Ar atmosphere to yield C/Fe_3O_4 nanoparticles.

2.2.12 Microwave synthesis of $C/LiFe_{1-x}Ni_xPO_4$ (x=0.05, 0.2, 0.15 and 0.2) nanostructures from heterometallic alkoxide precursor "$[FeLi_2Cl(O^tBu)_4(THF)_2]_n$"

Stoichiometric amounts of heterometallic alkoxide precursor "$[FeLi_2Cl(O^tBu)_4(THF)_2]_n$" (V), $NiC_2O_4 \cdot H_2O$, H_3PO_4 and 10, 15 or 20 transition metal weight % of PVP were thorougly mixed in 10 mL of ethylene glycol and then irradiated with microwaves for 1 hr at 240 ºC using a CEM Discover SP microwave synthesiser (2.45 GHz). The resulting products were washed thoroughly with ethanol (30 mL × 2), acetic

acid glacial 0.01 M in order to dissolve any Li_3PO_4 formed during the microwave synthesis (5 mL × 1), distilled H_2O (10 mL × 3) and acetone (30 mL × 3). The powders were then dried overnight in a vacuum oven at 80 °C to yield the $LiFe_{0.95}Ni_{0.05}PO_4$, $LiFe_{0.9}Ni_{0.1}PO_4$, $LiFe_{0.85}Ni_{0.15}PO_4$ and $LiFe_{0.8}Ni_{0.2}PO_4$ nanostructures. Similar reactions for the preparation of $LiFe_{0.95}Ni_{0.05}PO_4$ were conducted using the "$[NiLi_2Cl(O^tBu)_4(THF)_2]_n$" heterometallic alkoxide precursor as Ni source. Finally, the powders were heat treated in a tube furnace for 1 hr at 700 °C under Ar flow in an effort to carbonise the PVP and form a uniform and thin carbon coating without the need of any additional carbon source.

The same synthetic procedure was followed for the preparation of $LiMn_{0.95}Ni_{0.05}PO_4$ nanostructures. Stoichiometric amounts of heterometallic alkoxide precursor "$[MnLi_2Br(O^tBu)_4(THF)_2]_n$" (VI), $NiC_2O_4{\cdot}H_2O$, H_3PO_4 crystalline and 15 transition metal weight % of PVP were thoroughly mixed in 10 mL of ethylene glycol and then irradiated with microwaves for 1 hr at 240 °C. The obtained powders were also heat treated for 1 hr at 700 °C under Ar to carbonise the PVP.

2.2.13 Ultrasound-assisted synthesis of C/NiO from "$[NiLi_2Cl(O^tBu)_4(THF)_2]_n$" alkoxide precursor

The remaining "$[NiLi_2Cl(O^tBu)_4(THF)]_2$" (VIII) and LiCl precipitate was hydrolysed with 40 mL of degassed H_2O and then irradiated with ultrasound for 1 hr at room temperature. The H_2O was slowly evaporated by heating at 120 °C under vigorous stirring. After that, the dry precipitate was mixed with 15% wt. C from sucrose and a mixture 1:1 V:V of distilled H_2O:ethanol was added. The suspension was sonicated for 20 min and then the solvent was slowly evaporated by heating under vigorous stirring. The C/NiO powders were obtained by a heat treatment for 3 hr at 500 °C under air.

2.3 Characterisation methods

2.3.1 Structural characterisation

The main purpose of structural analysis is to relate the atomic structure to the properties displayed by the material, enabling the understanding of the materials properties from the atomistic point of view. This understanding can lead to important improvements of the material or even the design of new ones with enhanced properties. Various analytical techniques are required to fully characterise the nanomaterials on all length scales.

2.3.1.1 Powder X-ray diffraction (PXRD)

Powder X-ray diffraction (PXRD) is one of the most powerful characterisation tools and is a non-destructive technique for characterising the atomic structure of crystalline materials. It allows phase identification of a crystalline material and determination of the unit cell dimensions. The term "powder" relates to crystalline domains which are randomly oriented in the sample. In a PXRD experiment, the material under investigation

is finely ground, homogenised and the average bulk composition is determined. A monochromatic X-ray beam is focused onto a sample. Usually, crystalline materials are composed of repeating and uniform atomic planes which constitute their crystal structure. Polychromatic X-rays are normally produced within a closed tube under vacuum. Application of 15-60 kV current within the tube releases electrons which hit a Cr, Fe, Co, Cu, Mo or Ag anode, from which X-ray beams are generated. For X-ray diffraction, the metal most frequently used is copper. Copper emits two distinct wavelengths of X-rays, K_α and K_β, due to electrons decaying from the 2*p* and 3*p* orbitals. However, for diffraction purposes only K_α is selected and this is accomplished by passing the X-ray beam through a monochromator. Copper is generally chosen as the X-rays that are produced have a wavelength of 1.5406 Å, which is in similar size to the spacing of atoms in a crystal lattice. After filtering the polychromatic X-rays through a monochromator, monochromatic X-rays are produced, which are then collimated and directed onto the powder sample. Interactions of the incident X-rays with the samples create diffracted, transmitted, refracted and absorbed beams according to Bragg´s law:

$$n\lambda = 2d\ sin\theta \qquad (2.1)$$

where *n* is an integer defining the order of the diffracted beam, λ represents the wavelength of the incident X-ray beam, *d* marks the distance between near atomic planes or *d*-spacing, and θ represents the angle of incident X-rays. Figure 2.1 depicts a schematic illustration of the Bragg´s law condition.[205] Two beams with identical wavelength phase are directed towards a crystalline solid and are scattered by two different atoms within it. The lower beam traverses an extra length of 2*d*sinθ. Constructive interference occurs when this length is equal to an integer multiple of the radiation wavelength.[206]

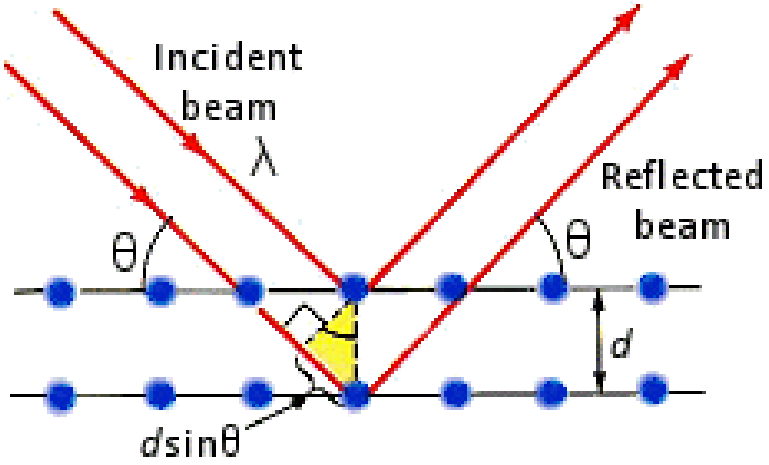

Figure 2.1. Schematic illustration of Bragg´s law condition.[206]

The degree of diffracted X-rays directly depends on the arrangement of the material's atomic planes within the crystal lattice. Bragg's law correlates diffraction angle and lattice atomic planes spacing at a specific wavelength of the electromagnetic radiation.

A detector is used to measure diffracted X-rays followed by processing and counting of the diffracted rays to give rise the diffracted pattern. Typically materials are identified by comparing the diffracted pattern beams with several reference patterns gathered in databases. In particular, the powder diffraction patterns of most inorganic solids can be found on the *Inorganic Crystal Structure Database (ICSD)*.[207] Diffraction data are a set of intensity values measured at specific momentum transfer *Q* values which are usually expressed as degrees 2θ. PXRD analysis can provide information about material's identity, crystallinity, residual stress and textural features with minimum invasion. As a popular analytical tool, PXRD has widespread applications in a wide range of fields such as geology, pharmaceuticals, materials, polymers and environmental and forensic science.[206]

The crystallite size can be estimated from the resulting PXRD pattern using the Scherrer equation. The Scherrer equation is a formula that relates the size of sub-micrometre particles, or crystallites, in a solid to the broadening of a peak in a PXRD pattern.[208] The mathematical formula can be written as equation 2.2:

$$\tau = \frac{K\lambda}{\beta \cos\theta} \qquad (2.2)$$

where τ is the mean size of the ordered (crystalline) domains, which may be smaller or equal to the grain size; *K* is a dimensionless shape factor, with a value close to unity. The shape factor has a typical value of about 0.9, but varies with the actual shape of the crystallite; λ is the X-ray wavelength; *B* is the broadening at half the maximum (FWHM), in radians and θ is the Bragg angle.

PXRD characterisation of the materials in this thesis were carried out using a PANalytical X' Pert powder diffractometer using Cu Kα radiation operated at 40 kV and 40 mA. The diffraction data were collected in the 2θ range between 10 and 70 ° in steps size of 0.02 (2θ) and an integration time of 2 s per step. When longer scan times were required, a step size of 0.00128 (2θ) was used. The samples are mounted in a flat plate spinner stage or in a glass slide bracket stage depending on the amount of sample available.

2.3.1.1.1 Rietveld Method

To have a complete structural analysis of a material, a structure refinement is often required in order to asses how well the collected diffraction data agrees with a structural model. A structural analysis based on the Rietveld method is usually used to fit powder X-ray and neutron diffraction data. Rietveld analysis is a sophisticated form of crystallographic modeling that consists on fitting a structural model (or known crystal structure) to a powder diffraction data using a least squares minimisation algorithm. The method considers the entire powder X-ray diffraction pattern and by varying an array of refinable parameters aims to deliver a fitted structure. This process requires determining the structural parameters (unit cell, atom positions and displacement/thermal parameters, etc.) for all crystalline phases present, as well as different instrumental and

sample parameters that describe the experimental and sample conditions: scale factor, the background, peak broadening, atomic positions, thermal factors, preferred orientation, etc. In most cases, Rietveld analysis is mainly performed to determine the lattice parameters, but increasingly, the method is also employed to estimate relative amounts of the crystallographic phases, the amount and type of peak broadening, the preferred orientation or similar types of sample characterisation.[209]

Rietveld analysis works by using non-linear least-squares fitting in order to optimise several instrumental and sample parameters. The refinement process must start with approximate values for all parameters that will be fit and this fit is subsequently optimised by allowing variation of a small subset of the parameters. The refinement is finally complete once a minimum difference between the calculated and observed profiles is reached. The process only works well if the starting model is sufficiently good. Scale factor, zero point, lattice parameters, atomic positions and thermal factors are frequently iteratively refined. During the refining process, statistical values are employed to judge the goodness of a refinement and the level of agreement between observed and calculated structure factors, which is often indicated by R factors and the Goodness of Fit (GoF) values. The Rietveld algorithm optimises the model function to minimise the weighted sum of squared differences between the observed and computed intensity values, for example, to minimise $\Sigma_i w_i(Y_{C,i}-Y_{O,i})^2$, where the weight labelled as w_i is $w_i=1/\sigma^2[Y_{O,i}]$, $\sigma^2[Y_{O,i}]$ is an uncertainity estimate for $Y_{O,I}$, i is the step, w_i is the weight, $Y_{O,i}$ is the observed intensity and $Y_{C,i}$ is the calculated intensity. The most straightforward discrepancy index, the weighted profile R-factor (R_{wp}), derives directly from the square root of the quantity minimised, scaled by the weighed intensities: $R_{wp}^2= \Sigma_i w_i(Y_{C,i}-Y_{O,i})^2/ \Sigma_i w_i(Y_{O,i})^2$. The best possible R_{wp} value is the expected R factor (R_{exp}). R_{exp} is calculated with this expression $R_{exp}^2= N/ \Sigma_i w_i(Y_{O,i})^2$, being N the number of data points. The smaller the R_{wp} and R_{exp} values implies a better fit. Also, the goodness of fit can be determined from the expected and weighed profile R factors as $x^2=(R_{wp}/R_{exp})^2$.[210-212] The value of x^2 indicates a better fit when is closer to 1. Visual inspection of the fit can also give an indication of how good is the fit.

Throughout this thesis, in the Rietveld fits the observed intensity $Y_{obs.}$ (experimental data) and the calculated intensity $Y_{calc.}$ will be represented by blue circle signs and an orange solid line, respectively. The grey curve at the bottom will represent the residual difference, $Y_{obs.}$-$Y_{calc.}$.

2.3.1.2 Synchrotron powder X-ray diffraction

A synchrotron is a circular particle accelerator and an extremely powerful source of X-rays. It works by accelerating charged particles (electrons) through sequences of focusing and bending magnets until they reach almost the speed of light. These fast-moving electrons generate very bright light (predominantly in the X-ray region), which is

millions of times brighter than light produced from conventional sources. When it comes to data quality, synchrotron X-ray diffraction can be generally superior to laboratory XRD in terms of angular resolution, counting statistics, energy tunability and fast acquisition time.

High resolution synchrotron powder X-ray diffraction (PXRD) were collected at room temperature at the I11 beamline at Diamond Light Source using 0.5 mm diameter glass capillaries using the multi-analysing crystal (MAC) system and robotic sample changer. Data were collected at an angular range of 2θ=3-150°, binned at 0.001° step and a scan time of 30 min. These high intensity X-rays (λ=0.825704 Å) can probe more deeply into the sample than conventional laboratory diffractometers and allow one to perform a more detailed structural analysis of materials. Using these high intensity X-rays is especially beneficial because the common problem of fluorescence from Fe rich samples typically observed when using a Cu Kα source can be avoided. Furthermore, unit cell parameters can be more accurately determined and the presence of impurity phases or phase segregation can be examined more in detail.

2.3.1.3 High resolution powder neutron diffraction (PND)

Neutron diffraction or elastic neutron scattering experiments aim to determine the atomic and/or magnetic structure of a material. The sample to be studied is placed in a beam of neutrons to obtain a diffraction pattern that provides valuable information of the material under investigation. When a beam of neutrons is slowed down and selected properly by their speed, their wavelength lies near one angstrom (0.1 nanometer), the typical separation between atoms in a solid material. Impinging on a crystalline sample the beam will scatter under a limited number of well-defined angles according to Bragg´s law.[213] Whereas X-rays are scattered from the electron cloud of the atoms, neutrons are scattered primarily by atomic nuclei. Furthermore, in the special case of magnetic materials, neutrons are also scattered by the interaction of the neutron magnetic moment with the magnetic moment(s) of the atoms. This means that the scattering power of an atom is not strongly related to its atomic number, unlike X-rays where the scattering power increases in proportion to the number of electrons in the atom. This has three main advantages: (i) It is easier to sense light atoms, such as hydrogen or lithium, in the presence of heavier ones. (ii) Neighbouring elements in the periodic table generally have substantially different scattering cross sections and can be distinguished (for example Fe and Mn). (iii) The nuclear dependence of scattering allows isotopes of the same element to have substantially different scattering lengths for neutrons. Isotopic substitution can be used to label different parts of the molecules making up a material. Moreover, the interaction of a neutron with the nucleus of an atom is weak, making them a highly penetrating probe and allowing the investigation of the interior of the materials rather than the surface layer probed by techniques such as X-ray scattering. Therefore, neutrons

are a non-destructive probe even to complex and delicate biological or polymeric samples. In addition, neutrons are weakly absorbed by most of the materials and the atom scattering power remains approximately constant with the angle.[214] Neutrons are produced by accelerating "bunches" of protons in a synchrotron and then colliding these with a heavy tungsten metal target under a constant cooling load to dissipate the heat from the 160 kW proton beam.

In particular, time-of-flight (TOF) neutron diffraction employs a polychromatic beam and a pulsed source of neutrons and exploits the fact that a neutron's wavelength is inversely proportional to its velocity, as postulated by the De Broglie relationship. Long-wavelength neutrons are slower than short-wavelength neutrons and take more time to travel from the source to the detector. A TOF neutron diffraction experiment is carried out at a fixed angle and varying the energy (or wavelength) of the incident neutrons. The energy dispersion is obtained by measuring the time-of-flight *t* that a neutron takes to cover the distance *L* from the source to the detector. Under the assumption that the neutrons do not suffer a change in the energy during the scattering process, the time-of-flight values are directly related to the distance *d* between the crystallographic planes. By measuring the arrival time of each neutron of a particular pulse in the detector, its wavelength and the corresponding *d*-spacing of the diffracting planes can be calculated using the following equation 2.3:

$$\lambda = {}^{h}/_{m_n} = {}^{ht}/_{m_n L} = 2d\,\sin\theta \qquad (2.3)$$

where *t* is the time-of-flight and *L* is the length of the flight path.[215, 216] TOF instruments have no moving detectors, which can be an advantage with complex sample environments, such as high-pressure cells, where fixed entrance and exit windows can be designed into the apparatus. Banks of detectors covering a large proportion of the volume around the sample are common in TOF experiments.

High resolution powder neutron diffraction (NPD) data were collected at the Polaris beamline at the UK pulsed spallation neutron and muon source ISIS, at Rutherford Appleton Laboratory. The Polaris instrument is a high intensity, medium resolution powder diffractometer optimised for rapid structural characterisation, with the collection of data sets in short periods of times down to ~5 min. Isotopically enriched lithium (^{7}Li) was used to prepare samples because of its lower neutron absorption cross section and to remove uncertainties in the correct bound coherent neutron scattering length that can exist with natural lithium. This can greatly improve data quality because the natural abundance of 7.5% of ^{6}Li can cause about $1.5 \cdot 10^{4}$ larger absorption, about 15% decrease of coherent scattering length and larger incoherent scattering.[56] Approximately 3 g of sample was transferred into vanadium cans (8 mm in diameter), which were loaded into a cryostat. Ideally the container should be made of a purely incoherent scattering

material such as vanadium, which hardly scatters neutrons. This material is needed otherwise the Bragg reflections from the container can be difficult to subtract completely.

2.3.1.4 X-ray and neutron pair distribution function (PDF)

Perfectly periodic materials are generally well described by traditional crystallographic characterisation techniques but, nowadays novel materials and their properties usually exhibit varying degrees of disorder, requiring alternative characterisation methods in which Bragg analysis can be complemented by local structure analysis. Therefore, new experimental techniques probing local structure details have gained increased importance in the crystallographic investigation.[217-219]

Traditionally, the local structure analysis of crystalline materials has been usually examined by extended X-ray absorption fine structure (EXAFS) and solid state nuclear magnetic resonance (NMR), which have different targets and sensitivities in comparison with crystallographic methods. The dominant contribution to these techniques is given by the structural correlations between nearest neighbours, providing very useful information on the coordination environment with respect to a reference atom but, on the other hand, they are unable to provide any information regarding longer distances. As a result, this difference in target information sometimes generates structural results which could be apparently in contradiction between EXAFS/NMR and crystallography.[220] In this context, the need for a probe which can act as a bridge between the two domains of the average and local structures, providing an effective description of the structure of a material on different length scales considering both the long range order and the possible deviation from it at the local level, is evident. In order to meet this need, new experimental approaches have been recently developed. In particular, total scattering methods coupled with the pair distribution function analysis (PDF) are gaining a more central role in the understanding of the structure–property correlation of complex materials. It is clearly needed to go beyond the analysis of Bragg scattering and to explore the local atomic structure using total scattering techniques, which take into account both, Bragg and diffuse scattering. The Bragg component in the diffraction pattern reveals information about the average and periodic structure of a material. However, diffuse scattering is originated from scattering arsing from any kind of departures from perfectly regular units and it contains valuable information regarding local deviations from the average structure. Diffuse scattering often appears as a smooth background in the diffraction pattern and mainly dominating at higher scattering angles. The limitation of conventional crystallographic structure solution approaches is the fact that it only yields the long range average structure of the material. Furthermore, the atomic structures of nanostructured materials are not always accessible by conventional crystallographic methods because of the absence of long-range order. Nowadays, this drawback is known as the “nanostructure problem”, as traditional crystallography breaks down on the nanoscale. For this reason

total scattering methods such as pair distribution function (PDF) are needed to elucidate the structures of nanostructured and complex materials.[221] The study of both Bragg and diffuse scattering provides information about the local atomic arrangements, a key factor to understand increasingly complex materials. The PDF technique is therefore an essential complement to the traditional crystallographic approaches for structure determination that are mostly sensitive to the long-range ordering in materials and gives information on the atom-atom distance.

The pair distribution function analysis method is a powerful tool for the study of glasses, liquids and amorphous materials, as well as crystalline or partly crystalline materials. The pair distribution function analysis involves the direct Fourier transformation of X-ray or neutron total scattering data giving the probability of finding any two atoms at a given interatomic distance. Therefore, the PDF represents basically a histogram of interatomic spacings weighted by the relative concentration and scattering power of the different atom types present in the sample. Recently, this method has found many applications in the study of local structure in both crystalline and non-crystalline materials, yielding crucial information about atomic-scale structures of nanosized and disordered materials in real space.[222] The position of a peak in the PDF indicates the existence of a pair of atoms with that separation. In crystals, because of the long-range order of the structure, all neighbors at all lengths are well defined and give rise to sharp PDF peaks. The positions of these peaks give the separations of pairs of atoms in the structure directly and the width contains information about thermal motion of the atoms, or static disorder. Moreover, when a well-defined PDF peak can be observed, it is possible to determine information about the number of neighbours in that coordination shell around an origin atom by integrating the intensity under that peak. Figure 2.2 illustrates a schematic of the PDF principle in which interatomic distances r cause maxima in the PDF $G(r)$.

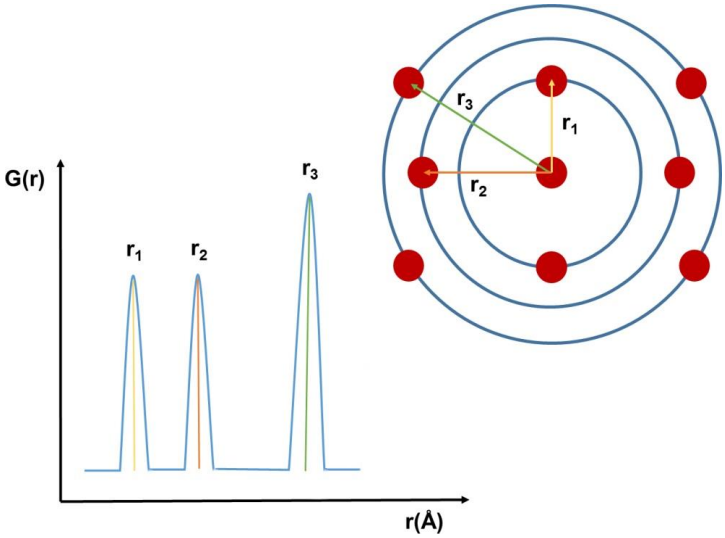

Figure 2.2. Principle of the PDF. Interatomic distances r_i cause maxima in the PDF G(r). The area below the peaks correspond to the number of neighbors, scaled by the scattering power of the respective atom.

The atomic PDF, G(r), is defined as equation 2.4:

$$G(r) = 4\pi[\rho(r) - \rho_0] \quad (2.4)$$

where ρ_o is the average atomic number density, $\rho(r)$ is the atomic pair density and r is a radial distance. The function G(r) gives information about the number of atoms in a spherical shell of unit thickness at a distance r from a reference atom. It peaks at characteristic distances separating pairs of atoms. G(r) is an experimentally accessible function and it is related to the measured X-ray or neutron powder diffraction pattern through a Fourier transform. PDFs are calculated from the Fourier transformation of the normalised scattering function S(Q) as described in equation 2.5:

$$G(r) = \frac{2}{\pi}\int_0^\infty Q[S(Q) - 1]\sin(Qr)\,dQ \quad (2.5)$$

where S(Q), the total scattering structure function, contains the measured intensity from an isotropic sample. Q is the magnitude of the scattering vector and is derived from the expression $Q=4\pi \sin(\theta)/\lambda$.

The structure function S(Q) is related to the coherent part of the total diffracted intensity of the material by the following equation 2.6:

$$S(Q) = \frac{I^{coh}(Q) - \sum c_i|f_i(Q)|^2}{\sum c_i|f_i(Q)|^2} + 1 \quad (2.6)$$

where $I^{coh.}(Q)$ is the measured scattering intensity from a powder sample that has been properly corrected for background and other experimental effects and normalised by the flux and number of atoms in the sample. Here, c_i and f_i are the atomic concentration and X-ray atomic form factor, respectively, for the atomic species of type i. In the case of neutron experiments the f's are replaced by Q-independent neutron scattering lengths, b, and the sums run over all isotopes and spin-states as well as over the atomic species. In PDF experiments, it is important to measure data over a wide range of momentum

transfer, Q, in order to obtain high accuracy and adequate real-space resolution of the PDF peaks. This implies that short wavelength, high energy X-rays or neutrons are required. X-rays of > 45 keV (λ = 0.27 Å) and up to 100 keV (λ = 0.12 Å) or more are typically used.[217, 223]

Here, data was collected using the Polaris diffratometer at ISIS. Data collected from all 5 detector banks was included to obtain the total scattering function *S(Q)* which was Fourier transformed using Q_{max}=36 $Å^{-1}$. Each data collection was run for 8 hr. Raw data were corrected for contributions from the background, empty container, attenuation, and multiple scattering to give the structure factor, *S*(*Q*), where the modulus of the scattering vector $Q=4\pi(\sin\theta)/\lambda$. Data processing including background subtraction to obtain *S(Q)* that can be Fourier transformed was carried out using GudrunN.[224] High Q_{max} values are required, which results in the data extending over a wider range of *r*. High-momentum transfers leads to high-real space resolution at short interatomic distances in the pair distribution function, which significantly aids to accurately distinguish between two average bond distances that are very close together. Moreover, termination ripples and other artefacts coming from improper data normalisation are not a problem if data are collected to high enough Q_{max} values. In order to reach higher Q_{max} it is necessary to use short wavelength particles, which can be obtained with higher energy X-rays and epithermal neutrons. Finally, the radial distribution function, G(*r*), was obtained from the Fourier transformation of *S*(*Q*) using stog programme.[225]

An X-ray total scattering experiment is very similar to a standard X-ray powder diffraction experiment. However, to interpret the diffuse scattering signal in the data and thus obtain information about local structural order, it is necessary to obtain data to high values of momentum transfer Q (< 16 $Å^{-1}$, where $Q=4\pi\sin\theta/\lambda$). As mentioned before, the Q_{max} value affects the resolution of data analysis in real space on the order of $\Delta r \approx \pi/Q_{max}$ and for this reason, high energy X-rays (40-100 keV) are required for total scattering experiments. In general, the rapid acquisition PDF (RA-PDF) method is usually applied, in which a large 2D detector combined with a small distance between sample and dectector ensures fast data collection as well as good counting statistics at high Q-values.[226] X-ray diffraction experiments were conducted using X-rays of energy 65.7065 keV (λ = 0.188682 Å) on the XPD beamline at National Synchrotron Light Source (NSLS), Brookhaven National Laboratory. The high energy X-rays were used to extend the region of reciprocal space covered, which is required for high real-space resolution in the PDF. The data collection time was 20 min for each sample. Fit2D was used to integrate and convert 2D data to 1D intensity versus wave vector (Q).[227] The sample-to-detector distance, the beam center position and the tilt angles of the detector, relative to the beam path, were calibrated using a Si standard. X-ray PDFs were calculated at Q_{max} = 18 $Å^{-1}$ using xPDFsuite programme.[228] Both the neutron and X-ray PDFs were modelled individually to an average

olivine structure using PDFgui software.[229] The structure was modeled as for the Rietveld refinements, however with the difference that the metal occupancies were not refined. The pair distribution *r*-ranges from 1–5 Å, 1–15 Å and 5–30 Å were considered in the analysis. The scale factor, the structural parameters (lattice parameters and atomic positions) and the quadratic dynamic correlation factor (delta2) were refined. For the X-ray PDF analysis, the two instrumental resolution parameters, the damping (Q_{damp}) and broadening (Q_{broad}) factors, were fixed in the fits. These parameters (Q_{damp}=0.0284 $Å^{-1}$; Q_{broad}=0.0095 $Å^{-1}$) were derived by fitting the PDF of a Si standard. For the neutron data, Q_{damp} and Q_{broad} were allow to refine in the 5–30 Å *r*-range model and kept fixed in the obtained values for the 1–5 Å and 1–15 Å *r*-ranges. Q_{broad} models the PDF peak broadening and Q_{damp} the intensity dampening, both as a result of the Q resolution of the diffractometer.

The progress of the refinement is assessed by computing a reliability factor, R_w, which is calculated from equation 2.7:

$$R_w = \left(\frac{\sum w_i \left(G_i^{exp} - G_i^{calc} \right)^2}{\sum w_i \left(G_i^{exp} \right)^2} \right)^{1/2} \qquad (2.7)$$

where G_i^{exp} and G_i^{calc} are the experimental and calculated PDFs, respectively, and w_i are weighting factors reflecting the statistical quality of the individual data points. Real space Rietveld analysis was also performed to obtain information on the cell parameters and atomic positions.

2.3.1.5 Single crystal X-ray diffraction (SCXRD)

Single crystal X-ray diffraction (SCXRD) is a non-destructive structural characterisation technique which provides detailed information about the crystalline lattice of compounds including unit cell dimensions, bond lengths, bond angles and details of site-ordering. However, it is generally more complicated and time consuming (data collection generally takes between 24 and 72 hours) than PXRD. Furthermore, it requires higher degree of homogeneity of the selected crystal. Samples for single crystal diffraction should be unfractured and optically clear crystals, ideally of between 150 and 250 microns in size. The crystal is carefully mounted into the goniometer head and the X, Y and Z directions adjusted until the sample is centered for all crystal orientations. A single crystal refinement of the data generated is then conducted to solve the crystal structure.[230]

SCXRD data were collected at 100 K on a Bruker APEX-II CCD diffractometer (Mo Kα radiation, λ=0.71073 Å) equipped with an Oxford Cryosystems N-Helix cooling device. The structure was solved using ShelXS and refined using full-matrix least-squares refinement on F^2 using SHELXL2014 in OLEX2.[231] All non-hydrogen atoms were refined with anisotropic atomic displacement parameters. All CH_2 hydrogen atoms were placed in geometrically

calculated positions and included in the refinement as part of a riding model, CH_3 hydrogen atoms were refined as part of a rigid rotor. All hydrogen atoms were assigned Uiso values at 1.5 (Ueq) for the parent carbon atom.

2.3.2 Electron microscopy

Electron microscopy is a powerful characterisation technique for the visualisation of nanoparticles and their atomic arrangement. An electron microscope uses a beam of accelerated electrons as a source of illumination.

2.3.2.1 Scanning electron microscopy (SEM)

A scanning electron microscope (SEM) generates images of a sample by probing its surface with a focused beam of electrons. The electrons interact with atoms producing various signals that contain information about the surface topography and composition of the sample. When the electron beam interacts with the specimen, it loses energy by a variety of mechanisms. The lost energy is converted into alternative forms such as heat, emission of low-energy secondary electrons and high-energy backscattered electrons, light emission (cathodoluminescence) or X-ray emission, all of which provide signals carrying information about the properties of the specimen surface, such as its topography and composition.[232]

SEM images were taken in a Philips XL30 ESEM tungsten filament electron microscope operating at an acceleration voltage of 20 kV. Powder samples were deposited onto conductive carbon tabs mounted on an aluminium stub and coated using a Polaron SC7640 plasma sputter coater with a 99:1 Au:Pt target in order to avoid charging feedback. High resolution scanning electron microscopy (HR SEM) analysis of the powders was conducted using a Carl Zeiss Sigma variable pressure analytical SEM with Oxford microanalysis. The operating voltage was between 5 and 15 kV and an In-lens secondary detector was used.

2.3.2.2 Energy-dispersive X-ray spectroscopy (EDS)

Energy-dispersive X-ray spectroscopy (EDS) is an analytical technique used for the elemental analysis of a sample. In this technique, a high-energy beam of electrons is focused onto the sample to stimulate the emission of characteristic X-rays from the specimen. In this process the incident beam may excite an electron from an inner shell, ejecting it from that shell while creating an electron hole. An electron from an outer, higher-energy shell may fill the hole, and the difference in energy between the higher-energy shell and the lower energy shell may be released in the form of X-rays. The energies and number of the emitted X-rays are characteristic of the difference in energy between the two shells and the atomic structure of the emitting element, allowing the elemental composition of the specimen to be examined.[233]

2.3.2.3 Transmission electron microscopy (TEM)

The transmission electron microscope (TEM) uses a high voltage electron beam to generate an image. The electron beam is generally produced by an electron gun, commonly fitted with a tungsten filament cathode as the electron source. The electron beam is then accelerated by an anode typically at ~100 keV with respect to the cathode, focused by electrostatic and electromagnetic lenses, and transmitted through the sample that is in part transparent to electrons and in part scatters them out of the beam. The emerging electron beam carries information about the structure of the specimen that is magnified by the objective lens system of the microscope. The spatial variation in the image may be viewed by projecting the magnified electron image onto a fluorescent viewing screen coated with a phosphor or scintillator material such as zinc sulfide. TEM studies are often subject to several important limitations. First, the sample to be examined must be electron transparent, meaning that the sample thickness should be of the order of 100 nm or less. Careful and time consuming sample preparation may therefore be required. Furthermore, many samples are vulnerable to radiation damage caused by the incident beam of electrons.[234]

Because the wavelength of high-energy electrons is a few thousandths of a nanometer and the spacing between atoms in a solid is around a hundred times larger, the atoms can act as a diffraction grating to the electrons. Therefore, some fraction of the electron beam will be scattered to specific angles determined by the crystal structure of the sample while others will continue to pass through the sample without deflection. As a result, the image shows a series of spots corresponding to the satisfied conditions of the sample´s crystal structure. An aperture in the image plane is used to select the diffracted region of the specimen, providing site-selective diffraction analysis. Selected area of electron diffraction (SAED) patterns are a projection of the reciprocal lattice, with lattice reflections showing sharp diffraction spots. Single diffraction spots appear only when the electron beam is diffracted by a single crystal. Polycrystalline materials give generally ring patterns analogous to those from PXRD.[235]

TEM and SAED were performed on a FEI Tecnai TF20 microscope in the School of Physics and Astronomy at Glasgow University. The microscope is fitted with a field emission gun, operated at 200 keV. A reduced TEM excitation voltage of 120 kV is sometimes used to reduce the rate of sample damage. The spherical aberration coefficient is 1.2 mm, giving a point resolution of 2.4 and line resolution of 1.5. Powder samples were dispersed in ethanol, sonicated for 2 min and the resulting solution was then dropped onto an amorphous holey carbon coated grid. Finally, the samples were heated at 80 ºC for ~10 min in an oven to evaporate residual solvents.

2.3.3 Muon spin relaxation (μ^+SR)

Muon spin relaxation (μ^+SR) has been used as a local magnetic probe in magnetism, superconductivity and charge transport studies. Spin relaxation in solids is subject to essentially the same processes as for the case of nuclear magnetic resonance. μ^+SR technique is based on the implantation of spin polarised muons in matter and the detection of the influence of atomic, molecular or crystalline surroundings on the muon spin motion. Muons stop at interstitial sites and decay with a mean lifetime of 2.2 μs. Whilst implanted in the sample, the muon spin direction is affected by the local magnetic field at the muon stopping site or by species diffusing nearby. After 2.2 μs the muon decays into a positron and two neutrinos. The positron is preferentially emitted in the direction of the muon spin at the instant of the decay and the time evolution of the muon polarisation can be measured by detecting the position of the decayed positrons. The muon spin polarisation is then followed as a function of time by measuring the asymmetry in the count rate of the decaying positrons, *a (t)*, in two detector banks located on opposite sides of the sample. Figure 2.3 illustrates the fundamental working principle of a μ^+SR experiment.

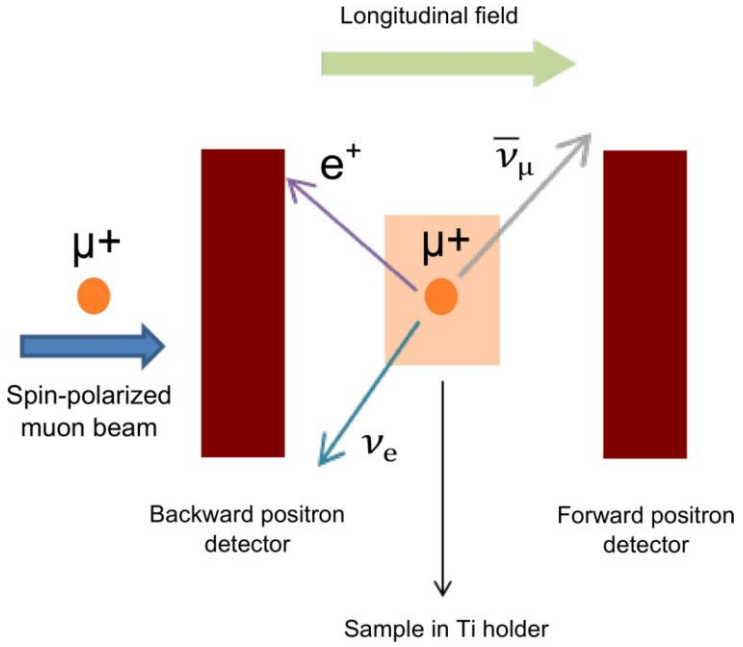

Figure 2.3. Schematic of a μ^+SR experiment. A spin-polarised beam of muons is implanted in the sample. After muon decay, positrons are detected by the forwards and backwards detector.

The time evolution of the muon polarisation can be obtained by studying the number of positrons detected in the backward and forward detectors, and the difference between these normalised functions is the asymmetry function *a(t)*, which is described by the following equation 2.8:

$$a(t) = a_0 G_z(t) = \frac{N_F(t) - \alpha N_B(t)}{N_F(t) + \alpha N_B(t)} \qquad (2.8)$$

with a_0 being the initial asymmetry, $G_Z(t)$ the depolarisation function (defined as the average spin polarisation of an ensemble of muons spin at time t after the implantation of muons), N_F and N_B the number of decay positrons detected by the forward and backwards counters, respectively, and a an experimental constant that is dependent on sample position and detector efficiencies.

Since lithium diffusion is one of the primary parameters that govern the charge and discharge rates in LIBs, the μ^+SR technique has been employed here to probe the microscopic Li^+ diffusion properties. As well as being a sensitive probe of magnetic ordering, μ^+SR provides a means of investigating diffusion processes of both the muon and other species that perturbs its environment such as the Li^+ diffusion process. The transport of ions is a very complex process and a deeper understanding of the Li^+ dynamics in the electrode nanostructures for Li-ion batteries is needed. Previous investigations have proved that Li^+ diffusion can perturb the muon decay process and yield information about the Li^+ kinetics.[236] The Li^+ diffusion coefficient and the activation energy for that process are key factors in helping to understand the electrochemical performance of electrode materials in Li-ion batteries. Muons are produced in a variety of high energy processes and elementary particle decays, however, the μ^+SR technique requires low energy muons that will stop in the samples being studied. Low energy muons are available in the required intensities only from ordinary two-body pion decay. Pions are produced in sufficient numbers from collisions of high-energy protons (>500 MeV) with the nuclei of an intermediate target. A light element such as carbon or beryllium is used for the primary target in order to maximise pion production, while minimising multiple scattering of the proton beam. The charged pions that are produced live for only about 26 billionths of a second and then they decay into a muon and muon neutrino.[236]

μ^+SR experiments were carried out using the EMU instrument at the ISIS pulsed neutron and muon source and data was analysed using the WIMDA program.[237] EMU is a 96-detector μ^+SR spectrometer optimised for zero field and longitudinal field measurements. In this instrument fields of up to 4500 G can be applied and sample temperatures in the range of 50 mK to 1500 K can be produced using a variety of sample environment equipment.[238] The samples were placed in titanium sample holders with a titanium foil window. Ti depolarises muons very weakly and allows an easy subtraction of the background. Measurements were carried out over a temperature range from 100 K to 400 K and at ZF (zero field) and LF (longitudinal field) of 5, 10 and 20 G. This temperature range was chosen because it includes the thermally activated region in which an increase in the lithium diffusion is observed. By applying different longitudinal magnetic fields parallel to the direction of the beam, any interactions between the muon and the local magnetic field distribution of the Fe and Mn magnetic moments can be eliminated. Furthermore, multiple magnetic field measurements at each temperature give more reliable

determinations of simultaneously fitted parameters. In previous muon spin resonance studies on $LiFePO_4$ samples, it was shown that a magnetic field of 10 G was strong enough to decouple the Fe(II) magnetic moment. However, in the present experiments, due to the presence of Mn in these materials, more intense magnetic fields were required to decouple the contributions coming from Mn and data were also collected at 20 G. Before collecting the μ^+SR data for any new compound, measurements at applied TF (transverse field) of 20 G are required in order to obtain the calibration constant α_c and the background; otherwise, no reliable study when fitting the μ^+SR data can be performed.

2.3.4 Electrochemical characterisation

Electrochemistry studies the loss of electrons (oxidation) or gain of electrons (reduction) that a material undergoes during the electrical stimulation. These reduction and oxidation reactions are commonly known as redox reactions and can provide information about the concentration, kinetics, reaction mechanisms and chemical status of the species under investigation.

2.3.4.1 Galvanostatic cycling with potential limitations (GCPL)

Galvanostatic cycling with potential limitation (GCPL) is a standard potentiodynamic technique used to investigate the electrochemical performance and cycling life of battery materials. GCPL experiments rely on the application of a constant current to a cell while the evolution of potential is measured. It is the most widely used tool to evaluate the ability of battery materials to retain their capacity upon extended cycling. Several charge and discharge cycles are performed at constant current over a set voltage range. The performance of a battery is determined as a function of its charge and discharge conditions: a given rate, within a given potential range. For batteries, the galvanostatic rate is usually expressed as C/h, with h being the number of hours at which the nominal charge or discharge of the battery will be passed through and C is the charge corresponding to the total expected reduction/oxidation of that electrode. Often the specific capacity of an electrode material is expressed per weight ($mAh \cdot g^{-1}$) and the galvanostatic rate in current per active material mass ($mA \cdot g^{-1}$). Therefore, knowing the electrode characteristics, the charge/discharge currents can be determined depending on the rate to be applied.[239] The battery capacity is the total number of mA·h that can be withdrawn from a fully charged cell under specified charge-discharge conditions. It is basically a measure of the charge stored by the battery and is determined by the mass of active material contained in it. In short, the battery capacity represents the maximum amount of energy that can be extracted from the cell under certain conditions. However, the energy storage capabilities of the battery can vary significantly from the theoretical capacity, as the battery capacity depends strongly on the charging or discharging regimes and the temperature.[240] For example, if the battery is being discharged very fast (the discharge current is high), then the amount of energy that can be extracted from the

battery is reduced and the battery capacity significantly decreases. This is mainly attributed to the fact that the required components for the reaction to occur do not necessarily have enough time to rearrange and only a fraction of the total reactants are converted to appropriate forms leading to a reduction of the energy available. On the other hand, if the battery is discharged at a very slow rate using a low current, more energy can generally be extracted from the battery and the battery capacity is higher.[240] For the particular case of $LiFePO_4$, the theoretical capacity can be determined by Faraday's law (Equation 2.9) knowing that the molecular weight (M_w) of $LiFePO_4$ is 157.76 $g \cdot mol^{-1}$, n = 1 (one e^- is exchanged in the process) and the Faraday constant (F) is 96485.3365 $sA \cdot mol^{-1}$

$$Q = \frac{nF \times 1000}{3600 \times Mw} \quad \mathrm{mAh} \cdot \mathrm{g}^{-1} \qquad (2.9)$$

The calculated theoretical capacity for the $LiFe_{1-x}Mn_xPO_4$ species is also ~170 $mAh \cdot g^{-1}$ due to the similar atomic weight of Fe and Mn.

Galvanostatic cycling experiments (constant current) of the electrode materials were conducted in a BioLogic VSP potentiostat using Swagelok type cells (Figure 2.4). The batteries were assembled in an Ar-filled glovebox using a pellet of the electrode material (active material:C black:PTFE 60:30:10 wt. % ratio), a Whatman glass microfiber filter as separator, 1 M lithium hexafluorophosphate ($LiPF_6$) in ethylene carbonate (EC) and dimethyl carbonate (DMC) 1:1 v/v as electrolyte and Li metal as counter electrode. High loading of conductive carbon reduces the volumetric energy but is effective in stabilising high rate capabilities of the active cathode material.[241] The cells were disassembled after electrochemical test in an Ar-filled glovebox and the active electrodes collected, thoroughly washed with dry THF and dried prior to powder XRD analysis to study structural changes in post-cycled materials.

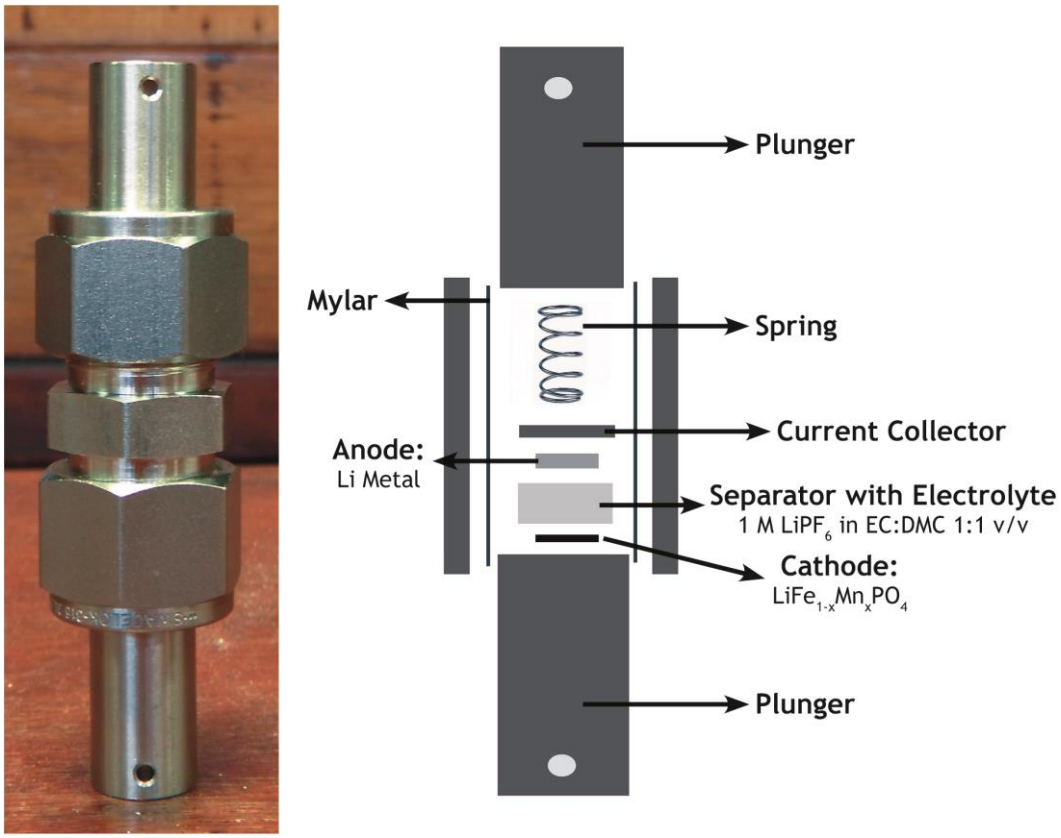

Figure 2.4. Schematic showing Swagelok battery set-up.

2.3.4.2 Cyclic voltammetry (CV)

Cyclic voltammetry (CV) is a common electrochemical technique used for the investigation of electroactive species. Its versatility combined with ease of measurement has resulted in extensive use of CV in the fields of electrochemistry, organic chemistry, inorganic chemistry and biochemistry. CV is a potentiodynamic electrochemical technique in which a cyclic linear potential sweep is imposed on the electrode and the resulting current is recorded. Once the set potential is reached, the working electrode's potential is ramped in the opposite direction in order to return to the initial potential. During the potential sweep, the potentiostat measures the current intensity resulting from the electrochemical reactions (consecutive to the applied potential). The CV is the current response at the working electrode as a function of the applied potential, as shown in Figure 2.5. This technique provides information about redox active processes offering a rapid determination of the redox potential of electroactive species. A typical CV plot shows four important values: the cathodic peak height (I_p^c), the anodic peak height (I_p^a), the cathodic peak potential (E_p^c) and the anodic peak potential (E_p^a).

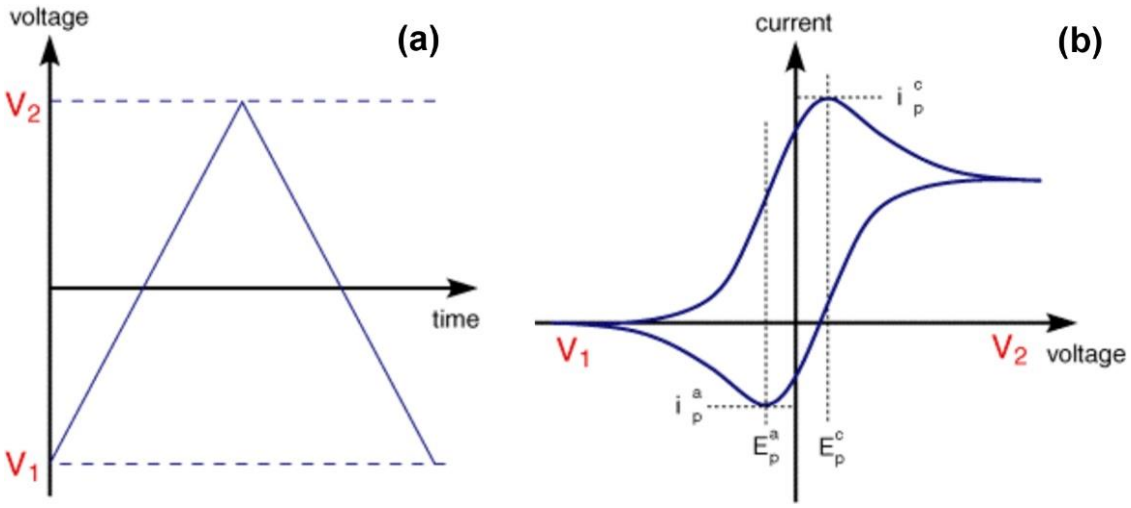

Figure 2.5. (a) In CV a voltage is swept between two values (V_1 and V_2) at a fixed rate. When the voltage reaches V_2 the scan is reversed and the voltage swept back to V_1. **(b)** Typical CV for a reversible single electrode transfer reaction containing only a single electrochemical reactant.[46]

When a redox couple is reversible, during the reverse scan the reduced species will start to be re-oxidised producing a current of reverse polarity. The more reversible the redox couple is, the more similar the oxidation peak will be in shape to the reduction peak. For a reversible electrochemical reaction, the recorded CV often has certain well defined characteristics: (i) the voltage separation between the current peaks is around 56 mV at 25 ºC ($\Delta E = E_p^a - E_p^c = \frac{56}{n} mV$) and the positions of peak voltage do not alter as a function of voltage scan rate, (ii) the ratio of the cathodic and anodic peak currents is unity $\left|\frac{I_p^a}{I_p^c}\right| = 1$ and (iii) the peak currents are proportional to the square root of the scan rate, based on a diffusion-controlled process.[242] Reversibility is generally greater at slower scan rates where there is ample time for the reacting species to reach equilibrium. For a reversible reaction, the diffusion equation can be solved under a linear voltage sweep condition to give a relationship between peak current (I_p) and diffusion constant (D), as shown in equation 2.10:

$$I_p = 0.4463F\left(\frac{F}{RT}\right)^{1/2} C v^{1/2} A D^{1/2} \qquad (2.10)$$

where I_p is the peak current in amperes, F is the Faraday constant, C is the initial concentration of Li in mol/cm^3 , v is scan rate in V/s, A is electrode area in cm^2 , and D is the diffusion constant in cm^2/s .[243, 244]

The cyclic voltammetry experiments were also conducted in a BioLogic VSP potentiostat using the same Swagelok cells as for the galvanostatic cycling tests.

2.3.5 Gas Uptake analysis

Brunauer-Emmet-Teller (BET) analysis allows for the study of the physical adsorption process of gas molecules on a solid surface, by providing a measurement of the specific surface area of the material under study by nitrogen multilayer adsorption

measured as a function of relative pressure. The technique encompasses external area and pore area evaluations to determine the total specific surface area in m^2/g, yielding important information in studying the effects of surface porosity and particle size. Barret-Joyner-Halenda (BJH) pore size and volume analysis can also be employed to determine specific pore volume using adsorption and desorption techniques. Physical adsorption results from relatively weak forces (van der Waals forces) between the adsorbate gas molecules and the adsorbent surface area of the test powder. The determination is usually performed at the temperature of liquid nitrogen. The amount of gas adsorbed can be measured by a volumetric or continuous flow procedure.[245, 246] For the gas uptake analysis, N_2 adsorption isotherms were conducted at 77 K using a Quantachrome Autosorb iQ gas sorption analyser. Samples were degassed under vacuum at 120 °C for 20 hours using the internal turbo pump. BET surface areas were calculated from the isotherms using the Micropore BET Assistant and pore-size distribution analysis was carried out using QSDFT (N_2 on carbon at 77 K, slit/cylindrical pore model) both in the Quantachrome ASiQwin operating software.

2.3.6 CHN elemental analysis

Elemental analysis is a process to determine the elemental and sometimes isotopic composition of a sample. This can be qualitative (determination of what elements are present), or quantitative (determination of how much of each element is present). CHN analysis is accomplished by combustion analysis of the sample where the sample is burned in excess oxygen and several traps are used to collect the combustion products: mainly carbon dioxide, water and nitric oxide. The masses of these combustion products can be then used to calculate the composition of the unknown sample.[247]

CHN analysis was conducted using an Exeter CE-440 Elemental analyser. To achieve a successful analysis approximately 5 mg of sample are required and the measurements are run in duplicate. For the results to verify the expected sample, the results must be within ±0.3% of the theoretical value.

2.3.7 Atomic absorption spectroscopy (AAS)

Atomic absorption spectroscopy (AAS) is a spectroanalytical technique used for the quantitative determination of chemical elements based on the absorption of optical radiation (light) by free atoms in the gaseous state. The sample is atomised using flames of electrothermal atomisers and then irradiated by optical radiation. The radiation passes through a monochromator in order to separate the element-specific radiation from any other radiation emitted, which is finally measured by a detector. The technique makes use of the absorption spectrometry to assess the concentration of an analyte in a sample. It requires standards with known analyte content to establish the relation between the measured absorbance and the analyte concentration and relies therefore on the Beer-Lambert law. Essentially, the electrons of the atoms in the atomiser can be promoted to

higher orbitals (excited states) for a short period of time by absorbing a defined quantity of energy. This amount of energy is element specific and particular to an electron transition. In general, each wavelength corresponds to only one element, and the width of an absorption line is only of the order of few picometers, which give the technique its elemental selectivity. The radiation flux with and without a sample in the atomiser is measured using a detector, and the ratio between the two values (absorbance) is converted to analyte concentration or mass using the Beer-Lambert law.[248]

AAS analysis was performed with a PerkinElmer AAnalyst 400. The powder material was digested and diluted in aqua regia (6M HCl:69% H_2NO_3 3:1) for the analysis.

2.3.8 ^{1}H NMR

Nuclear magnetic resonance (NMR) is one of the most important techniques in chemistry for structure elucidation. It exploits the magnetic properties of certain atomic nuclei based on a physical phenomenon in which nuclei in a magnetic field absorb and re-emit electromagnetic radiation. NMR determines physical and chemical properties of atoms or the molecules in which they are contained providing detailed information about the structure, dynamics, reaction state and chemical environment of molecules. When placed in a magnetic field, NMR active nuclei (such as ^{1}H or ^{13}C) absorb electromagnetic radiation at a frequency characteristic of the isotope. The resonant frequency, energy of the absorption and the intensity of the signal are proportional to the strength of the magnetic field and the magnetic properties of the isotope of the atoms.

A solution of the sample in a uniform glass tube is oriented between the poles of a powerful magnet, and is spun to average any magnetic field variations, as well as tube imperfections. The majority of nuclei in a solution generally belong to the solvent and most regular solvents are hydrocarbons and contain NMR-reactive protons. Therefore, deuterated solvents are generally used in NMR experiments. Radio frequency radiation of appropriate energy is broadcast into the sample from an antenna coil. A receiver coil surrounds the sample tube, and emission of absorbed radio-frequency energy is monitored by dedicated electronic devices and a computer. Upon excitation of the sample with a radio frequency (60-100 MHz) pulse, a NMR response, a free induction decay, is obtained. A Fourier transform is carried out to extract the frequency-domain spectrum from the raw-time domain. The obtained NMR spectra is often calibrated against the known solvent residual proton peak.[249, 250]

^{1}H NMR analysis of the metal alkoxide precursors was performed with a Bruker AVIII 400MHz or 500MHz Spectrometer using Young valve NMR tubes for air sensitive materials and dry benzene-d^6.

2.3.9 FT-IR Spectroscopy

Fourier transform infrared spectroscopy (FT-IR) is a technique based on the vibration of the atoms in a molecule. Infrared radiation with wavelength of around 1000

and 4000 nm is shone through a sample and an infrared spectrum is commonly obtained by determining what fraction of the incident radiation is absorbed at a particular energy. FT-IR exploits the fact that molecules absorb specific frequencies that are characteristic of their structure. Some of the infrared radiation is absorbed by the sample and some of it is passed through (transmitted). These absorptions are resonant frequencies where the frequency of the absorbed radiation matches the transition energy of the bond or group of atoms that vibrates. An infrared spectrum therefore represents a fingerprint of a sample with absorption peaks corresponding to the frequencies of vibrations between the bonds of the atoms constituting the material. The energy at which any peak in an absorption spectrum appears corresponds to the frequency of a vibration of a specific part of a sample molecule. Because each different material constitutes a unique combination of atoms, each compound produce a characteristic infrared spectrum.[251]

FT-IR measurements were conducted with a FT-IR Shimadzu spcectrophotometer. The powders were mixed with Nujol and placed between two NaCl plates. All the manipulations were conducted in an Ar-filed glovebox in order to avoid oxidation of the product.

3 Local Structure and Li^+ Diffusion Studies of Microwave Synthesised $LiFe_{1-x}Mn_xPO_4$ olivines

3.1 Introduction

Olivine nanostructured $LiFe_{1-x}Mn_xPO_4$ have received increasing attention as they exhibit higher energy density and enhanced redox kinetics, due to the improved electronic conductivity, in comparison to the pure olivines. These mixed-metal phosphates phases are isostructural with the end-members $LiFePO_4$ and $LiMnPO_4$, showing the same olivine-type lattice. Partial substitution of Fe by Mn in these olivine structures leads to electrode materials with increased voltage due to the higher $Mn^{3+/2+}$ redox potential compared to the pair $Fe^{3+/2+}$.[66] However, the existence of Mn^{3+} ions in delithiated $MnPO_4$ triggers a Jahn-Teller distortion leading to interfacial strain, which is detrimental to ion and electron hopping during the charge/discharge process. The Jahn-Teller effect induces volume and cell distortion of the electrode, leading to a rapid mechanical degradation of the electrode and consequently, poor electrochemical performance. Previous investigations by Padhi *et al*. on the electrochemical performance of $LiFe_{1-x}Mn_xPO_4$ (x=0.25, 0.50, 0.75, 1.0) materials revealed that the specific capacity significantly decreases when $x > 0.75$.[34] Yamada *et al*. also reported that Mn-rich $LiFe_{1-x}Mn_xPO_4$ ($x > 0.8$) phases are not the best performing mixed metal phosphates due to the large anisotropic distortion of Mn^{3+} during cycling.[78, 79] Therefore there is much scope for the study and improvement of these important energy storage electrodes.

In this chapter, a simple and low cost microwave-assisted solvothermal synthesis of single-phase $LiFe_{1-x}Mn_xPO_4$ (x=0.25, 0.50, 0.75, 1.0) olivines is presented, which allows for up to 4 times faster reaction times compared to traditional solvothermal methods. To have a complete characterisation and a better understanding of the structure-property relationship of these nanocrystalline phases, high resolution powder neutron diffraction (PND) and neutron pair distribution function (PDF) analyses of these microwave synthesised electrode materials have been conducted. These techniques allow elucidation of the local structure, the cation distribution, the presence of defects and the Li content. Furthermore, muon spin relaxation (μ^+SR) has been successfully applied to examine the Li^+ diffusion in these Li-ion battery materials, where the Li^+ diffusion perturbs the muon environment. Also, of interest here is whether the microwave synthetic approach eliminates potential defects in these materials. The presence of, for example, antisite defects in this olivine structure precludes Li^+ diffusion along the *b*-axis leading to a significant decrease in reversible capacities. Finally, the electrochemical performance as active electrodes in Li-ion batteries has also been examined.

3.2 Results and discussion

3.2.1 Synthesis and characterisation of $LiFe_{1-x}Mn_xPO_4$ olivines

Single-phase LiH_2PO_4 and $LiFe_{1-x}Mn_xPO_4$ were prepared as described in sections 2.2.1 and 2.2.2. Schematic 3.1 depicts the reaction schematic for the synthetic procedure of $LiFe_{1-x}Mn_xPO_4$ olivines and Table 3.1 lists the LiH_2PO_4 starting material and $LiFe_{1-x}Mn_xPO_4$ products prepared from commercial starting materials.

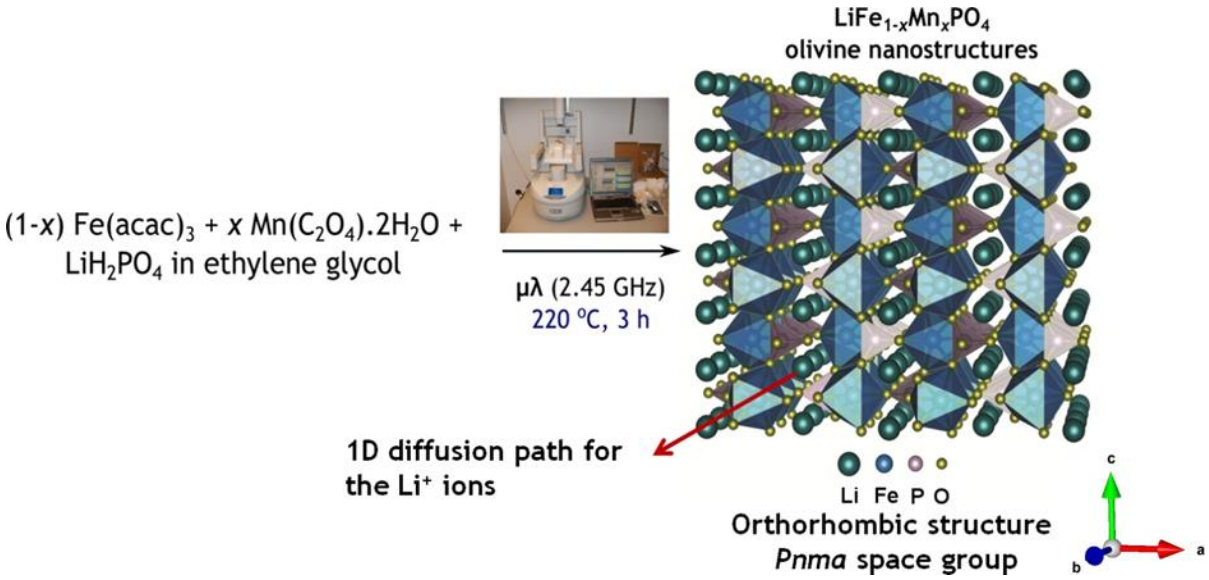

Schematic 3.1. Reaction schematic for the solvothermal microwave-assisted synthesis of $LiFe_{1-x}Mn_xPO_4$ (x=0, 0.25, 0.5, 0.75, 1) olivines showing the CEM Discover/Explorer SP microwave synthesiser and the crystal structure of $LiFePO_4$.

3.2.1.1 PXRD of LiH_2PO_4 and $LiFe_{1-x}Mn_xPO_4$ phases

Initially, attempts to synthesise olivine $LiFePO_4$ phases through a solvothermal microwave-assisted route employing $Fe(acac)_3$ and commercial LiH_2PO_4 in ethylene glycol were investigated. The use of freshly prepared LiH_2PO_4 (made from reaction of $LiOH{\cdot}H_2O$ with H_3PO_4) in a similar synthesis of $LiFePO_4$ was also investigated to check the effect of the starting material in the resulting product (see Figure A3.1 for PXRD pattern confirming purity). Figure 3.1 shows that the synthesis of $LiFePO_4$ using the freshly prepared LiH_2PO_4 led to single-phase $LiFePO_4$ nanostructures, while employing the commercial LiH_2PO_4 gave rise to $LiFePO_4$ with undesirable Li_3PO_4 impurities. These results reveal that Li_3PO_4 is an important intermediate in this reaction. These observations could be explained by the significantly smaller particle size of the prepared LiH_2PO_4 compared to the commercial one, allowing the reaction to proceed easily, which will be confirmed later by scanning electron microscopy (SEM) analysis.

Table 3.1. List of LiH_2PO_4 and $LiFe_{1-x}Mn_xPO_4$ samples prepared from commercial starting materials.

Samples	Reactants	Reaction conditions
LiH_2PO_4	$LiOH{\cdot}H_2O$ (9.00 g, 0.092 mol) + 16.7 mL H_3PO_4(+ 1 mL excess) + 90 mL distilled H_2O	
$^7LiH_2PO_4$	$^7LiOH{\cdot}H_2O$ (9.00 g, 0.092 mol) + 16.7 mL H_3PO_4(+ 1 mL excess) + 90 mL distilled H_2O	
$LiFePO_4$_MW_Com.	$Fe(acac)_3$ (0.7063 g, 2 mmol)+LiH_2PO_4 (0.2079 g, 2 mmol) + 10 mL EG	Microwave synthesis (2.45 GHz) 3 hr 220 ºC
$LiFe_{0.75}Mn_{0.25}PO_4$_MW_Com.	$Fe(acac)_3$ (0.5298 g, 1.5 mmol)+$MnC_2O_4{\cdot}2H_2O$ (0.0895 g, 0.5 mmol)+LiH_2PO_4 (0.2079 g, 2 mmol) + 10 mL EG	Microwave synthesis (2.45 GHz) 3 hr 220 ºC
$LiFe_{0.5}Mn_{0.5}PO_4$_MW_Com.	$Fe(acac)_3$ (0.3532 g, 1 mmol)+$MnC_2O_4{\cdot}2H_2O$ (0.1790 g, 1 mmol)+LiH_2PO_4 (0.2079 g, 2 mmol) + 10 mL EG	Microwave synthesis (2.45 GHz) 3 hr 220 ºC
$LiFe_{0.25}Mn_{0.75}PO_4$_MW_Com.	$Fe(acac)_3$ (0.1766 g, 0.5 mmol)+$MnC_2O_4{\cdot}2H_2O$ (0.2685 g, 1.5 mmol)+LiH_2PO_4 (0.2079 g, 2 mmol) + 10 mL EG	Microwave synthesis (2.45 GHz) 3 hr 220 ºC
$LiMnPO_4$_MW_Com. (1)	$Mn(acac)_3$ (0.7045 g, 2 mmol)+LiH_2PO_4 (0.2079 g, 2 mmol) + 10 mL EG	Microwave synthesis (2.45 GHz) 3 hr 220 ºC
$LiMnPO_4$_MW_Com. (2)	$MnC_2O_4.2H_2O$ (0.3578 g, 2 mmol)+LiH_2PO_4 (0.2079 g, 2 mmol) + 10 mL EG	Microwave synthesis (2.45 GHz) 3 hr 220 ºC
$LiMnPO_4$_MW_Com. (3)	$MnCO_3$ (0.2299 g, 2 mmol)+LiH_2PO_4 (0.2079 g, 2 mmol) + 10 mL EG	Microwave synthesis (2.45 GHz) 3 hr 220 ºC
$LiMnPO_4$_MW_Com. (4)	$MnSO_4{\cdot}H_2O$ (0.3380 g, 2 mmol)+LiH_2PO_4 (0.2079 g, 2 mmol) + 10 mL EG	Microwave synthesis (2.45 GHz) 3 hr 220 ºC
$^7LiFePO_4$_MW_Com.	$Fe(acac)_3$ (0.7063 g, 2 mmol)+$^7LiH_2PO_4$ (0.2079 g, 2 mmol) + 10 mL EG	Microwave synthesis (2.45 GHz) 3 hr 220 ºC
$^7LiFe_{0.75}Mn_{0.25}PO_4$_MW_Com.	$Fe(acac)_3$ (0.5298 g, 1.5 mmol)+$MnC_2O_4{\cdot}2H_2O$ (0.0895 g, 0.5 mmol)+$^7LiH_2PO_4$ (0.2079 g, 2 mmol) + 10 mL EG	Microwave synthesis (2.45 GHz) 3 hr 220 ºC
$^7LiFe_{0.5}Mn_{0.5}PO_4$_MW_Com.	$Fe(acac)_3$ (0.3532 g, 1 mmol)+$MnC_2O_4{\cdot}2H_2O$ (0.1790 g, 1 mmol)+$^7LiH_2PO_4$ (0.2079 g, 2 mmol) + 10 mL EG	Microwave synthesis (2.45 GHz) 3 hr 220 ºC
$^7LiFe_{0.25}Mn_{0.75}PO_4$_MW_Com.	$Fe(acac)_3$ (0.1766 g, 0.5 mmol)+$MnC_2O_4{\cdot}2H_2O$ (0.2685 g, 1.5 mmol)+$^7LiH_2PO_4$ (0.2079 g, 2mmol) + 10 mL EG	Microwave synthesis (2.45 GHz) 3 hr 220 ºC
$^7LiMnPO_4$_MW_Com.	$Mn(acac)_3$ (0.7045 g, 2 mmol)+$^7LiH_2PO_4$ (0.2079 g, 2 mmol) + 10 mL EG	Microwave synthesis (2.45 GHz) 3 hr 220 ºC

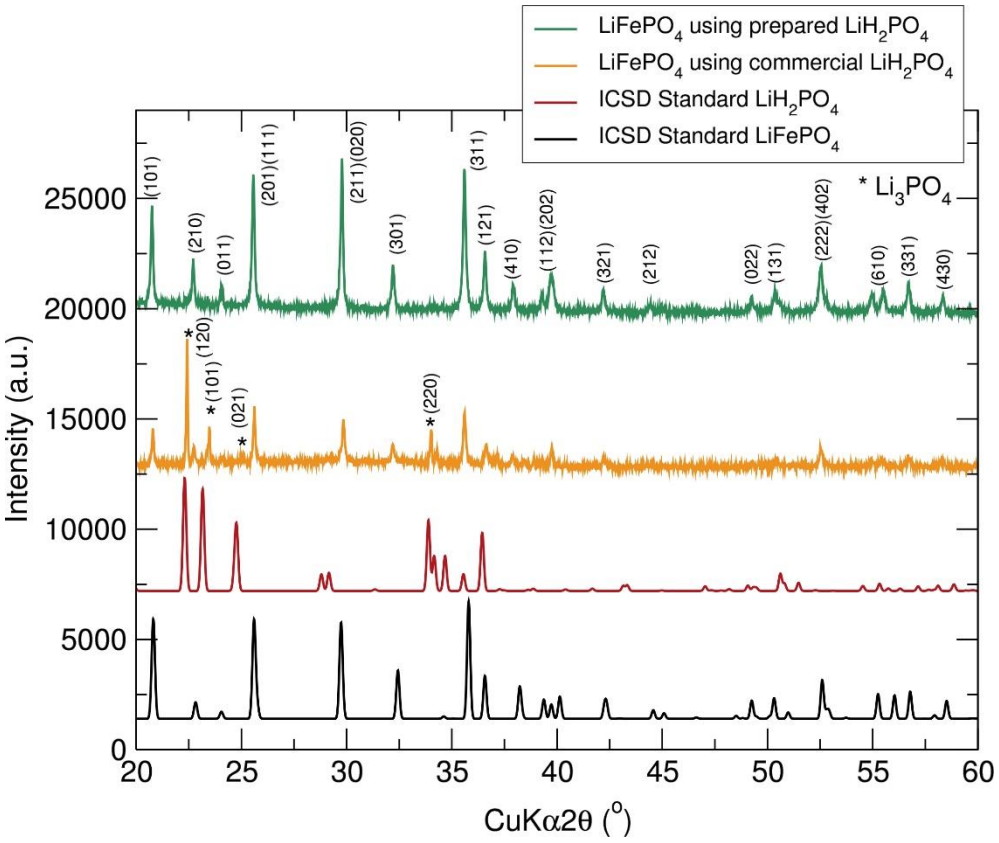

Figure 3.1. PXRD patterns of $LiFePO_4$ prepared using commercial LiH_2PO_4 and $LiFePO_4$ prepared using synthesised LiH_2PO_4. * indicates Li_3PO_4 impurities.

In an effort to find a suitable Mn containing precursor for the preparation of single phase $LiMnPO_4$, different Mn based starting materials including $MnSO_4{\cdot}H_2O$, $MnCO_3$, $Mn(acac)_3$ and $MnC_2O_4{\cdot}2H_2O$ were individually reacted with the freshly prepared LiH_2PO_4 in 10 mL of ethylene glycol to find the best synthesis conditions. As shown in Figure 3.2, PXRD characterisation of the reaction products revealed that only single phase $LiMnPO_4$ was obtained when $Mn(acac)_3$ was employed ($LiMnPO_4$_MW_Com. (1)). The microwave reaction employing the other three Mn containing precursors $MnCO_3$, $MnC_2O_4{\cdot}2H_2O$ and $MnSO_4.H_2O$ did not provide the desired olivine phase.

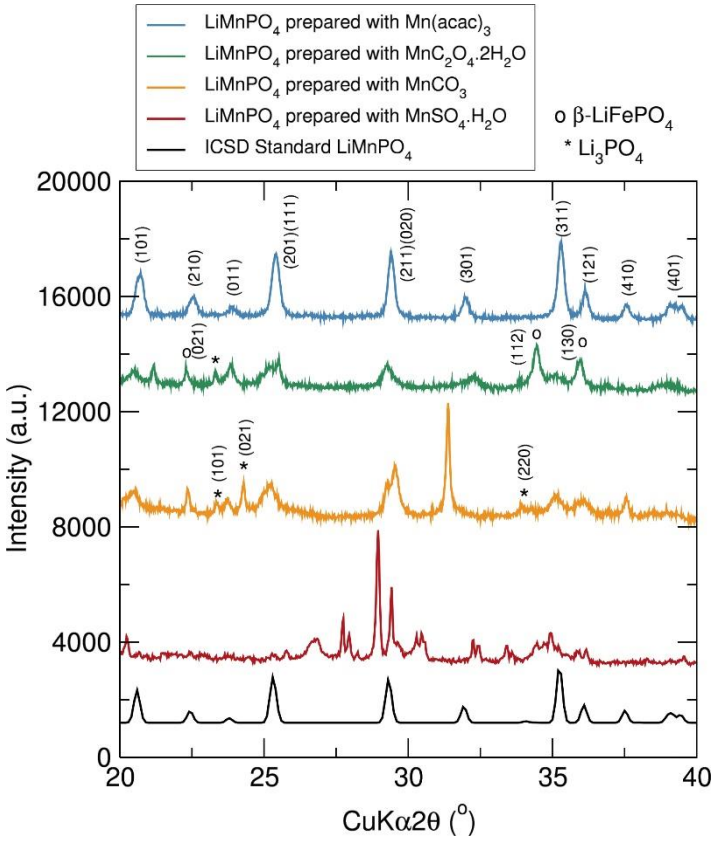

Figure 3.2. Comparative PXRD patterns of $LiMnPO_4$ samples prepared using $MnSO_4 \cdot H_2O$, $MnCO_3$, $MnC_2O_4 \cdot 2H_2O$ and $Mn(acac)_3$ after microwave synthesis for 3 hr at 220 °C. * indicates Li_3PO_4 impurities and ° possible peaks coming from a *Cmcm* high pressure phase of $LiMnPO_4$.

Heat treatments of the $LiMnPO_4$ products obtained from $MnC_2O_4 \cdot 2H_2O$ and $MnCO_3$ were performed in a tube furnace at 500 ºC for 1 hr under Ar atmosphere in an effort to obtain phase pure $LiMnPO_4$. PXRD analysis shown in Figure 3.3 (a) indicates that the product obtained after the microwave synthesis of $LiMnPO_4$ using $MnC_2O_4 \cdot 2H_2O$ ($LiMnPO_4$_MW_Com. (2)) afforded a mixture of the *Pnma* and high pressure *Cmcm* phases, together with Li_3PO_4 impurity. After heat treatment, the desired *Pnma* $LiMnPO_4$ phase was obtained with some small amounts of Li_3PO_4. To overcome this problem, a quick washing with acetic acid 0.01 M was performed to dissolve this remaining impurity. As reported by Niederberger *et al.*, when high pressure and elevated temperatures are applied, a high-pressure *Cmcm* space group phase denoted as ß-$LiFePO_4$ may form. They have demonstrated that this ß-phase irreversibly may transform into the α-phase upon heat treatment without alteration of the morphology.[50] Moreover, it is also worth mentioning that the Li^+ diffusion behaviour is strikingly different in both phases. ß-$LiFePO_4$ is significantly less electrochemically active than the α-phase, mainly due to the longer Li-Li hoping distances in the *Cmcm* space group phase. Recent muon studies on Li^+ diffusion indicate that the Li^+ diffusion is significantly more impeded in the presence of this high pressure *Cmcm* phase, showing a lower D_{Li} of 3.96 x 10^{-10} cm^2 s^{-1} compared to the D_{Li} of 6.25 x 10^{-10} cm^2 s^{-1}obtained for *Pnma* $LiFePO_4$ phase.[51] In the present case, from the resulting PXRD pattern, the reaction

carried out employing $MnC_2O_4{\cdot}2H_2O$ proceeds through a reaction pathway in which the high pressure ß-phase may be an important reaction intermediate, possibly due to a higher pressure generated in the microwave vessel by the two hydration water molecules contained in the $MnC_2O_4{\cdot}2H_2O$ precursor. Pressure readings during the microwave synthesis indicated a maximum pressure of 98 psi when using $MnC_2O_4{\cdot}2H_2O$ precursor instead of 42 psi for the reaction with $Mn(acac)_3$. The preparation of *Cmcm* $LiMnPO_4$ phase with some olivine $LiMnPO_4$ and $Mn_2P_2O_7$ impurities *via* a similar solvothermal microwave-assisted method has recently been reported using $MnC_2O_4{\cdot}2H_2O$ precursor in tetraethylene glycol.[158] In the case of the $LiMnPO_4$ phase prepared with $MnCO_3$ ($LiMnPO_4$_MW_Com. (3)), PXRD patterns in Figure 3.3 (b) indicate that the heat treatment transforms the product obtained after the microwave reaction into the desired *Pnma* $LiMnPO_4$ product. Furthermore, from these results, it can also be concluded that in this reaction process Li_3PO_4 could also potentially be an important reaction intermediate. There is no evidence for the formation of ß-$LiMnPO_4$ *Cmcm* phase in this reaction.

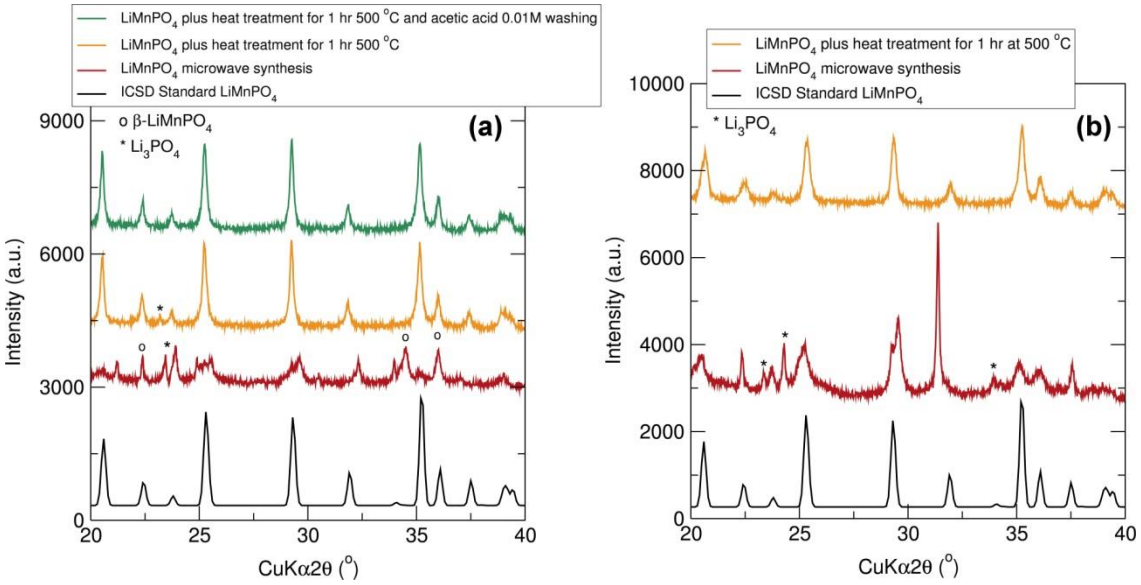

Figure 3.3. PXRD patterns of $LiMnPO_4$ after the microwave synthesis for 3 hr at 220 ºC, $LiMnPO_4$ after the microwave synthesis and heat treatment for 1 hr at 500 ºC and $LiMnPO_4$ after the microwave synthesis, heat treatment for 1 hr at 500 ºC and acetic acid 0.01M washing. **(a)** $LiMnPO_4$ prepared using $MnC_2O_4{\cdot}2H_2O$. **(b)** $LiMnPO_4$ prepared using $MnCO_3$. * indicates Li_3PO_4 impurities and º possible peaks from *Cmcm* $LiMnPO_4$ high pressure phase.

Figure 3.4 shows the Rietveld analysis of the PXRD data from the two *Pnma* $LiMnPO_4$ phases prepared using $MnCO_3$ and $MnC_2O_4{\cdot}2H_2O$ after the heat treatments for 1 hr at 500 ºC under Ar flow. The fitting was performed from 20 º to 40 º 2θ with *Pnma* $LiMnPO_4$ (ICSD No. 01-072-7844) as the starting structure. The good agreement between the experimental data and the calculated model (R_{wp} values of 15%) indicates that phase pure $LiMnPO_4$ materials have been successfully obtained. Table 3.2 summarises the results from

the Rietveld analysis of $LiMnPO_4$_MW_Com. (2) and $LiMnPO_4$_MW_Com. (3) samples showing that similar values for the lattice parameters and cell volume are obtained.

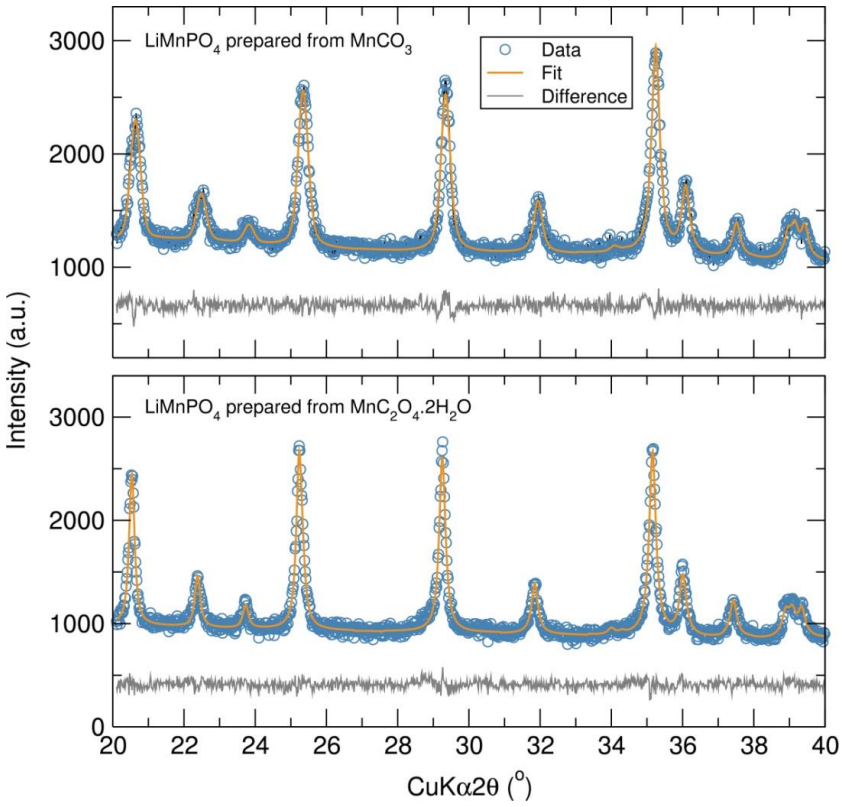

Figure 3.4. Rietveld analysis of PXRD data from $LiMnPO_4$ phases to an orthorhombic *Pnma* structure. Samples prepared through a microwave synthesis (3 hr 220 ºC) and post-heat treatment for 1 hr at 500 ºC using $MnC_2O_4{\cdot}H_2O$ or $MnCO_3$.

Table 3.2. Calculated lattice parameters from Rietveld refinements for $LiMnPO_4$ phases prepared using using $MnC_2O_4{\cdot}H_2O$ or $MnCO_3$.

Sample	$LiMnPO_4$_MW_Com. (2)	$LiMnPO_4$_MW_Com. (3)
Space group	*Pnma*	*Pnma*
a (Å)	10.444(1)	10.454(2)
b (Å)	6.100(1)	6.109(1)
c (Å)	4.744(1)	4.751(2)
V (Å^{-3})	302.2(1)	303.4(1)
R_{wp}	15.4 %	15.3 %
R_{exp}	13.13 %	13.28 %
X^2	1.37	1.32

The possibility of improved energy density over $LiFePO_4$ has therefore generated continued interest in the mixed transition metal phosphates $LiFe_{1-x}Mn_xPO_4$. Despite the fact that $MnC_2O_4{\cdot}2H_2O$ was not a suitable precursor for the microwave synthesis of phase pure $LiMnPO_4$, mixed metal phosphates $LiFe_{0.75}Mn_{0.25}PO_4$, $LiFe_{0.5}Mn_{0.5}PO_4$ and $LiFe_{0.25}Mn_{0.75}PO_4$ were successfully prepared using stoichiometric amounts of $Fe(acac)_3$,

$MnC_2O_4 \cdot 2H_2O$ and freshly prepared LiH_2PO_4 in ethylene glycol. In Figure 3.5, the PXRD patterns of the $LiFe_{1-x}Mn_xPO_4$ (x=0, 0.25, 0.5, 0.75 and 1) nanostructures are shown. These results reveal that all five $LiFe_{1-x}Mn_xPO_4$ samples were isostructural and exhibited a pure phase material with an olivine structure indexed to an orthorhombic *Pnma* space group. Moreover, no peaks of impurity phases or evidence of phase segregation were detected from PXRD analysis. A slight shifting of the peaks towards lower angles is noted with increasing Mn content. This is a signature of an increase in average lattice parameter due to the larger cation size of Mn^{2+} (83 pm ionic radius) in comparison to Fe^{2+} (78 pm ionic radius).[252] According to the Bragg Formula $2d\sin\theta=n\lambda$, a larger lattice parameter d corresponds to a smaller peak angle θ. This explains the slight shift of the peaks to smaller 2θ angles with increasing Mn content. Because of the smaller ionic radius of Fe^{2+}, the average M-O (M=Fe and Mn) bond length increases after substitution of Fe with higher Mn contents. The shorter average bond length decreases the ionicity of the Fe-O bonds in $LiFe_{1-x}Mn_xPO_4$ relative to the Mn-O bonds in $LiMnPO_4$, which could improve the electron polaron hopping between adjacent cationic centers. A slight peak broadening of the peaks in the PXRD patterns is observed when increasing the Mn content in $LiFe_{1-x}Mn_xPO_4$, which suggests a decrease in particle size with higher amounts of Mn in $LiFe_{1-x}Mn_xPO_4$.

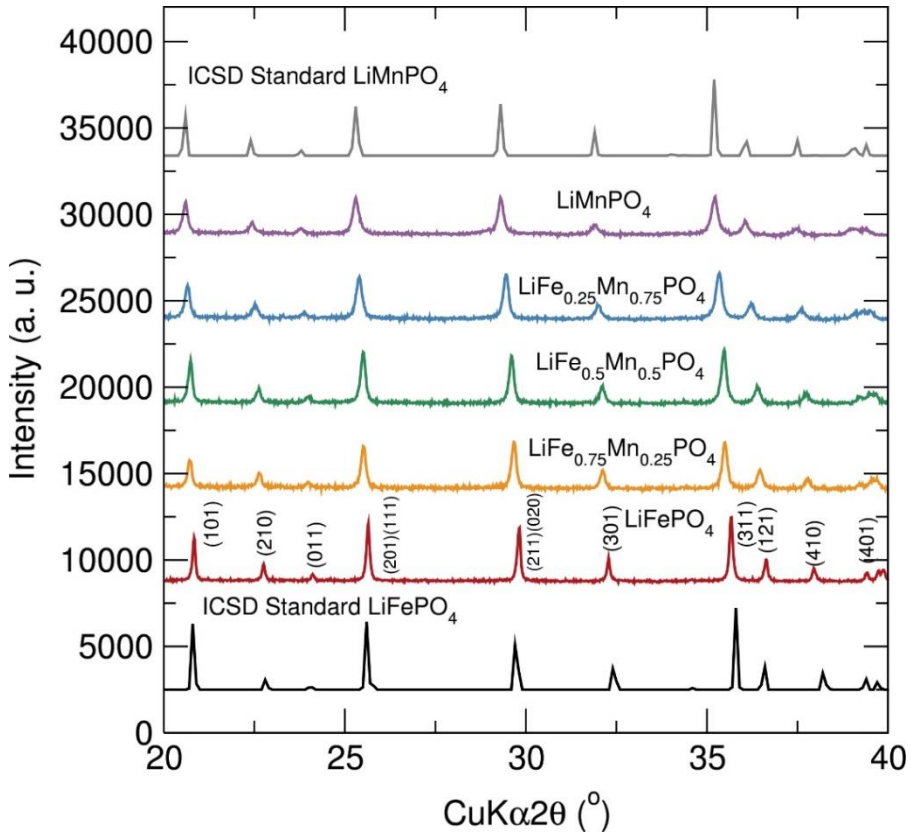

Figure 3.5. Comparative PXRD patterns of $LiFe_{1-x}Mn_xPO_4$ (x=0, 0.25, 0.5, 0.75, 1) olivine phases. Samples prepared by a solvothermal microwave-assisted synthesis (3 h at 220 °C) using a stoichiometric mixture of LiH_2PO_4, $Fe(acac)_3$, and $MnC_2O_4 \cdot 2H_2O$ in ethylene glycol ($LiMnPO_4$ prepared using $Mn(acac)_3$).

PXRD data of this family of mixed metal phosphates was analysed by Rietveld refinements and fit to the orthorhombic *Pnma* $LiFePO_4$ (ICSD No. 01-072-7845) and $LiMnPO_4$ (ICSD No. 01-072-7844) structures from the Inorganic Crystal Structure Database (ICSD)[49] using GSAS.[253] As observed in the difference curves in Figure 3.6, a good fit was obtained in all five compounds. Table 3.3 summarises the calculated lattice parameters of all $LiFe_{1-x}Mn_xPO_4$ olivine phases determined by Rietveld analysis, revealing a clear increase in the lattice parameters when doping $LiFePO_4$ with higher Mn content. These results imply that Fe^{2+} atoms have been successfully substituted by Mn^{2+} in and are effectively located in the olivine structure. Moreover, the determined lattices parameters are similar to previous values reported for microwave synthesised $LiFePO_4$ (a=10.3175 Å, b=5.9935 Å and c=4.7016 Å) and $LiMnPO_4$ (a=10.4632 Å, b=6.1074 Å and c=4.7507 Å) samples.[45]

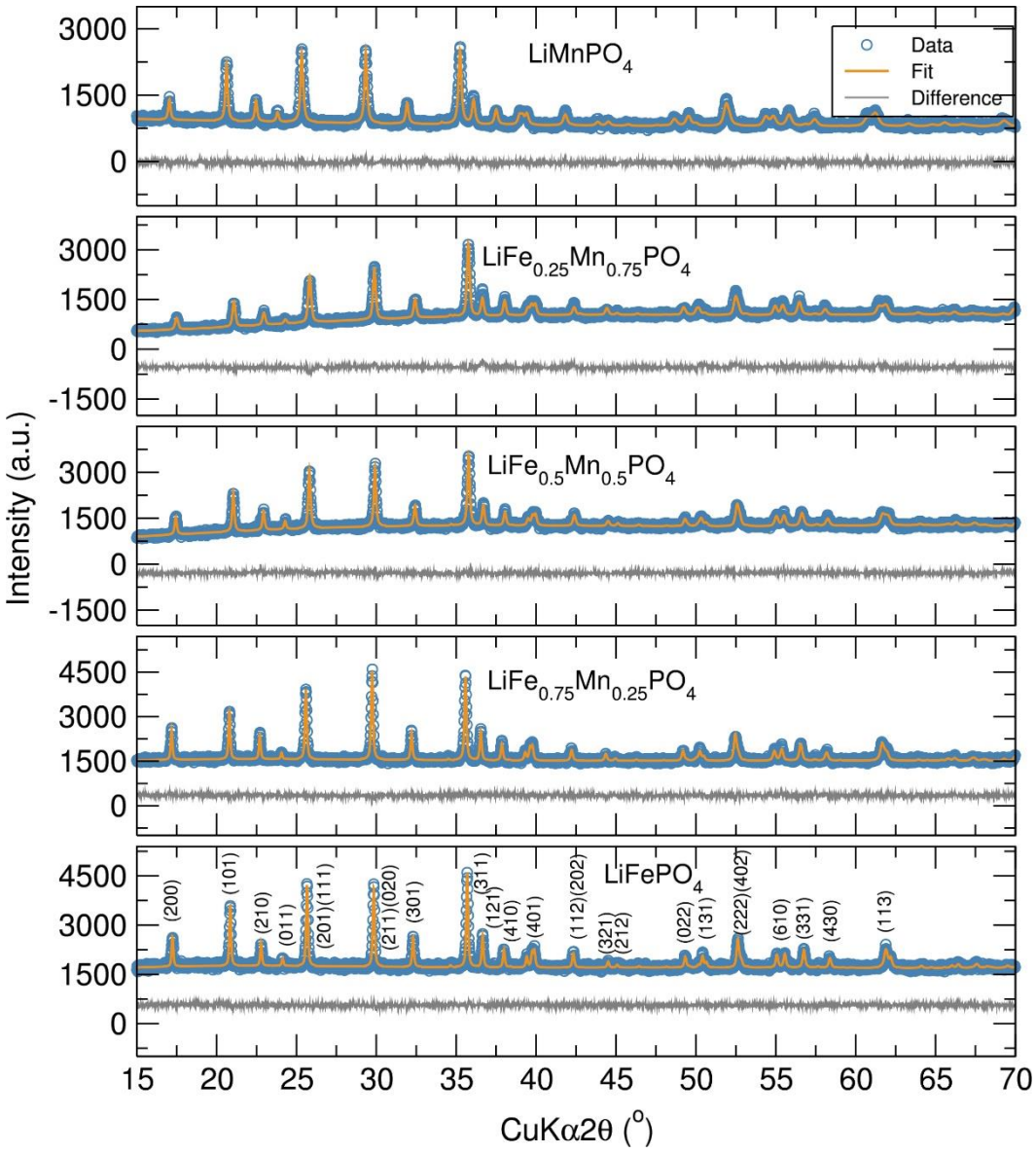

Figure 3.6. Rietveld analysis of PXRD data from $LiFe_{1-x}Mn_xPO_4$ (x=0, 0.25, 0.5, 0.75, 1) olivine phases to an orthorhombic *Pnma* structure.

Table 3.3. Calculated lattice parameters for the $LiFe_{1-x}Mn_xPO_4$ olivine phases obtained from Rietveld refinements.

Sample	$LiFePO_4$_MW_Com.	$LiFe_{0.75}Mn_{0.25}PO_4$_MW_Com.	$LiFe_{0.5}Mn_{0.5}PO_4$_MW_Com.	$LiFe_{0.25}Mn_{0.75}PO_4$_MW_Com.	$LiMnPO_4$_MW_Com.
Space group	*Pnma*	*Pnma*	*Pnma*	*Pnma*	*Pnma*
a (Å)	10.3303(5)	10.3628(5)	10.3899(7)	10.4213(9)	10.4504(8)
b (Å)	6.0000(3)	6.0200(3)	6.0460(4)	6.0761(5)	6.1043(5)
c (Å)	4.6948(3)	4.7052(3)	4.7197(4)	4.7344(5)	4.7471(5)
V ($Å^{-3}$)	291.00(4)	293.53(4)	296.48(5)	299.78(7)	302.83(7)
R_{wp}	0.0254	0.0272	0.0328	0.0400	0.0373
R_p	0.0202	0.0218	0.0260	0.0316	0.0298
X^2	1.164	1.196	1.360	1.577	1.293

3.2.1.2 SEM of LiH_2PO_4 and $LiFe_{1-x}Mn_xPO_4$ phases

The particle size and morphology of the LiH_2PO_4 starting material and $LiFe_{1-x}Mn_xPO_4$ (x=0, 0.25, 0.5, 0.75, 1) phases were examined by SEM. From Figure 3.7, smaller particle size of the LiH_2PO_4 powders synthesised using $LiOH{\cdot}H_2O$ and H_3PO_4 (~80 µm) compared to commercial LiH_2PO_4 (~500 µm) are clearly observed. This significant decrease in the particle size is believed to make the reaction between $Fe(acac)_3$ and LiH_2PO_4 to proceed easily towards the formation of phase-pure $LiFePO_4$, as demonstrated by the PXRD experiments shown previously. SEM images shown in Figure 3.8 of the $LiFePO_4$ phase synthesised with the freshly prepared LiH_2PO_4 exhibited a non-uniform platelet-like morphology with average particle sizes in the order of 200-500 nm. SEM images of the $LiFe_{1-x}Mn_xPO_4$ powders highlight that increasing the Mn content in these olivine phases has a pronounced effect on the resulting particle morphology and size. From the SEM micrographs in Figure 3.9, it is interesting to note that increasing the Mn content clearly affords a reduction in the size and width of the oval-shaped platelets, going from larger crystallites to thin nanowires. For example, there is a clear reduction in the size and width of particles on going from $LiFe_{0.75}Mn_{0.25}PO_4$ and $LiFe_{0.5}Mn_{0.5}PO_4$ (larger oval-shaped particles, with typical widths of 580 and 540 nm, respectively) to $LiFe_{0.25}Mn_{0.75}PO_4$ (thinner and longer oval particles of typical width 220 nm) and $LiMnPO_4$ (wires, typically 150 nm wide). The typical sizes of these particles are given in Table 3.4. Between 10 and 30 particle sizes were measured. These results clearly evidence a control over particle size depending on the transition metal content (Fe/Mn) in these olivine $LiFe_{1-x}Mn_xPO_4$ phases.

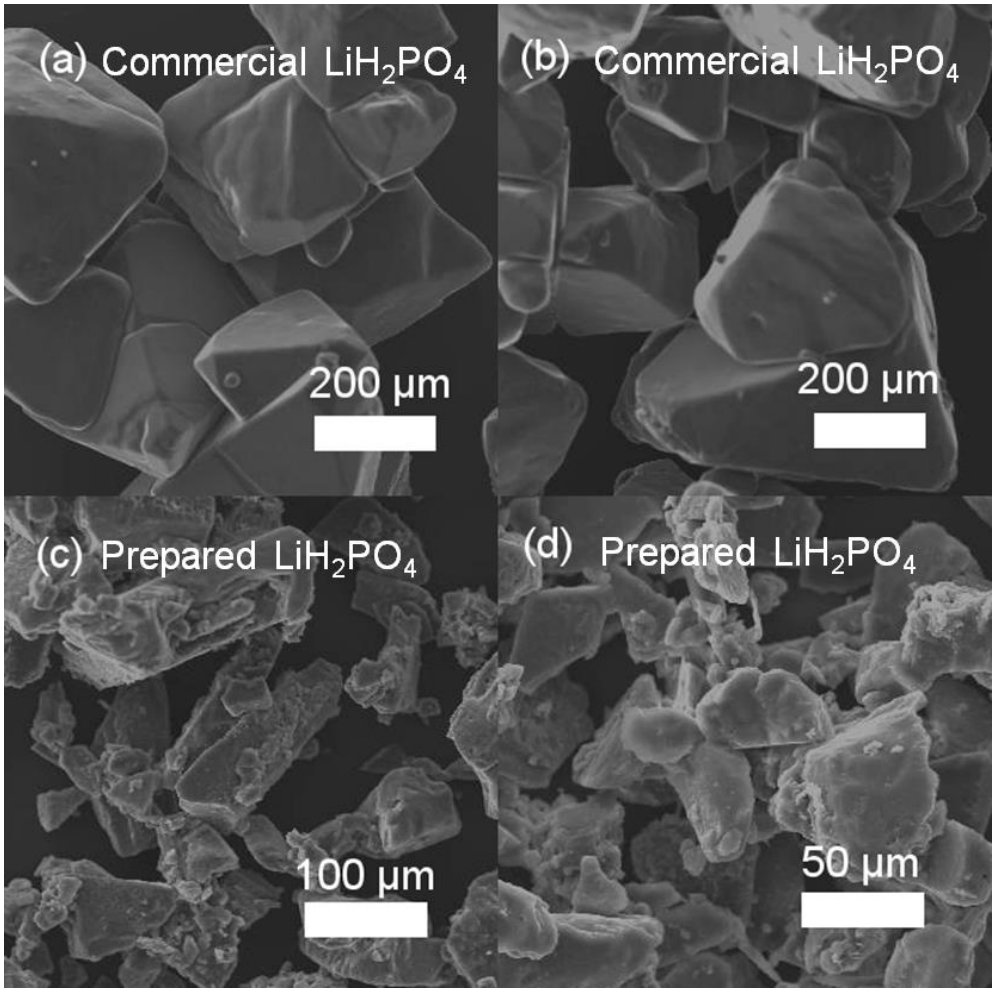

Figure 3.7. SEM images of **(a, b)** commercial LiH_2PO_4. **(c, d)** LiH_2PO_4 powders prepared with $LiOH{\cdot}H_2O$ and H_3PO_4.

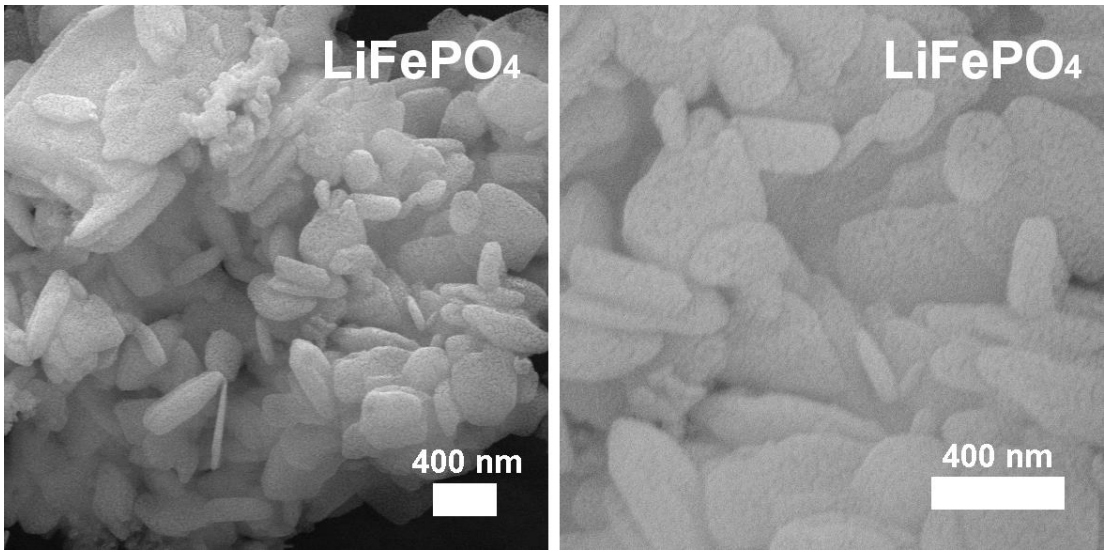

Figure 3.8. SEM images of $LiFePO_4$ powders prepared using synthesised LiH_2PO_4.

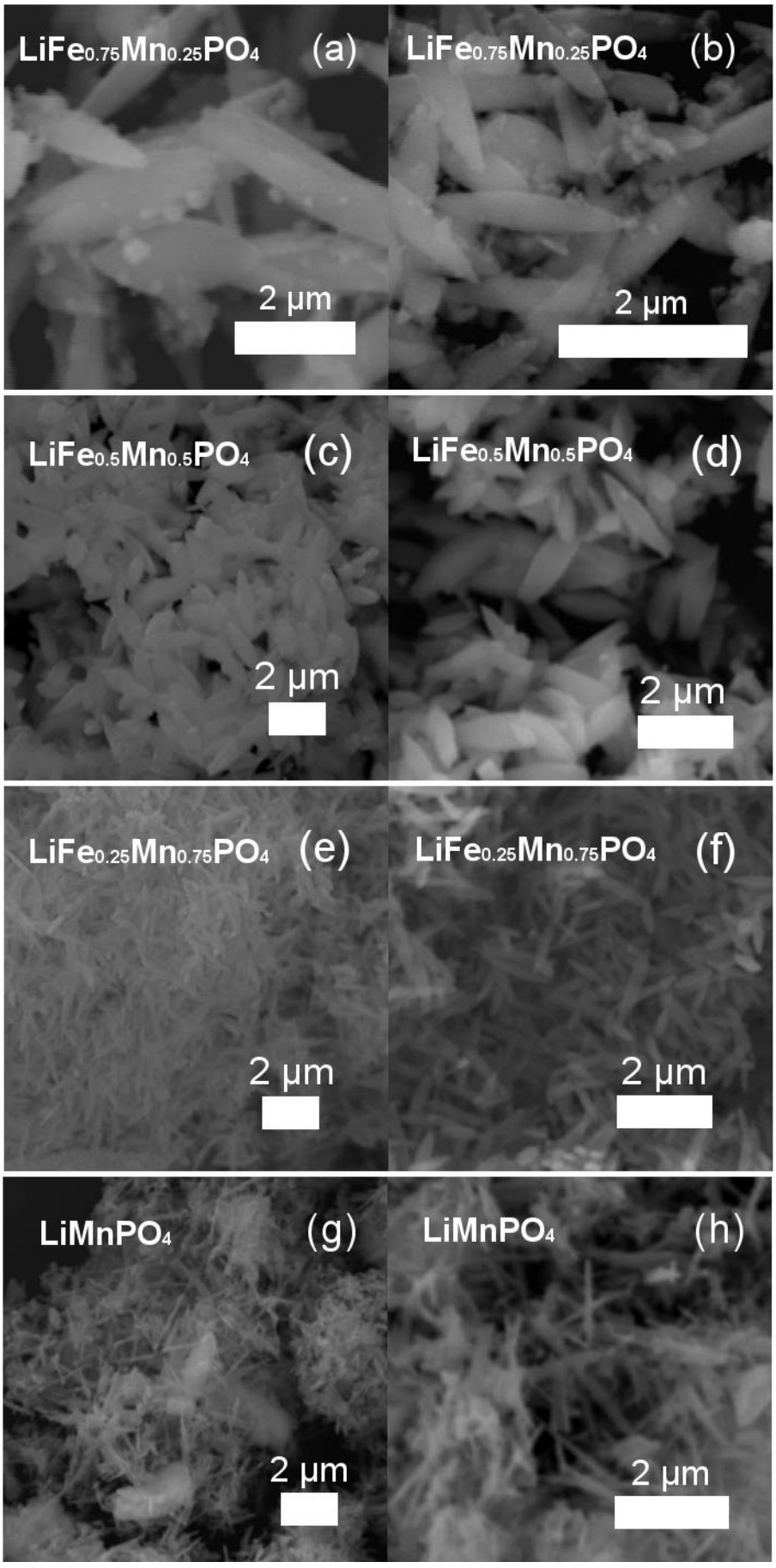

Figure 3.9. SEM images of $LiFe_{1-x}Mn_xPO_4$ (x=0.25, 0.5, 0.75, 1) olivine phases. **(a, b)** $LiFe_{0.75}Mn_{0.25}PO_4$. **(c, d)** $LiFe_{0.5}Mn_{0.5}PO_4$. **(e, f)** $LiFe_{0.25}Mn_{0.75}PO_4$. **(g, h)** $LiMnPO_4$.

Table 3.4. Typical sizes of $LiFe_{1-x}Mn_xPO_4$ olivine phases obtained from SEM.

Compound	Length (μm)	Width (nm)
$LiFe_{0.75}Mn_{0.25}PO_4$	1.37±0.07	580±40
$LiFe_{0.5}Mn_{0.5}PO_4$	1.58±0.07	540±20
$LiFe_{0.25}Mn_{0.75}PO_4$	1.49±0.08	220±10
$LiMnPO_4$	2.64±0.19	150±10

3.2.1.3 High resolution powder neutron diffraction of $LiFe_{1-x}Mn_xPO_4$ olivines

A detailed examination of the Li content and crystallographic properties of this family of $LiFe_{1-x}Mn_xPO_4$ olivines is required in order to further understand their electrochemical behaviour. PXRD has already confirmed phase pure olivine $LiFe_{1-x}Mn_xPO_4$. However, X-ray based techniques are not able to reliably quantify the Li content because Li is too light to scatter X-rays. Furthermore, XRD methods can not sensibly distinguish between Fe and Mn atoms due to their similar scattering power. Neutron based methods allow evaluation of light atoms such as Li and also allows the distinction between neighbouring atoms in the periodic table. Therefore, the crystallographic properties of the $LiFe_{1-x}Mn_xPO_4$ phases and their detailed Li content were investigated using high resolution powder neutron diffraction (PND) experiments combined with Rietveld refinement analysis. The high resolution PND data of the series of $LiFe_{1-x}Mn_xPO_4$ (x=0, 0.25, 0.5, 0.75 and 1) olivine was analysed by Rietveld refinements using GSAS in combination to the user interface EXPGUI.[253, 254] Data collected in the detector banks 3, 4 and 5 from the POLARIS diffractometer at ISIS were simultaneously fitted in the refinement process. The structural and profile parameters were refined according to a pseudo-Voigt profile function and the refinement process order used was the following: (i) scale factor (ii) the background was carefully modelled using a 6-coefficient Shifted Chebyschev function (iii) the diffractometer constants DIFC and DIFA, (iv) cell parameters, (v) profile parameters, (vi) atomic positions (the crystallographic sites for Fe and Mn atoms were constrained to be the same in the mixed metal phosphates), (vii) fraction occupancies of Li, Fe and Mn atoms in which the total occupancy of Fe and Mn was constrained to 1, and finally (viii) isotropic atomic thermal displacement parameters (B_{iso}) constraining Li and Fe/Mn to have the same value and also the oxygen atoms to be same. Figure 3.10 shows that an excellent fit was obtained for all five $LiFe_{1-x}Mn_xPO_4$ mixed metal phosphates. Tables A3.1, A3.2, A3.3, A3.4 and A3.5 summarise the structural parameters of the $LiFe_{1-x}Mn_xPO_4$ samples determined from Rietveld analysis of high resolution PND data at room temperature. There is also excellent agreement between the calculated lattice parameter from Rietveld analysis of PXRD and the high resolution PND data.

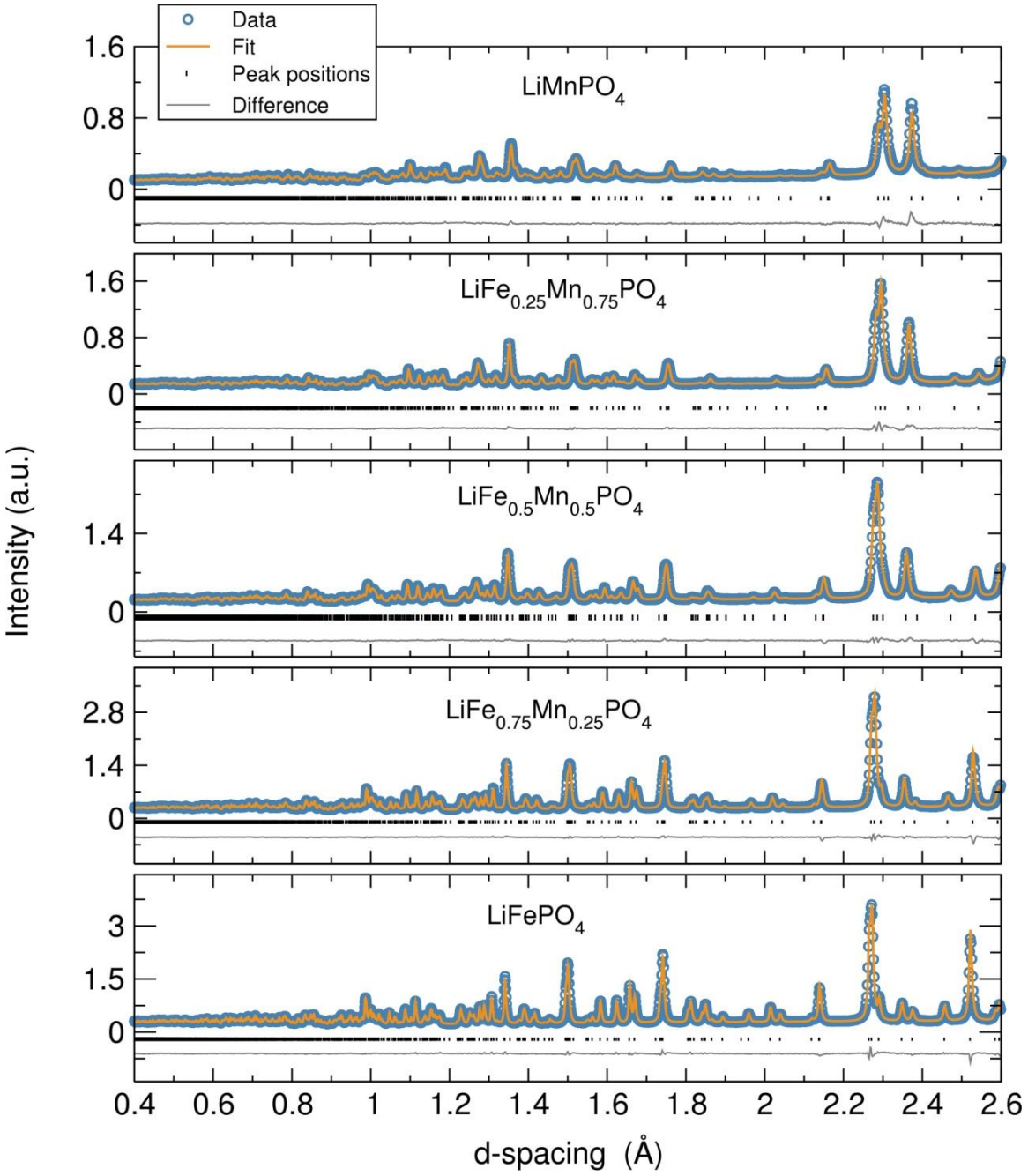

Figure 3.10. Rietveld refinements of high resolution powder neutron diffraction data collected at room temperature of $LiFe_{1-x}Mn_xPO_4$ (x=0, 0.25, 0.5, 0.75 and 1) olivine phases (detector bank 5).

The changes of the lattice parameters with the increasing amount of Mn in the $LiFe_{1-x}Mn_xPO_4$ olivines were studied considering Vegard's law, an empirical rule which holds that a linear relation exists, at constant temperature, between the crystal lattice parameter of a compound and the content of the constituent elements.[255] Results from the Rietveld refinements of the $LiFe_{1-x}Mn_xPO_4$ phases at room temperature revealed that these series of $LiFe_{1-x}Mn_xPO_4$ compounds obey Vegard's law. Figure 3.11 shows a linear increase of the lattice parameters with higher Mn content due to the slightly larger ionic radius of Mn^{2+} compared to Fe^{2+}. These results clearly confirm that substitution of Fe by Mn in $LiFe_{1-x}Mn_xPO_4$ linearly increases the unit cell volume.

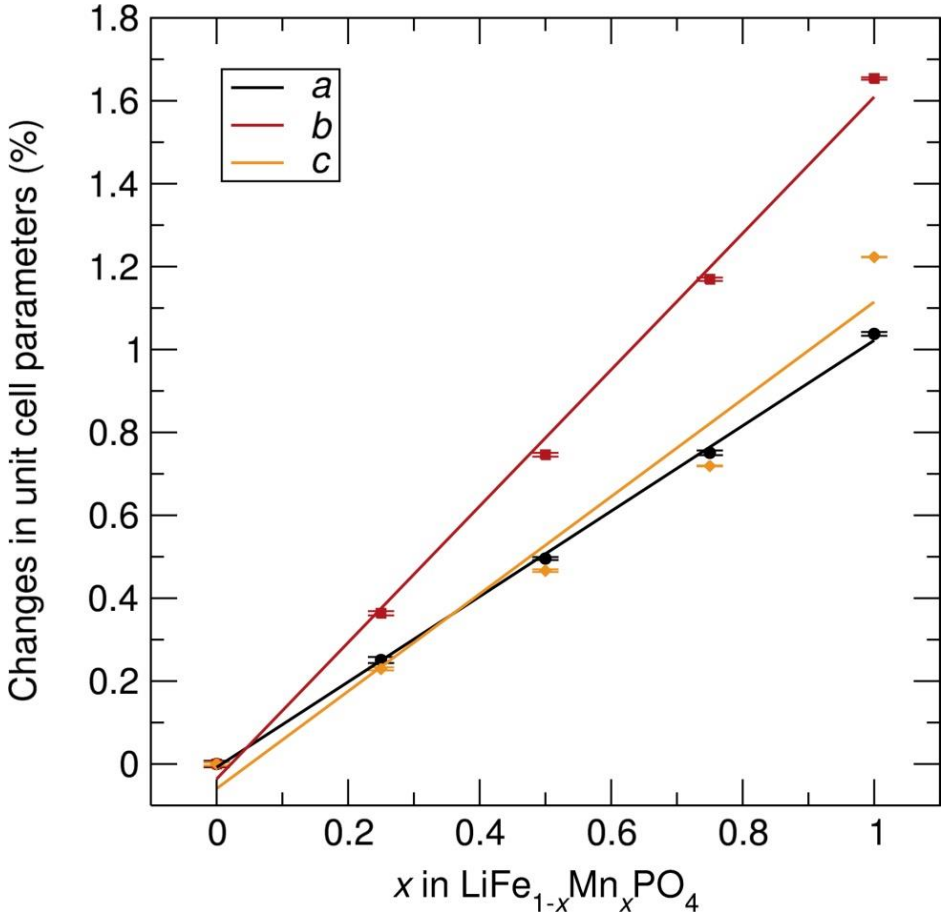

Figure 3.11. Changes in the unit-cell parameters as a function of the Mn content obtained from after Rietveld refinements of high resolution PND data at room temperature of $LiFe_{1-x}Mn_xPO_4$ (x=0, 0.25, 0.50, 0.75, 1) olivine phases.

The Li, Fe and Mn content in these $LiFe_{1-x}Mn_xPO_4$ compound and the R factors obtained from the Rietveld refinements data of the PND experiments at room temperature are summarised in Table 3.5. Interestingly, it is observed that all samples display a slight Li deficiency with a Li:transition metal ratio consistently less than 1 and the Li deficiency decreases with increasing Mn content. This observation is in good agreement with previous high resolution PND analyses which showed a slight Li deficiency in $LiFePO_4$ samples and a lower Li deficiency in Mn containing $LiFe_{1-x}Mn_xPO_4$ phases.[131] Moreover, in the mixed transition metal phases $LiFe_{0.75}Mn_{0.25}PO_4$ and $LiFe_{0.5}Mn_{0.5}PO_4$, the Fe content is slightly higher than the expected stoichiometric value, while the Mn content is lower. These results could be attributed to the fact that the $Fe(acac)_3$ precursor is more soluble than $MnC_2O_4{\cdot}2H_2O$ in ethylene glycol, which may facilitate the introduction of Fe in the olivine structure rather than Mn. These results may indicate that Fe atoms could also be occupying Li or interstitial positions, what could be explained by the fact that during the synthesis of these electrode materials Fe could potentially be introduced in the olivine structure faster than Mn.

Table 3.5. Li, Fe and Mn content in $LiFe_{1-x}Mn_xPO_4$ olivine phases from the Rietveld refinements of PND data at room temperature.

Sample	Li content	Fe content	Mn content	R_{wp}	R_{exp}
$LiFePO_4$	0.777(7)	1.001(2)	0.000	0.0153	0.0193
$LiFe_{0.75}Mn_{0.25}PO_4$	0.839(7)	0.771(1)	0.229(1)	0.0144	0.0174
$LiFe_{0.5}Mn_{0.5}PO_4$	0.888(8)	0.521(1)	0.479(1)	0.0150	0.0176
$LiFe_{0.25}Mn_{0.75}PO_4$	0.913(8)	0.249(1)	0.751(1)	0.0169	0.0234
$LiMnPO_4$	0.975(13)	0.000	1.045(7)	0.0205	0.0287

3.2.1.4 Neutron Pair Distribution Function (PDF) of $LiFe_{1-x}Mn_xPO_4$ olivines

In order to probe the presence of defects and changes in the local structure as a function of the Mn content, neutron PDFs were calculated from the time of flight PND data collected at room temperature for the $LiFe_{1-x}Mn_xPO_4$ (x=0, 0.25, 0.5, 0.75 and 1) samples. Here, the raw neutron PDF data collected at room temperature for the $LiFePO_4$ and $LiMnPO_4$ samples in the range from 1 -100 Å are shown in Figure 3.12.

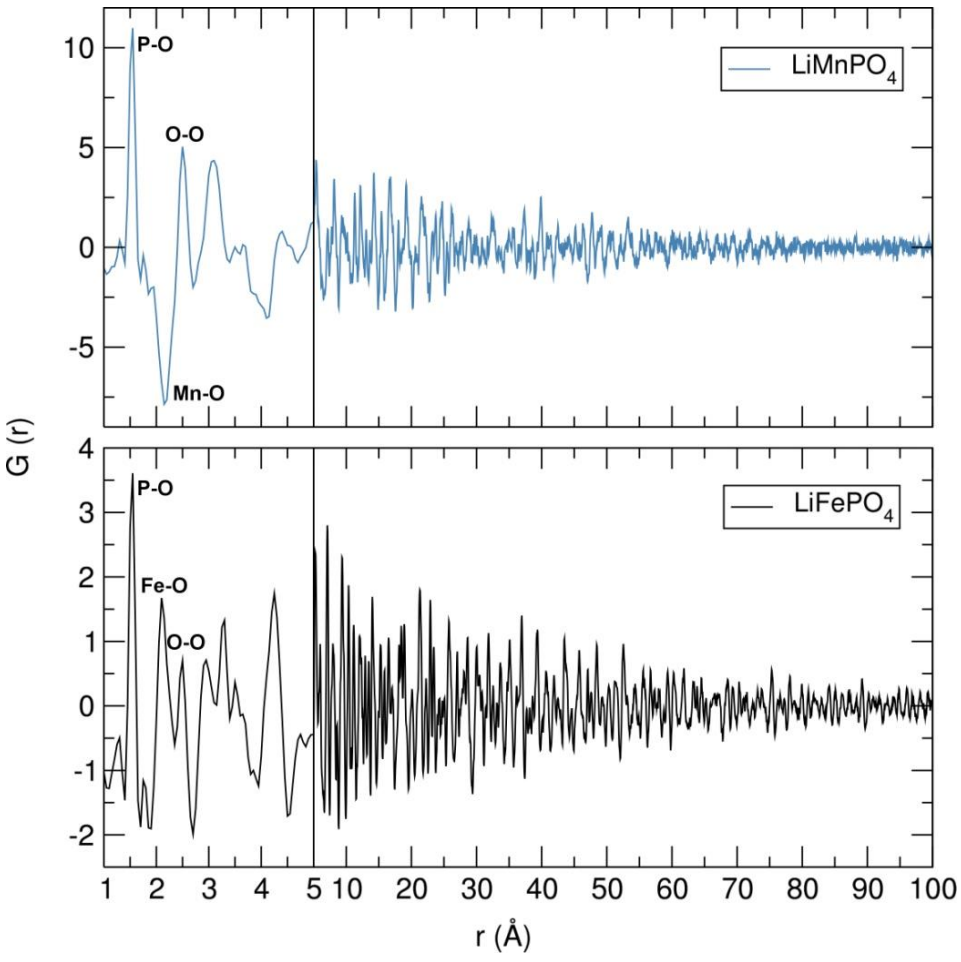

Figure 3.12. Raw neutron PDF data obtained for single-phase $LiFePO_4$ and $LiMnPO_4$ at room temperature in the range from 1 -100 Å. The scattering data was terminated at Q_{max}=36 $Å^{-1}$.

The peak seen at 1.5 Å originates from the P–O distance, while the range from 2 to 2.7 Å covers the first Li–O and Fe–O distances. The first metal–P distance is seen at around 3.2 Å. The noticeable dampening in the intensities of the peaks at higher *r* values indicates that the size of the particles is close to the nano range, as this indicates a decrease in long range order typically associated with crystalline materials. A sharper dampening in the intensities for the $LiMnPO_4$ sample in comparison to the $LiFePO_4$ is noted, suggesting smaller particle sizes for the Mn containing olivines, which is in agreement with the smaller particle size of $LiMnPO_4$ observed in the SEM analysis. Figure 3.13 shows a highlighted region from 1 Å to 5 Å in the neutron PDF data at room temperature of the $LiFe_{1-x}Mn_xPO_4$ (x=0, 0.25, 0.5, 0.75 and 1) phases, revealing a change in the peak at 2.1 Å, which goes from a positive peak to a negative peak when doping $LiFePO_4$ with increasing amounts of Mn. These results can be explained by the difference of sign in the neutron scattering length of the constituent atoms, which are Fe (+9.45 fm), Mn (-3.73 fm), ^{7}Li (-2.22 fm), P (+5.13 fm) and O (+5.803 fm) (NIST scattering lengths).[256] As a result, negative peaks for the Mn–O correlation and positive peaks for Fe–O and P–O correlations are observed.[79] With neutron diffraction, the scattering process involves an interaction between the neutron and the atomic nucleus over a distance very much shorter than the neutron's wavelength, meaning that the scattering power is dependent on properties of the nucleus itself. In neutron diffraction, there is an almost random variation in scattering power, termed the scattering length, with atomic number. The scattering length *b* is an important quantity in neutron diffraction, which depends on the detailed nuclear structure of the element. The constant *b* measures the strength of the interaction between the neutron and the nucleus. The minus sign means that *b* is a positive number for a repulsive interaction between neutron and nucleus. In many cases, elements adjacent to each other in the periodic table (and even different isotopes of the same element) can have vastly different neutron scattering lengths, e.g. Fe, Co and O and in some cases the neutron scattering length is negative, e.g. Li, Mn and Ti.[214]

The neutron PDF data collected for the $LiFe_{1-x}Mn_xPO_4$ phases was modelled by least-squares refinement to an average crystallographic structure using PDFgui.[229] This program allows structural parameters such as lattice parameters, anisotropic atomic displacements parameters, positions and site occupancies to be refined. The resulting fits in the *r* range from 1 to 30 Å for the series of $LiFe_{1-x}Mn_xPO_4$ olivines is shown in Figure 3.14. As seen from the difference curves, a good fit (R_w values from 0.13-0.18) was obtained for the $LiFe_{1-x}Mn_xPO_4$ data sets in the *r*-range from 5 Å to 30 Å, indicating that in this region the average crystallographic model obtained form PND Rietveld analysis matches well to the experimental PDFs. The higher R_w value for the $LiMnPO_4$ (R_w =0.1849) compared to the rest of the samples (R_w values from 0.13-0.15) could be ascribed to the lack of enriched Li in the $LiMnPO_4$ sample ($LiMnPO_4$ was the only sample not prepared with

enriched Li), which would give more noise in the PDF and thus a worse fit. The slight dampening in the peak intensities at higher *r* values again suggests that the particle sizes of these insertion electrodes are close to the nano range. Changes in the lattice parameters with the increasing amount of Mn in the olivine $LiFe_{1-x}Mn_xPO_4$ phases were calculated from the neutron PDF fits from 1-30 Å and they also agreed with Vegard's law (Table A3.6). Figure A3.2 shows a linear increase of the lattice parameters with higher amounts of Mn in these compounds, most likely due to the slightly larger ionic radius of Mn^{2+} compared to Fe^{2+}. These results confirm that substitution of Fe by Mn increases the unit cell volume. Furthermore, there is an excellent agreement in the variation of the unit cell parameters of the $LiFe_{1-x}Mn_xPO_4$ nanostructures determined from Rietveld analysis of high resolution PND and neutron PDF data was observed, suggesting that the average crystal structure and the local strurture are similar. Table A3.7 summarises the bond length of the $LiFe_{1-x}Mn_xPO_4$ phases determined from the neutron PDF fits at room temperature. It is notable that the Li-Li distance slightly increases with higher Mn content. When fits to the model at *r* values below 5 Å are examined, some of the peak intensities in the experimental PDF are not so well described. This poorer fit at low *r* may suggest that local disorder could be induced by the presence of antisite defects (i.e. Fe^{2+} at the Li^+ sites) or distortions in the MO_6 (*M*=Fe or Mn) octahedra. It is important to note that the peak at 2.5 Å, which can be attributed to one of the oxygen-oxygen distances, is the poorest described peak in these fits, which may point to distortions in the MO_6 (*M*=Fe or Mn) octahedra and this is most pronounced in the $LiMnPO_4$ sample. Previous olivine $LiFe_{1-x}Mn_xPO_4$ compounds synthesised by a solvothermal method were characterised by synchrotron radiation-X-ray absorption spectroscopy combined with first principle calculations and energy-dispersive X-ray measurement and results indicated that when increasing the Mn doping concentration the distortion of the MO_6 octahedra was more evident.[82] Considering the possibility of either Li/Fe antisite defects, a model allowing the occupancy of the Li and Fe atoms to be exchanged was applied. The results suggested that the $LiFePO_4$ was the only one which presented a small amount of Li/Fe antisite defects (~2%). No Mn-containing phases showed any evidence for the presence of antisite defects. When the fits were performed allowing some excess of Fe atoms to reside on the Li sites (full occupancy of the Fe^{2+} sites is assumed and the Fe^{2+} excess is occupying some Li^+ positions), it was found again that ~2% of Fe atoms could be located on the Li sites in Li defective $LiFePO_4$. However, no Fe on Li positions were observed in the Mn containing $LiFe_{1-x}Mn_xPO_4$ phases. It was also not seen any apparent presence of Mn on the Li sites in the case of $LiMnPO_4$. The possibility of a two phase model in which separate nanodomains of $LiFePO_4$ and $LiMnPO_4$ could be present in the mixed metal phases was also ruled out by fitting such a model to the data. However, this model did not lead to an improvement in the fits.

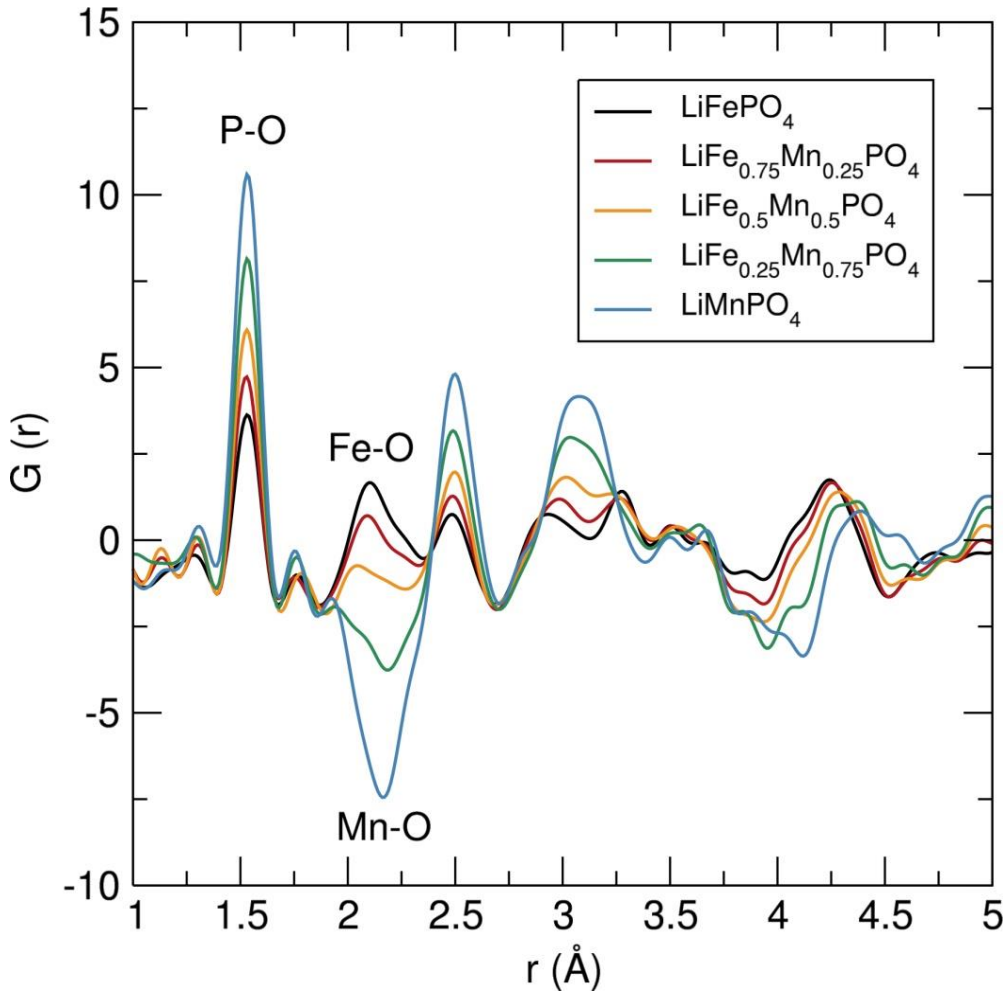

Figure 3.13. Raw neutron PDF data obtained for single-phases $LiFe_{1-x}Mn_xPO_4$ (x=0, 0.25, 0.5, 0.75, 1) at room temperature in the range from 1 to 5 Å.

In previous investigations carried out by Jensen *et al.*, the crystal structure and defect chemistry of hydrothermally synthesised $LiFe_{1-x}Mn_xPO_4$ particles were characterised by simultaneous neutron and X-ray Rietveld refinement as well as X-ray and neutron pair distribution function analysis.[257] These results indicated that the fast (from 40 min to 7 hr) hydrothermal synthesis of $LiFePO_4$ conducted at 170 °C triggers partial Fe occupancy and vacancies on the Li (M1) site, while the Fe (M2) site is always fully occupied by iron. They also found out that crystalline, defective $Li_xFe_yPO_4$ coexists with amorphous lithium and iron phosphate structures displaying only short-range order. With this in mind, neutron PDF data were fitted in the *r*-ranges from 1 Å to 5 Å (Figure 3.15) and from 5 Å to 30 Å (Figure A3.3) independently, both using the same $LiFePO_4$. The resulting fits revealed that in both regions the average crystallographic model matches very well with the experimental PDFs. However, significant differences in the scale factors of both *r*-range modelled datasets were found, with the scale factor being larger in the low *r* region fits. This may indicate that there could be some population of short-range ordered (i. e. amorphous) Li/Fe/Mn-PO_4 coexisting with highly crystalline $LiFe_{1-x}Mn_xPO_4$ nanoparticles. The lower *r*-region fits from 1 Å to 5 Å fitted well to the crystalline $LiFe_{1-x}Mn_xPO_4$ structural

models, suggesting that the local structure of any amorphous component is very closely related to the bulk phase. From the ratio between the scale factors obtained for the 1 Å to 5 Å and the 5 Å to 30 Å, results showed that the $LiMnPO_4$ sample may have a higher amount of "amorphous $LiMnPO_4$" compared to the $LiFePO_4$ sample and also that the mixed metal phosphates presented a slightly lower "amorphous" content in comparison with both end members of this family of $LiFe_{1-x}Mn_xPO_4$ (x=0, 0.25, 0.5, 0.75 and 1) phases. Table 3.6 shows the R_w values obtained from neutron PDF fits of single-phase $LiFe_{1-x}Mn_xPO_4$ olivines at different r ranges and Table 3.7 the scale factor values. In general, these results are in agreement with previous PDF studies on hydrothermally synthesised $LiFe_{0.5}Mn_{0.5}PO_4$ sample conducted by Jensen *et al.*, in which they believe that the poor fits to the lower r-region can be ascribed to the presence of amorphous content. Furthermore, they concluded that local disorder induced by the split of cation site (from both Fe, Mn and Li) was not apparent in their refinements.[257]

To quantify the amorphous content in this series of $LiFe_{1-x}Mn_xPO_4$ olivines, two-phase model refinements from 1 to 30 Å in which the two phases have the same average olivine structure but allowing only the *spdiameter* (particle diameter for the PDF shape damping function) in one of the phases to refine were performed. When the second phase with a small *spdiameter* is included, that structure would represent the amorphous fraction in the material while the *spdiameter* would give the coherence length of the atomic structure in the amorphous phase. These refinements suggest that the amorphous phase has order to about ~1-2 nm. Table A3.8 shows the calculated scale factors and amorphous contents for the $LiFe_{1-x}Mn_xPO_4$ olivine phases obtained from these two isostructural phases refinements. Results suggested a higher presence of amorphous material in the $LiMnPO_4$ phase compared to the other Fe containing olivines (for example ~8% amorphous content in $LiMnPO_4$ *vs.* ~5% in $LiFe_{0.75}Mn_{0.25}PO_4$), which agrees with the trend observed from the refinement at different r ranges. A slight improvement in the fit quality was obtained when adding the second phase.

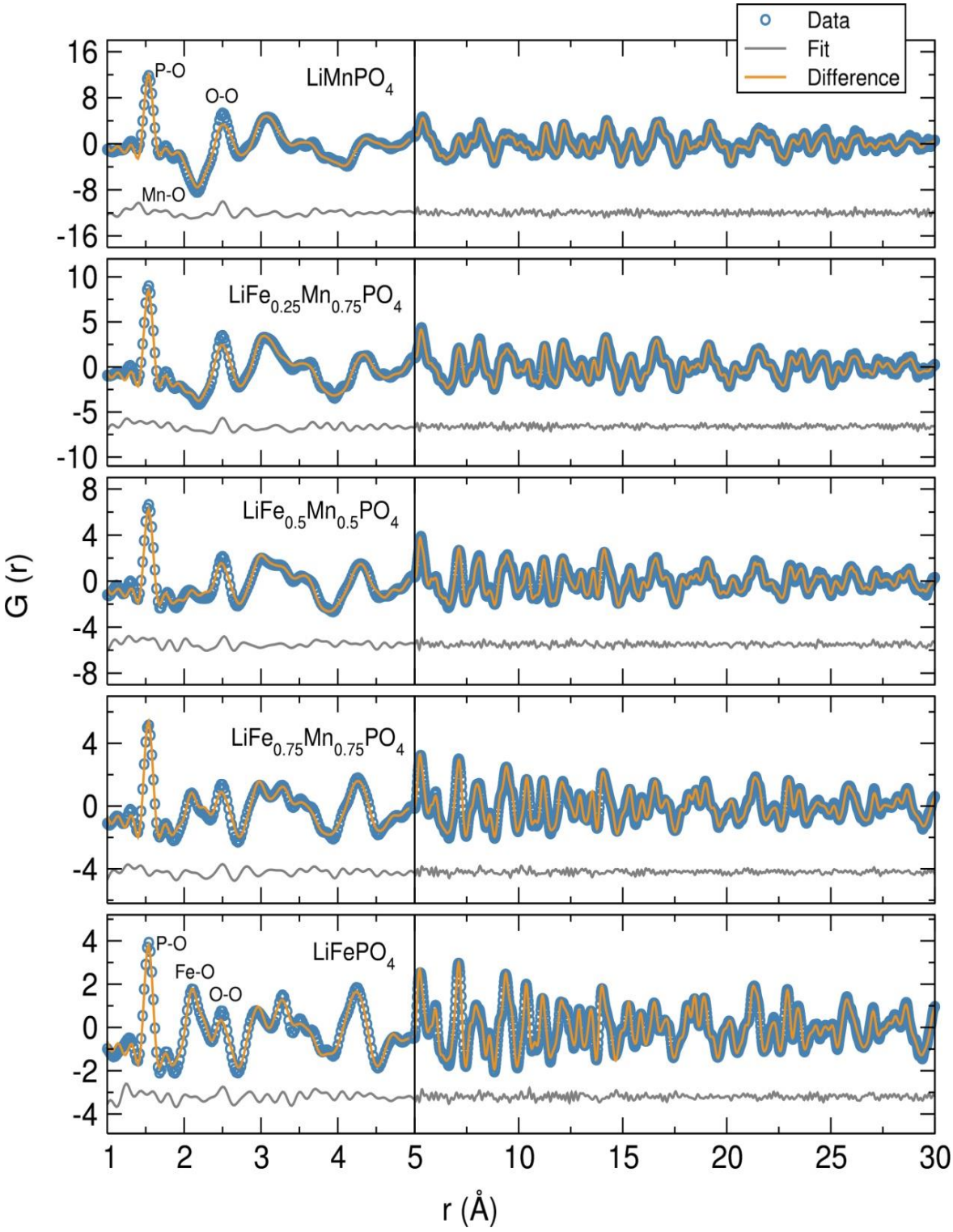

Figure 3.14. Fits of neutron PDF data obtained for single-phase $LiFe_{1-x}Mn_xPO_4$ (x = 0, 0.25, 0.5, 0.75 and 1) olivines at room temperature in the r range from 1 - 30 Å.

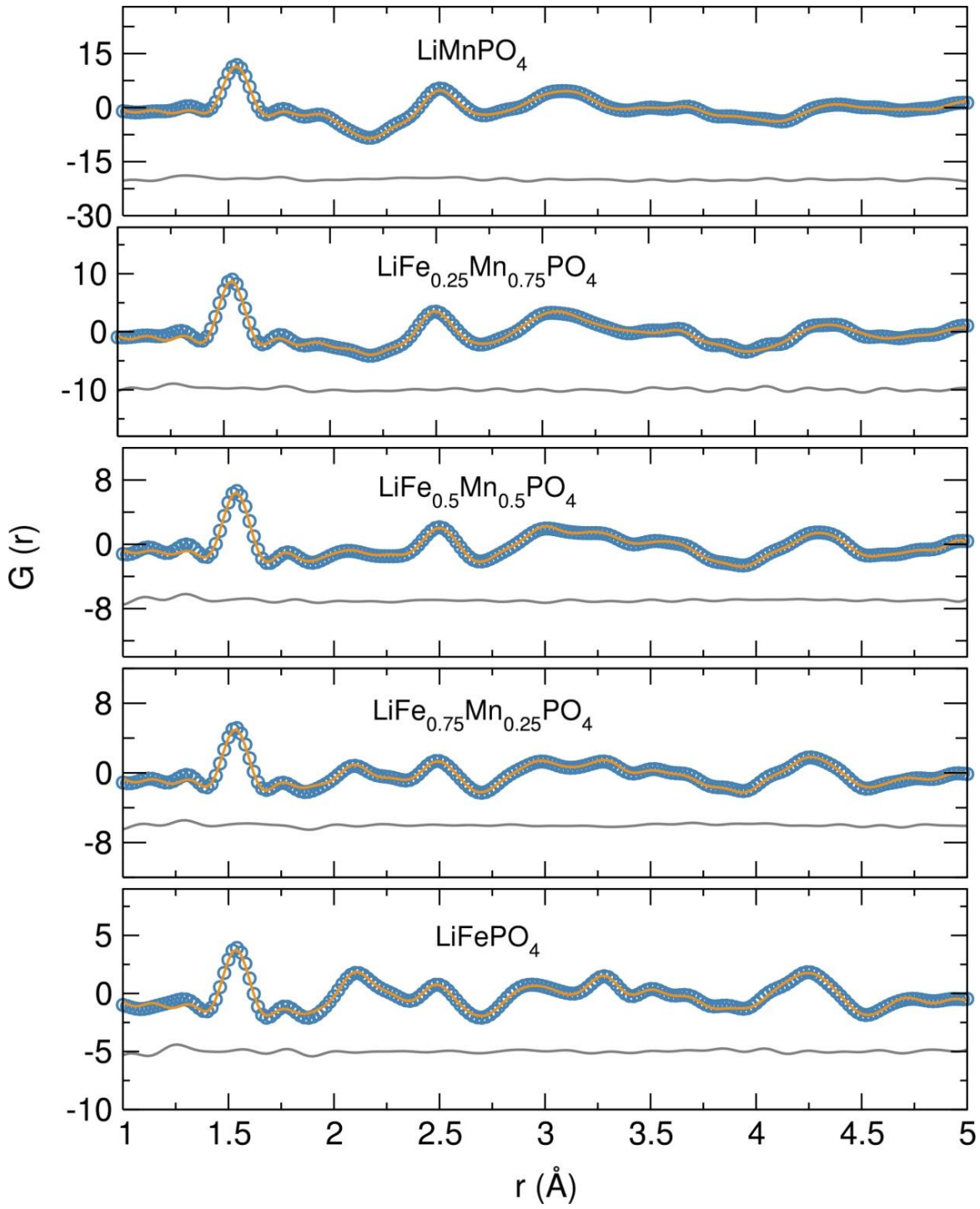

Figure 3.15. Fits of neutron PDF data obtained for single-phase $LiFe_{1-x}Mn_xPO_4$ (x = 0, 0.25, 0.5, 0.75 and 1) olivines at room temperature in the r range from 1 Å to 5 Å. Dots represent observed data and solid line the calculated pattern. The lower line is the difference curve.

Table 3.6. R_w values obtained from neutron PDF fits of single-phase $LiFe_{1-x}Mn_xPO_4$ (x=0, 0.25, 0.5, 0.75 and 1) olivines at different r ranges.

R_w	$LiFePO_4$	$LiFe_{0.75}Mn_{0.25}PO_4$	$LiFe_{0.5}Mn_{0.5}PO_4$	$LiFe_{0.25}Mn_{0.75}PO_4$	$LiMnPO_4$
1 - 5 Å	0.1244	0.1211	0.1140	0.1289	0.1085
5 - 30 Å	0.1074	0.1088	0.1336	0.124344	0.1776
1 - 30 Å	0.1299	0.1331	0.1577	0.1468	0.1849

Table 3.7. Scale factor values obtained from neutron PDF fits of single-phase $LiFe_{1-x}Mn_xPO_4$ (x=0, 0.25, 0.5, 0.75 and 1) olivines at different r ranges.

Scale factor	$LiFePO_4$	$LiFe_{0.75}Mn_{0.25}PO_4$	$LiFe_{0.5}Mn_{0.5}PO_4$	$LiFe_{0.25}Mn_{0.75}PO_4$	$LiMnPO_4$
1 - 5 Å	0.76(8)	0.68(9)	0.72(7)	0.75(3)	0.82(2)
5 - 30 Å	0.69(5)	0.68(2)	0.69(3)	0.70(4)	0.66(3)
1 - 30 Å	0.70(4)	0.68(3)	0.70(3)	0.73(2)	0.68(2)

To examine the possible presence of amorphous material in the $LiFe_{1-x}Mn_xPO_4$ series, high resolution TEM analysis was performed on the $LiFe_{0.25}Mn_{0.75}PO_4$ sample. Analysis of the $LiFe_{0.25}Mn_{0.75}PO_4$ sample revealed that most particles are crystalline with an elongated oval shape (Figure 3.16 (a)), and exhibit lattice fringes up to within less than ~ 1nm of the edge (Figure 3.16 (b)). Very few particles have a large amorphous coating or appear to be amorphous. The HRTEM fringe spacing in particle regions of a clear single layer is 0.39 nm. Electron diffraction measurements can be indexed to a *Pnma* crystal structure (Figure 3.16 (c)). Dark field images showed elongated oval shaped porous particles ~225 nm in width and 1.5 μm in length. Interestingly, pores of approximately 10 nm could be observed (Figure 3.16 (d)).

To investigate how the surface area and pore size change in this family of $LiFe_{1-x}Mn_xPO_4$ (x=0, 0.25, 0.5, 0.75 and 1) olivines, N_2 adsoption isotherms at 77 K were conducted. Pore size distributions calculated using QSDFT revealed average pore size diameter in the range from 17 to 26 Å for the five $LiFe_{1-x}Mn_xPO_4$ samples. Figure 3.17 illustrates the N_2 sorption isotherms for the $LiFe_{1-x}Mn_xPO_4$ samples and Table 3.8 lists the specific surface area and average pore size from BET analysis, as derived from their N_2 sorption isotherms. The results show that the $LiMnPO_4$ sample exhibited the highest surface area (23.5 m^2/g compared to $LiFePO_4$ of 6.6 m^2/g, see Table 3.8). These results correlate well with observations from neutron PDF data, which suggest a higher degree of disorder in the $LiMnPO_4$ phase. Larger surface areas are associated with progressively greater Mn content. Increasing the surface area of the particles leads to greater opportunities for disorder of the atoms at those surfaces, due to the potential for greater relaxation in the crystallinity at the surface. This hypothesis directly agrees with the observations from the neutron

PDF analysis, which showed that at a local level (below 5 Å), a greater deviation of the data from the average structural model provided from PND Rietveld analysis was observed. This is most likely an increased surface effect due to the emergence of porosity in these olivine samples and this nanostructured disorder drives changes in the total scattering function observed.

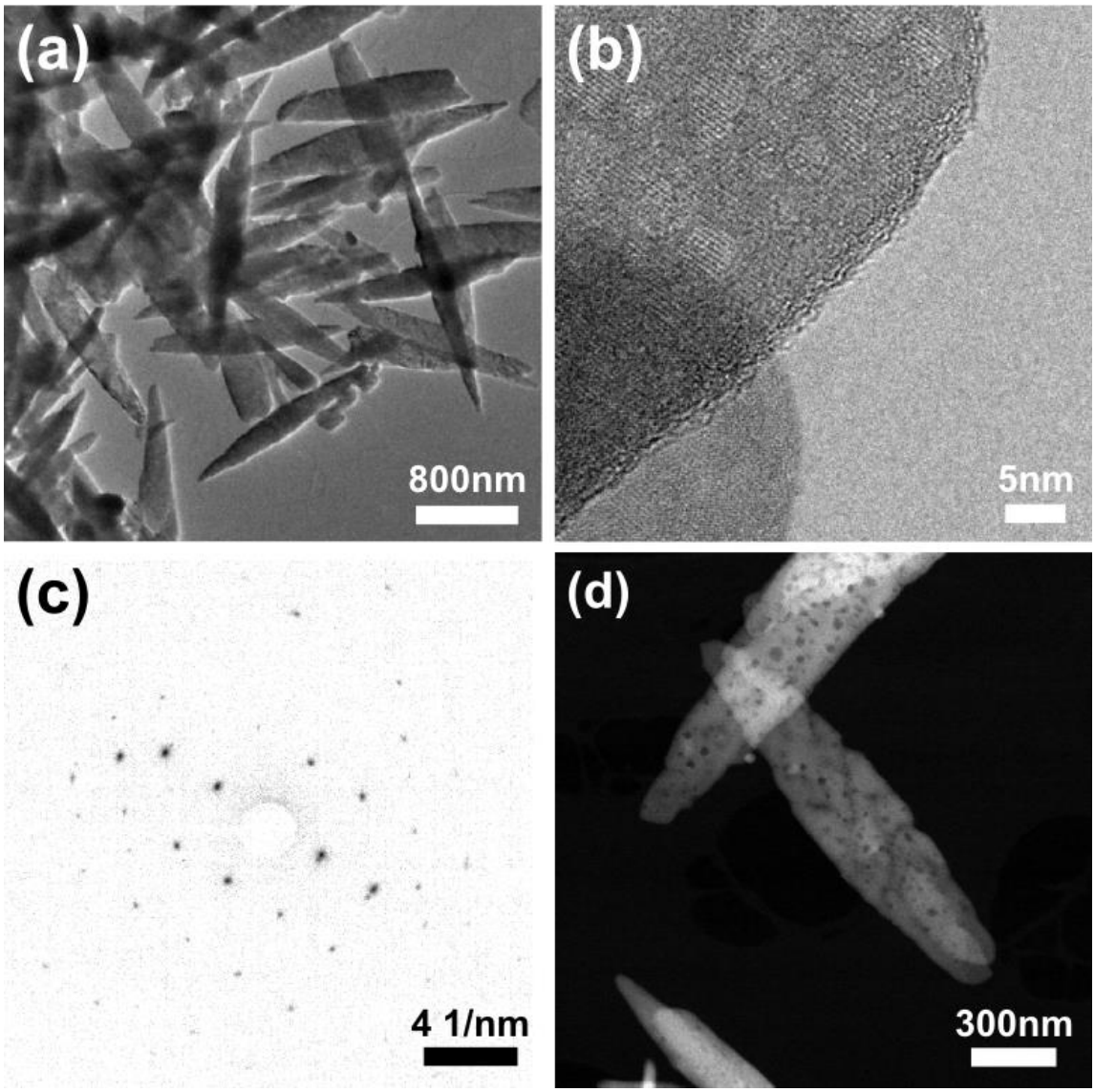

Figure 3.16. High resolution TEM images of **(a, b)** $LiFe_{0.25}Mn_{0.75}PO_4$ powders, with SAED confirming *Pnma* crystal structure. **(d)** Dark field imaging reveals pores in the particle of typically 10 nm in diameter.

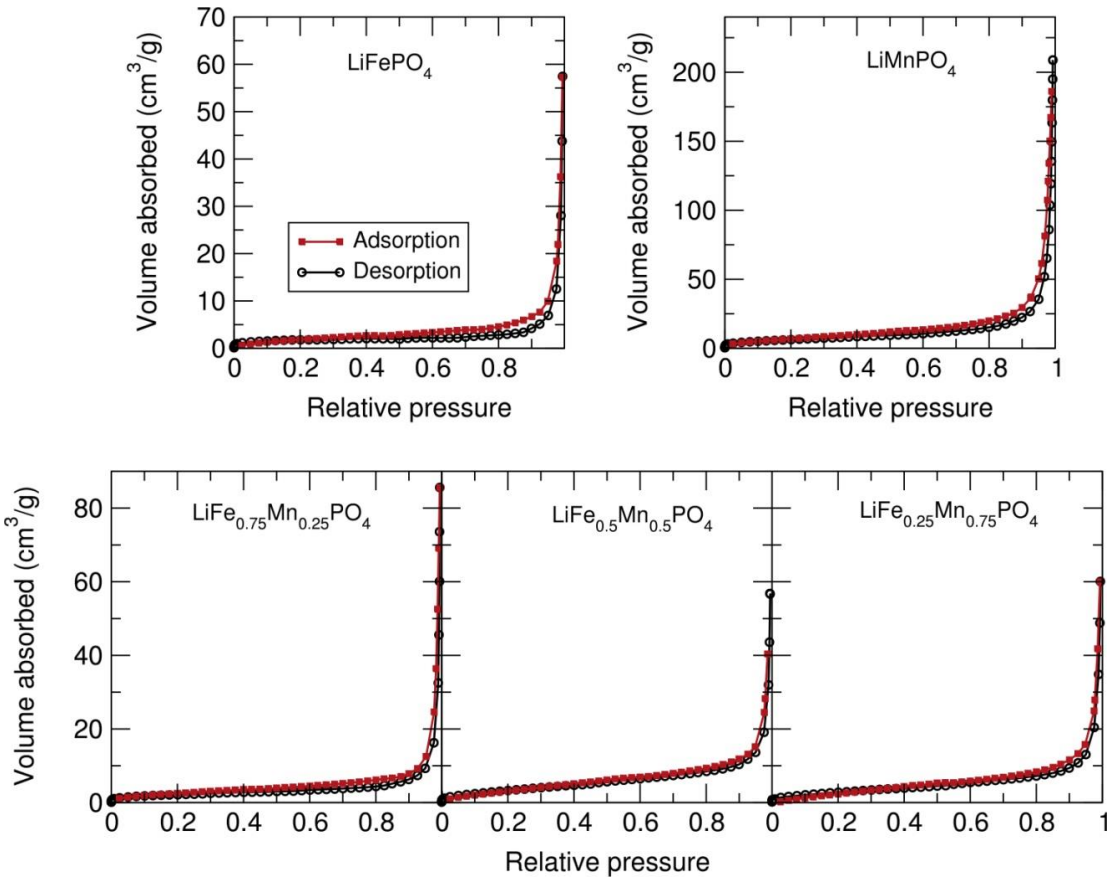

Figure 3.17. N_2 sorption isotherms at 77 K for $LiFe_{1-x}Mn_xPO_4$ (x=0, 0.25, 0.5, 0.75 and 1) olivine phases.

Table 3.8. Specific Surface Area and Average Pore Size from BET analysis for $LiFe_{1-x}Mn_xPO_4$ (x=0, 0.25, 0.5, 0.75 and 1) olivine phases, as derived from their N_2 sorption isotherms.

Sample	specific surface area (m^2/g)	average pore size (Å)
$LiFePO_4$	6.6	20
$LiFe_{0.75}Mn_{0.25}PO_4$	7.8	17
$LiFe_{0.5}Mn_{0.5}PO_4$	14.1	24
$LiFe_{0.25}Mn_{0.75}PO_4$	11.6	26
$LiMnPO_4$	23.5	20

3.2.1.5 Muon spin spectroscopy (μ^+SR) of $LiFe_{1-x}Mn_xPO_4$ olivines

Since lithium diffusion is one of the primary parameters that govern the charge and discharge rates in LIBs, the muon spin relaxation (μ^+SR) technique has been employed here to probe the microscopic Li^+ diffusion properties in the Mn-containing olivine $LiFe_{1-x}Mn_xPO_4$ (x=0.25, 0.5 and 0.75) samples. Spin polarised positive muons were implanted into $LiFe_{1-x}Mn_xPO_4$ samples and the data were fit using an exponentially relaxing dynamic Kubo-Toyabe function,[258] which provides information on the Li^+ diffusion behaviour in these materials, including the field fluctuation rate, ν, and the local field distribution at the muon stopping site, Δ. Figure 3.18 (a) (b) and (c) shows the obtained fits of the raw

μ⁺SR data for $LiFe_{1-x}Mn_xPO_4$ (x=0.25, 0.5 and 0.75) samples collected at 300 K and at 0, 5, 10 and 20 G. At each temperature, the ZF and LF spectra of the $LiFe_{1-x}Mn_xPO_4$ samples consist of a fast initial relaxation signal followed by a later slowly relaxing signal. The former trend can be explained by the muon interactions with the magnetic moments (H_{int}^{3d}) due to the 3*d* electrons of the Fe^{2+} and Mn^{2+} ions, while the latter is caused by the interactions between the muon and the nuclear magnetic moments fields (H_{int}^{N}) from the ^{6}Li, ^{7}Li, ^{57}Fe, ^{55}Mn and ^{31}P. Also, the applied LF (5, 10 and 20 Gauss) clearly reduces the relaxation rate of the slowly relaxing signal. Attempts to measure the $LiMnPO_4$ sample were not successful because contributions arising from the high magnetic moment on the Mn^{2+} were still present even when applying longitudinal magnetic fields up to 20 G (see Figure 3.19). Therefore, any contributions to the spectra from Li^+ ions diffusion were masked and the data could not be reliably described by any fitting functions. From the results of the fits at different temperatures shown in Figure 3.18 (d), (e), (f), (g), (h) and (i), the temperature dependence of *v* follows a similar trend in the three mixed-metal phosphates studied, where a slight decrease from the lowest measured temperature at 100 K, followed by a significant rise from ~190 K to ~260 K over the thermally activated region, and then a sharp drop. The observed decrease of v above 260 K could be explained from the Li^+ diffusion being too fast for μ⁺SR technique to be able to measure it. On the other hand, the Δ values show a trend in which a low-temperature plateau is followed by a smooth decrease to a high-temperature plateau. This slight decrease in the Δ values over the thermally activation region could be explained by changes in the local magnetic field distribution caused by the lithium diffusion process. Considering that the primary hopping pathway for Li^+ ions is along the *b*-axis in these compounds, the diffusion coefficient can be estimated taking into account the following equation $D_{Li}=b^2v/4$, where *v* is the field fluctuation rate and *b* is the refined *b* lattice parameter obtained from Rietveld refinements of the high resolution PND data. Extrapolating the values to 300 K gives an estimation of the lithium hopping rate at room temperature. For the determination of the activation energy of Li^+ diffusion in these materials, the Arrhenius equation was plotted in order to represent the ln(v) over 1/T over the thermally activated region to obtain E_{act}, considering the following expression for the Arrhenius equation 3.1:

$$ln(v) = \frac{-E_{act}}{K_B T} + ln(A) \qquad (3.1)$$

where K_B is the Boltzman constant ($1.3806488 \times 10^{-23}$ J/K) and A is a pre-exponential factor (prefactor). In Table 3.9, the estimated values of the Li^+ diffusion coefficients and the activation energies both at 300 K for the three $LiFe_{1-x}Mn_xPO_4$ (x=0.25, 0.5 and 0.75) mixed metal phosphates calculated from μ⁺SR studies are listed. These results reveal that the D_{Li} and E_{act} slightly decrease with higher Mn content. μ⁺SR has thus been used to provide a new method of investigating the diffusive properties of this series of $LiFe_{1-}$

$_xMn_xPO_4$ (x=0.25, 0.5 and 0.75) olivine phosphates, finding a lithium diffusion constant D_{Li} in the order of 10^{-10} cm^2s^{-1} and an energy barrier of E_a 100 meV. These results are in excellent agreement with previous μ^+SR studies on $LiFePO_4$ polymorphs also prepared through a solvothermal microwave-assisted approach.[51] On the other hand, previous determinations of the D_{Li} constants in $LiFe_{1-x}Mn_xPO_4$ phases using electrochemical impedance spectroscopy showed slightly lower values ranging from 10^{-13} cm^2s^{-1} to 10^{-12} cm^2s^{-1}.[259] The more elevated D_{Li} values obtained wtih μ^+SR technique can be ascribed to the fact that in the μ^+SR measurements there are no contributions from intragrain and grain boundaries. This coud also explain the low activation energies of ionic conductivity obtained here (75-125 ± 10 meV) compared to other manganese-doped $LiFePO_4$ olivines reported in the literature showing values in the range of 600 meV.[81] Previous investigations of the lithium diffusion behaviour in battery materials indicate a significant difference between microscopic and bulk determinations of D_{Li} depending on the characterisation technique employed.[260, 261] Di Lecce *et al.* carefully investigated the lithium transport properties in $LiMn_{1-x}Fe_xPO_4$ olivines by cyclic voltammetry (10^{-12} cm^2s^{-1} for $LiMnPO_4$, 10^{-9} cm^2s^{-1} for $LiFePO_4$ and 10^{-11} cm^2s^{-1} for $LiFe_{0.5}Mn_{0.5}PO_4$), electrochemical impedance spectroscopy (10^{-13} cm^2s^{-1} for $LiMnPO_4$, 10^{-12} cm^2s^{-1} for $LiFePO_4$ and 10^{-13} cm^2s^{-1} for $LiFe_{0.5}Mn_{0.5}PO_4$) and galvanostatic intermittent titration techniques (10^{-14} - 10^{-10} cm^2s^{-1} for $LiMnPO_4$ and $LiFePO_4$, and 10^{-13} - 10^{-10} cm^2s^{-1} for $LiFe_{0.5}Mn_{0.5}PO_4$) and concluded that the wide diffusion coefficient window obtained by changing the adopted characterisation technique suggested a complex trend of the lithium diffusion in olivines and revealed that the techinique may significantly influence the materials evaluation.[259]

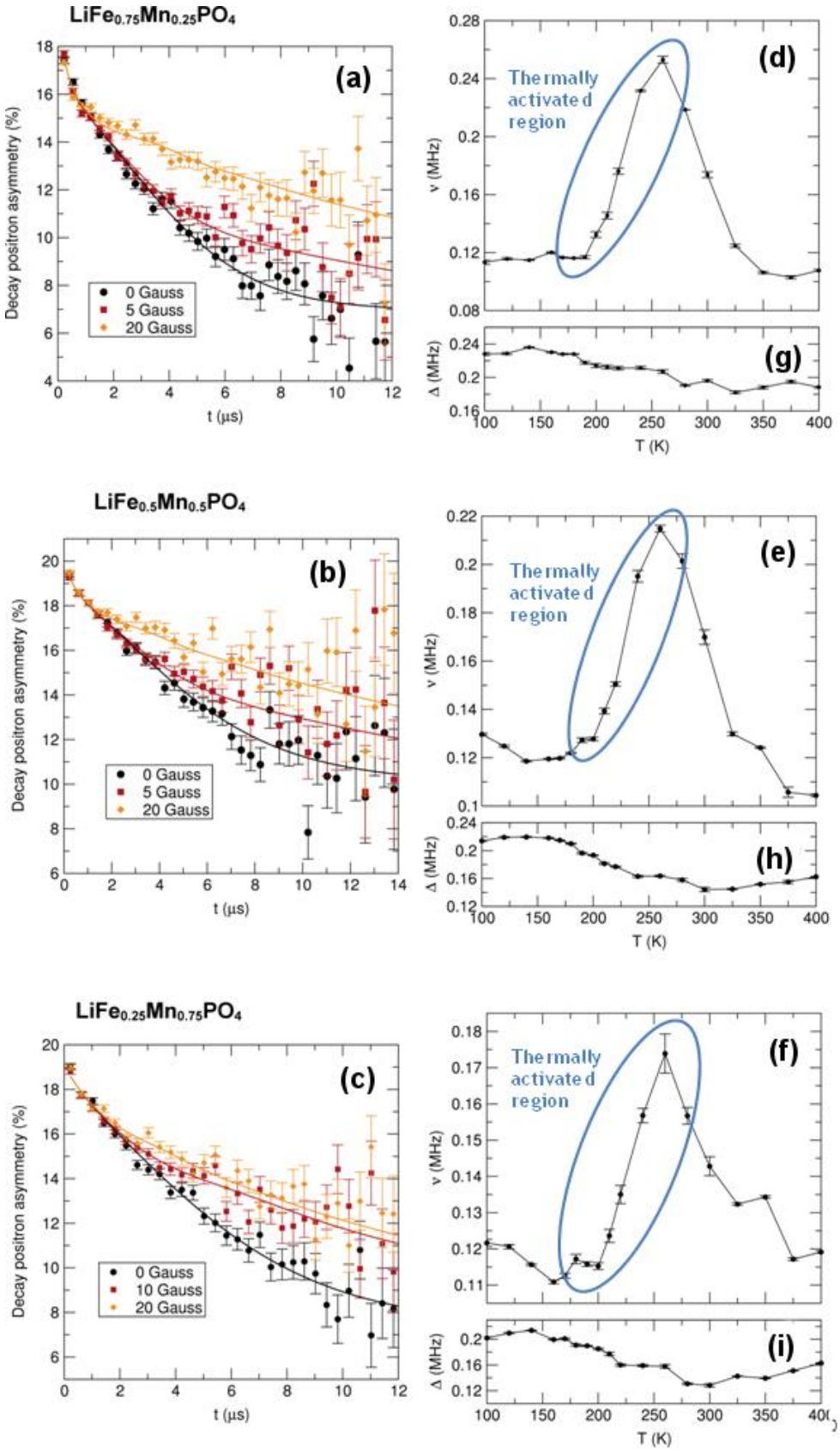

Figure 3.18. (a) (b) (c) Raw μ^+SR data for $LiFe_{1-x}Mn_xPO_4$ (x=0.25, 0.5 and 0.75) at 300 K at zero field (ZF) [circles] and applied longitudinal fields of 10 G [squares] and 20 G [diamonds]. Temperature dependence of **(d) (e) (f)** fluctuation rate (ν) and **(g) (h) (i)** field distribution width (Δ) at muon stopping site, measured from 100 K to 400 K at 0, 10 and 20 G longitudinal fields.

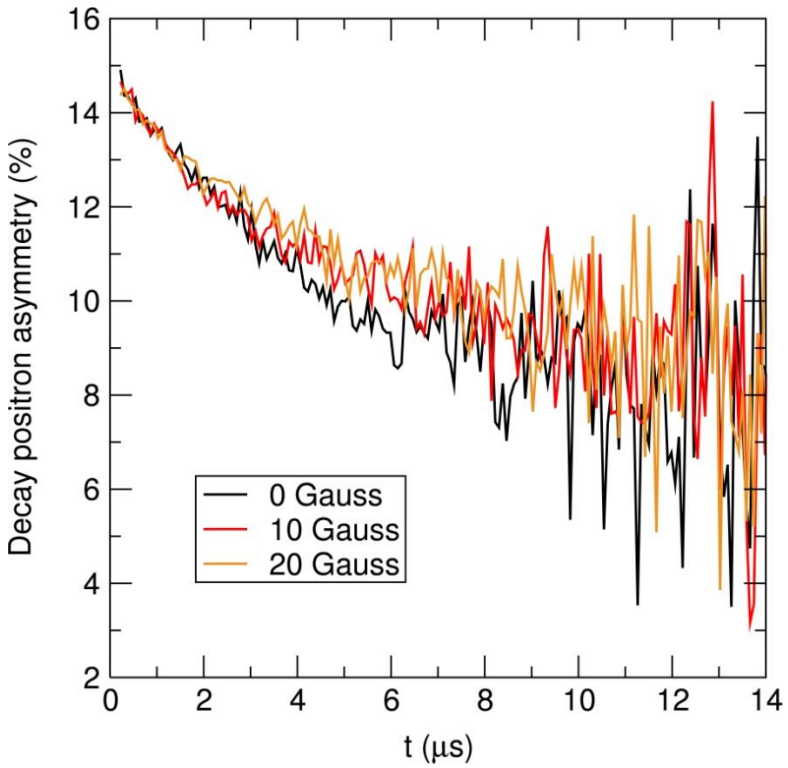

Figure 3.19. Raw μ^+SR data for $LiMnPO_4$ at 300 K at zero field (ZF) and applied longitudinal fields of 10 G and 20 G.

Table 3.9. D_{Li} and E_{act} at room temperature of $LiFe_{1-x}MnPO_4$ (x=0.25, 0.5 and 0.75) samples from μ^+SR data.

Sample	D_{Li} at 300 k (cm^2s^{-1})	E_{act} (meV)
$LiFe_{0.75}Mn_{0.25}PO_4$	3.2×10^{-10}	122 ± 18
$LiFe_{0.5}Mn_{0.5}PO_4$	2.6×10^{-10}	100 ± 11
$LiFe_{0.25}Mn_{0.75}PO_4$	2.0×10^{-10}	75 ± 3

3.2.1.6 Electrochemical performance of $LiFe_{1-x}Mn_xPO_4$ olivines

Galvanostatic cycling with potential limitation (constant current) of the electrode nanostructures in a Swagelok type cell was conducted at a C/20 rate in a potential range from 2.2 V to 4.5 V depending on the Mn content. Moreover, galvanostatic cycling experiments at different charge-discharge rates were also performed to examine the rate capabilities of these olivine materials. Finally, CV studies were carried out to determine the oxidation and reduction potentials of the electrochemically active species and to confirm the reversibility of these electrochemical systems. Due to the poor electronic conductivity of these materials, the $C/LiFe_{1-x}Mn_xPO_4$ powders were mixed with conductive carbon black and polytetrafluoroethylene (PTFE) in 60:30:10 % wt. ratio and the mixture was then pressed into a pellet. Although such high carbon loadings are inappropriate for real batteries, they are useful in establishing the true rate capability of the active material and are commonly used in the testing of high-rate nanomaterials.[63, 262, 263]

In this electrochemical system using $LiFePO_4$, Li^+ is extracted during charge and Li_xFePO_4 ($x<1$ and with Fe changing oxidation state from 2+ to 3+) is formed. After that, while discharging, Li^+ is inserted back into the Li_xFePO_4 structure, where Fe^{3+} is reduced to Fe^{2+}. The voltage-capacity profile from the galvanostatic cycling test of the C/$LiFePO_4$ sample (Figure 3.20 (a)) displays a clear flat voltage plateau at ~3.45 V corresponding to the Fe^{3+}/Fe^{2+} redox pair. Moreover, charge and discharge capacities of approximately 160 $mAh{\cdot}g^{-1}$ were reached, values that are quite close to the theoretical capacity of this electrode material (170 $mAh{\cdot}g^{-1}$) and in accordance with data reported in similar electrochemical studies on microwave synthesised $LiFePO_4$ electrodes.[45, 46] Furthermore, this cycling study revealed that this insertion electrode exhibits no capacity fading over at least 50 cycles (Figure 3.20(b)).

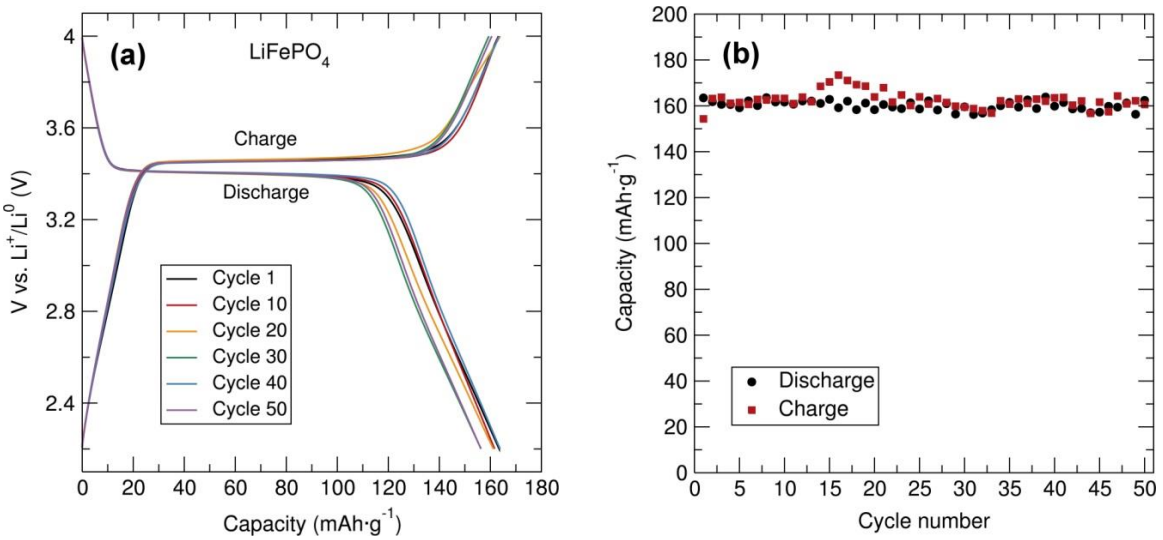

Figure 3.20. (a) Voltage-capacity profile and **(b)** cycling stability of C/$LiFePO_4$ (15% wt. C from sucrose) with C black and PTFE in 60:30:10 % wt. ratio between 2.2 V and 4.0 V at C/20 rate.

Cycling studies of the mixed metal phosphates C/$LiFe_{1-x}Mn_xPO_4$ were also conducted to examine the relationship between particle morphology, Mn content and electrochemical performance. Similar electrochemical tests for the different C/$LiFe_{1-x}Mn_xPO_4$ samples indicated a significantly better electrochemical performance of $LiFePO_4$ (~160 $mAh{\cdot}g^{-1}$) in comparison to the Mn-containing phases (Figure 3.21). In particular, the $LiMnPO_4$ exhibited much lower discharge capacities (only ~50 $mAh{\cdot}g^{-1}$). This capacity is markedly lower than the initial specific charge capacity of 125 $mAh{\cdot}g^{-1}$ that faded to 75 $mAh{\cdot}g^{-1}$ after 100 cycles reported by Niederberger *et al* on a C/$LiMnPO_4$ prepared through a 3 min microwave synthesis.[45] $LiMnPO_4$ is an insulator and exhibits more sluggish kinetics than $LiFePO_4$. The limiting factor in the reversible $MnPO_4/LiMnPO_4$ redox reaction is then mostly its low ionic and electronic transport within $LiMnPO_4$.[264] Therefore, the generation of electrochemically $LiMnPO_4$ is more challenging and specific synthetic procedures are required to enhace its electrochemical performance. The Fe/Mn containing olivines also

delivered lower discharge capacities than the C/$LiFePO_4$ sample. As observed in Figure 3.21, the mixed transition metal phosphates displayed two clear voltage plateaus at ~3.45 V and ~4.1 V due to the Fe^{3+}/Fe^{2+} and Mn^{3+}/Mn^{2+} redox pair, respectively, the lengths of which are correlated to the Fe/Mn contents in C/$LiFe_{1-x}Mn_xPO_4$. Reversible discharge capacities in the order of 120 mAh·g^{-1} were obtained for the three C/$LiFe_{1-x}Mn_xPO_4$ (x=0.25, 0.50 and 0.75) samples. Furthermore, it must be added that no capacity fading was observed in any of the C/$LiFe_{1-x}Mn_xPO_4$ phases at least over the first 20 cycles (Figure 3.22 (a)). PXRD patterns of the post-cycled material in the discharge state shown in Figure 3.22 (b) indicated that the cycling process did not modify the structure of these materials, confirming the good structural stability of this family of mixed metal phosphates upon cycling. Furthermore, the slight shift of the diffraction peaks towards lower 2θ angles with higher Mn contents in C/$LiFe_{1-x}Mn_xPO_4$ was still evident after the cycling process.

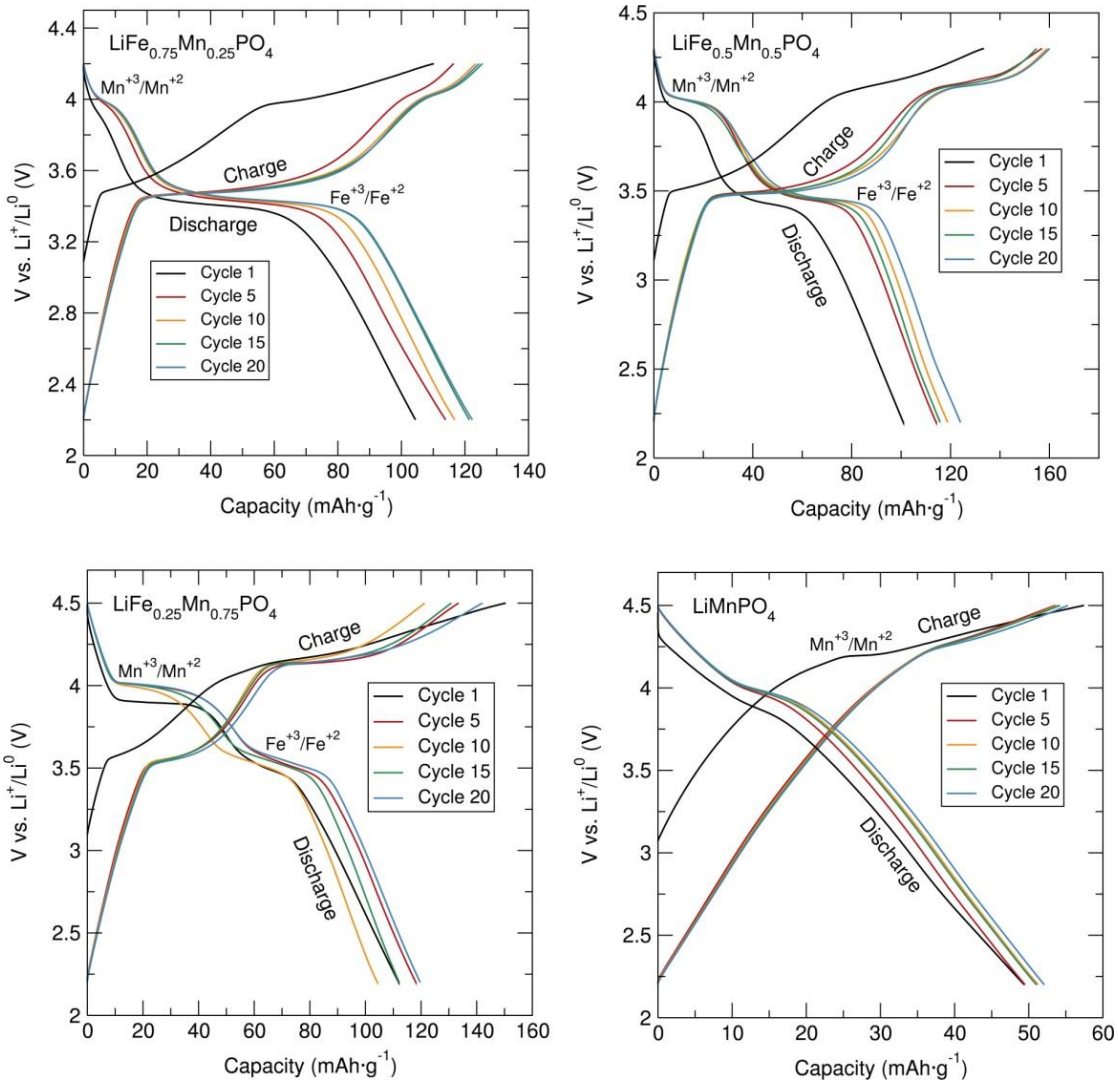

Figure 3.21. Voltage-capacity profiles of C/$LiFe_{1-x}Mn_xPO_4$ (x=0.25, 0.50, 0.75 and 1) (15% wt. C from sucrose), C black and PTFE in 60:30:10 (% wt.) between 2.2 V and 4.5 V (depending on Mn content) at C/20 rate.

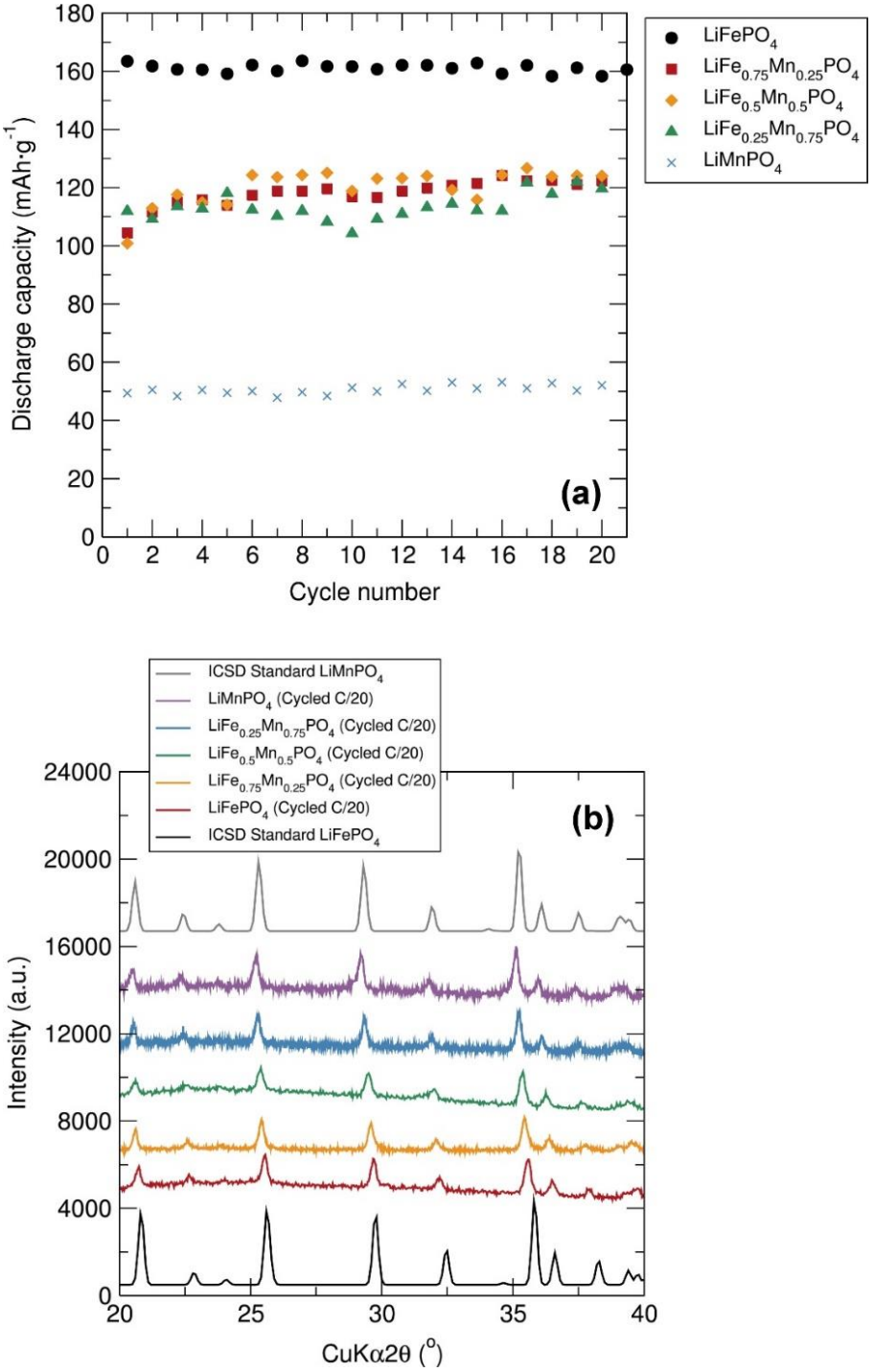

Figure 3.22. (a) Cycling stability between 2.2 V and 4.5 V at C/20 rate of C/LiFe$_{1-x}$Mn$_x$PO$_4$ (15% wt.C sucrose), C black and PTFE in a 60:30:10 % wt. ratio. **(b)** PXRD of cycled C/LiFe$_{1-x}$Mn$_x$PO$_4$ nanostructures in the discharged state.

The rate behaviour of the C/LiFe$_{1-x}$Mn$_x$PO$_4$ phases at room temperature was investigated in order to elucidate the rate capabilities as a function of particle morphology and Mn content. It was found that in all cases, the discharge capacity decreased regularly with increased rates and that the capacity was recovered when returned to a C/10 rate. Upon increasing the charge/discharge rates, the polarisation (displacement of the electrode potential from the equilibrium value) significantly increased and the amount of Li^+ reversibly inserted and extracted decreased. Slower charge/discharge rates allow major

structural rearrangements to take place and more Li^+ can be exchanged during the lithium extraction/insertion process. The best rate performing material was again C/$LiFePO_4$ compared to the other C/$LiFe_{1-x}Mn_xPO_4$ composites (x=0.25, 0.5, 0.75 and 1) (Figure 3.23 (a)). This C/$LiFePO_4$ sample displayed a regular decrease in the discharge capacity from 155 mAh·g^{-1} to 66 mAh·g^{-1} when increasing the discharge rates from 0.1 to 10 C. Similar rate capabilities have been reported by Hou *et al.* on $LiFePO_4$ nanocrystals prepared through a liquid phase reduction synthesis (66.7 mAh·g^{-1} at 10 C after 80 cycles).[265] Moreover, poorer rate capabilities were clearly observed when introducing Mn in the $LiFePO_4$ structure, reaching only ~10 mAh·g^{-1} at 10 C in the case of the C/$LiMnPO_4$ powders. Similar rate behaviour has been reported on $LiMnPO_4$ olivines by Hong *et al.*[132] Cycling results revealed slightly better rate capabilities for the C/$LiFe_{0.5}Mn_{0.5}PO_4$ phase at higher C rates in comparison to the C/$LiFe_{0.75}Mn_{0.25}PO_4$ and C/$LiFe_{0.25}Mn_{0.75}PO_4$ materials, yielding discharge capacities of ~120 mAh·g^{-1} and ~95 mAh·g^{-1} at C/10 and 2 C, respectively. Moreover, at the fastest C rates C/$LiFe_{0.25}Mn_{0.75}PO_4$ showed a more pronounced decrease in discharge capacities that C/$LiFe_{0.75}Mn_{0.25}PO_4$ and C/$LiFe_{0.5}Mn_{0.5}PO_4$, displaying only ~25 mAh·g^{-1} at 10 C. Comparable rate behavior in C/$LiFe_{1-x}Mn_xPO_4$ (x=0.7, 0.8 and 0.9) samples has been observed by Zhang *et al* which delivered 90-70 mAh·g^{-1} at 2 C rate.[266] *Ex-situ* PXRD characterisation of the C/$LiFe_{1-x}Mn_xPO_4$ cycled material in the discharge state after the cycling experiment at different discharge/charge rates shown in Figure 3.23 (b) indicated that the Li^+ (de)intercalation process did not affect the structure of these battery materials after the fast charge/discharge tests, confirming the structural stability of these family of mixed metal phosphates upon cycling at fast charge/discharge rates.

CV experiments at room temperature were performed at a scan rate of 0.1 mV·s^{-1} over a voltage range of 2.8−4.0 V *vs.* Li^+/Li^0 for the C/$LiFePO_4$ and 2.5−4.5 V *vs.* Li^+/Li^0 for the Mn containing C/$LiFe_{1-x}Mn_xPO_4$ olivines. The CVs for the C/$LiFe_{1-x}Mn_xPO_4$ phases depicted in Figure 3.24 show the oxidation and reduction peaks around 3.5 and 4.1 V for Fe^{3+}/Fe^{2+} and Mn^{3+}/Mn^{2+} redox pairs, respectively, with varying peak intensities dependent on the degree of manganese substitution. The ratio between the Mn and Fe peak heights should correspond to the material's composition. However, the CVs suggested a more prounced participation of the Fe component over Mn in these electrochemical processes. Furthermore, the substitution of higher amounts of Fe by Mn in the $LiFePO_4$ structure generally increases the Fe^{+3}/Fe^{+2} and Mn^{+3}/Mn^{+2} redox potentials. Similar studies by Kobayashi *et al.* have also shown a shift in the redox potential of Fe^{+3}/Fe^{+2} and Mn^{+3}/Mn^{+2} as the value of x in $LiFe_{1-x}Mn_xPO_4$ is increased. This shift was attributed to the inductive effect in the M–O–P bonding, which increases the ionic character of the transition metal atoms.[267] The overall volume expansion upon Mn substitution in the $LiFe_{1-x}Mn_xPO_4$ system possibly increases the average metal-oxide bond length and hence the ionicity of each transition metal.[267] These results are also in agreement with previous cyclic voltammetry

investigations on an array of $LiFe_{1-x}Mn_xPO_4$ samples prepared with different degrees of carbon coating to assist electron transfer.[268] Finally, it must be remarked the good reversibility of this family of $C/LiFe_{1-x}Mn_xPO_4$ phases after the first cycle, as it can be observed by the excellent overlapping of the CV curves.

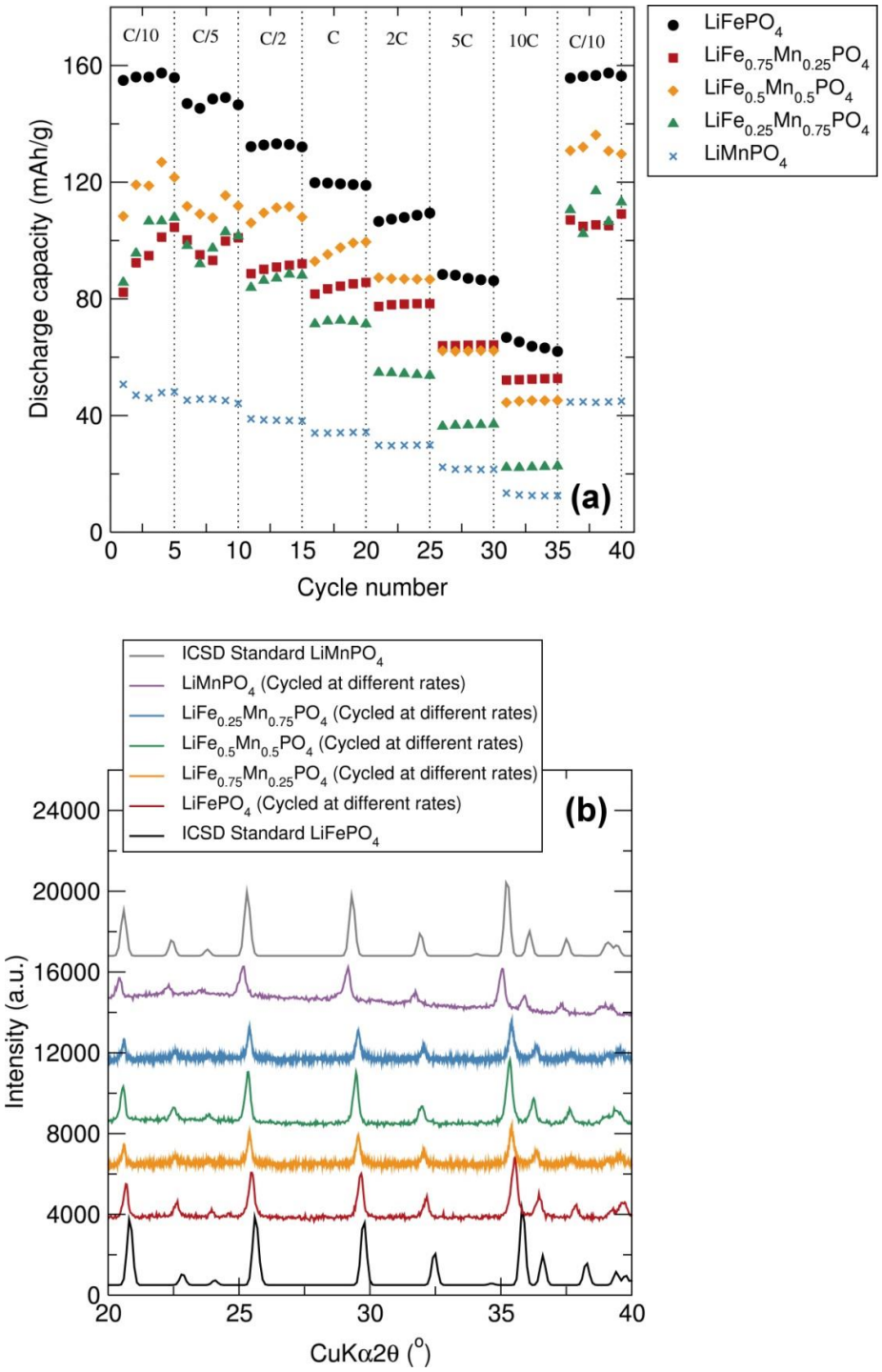

Figure 3.23. (a) Comparative rate performance of $C/LiFe_{1-x}Mn_xPO_4$ (15% wt. C from sucrose), C black and PTFE in 60:30:10 (% wt.). **(b)** PXRD of cycled at different rates $C/LiFe_{1-x}Mn_xPO_4$ materials in the discharged state.

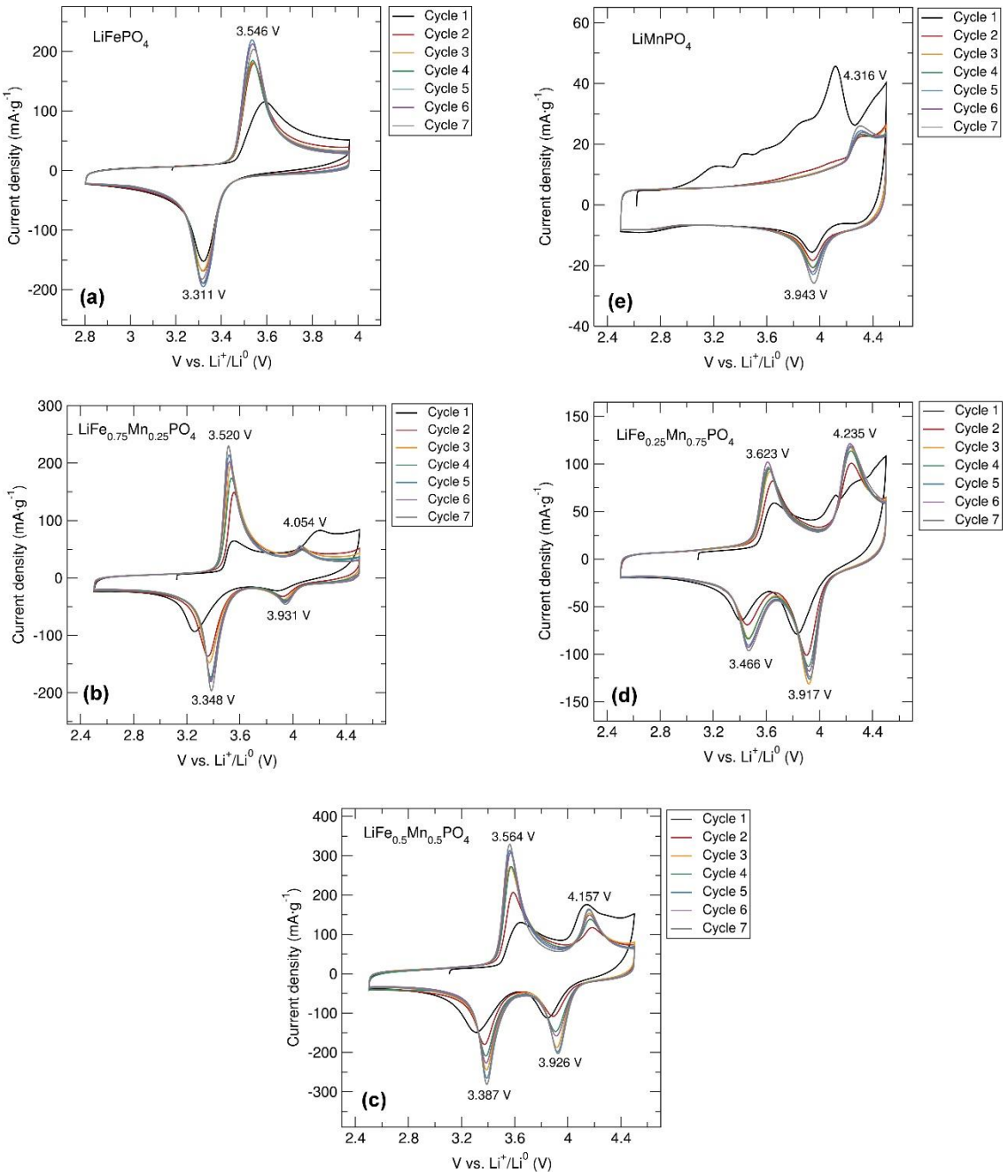

Figure 3.24. CVs at 0.1 mV·s^{-1} scan rate between 2.5 V and 4.5 V of C/$LiFe_{1-x}Mn_xPO_4$ (15% wt. C from sucrose), C black and PTFE in 60:30:10 (% wt.). **(a)** $LiFePO_4$, **(b)** $LiFe_{0.75}Mn_{0.25}PO_4$, **(c)** $LiFe_{0.5}Mn_{0.5}PO_4$, **(d)** $LiFe_{0.25}Mn_{0.75}PO_4$ and **(e)** $LiMnPO_4$ olivine phases.

3.3 Conclusions

In this chapter, solvothermal microwave-assisted synthesis has been demonstrated as a powerful method for the preparation of phase-pure $LiFe_{1-x}Mn_xPO_4$ olivines for use as positive insertion electrodes in Li-ion batteries. First, the importance of reducing the particle size of the precursor materials (in this case LiH_2PO_4) for the preparation of single phase $LiFePO_4$ olivine materials has been highlighted. From a series of optimisation reactions for the best Mn-containing precursor for the preparation of single phase *Pnma* $LiMnPO_4$ *via* microwave processes, $Mn(acac)_3$ is the most suitable candidate in comparison to $MnSO_4{\cdot}H_2O$, $MnCO_3$ and $MnC_2O_4{\cdot}2H_2O$. Particle size and morphology has a strong

dependence on the transition metal content in these materials. After that, to better understand the structure-property relationship of these mixed metal phosphates, neutron total scattering measurements for Rietveld analysis, neutron PDF analysis and μ^+SR experiments have been performed, which allow elucidation of the local structure, cation distribution, presence of defects, Li^+ content and Li^+ diffusion behaviour. The good fit observed in the neutron PDF refinements of this family of mixed metal phosphates suggested that the synthetic method presented here affords highly crystalline materials exhibiting less disorder or structural distortions than similar olivine structures synthesised through a conventional solvothermal approach. Interestingly, μ^+SR analysis has been applied for the first time to Mn-containing olivine $LiFe_{1-x}Mn_xPO_4$ phases, suggesting that the D_{Li} and E_{act} slightly decreased with higher Mn content. Finally, electrochemical testing of this series of metal phosphates showed that the $LiFePO_4$ sample was the best performing material among this family of Fe/Mn containing olivines, reaching charge and discharge capacities near theoretical values (170 $mAh \cdot g^{-1}$) with no capacity fading over at least 50 cycles.

4 Microwave Treatments of Single Source Alkoxides for Nanostructured Li-ion Battery Electrodes

4.1 Introduction

Control over the design of inorganic nanostructures of preferred crystal structure, particle size and particle morphology is highly desirable and challenges still remain in achieving this in a reliable and reproducible manner. In particular, fast and low temperature syntheses are highly desirable for the preparation of high quality functional inorganic nanoparticles. Previously, metal alkoxides and their derivatives have been shown to be excellent starting materials for the preparation of metal oxide thin films due to their easy hydrolysis and thermolysis.[269] As previously reported by Gun'ko *et al.*, Fe^{2+} alkoxide complexes are considered promising precursors for the synthesis of important iron-based compounds and nanomaterials.[204, 270]

In this chapter, a series of metal alkoxide precursors have been prepared and employed for the preparation of nanostructured Li-ion battery electrodes. Microwave or ultrasonic treatment of metallorganic precursors has been investigated as a potentially fast and low cost route to both anode and cathode nanomaterials for Li-ion battery applications. In particular, the formation of $LiMPO_4$ (*M*=Fe, Mn) and Mn_3O_4 nanostructures *via* relatively fast and low temperature synthetic methods is examined. Realising such routes could open up a new avenue for the targeted design of nanoparticulate electrode materials, where co-location of the desired metals in a single starting material shortens reaction times and temperatures due to a decrease in diffusional energy requirements usually needed for such reactions to proceed. Furthermore, thermal decomposition of these metal alkoxides should be achievable at relatively low temperatures, allowing decreased temperatures during the synthesis and making the process more environmentally benign while also driving down reaction times.

4.2 Results and discussion

4.2.1 Synthesis and characterisation of $[Fe(O^tBu)_2(THF)]_2$ (I)

The metallorganic alkoxide precursor $[Fe(O^tBu)_2(THF)]_2$ (I) was synthesised *via* a straightforward salt elimination reaction at room temperature using two equivalents of NaO^tBu and one equivalent of $FrBr_2$ in dry THF, as previously reported by Gun'ko *et al.*[203] (see Schematic 4.1 and section 2.2.3). This reaction results in the formation of a black-dark greenish solution and a greyish precipitate of NaBr. The $[Fe(O^tBu)_2(THF)]_2$ (I) is composed by two Fe^{2+} centers coordinated to two bridging O^tBu groups and a terminal O^tBu group. The tetrahedral coordination Fe^{2+} is then completed with a THF molecule. This metal akoxide is extremely air and moisture sensitive and demonstrates a colour change from dark green to reddish orange upon exposure to air due the oxidation of Fe^{2+} to Fe^{3+}.

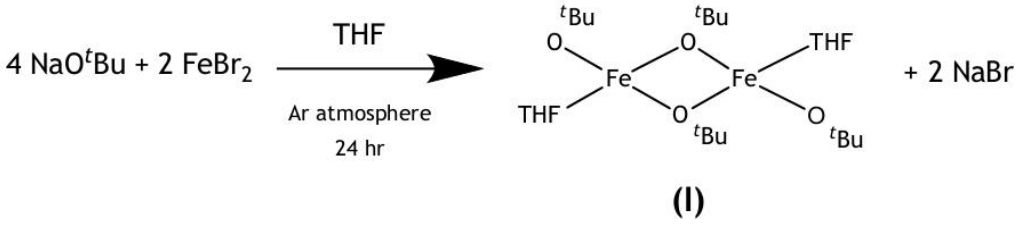

(I)

Schematic 4.1. Synthesis of $[Fe(O^tBu)_2(THF)]_2$ (I) metal alkoxide precursor.

The obtained dry greenish powders of $[Fe(O^tBu)_2(THF)]_2$ (I) were characterised by ^{1}H NMR and FT-IR spectroscopy. The ^{1}H NMR spectrum conducted in dry C_6D_6 is shown in Figure A4.1 and revealed two peaks from the *tert*-butoxide protons, one at 0.3 ppm corresponding to the μ_2-O^{t}Bu bridging groups and another at 1.1 ppm representing the terminal O^{t}Bu groups. Two broad peaks corresponding to the THF group were found at 3.8 and 1.5 ppm. There is a significant broadening of the peaks due to the presence of paramagnetic Fe^{2+} ions. The FT-IR spectra of $[Fe(O^tBu)_2(THF)]_2$ (I) was carried out in Nujol using NaCl plates to prevent oxidation of the transition metal. The FT-IR spectrum for the $[Fe(O^tBu)_2(THF)]_2$ (I) in Nujol is depicted in Figure A4.2. The Nujol bands at 1461 and 1385 cm^{-1} are easily distinguishable (the Nujol major absorption bands appear between 2950-2800, 1465-1450, and 1380–1370 cm^{-1}). The 723 and 854 cm^{-1} vibrations for this metal *tert*-butoxide could be assigned to a symmetrical skeletal vibration of the *tert*-butyl group. The asymmetric stretch due to the C-O-C group in THF was seen at 971 cm^{-1}. The 1133 cm^{-1} band corresponds to a C-O stretch vibration characteristic of the *tert*-butoxy group. In general, the *tert*-butyl group is consistently characterised by strong absorptions at about 1200 - 1250 cm^{-1}.[271, 272]

4.2.2 Synthesis and characterisation of "$[Mn(O^tBu)_2(THF)]_2$" (II)

The equivalent Mn containing alkoxide precursor with expected chemical formula "$[Mn(O^tBu)_2(THF)]_2$" (II) ("" is used to denote suggested chemical formula in the absence of single cystal XRD data) was synthesised through a similar straightforward salt elimination reaction at room temperature using two equivalents of NaO^{t}Bu and one equivalent of $MnBr_2$ in dry THF. This reaction resulted in the formation of a dark brown-pinkish solution and a greyish precipitate of NaBr. The "$[Mn(O^tBu)_2(THF)]_2$" (II) product was also air and moisture sensitive, as when exposing it to air the brown-pinkish Mn(II) ions could be oxidised to blackish Mn(III). The ^{1}H NMR spectrum of the "$[Mn(O^tBu)_2(THF)]_2$" (II) dry product (Figure A4.3) revealed two peaks from the *tert*-butoxide protons, a major one at 0.3 ppm corresponding to the μ_2-O^{t}Bu bridging and other at 0.9 ppm representing the terminal O^{t}Bu groups. The higher intensity of the 0.3 ppm peak compared to the 0.9 ppm peak suggests a major presence of μ_2-O^{t}Bu bridging groups in comparison to O^{t}Bu terminal groups in the "$[Mn(O^tBu)_2(THF)]_2$" (II) complex. Therefore, these results could indicate that a cubane architecture with $[Mn_4(O^tBu)_4]^{2+}$ may be formed. Iron and manganese alkoxide cubes have already been fabricated by a similar single-step synthetic

approach presented here using MCl_2 (*M*=Fe, Mn), β-diketone and two equivalents of lithium alkoxide. The $[M_4(OR)_4]^{n+}$ cores contain iron or manganese with triply bridging alkoxide ligands arranged at alternating vertices of a cube. The terminal positions are then completed by either alcohol or alkoxide and β-diketonate or benzoate ligands.[273] A broad peak most likely corresponding to the THF group was found at 1.3 ppm. The FT-IR spectrum for the "$[Mn(O^tBu)_2(THF)]_2$" (II) in Nujol depicted in Figure A4.4 showed the Nujol bands at 1470 and 1379 cm^{-1}. The symmetrical skeletal vibration of the *tert*-butyl group was observed at 723 and 900 cm^{-1}. The asymmetric stretch from the C-O-C group in THF corresponds to the band 974 cm^{-1}. The 1128 cm^{-1} band could be assigned to a C-O stretch vibration characteristic of the *tert*-butoxy group. The absorption band at 1205 cm^{-1} is typical of the *tert*-butyl group.

4.2.3 Synthesis and characterisation of "$[Fe_{0.5}Mn_{0.5}(O^tBu)_2(THF)]_2$" (III)

In an effort to prepare a bimetallic *tert*-butoxide compound containing Fe and Mn, a similar synthetic approach was followed by reacting four equivalents of NaO^tBu, one equivalent of $FeBr_2$ and one equivalent of $MnBr_2$ in dry THF. The obtained dark-brownish product with expected chemical formula "$[Fe_{0.5}Mn_{0.5}(O^tBu)_2(THF)]_2$" (III) was also characterised by ^1H NMR and FT-IR spectroscopy. The ^1H NMR spectrum of the "$[Fe_{0.5}Mn_{0.5}(O^tBu)_2(THF)]_2$" (III) product (Figure A4.5) revealed three main peaks from the *tert*-butoxide protons, similar to those observed for the monometallic precursors (0.3 ppm corresponding to the μ_2-O^tBu bridging and 0.9 and 1.0 ppm for the terminal O^tBu groups). Peaks attributed to the THF groups were found at 1.4, 2.1 and 3.6 ppm. The FT-IR spectrum for the "$[Fe_{0.5}Mn_{0.5}(O^tBu)_2(THF)]_2$" (III) powder in Nujol depicted in Figure A4.6 showed the Nujol bands at 1463 and 1382 cm^{-1}. The 804, 879 and 1033 cm^{-1} vibrations are assigned to a symmetrical skeletal vibration of the *tert*-butyl group. The asymmetric stretch of the C-O-C group in THF appears at 1102 cm^{-1}, with a band at 1186 cm^{-1} for the C-O stretch vibration of the *tert*-butoxy group. The absorption band at 1265 cm^{-1} is characteristic of the *tert*-butyl group.

The similar FT-IR spectra obtained for $[Fe(O^tBu)_2(THF)]_2$ (I), "$[Mn(O^tBu)_2(THF)]_2$" (II) and "$[Fe_{0.5}Mn_{0.5}(O^tBu)_2(THF)]_2$" (III) metal alkoxides suggested that there are no differences in the functional groups of these transition metal complexes. Furthermore, ^1H NMR spectra of the three complexes showed the signals characteristic of the terminal and bridging *tert*-butoxide protons and the THF group. In order to quantify the transition metal content in these metal alkoxides, atomic absorption spectroscopy (AAS) measurements were conducted. The $[Fe(O^tBu)_2(THF)]_2$ (I) metal alkoxide exhibited Fe contents close to the expected values. Nevertheless, the Mn contents in "$[Mn(O^tBu)_2(THF)]_2$" (II) were higher than the theoretical values. Results also showed that in the case of the mixed transition metal alkoxide precursor "$[Fe_{0.5}Mn_{0.5}(O^tBu)_2(THF)]_2$" (III) similar Fe and Mn contents are observed.

Ultimately, single crystal XRD analysis on each alkoxide precursor would be required to obtain a complete picture of the structure of each alkoxide precursor. Unfortunately, it has not been possible to obtain single crystals of sufficient quality for diffraction studies. It should also be noted that it would not be possible to discern between iron and manganese from single crystal XRD analysis. These precursors were therefore employed in subsequent syntheses on the basis of their predicted formulae.

Table 4.1. Fe and Mn contents of "$[Fe(O^tBu)_2(THF)]_2$" (I), "$[Mn(O^tBu)_2(THF)]_2$" (II) and "$[Fe_{0.5}Mn_{0.5}(O^tBu)_2(THF)]_2$" (III) metal alkoxide precursors obtained from AAS analysis.

	Found		Expected	
Sample	**Fe (% mol)**	**Mn (% mol)**	**Fe (% mol)**	**Mn (% mol)**
$[Fe(O^tBu)_2(THF)]_2$ (I)	23.13	-	20.37	-
"$[Mn(O^tBu)_2(THF)]_2$ " (II)	-	44.70	-	20.04
"$[Fe_{0.5}Mn_{0.5}(O^tBu)_2(THF)]_2$" (III)	18.32	22.25	10.20	10.03

4.2.4 Synthesis and characterisation of $LiFe_{1-x}Mn_xPO_4$ and Mn_3O_4 nanostructures from "$[M(O^tBu)_2(THF)]_2$" (*M*=Fe, Mn) metal alkoxides

The synthesis of single phase $LiFe_{1-x}Mn_xPO_4$ and M_3O_4 hausmannite nanostructures was attempted using "$[M(O^tBu)_2(THF)]_2$" (*M*=Fe, Mn) (I, II and III) metal alkoxide precursors (see section 2.2.3), $LiOH{\cdot}H_2O$ and H_3PO_4 as reactants according to the reaction schematic 4.2 and experimental sections 2.2.4 and 2.2.5, respectively. Table 4.2 shows the full list of reactions attempted, including the nature of the metal alkoxide precursors "$[M(O^tBu)_2(THF)]_2$" (*M*=Fe, Mn) (I, II and III) and the $LiFe_{1-x}Mn_xPO_4$ and Mn_3O_4 hausmannite nanophases prepared from each precursor.

4.2.4.1 PXRD of $LiFe_{1-x}Mn_xPO_4$ nanostructures prepared from "$[Fe_{1-x}Mn_x(O^tBu)_2(THF)]_2$" (*x*=0, 0.5 and 1)

The microwave-assisted synthesis of $LiFePO_4$ nanoparticles from the metal alkoxide precursor $[Fe(O^tBu)_2(THF)]_2$ (I) as a starting material was attempted initially *via* a series of reactions using $LiOH{\cdot}H_2O$, Li_2CO_3, LiH_2PO_4 and H_3PO_4 as Li^+ and PO_4^{3-} sources in benzyl alcohol. Benzyl alcohol ($tan\delta=0.667$)[274] is a strong microwave absorbing solvent that has already been successfully used for the preparation of olivine $LiFePO_4$, $LiMnPO_4$ and $LiMn_{0.65}Fe_{0.35}PO_4$ nanostructures *via* fast microwave assisted methods.[45] These preliminary reactions were designed so as to identify the most suitable Li^+ and PO_4^{3-} starting materials for the preparation of single phase nanocrystalline $LiFePO_4$ through fast microwave treatments of metal alkoxides. Reaction times and temperatures were limited to 10 mins and 240 °C, respectively. Furthermore, in an effort to demonstrate that metal alkoxide precursors yield better quality materials, a similar reaction using the commercial starting materials $Fe(acac)_3$ and LiH_2PO_4 in benzyl alcohol was also performed. PXRD patterns of the reaction products (shown in Figure 4.1) revealed that phase pure $LiFePO_4$ was only obtained when the $[Fe(O^tBu)_2(THF)]_2$ (I) metal alkoxide was reacted with

$LiOH{\cdot}H_2O$ and H_3PO_4 in benzyl alcohol. When reacted with Li_2CO_3, a mixture of $LiFePO_4$ and Li_3PO_4 was formed. When LiH_2PO_4 was employed, olivine $LiFePO_4$ was not obtained and instead Fe_3O_4 magnetite was the major product. These results could be explained by the fact that a slightly acidic pH provided by the phosphoric acid could potentially avoid the formation of iron oxide, leading to the phase pure olivine when $LiOH{\cdot}H_2O$ and H_3PO_4 were employed. Finally, the amorphous product obtained when using $Fe(acac)_3$ as a starting material, which was evidenced by the lack of diffraction peaks in the PXRD pattern, confirmed that reducing the reaction times to 10 min was only feasible when metal alkoxide precursors such as $[Fe(O^tBu)_2(THF)]_2$ are used. In the synthesis of $LiFePO_4$ using $Fe(acac)_3$ precursor, the reduction from Fe^{3+} to Fe^{2+} needs to take place, which is one possible reason why longer reaction times may be required.

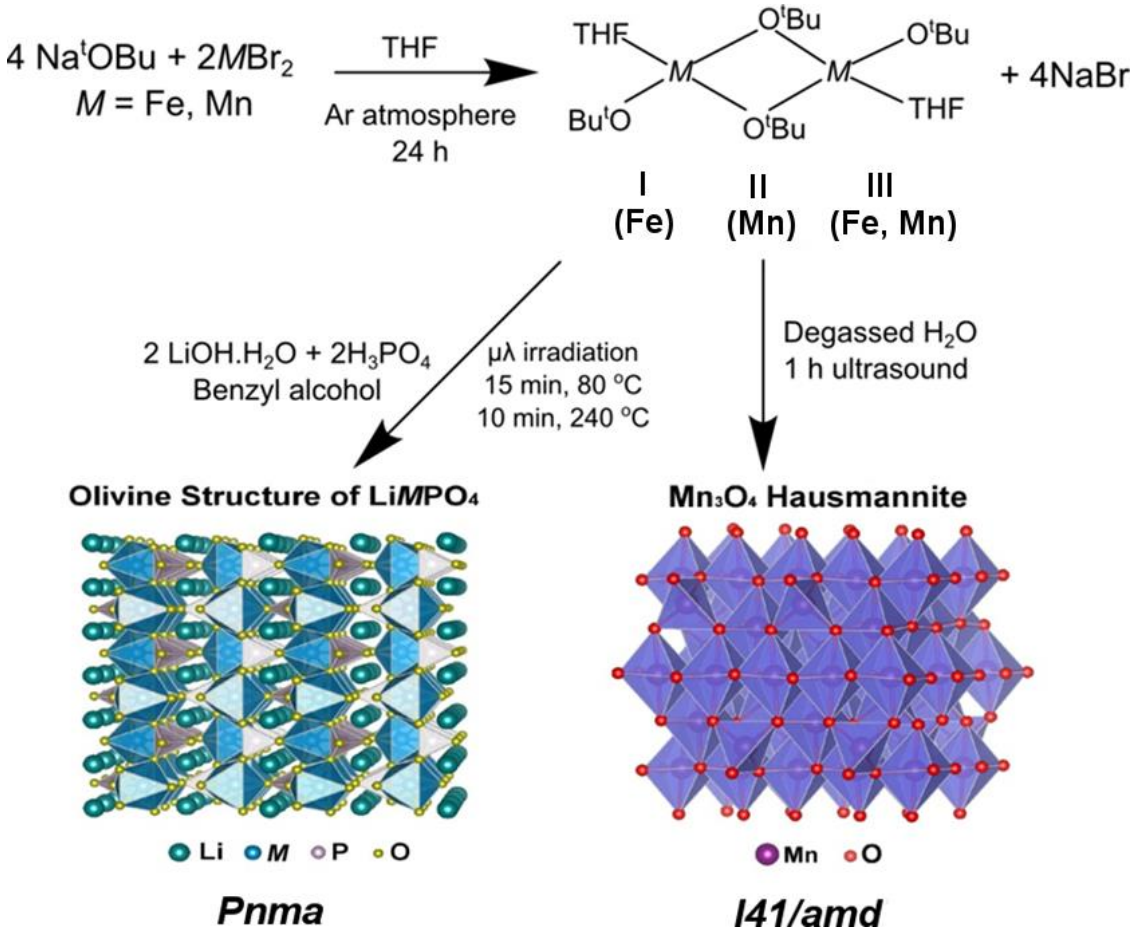

Schematic 4.2. Reaction schematic for the synthesis of $LiFe_{1-x}Mn_xPO_4$ (x=0, 0.5 and 1) and Mn_3O_4 hausmannite nanostructures using "$[M(O^tBu)_2(THF)]_2$" (I, II and III) metal alkoxide precursors.

Table 4.2. Preparation of "[*M*(O^tBu)$_2$(THF)]$_2$" (*M* = Fe, Mn) (I, II and III) alkoxide precursors and the reactions attempted with these precursors to obtain $LiFe_{1-x}Mn_xPO_4$ (*x* = 0, 0.5 and 1) and Mn_3O_4 nanoparticles.

Samples	Reactants	Reaction conditions
[Fe(O^tBu)$_2$(THF)]$_2$ (I)	2 $FeBr_2$ (6.470 g, 30 mmol) + 4 NaO^tBu (5.766 g, 60 mmol) + 90 mL THF	24 hr stirring at RT
"[Mn(O^tBu)$_2$(THF)]$_2$" (II)	2 $MnBr_2$ (6.443 g, 30 mmol) + 4 NaO^tBu (5.766 g, 60 mmol) + 90 mL THF	24 hr stirring at RT
"[$Fe_{0.5}Mn_{0.5}$(O^tBu)$_2$(THF)]$_2$" (III)	$MnBr_2$ (3.221 g, 15 mmol) + $FeBr_2$ (3.235 g, 15 mmol) + 4 NaO^tBu (5.766 g, 60 mmol) + 90 mL THF	24 hr stirring at RT
$LiFePO_4$_I	[Fe(O^tBu)$_2$(THF)]$_2$ (0.0300g, 0.07 mmol) + 2 H_3PO_4 (0.0134 g, 0.14 mmol) + 2 $LiOH{\cdot}H_2O$ (0.0057 g, 0.14 mmol) + 4 mL benzyl alcohol	Microwave synthesis (2.45 GHz) 15 min 80 ºC and 10 min 240 ºC
$LiMnPO_4$_II	"[Mn(O^tBu)$_2$(THF)]$_2$" (0.0300 g, 0.07 mmol) + 2 H_3PO_4 (0.0134 g, 0.14 mmol) + 2 $LiOH{\cdot}H_2O$ (0.0058 g, 0.14 mmol) + 4 mL benzyl alcohol	Microwave synthesis (2.45 GHz) 15 min 80 ºC and 10 min 240 ºC
$LiFe_{0.5}Mn_{0.5}PO_4$_I-II	"[Fe(O^tBu)$_2$(THF)]$_2$" (0.0150 g, 0.035 mmol) + "[Mn(O^tBu)$_2$(THF)]$_2$" (0.0150 g, 0.035 mmol) + 2 H_3PO_4 (0.0134 g, 0.14 mmol) + 2 $LiOH{\cdot}H_2O$ (0.0057 g, 0.14 mmol) + 4 mL benzyl alcohol	Microwave synthesis (2.45 GHz) 15 min 80 ºC and 10 min 240 ºC
$LiFe_{0.5}Mn_{0.5}PO_4$_III	"[$Fe_{0.5}Mn_{0.5}$(O^tBu)$_2$(THF)]$_2$" (0.0300 g, 0.07 mmol) + 2 H_3PO_4 (0.0134 g, 014 mmol) + 2 $LiOH{\cdot}H_2O$ (0.0057 g, 0.14 mmol) + 4 mL benzyl alcohol	Microwave synthesis (2.45 GHz) 15 min 80 ºC and 10 min 240 ºC
Mn_3O_4 hausmannite	"[Mn(O^tBu)$_2$(THF)]$_2$" + degassed H_2O (6 x 60 mL)	1 hr ultrasound

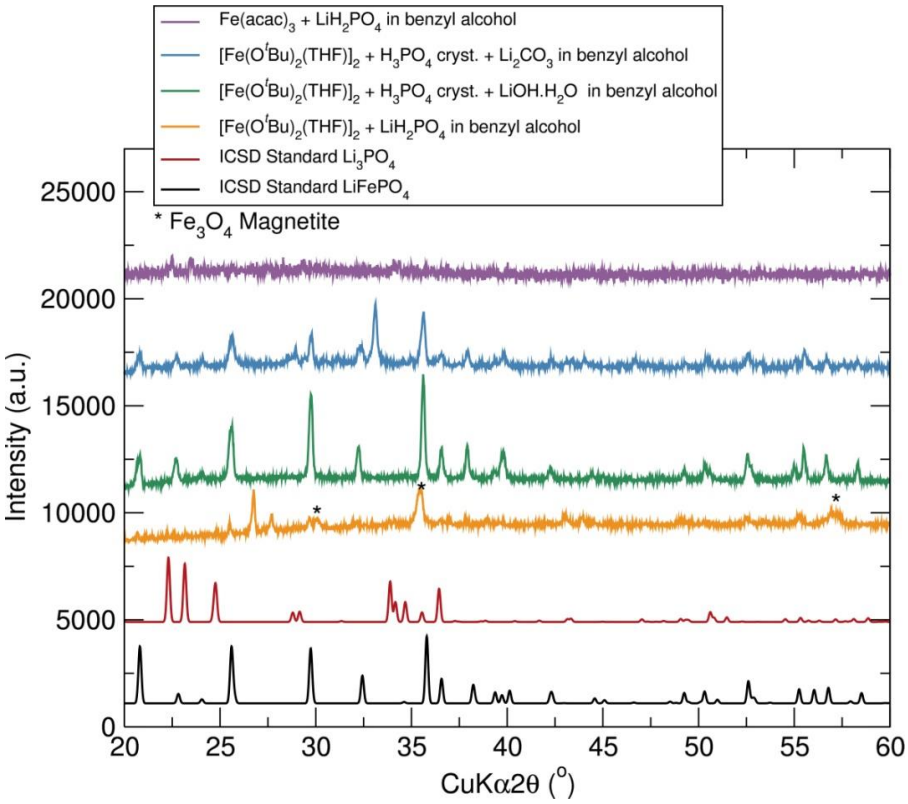

Figure 4.1. PXRD patterns of $LiFePO_4$ samples prepared using a $[Fe(O^tBu)_2(THF)]_2$ precursor and different lithium and phosphate sources after fast microwave synthesis.

Having established the most suitable route, $LiFe_{1-x}Mn_xPO_4$ (x=0, 0.5, 1) nanostructures were prepared using "$[M(O^tBu)_2(THF)]_2$" (M=Fe, Mn) metal alkoxide precursors, $LiOH{\cdot}H_2O$ and H_3PO_4 in benzyl alcohol. First, $LiFePO_4$_I and $LiMnPO_4$_II were prepared using the $[Fe(O^tBu)_2(THF)]_2$ (I) and "$[Mn(O^tBu)_2(THF)]_2$" (II) alkoxide precursors, respectively. Figure 4.2 and 4.3 show that single phase olivine materials were obtained after microwave treatment and also after a post-heat treatment for 1 hr at 500 ºC under Ar atmosphere. The heat treatment is conducted to check the thermal stability of the materials and confirm that there are no changes in the crystallinity upon heating. Moreover, phase pure $LiFePO_4$ and $LiMnPO_4$ olivines were maintained after carbon coating with 15% wt. C from sucrose and heat treatment for 1 hr at 700 ºC under Ar. Stoichiometric amounts of $[Fe(O^tBu)_2(THF)]_2$ (I) and "$[Mn(O^tBu)_2(THF)]_2$" (II) alkoxide precursors were reacted to prepare the mixed transition metal olivine $LiFe_{0.5}Mn_{0.5}PO_4$_I-II following the same synthetic procedure. As observed in Figure 4.4, PXRD analysis of the resulting product indicated that $LiFe_{0.5}Mn_{0.5}PO_4$ phase with some Fe_3O_4 magnetite impurities was obtained after the heating process for 1 hr at 500 ºC under Ar flow.

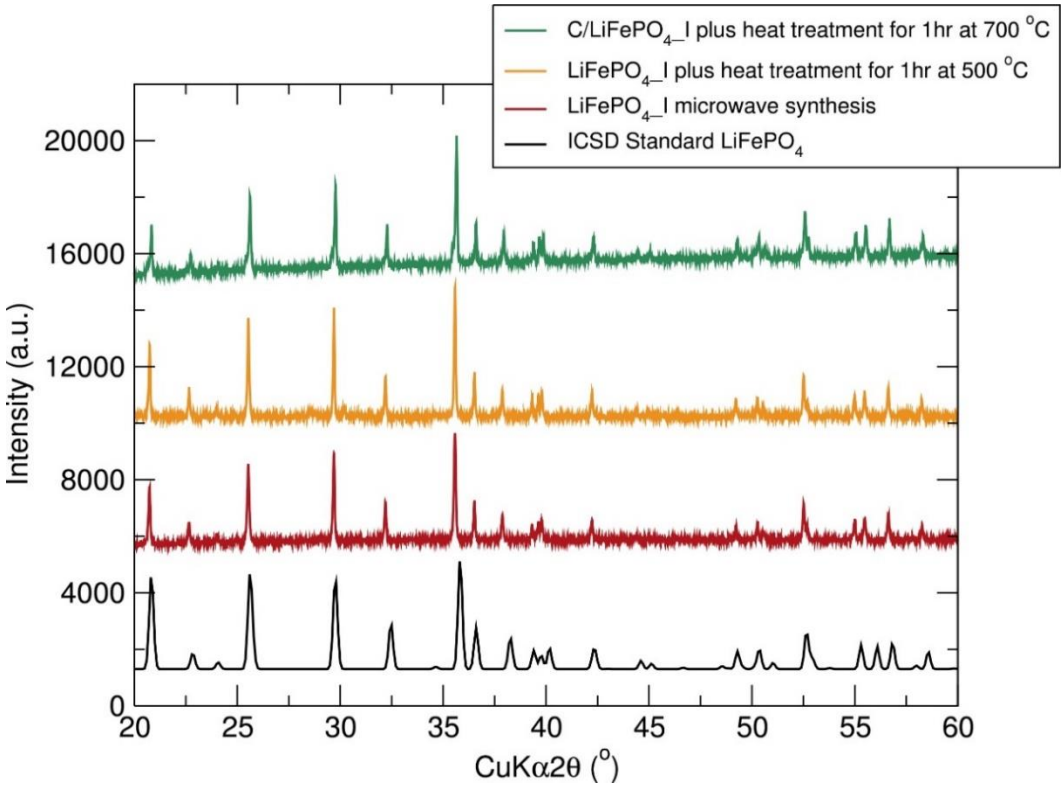

Figure 4.2. PXRD pattern of $LiFePO_4$ prepared using $[Fe(O^tBu)_2(THF)]_2$ (I) precursor, $LiOH.H_2O$ and H_3PO_4 in a 1:2:2 molar ratio in benzyl alcohol.

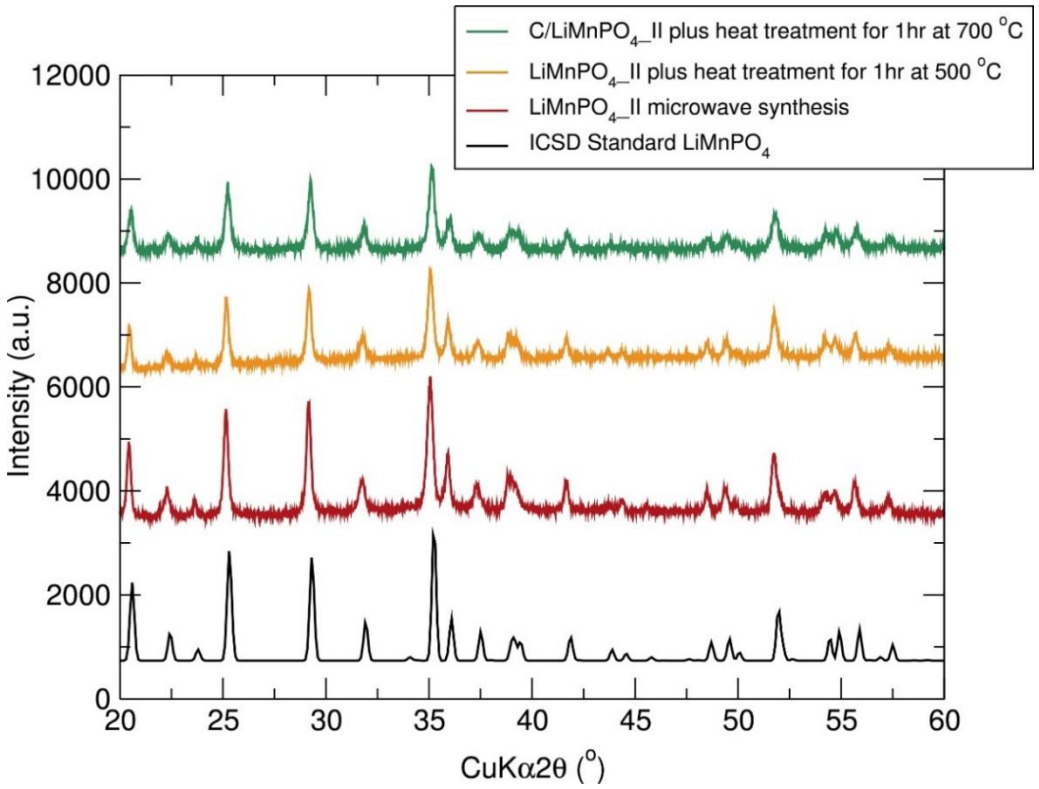

Figure 4.3. PXRD pattern of $LiMnPO_4$ prepared using "$[Mn(O^tBu)_2(THF)]_2$" (II) precursor, $LiOH.H_2O$ and H_3PO_4 in a 1:2:2 molar ratio in benzyl alcohol.

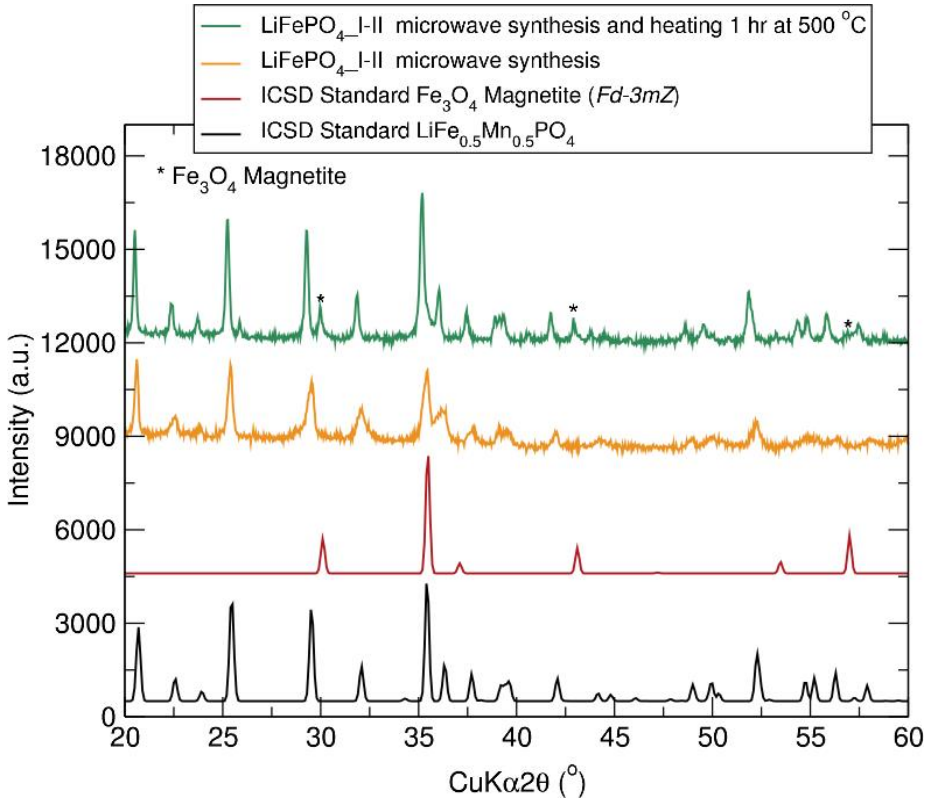

Figure 4.4. PXRD pattern of $LiFe_{0.5}Mn_{0.5}PO_4$_I-II prepared from stoichiometric mixture of $[Fe(O^tBu)_2(THF)]_2$ (I) and "$[Mn(O^tBu)_2(THF)]_2$" (II) alkoxide precursors. * indicates Fe_3O_4 impurities.

In an effort to avoid the formation of undesired Fe_3O_4 during the preparation of transition mixed metal phosphates, $LiFe_{0.5}Mn_{0.5}PO_4$ nanostructures were prepared through the same fast microwave synthesis using the bimetallic alkoxide precursor "$[Fe_{0.5}Mn_{0.5}(O^tBu)_2(THF)]_2$" (III). Figure 4.5 shows the resulting PXRD pattern, which indicates that no undesirable side products were formed. These results demonstrate the suitability of having the two transition metals in a single source precursor for the preparation of phase pure $LiFe_{0.5}Mn_{0.5}PO_4$ olivine nanomaterials. This also lends some evidence to the presumption that the mixed heterometallic alkoxide is not, in fact, simply a mixture of the iron and manganese homometallic precursors. Comparative PXRD patterns of the $LiFePO_4$_I, $LiFe_{0.5}Mn_{0.5}PO_4$_III and $LiMnPO_4$_II nanostructures in Figure 4.6 revealed that all three samples are single phase materials with an olivine structure indexed to an orthorhombic *Pnma* space group. The diffraction patterns were matched well with the standards $LiFePO_4$ (ICSD No. 01-072-7845), $LiFe_{0.5}Mn_{0.5}PO_4$ (ICSD No. 01-073-7355) and $LiMnPO_4$ (ICSD No. 01-072-7844).[49, 275] It is also interesting to note the slight shifting of the peaks towards lower angles when substituting Fe by Mn, a signature of the larger cation size of Mn^{2+} (83 pm) in comparison to Fe^2 (78 pm).[252] There is also a significant broadening in the peaks observed in the PXRD pattern with increasing Mn content in $LiFe_{1-x}Mn_xPO_4$, which may suggest a smaller crystallite size for the Mn

containing olivines. The estimated crystallite sizes of the $LiFePO_4$_I, $LiFe_{0.5}Mn_{0.5}PO_4$_III and $LiMnPO_4$_II nanostructures were calculated using the Scherrer equation[208] (equation 2.2) applied to the (200) diffraction peak and they were 105, 71 and 33 nm, respectively.

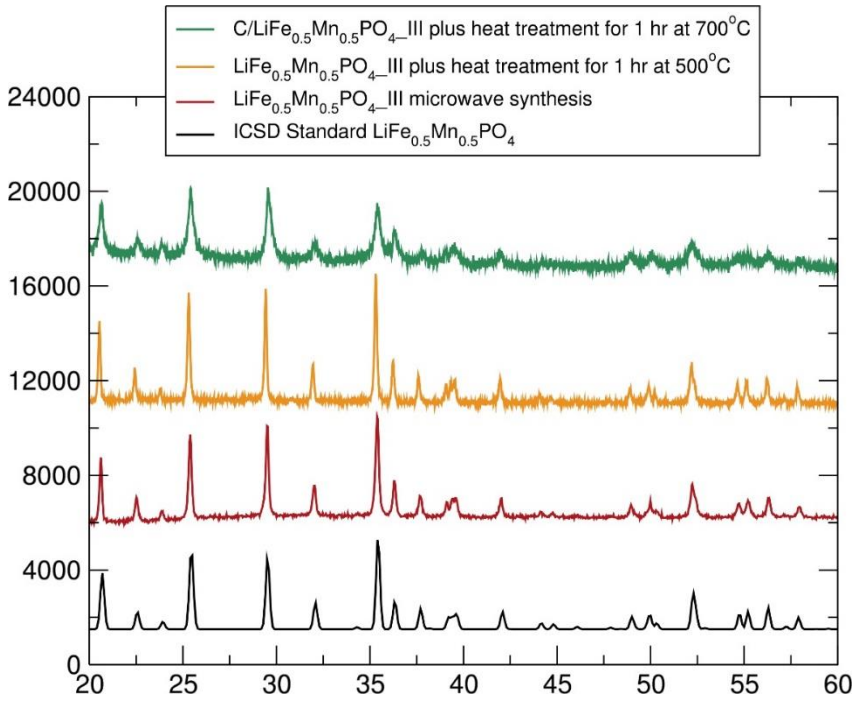

Figure 4.5. PXRD pattern of $LiFe_{0.5}Mn_{0.5}PO_4$_III prepared from stoichiometric mixture of $[Fe(O^tBu)_2(THF)]_2$ (I) and "$[Mn(O^tBu)_2(THF)]_2$" (II) alkoxide precursors.

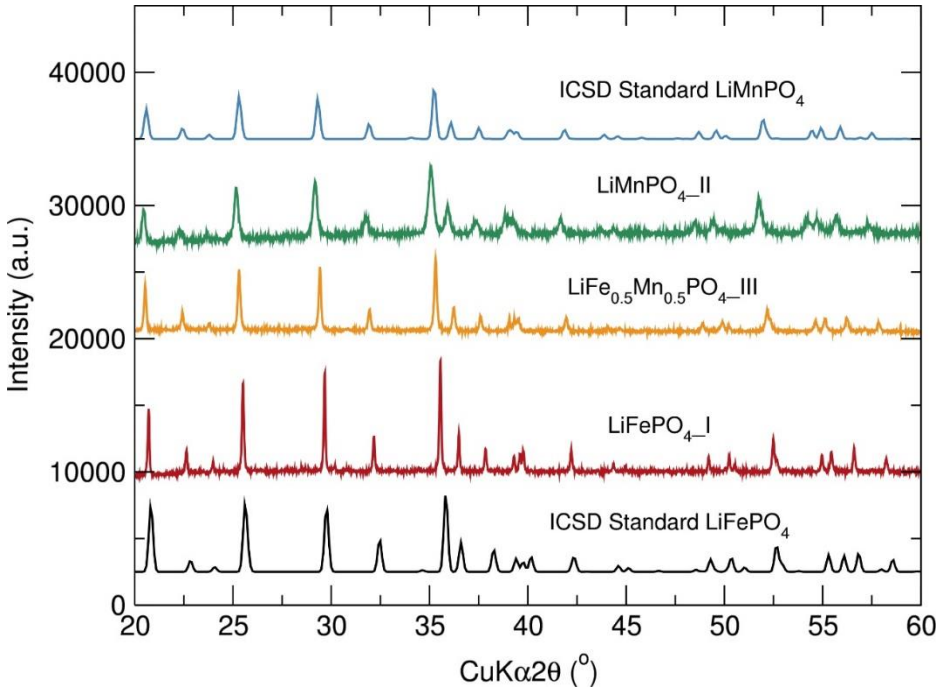

Figure 4.6. PXRD pattern of $LiFe_{1-x}Mn_xPO_4$ (x=0, 0.5 and 1) nanostructures from "$[M(O^tBu)_2(THF)]_2$"(M=Fe, Mn) (I, II and III) after heat treatment for 1 hr at 500 ºC in Ar.

High resolution PXRD analysis of the $LiFePO_4$_I, $LiFe_{0.5}Mn_{0.5}PO_4$_III and Li*M*nPO_4_II nanostructures prepared *via* a rapid microwave synthesis using "$[M(O^tBu)_2(THF)]_2$" (*M*=Fe, Mn) (I, II and III) alkoxide precursors were conducted at the I11 beamline at the Diamond Light Source. High resolution PXRD patterns of the Li*M*PO_4 (*M*=Fe, Mn) nanophases confirmed that the three samples were phase pure materials with an olivine structure indexed to an orthorhombic *Pnma* space group. Furthermore, no peaks of impurity phases or evidence of phase segregation were detected from PXRD analysis. PXRD data was fit by Rietveld analysis to the orthorhombic *Pnma* space group using Fullprof programme.[276] The structural and profile parameters were refined according to a pseudo-Voigt profile function and the refinement process order was the following: (i) scale factor (ii) the background was carefully modelled using a 6-coefficient polynomial function (iii) zero point and sample displacement correction, (iv) cell parameters, (v) profile parameters, (vi) atomic positions and finally (vii) isotropic atomic thermal displacement parameters (B_{iso}) constraining Li and Fe/Mn to have the same value and also the oxygen atoms to be same. As shown in Figure 4.7, an excellent agreement between the observed and calculated data was obtained, confirming the phase purity of these $LiFe_{1-x}Mn_xPO_4$ nanomaterials. Table 4.3 details the calculated lattice parameters for each sample, revealing an increase in the lattice parameters when doping $LiFePO_4$ with Mn. These results imply that Fe^{2+} atoms have been successfully substituted by Mn^{2+} in and are effectively located in the olivine structure.

4.2.4.2 Electron microscopy of $LiFe_{1-x}Mn_xPO_4$ (*x*=0, 0.5 and 1) nanostructures prepared from "$[Fe_{1-x}Mn_x(O^tBu)_2(THF)]_2$" (*x*=0, 0.5 and 1)

SEM analysis of the $LiFePO_4$_I, $LiFe_{0.5}Mn_{0.5}PO_4$_III and Li*M*nPO_4_II powders was conducted to examine the particle size and morphology. SEM images of the $LiFePO_4$_I sample revealed non-uniform platelet shaped morphology with particle sizes ranging from ~60 to 250 nm (Figure 4.8 (a)). The $LiFe_{0.5}Mn_{0.5}PO_4$_III powders appeared as thinner and slightly more elongated platelets (~130 nm wide and 300 nm long) (Figure 4.8 (b)). Finally, Li*M*nPO_4_II sample adopted a rod-like morphology (~60 nm width and 350-500 nm length), confirming the strong influence of the Mn content in the resulting particle morphology and size (Figure 4.8 (c)). HR TEM of the $LiFePO_4$_I, $LiFe_{0.5}Mn_{0.5}PO_4$_III and Li*M*nPO_4_II nanostructures confirmed the change in morphology and particle size with higher Mn content. TEM analysis shown in Figure 4.9 also confirmed the long-range crystallographic nature of these particles with lattice spacings consistent with the *Pnma* Li*M*PO_4 space group observed. The visible fringes demonstrated that the samples are crystalline and that the lattice spacings are consistent with the planes indicated in the images. The calculated average interplanar distances for the $LiFePO_4$, $LiFe_{0.5}Mn_{0.5}PO_4$ and Li*M*nPO_4 samples were found to be 0.387 nm, 0.403 nm and 0.634 nm, corresponding to the (210),

(210) and (010) planes, respectively. The insets show Fourier transforms of the TEM images revealing these materials to be single crystals over the imaged area. Indexing of the electron diffraction patterns revealed that the crystal long-axis, indicated by the green lines in the images, lies within a few degrees of the [020], [112] and [101] axes for the $LiFePO_4$, $LiFe_{0.5}Mn_{0.5}PO_4$ and $LiMnPO_4$ samples, respectively.

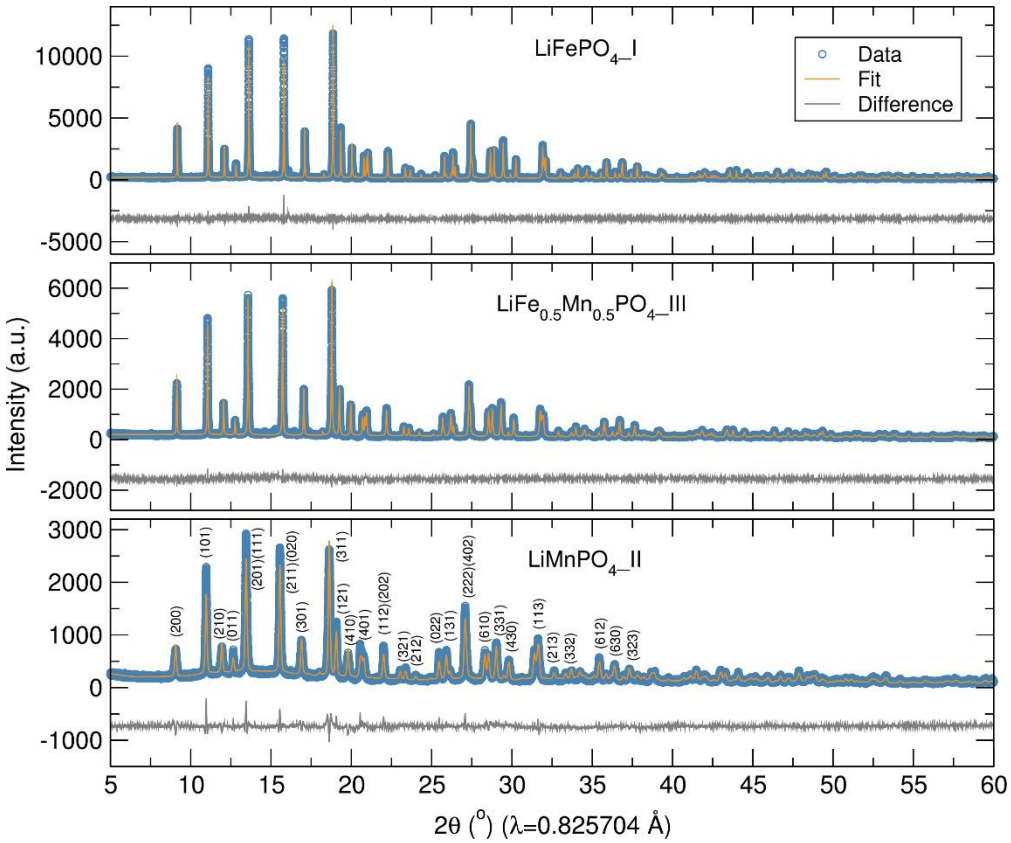

Figure 4.7. Rietveld analysis of high resolution PXRD data of $LiFePO_4$_I, $LiFe_{0.5}Mn_{0.5}PO_4$_III and $LiMnPO_4$_II nanostructures after microwave-assisted synthesis and heating for 1 h at 500 ºC under Ar flow.

Table 4.3. Calculated lattice parameters from Rietveld refinements for the different lithium metal phosphates prepared from "$[M(O^tBu)_2(THF)]_2$" (*M*=Fe, Mn) (I, II and III) metal alkoxide precursors.

Sample	**$LiFePO_4$_I**	**$LiFe_{0.5}Mn_{0.5}PO_4$_III**	**$LiMnPO_4$_II**
Space group	*Pnma*	*Pnma*	*Pnma*
a (Å)	10.3266(3)	10.36628(3)	10.44926(7)
b (Å)	6.0058(2)	6.03484(2)	6.10167(4)
c (Å)	4.6924(1)	4.70931(2)	4.74596(3)
V (Å^{-3})	291.017(1)	294.609(1)	302.593(3)
R_{wp}	19.1 %	20.5 %	25.0 %
R_{exp}	10.80 %	13.45 %	16.88 %
X^2	3.10	2.32	2.19

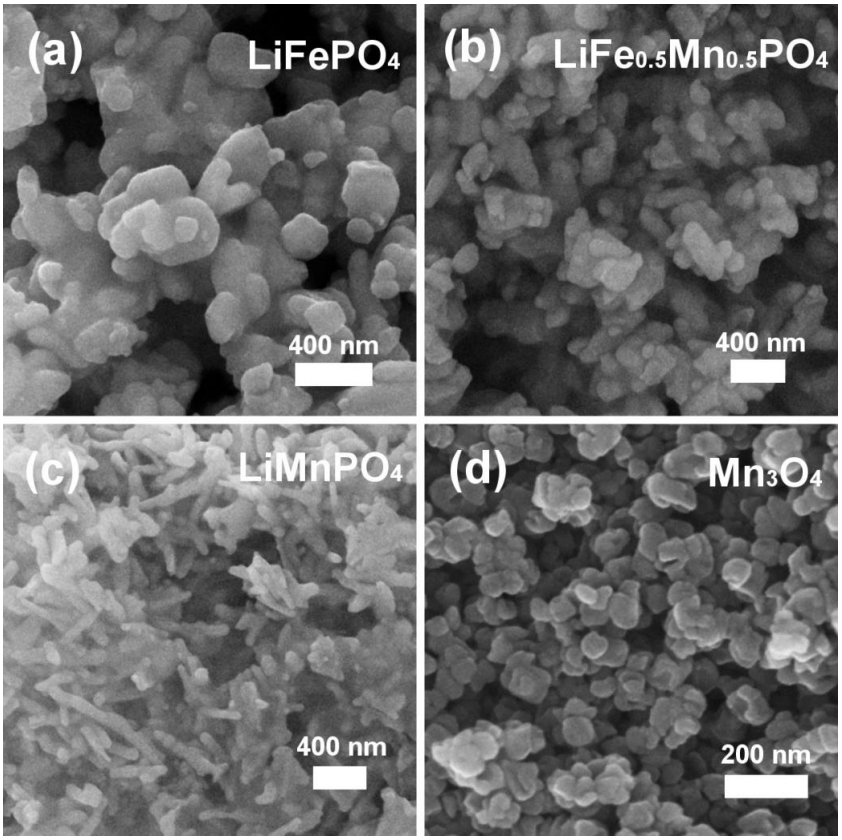

Figure 4.8. SEM images of **(a)** $LiFePO_4$_I, **(b)** $LiFe_{0.5}Mn_{0.5}PO_4$_III, **(c)** $LiMnPO_4$_II and **(d)** Mn_3O_4 nanostructures from "$[M(O^tBu)_2(THF)]_2$" (*M*=Fe, Mn) (I, II and III) metal alkoxide precursors.

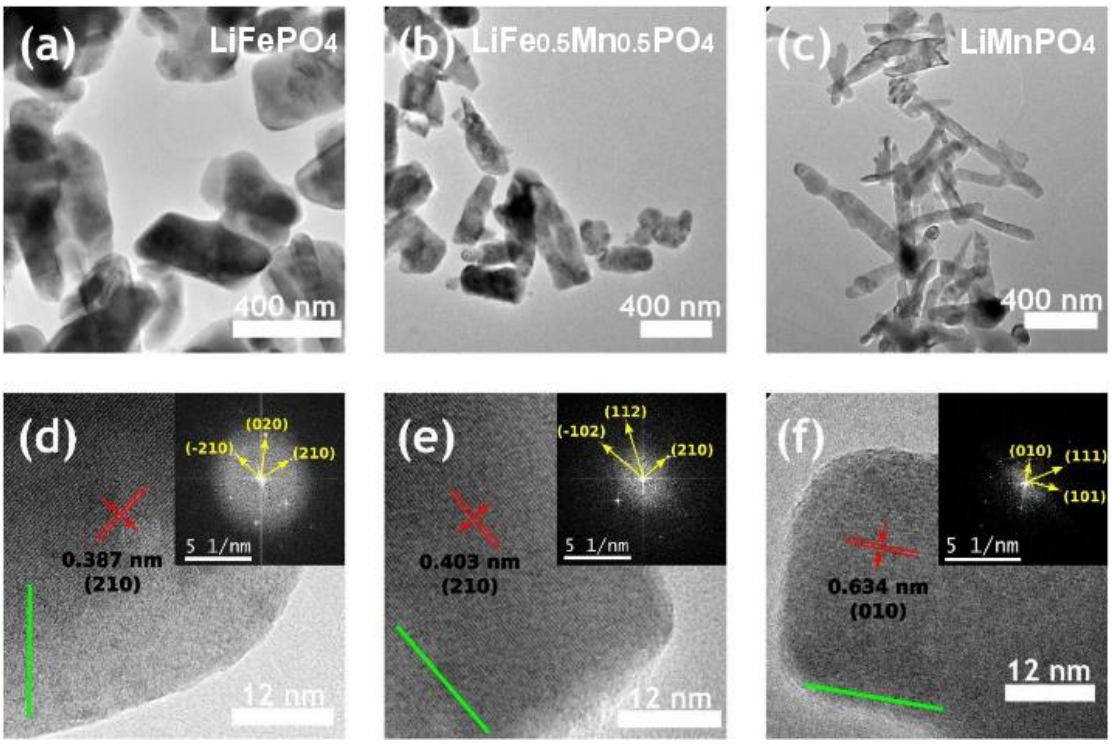

Figure 4.9. High resolution TEM images of **(a, d)** $LiFePO_4$_I, **(b, e)** $LiFe_{0.5}Mn_{0.5}PO_4$_III and **(c, f)** $LiMnPO_4$_II nanostructures from "$[M(O^tBu)_2(THF)]_2$" (*M*=Fe, Mn) (I, II and III).

4.2.4.3 Electrochemical performance of $LiFe_{1-x}Mn_xPO_4$ nanostructures prepared from "$[Fe_{1-x}Mn_x(O^tBu)_2(THF)]_2$" ($x$=0, 0.5 and 1)

The electrochemical behavior of the C/$LiFePO_4$_I, C/$LiFe_{0.5}Mn_{0.5}PO_4$_III and C/$LiMnPO_4$_II nanostructures was investigated *via* galvanostatic cycling and CV measurements. Galvanostatic cycling at room temperature of the C/$LiFePO_4$_I, C/$LiFe_{0.5}Mn_{0.5}PO_4$_III and C/$LiMnPO_4$_II samples was conducted over the voltage range of 2.2-4.0 V, 2.2-4.3 V and 2.2-4.5 V, respectively, at a C/20 rate. The positive electrodes consisted of a C/Li*M*PO_4:carbon black:PTFE mixture in a 60:30:10 weight ratio pressed into a pellet. The representative charge and discharge voltage profile for the C/$LiFePO_4$_I sample shown in Figure 4.10 (a) indicated that charge and discharge capacities of approximately 150 mAh·g^{-1} were reached. Furthermore, as shown in Figure 4.10 (b), this cycling study revealed that this electrode material exhibited almost no capacity fading over at least 20 cycles, with coulombic efficiencies of almost 99 % observed. Galvanostatic cycling at room temperature of the C/$LiFe_{0.5}Mn_{0.5}PO_4$_III sample at C/20 from 2.2 to 4.3 V displayed discharge and charge capacities of around 140 mAh·g^{-1} and 180 mAh·g^{-1}, respectively, with no noticeable capacity fading over the first 10 charge/discharge cycles (Figure 4.10 (c) and (d)). A lower electrochemical activity was observed for the Mn^{3+}/Mn^{2+} redox pair in comparison to Fe^{3+}/Fe^{2+}, as evidenced by the shorter redox plateau at 4.0 V compared to the 3.45 V plateau. Furthermore, the appearance of an additional discharge plateau is noted at around 3.6 V over cycling, which has also been previously observed by Wang *et al*. They demonstrate by capacity analysis, CV and galvanostatic intermittent titration technique that the additional discharge plateau can still be attributed to Mn^{3+} reduction, but with a different mechanism than in pure $LiMnPO_4$.[277] Galvanostatic cycling of the C/$LiMnPO_4$_II sample at C/20 from 2.2 V to 4.5 V demonstrated a poorer electrochemical performance delivering charge and discharge capacities of around 120 mAh·g^{-1} and 100 mAh·g^{-1}, respectively, over the first 20 charge/discharge cycles (Figure 4.10 (e) and (f)). In the cycling studies of C/$LiFe_{0.5}Mn_{0.5}PO_4$_III and C/$LiMnPO_4$_II a significant difference in charge and discharge capacities was observed, which may indicate that some electrolyte decomposition is taking place at voltages higher than 4 V *vs*. Li^+/Li^0.

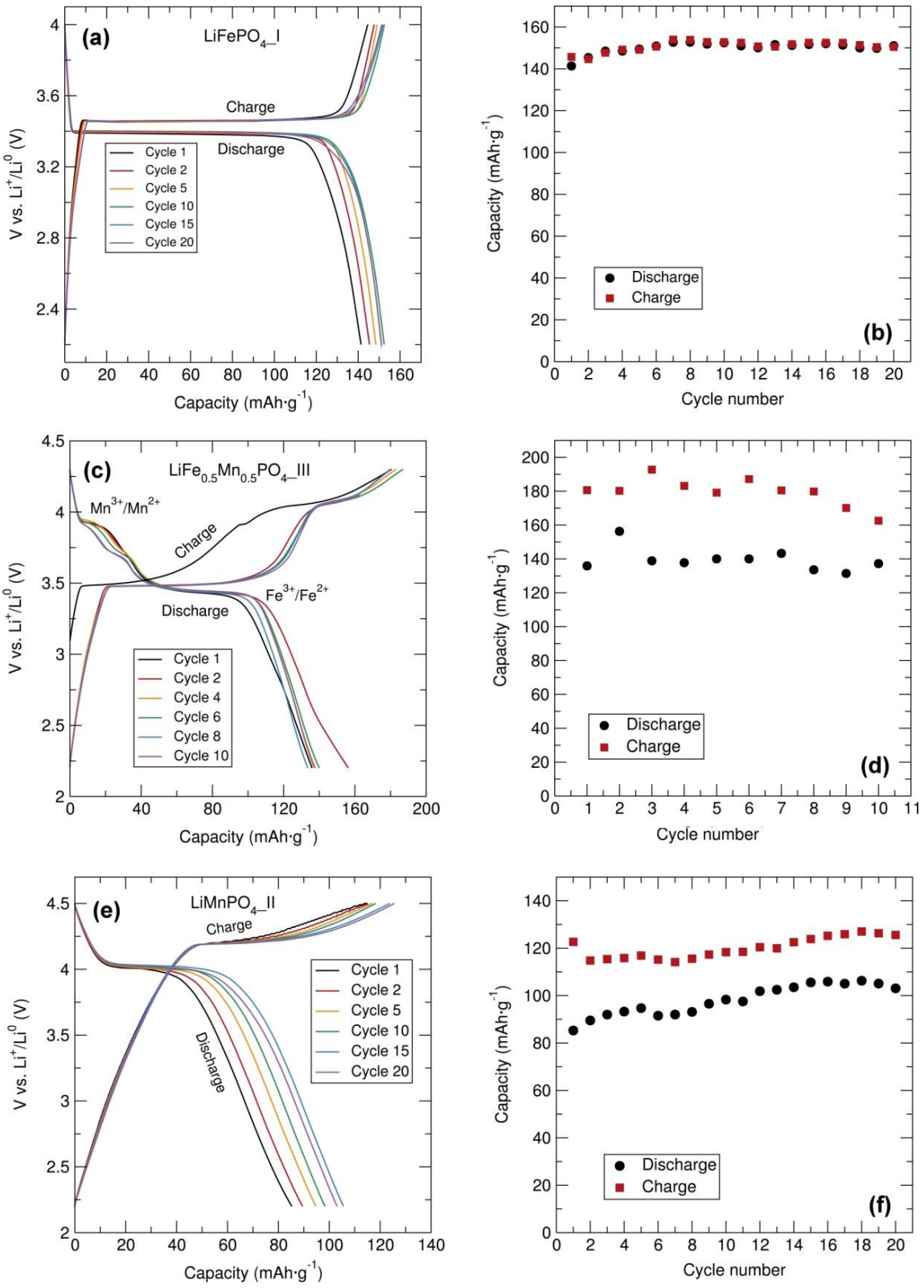

Figure 4.10. Voltage-capacity profiles and cycling stability between 2.2 V and 4.0, 4.3 or 4.5 V at C/20 rate of **(a)** and **(b)** C/$LiFePO_4$_I (15% wt. C from sucrose), **(c)** and **(d)** C/$LiFe_{0.5}Mn_{0.5}PO_4$_III (15% wt. C from sucrose), and **(e)** and **(f)** C/$LiMnPO_4$_II (15% wt. C from sucrose).

The rate behaviour of the C/$LiFePO_4$_I, C/$LiMnPO_4$_II and C/$LiFe_{0.5}Mn_{0.5}PO_4$_III phases was investigated to examine the rate capabilities as a function of Mn content and particle size and morphology. The results observed in Figure 4.11 indicated that the discharge capacity

regularly decreased with higher C rates. This effect was more pronounced for the $LiMnPO_4$ sample. High C rates up to 10 C delivered discharge capacities of 75 $mAh \cdot g^{-1}$, 50 $mAh \cdot g^{-1}$ and 25 $mAh \cdot g^{-1}$ for the $C/LiFe_{0.5}Mn_{0.5}PO_4$_III, $C/LiFePO_4$_I and $C/LiMnPO_4$_II phases, respectively. The $C/LiFe_{0.5}Mn_{0.5}PO_4$ presented here showed an improved rate capability at 10 C in comparison to the ~55 $mAh \cdot g^{-1}$ at 8 C reported previously for $LiFe_{0.5}Mn_{0.5}PO_4$ prepared *via* a more elaborate electrospun synthetic procedure.[278] This suggests that the fast microvawe treatment of metal alkoxide precursors presents a promising synthetic approach for the simple and low cost generation of olivine structured mixed metal phosphates with good electrochemical performance. In each of the three samples the capacity was fully recovered when the cycling rate returned back to C/10 rate after increasingly faster rates. An improved rate capability is clearly observed in the $C/LiFe_{0.5}Mn_{0.5}PO_4$ sample prepared using the "$[Fe_{0.5}Mn_{0.5}(O^tBu)_2(THF)]_2$" (III) metal alkoxide precursor in comparison to the $LiFe_{0.5}Mn_{0.5}PO_4$ sample synthesised with commercial starting materials presented in Chapter 3 (for example, 120 $mAh \cdot g^{-1}$ *vs.* 80 $mAh \cdot g^{-1}$ at C rate and 75 $mAh \cdot g^{-1}$ *vs.* 50 $mAh \cdot g^{-1}$ at 10 C rate). This could be attributed to the reduced particle size of $C/LiFe_{0.5}Mn_{0.5}PO_4$_III (~130 nm in width) compared to $C/LiFe_{0.5}Mn_{0.5}PO_4$_MW_com (~540 nm in width). These results also suggest that partial substitution of Fe^{2+} by Mn^{2+} in the olivine structure affords a noticeable enhancement in the rate capability of these electrodes. The observed improvement in the electrochemical performance of the $C/LiFe_{0.5}Mn_{0.5}PO_4$ material in comparison to $C/LiFePO_4$ could also be related to the decrease in particle size. Zhao *et al*. have studied the effect of particle size on the electrochemical performance of $LiFePO_4/C$ materials and demonstrated an increase in the discharge capacities of $LiFePO_4/C$ as the particle size decreased, which may be due to the fact that reduced particle sizes shortened the Li^+ diffusion distance through the $LiFePO_4/C$ bulk.[279] PXRD characterisation of the post-cycled materials in the discharge state shown in Figure 4.12 indicated that the Li^+ extraction/insertion process did not affect the structure of the $C/LiFe_{1-x}Mn_xPO_4$ composites, confirming the good structural stability of these positive insertion electrodes upon cycling even at high C rates.

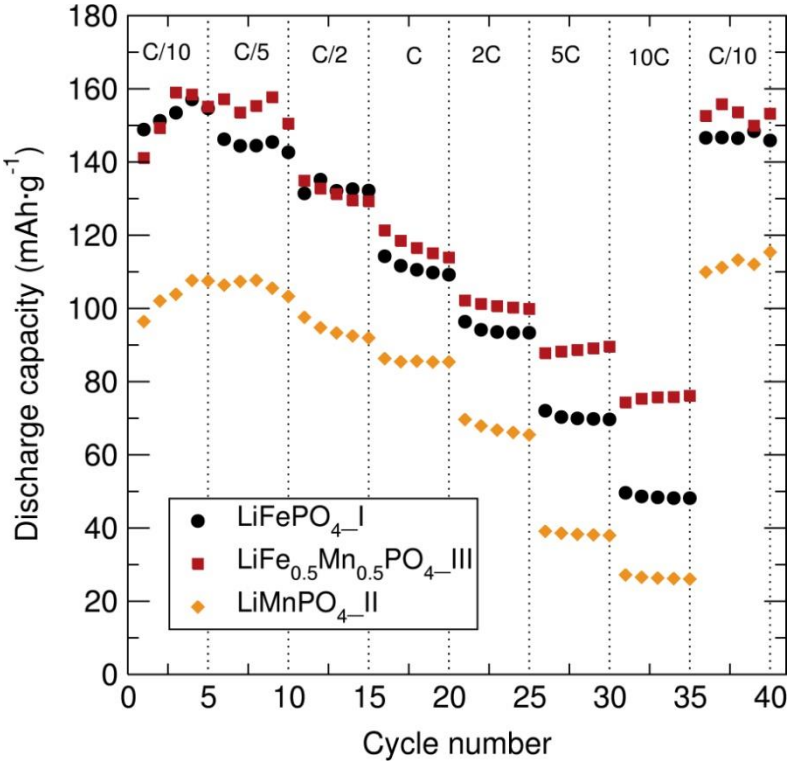

Figure 4.11. Comparative rate behaviour of C/$LiFePO_4$_I, C/$LiFe_{0.5}Mn_{0.5}PO_4$_III and C/$LiMnPO_4$_II (15% wt. C from sucrose) with C black and PTFE in 60:30:10 wt. ratio at different charge-discharge C rates.

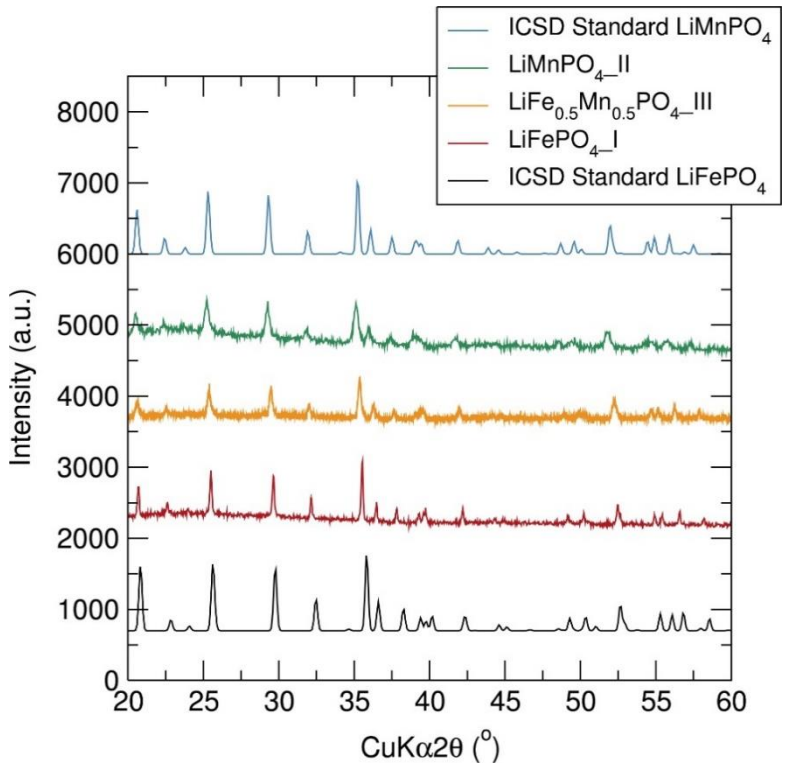

Figure 4.12. PXRD of post-cycled C/$LiFePO_4$_I, C/$LiFe_{0.5}Mn_{0.5}PO_4$_III and C/$LiMnPO_4$_II at different rates in the discharged state.

CV measurements for the C/$LiFePO_4$_I, C/$LiMnPO_4$_II and C/$LiFe_{0.5}Mn_{0.5}PO_4$_III nanocomposites prepared with "[*M*(O^tBu)$_2$(THF)]$_2$" (*M*=Fe, Mn) (I, II and III) metal alkoxide precursors were conducted at a scan rate of 0.1 mV·s^{-1} between 2.5 V and 4.5 V. The CV results for the C/$LiFePO_4$_I sample showed anodic and cathodic peaks at ~3.60 V and 3.23 V, respectively, due to the Fe^{+3}/Fe^{+2} redox pair (Figure 4.13 (a)). The CV curve for the C/$LiFe_{0.5}Mn_{0.5}PO_4$_III sample exhibited two oxidation (3.56 V and 4.14 V) and two reduction peaks (3.38 V and 3.84 V) characteristic from the Fe^{3+}/Fe^{2+} and Mn^{3+}/Mn^{2+} redox pairs (Figure 4.13 (c)). The significantly more intense peaks from the Fe^{3+}/Fe^{2+} pair in comparison to the Mn^{3+}/Mn^{2+} confirmed the stronger contribution of Fe over Mn in this electrochemical process. Furthermore, an additional reduction peak was observed at 3.6 V, in agreement with the additional discharge plateau observed in the galvanostatic cycling tests. This extra reduction peak has been also previously observed by Mathur *et al*, which they attribute to a $Mn_2P_2O_7$ impurity phase formed during the heat treatment process.[278] However, this impurity could not be detected in the PXRD pattern. Finally, the CV for the C/$LiMnPO_4$_II compound showed the oxidation and reduction peaks at ~4.31 and 3.95 V, repectively, due to the Mn^{+3}/Mn^{+2} redox pair (Figure 4.13 (b)). The good overlap of the CV curves after the first cycle confirmed the good reversibility of these electrochemical systems.

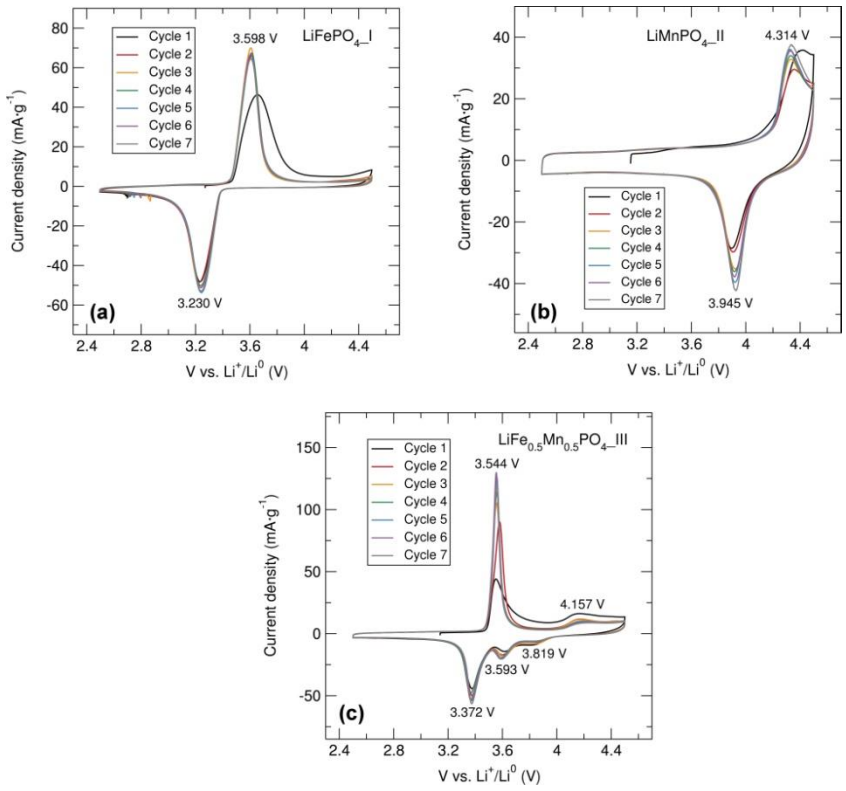

Figure 4.13. CVs at a 0.1 mV·s^{-1} scan rate between 2.5 V and 4.5 V of **(a)** C/$LiFePO_4$_I, **(b)** C/$LiMnPO_4$_II, and **(b)** C/$LiFe_{0.5}Mn_{0.5}PO_4$_III nanostructures prepared with "[*M*(O^tBu)$_2$(THF)]$_2$" (*M*=Fe, Mn) (I, II and III) metal alkoxide precursors.

4.2.4.4 PXRD and SEM of Mn_3O_4 nanoparticles prepared from hydrolysis of "$[Mn(O^tBu)_2(THF)]_2$" metal alkoxide

Mn_3O_4 hausmannite has received increasing attention as promising alternative anode material to graphite due to its high theoretical capacity (937 $mAh \cdot g^{-1}$), low conversion potential, natural abundance and environmental benignity, which are desirable for the practical application of LIBs. Mn_3O_4 has a spinel structure with Mn^{3+} and Mn^{2+} ions occupying the octahedral and tetrahedral positions, respectively.[280] The brownish Mn_3O_4 powder synthesised through a room temperature ultrasound-assisted hydrolysis route of "$[Mn(O^tBu)_2(THF)]_2$" (II) was characterised by PXRD. The volatile metallorganic compound can fully dissociate their O^tBu groups inside a bubble during the acoustic cavitation process of ultrasound and the resulting metal atoms can agglomerate to form the nanostructured oxide. Rietveld refinements to Mn_3O_4 (ICSD No 01-080-0382 24-734)[281] tetragonal structure belonging to $I4_1/amd$ space group confirmed that phase pure Mn_3O_4 hausmannite was obtained. Figure 4.14 indicates that a good fit between the experimental PXRD data and the calculated pattern was achieved. The estimated crystallite size of the Mn_3O_4 nanostructure was calculated using the Scherrer equation[208] applied to the (211) diffraction peak and was ~37 nm. SEM images of the Mn_3O_4 powders demonstrated quasi-spherical discs with an average particle size of around 80 nm (Figure 4.8 (d)). Heat treatment in a tube furnace of the Mn_3O_4 powder mixed with 15 % wt. C from sucrose at 500 ºC and 700 ºC for 1 hr under air was conducted. As observed in Figure 4.15, PXRD patterns of this sample indicate that heating at 500 ºC still afforded Mn_3O_4 hausmannite. However, heat treatment at elevated temperatures of 700 ºC in air led to the complete oxidation of the Mn^{2+} ions in Mn_3O_4 to Mn^{3+} forming Mn_2O_3. Similar heat treatment performed under Ar flow afforded the formation of the reduced product MnO due to the reducing nature of the sucrose (Figure 4.16).

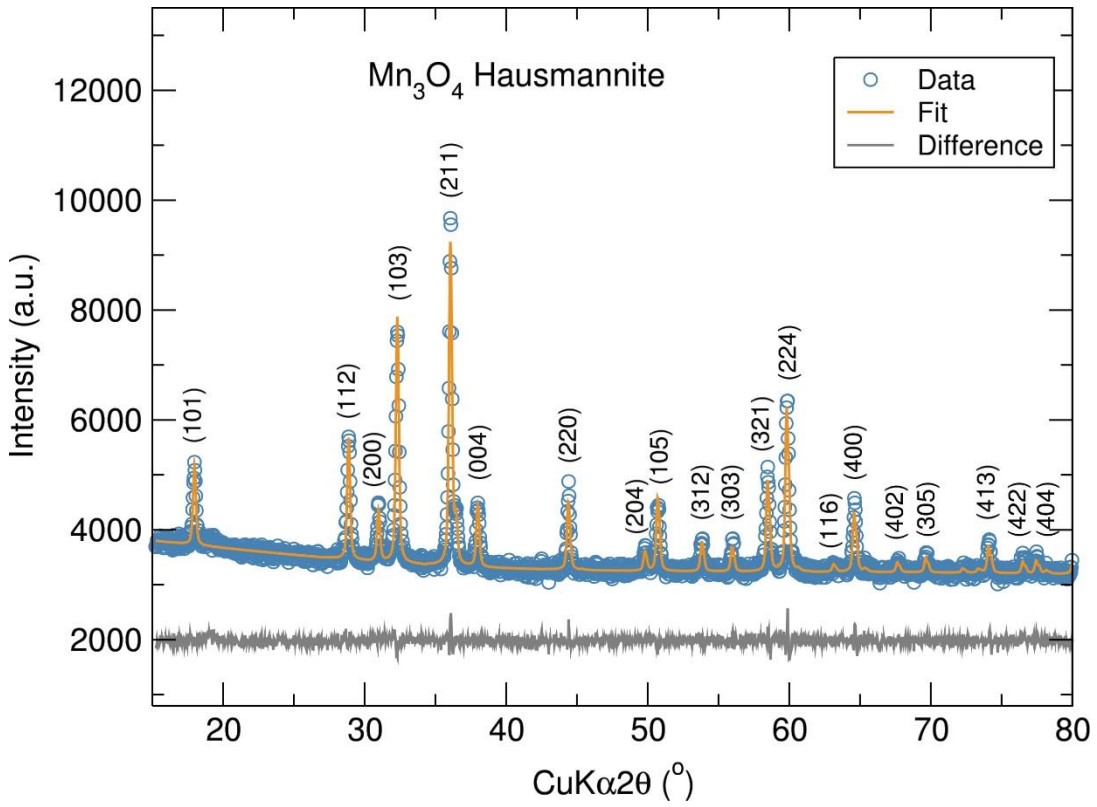

Figure 4.14. Rietveld analysis of PXRD data of hausmannite Mn_3O_4 nanostructure. [R_{wp}=19.5 %, R_{exp}=15.87 %, x^2=1.51, *a*=5.7655(3) Å, *b*=5.7655(3) Å and *c*=9.4634(7) Å].

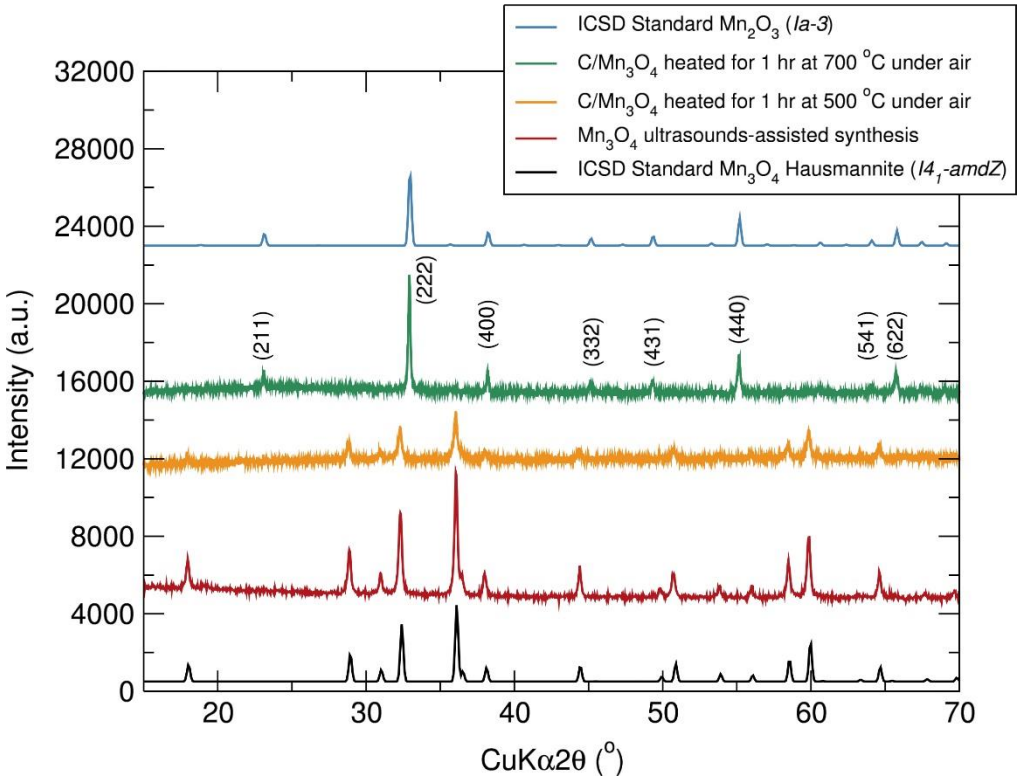

Figure 4.15. PXRD pattern of Mn_3O_4 hausmannite prepared through a room temperature ultrasound-assisted synthesis and post-heat treatment of Mn_3O_4 mixed with 15% wt. C from sucrose at 500 °C and 700 °C for 1 hr under air.

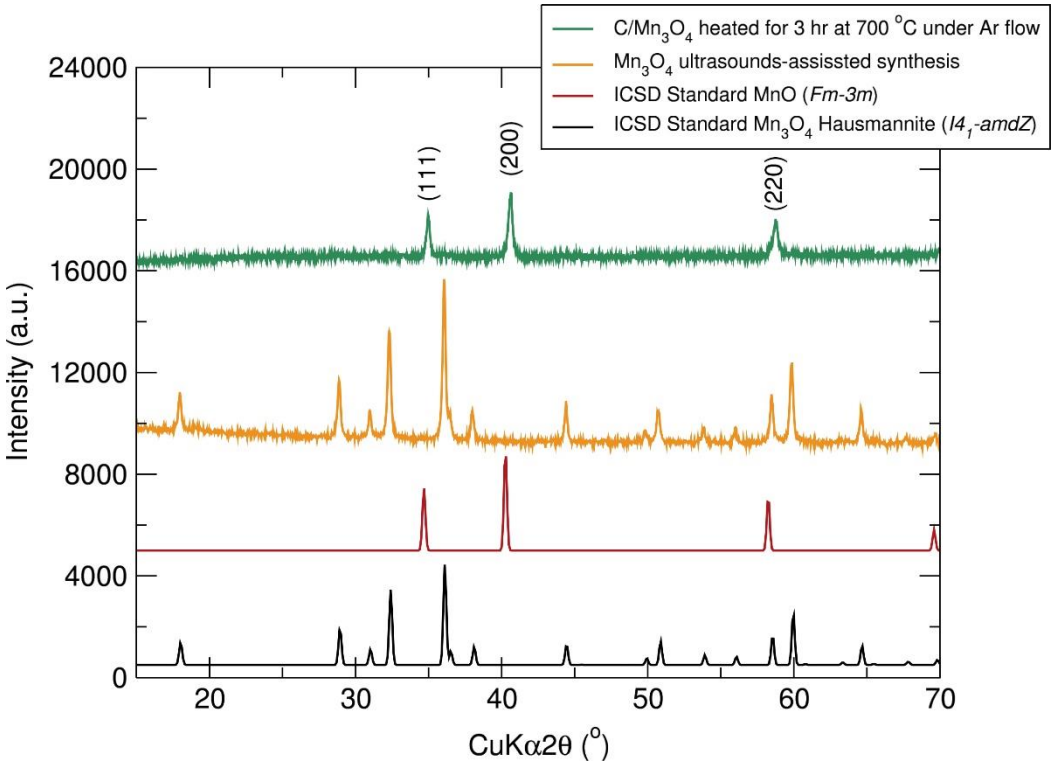

Figure 4.16. PXRD pattern of Mn_3O_4 hausmannite prepared through a room temperature ultrasound-assisted synthesis and post-heat treatment of Mn_3O_4 hausmannite mixed with 15% wt. C from sucrose at 700 °C for 3 hr under Ar flow.

4.2.4.5 Electrochemical performance of Mn_3O_4 nanoparticles prepared from hydrolysis of "$[Mn(O^tBu)_2(THF)]_2$"

The electrochemical performance of bare Mn_3O_4 hausmannite and C/Mn_3O_4 composite prepared using 15% wt. C from sucrose were examined to investigate the influence of the carbon coating on the cycling capability. Galvanostatic cycling studies of the bare Mn_3O_4 sample as an anode at a current density of 100 $mA \cdot g^{-1}$ over a voltage range between 0.01 V and 3.00 V revealed an initial discharge capacity of ~2300 $mAh \cdot g^{-1}$ that sharply faded to ~750 $mAh \cdot g^{-1}$ at the second cycle (Figure A4.7 (b)). By the 20th cycle, a discharge capacity of ~300 $mAh \cdot g^{-1}$ was still obtained (Figure A4.7 (c)). On the other hand, electrochemical measurements on the C/Mn_3O_4 sample (carbon coated with 15% wt. C from sucrose) at a same current density of 100 $mA \cdot g^{-1}$ over the same voltage range displayed a first discharge capacity of ~3200 $mAh \cdot g^{-1}$ that sharply decreased to approximately 1300 $mAh \cdot g^{-1}$ at the second cycle. These elevated initial discharge capacities of bare Mn_3O_4 and C/Mn_3O_4 hausmannite could be attributed to the contribution of carbon to the storage of Li^+ ions. Moreover, these first discharge capacities are significantly larger than in any previous reports.[282-285] The large capacity drop after the first cycle could be attributed to inevitable irreversible processes such as solid electrolyte interface (SEI) formation and electrolyte decomposition. These irreversible processes still occurred irrespective of a change in the lower voltage limit. Figure A4.8 shows the

galvanostatic cycling test of the C/Mn_3O_4 sample at a current density of 100 mA·g^{-1} over a voltage range between 0.1 V and 3.0 V, confirming that the marked capacity fading is still present even when increasing the lower voltage limit. The voltage-composition profile of the C/Mn_3O_4 sample indicates that approximately 8 Li^+ were inserted and extracted after the first cycle (Figure 4.17 (a)). Furthermore, Figure 4.17 (b) shows a marked decrease in capacity over cycling, although discharge capacities of around 460 mAh·g^{-1} were still reached at the 20th cycle, which is still higher than the theoretical capacity of standard graphite anodes (372 mAh·g^{-1}).[286, 287] The sharp capacity loss upon cycling could be explained by the fact that amorphous Li_2O and Mn metal is formed during the cycling process. Transition metal oxides store and release Li^+ ions throught the following conversion reaction: $MO_x + 2xe^- + 2xLi^+ \leftrightarrow M^0 + xLi_2O$. The full reduction of the transition metal oxides results in the formation of a composite material composed of metallic nanoparticles dispersed in the amorphous Li_2O matrix.[93, 188] Moreover, some Mn dissolution in the electrolyte solution could be also contributing to the drastic capacity fading observed.[288] These electrochemical studies clearly confirmed the improved cycling capability of C/Mn_3O_4 compared to bare Mn_3O_4, indicating that the presence of a carbon coating significantly enhances the electrochemical behavior of this electrode material. For example, well-dispersed ultrafine Mn_3O_4 nanocrystals on reduced graphene oxide delivered discharge capacities of 1912 mAh·g^{-1} and 1198 mAh·g^{-1} at 100 mA·g^{-1} after the 1st and 10th cycle, repectively.[282] Also, it has been reported that porous Mn_3O_4 nanorods displayed an outstanding electrochemical performance with high specific capacity (901.5 mAh·g^{-1} at a current density of 500 mA·g^{-1}), long cycling stability (coulombic efficiency of 99.3% after 150 cycles) and high rate capability (387.5 mAh·g^{-1} at 2000 mA·g^{-1}).[116] PXRD pattern of the cycled C/Mn_3O_4 presented here clearly suggested that the significant volume changes ocurring upon cycling degrades the structure, evidenced by the lack of diffraction peaks which suggest the formation of an amorphous material (Figure 4.17 (c)). Further examination of the PXRD pattern of C/Mn_3O_4 hausmannite after 20 cycles shows the possible presence of conversion product Li_2O after repeated cycles (see Figure A4.9). Moreover, rate behavior investigations on the C/Mn_3O_4 electrode material were conducted at current densities of 200 mA·g^{-1}, 400 mA·g^{-1}, 800 mA·g^{-1}, 1200 mA·g^{-1}, 2000 mA·g^{-1} and 200 mA·g^{-1} to probe the rate capabilities of this anode. Results showed a decrease in rate performance of this C/Mn_3O_4 nanostructure with increasing rate, displaying approximately 800 mAh·g^{-1} at 200 mA·g^{-1}, 400 mAh·g^{-1} at 400 mA·g^{-1}, 100 mAh·g^{-1} at 800 mA·g^{-1} and capacities lower than 50 mAh·g^{-1} at 1200 and 2000 mA·g^{-1} (Figure 4.18). Furthermore, a discharge capacity of ~350 mAh·g^{-1} was reached when cycling back at the current density of 200 mA·g^{-1}.

Results from the CV studies of C/Mn_3O_4 at 0.1 $mV \cdot s^{-1}$ scan rate between 0.01 V and 3.00 V indicated that the CV curves change significantly after the first cycle, with quite good overlap in subsequent cycles confirming the good reversibility of this electrochemical system during cycling (Figure 4.19). An intense cathodic peak at around 0.3 V and an anodic peak at approximately 1.38 V were observed in the CV scan, indicating the reversibility of the electrochemical reactions of Mn_3O_4 after the second cycle. In the anodic process, the broad peak that appeared at 1.38 V is attributed to the oxidation of metal Mn to MnO and the decomposition of Li_2O. The intense peak that emerges at low potential (0.3 V) is ascribed to the reduction of MnO to metallic Mn.[116]

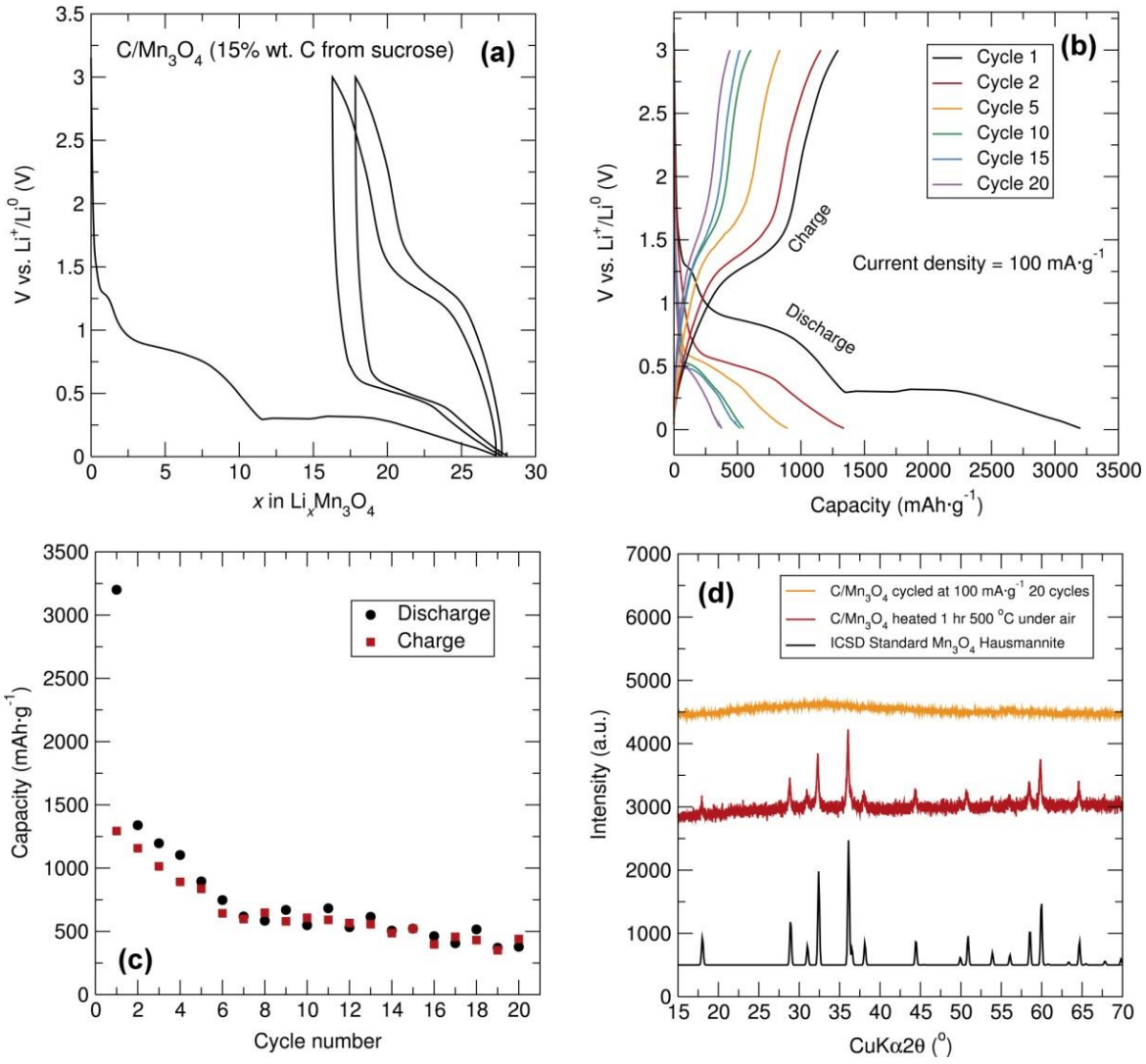

Figure 4.17. (a) Voltage-composition profile, **(b)** voltage-capacity profile, **(c)** cycling stability of C/Mn_3O_4 (15% C from sucrose) with C black and PTFE in 60:30:10 % wt. ratio over the potential range of 0.01 V-3.00 V at 100 $mA \cdot g^{-1}$. **(d)** PXRD of cycled C/Mn_3O_4 in the charged state.

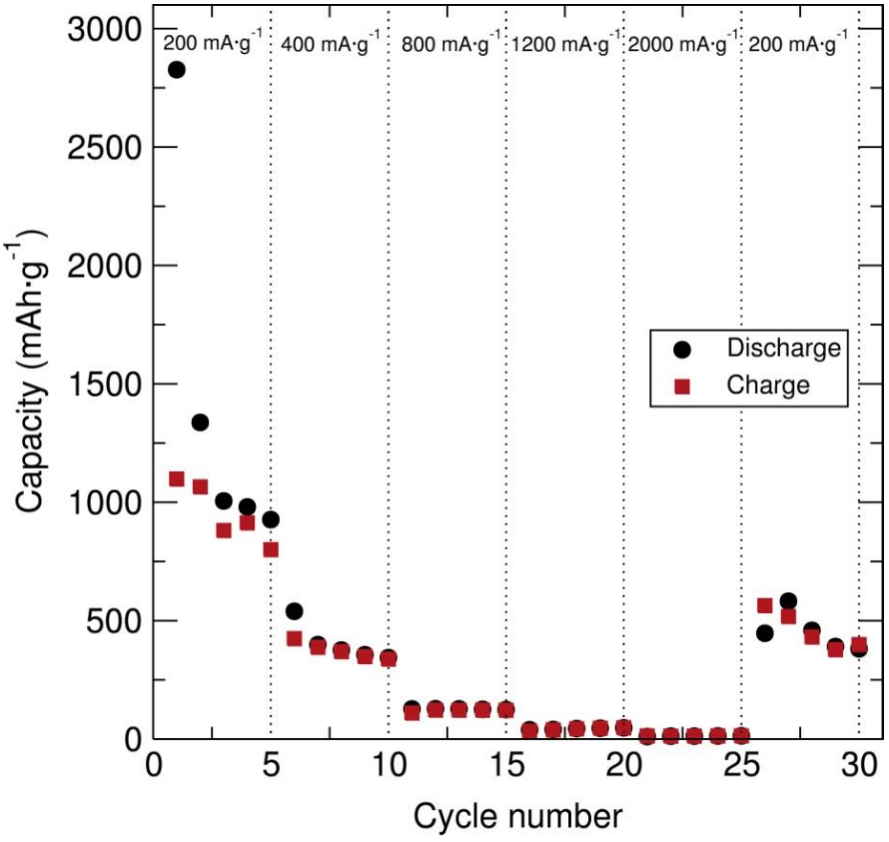

Figure 4.18. Rate behavior of C/Mn_3O_4 (15% wt. C from sucrose) mixed with C black and PTFE in 60:30:10 % wt. ratio over the potential range between 0.01 V and 3.00 V at different charge/discharge rates.

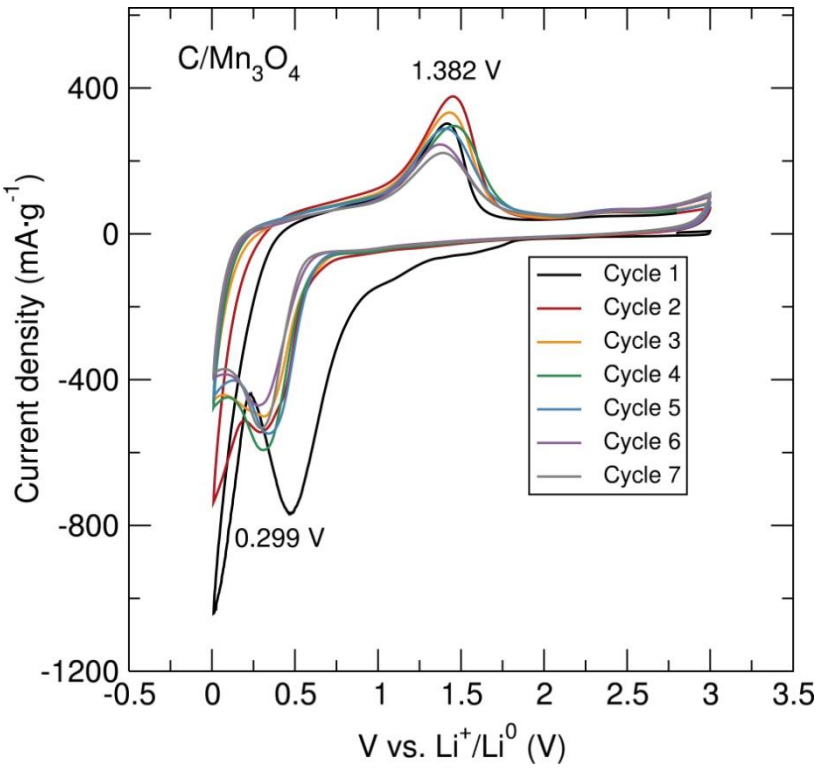

Figure 4.19. CV of C/Mn_3O_4 hausmannite at a 0.1 $mV \cdot s^{-1}$ scan rate between 0.01 V and 3.00 V.

4.3 Conclusions

In this chapter, a low cost and energy-efficient synthetic approach for the preparation of metal alkoxides to be used as precursors in the synthesis of phase pure olivine nanostructured $LiFe_{1-x}Mn_xPO_4$ (x=0, 0.5 and 1) and Mn_3O_4 hausmannite nanoparticles through fast microwave and ultrasound-assisted routes, respectively, has been presented. As previously observed for the $LiFe_{1-x}Mn_xPO_4$ olivines studied in Chapter 3, the particle size and morphology in the $LiFe_{1-x}Mn_xPO_4$ (x=0, 0.5 and 1) nanostructures has a strong dependence on the transition metal composition, going from larger platelets to thiner nanorods with increased Mn contents. Electrochemical testing of $LiFePO_4$ and $LiFe_{0.5}Mn_{0.5}PO_4$ samples revealed excellent cyclability with charge/discharge capacities close to theoretical values (~155 mAh g^{-1} vs. 170 mAh g^{-1}at C/20 rate). These positive insertion electrodes also displayed rate capabilities comparable to the best performing olivine-structured metal phosphates in the literature, demonstrating the suitability of the metal alkoxide precursors presented here in the generation of high performance olivine mixed-metal phosphates *via* a fast microwave-assisted synthesis. On the other hand, C/Mn_3O_4 hausmannite nanoparticles prepared by a straightforward room temperature ultrasound-assisted hydrolysis and carbon coated using sucrose (heat treatment for 1 hr at 500 ºC under air, as higher temperatures or heating in Ar atmosphere led to the oxidised or reduced product, respectively) showed a good electrochemical behaviour displaying an initial discharge capacity of ~3200 mAh·g^{-1} and reaching 460 mAh·g^{-1}after the 20th cycle. Nevertheless, a sharp capacity fading over subsequent cycling and poor rate capabilities were observed. Further improvements in the carbon coating of this metal oxide nanoparticles synthesised may dramatically enhance the battery cycling performance.

5 Microwave Treatments of Single Source Heterometallic Alkoxides for Nanostructured Li-ion Battery Electrodes

5.1 Introduction

To expand the use of transition metal alkoxide precursors for the preparation of electrode nanomaterials, the current chapter details efforts towards designing a series of heterometallic alkoxides containing Li and one or two transition metals (Fe, Mn) in a single compound. Such heterometallic complexes have been of interest as precursors to oxide based thin films.[289-291] Here, they are employed as single source precursors for the preparation of $LiFe_{1-x}Mn_xPO_4$ (x=0, 0.5 and 1) olivine nanostructures *via* fast and low temperature microwave-assisted synthesis in ethylene glycol or a ionic liquid. Co-location of all required metals in these metallorganic precursors should further decrease reaction times and temperatures, an important consideration for industrial scale-up. X-ray PDF analyses of these olivine $LiFe_{1-x}Mn_xPO_4$ nanostructures have also been conducted to examine the local structure and defect chemistry as a function of the Mn content and the reaction media.

5.2 Results and discussion

5.2.1 Synthesis and characterisation of "$[MLi_2X(O^tBu)_4(THF)_2]_n$" ($M$=Fe, Mn and X=Br, Cl) heterometallic alkoxide precursors

5.2.1.1 Synthesis and characterisation of $[FeLi_2Br(O^tBu)_4(THF)_2]_n$ (IV)

Knowing that the reaction between $FeBr_2$ and three molar equivalents of NaO^tBu in THF solution affords the heterometallic alkoxide $[NaFe(O^tBu)_3(THF)]_2$ previously reported by Gun'ko *et. al*,[292] the preparation of the structural analogue "$[LiFe(O^tBu)_3(THF)]_2$" was pursued. A similar reaction between $FeBr_2$ and three molar equivalents of LiO^tBu in THF was carried out. As observed by Barley *et al*,[293] this attempt failed and the product obtained was the bromide containing metallorganic compound $[FeLi_2Br(O^tBu)_4(THF)_2]_n$ (see Schematic 5.1 and section 2.2.6). The $[FeLi_2Br(O^tBu)_4(THF)_2]_n$ (IV) product is very air and moisture sensitive and demonstrates a colour change from light green to reddish upon exposure to air due the oxidation of Fe^{2+} to Fe^{3+}.

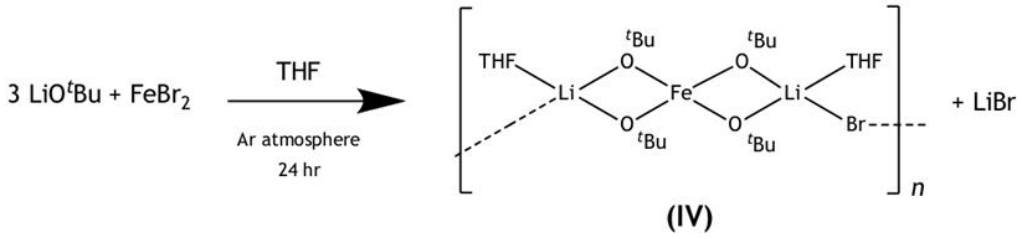

Schematic 5.1. Synthesis of $[FeLi_2Br(O^tBu)_4(THF)_2]_n$ (IV) heterometallic alkoxide precursor.

Single crystal XRD studies of the heterometallic alkoxide confirmed the formation of the $[FeLi_2Br(O^tBu)_4(THF)_2]_n$ metallorganic complex previously reported by Barley *et* al.[293] As shown in Figure 5.1, in this compound the lithium bound bromide acts as a bridge between lithium atoms in different four member ring systems, resulting in a 1D polymeric structure. The bonding at each Li atom is completed by complexation of a THF molecule. Table 5.1 summarises the crystallographic information obtained from the structure refinement of $[FeLi_2Br(O^tBu)_4(THF)_2]_n$ (IV).

The ^1H NMR spectrum of the $[FeLi_2Br(O^tBu)_4(THF)_2]_n$ (IV) powder conducted in dry C_6D_6 (Figure A5.1) showed two peaks at 0.3 and 1.2 ppm corresponding to the bridging and terminal O^tBu groups, respectively. Broader peaks from the THF groups were found at 1.4 ppm and 3.6 ppm. FT-IR spectrum in Nujol of the dry powder $[FeLi_2Br(O^tBu)_2(THF)_2]_n$ (IV) heterometallic alkoxide precursor depicted in Figure A5.2 showed the characteristic Nujol bands at 1460 and 1370 cm^{-1}. Considering previous infrared spectroscopy studies on metal alkoxides, the 724 and 772 cm^{-1} vibrations for this heterometallic *tert*-butoxide could be assigned to a symmetrical skeletal vibration of the *tert*-butyl group. The 893 cm^{-1} absorption band could also be attributed to a skeletal vibration of the *tert*-butoxy group. The asymmetric stretch from the C-O-C group in THF is seen at 962 cm^{-1}. The band at 1048 cm^{-1} could correspond to a C-C vibration within the *tert*-butoxy group, while the 1191 cm^{-1} band could be due to a C-O stretch vibration typical of the *tert*-butyl group. In general, the *tert*-butyl group is often characterised by strong absorptions at about 1200 - 1250 cm^{-1}.[271, 272]

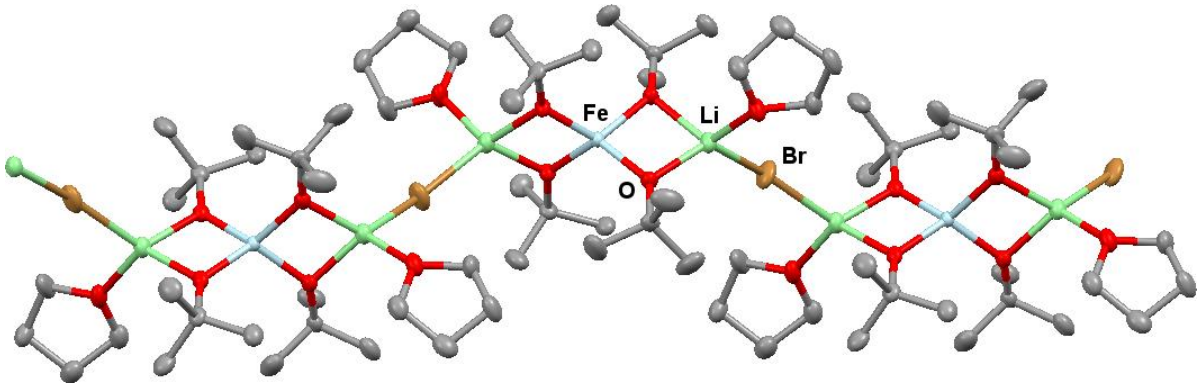

Figure 5.1. Propagation of the crystal structure of $[FeLi_2Br(O^tBu)_4(THF)_2]_n$ (IV) in the *c* direction to form a polymeric chain.

Table 5.1. Crystal data and structure refinement of $[FeLi_2Br(O^tBu)_4(THF)_2]_n$ (IV).

$[FeLi_2Br(O^tBu)_2(THF)_2]_n$ (IV)	
Mw=586.29 g/mol	Mo K_α Radiation (λ=0.71073 Å)
Monoclinic, $P2_1/c$	ρ_{cal}=1.248 g/cm^3
a =18.635 (5) Å	μ=1.79 mm^{-1}
b=9.087 (2) Å	2 θ range of data collection 2.186° to 50.05°
c =18.425 (4) Å	Reflections collected 21611
β=90.502 (6)°	Independent refelctions 5352 (R_{int}=0.1500, R_{sigma}=0.1636)
V=3119.7 (13) Å^3	T=100 K
Z=4	Crystal size 0.35x0.3x0.11 mm
F (000)=1244.0	*h*=21 →22
Goodness of fit on F^2 1.00	k=10 →10
R indexes R_1=0.1600, wR_2=0.1644	*l*=21 → 21

5.2.1.2 Synthesis and characterisation of "$[FeLi_2Cl(O^tBu)_4(THF)_2]_n$" (V)

A similar heterometallic precursor to $[FeLi_2Br(O^tBu)_4(THF)_2]_n$ (IV) was prepared using $FeCl_2$ instead of $FeBr_2$ in order to investigate the influence of the halogen in the resulting metal alkoxide complex. The different reactivity and ionic radius of Cl and Br may trigger some the differences in the resulting heterometallic alkoxide. The heterometallic alkoxide with suggested formula "$[FeLi_2Cl(O^tBu)_4(THF)_2]_n$" (V) was synthesised as described in section 2.2.6.

Single crystal XRD data from the "$[FeLi_2Cl(O^tBu)_4(THF)_2]_n$" (V) crystals was not of enough quality to conduct a refinement sensibly, so unfortunately it was not possible to obtain a reliable crystal structure. Nevetheless, the data collected suggested that the "$[FeLi_2Cl(O^tBu)_4(THF)_2]_n$" (V) crystals exhibit an analogous crystal structure to the $[(THF)_2Li_2Al(O^tBu)_4Cl]$ compound previously reported by Pauls *et al.*, which was fabricated by reaction of four equivalents of LiO^tBu on $AlCl_3$ in THF.[294] The $[(THF)_2Li_2Al(O^tBu)_4Cl]$ complex displays a similar structure to $[FeLi_2Br(O^tBu)_4(THF)_2]_n$ but with Cl atoms acting as a bridge between Li atoms instead of Br. The ^{1}H NMR spectrum of the "$[FeLi_2Cl(O^tBu)_4(THF)_2]_n$" (V) powder conducted in dry C_6D_6 (Figure A5.3) revealed two peaks from the *tert*-butoxide protons, a major one at 0.3 ppm corresponding to the μ_2-O^tBu bridging and other at 1.2 ppm representing the terminal O^tBu groups. Broader peaks from the THF grous again appeared at 1.4 and 3.6 ppm. The FT-IR spectrum in Nujol of the dry powder "$[FeLi_2Cl(O^tBu)_2(THF)_2]_n$" (V) depicted in Figure A5.4 showed 724 and 758 cm^{-1} vibrations corresponding to a symmetrical skeletal vibration of the *tert*-butyl group. The 896 cm^{-1} absorption band may be ascribed to a skeletal vibration of the *tert*-butoxy

group. The asymmetric stretch from the C-O-C group in THF appears at 958 cm^{-1}. The band at 1046 cm^{-1} could be originated from a C-C vibration within the *tert*-butoxy group, while the 1199 cm^{-1} band could be assigned to a C-O stretch vibration from the *tert*-butyl group.

5.2.1.3 Synthesis and characterisation of "$[MnLi_2Br(O^tBu)_4(THF)_2]_n$" (VI)

The equivalent Mn containing alkoxide precursor with expected chemical formula "$[MnLi_2Br(O^tBu)_4(THF)_2]_n$" (VI) was prepared in a similar manner using three equivalents of LiO^tBu and one equivalent of $MnBr_2$ in dry THF. This reaction resulted in the formation of a light brown-pinkish solution and a greyish precipitate of LiBr. The "$[MnLi_2Br(O^tBu)_4(THF)_2]_n$" (VI) product was also air and moisture sensitive, as when exposing it to air pinkish Mn^{2+} ions could be oxidised to blackish Mn^{3+} ions.

Again, single crystals of the "$[MnLi_2Br(O^tBu)_4(THF)_2]_n$" (VI) heterometallic alkoxide with enough quality for single crystal XRD experiments were not obtained. However, similar ^1H NMR and FT-IR spectra as the previous heterometallic compounds shown in this chapter were obtained for this complex (see Figure A5.5 and A5.6). From this, it may be inferred that a similar structure is formed and for the rest of this thesis the structure is referred as "$[MnLi_2Br(O^tBu)_4(THF)_2]_n$" (VI).

5.2.1.4 Synthesis and characterisation of "$[Fe_{0.5}Mn_{0.5}Li_2Br(O^tBu)_4(THF)_2]_n$" (VII)

Finally, in an effort to prepare a trimetallic *tert*-butoxide compound containing Li, Fe and Mn, a similar synthetic approach was followed by reacting six equivalents of LiO^tBu, one equivalent of $FeBr_2$ and one equivalent of $MnBr_2$ in dry THF.

Single crystal XRD analysis on "$[Fe_{0.5}Mn_{0.5}Li_2Br(O^tBu)_4(THF)_2]_n$" (VII) crystals revealed a similar unit cell than $[FeLi_2Br(O^tBu)_4(THF)_2]_n$ (IV), however, using X-ray based techniques it is not possible to reliably distinguish between Fe and Mn atoms.The obtained dark-brownish product with expected chemical formula "$[Fe_{0.5}Mn_{0.5}Li_2Br(O^tBu)_4(THF)_2]_n$" (VII) was also characterised by ^1H NMR and FT-IR spectroscopy. Again similar ^1H NMR and FT-IR spectra as the rest of heterometallic compounds presented here were obtained (see Figure A5.7 and A5.8). Therefore, this suggests that this metallorganic complex may exhibit a similar structure.

Results from the CHN microanalysis of the dry powders $[FeLi_2Br(O^tBu)_4(THF)_2]_n$ (IV), "$[MnLi_2Br(O^tBu)_4(THF)_2]_n$" (VI) and "$[Fe_{0.5}Mn_{0.5}Li_2Br(O^tBu)_4(THF)_2]_n$" (VII) heterometallic alkoxides shown in Table 5.2 revealed C and H contents lower than the expected theoretical values. The decrease in the C and H content could be attributed to the fact that during the drying process under vacuum some of the THF groups in these compounds could be removed leading to the noticeable decrease in the C and H content observed.

Results showed a better agreement to the expected C and H contents for the "$FeLi_2Br(O^tBu)_4$" product assuming that the THF molecules are lost.

AAS investigations to determine the metal contents in these heterometallic alkoxides confirmed that the "$[Fe_{0.5}Mn_{0.5}Li_2Br(O^tBu)_4(THF)_2]_n$"(VII) alkoxide precursor exhibited similar Fe and Mn contents, in excellent agreement with the expected stoichiometry for this compound. Each of the four $[FeLi_2Br(O^tBu)_2(THF)_2]_n$ (IV), "$[FeLi_2Cl(O^tBu)_2(THF)_2]_n$" (V), "$[MnLi_2Br(O^tBu)_2(THF)_2]_n$" (VI) and "$[Fe_{0.5}Mn_{0.5}Li_2Br(O^tBu)_2(THF)_2]_n$" (VII) heterometallic alkoxide precursors had similar Li contents. The Li contents were higher than expected, what suggests that all the precursors may still contain some LiBr/LiCl.

Table 5.2. CHN Microanalysis of $[FeLi_2Br(O^tBu)_2(THF)_2]_n$, "$[MnLi_2Br(O^tBu)_2(THF)_2]_n$" and "$[Fe_{0.5}Mn_{0.5}Li_2Br(O^tBu)_2(THF)_2]_n$" heterometallic alkoxide precursors.

	Found		Expected	
Sample	**C**	**H**	**C**	**H**
$[FeLi_2Br(O^tBu)_4(THF)_2]_n$ (IV)	34.18 %	6.22 %	49.17 %	8.94 %
"$[MnLi_2Br(O^tBu)_4(THF)_2]_n$" (VI)	37.94 %	6.93 %	49.24 %	8.95 %
"$[Fe_{0.5}Mn_{0.5}Li_2Br(O^tBu)_4(THF)_2]_n$" (VII)	38.31 %	6.97 %	49.20 %	8.95 %
"$FeLi_2Br(O^tBu)_4$"	-	-	32.78 %	6.19 %
"$MnLi_2Br(O^tBu)_4$"	-	-	32.83 %	6.20 %
"$Fe_{0.5}Mn_{0.5}Li_2Br(O^tBu)_4$"	-	-	32.80 %	6.19 %

Table 5.3. Fe, Mn and Li contents of $[FeLi_2Br(O^tBu)_2(THF)_2]_n$ (IV), "$[FeLi_2Cl(O^tBu)_2(THF)_2]_n$" (V), "$[MnLi_2Br(O^tBu)_2(THF)_2]_n$" (VI) and "$[Fe_{0.5}Mn_{0.5}Li_2Br(O^tBu)_2(THF)_2]_n$" (VII) heterometallic alkoxide precursors obtained from AAS analysis.

	Found			Expected		
Sample	**Fe (% mol)**	**Mn (% mol)**	**Li (% mol)**	**Fe (% mol)**	**Mn (% mol)**	**Li (% mol)**
$[FeLi_2Br(O^tBu)_4(THF)_2]_n$ (IV)	5.59	-	4.69	9.52	-	2.37
"$[FeLi_2Cl(O^tBu)_4(THF)_2]_n$" (V)	9.07	-	4.92	10.31	-	2.56
"$[MnLi_2Br(O^tBu)_4(THF)_2]_n$" (VI)	-	11.01	4.19	-	9.38	2.37
"$[Fe_{0.5}Mn_{0.5}Li_2Br(O^tBu)_4(THF)_2]_n$"(VII)	4.02	4.15	4.13	4.77	4.69	2.37

5.2.2 Synthesis and characterisation of $LiFe_{1-x}Mn_xPO_4$ nanostructures from "$[MLi_2X(O^tBu)_4(THF)_2]_n$" (*M*=Fe, Mn and *X*=Br, Cl)

Olivine $LiFe_{1-x}Mn_xPO_4$ (x=0, 0.5 and 1) nanostructures were prepared using "$[MLi_2X(O^tBu)_4(THF)_2]_n$" (*M*=Fe, Mn; *X*=Br, Cl) heterometallic alkoxides (see section 2.2.6) and H_3PO_4 as reactants according to the reaction schematics 5.2 and 5.3, and as described in section 2.2.7. Table 5.4 lists the "$[MLi_2X(O^tBu)_4(THF)_2]_n$" (M=Fe, Mn, *X*=Br, Cl) heterometallic alkoxide precursors employed here and the attempted olivine $LiFe_{1-x}Mn_xPO_4$ nanophases prepared from these.

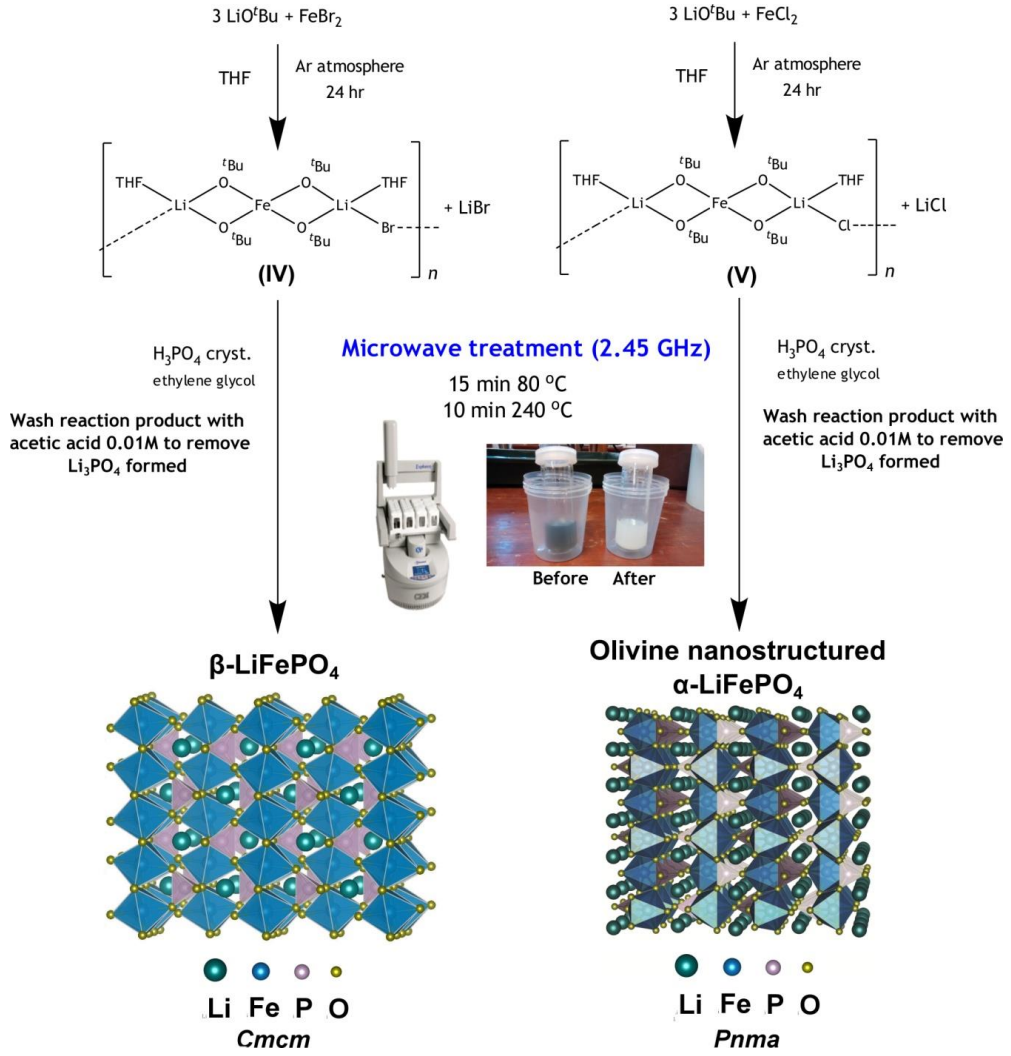

Schematic 5.2. Reaction schematic for the preparation of $LiFePO_4$ polymorphs from $[FeLi_2Br(O^tBu)_4(THF)_2]_n$ (IV) and "$[FeLi_2Cl(O^tBu)_4(THF)_2]_n$" (V) single source heterometallic alkoxide precursors using microwave methods.

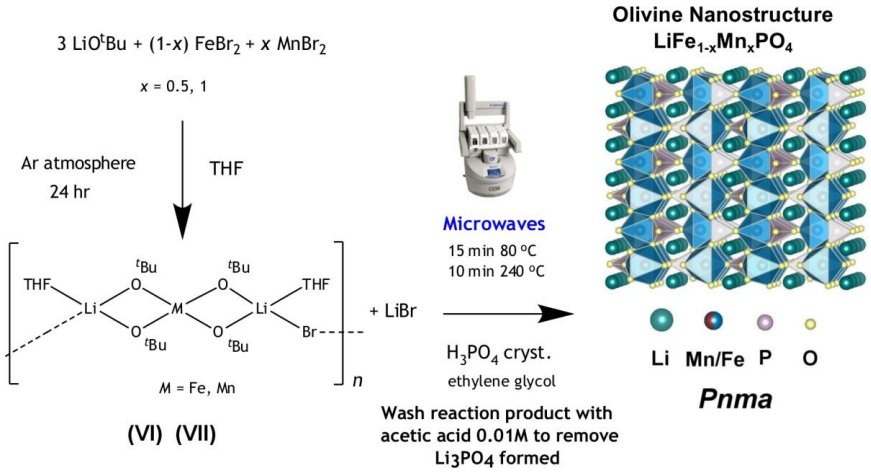

Schematic 5.3. Reaction schematic for the preparation of $LiFe_{0.5}Mn_{0.5}PO_4$ and $LiMnPO_4$ from "$[MnLi_2Br(O^tBu)_4(THF)_2]_n$" (VI) and "$[Fe_{0.5}Mn_{0.5}Li_2Br(O^tBu)_4(THF)_2]_n$" (VII) single source heterometallic alkoxide precursors using microwave methods.

Table 5.4. Preparation of "$[MLi_2X(O^tBu)_4(THF)_2]_n$" (*M*=Fe, Mn; *X*=Br, Cl) (IV, V, VI and VII) single source heterometallic alkoxide precursors and the reactions attempted with these precursors to obtain $LiFe_{1-x}Mn_xPO_4$ (*x*=0, 0.5 and 1) nanostructures.

Samples	Reactants	Reaction conditions
$[FeLi_2Br(O^tBu)_4(THF)_2]_n$ (IV)	$FeBr_2$ (1.078 g, 5 mmol) + 3 LiO^tBu (1.201 g, 15 mmol) + 40 mL THF	24 hr stirring at RT
"$[FeLi_2Cl(O^tBu)_4(THF)_2]_n$" (V)	$FeCl_2$ (0.634 g, 5 mmol) + 3 LiO^tBu (1.201 g, 15 mmol) + 40 mL THF	24 hr stirring at RT
"$[MnLi_2Br(O^tBu)_4(THF)_2]_n$" (VI)	$MnBr_2$ (1.074 g, 5 mmol) + 3 LiO^tBu (1.201 g, 15 mmol) + 40 mL THF	24 hr stirring at RT
"$[Fe_{0.5}Mn_{0.5}Li_2Br(O^tBu)_4(THF)_2]_n$" (VII)	$MnBr_2$ (0.537 g, 2.5 mmol) + $MnBr_2$ (0.539 g, 2.5 mmol) + 3 LiO^tBu (1.201 g, 15 mmol) + 40 mL THF	24 hr stirring at RT
β-$LiFePO_4$_IV	$[FeLi_2Br(O^tBu)_4(THF)_2]_n$ (0.2000 g, 0.34 mmol) + H_3PO_4 (0.0334 g, 0.34 mmol) + 10 mL EG	Microwave synthesis (2.45 GHz) 15 min 80 ºC and 10 min 240 ºC
α-$LiFePO_4$_V	"$[FeLi_2Cl(O^tBu)_4(THF)_2]_n$" (0.2000 g, 0.37 mmol) + H_3PO_4 (0.0362 g, 0.37 mmol) + 10 mL EG	Microwave synthesis (2.45 GHz) 15 min 80 ºC and 10 min 240 ºC
$LiMnPO_4$_VI	"$[MnLi_2Br(O^tBu)_4(THF)_2]_n$" (0.2000 g, 0.34 mmol)+ H_3PO_4 (0.0335 g, 0.34 mmol) + 10 mL EG	Microwave synthesis (2.45 GHz) 15 min 80 ºC and 10 min 240 ºC
$LiFe_{0.5}Mn_{0.5}PO_4$_VII	"$[Fe_{0.5}Mn_{0.5}(O^tBu)_2(THF)]_n$" (0.3000 g, 0.51 mmol) + H_3PO_4 (0.0503 g, 0.51 mmol) + 15 mL EG	Microwave synthesis (2.45 GHz) 15 min 80 ºC and 10 min 240 ºC
$LiFe_{0.5}Mn_{0.5}PO_4$_IV-VI	0.5 "$[FeLi_2Br(O^tBu)_4(THF)_2]_n$" (0.1500 g, 0.25 mmol) + 0.5 "$[MnLi_2Br(O^tBu)_4(THF)_2]_n$" (0.1500 g, 0.25 mmol)+ H_3PO_4 (0.0501 g, 0.51 mmol) + 15 mL EG	Microwave synthesis (2.45 GHz) 15 min 80 ºC and 10 min 240 ºC
$LiFe_{0.5}Mn_{0.5}PO_4$_V-VI	0.5 "$[FeLi_2Cl(O^tBu)_4(THF)_2]_n$" (0.1350 g, 0.25 mmol) + 0.5 "$[MnLi_2Br(O^tBu)_4(THF)_2]_n$"(0.1500 g, 0.25 mmol)+ H_3PO_4 (0.0501 g, 0.51 mmol) + 15 mL EG	Microwave synthesis (2.45 GHz) 15 min 80 ºC and 10 min 240 ºC
$LiFePO_4$_V_IL_10 min	"$[FeLi_2Cl(O^tBu)_4(THF)_2]_n$" (0.1500 g, 0,28 mmol) + H_3PO_4 (0.0271 g, 0.28 mmol) + 5 mL 1-ethyl-3-methylimidazolium trifluoromethanesulfonate	Microwave synthesis (2.45 GHz) 15 min 80 ºC and 10 min 240 ºC
$LiFePO_4$_V_IL_1 hr	"$[FeLi_2Cl(O^tBu)_4(THF)_2]_n$" (0.1500 g, 0,28 mmol) + H_3PO_4 (0.0271 g, 0.28 mmol) + 5 mL 1-ethyl-3-methylimidazolium trifluoromethanesulfonate	Microwave synthesis (2.45 GHz) 1 hr 240 ºC
β-$LiFePO_4$_IV_TEG	$[FeLi_2Br(O^tBu)_4(THF)_2]_n$ (0.2000 g, 0.34 mmol) + H_3PO_4 (0.0334 g, 0.34 mmol) + 10 mL TEG	Microwave synthesis (2.45 GHz) 15 min 80 ºC and 10 min 240 ºC

5.2.2.1 PXRD and X-ray PDF analysis of $LiFe_{1-x}Mn_xPO_4$ nanostructures prepared from "$[MLi_2X(O^tBu)_4(THF)_2]_n$" (*M*=Fe, Mn and *X*=Br, Cl)

PXRD characterisation of $LiFePO_4$ obtained from the fast microwave-assisted synthesis (15 min 80 °C and 10 min 240 °C) employing the $[FeLi_2Br(O^tBu)_4(THF)_2]_n$ (IV) heterometallic alkoxide precursor and H_3PO_4 in ethylene glycol revealed the formation of the ß-$LiFePO_4$_IV polymorph belonging to the *Cmcm* space group. The formation energy for the ß-$LiFePO_4$ phase is lower than that of α-$LiFePO_4$, making it an intermediate and metastable polymorph which usually displays a phase transformation to olivine α-$LiFePO_4$ when the temperature is increased above 475 °C.[52] While the Li^+ ions in olivine-structured α-$LiFePO_4$ are in an octahedral [LiO_6] environment, the Li^+ ions in the ß-$LiFePO_4$ are tetrahedrally coordinated and [LiO_4] tetrahedra share a corner with the nearest octahedral [FeO_6] and the nearest tetrahedral [PO_4]. Consequently, the 1D migration channels for Li-ion diffusion observed in α-$LiFePO_4$ along the *b*-axis direction disappear in the ß-$LiFePO_4$ phase. Therefore, the Li^+ ions in ß-$LiFePO_4$ stay in a more captive state and are surrounded by octahedral [FeO_6] and tetrahedral [PO_4].[49, 158] As a result, the Li^+ migration is hampered due to the very long diffusion distance between two adjacent Li^+ ion sites and very high energy barriers for Li^+ migration.[51] As observed by Nierderberger *et al.*,[24] heat treatment of the ß-$LiFePO_4$_IV polymorph with 15 % wt. C from sucrose in a tube furnace for 1 hr at 700 °C under Ar flow yielded a phase transformation to the phase pure electrochemically active olivine α-$LiFePO_4$_IV polymorph (*Pnma* space group). Unfortunately, several attempts to prepare the phase pure ß-$LiFePO_4$ polymorph using $[FeLi_2Br(O^tBu)_4(THF)_2]_n$ (IV) afforded a mixture of both α and ß phases (see Figure A5.9). Figure 5.2 depicts the Rietveld refinements of the PXRD data from the α and ß-$LiFePO_4$_IV polymorphs to a *Pnma* $LiFePO_4$ (ICSD No. 01-072-7845) and *Cmcm* $LiFePO_4$ (ICSD No. 01-072-7847) crystal structures, respectively.[49] Results indicated that a good fit between the experimental data and the calculated model was achieved, confirming the phase purity of both $LiFePO_4$ polymorphs. Recently, Wu *et al.* have investigated the phase transformation of solvothermally synthesised *Cmcm* type β-$LiFePO_4$ to *Pnma* type α-$LiFePO_4$ *via* thermal annealing. They propose that the conversion mechanism could be explained with reconstruction of PO_4 tetrahedra and FeO_6 octahedra taking place during the heat treatment as the coordination between the PO_4 tetrahedra and FeO_6 must be altered. TG-DSC and HRTEM analysis revealed that ß-$LiFePO_4$ experiences a two-step phase transformation to α-$LiFePO_4$ rather than a direct conversion during the annealing process.[295] The effect of the solvent in the microwave reaction using the single source $[FeLi_2Br(O^tBu)_4(THF)_2]_n$ (IV) heterometallic alkoxide precursor was also evaluated by performing the same reaction in tetraethylene glycol instead of ethylene glycol, as previously *Cmcm* Li*M*PO_4 (*M*=Fe, Co, Ni) phases have been successfully fabricated by fast

microwave treatments in tetraethylene glycol.[158] PXRD analysis of the product (ß-$LiFePO_4$_IV_TEG) shown in Figure A5.10 indicated that phase pure ß-$LiFePO_4$ was obtained, suggesting that the higher viscosity of tetraethylene glycol (11.4 cP) compared to ethylene glycol (5.2 cP)[296] may favour the formation of the metastable non-olivine ß-$LiFePO_4$ polymorph. Solvents with elevated viscosities may allow highly localised temperatures during microwave heating facilitating the formation of metastable phases.

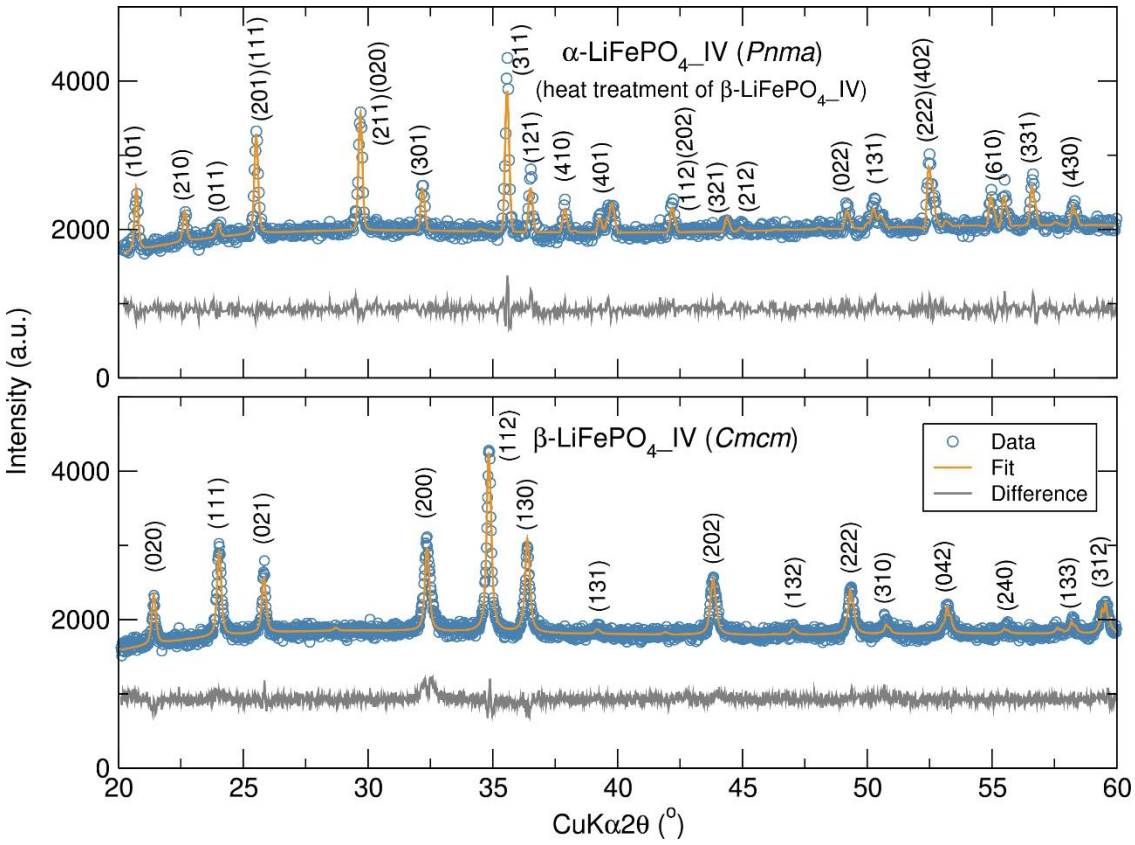

Figure 5.2. Rietveld analysis of pXRD data of α-$LiFePO_4$_IV and β-$LiFePO_4$_IV nanostructures prepared using $[FeLi_2Br(O^tBu)_4(THF)_2]_n$ (IV) alkoxide precursor.

PXRD analysis of the $LiFePO_4$_V and $LiMnPO_4$_VI samples synthesised using the "$[FeLi_2Cl(O^tBu)_4(THF)_2]_n$" (V) and "$[MnLi_2Br(O^tBu)_4(THF)_2]_n$" (VI) precursors in ethylene glycol, respectively, also showed phase pure olivine materials. The reaction using the "$[FeLi_2Cl(O^tBu)_4(THF)_2]_n$" (V) heterometallic alkoxide precursor clearly proceeds towards the formation of the olivine α-$LiFePO_4$ polymorph with no evidence of ß-$LiFePO_4$ phase, as no reflections associated to the *Cmcm* space group were observed. In terms of the reactivity of Br or Cl containing precursors, the smaller ionic radius of Cl^- (1.81 pm) compared to Br^- (1.96 pm),[252] both acting as a bridge between Li atoms in the polymeric "$[FeLi_2X(O^tBu)_4(THF)_2]_n$" (*X*=$Cl^-$ or Br^-) heterometallic alkoxide precursors, may favour the formation of the olivine α-$LiFePO_4$ phase where the Li-Li distance is shorter than in ß-$LiFePO_4$ (~3.00 Å for α-$LiFePO_4$ and ~4.31 Å for ß-$LiFePO_4$). These results clearly demonstrate the versatility of these single source heterometallic alkoxide precursors for

the fast generation of both α and ß-$LiFePO_4$ polymorphs. Figure 5.3 shows that single phase α-$LiFePO_4$_V was obtained after the 10 min microwave treatment at 240 ºC, with no additional phases observed after the post-heat treatment for subsequent carbon coating. These results also confirm that the heat treatment of α-$LiFePO_4$_V with sucrose does not influence the olivine structure. PXRD analysis of the Li*M*nPO_4_VI sample depicted in Figure 5.4 shows that single phase olivine Li*M*nPO_4 was obtained after the fast microwave synthesis and also after heat treatment for carbon coating. There is a significant broadening of the diffraction peaks in the PXRD pattern of Li*M*nPO_4_VI compared to the $LiFePO_4$ samples, suggesting a smaller particle size compared to the $LiFePO_4$_V sample. The estimated crystallite sizes of the $LiFePO_4$_V and Li*M*nPO_4_VI samples were ~33 nm and 17 nm, respectively, which were calculated through the full width at the half maximum (FWHM) of the PXRD patterns using the Scherrer equation[208] from the (211) diffraction peaks. Figure 5.5 illustrates the Rietveld fits of the PXRD data from the $LiFePO_4$_V and Li*M*nPO_4_VI nanostructures to a *Pnma* $LiFePO_4$ (ICSD No. 01-072-7845) and Li*M*nPO_4 (ICSD No. 01-072-7844) crystal structures, respectively.[49] The results show that a good fit between the experimental data and the calculated model was achieved, with no evidence for any additional phases observed. Table 5.5 summarises the calculated lattice parameters from Rietveld refinements of these Li*M*PO_4 (*M*=Fe, Mn) samples prepared from single source heterometallic alkoxide precursors. As expected due to the larger ionic radius of Mn^{2+} in comparison to Fe^{2+}, $LiFePO_4$_V exhibited smaller cell parameters than Li*M*nPO_4_VI.[252] Furthermore, olivine α-$LiFePO_4$_IV fabricated from a heat treatment of β-$LiFePO_4$_IV showed slightly larger cell volume than $LiFePO_4$_V, suggesting that the heating process may lead towards an increase in the unit cell volume of the $LiFePO_4$ olivine structure.

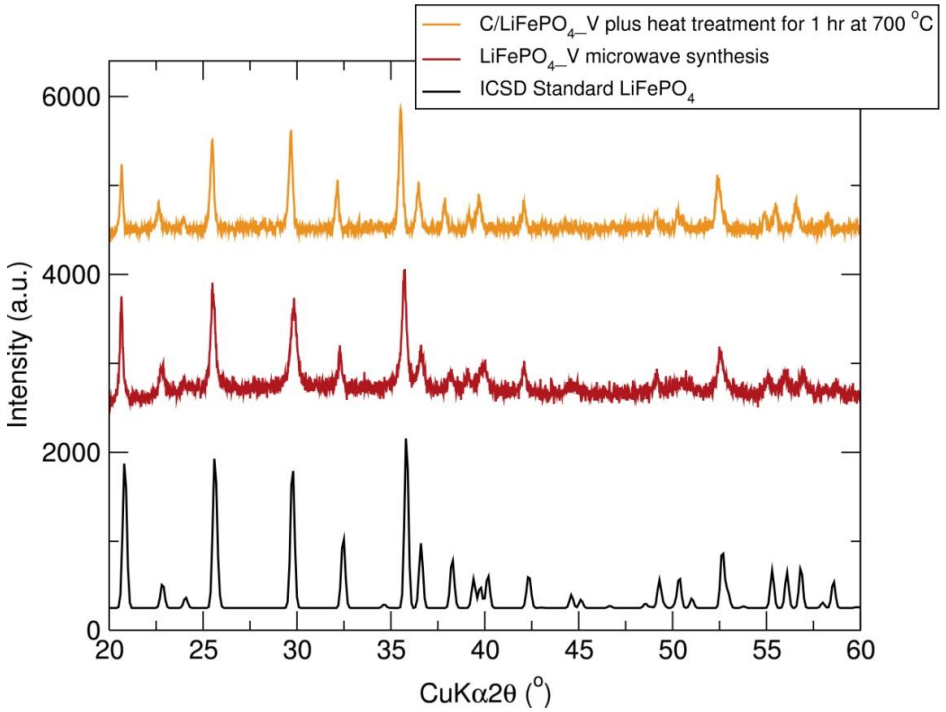

Figure 5.3. PXRD pattern of $LiFePO_4$_V after fast microwave synthesis and after heat treatment in tube furnace for 1 hr at 700 ºC under Ar atmosphere. Sample prepared using "$[FeLi_2Cl(O^tBu)_4(THF)_2]_n$" (V) heterometallic precursor and H_3PO_4 in a 1:1 molar ratio in ethylene glycol.

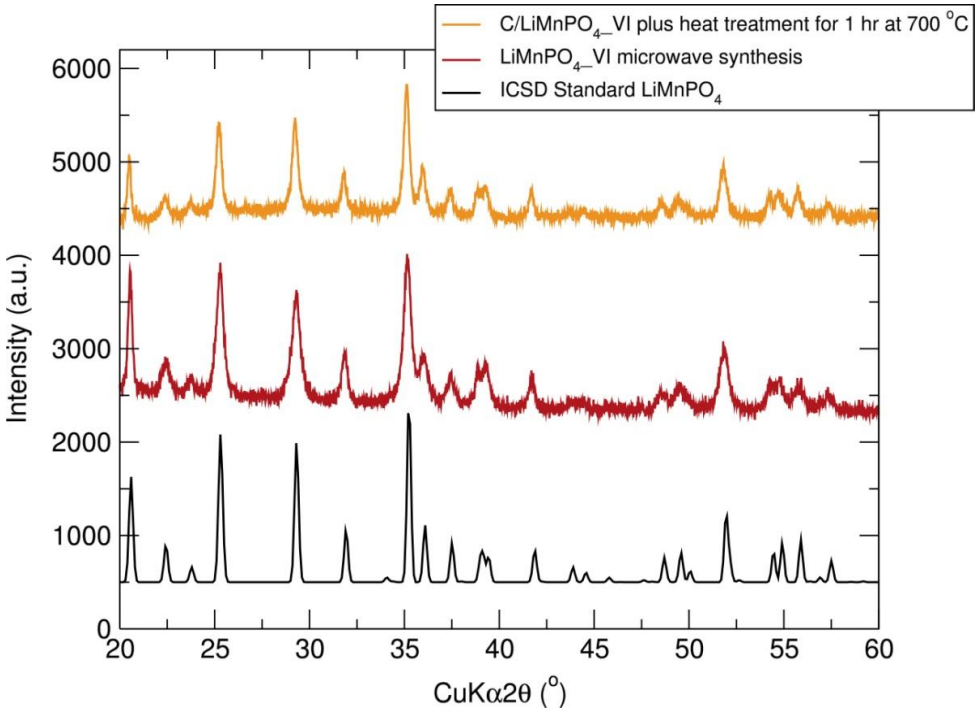

Figure 5.4. PXRD pattern of $LiMnPO_4$_VI after fast microwave synthesis and after heat treatment in tube furnace for 1 hr at 700 ºC under Ar atmosphere. Sample prepared using "$[MnLi_2Br(O^tBu)_4(THF)_2]_n$" (VI) heterometallic alkoxide precursor and H_3PO_4 in a 1:1 molar ratio in ethylene glycol.

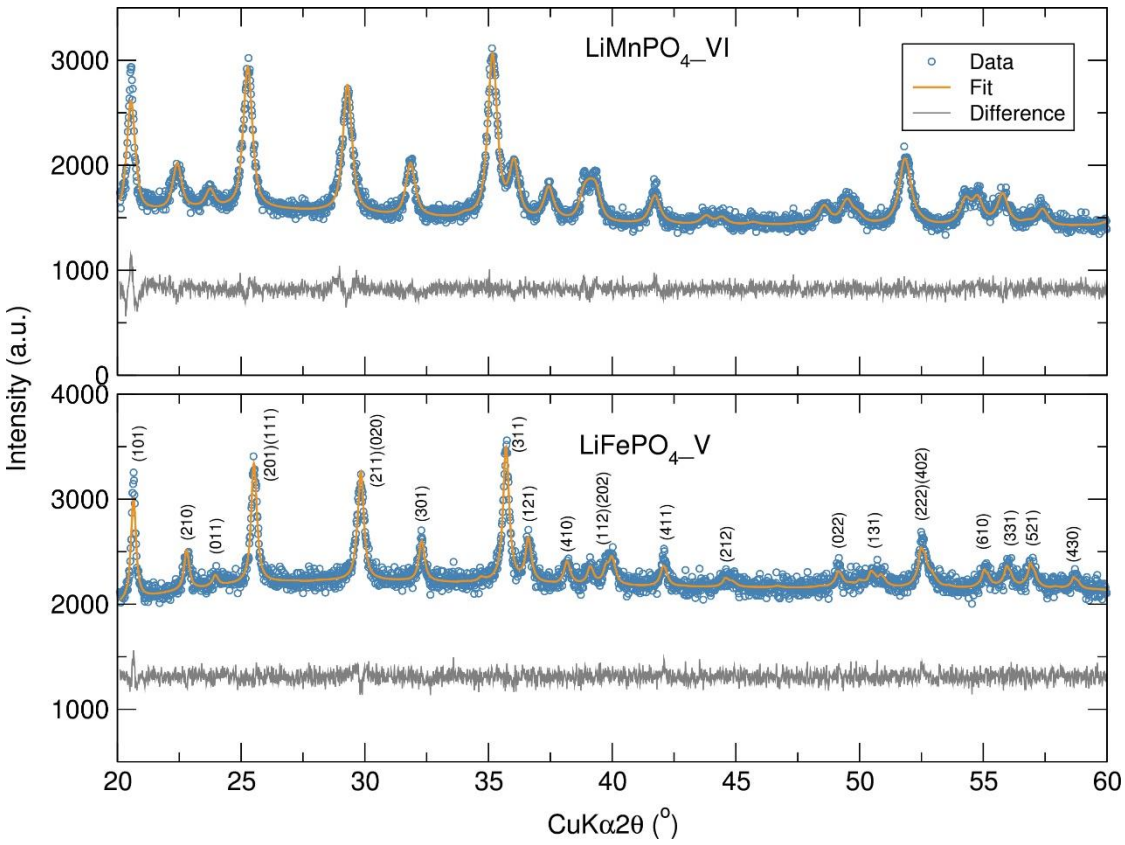

Figure 5.5. Rietveld analysis of PXRD data of $LiFePO_4$_V and $LiMnPO_4$_VI nanostructures prepared using "$[FeLi_2Cl(O^tBu)_4(THF)_2]_n$" (V) and "$[MnLi_2Br(O^tBu)_4(THF)_2]_n$" (VI), respectively.

Table 5.5. Calculated lattice parameters from Rietveld refinements for the ß and α-$LiFePO_4$_IV polymorphs, $LiFePO_4$_V and $LiMnPO_4$_VI nanostructures prepared from "$[MLi_2X(O^tBu)_4(THF)_2]_n$" (*M*=Fe, Mn; *X*=Br, Cl) (IV, V and VI) heterometallic alkoxide precursors.

Sample	ß-$LiFePO_4$_IV	α-$LiFePO_4$_IV	$LiFePO_4$_V	$LiMnPO_4$_VI
Space group	*Cmcm*	*Pnma*	*Pnma*	*Pnma*
a (Å)	5.5115(4)	10.3212(8)	10.235(2)	10.457(2)
b (Å)	8.2505(5)	6.0037(4)	5.969(1)	6.101(1)
c (Å)	6.1936(3)	4.6957(4)	4.715(1)	4.753(1)
V (Å^{-3})	281.64(3)	290.97(4)	288.07(9)	303.3(1)
R_{wp}	28.6 %	31.4 %	29.8 %	19.0 %
R_{exp}	22.60 %	25.08 %	27.07 %	16.08 %
X^2	1.61	1.57	1.21	1.40

Evaluation of the local structure and underlying defect chemistry in these olivine nanostructures is crucial to developing a greater understanding of their structure-property relationship and resulting electrochemical behavior. It has been reported that the most favorable intrinsic defect is Li-Fe antisite pair, in which a Li^+ ion (M1 site) and the Fe^{2+} ion (M2 site) are exchanged.[54] Knowing that, it is highly probable that the Li-Fe

antisite defects can block the diffusion pathways down [010] channels leading to an inhibition of the long-range Li^+ migration. Total scattering methods can provide means to examining disordered materials at the local level, e.g. Jensen *et al.*[257] Theoretical calculations, for example by Gardiner *et al.*, reported that migration energies for Fe and Mn for antisite cations on Li sites suggests that Mn defects would impede bulk Li mobility in $LiFe_{0.5}Mn_{0.5}PO_4$ to a greater extent than Fe antisite defects in $LiFePO_4$.[55] To study the local structure and presence of defects as a function of Mn content in these microwave synthesised $LiFe_{1-x}Mn_xPO_4$ nanostructures using single source heterometallic alkoxide precursors presented here, X-ray total scattering experiments were performed and PDF analysis carried out on the data collected. X-ray PDF investigations of the ß-$LiFePO_4$_IV, α-$LiFePO_4$_V and Li$MnPO_4$_VI nanostructures prepared through a fast microwave synthesis using single source $[FeLi_2Br(O^tBu)_4(THF)_2]_n$ (IV), "$[FeLi_2Cl(O^tBu)_4(THF)_2]_n$" (V), and "$[MnLi_2Br(O^tBu)_4(THF)_2]_n$" (VI) heterometallic alkoxide precursors, respectively, were conducted in an effort to study the local structure in different $LiFePO_4$ polymorphs and examine if fast microwave treatments of single source heterometallic alkoxides yield highly crystalline and non-defective electrode nanomaterials. From fitting the X-ray PDF data of the α-$LiFePO_4$_V nanostructure in the *r* range from 1 to 15 Å using a fully ordered olivine structured model, a good agreement (R_w=0.1806) between the experimental data and the calculated model was obtained, suggesting that there is no evident presence of defects or significant local structure deviations in α-$LiFePO_4$_V (Figure 5.6). The X-ray PDF based fit for the $LiFePO_4$_V nanostructure yielded structural parameters that are in excellent agreement with the Rietveld analysis results of the PXRD data, indicating that the local and average crystal structure are very similar. Nevertheless, a poorer fit (R_w=0.2679) was observed for the olivine Li$MnPO_4$_V nanophase, which may suggest that the presence of Mn in the olivine structure leads to a slightly more disordered olivine structure and/or higher content of amorphous material. The possibility of Mn^{2+} disorder in Li$MnPO_4$ has also been studied using PXRD and X-ray absorption fine structure analysis. Results suggested some Mn^{2+} excess on the Li^+ sites which could be suppressed by increasing the reaction temperature in the prosposed hydrothermal synthesis.[297] Therefore, a model allowing some Mn^{2+} ions on Li^+ positions was applied to the Li$MnPO_4$_VI X-ray PDF data but no improvement in the refinement process was observed. Also, refinements of the ß-$LiFePO_4$_IV X-ray PDF data to a fully ordered non-olivine orthorhombic *Cmcm* crystal structure demonstrated smaller R_w values for the olivine α-$LiFePO_4$_V (R_w=0.1806) in comparison to ß-$LiFePO_4$_IV (R_w=0.2764), which could be an indication that the non-olivine ß-$LiFePO_4$ polymorph is more prone to exhibit some short range disorder. Table 5.6 summarises the calculated lattice parameters and R_w from the X-ray PDF fits for the $LiFePO_4$_IV, $LiFePO_4$_V and Li$MnPO_4$_VI nanostructures prepared using single source heterometallic alkoxide precursors. Previous X-ray PDF investigations

on microwave synthesised $LiFePO_4$ conducted by Bini *et al* revealed the presence of structural disorder possibly due to Li-Fe exchange. A 5% amount of Fe in the Li site was detected both by PDF as well as by Mossbauer spectroscopy, which showed a small percentage of Fe^{3+} on the regular sites.[298] A possible reason why less disordered olivine $LiFePO_4$ nanostructures have been obtained here in comparison to Bini *et al*. may be attributed to the higher reaction temperatures in which the microwave synthesis has been performed here (240 ºC *vs.* 170 ºC). Also, having the Li and Fe atoms initially closer at the atomic level by using single source precursors should contribute to the formation of a less defective olivine structure.

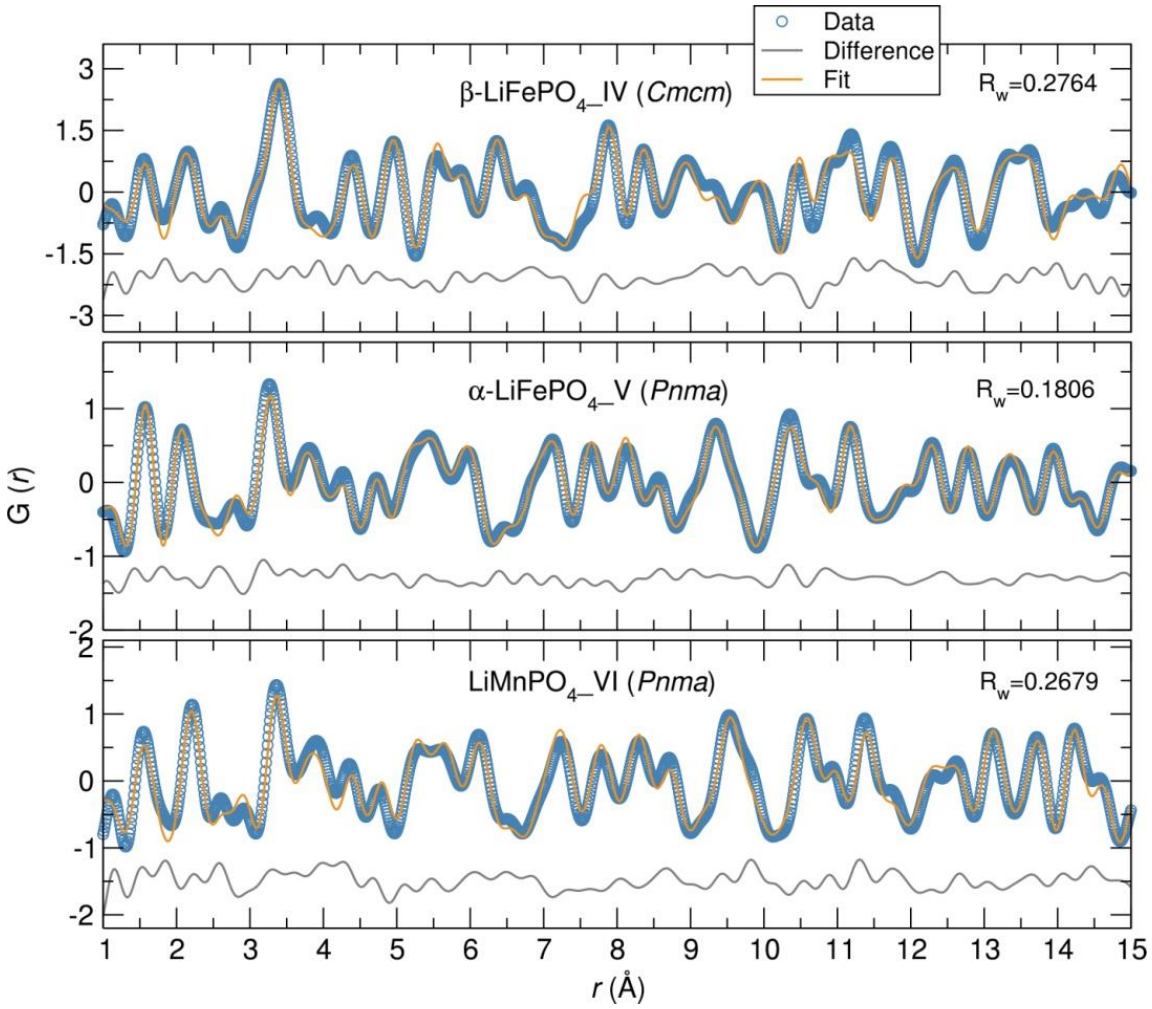

Figure 5.6. Fits of X-ray PDF data collected at 100 K for ß-$LiFePO_4$_IV, α-$LiFePO_4$_V, and $LiMnPO_4$_VI prepared through a fast microwave synthesis using heterometallic alkoxide precursors in the *r* range from 1-15 Å.

Table 5.6. Calculated lattice parameters from X-ray PDF fits for the ß-$LiFePO_4$_IV, α-$LiFePO_4$_V and $LiMnPO_4$_VI nanostructures prepared using heterometallic alkoxide precursors.

Sample	ß-$LiFePO_4$_IV	α-$LiFePO_4$_V	$LiMnPO_4$_VI
Space group	*Cmcm*	*Pnma*	*Pnma*
a (Å)	5.56(1)	10.24(3)	10.50(2)
b (Å)	8.30 (1)	6.00(2)	6.16(1)
c (Å)	6.25(1)	4.71(1)	4.78(1)
R_w	0.2764	0.1806	0.2679

Several routes to mixed transition metal phosphates $LiFe_{0.5}Mn_{0.5}PO_4$ nanoparticles were also investigated using a series of heterometallic alkoxide precursors:

1. $LiFe_{0.5}Mn_{0.5}PO_4$_IV-VI was prepared with stoichiometric amounts of "$[FeLi_2Br(O^tBu)_4(THF)_2]_n$" (IV) and "$[MnLi_2Br(O^tBu)_4(THF)_2]_n$" (VI).
2. $LiFe_{0.5}Mn_{0.5}PO_4$_V-VI was obtained by reaction of stoichiometric amounts of "$[FeLi_2Cl(O^tBu)_4(THF)_2]_n$" (V) and "$[MnLi_2Br(O^tBu)_4(THF)_2]_n$" (VI).
3. $LiFe_{0.5}Mn_{0.5}PO_4$_VII was synthesised using the single-source trimetallic alkoxide "$[Fe_{0.5}Mn_{0.5}Li_2Br(O^tBu)_4(THF)_2]_n$" (VII).

PXRD patterns of the resulting $LiFe_{0.5}Mn_{0.5}PO_4$ products indicate that phase pure olivine nanomaterials were obtained in all three cases. Rietveld analysis of the three $LiFe_{0.5}Mn_{0.5}PO_4$ compounds confirmed the phase purity of these olivine mixed metal phosphates, as evidenced by the excellent agreement between the experimental data and the calculated model (Figure 5.15). Table 5.7 summarises the calculated lattice parameters from Rietveld refinements for the different $LiFe_{0.5}Mn_{0.5}PO_4$ nanostructures, indicating that there are no significant variations in the unit cell parameters. Moreover, slightly sharper peak intensities observed in the $LiFe_{0.5}Mn_{0.5}PO_4$_VII sample prepared using the "$[Fe_{0.5}Mn_{0.5}Li_2Br(O^tBu)_4(THF)_2]_n$" (VII) heterometallic precursor suggests the formation of better crystallised olivine $LiFe_{0.5}Mn_{0.5}PO_4$ materials for this ternary metallic precursor route than for mixtures of bimetallic precursors. This suggests that the co-location of all metals in a single precursor may be favourable for the fast formation of more crystalline nanomaterials. Estimation of the crystallite sizes from the PXRD of the three $LiFe_{0.5}Mn_{0.5}PO_4$ nanostructures using the Scherrer equation applied to the (201) diffraction peak revealed crystallite sizes ranging from ~25 to 37 nm.

The local structure of the $LiFe_{0.5}Mn_{0.5}PO_4$ nanophases was also investigated by X-ray PDF analysis. Least-squares fits to the $LiFe_{0.5}Mn_{0.5}PO_4$ X-ray PDFs in the *r* range from 1 to 15 Å to a completely ordered olivine $LiFe_{0.5}Mn_{0.5}PO_4$ structure also showed a good fit between the experimental data and the calculated model for the three olivine $LiFe_{0.5}Mn_{0.5}PO_4$

nanophases, although significantly higher R_w values than for $LiFePO_4$_V were obtained (Figure 5.8). These results confirmed that introducing Mn to the olivine $LiFePO_4$ may lead to significant local structural disorder. On the other hand, it must be highlighted that a slightly better fit was obtained for the $LiFe_{0.5}Mn_{0.5}PO_4$_VII nanophase in comparison to $LiFe_{0.5}Mn_{0.5}PO_4$_IV-VI and $LiFe_{0.5}Mn_{0.5}PO_4$_V-VI. This may point to the theory that having all the required metals in a single source precursor may be beneficial towards the generation of highly crystalline and non-defective nanomaterials. Table 6.8 shows the calculated lattice parameters and R_w from X-ray PDF fits for the different $LiFe_{0.5}Mn_{0.5}PO_4$ nanostructures prepared using single source heterometallic alkoxide precursors. Similar cell parameters were obtained for the three $LiFe_{0.5}Mn_{0.5}PO_4$ nanostructures.

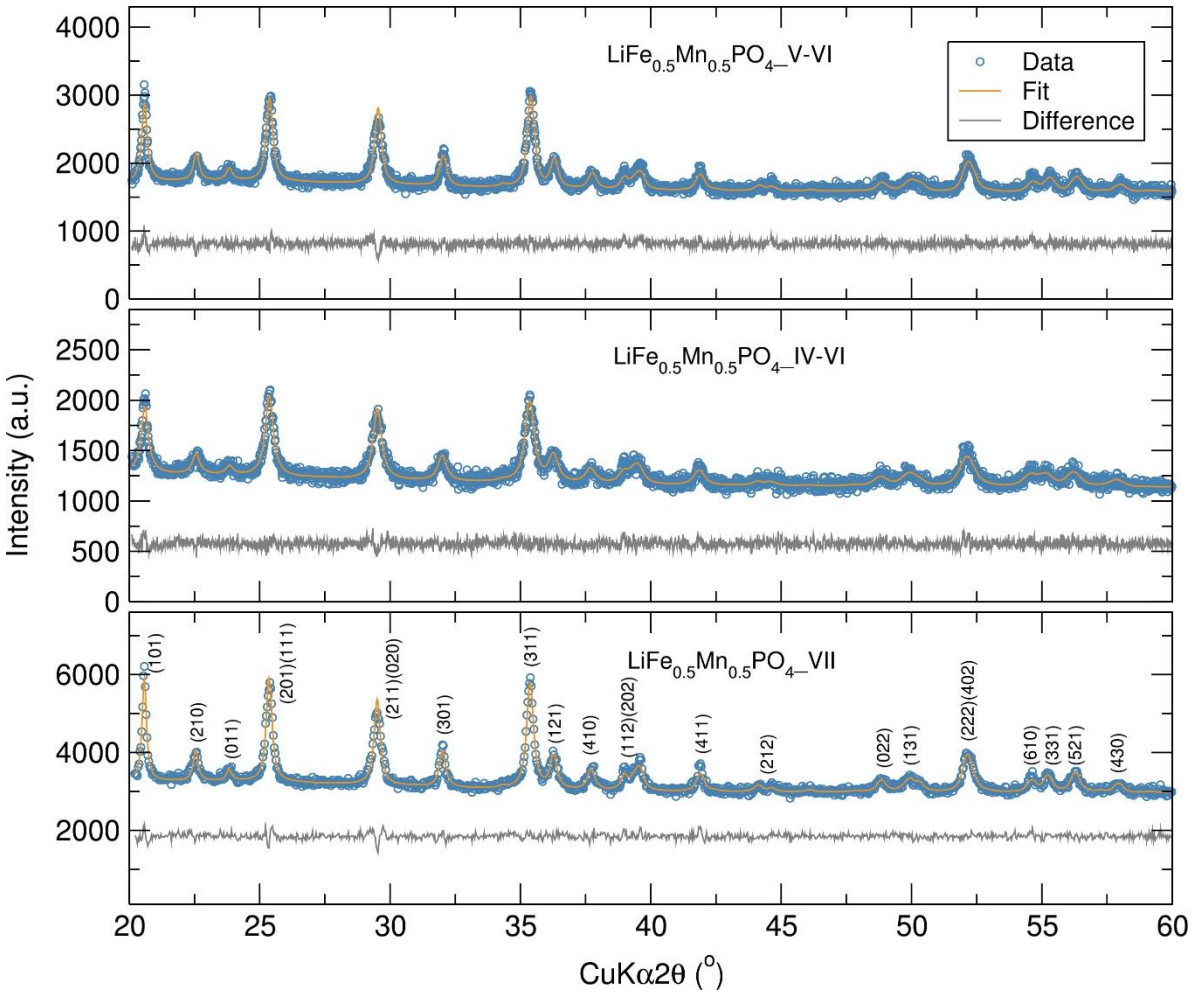

Figure 5.7. Rietveld analysis of PXRD pattern of different $LiFe_{0.5}Mn_{0.5}PO_4$ nanostructures prepared from heterometallic alkoxide precursors "$[Fe_{0.5}Mn_{0.5}Li_2Br(O^tBu)_4(THF)_2]_n$" (VII), $[FeLi_2Br(O^tBu)_4(THF)_2]_n$ (IV), "$[FeLi_2Cl(O^tBu)_4(THF)_2]_n$" (V).and "$[MnLi_2Br(O^tBu)_4(THF)_2]_n$" (VI).

Table 5.7. Calculated lattice parameters from Rietveld refinements for the different $LiFe_{0.5}Mn_{0.5}PO_4$ nanostructures.

Sample	$LiFe_{0.5}Mn_{0.5}PO_4$_IV-VI	$LiFe_{0.5}Mn_{0.5}PO_4$_V-VI	$LiFe_{0.5}Mn_{0.5}PO_4$_VII
Space group	*Pnma*	*Pnma*	*Pnma*
a (Å)	10.398(1)	10.3608(8)	10.3718(8)
b (Å)	6.0553(8)	6.0386(5)	6.0438(5)
c (Å)	4.7444(9)	4.7351(5)	4.7338(5)
V ($Å^{-3}$)	298.72(8)	296.25(5)	296.74(5)
R_{wp}	27.8 %	24.7 %	18.8 %
R_{exp}	25.46 %	21.82 %	15.45 %
X^2	1.19	1.28	1.48

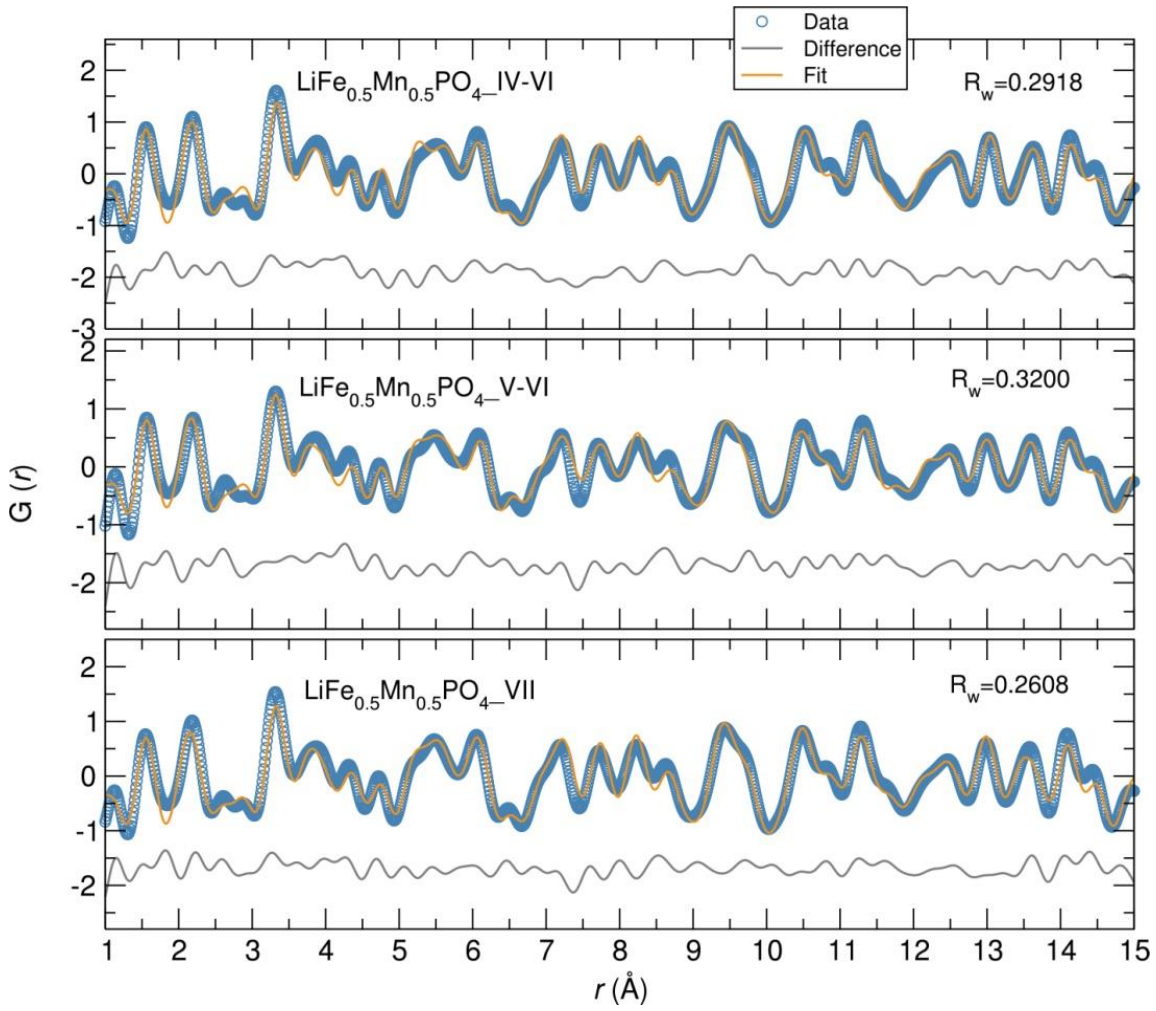

Figure 5.8. Fits of X-ray PDF data collected at 100 K for $LiFe_{0.5}Mn_{0.5}PO_4$ nanostructures prepared through a fast microwave synthesis using heterometallic alkoxide precursors in the *r* range from 1-15 Å.

Table 5.8. Calculated lattice parameters from X-ray PDF fits for the different $LiFe_{0.5}Mn_{0.5}PO_4$ nanostructures prepared using heterometallic alkoxide precursors.

Sample	$LiFe_{0.5}Mn_{0.5}PO_4$_IV-VI	$LiFe_{0.5}Mn_{0.5}PO_4$_V-VI	$LiFe_{0.5}Mn_{0.5}PO_4$_VII
Space group	*Pnma*	*Pnma*	*Pnma*
a (Å)	10.40(2)	10.43(3)	10.39(2)
b (Å)	6.11(1)	6.11(2)	6.09(1)
c (Å)	4.77(1)	4.76(1)	4.76(1)
R_w	0.3200	0.2918	0.2608

To further examine changes in the local structure as a function of the Mn content, X-ray PDF data of the $LiFePO_4$_V, $LiFe_{0.5}Mn_{0.5}PO_4$_VII and $LiMnPO_4$_VI nanostructures were also fitted at different *r* ranges from 1-5 Å and 1-10 Å. Good fits using a fully ordered olivine model were obtained in the 1-5 Å *r* range for the three $LiFe_{1-x}Mn_xPO_4$ (*x*=0, 0.5 and 1) nanostructures (R_w values from 0.13 to 0.16), as it can be observed in Figure 5.17. The better fit at lower *r* distances could be explained by the fact that crystalline defective $LiFe_{1-x}Mn_xPO_4$ could coexist with any possible amorphous Li/Fe/Mn-PO_4 structures which would exhibit short range order, as previously reported by Jensen *et al*.[257] The slight shift of the peak at 2.1 Å (which corresponds to the transition metal-oxygen distance) towards high *r* values with higher Mn content in these $LiFe_{1-x}Mn_xPO_4$ olivine nanophases indicates that the transition metal-oxygen distance increased (Figure 5.9), possibly due to the higher ionic radius of Mn^{2+} compared to Fe^{2+}. The Fe-O bond slightly decreased from 2.04(1) Å in the $LiFePO_4$ sample to 1.95(2) Å in $LiFe_{0.5}Mn_{0.5}PO_4$, while the Mn-O bond increased from 1.96(2) Å in the $LiFe_{0.5}Mn_{0.5}PO_4$ nanostructure to 2.17(1) Å in $LiMnPO_4$. A similar trend was observed for solvothermally synthesised olivine $LiFe_{1-x}Mn_xPO_4$ materials examined by a combination of synchrotron X-ray absorpotion spectroscopy, energy-dispersive X-ray spectroscopy and first-principle calculations.[82] It is also worth noting the slight increase in the Li-Li distances with increased Mn content (2.99(3) Å in $LiFePO_4$_V, 3.06(1) Å in $LiFe_{0.5}Mn_{0.5}PO_4$_VII and 3.18(1) Å in $LiMnPO_4$_VI). Table A5.2 lists the atom-atom distances in the $LiFe_{1-x}Mn_xPO_4$ samples determined from fits of X-ray PDF data in the *r* range from 1-5 Å. On the other hand, the scale factors (which can be regarded as an indication of the amount of crystalline material present) decreased when increasing the *r* range in which the data were fitted. This may suggest that some amorphous material is present. These results are in good agreement with the neutron PDF data of $LiFe_{1-x}Mn_xPO_4$ phases prepared from commercial starting materials presented in Chapter 3, which also demonstrated a decrease in the scale factors when increasing the *r* range fitted. Especially significant was the variation in the scale factors for the $LiMnPO_4$_VI sample, which could be an indication that the

presence on Mn leads to the formation of more amorphous material. Table 5.9 shows the lattice parameters, the scale factors and R_w values obtained from X-ray PDF fits of $LiFePO_4$_V, $LiFe_{0.5}Mn_{0.5}PO_4$_VII and $LiMnPO_4$_VI nanostructures at different *r* ranges. Furthermore, a more significant variation in the lattice parameters calculated from the refinements at different *r* ranges was observed for the $LiMnPO_4$_VI olivine compared to $LiFePO_4$_VI, further suggesting the more pronounced mismatch between the local and average structure when introducing Mn in olivine $LiFePO_4$.

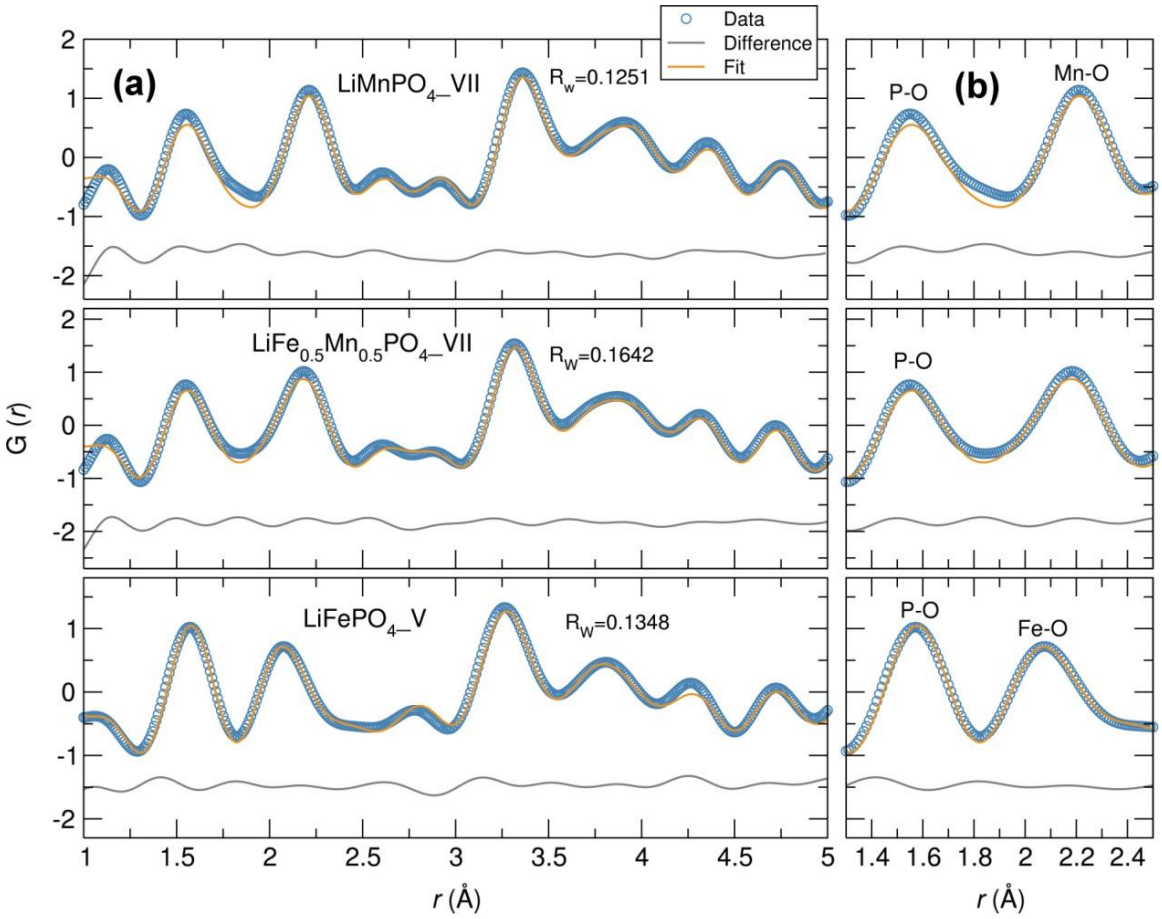

Figure 5.9. (a) Fits of X-ray PDF data collected at 100 K for single-phase olivine $LiFePO_4$_V, $LiFe_{0.5}Mn_{0.5}PO_4$_VII and $LiMnPO_4$_VI nanostructures prepared through a fast microwave synthesis using heterometallic alkoxide precursors in the *r* range from 1-5 Å. **(b)** Extention of the fit in the range from 1.3–2.5 Å.

Finally, to investigate if the heterometallic alkoxide precursors could provide some residual carbon in $LiFe_{1-x}Mn_xPO_4$ nanophases obtained after the fast microwave treatments, CHN microanalysis of the $LiFePO_4$_IV, $LiFePO_4$_V, $LiFe_{0.5}Mn_{0.5}PO_4$_VII and $LiFePO_4$_VI powders was conducted to determine the carbon content. From the results gathered in Table A5.1 it is shown that the $LiFe_{1-x}Mn_xPO_4$ nanostructures have approximately 2% of carbon. This low carbon content may be attributed to some residual ethylene glycol left

from the synthesis and also to some decomposition product from the metal alkoxide precursors.

Table 5.9. Calculated lattice parameters, scale factors and R_w values from X-ray PDF fits at different *r* ranges for $LiFePO_4$_V, $LiFe_{0.5}Mn_{0.5}PO_4$_VII and $LiFePO_4$_VI nanostructures prepared through a fast microwave synthesis using heterometallic alkoxide precursors.

		1-5 Å	1-10 Å	1-15 Å
$LiFePO_4$_V	Scale factor	0.42(5)	0.37(4)	0.36(2)
	a (Å)	10.24(2)	10.24(7)	10.23(3)
	b (Å)	5.99(7)	5.99(3)	6.00(2)
	c (Å)	4.71(4)	4.71(2)	4.71(1)
	R_w	0.1348	0.1715	0.1806
$LiFe_{0.5}Mn_{0.5}PO_4$_VII	Scale factor	0.47(5)	0.41(3)	0.43(3)
	a (Å)	10.25(9)	10.36(3)	10.39(2)
	b (Å)	6.11(3)	6.10(2)	6.09(1)
	c (Å)	4.74(4)	4.75(2)	4.76(1)
	R_w	0.1642	0.2383	0.2609
$LiMnPO_4$_VI	Scale factor	0.56(5)	0.34(3)	0.35(2)
	a (Å)	10.36(8)	10.62(5)	10.49(2)
	b (Å)	6.36(1)	6.19(3)	6.16(1)
	c (Å)	4.73(3)	4.76(1)	4.78(1)
	R_w	0.1251	0.2437	0.2679

5.2.2.2 Electron microscopy of $LiFe_{1-x}Mn_xPO_4$ nanostructures prepared from "$[MLi_2X(O^tBu)_4(THF)_2]_n$" (*M*=Fe, Mn and *X*=Br, Cl)

SEM analysis of the β-$LiFePO_4$_IV and α-$LiFePO_4$_V powders revealed a clear dependence of the particle size and morphology on the heterometallic alkoxide precursor employed. SEM micrographs of the β-$LiFePO_4$_IV sample showed large, flat platelets with an average particle size of 200-300 nm in width and ~600 nm in length (Figure 5.10 (a)). In contrast, the α-$LiFePO_4$_V nanostructures adopted a non-uniform and more elongated platelet morphology, with particles sizes ranging from approximately 40 to 150 nm (Figure 5.10 (b)). These results suggest that the nature of the single source metal alkoxide precursors has a strong influence in the resulting particle shape and size. Moreover, it must be highlighted that fast microwave processes using single source heterometallic alkoxide precursors afforded smaller olivine $LiFePO_4$ particles in comparison to when homometallic alkoxides or commercial starting materials are used [40-150 nm for $LiFePO_4$_V (Heterometallic) *vs.* 60-250 nm for $LiFePO_4$_I (Homometallic) and 200-500 nm for $LiFePO_4$_MW_Commercial]. Examination of the $LiMnPO_4$_VI and $LiFe_{0.5}Mn_{0.5}PO_4$_VII nanophases by electron microscopy also demonstrated a noticeable change in morphology

and particle size depending on the transition metal content, going from larger platelet-shaped particles to thin nanowires with increasing Mn content. The detailed morphological and structural features of the $LiFe_{0.5}Mn_{0.5}PO_4$_VII, $LiFe_{0.5}Mn_{0.5}PO_4$_V-VI and $LiMnPO_4$_VI nanostructures were also examined by HR TEM. More elongated particles with thickness around 15 nm were obtained for the $LiFe_{0.5}Mn_{0.5}PO_4$_VII and $LiFe_{0.5}Mn_{0.5}PO_4$_V-VI nanophases (Figure 5.19 (a) and (b)). Finally, wires thinner than 15 nm were found for the $LiMnPO_4$_VI nanopowders (Figure 5.19 (c)). HRTEM imaging of the $LiFe_{0.5}Mn_{0.5}PO_4$_VII, $LiFe_{0.5}Mn_{0.5}PO_4$_V-VI and $LiMnPO_4$_VI nanoparticles confirmed the long-range crystallographic order of the nanostructures with lattice spacings of 0.26, 0.55, and 0.45 nm, respectively. Electron diffraction also demonstrated the polycrystalline nature of these olivine phases.

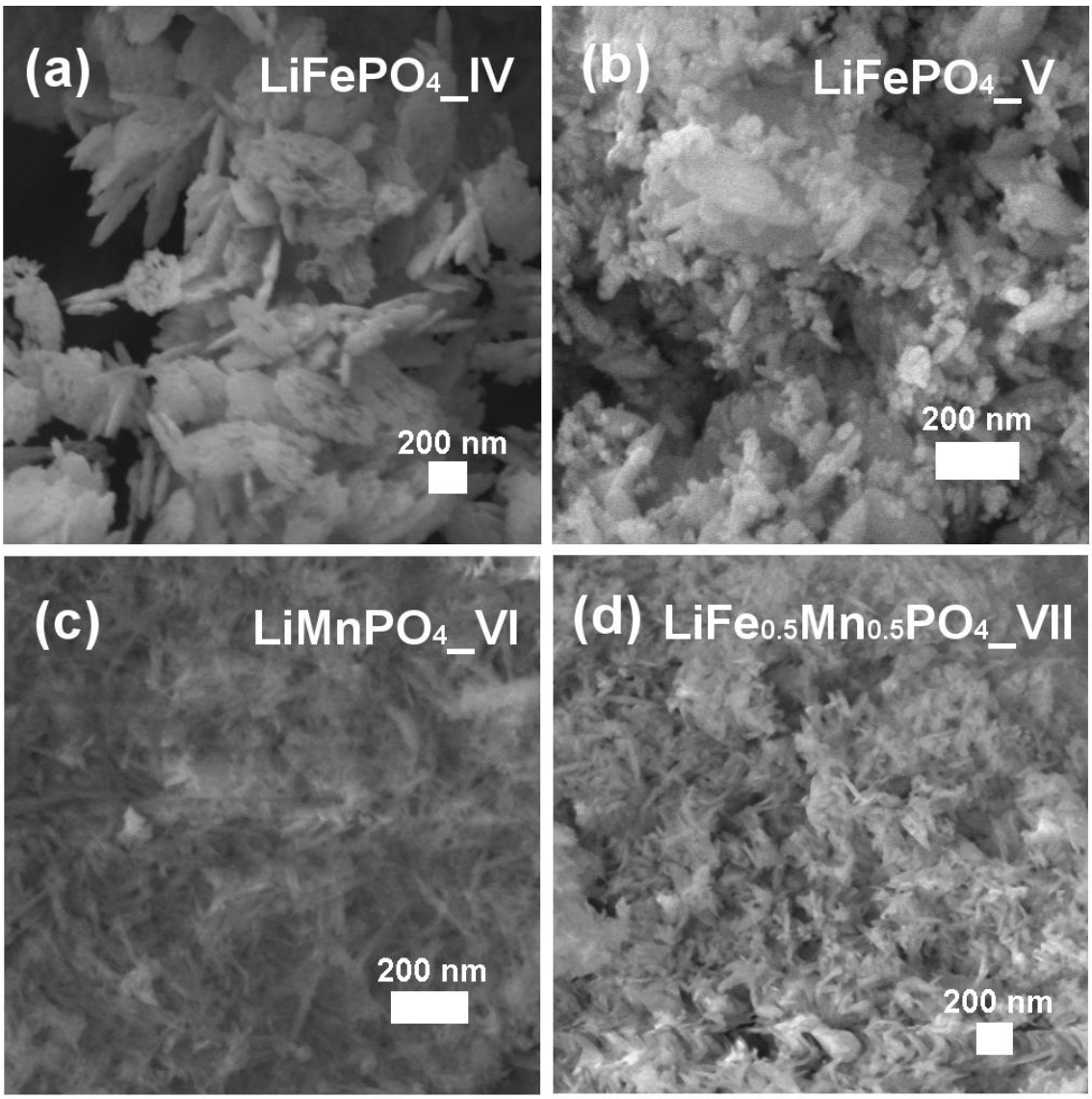

Figure 5.10. SEM images of **(a)** ß-$LiFePO_4$_IV, **(b)** α-$LiFePO_4$_V, **(c)** $LiMnPO_4$_VI and **(d)** $LiFe_{0.5}Mn_{0.5}PO_4$_VII nanostructures.

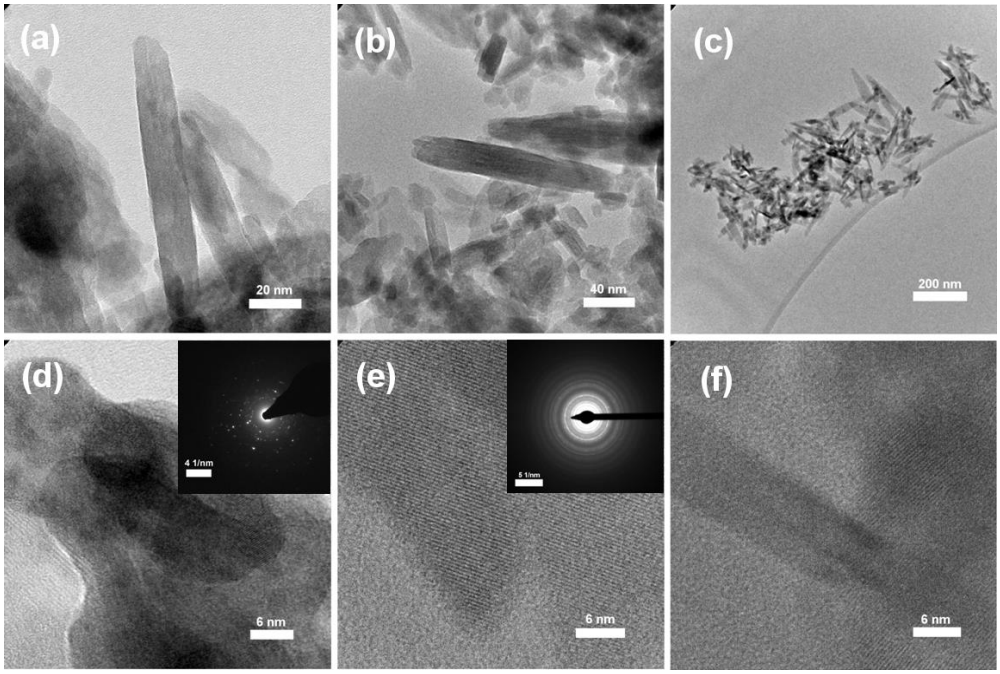

Figure 5.11. HR TEM images of **(a, d)** $LiFe_{0.5}Mn_{0.5}PO_4$_VII, **(b, e)** $LiFe_{0.5}Mn_{0.5}PO_4$_V-VI and **(c, f)** $LiMnPO_4$_VI nanostructures.

5.2.2.3 Electrochemical performance of C/$LiFe_{1-x}Mn_xPO_4$ nanostructures prepared from "[*M*Li_2*X*(O^tBu)$_4$(THF)$_2$]$_n$" (*M*=Fe, Mn and *X*=Br, Cl)

Galvanostatic cycling tests and CV scans of the $LiFe_{1-x}Mn_xPO_4$ (*x*=0, 0.5 and 1) nanostructures synthesised *via* fast microwave treatments of single source heterometallic alkoxide precursors [$FeLi_2Br(O^tBu)_4(THF)_2]_n$ (IV), "[$FeLi_2Cl(O^tBu)_4(THF)_2]_n$" (V), "[$MnLi_2Br(O^tBu)_4(THF)_2]_n$" (VI) and "[$Fe_{0.5}Mn_{0.5}Li_2Br(O^tBu)_4(THF)_2]_n$" (VII) were conducted to investigate the electrochemical behaviour and rate capabilities. Initially, the electrochemical performance of the *Cmcm* β-$LiFePO_4$_IV phase was evaluated. As previous reports have demonstrated, theball milling can efficiently enhance the electrochemical performance of non-olivine β-$LiFePO_4$,[52] the pristine β-$LiFePO_4$_IV powders were mixed with C black (60:40 % wt. ratio) and the mixture ball milled for 2 hr. Galvanostatic cycling at room temperature of the non-olivine β-$LiFePO_4$_IV phase at C/20 rate in the voltage range from 1.8 V to 4.0 V displayed charge and discharge capacities of around 70 $mAh{\cdot}g^{-1}$ and 50 $mAh{\cdot}g^{-1}$, respectively, over the first 20 cycles without a noticeable capacity loss (see Figure A5.11). Optimisation of the ball milling time and also the carbon content of the final electrode mixture could significantly increase the electrochemical performance of this ß-$LiFePO_4$ polymorph. Such materials activated by disorder could be promising candidate cathodes for LIBs, and the related mechanism of storage and effective migration of Li^+ ions also provides new clues for future design of disordered-electrode materials with high capacity and energy density. On the other hand, galvanostatic cycling at room temperature of the olivine carbon coated (15% C wt. from sucrose) C/$LiFePO_4$_IV, C/$LiFePO_4$_V and C/$LiMnPO_4$_VI nanostructures prepared from the [$FeLi_2Br(O^tBu)_4(THF)_2]_n$

(IV), "$[FeLi_2Cl(O^tBu)_4(THF)_2]_n$" (V), "$[MnLi_2Br(O^tBu)_4(THF)_2]_n$" (VI) heterometallic alkoxide precursors, respectively, were conducted over the voltage range between 2.2 V and 4.5 Vat a C/20 rate. The representative charge/discharge voltage profile for the C/$LiFePO_4$_IV sample shown in Figure 5.18 (a) indicated that capacities of around 138 $mAh \cdot g^{-1}$ were reached with no significant capacity fading over 20 cycles. On the other hand, galvanostatic cycling at C/20 from 2.2 V to 4.0 V of the C/$LiFePO_4$_V sample delivered discharge capacities of approximately 142 $mAh \cdot g^{-1}$ with a good capacity retention during the first 20 cycles (Figure 5.18 (c) and (d)). These results demonstrated that C/$LiFePO_4$_IV and C/$LiFePO_4$_V nanostructures displayed similar electrochemical behaviour. This suggests that using $[FeLi_2Br(O^tBu)_4(THF)_2]_n$ (IV) instead of "$[FeLi_2Cl(O^tBu)_4(THF)_2]_n$" (V) in the presented fast microwave-assisted synthesis of olivine $LiFePO_4$ nanostructures does not lead to significant difference in the resulting electrochemical performance. Galvanostatic cycling of the C/$LiMnPO_4$_VI sample in the voltage range from 2.2 V to 4.5 V reveals that initial discharge capacities of approximately 150 $mAh \cdot g^{-1}$ were reached, values that slowly faded to ~135 $mAh \cdot g^{-1}$ over the first 20 cycles (Figure 5.18 (e) and (f)). However, charge capacities between 400 and 250 $mAh \cdot g^{-1}$ were reached during the charge process. This may be attributed to some electrolyte decomposition and/or Mn dissolution taking place at high voltages in the charge process. Moreover, electrolyte decomposition can be intensified in the case of such small $LiMnPO_4$ nanoparticles (~15 nm thick nanorods). From these results, it must be highlighted that a significant improvement in the electrochemical behaviour of olivine $LiMnPO_4$ nanostructures is obtained when the synthesis is performed using the single source heterometallic alkoxide precursor "$[MnLi_2Br(O^tBu)_4(THF)_2]_n$" (VI) instead of the homometallic alkoxide "$[Mn(O^tBu)_2(THF)]_2$" (II) or commercial starting materials such as $Mn(acac)_3$ and LiH_2PO_4 (for example, 135 $mAh \cdot g^{-1}$ for $LiMnPO_4$_VI (Heterometallic) *vs.*100 $mAh \cdot g^{-1}$ for $LiMnPO_4$_II (Homometallic) and 50 $mAh \cdot g^{-1}$ for $LiMnPO_4$_MW_Commercial at C/20 rate). The electrochemical behaviour of $LiMnPO_4$_VI was also comparable to some C/$LiMnPO_4$ nanoparticles prepared by a two-stage microwave process which delivered an initial discharge capacity of 152.6 $mAh \cdot g^{-1}$ at 0.1 C rate and 128.4 $mAh \cdot g^{-1}$ after 100 cycles at 0.5 C.[299] Therefore, it has been demonstrated that microwave-assisted single source processes are a promising synthetic approach for the generation of electrochemically optimised $LiMnPO_4$ nanoparticles with good electrochemical performance. Nevertheless, such a noticeable enhancement in the electrochemical performance has not been observed in the case of olivine $LiFePO_4$ nanophases, which delivered capacities of ~160 $mAh \cdot g^{-1}$ when prepared with the commercial precursor $Fe(acac)_3$, ~148 $mAh \cdot g^{-1}$ when using homometallic alkoxide $[Fe(O^tBu)_2(THF)]_2$ (I) and ~140 $mAh \cdot g^{-1}$ with heterometallic alkoxide precursors $[FeLi_2X(O^tBu)_4(THF)_2]$ (*X*=Br, Cl).

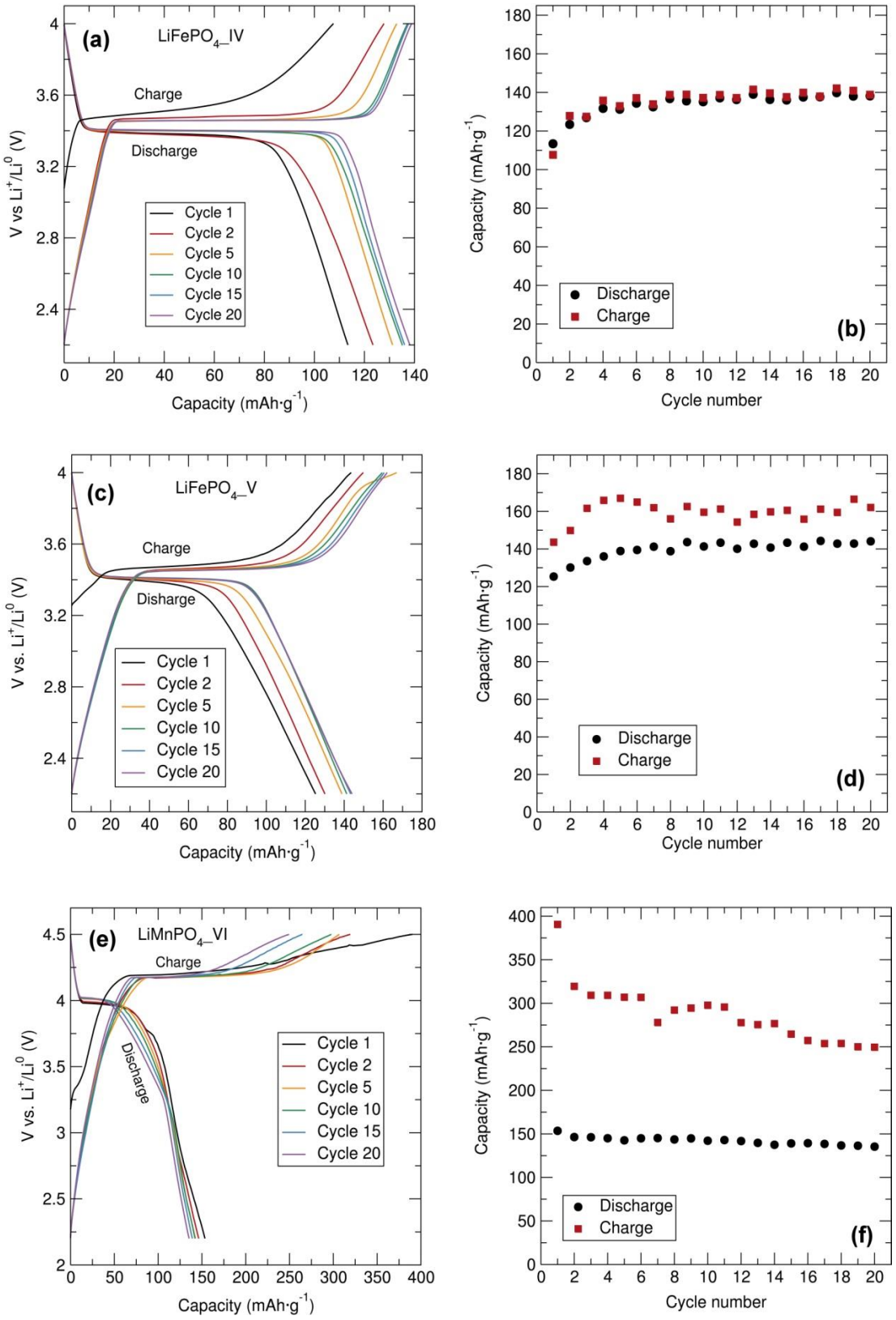

Figure 5.12. Voltage-capacity profiles and cycling stability at C/20 rate of **(a, b)** C/$LiFePO_4$_IV (15% wt. C from sucrose), **(c, d)** C/$LiFePO_4$_V (15% wt. C from sucrose), and **(e, f)** C/$LiMnPO_4$_VI (15% wt. C from sucrose). Samples prepared through a fast microwave synthesis (15 min 80 ºC and 10 min at 240 ºC) with from "$[ML i_2X(O^tBu)_2(THF)]_2$" (*M*=Fe, Mn; *X*=Br, Cl) (IV,V, VI) heterometallic alkoxide precursors and mixed with C black and PTFE in 60:30:10 (% wt. ratio).

Galvanostatic cycling studies from 2.2 to 4.3 V at C/20 rate of the C/$LiFe_{0.5}Mn_{0.5}PO_4$_IV-VI, C/$LiFe_{0.5}Mn_{0.5}PO_4$_V-VI and C/$LiFe_{0.5}Mn_{0.5}PO_4$_VII nanostructures demonstrated in all three cases that discharge capacities of approximately 150 mAh·g^{-1} were reached over the first 20 charge/discharge cycles with no evident capacity fading (Figure 5.13). From the voltage-capacity curves, two flat plateaus at 3.45 V and 4.10 V can be clearly observed due to the Fe^{3+}/Fe^{2+} and Mn^{3+}/Mn^{2+} redox couples, respectively. Moreover, the capacity associated with both plateaus is nearly the same, consistent with the Fe/Mn ratio of the $LiFe_{0.5}Mn_{0.5}PO_4$ sample. These results suggest that using a mixture of $[FeLi_2Br(O^tBu)_4(THF)_2]_n$ (IV)/"$[FeLi_2Cl(O^tBu)_4(THF)_2]_n$" (V) and "$[MnLi_2Br(O^tBu)_4(THF)_2]_n$ (VI) or the trimetallic alkoxide precursor "$[Fe_{0.5}Mn_{0.5}Li_2Br(O^tBu)_4(THF)_2]_n$" (VII) does not result in any significant difference in the resulting electrochemical performance. It must be noted that enhanced rate capabilities in $LiFe_{0.5}Mn_{0.5}PO_4$ olivines may be reached with more specific surface coating processes. For example, a 1% wt $Li_4Ti_5O_{12}$-coated $LiFe_{0.5}Mn_{0.5}PO_4$/C composite maintained high cycling stability at 1 C (141 mAh·g^{-1}) and 10 C (133 mAh·g^{-1}) rates at 55 ºC after 100 cycles in contrast to bare $LiFe_{0.5}Mn_{0.5}PO_4$/C, which deliverd only 60 mAh·g^{-1} at 10 C also at 55 ºC. Hybrid coating layers with a carbon layer and a $Li_4Ti_5O_{12}$-layer provide high conductivity for Li^+ ions and electrons, facilitate Li^+ solvation/desolvation *via* an ionic conductor layer, and provide reliable protection against HF attacks.[300]

The rate behaviour of the C/$LiFe_{1-x}Mn_xPO_4$ nanophases was also investigated to examine the rate capabilities as a function of Mn content, particle morphology and size. Figure 5.14 (a) shows that the discharge capacities of the C/$LiFe_{1-x}Mn_xPO_4$ nanostructures progressively decreased with increasing C rates, with a pronounced effect for the C/$LiMnPO_4$_VI sample (especially at faster charge/discharge rates). High C rates up to 10 C delivered discharge capacities of 60 mAh g^{-1}, 70 mAh·g^{-1}, 75 mAh·g^{-1} and 35 mAh·g^{-1} for the C/$LiFePO_4$_V, C/$LiFe_{0.5}Mn_{0.5}PO_4$_IV-VI, C/$LiFe_{0.5}Mn_{0.5}PO_4$_VII and C/$LiMnPO_4$_VI phases, respectively. The C/$LiFePO_4$_V exhibited excellent rate capability delivering ~125 mAh·g^{-1} at C/2, ~115 mAh·g^{-1} at 2 C and ~100 mAh·g^{-1} at 5 C. The mixed metal C/$LiFe_{0.5}Mn_{0.5}PO_4$_VII nanostructure presented here exhibited slightly improved rate capabilities in comparison to the C/$LiFePO_4$_V and C/$LiFe_{0.5}Mn_{0.5}PO_4$_IV-VI nanophases, suggesting that substituting Fe by Mn in this series of $LiFe_{1-x}Mn_xPO_4$ nanostructures can improve the rate behaviour. This enhancement of the rate capabilities could be attributed to the smaller particle sizes of the $LiFe_{0.5}Mn_{0.5}PO_4$_VII sample in comparison to $LiFePO_4$_V. Furthermore, these cycling studies also suggested that having all the required metals in a single precursor may be beneficial in the achievement of high rate performing olivine materials. On the other hand, the C/$LiMnPO_4$ nanostructure displayed a significantly poorer rate performance, in which the discharge capacities markedly faded from ~160 mAh·g^{-1} at C/10 to ~110 mAh·g^{-1}, 100 mAh·g^{-1}, 85 mAh·g^{-1} and 35 mAh·g^{-1} at C/2, 2 C and

5 C and 10 C, respectively. Also, the capacity was not completely recovered when cycling back to C/10 rate after the increasingly faster rates. This behaviour may be explained by the significant volume changes occurring during the $LiMnPO_4$-$MnPO_4$ phase transition during the cycling process triggering a slow structural degradation. In a previous report, a fast microwave-assisted method with a ball-milling pre-step afforded a $LiMnPO_4$/C composite exhibiting a similar electrochemical performance of 109.2 $mAh \cdot g^{-1}$ and 85.2 $mAh \cdot g^{-1}$ at C and 5 C, respectively.[301] The simplicity of the single source precursor synthesis presented here still has room for a wide range of opportunities to enhance the electrochemical behaviour of these olivine materials by using more sophisticated processing techniques or by using tailored surfactants and coating agents to prepare specific composites. Recently, a $LiFe_{0.5}Mn_{0.5}PO_4$/C composite with a hierarchical porous structure was fabricated *via* a spray dry process and achieved discharge capacities of 161, 160, 157, 146, 137, and 115 $mAh \cdot g^{-1}$ at 0.2, 0.5, 1, 3, 5, and 10 C, respectively.[238] In the case of $LiMnPO_4$, plate-like nanocrystals synthesised by a one-spot solvothermal process exhibited a slightly enhanced electrochemical performance yielding discharge capacities of 108.2 $mAh \cdot g^{-1}$ at 10 C and maintaining a discharge capacity of 133.5 $mAh \cdot g^{-1}$ after 100 cycles at 0.5 C.[302] Hong *et al*. also reported high performance $LiMnPO_4$ nanorods prepapared *via* an ethylene glycol-assisted solvothermal method displaying high reversible capacities of 168 $mAh \cdot g^{-1}$ and 110 $mAh \cdot g^{-1}$ at 0.05 C and 10 C, respectively. Such remarkable high performance can be attributed to the unique nanoscale rod-like morphology and to the uniform thin carbon layer on the surface.[303] PXRD analysis of the post-cycled C/$LiFePO_4$_V, C/$LiFe_{0.5}Mn_{0.5}PO_4$_VII and C/$LiFe_{0.5}Mn_{0.5}PO_4$_IV-VI products in the discharge state showed no evident degradation of the olivine structure over these cycling studies. PXRD characterisation of the post-cycled $LiMnPO_4$_VI in the discharge state showed some $MnPO_4$ product, indicating that the Li^+ extraction/insertion process in the $LiMnPO_4$-$MnPO_4$ system may not be fully reversible (especially at faster charge/discharge rates). The formation of this $MnPO_4$ phase in the cycling process may lead to a progressive loss of the capacity retention and may explain why the capacity is not fully recovered when cycling back to C/10 rate after the increasingly faster rates. Figure 5.14 (b) shows the PXRD patterns of the post-cycled C/$LiFePO_4$_V, C/$LiFe_{0.5}Mn_{0.5}PO_4$_VII, C/$LiFe_{0.5}Mn_{0.5}PO_4$_IV-VI and C/$LiMnPO_4$_VI materials.

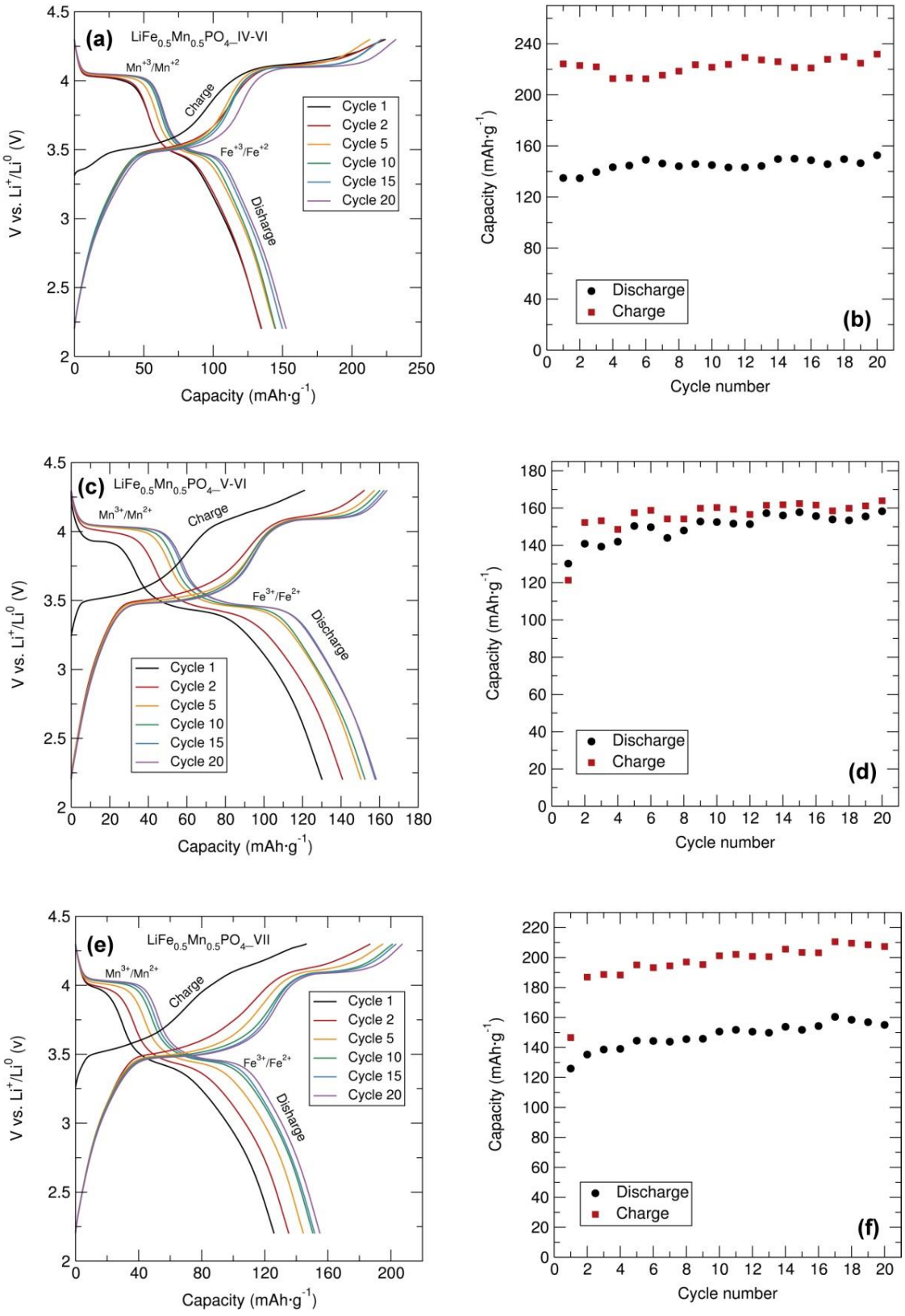

Figure 5.13. Voltage-capacity profiles and cycling stability at C/20 rate of **(a, b)** C/$LiFe_{0.5}Mn_{0.5}PO_4$_IV-VI (15% wt. C from sucrose), **(c, d)** C/$LiFe_{0.5}Mn_{0.5}PO_4$_V-VI (15% wt. C from sucrose), and **(e, f)** C/$LiFe_{0.5}Mn_{0.5}PO_4$_VII (15% wt. C from sucrose). Samples prepared through a fast microwave synthesis (15 min 80 ºC and 10 min at 240 ºC) with from "$[ML i_2X(O^tBu)_2(THF)]_2$" (*M*=Fe, Mn; *X*=Br, Cl) (IV, V, VI, VII) heterometallic alkoxide precursors and mixed with C black and PTFE in 60:30:10 (% wt. ratio).

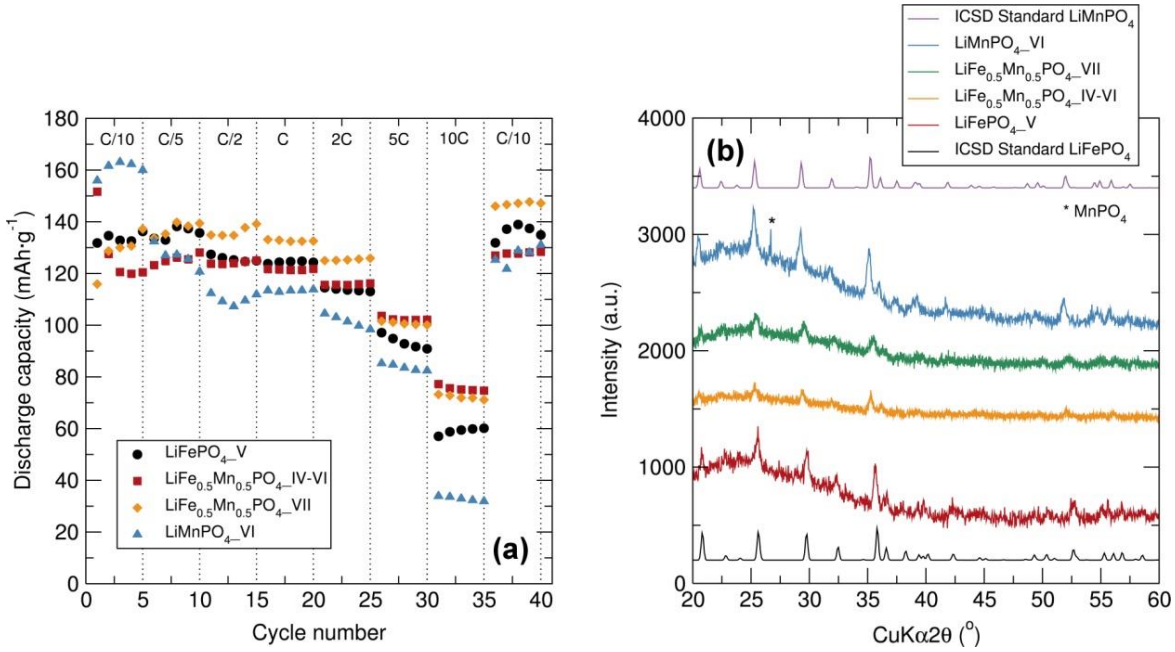

Figure 5.14. (a) Comparative rate performance of C/$LiFePO_4$_V, C/$LiFe_{0.5}Mn_{0.5}PO_4$_Mix IV and VI, C/$LiFe_{0.5}Mn_{0.5}PO_4$_VII and C/$LiMnPO_4$_VI (15% wt. C from sucrose) prepared with "$[FeLi_2Cl(O^tBu)_4(THF)_2]_n$" (IV), "$[Fe_{0.5}Mn_{0.5}Li_2Br(O^tBu)_4(THF)_2]_n$" (VII) and "$[MnLi_2Br(O^tBu)_4(THF)_2]_n$" (VI) alkoxide precursors, respectively. **(b)** PXRD of cycled C/$LiFePO_4$_V, C/$LiFe_{0.5}Mn_{0.5}PO_4$_VII, C/$LiFe_{0.5}Mn_{0.5}PO_4$_IV-VI and C/$LiMnPO_4$_VI at different C rates in the discharged state.

CV experiments at room temperature of the C/$LiFePO_4$_IV, C/$LiFePO_4$_V, C/$LiFe_{0.5}Mn_{0.5}PO_4$_VII and C/$LiMnPO_4$_VI nanophases were conducted at a scan rate of 0.1 $mV{\cdot}s^{-1}$ over the voltage range from 2.5 V to 4.5 V *vs.* Li^+/Li^0. The CV results for the C/$LiFePO_4$_IV and C/$LiFePO_4$_V samples showed anodic and cathodic peaks at ~3.53 V and 3.30 V, respectively, due to the Fe^{3+}/Fe^{2+} redox pair (Figure 5.15 (a) and (b)). The CV for the C/$LiFe_{0.5}Mn_{0.5}PO_4$_VII sample exhibited two oxidation (3.54 V and 4.15 V) and two reduction peaks (3.40 V and 3.96 V) corresponding to the Fe^{2+}/Fe^{3+} and Mn^{2+}/Mn^{3+} redox pairs, respectively (Figure 5.15 (c)). These results are in good agreement with the two discharge voltage plateaus at about 3.50 V and 4.10 V vs. Li^+/Li^0 associated, respectively, to the redox pairs of Fe^{3+}/Fe^{2+} and Mn^{3+}/Mn^{2+}. Finally, the CV curve of the C/$LiMnPO_4$_VI nanostructure displayed the expected anodic and cathodic peaks at ~4.34 V and 3.94 V, respectively, due to the Mn^{2+}/Mn^{3+} redox pair (Figure 5.15 (d)). The good superposition of all the CV curves confirmed the excellent reversibility of these electrochemical systems. Figure A5.12 depicts the superposition of the CV curves for the C/$LiFePO_4$_IV, C/$LiFe_{0.5}Mn_{0.5}PO_4$_VII and C/$LiMnPO_4$_VI nanostructures showing a slight increase in the Fe^{3+}/Fe^{2+} redox potential in C/$LiFe_{0.5}Mn_{0.5}PO_4$_VII compared to C/$LiFePO_4$_IV. Also, the anodic and cathodic Mn^{3+}/Mn^{2+} peak separation in C/$LiFe_{0.5}Mn_{0.5}PO_4$_VII is significantly smaller than in C/$LiMnPO_4$_VI, indicating a lower polarisation in the mixed metal phosphate olivine.

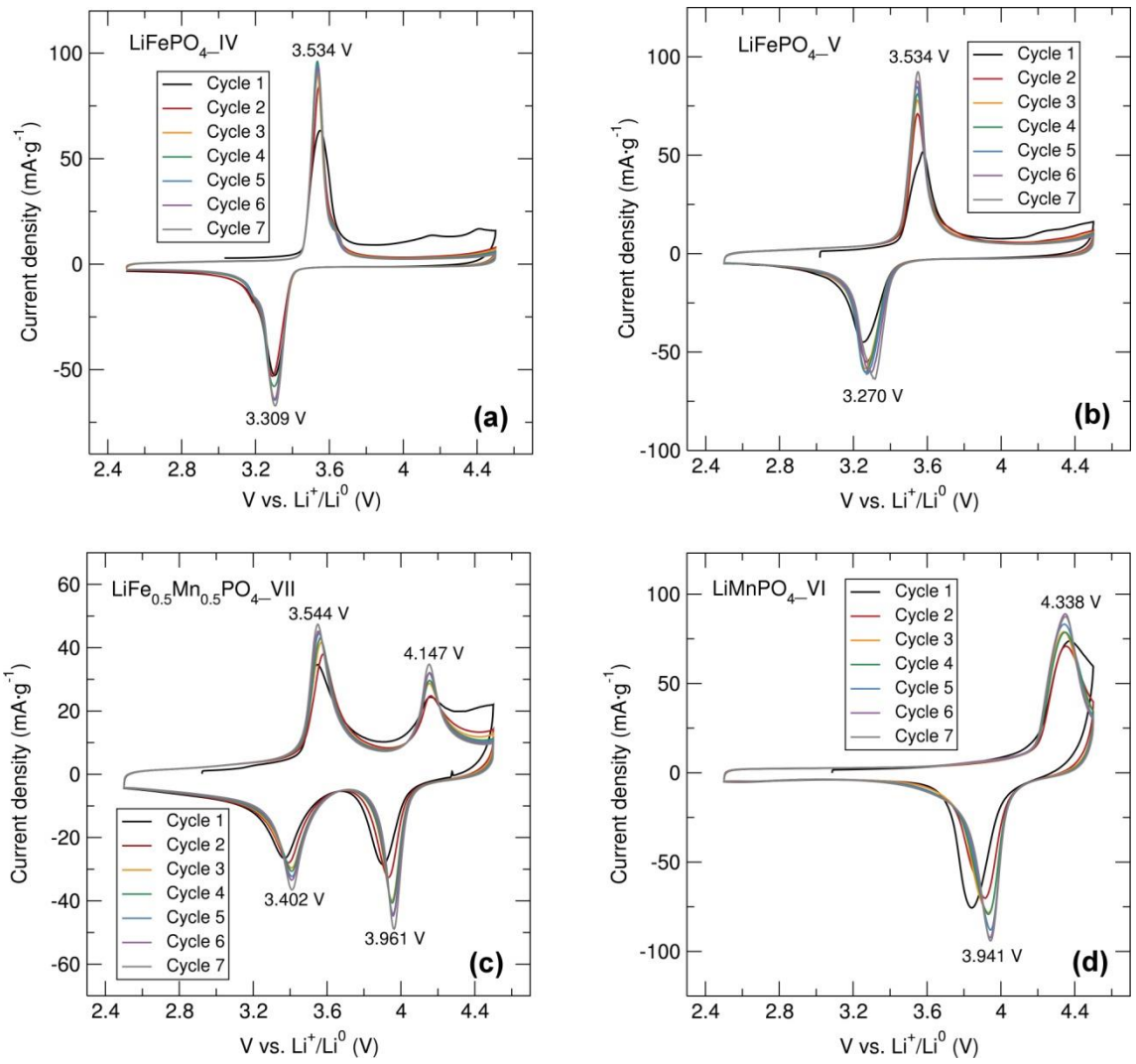

Figure 5.15. CVs at a 0.1 mV·s^{-1} scan rate between 2.5 V and 4.5 V of **(a)** C/$LiFePO_4$_IV, **(b)** C/$LiFePO_4$_V, **(c)** C/$LiFe_{0.5}Mn_{0.5}PO_4$_VII and **(d)** C/$LiMnPO_4$_VI nanostructures.

5.2.3 Ionothermal microwave synthesis of $LiFePO_4$ nanostructures from "$[FeLi_2Cl(O^tBu)_4(THF)_2]_n$" heterometallic alkoxide precursor

A rapid ionothermal microwave-assisted synthesis of $LiFePO_4$ nanostructures using the single source "$[FeLi_2Cl(O^tBu)_4(THF)_2]_n$" (V) heterometallic alkoxide precursor and 1-ethyl-3-methylimidazolium trifluoromethanesulfonate (EMI-TFMS) was conducted as depicted in Schematic 5.4 and according to the synthetic procedure detailed in section 2.2.8.

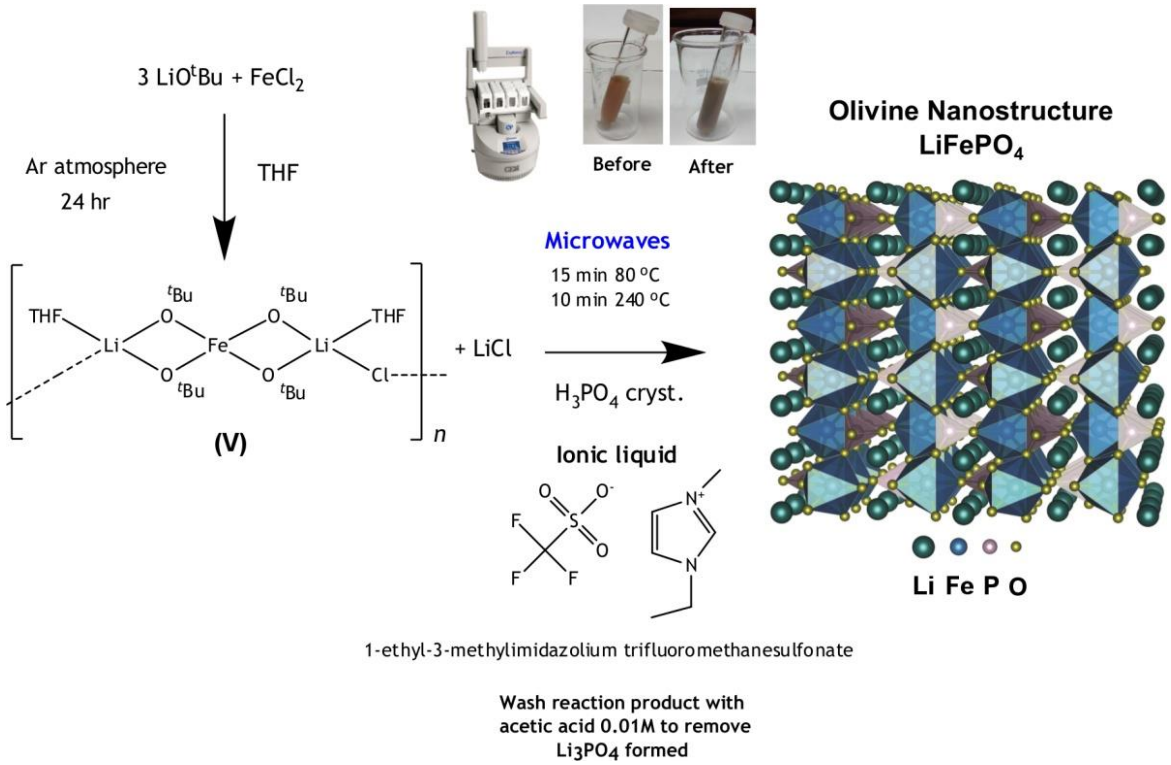

Schematic 5.4. Reaction schematic for the preparation of olivine $LiFePO_4$ *via* a fast ionothermal microwave synthesis using single source "$[FeLi_2Cl(O^tBu)_4(THF)_2]_n$" (V) heterometallic alkoxide precursor.

5.2.3.1 PXRD of $LiFePO_4$ nanostructures prepared from ionothermal microwave synthesis using "$[FeLi_2Cl(O^tBu)_4(THF)_2]_n$"

An ionothermal microwave-assisted synthesis using the "$[FeLi_2Cl(O^tBu)_4(THF)_2]_n$" (V) heterometallic alkoxide precursor with H_3PO_4 in the ionic liquid 1-ethyl-3-methylimidazolium trifluoromethanesulfonate (EMI-TFMS) was conducted for 1 hr at 240 °C to yield $LiFePO_4$_V_IL_1 hr nanostructures. In an effort to reduce the reaction times, the same microwave-assisted ionothermal reaction was performed for 15 min at 80 °C and 10 min at 240 °C. The ionic liquid 1-ethyl-3-methylimidazolium trifluoromethanesulfonate was chosen as this has previously been employed by Tarascon *et al* in the preparation of olivine $LiMnPO_4$, exhibiting an excellent electrochemical performance.[163] Furthermore, microwave dielectric measurements of EMI-TFMS revealed that it is an excellent microwave absorber to generate the temperatures required for this reaction to proceed.[51] Rietveld refinements of the PXRD data shown in Figure 5.16 indicate that an excellent fit between the experimental and calculated data was achieved. The intense and sharp peaks observed in the PXRD patterns suggest that this ionothermal reaction affords better crystallised olivine $LiFePO_4$ nanomaterials compared to when ethylene glycol is used. Table 5.10 summarises the calculated lattice parameters from Rietveld refinements for $LiFePO_4$_V_IL_10 min and $LiFePO_4$_V_IL_1 hr nanostructures prepared through this ionothermal microwave-assisted synthesis showing that increasing the reaction times

from 10 min to 1 hr slightly increases the lattice parameters of the $LiFePO_4$ nanophases. The estimated crystallite sizes of the $LiFePO_4$_V_IL_10 min and $LiFePO_4$_V_IL_1 hr samples were ~60 nm and 72 nm, respectively, which were calculated using the Scherrer equation[208] from the (211) diffraction peaks. These results suggested that longer reaction times may favour particle growth leading to larger particles. It is also worth noting the increased crystallite size of ionothermallly synthesised $LiFePO_4$_V_IL_10 min (~70 nm) compared to $LiFePO_4$_V prepared using ethylene glycol under the same reaction conditions (~33 nm).

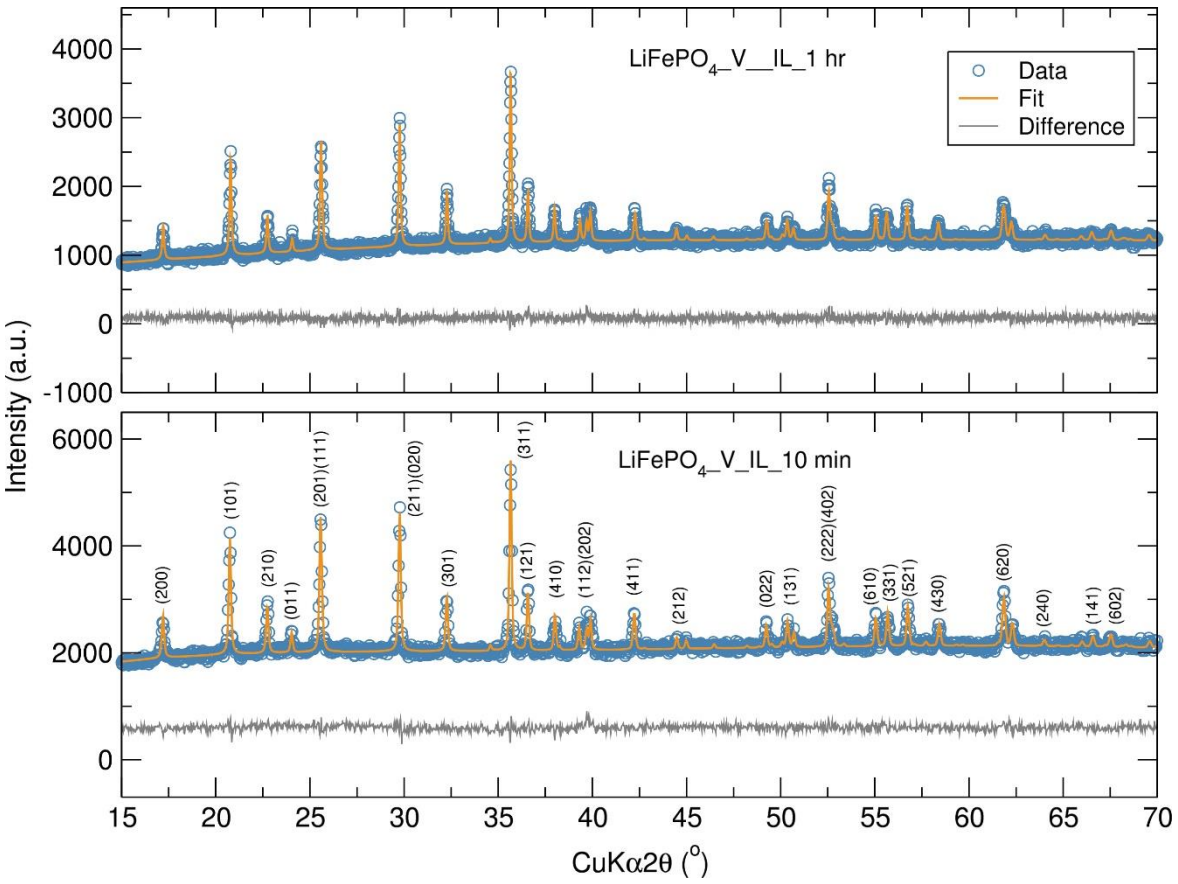

Figure 5.16. Rietveld analysis of PXRD data of $LiFePO_4$_V_IL olivines prepared using "$[FeLi_2Cl(O^tBu)_4(THF)_2]_n$" (V) heterometallic precursor and H_3PO_4 in ionic liquid EMI-TFMS after 10 min and 1 hr of microwave irradiation at 240 °C.

Table 5.10. Calculated lattice parameters from Rietveld refinements for $LiFePO_4$_V_IL olivines prepared through fast ionothermal microwave synthesis.

Sample	$LiFePO_4$_V_IL_1 hr	$LiFePO_4$_V_IL_10 min
Space group	*Pnma*	*Pnma*
a (Å)	10.3044(5)	10.2895(7)
b (Å)	5.9999(3)	5.9922(4)
c (Å)	4.6951(3)	4.6967(4)
V ($Å^{-3}$)	290.28(3)	289.58(4)
R_{wp}	29.2 %	25.2 %
R_{exp}	25.96 %	20.88 %
X^2	1.27	1.45

The local structure of the $LiFePO_4$_V_IL_10 min nanophase was also investigated by X-ray PDF analysis to demonstrate that this ionothermal process affords better crystallised nanostructures. From fitting the X-ray PDF data at different *r* ranges from 1 to 15 Å (1 to 15 Å, 1 to 10 Å and 1 to 5 Å) using a fully ordered olivine structured model, excellent agreements between the experimental data and the calculated models were obtained for the $LiFePO_4$_V_IL_10 min sample (R_w values from 0.06 to 0.1), suggesting that the local and average structure are very similar and that there is no evidence of defects or significant local structure deviations (Figure 5.17). These results indicate that single source precursor ionothermal processes in conjunction with microwave heating yields highly crystalline and non-defective olivine $LiFePO_4$ nanomaterials. Table 5.11 lists the calculated lattice parameters, scale factors and R_w values from X-ray PDF fits at different *r* ranges for the $LiFePO_4$_V_IL_10 min sample. The higher scale factor values for the $LiFePO_4$_V_IL_10 min nanostructure (~0.60) in comparison to $LiFePO_4$_V (~0.36), suggests a higher crystallinity for the ionothermally synthesised $LiFePO_4$_V_IL_10 min sample compared to the olivines prepared using ethylene glycol. Furthermore, a significant variation in the scale factors values when fitting the X-ray PDF data at varying *r* ranges is not observed in the $LiFePO_4$_V_IL_10 min olivine synthesised with the ionic liquid, further indicating this sample has better crystallinity.

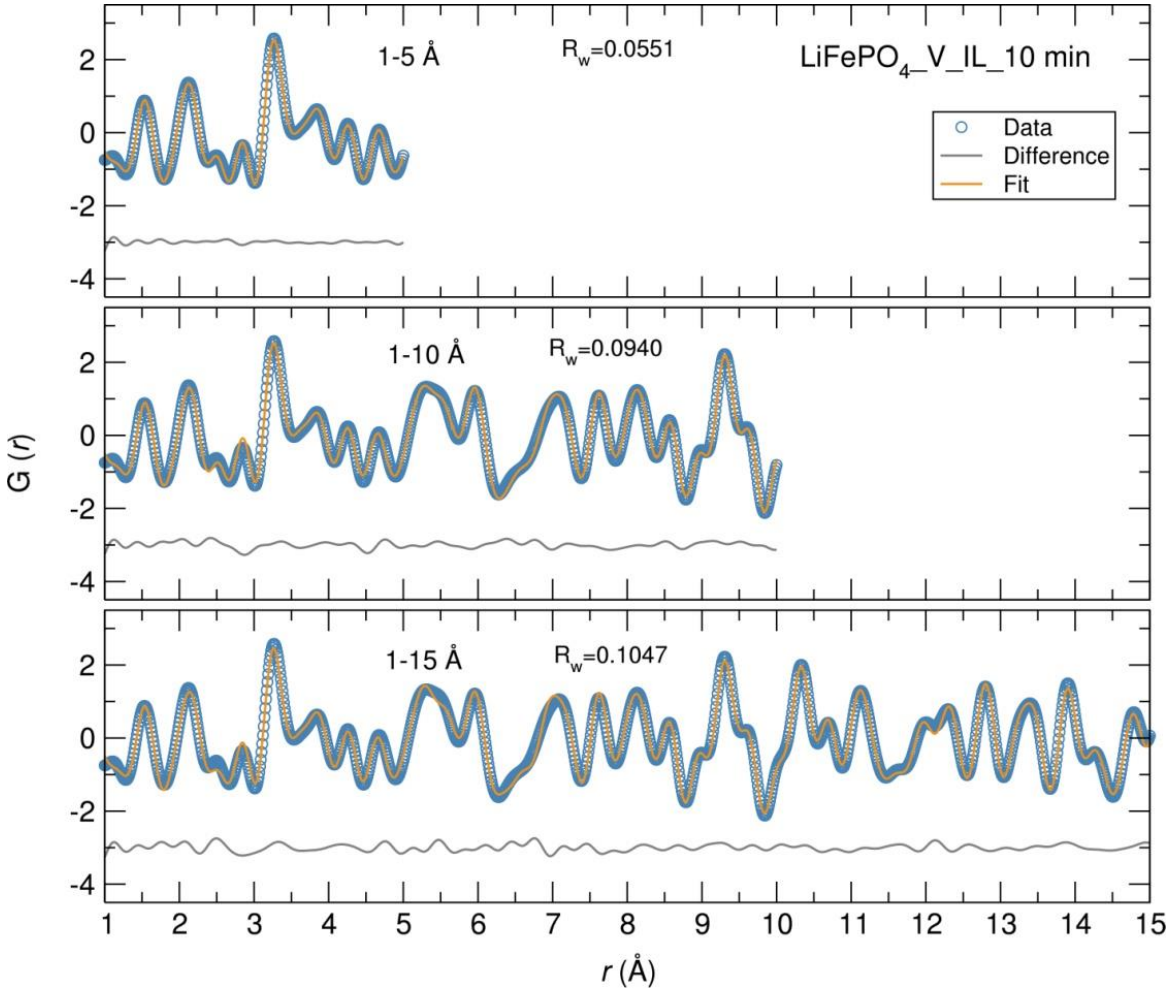

Figure 5.17. Fits at different *r* ranges of X-ray PDF data collected at 100 K for single-phase $LiFePO_4$_V_IL_10 min nanostructure prepared through a fast ionothermal microwave synthesis using heterometallic alkoxide precursors.

Table 5.11. Calculated lattice parameters, scale factors and R_w values from X-ray PDF fits at different *r* ranges for $LiFePO_4$_V_IL_10min nanostructure prepared through a fast ionothermal microwave synthesis.

$LiFePO_4$_V_IL_10 min	**1-5 Å**	**1-10 Å**	**1-15 Å**
Scale factor	0.61(6)	0.60(3)	0.60(3)
a (Å)	10.40(9)	10.27(3)	10.27(1)
b (Å)	5.94(8)	5.99(1)	5.99(1)
c (Å)	4.69(5)	4.68(1)	4.68(1)
R_w	0.0551	0.0940	0.1047

To quantify the amorphous content in this family of $LiFePO_4$_V, $LiFe_{0.5}Mn_{0.5}PO_4$_VII, $LiMnPO_4$_VI and $LiFePO_4$_V_IL_10 min olivines prepared from single source heterometallic alkoxide precursors, two phase model refinements from 1 to 15 Å in which the two phases have the same average olivine structure but allowing only the *spdiameter* in one of the phases to refine were performed as in Chapter 3. These refinements suggested that the amorphous phase has order to about ~1 nm. Table 5.12 shows the calculated scale factors,

amorphous contents and *spdiameters* for the $LiFe_{1-x}Mn_xPO_4$ olivine phases obtained from these two isostructural phases refinements. Results indicated a higher presence of amorphous material in the olivine $LiFe_{1-x}Mn_xPO_4$ nanophases prepared using ethylene glycol (~5-8% amorphous content) compared to the $LiFePO_4$_V_IL_10 min (~2% amorphous content), which confirms the higher crystallinity of the product obtained from the ionothermal synthesis. Also, a slight improvement in the fit quality was obtained when adding the second phase.

Table 5.12. Calculated scale factor, amorphous content and *spdiameters* for the $LiFe_{1-x}Mn_xPO_4$ olivine phases obtained from two isostructural phases refinements of neutron PDF data from 1 to 15 Å.

Sample	$LiFePO_4$_V	$LiFe_{0.5}Mn_{0.5}PO_4$_VII	$LiMnPO_4$_VI	$LiFePO_4$_V_IL_ 10 min
Scale factor Phase 1	0.36(2)	0.36(3)	0.42(4)	0.60(3)
Scale factor Phase 2	0.03(2)	0.02(9)	0.04(9)	0.01(9)
Amorphous content (%)	7.1	5.1	8.5	1.7
Spdiameter (Å)	2	7	10	8
R_{wp}	0.1803	0.2672	0.2593	0.1046

5.2.3.2 SEM of $LiFePO_4$ nanostructures prepared from ionothermal microwave synthesis using "$[FeLi_2Cl(O^tBu)_4(THF)_2]_n$"

High resolution SEM micrographs of LiFePO4_V_IL_10 min sample showed a clear dependence of the particle size and morphology on the choice of solvent. In comparison to the $LiFePO_4$_V sample prepared using ethylene glycol, where platelets with particle sizes around 40 to 150 nm were observed, the $LiFePO_4$_V_IL_10 min powders shown in Figure 5.18 adopted a non-uniform faceted morphology with particle sizes ranging from approximately 70 to 190 nm, similar to previous work conducted in the group where commercial starting materials ($FeC_2O_4 \cdot 2H_2O$ and LiH_2PO_4) and the same ionic liquid were employed.[51] ILs could potentially facilitate mass transport, bringing the reacting species together and affording well defined facets with salient edges, as reported previously by Recham *et al*.[162, 304]

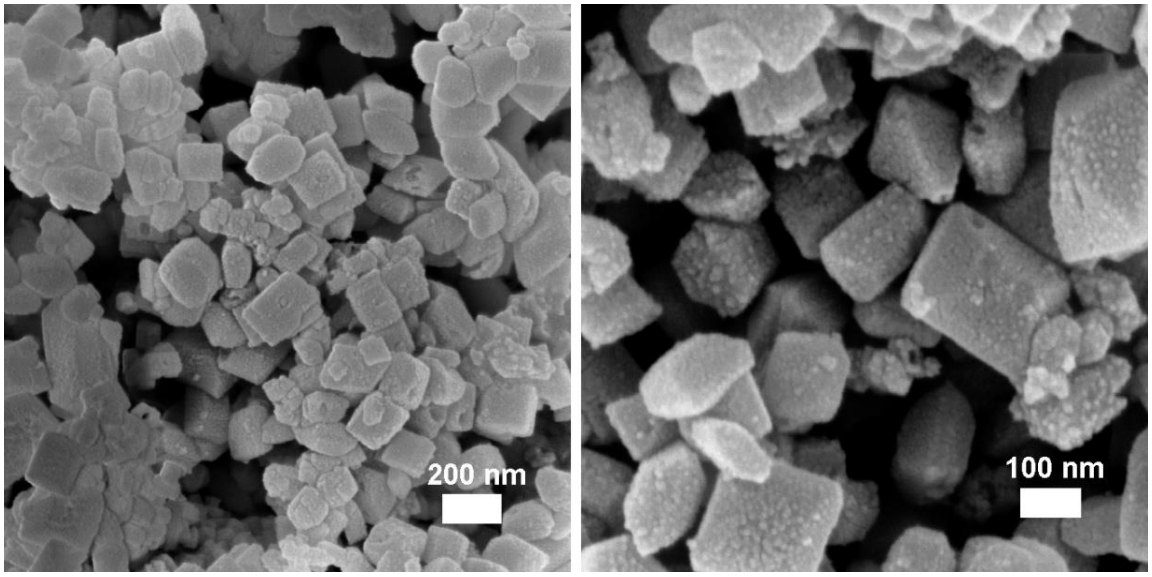

Figure 5.18. Hig resolution SEM images of $LiFePO_4$_V_IL_10 min nanostructures prepared using "$[FeLi_2Cl(O^tBu)_4(THF)_2]_n$" (V) heterometallic precursor and H_3PO_4 in ionic liquid EMI-TFMS after 10 min of microwave irradiation at 240 ºC.

5.2.3.3 Electrochemical performance of $LiFePO_4$ nanostructures prepared from ionothermal microwave synthesis using "$[FeLi_2Cl(O^tBu)_4(THF)_2]_n$"

Galvanostatic cycling at C/20 from 2.2 V to 4.0 V of C/$LiFePO_4$_V_IL_10 min displayed charge and discharge capacities of approximately 180 $mAh \cdot g^{-1}$ and 155 $mAh \cdot g^{-1}$, respectively (Figure 5.19 (a)). The charge and discharge capacities were retained for at least 20 cycles (Figure 5.19 (b)). The slight improvement in the electrochemical performance of C/$LiFePO_4$_V_IL_10 min compared to C/$LiFePO_4$_V could be ascribed to the better crystallinity of the olivine $LiFePO_4$ phase in the ionothermal process. The low polarisation observed between the charge and discharge process for C/$LiFePO_4$_V_IL_10 min (ΔV=0.024 V) in comparison to $LiFePO_4$_V (ΔV=0.064 V) suggests a faster electron transfer process in the $LiFePO_4$ sample prepared using the IL. Similar electrochemical performance has been previously reported for ionothermally synthesised $LiFePO_4$ using 1-ethyl-3-methylimidazolium bis(trifuoromethanesulfonyl)imide, which showed a reversible and sustainable capacity of 150 $mAh \cdot g^{-1}$ at C/10 rate.[162]

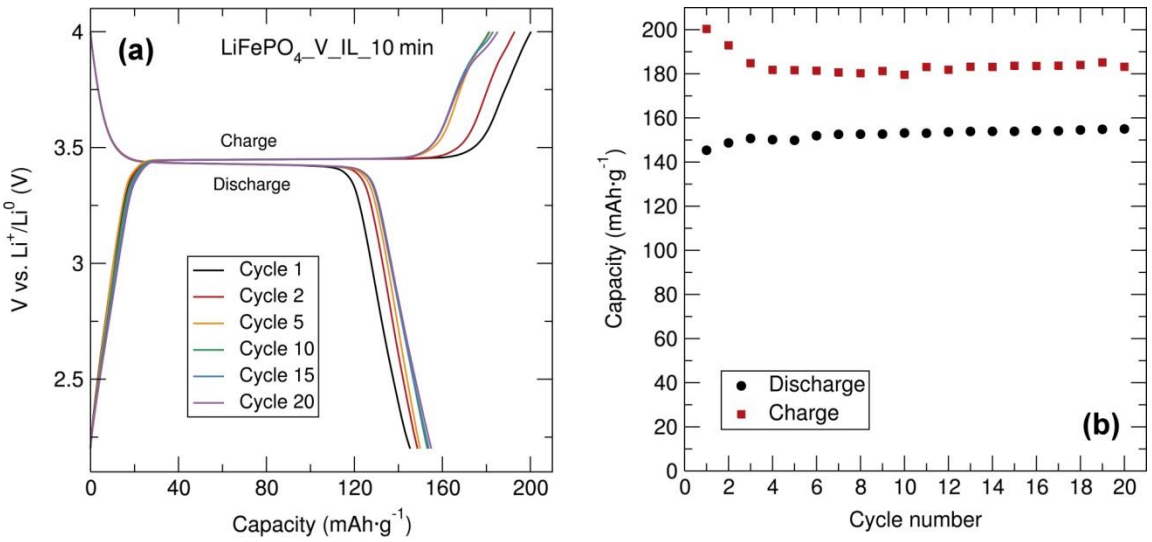

Figure 5.19. (a) Voltage-capacity profiles and **(b)** cycling stability of C/$LiFePO_4$_V_IL_10 min (15% wt. C from sucrose) prepared with "$[FeLi_2Cl(O^tBu)_4(THF)_2]_n$" (V) heterometallic alkoxide precursor in ionic liquid (EMI-TFMS) and mixed with C black and PTFE in 60:30:10 (% wt. ratio) between 2.2 V and 4.5 V at C/20 rate.

Investigations at different charge and discharge rates demonstrated an excellent rate capability of C/$LiFePO_4$_V_IL_10 min, reaching discharge capacities of 110 mAh·g^{-1} at 20 C (Figure 5.20). Slightly improved rate behaviour has been obtained in comparison to previously reported $LiFePO_4$ nanorods synthesised in an IL in the presence of ascorbic acid and dodecyl benzene sulfonic acid as surfactant, which delivered discharge capacities of 125 mAh·g^{-1} at 4 C.[305] Also, the ionothermally synthesised C/$LiFePO_4$_V_IL_10 min presented here displayed enhanced rate capabilities compared to $LiFePO_4$/C nano-plate thin films fabricated by drop casting a $LiFePO_4$ nano-plate/sucrose suspension, which delivered specific capacities of 162 mAh·g^{-1}, 90 mAh·g^{-1}, 67 mAh·g^{-1} and 44 mAh·g^{-1} at C, 10 C, 20 C and 50 C, respectively.[306] Even $LiFePO_4$ nanorods prepared by a rapid microwave-assisted solvothermal approach at higher temperatures of 300 ºC for 5 min, followed by coating with a mixed conducting polymer displayed a slightly lower rate performance than this C/$LiFePO_4$_V_IL_10 min nanostructure.[307] Similar rate capabilities have also been observed in a nanoporous spherical $LiFePO_4$ prepared by spray pyrolysis, which delivered as high as 123 mAh·g^{-1} and 106 mAh·g^{-1} at 10 C and 20 C, respectively.[308] These results indicated that the fast ionothermal microwave-assisted synthesis of $LiFePO_4$ employing single source heterometallic alkoxides affords among the best performing material at high C rates, establishing this synthetic approach as one to yield high performing electrode materials across the olivines. Furthermore, discharge capacities of 145 mAh·g^{-1} were recovered when cycling back to C/10. The C/$LiFePO_4$_V_IL_10 min nanostructure displayed charge capacities of around 200 mAh·g^{-1} at a C/10 rate after the increasingly faster C rates, suggesting that some decomposition processes contributing to a pronounced increase of the capacity may be taking place during charging. PXRD analysis

of the post-cycled C/$LiFePO_4$_V_IL_10 min material in the discharge state showed no degradation of the olivine structure over these cycling studies. Figure 5.21 depicts the Rietveld fit of the PXRD data of the post-cycled C/$LiFePO_4$_V_IL_10 min, suggesting that a slight increase in the unit cell parameters may has taken place after the cycling process.

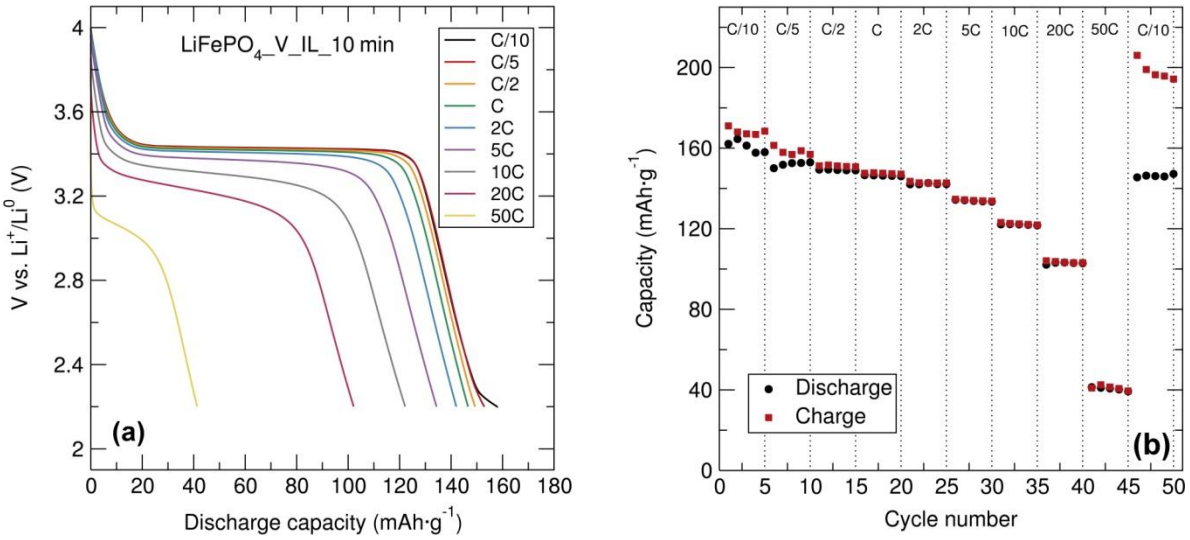

Figure 5.20. (a) Discharge capacity curves and **(b)** cycling stability at different charge-discharge C rates of C/$LiFePO_4$_V_IL_10 min (15% wt. C from sucrose) prepared with "$[FeLi_2Cl(O^tBu)_4(THF)_2]_n$" (V) alkoxide precursor in ionic liquid (EMI-TFMS) and mixed with C black and PTFE in 60:30:10 (% wt. ratio).

CV measurements at a 0.1 $mV \cdot s^{-1}$ scan rate between 2.2 V and 4.0 V of C/$LiFePO_4$_V_IL_10 min showed the anodic and cathodic peaks characteristic of the Fe^{3+}/Fe^{2+} redox pair with excellent overlap of the CV curves over cycling (Figure 5.22 (a)). CV experiments at different scan rates going from 0.1 to 1 $mV \cdot s^{-1}$ showed a slight shifting of the anodic peaks towards higher voltages at the same time that the cathodic peaks shifts towards smaller voltages, as expected for an electrode material exhibiting slow electron transfer processes. Furthermore, in Figure 5.22 (b) it is clearly shown that the intensity and area of the oxidation/reduction peak increase with scanning rate, suggesting that the electrode polarisation is also increasing.

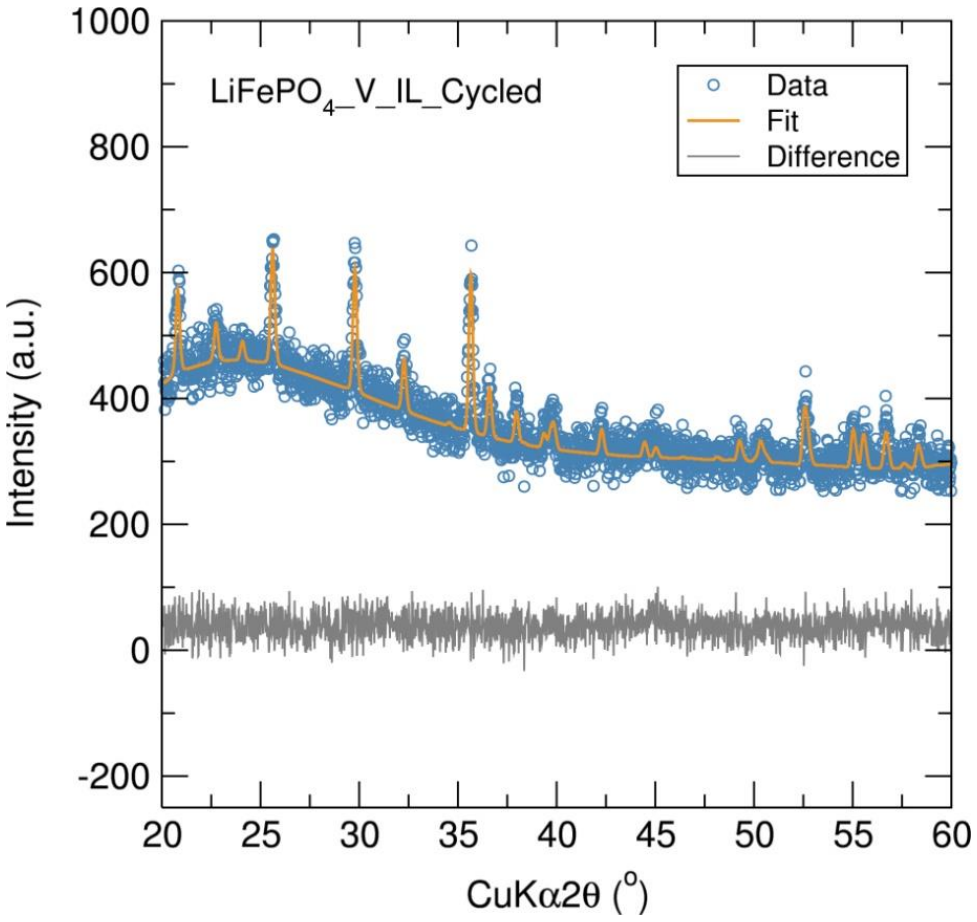

Figure 5.21. Rietveld analysis of PXRD data of post-cycled C/$LiFePO_4$_V_IL_10 min. [R_{wp}=60.4 %, R_{exp}=56.49 %, χ^2=1.14, *a*=10.329(3) Å, *b*=6.007(2) Å and *c*=4.699(2) Å].

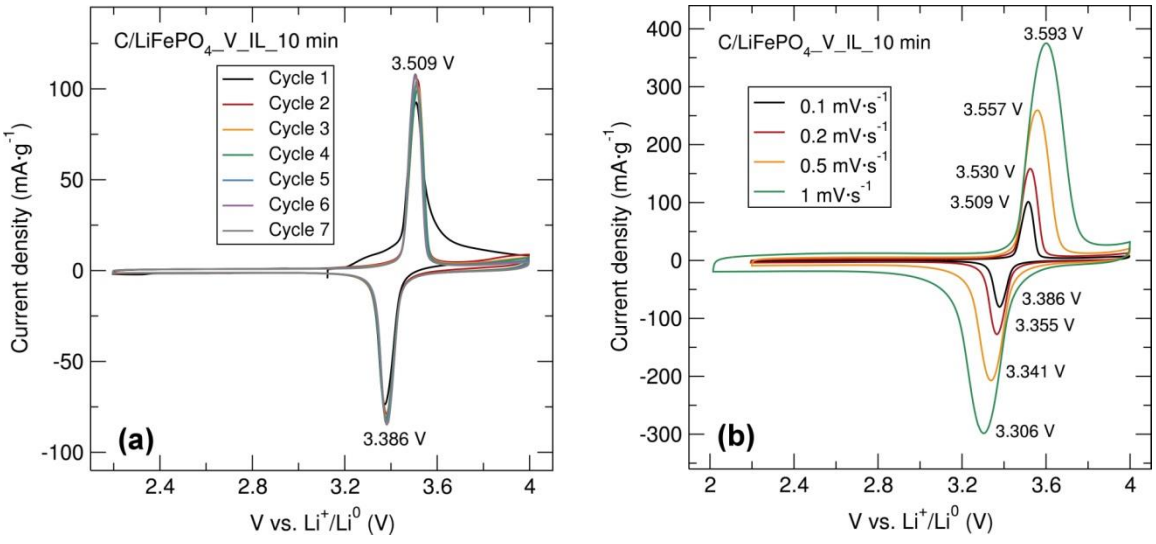

Figure 5.22. (a) CV at a 0.1 mV·s^{-1}scan rate between 2.2 V and 4.0 V of C/$LiFePO_4$_V_IL_10 min nanostructure prepared through a microwave-assisted ionothermal synthesis (15 min 80 ºC and 10 min 240 ºC) with "$[FeLiCl(O^tBu)_4(THF)_2]_n$" (V) heterometallic alkoxide precursor. **(b)** CV profiles of C/$LiFePO_4$_V_IL_10 min at different scan rates.

A rough estimation of the lithium diffusion coefficient for the C/$LiFePO_4$_V_IL_10 min nanostructure was determined from the CV study at different rates. For this calculation, it was considered that the pellet of the working electrode was 20 μm thick with a surface area of 0.126 cm^2. A plot of the peak currents *vs.* the square root of the scan rates ($v^{0.5}$) (Figure 5.23) shows a linear dependence between the peak current and $v^{0.5}$. Equation 2.10 can be applied to estimate the diffusion constant of Li^+ ions. Because the peak current of the CV profile is affected by the nature of the electrolyte, the obtained diffusion constant is an apparent value that incorporates both bulk Li^+ diffusion constant and Li^+ transfer through the interface in a particular electrolyte. The apparent anodic and cathodic diffusion constants of C/$LiFePO_4$_V_IL_10 min calculated using equation 2.10 with the slope of the peak current *vs.* $v^{0.5}$ plot were 5.12 x 10^{-9} and 3.41 x 10^{-9} $cm^2 \cdot s^{-1}$, respectively. The difference in the anodic and cathodic lithium diffusion constants can be attributed to the fact that $LiFePO_4$ undergoes a two-phase process during charge and discharge, and Li^+ ions are most easily transported through regions with $FePO_4$ or $LiFePO_4$.[59] Finally, similar lithium diffusion calculations by CV analysis at different scan rates applied the C/$LiFePO_4$_V nanostructure prepared in ethylene glycol revealed slightly smaller anodic and cathodic lithium diffusion coefficients of 4.61 x 10^{-9} and 3.40 x 10^{-9} $cm^2 \cdot s^{-1}$, respectively, (see Figure A5.13), suggesting a slight improvement in the Li^+ kinetics when using ILs as a reacting media. The smaller difference between the oxidation and reduction potentials in the CV curve of $LiFePO_4$_V_IL sample compared to $LiFePO_4$_V suggests a faster electron transfer process and lower resistance in the ionothermally synthesised $LiFePO_4$_V_IL10 min nanostructure (Figure 5.24). These results are in good agreement with the X-ray PDF data, which showed slightly shorter Li-Li distances and longer Li-O distances in $LiFePO_4$_V_IL_10 min (2.13(9) Å for Li-O and 2.97(4) Å for Li-Li) compared to $LiFePO_4$_V (2.05(4) Å for Li-O and 2.99(3) Å for Li-Li), factors with could potentially enhance the Li^+ diffusion in these materials.

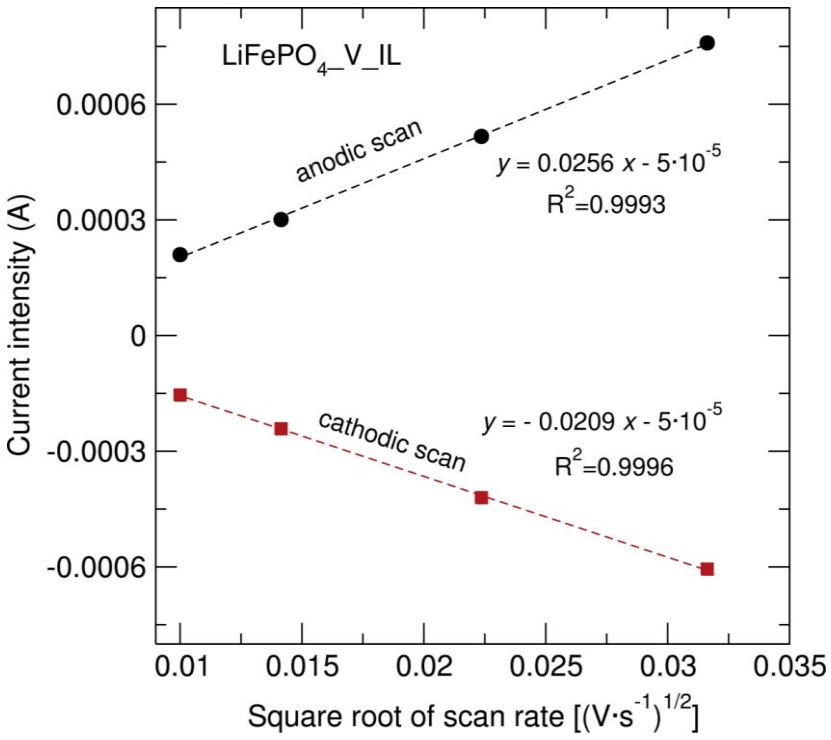

Figure 5.23. Peak current *vs.* square root of the scan rate for the C/$LiFePO_4$_V_IL_10 min (15% wt. C from sucrose) nanostructure prepared through an ionothermal microwave-assisted synthesis using "$[FeLiCl(O^tBu)_4(THF)_2]_n$" (V) heterometallic alkoxide precursor.

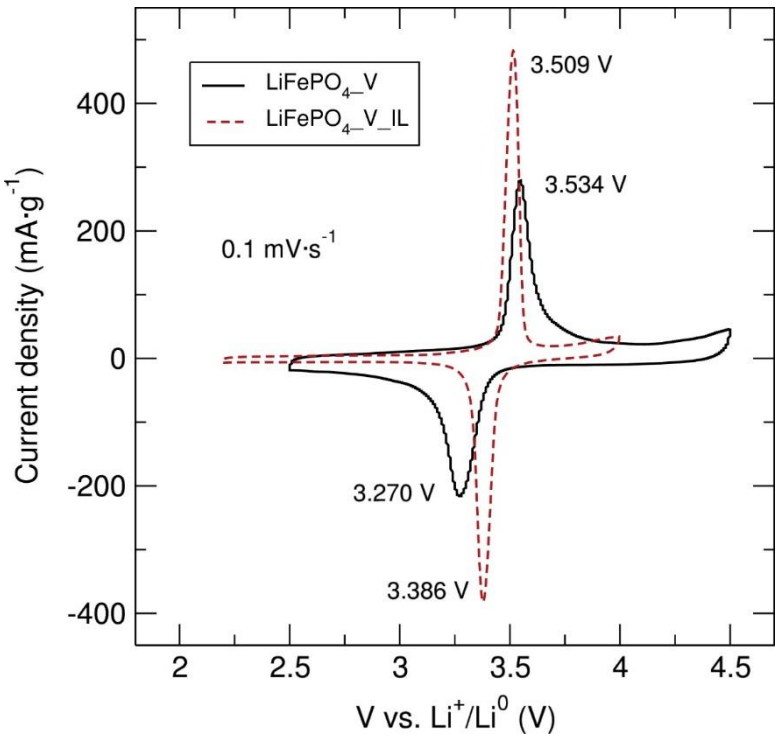

Figure 5.24. CVs at a 0.1 $mV \cdot s^{-1}$ scan rate of C/$LiFePO_4$_V_IL_10 min (15% wt. C from sucrose) and C/$LiFePO_4$_V (15% wt. C from sucrose) nanostructures prepared through fast microwave-assisted synthesis using "$[FeLiCl(O^tBu)_4(THF)_2]_n$" (V) heterometallic alkoxide precursor.

5.3 Conclusions

A facile and eco-efficient synthetic procedure for the preparation of heterometallic alkoxides "$[MLi_2X(O^tBu)_4(THF)_2]_n$" (*M*=Fe, Mn; *X*=Br, Cl) to be used as single source precursors in the fast microwave-assisted synthesis of single phase olivine $LiFe_{1-x}Mn_xPO_4$ (*x*=0, 0.5 and 1) nanostructures has been presented. Control over the $LiFePO_4$ polymorph formed depending on the nature of the heterometallic alkoxide precursor used has been demonstrated, as fast microwave treatments of the $[FeLiBr(O^tBu)_4(THF)_2]_n$ heterometallic alkoxide precursor generally afforded the ß-$LiFePO_4$ polymorph (*Cmcm* space group), while the similar Cl-containing heterometallic alkoxide precursor drove the microwave reaction towards the generation of olivine α-$LiFePO_4$ phase (*Pnma* space group). Furthermore, the strong influence of the transition metal (Fe, Mn) content and the choice of solvent on the resulting particle size and morphology of these olivine nanomaterials has been confirmed. X-ray PDF analysis suggests the suitability of single source heterometallic alkoxide precursors in conjunction with straightforward microwave-assisted routes for the generation of highly crystalline olivine $LiFePO_4$ with no evident presence of defects, especially when the ionic liquid EMI TFMS is used. Nevertheless, poorer fits to the X-ray PDF data were observed for the Mn containing olivine nanophases, which suggests that the presence of Mn could lead to a more disordered olivine structure and/or higher presence of amorphous material. Finally, electrochemical testing of $LiFe_{1-x}Mn_xPO_4$ (*x*=0, 0.5 and 1) nanostructures revealed outstanding electrochemical behaviour displaying rate capabilities comparable to the best performing olivine-structured metal phosphates in the literature. The improved electrochemical performance that can be achieved by employing single source precursor processes involving metal alkoxides precursors in comparison to conventional reactions employing commercial starting materials has therefore been confirmed. In particular, fast microwave treatments of single source heterometallic alkoxide precursor have been especially beneficial for the generation of electrochemically optimised $LiMnPO_4$ olivine nanostructures. On the other hand, the ionothermal microwave-assisted synthesis of olivine $LiFePO_4$ employing single source heterometallic alkoxide precursors afforded the best performing material at high C rates, establishing this synthetic approach as one to yield high performing electrode nanomaterials across the olivines.

6 Solvothermal Treatments of Single Source Heterometallic Alkoxides to Nanostructured Li-ion Battery Electrodes

6.1 Introduction

Low temperature solvothermal synthethic routes are increasingly being employed as a straightforward and energy-efficient synthetic method for the preparation of novel electrode materials exhibiting excellent electrochemical performances. In general, solvothermal syntheses allow for the precise control over the size, shape distribution, phase purity and crystallinity of nanostructures.[42, 309] In this chapter, the preparation of nanostructured olivine $LiFe_{1-x}Mn_xPO_4$ (x=0, 0.5 and 1) cathodes *via* a straightforward and conventional solvothermal process using single source "$[M Li_2Br(O^tBu)_4(THF)_2]_n$" ($M$=Fe, Mn) heterometallic alkoxide precursors in ethylene glycol is investigated. Ethylene glycol has been widely used in solvothermal syntheses of $LiFePO_4$ nanoparticles because is a weak reducing agent that prevents the oxidation of Fe^{2+} to Fe^{3+} during the reaction process and helps to ensure the phase purity of the product. Ethylene glycol also has a much higher viscosity than common solvents such as water and ethanol, which slows down the ion diffusion rate and prevents large particle growth.[310-312] Furthermore, ethylene glycol has been shown to be an optimal solvent for the solvothermal synthesis of $LiFePO_4$ nanoparticles with low defect concentration.[313-317] The use of ethylene glycol in the preparation of nanostructured $LiFe_{1-x}Mn_xPO_4$ solid solutions has also been previously reported, with materials exhibiting reversible capacities as high as 153 $mAh \cdot g^{-1}$ for $LiFe_{0.5}Mn_{0.5}PO_4$ nanoplates.[311] In order to demonstrate that the use of such tailored precursors indeed yields materials with enhanced electrochemical performance the same solvothermal reaction conducted using other common and commercially available starting materials was also investigated. Finally, in an effort to demonstrate the versatility of single source heterometallic alkoxide precursors in the generation of both cathode and anode materials, a simple ultrasound-assisted hydrolysis reaction of the $[FeLi_2Br(O^tBu)_4(THF)_2]_n$ heterometallic alkoxide precursor at room temperature was employed to obtain the corresponding metal oxide conversion anode Fe_3O_4 magnetite nanoparticles.

6.2 Results and discussion

6.2.1 Synthesis and characterisation of $LiFe_{1-x}Mn_xPO_4$ and Fe_3O_4 nanostructures prepared from heterometallic alkoxide precursors

Olivine $LiFe_{1-x}Mn_xPO_4$ (x=0, 0.5 and 1) nanostructures were solvothermally synthesised using single source "$[M Li_2Br(O^tBu)_4(THF)_2]_n$" ($M$=Fe, Mn) (IV, VI, VII) heterometallic alkoxide precursors and H_3PO_4 as reactants in ethylene glycol according to Schematic 6.1 and as described in section 2.2.9. For comparison, $LiFePO_4$ powders were

also prepared under the same reaction conditions using the commercially available starting materials $FeSO_4 \cdot 7H_2O$, $LiOH \cdot H_2O$ and H_3PO_4, as described in section 2.2.10. Alongside this, a hydrolysis reaction at room temperature of the $[FeLi_2Br(O^tBu)_4(THF)_2]_n$ (IV) heterometallic alkoxide promoted by ultrasound irradiation was performed in order to obtain Fe_3O_4 magnetite nanostructures (see section 2.211). Table 6.1 lists the solvothermally synthesised $LiFe_{1-x}Mn_xPO_4$ (x=0, 0.5 and 1) cathodes and the conversion anode Fe_3O_4 magnetite nanostructures prepared.

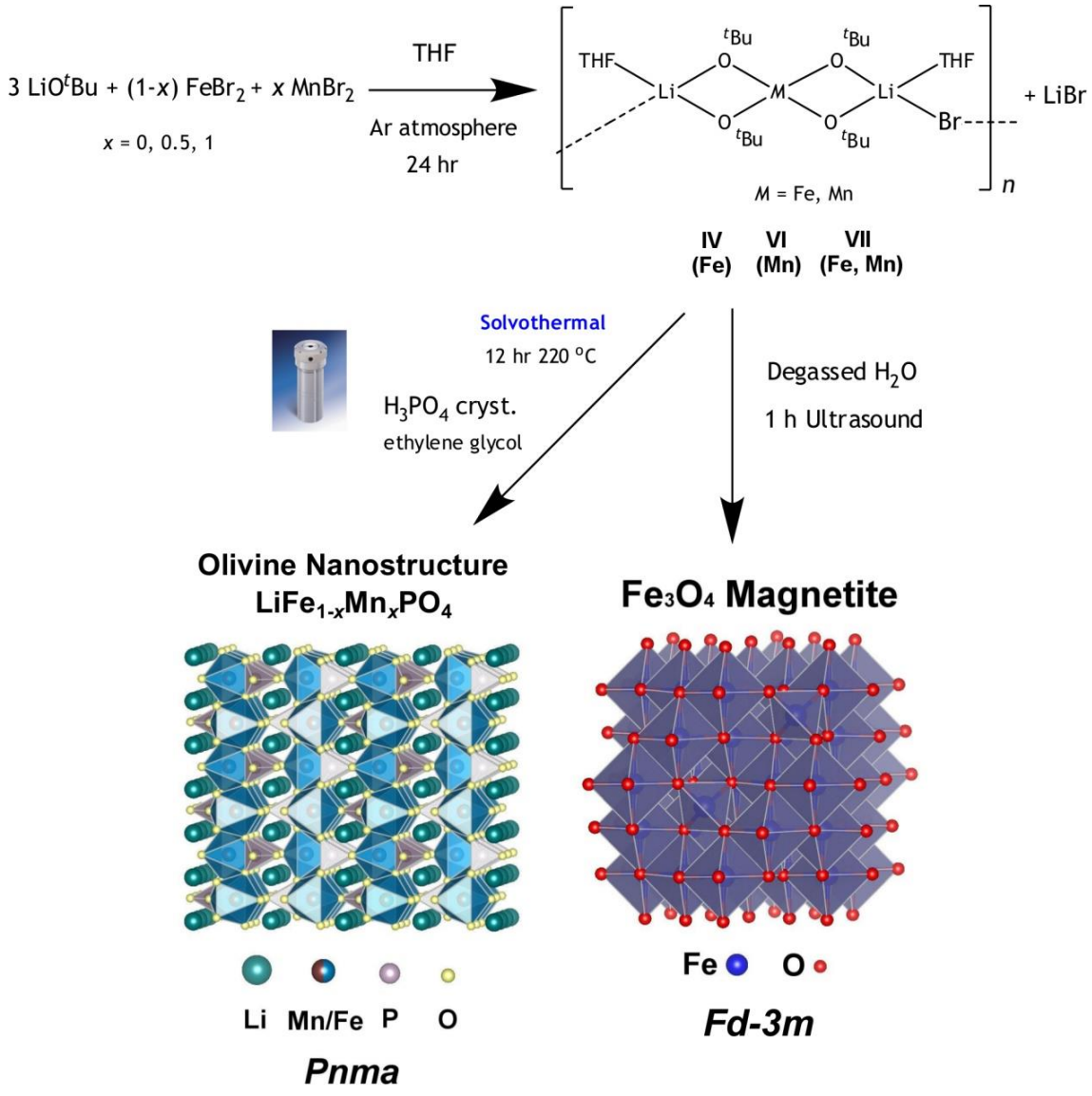

Schematic 6.1. Reaction schematic for the solvothermal synthesis of $LiFe_{1-x}Mn_xPO_4$ (x=0, 0.5 and 1) nanostructures and ultrasound synthesis of Fe_3O_4 nanoparticles using single source heterometallic alkoxide precursors "$[MLi_2Br(O^tBu)_4(THF)_2]_n$" ($M$=Fe, Mn) (IV, VI, VII).

Table 6.1. Preparation of solvothermally synthesised $LiFe_{1-x}Mn_xPO_4$ (x = 0, 0.5 and 1) nanostructures and Fe_3O_4 magnetite.

Samples	Reactants	Reaction conditions
$LiFePO_4$_S_Com._8	$FeSO_4 \cdot 7H_2O$ (0.5560 g, 2 mmol) + 2 $LiOH \cdot H_2O$ (0.1678 g, 4 mmol) + H_3PO_4 (0.1960 g, 2 mmol) + 30 mL EG	Solvothermal synthesis 8 hr at 220 °C
$LiFePO_4$_S_Com._10	$FeSO_4 \cdot 7H_2O$ (0.5560 g, 2 mmol) + 2 $LiOH \cdot H_2O$ (0.1678 g, 4 mmol) + H_3PO_4 (0.1960 g, 2 mmol) + 30 mL EG	Solvothermal synthesis 10 hr at 220 °C
$LiFePO_4$_S_Com._12	$FeSO_4 \cdot 7H_2O$ (0.5560 g, 2 mmol) + 2 $LiOH \cdot H_2O$ (0.1678 g, 4 mmol) + H_3PO_4 (0.1960 g, 2 mmol) + 30 mL EG	Solvothermal synthesis 12 hr at 220 °C
$LiFePO_4$_S_IV_1	$[FeLi_2Br(O^tBu)_4(THF)_2]_n$ (IV) (0.4000 g, 0.68 mmol) + H_3PO_4 (0.0669 g, 0.68 mmol) + 30 mL EG	Solvothermal synthesis 1 hr at 220 °C
$LiFePO_4$_S_IV_4	$[FeLi_2Br(O^tBu)_4(THF)_2]_n$ (IV) (0.4000 g, 0.68 mmol) + H_3PO_4 (0.0669 g, 0.68 mmol) + 30 mL EG	Solvothermal synthesis 4 hr at 220 °C
$LiFePO_4$_S_IV_8	$[FeLi_2Br(O^tBu)_4(THF)_2]_n$ (IV) (0.4000 g,0.68 mmol) + H_3PO_4 (0.0669 g, 0.68 mmol) + 30 mL EG	Solvothermal synthesis 8 hr at 220 °C
$LiFePO_4$_S_IV_10	$[FeLi_2Br(O^tBu)_4(THF)_2]_n$ (IV) (0.4000 g, 0.68 mmol) + H_3PO_4 (0.0669 g, 0.68 mmol) + 30 mL EG	Solvothermal synthesis 10 hr at 220 °C
$LiFePO_4$_S_IV_12	$[FeLi_2Br(O^tBu)_4(THF)_2]_n$ (IV) (0.4000 g, 0.68 mmol) + H_3PO_4 (0.0669 g, 0.68 mmol) + 30 mL EG	Solvothermal synthesis 12 hr at 220 °C
$LiMnPO_4$_S_VI_12 hr	"$[MnLi_2Br(O^tBu)_4(THF)_2]_n$" (VI) (0.4000 g, 0.68 mmol)+ H_3PO_4 (0.0670 g, 0.68 mmol) + 30 mL EG	Solvothermal synthesis 12 hr at 220 °C
$LiFe_{0.5}Mn_{0.5}PO_4$_S_VII_12 hr	"$[Fe_{0.5}Mn_{0.5}(O^tBu)_2(THF)]_n$" (VII) (0.4000 g, 0.68 mmol) + H_3PO_4 (0.0665 g, 0.68 mmol) + 30 mL EG	Solvothermal synthesis 12 hr at 220 °C
Fe_3O_4 magnetite	$[FeLi_2Br(O^tBu)_4(THF)_2]_n$ (IV) + degassed H_2O (6 x 60 mL)	1 hr Ultrasound, room temperature

6.2.1.1 PXRD of $LiFe_{1-x}Mn_xPO_4$ nanostructures prepared from "$[MLi_2Br(O^tBu)_4(THF)_2]_n$" (*M*=Fe, Mn)

Initially, olivine $LiFe_{1-x}Mn_xPO_4$ (x=0, 0.5 and 1) nanostructures were solvothermally synthesised (12 hr, 220 ºC) using single source "$[MLi_2Br(O^tBu)_4(THF)_2]_n$" (*M*=Fe, Mn) (IV, VI, VII) heterometallic alkoxide precursors in ethylene glycol. High resolution PXRD analysis of the $LiFePO_4$_S_IV_12 hr, $LiFe_{0.5}Mn_{0.5}PO_4$_S_VII_12 hr and $LiMnPO_4$_S_VI_12 hr nanostructures conducted at the I11 beamline at the Diamond Light Source indicated that the three samples were isostructural phase pure materials with an olivine structure indexed to the orthorhombic *Pnma* space group. No evidence of impurity phases or phase segregation was observed. PXRD data were fit by Rietveld analysis to $LiFePO_4$ (ICSD No. 01-072-7845) and $LiMnPO_4$ (ICSD No. 01-072-7844) orthorhombic *Pnma* structures[318] in a similar manner to that outlined in Chapter 4. Figure 6.1 shows that a good fit between the experimental data and the calculated model were obtained for these $LiFe_{1-x}Mn_xPO_4$ nanostructures (R_{exp} values of 10-12%). Again, slight shifting of the peaks towards lower angles is observed when comparing $LiMnPO_4$_S_VI_12 hr to $LiFePO_4$_S_IV_12 hr due to the larger Mn^{2+} cation size. The calculated lattice parameters clearly increase with higher Mn content, confirming the successful incorporation of the Mn^{2+} ions in the $LiFePO_4$ olivine structure. Results from the Rietveld analysis are summarised in Table 6.2. Estimation of the crystallite sizes for the $LiFe_{1-x}Mn_xPO_4$ (x=0, 0.5 and 1) nanostructures using the Scherrer equation[208] applied to the (211) peak revealed crystallite sizes of ~35 nm for the three olivine nanophases. A previous report by Saravanan *et al*. showed that temperatures of 290 ºC or above were required to obtain well crystallised $LiMnPO_4$ when using $MnCO_3$ precursor in a conventional solvothermal synthesis in ethylene glycol. Moreover, they also reported that using $Mn(OAc)_2$ required even higher temperatures to afford phase pure $LiMnPO_4$ nanoplates.[311] Therefore, the single source precursor method presented here can substantially decrease reaction temperatures in the solvothermal synthesis of olivine $LiMnPO_4$ without compromising phase purity or particle crystallinity.

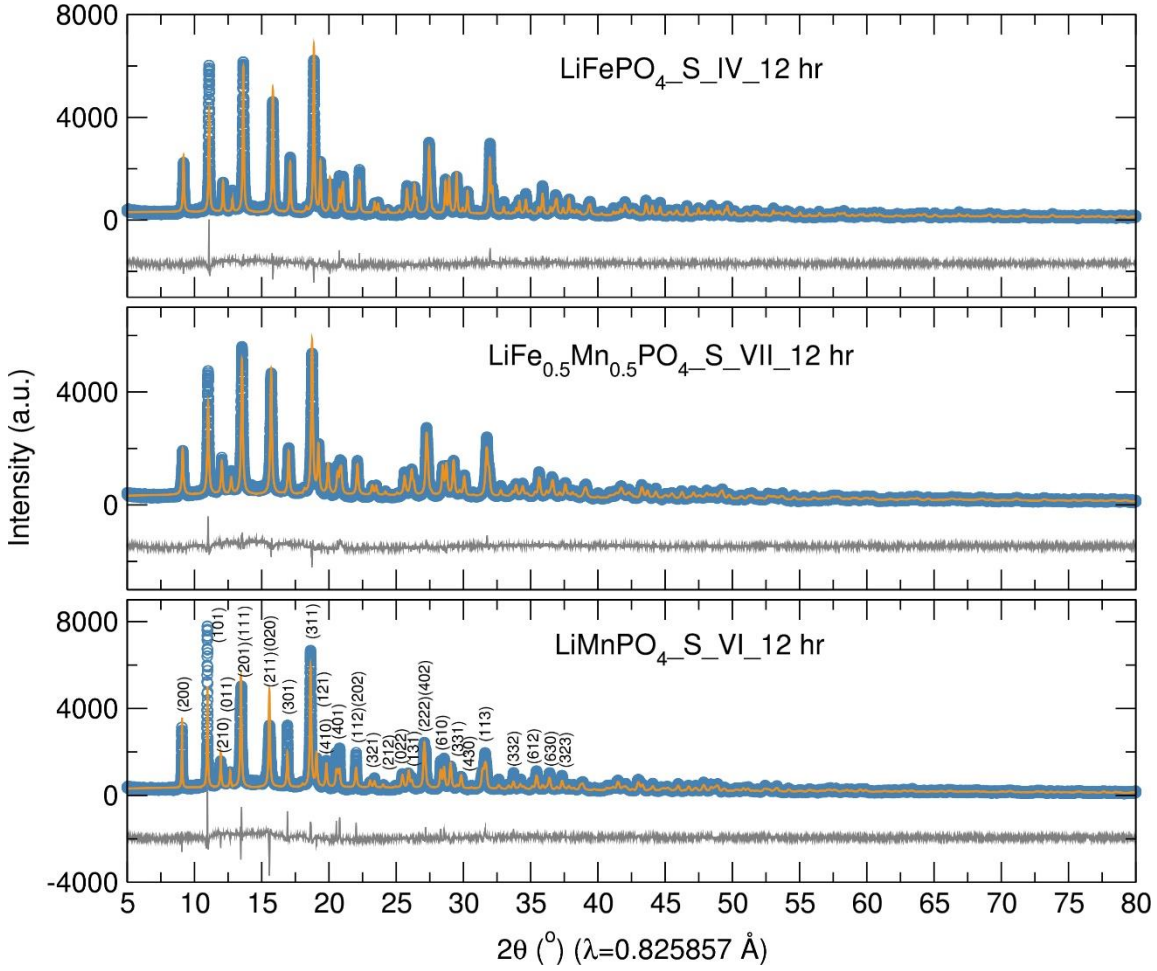

Figure 6.1. Rietveld analysis of high resolution PXRD data of $LiFe_{1-x}Mn_xPO_4$ (x=0, 0.5 and.1) nanostructures prepared through a solvothermal synthesis (12 hr at 220 °C) using single source "$[MLi_2Br(O^tBu)_4(THF)_2]_n$" ($M$=Fe, Mn) (IV, VI, VII) heterometallic alkoxide precursors.

Table 6.2. Calculated lattice parameters from Rietveld refinements for the different $LiFe_{1-x}Mn_xPO_4$ (x=0, 0.5 and 1) nanostructures prepared through a solvothermal synthesis (12 hr at 220 °C) using single source "$[MLi_2Br(O^tBu)_4(THF)_2]_n$" ($M$=Fe, Mn) (IV, VI, VII) heterometallic alkoxide precursors.

Sample	$LiFePO_4$_S_IV_12 hr	$LiFe_{0.5}Mn_{0.5}PO_4$_S_VII_12 hr	$LiMnPO_4$_S_VI_12 hr
Space group	*Pnma*	*Pnma*	*Pnma*
a (Å)	10.3139(1)	10.3867(2)	10.4460(2)
b (Å)	5.99802(6)	6.04582(9)	6.0966(1)
c (Å)	4.69870(5)	4.72886(7)	4.7493(1)
V (Å^{-3})	290.676(5)	296.955(8)	302.61 (1)
R_{wp}	23.5 %	23.2 %	33.8 %
R_{exp}	11.09 %	10.97 %	12.03 %
X^2	4.50	4.46	7.89

The effect of reaction time on the quality of the resulting products was also investigated using the $[FeLi_2Br(O^tBu)_4(THF)_2]_n$ (IV) single source heterometallic alkoxide precursor over 8 and 10 hr at 220 °C. Rietveld refinements of the PXRD data indicate that phase pure

$LiFePO_4$ nanostructures were obtained at both reaction times (Figure 6.2). It was found that the diffraction peak at $2\theta=30^\circ$ corresponding to the (020) or (211) direction became slightly more intense with longer reactions times. This may be indicative of increased regularity in the horizontal arrangement of the $LiFePO_4$ nanoplates with exposed (020) (corresponding also to (010) face) or (211) faces with longer processing times, as previously reported by Nan *et al.*[313] These results are also in agreement with previous studies conducted by Qin *et al.*, where they demonstrate preferential adsorption of ethylene glycol molecules in the (010) faces of the $LiFePO_4$ crystals inhibiting the growth along the [010] direction.[317] This would effectively reduce the path length of Li^+ ion diffusion and electronic conduction due to the decreased thickness along the [010] direction, thereby resulting in a higher Li^+ ion diffusion coefficient and electronic conductivity. Table 6.3 summarises the calculated lattice parameters from Rietveld refinements for the $LiFePO_4$ nanostructures prepared at different reaction times, indicating that longer processing times leads to a slight decrease in the unit cell parameters. The observed lattice volume contraction could be ascribed to a reduced extent of Fe^{2+} disorder on the Li^+ sites.[138, 319] Estimation of the crystallite sizes from the Scherrer equation applied to the (211) diffraction peak for the $LiFePO_4$_S_IV_12 hr, $LiFePO_4$_S_IV_10 hr and $LiFePO_4$_S_IV_8 hr nanoparticles suggests a slight decrease in the crystallite size with longer reaction times, with crystallite sizes ~35, 44 and 56 nm, respectively. From the solvothermal reactions for 1 and 4 hr at 220 ºC using the heterometallic alkoxide precursor $[FeLi_2Br(O^tBu)_4(THF)_2]_n$ (IV), the crystallisation of the Li_3PO_4 phase was observed after 1 hr. However, after 4 hr of solvothermal treatment, poorly crystalline olivine $LiFePO_4$ was formed (Figure 6.3). These results suggest that PO_4^{3-} groups in the solution mixture may more readily react with Li^+ ions than with Fe^{2+}, since most of the Fe^{2+} ions may be coordinated by ethylene glycol molecules to form complexes, leading to the initial formation of Li_3PO_4 product. Ethylene glycol molecules exist in long hydrogen bonded chains, which may trap cations in the reaction mixture. It has previously been reported that Li_3PO_4 impurities are commonly formed along with partially crystallised olivine $LiFePO_4$ when low temperatures are used in the solvothermal synthesis of $LiFePO_4$.[311, 312] This study confirms that the crystallisation of $LiFePO_4$ in conventional solvothermal process phases takes place slower than in microwave-assisted methods, as in previous chapters the formation of olivine $LiFePO_4$ has been demonstrated after only 10 min at 240 ºC under microwave irradiation.

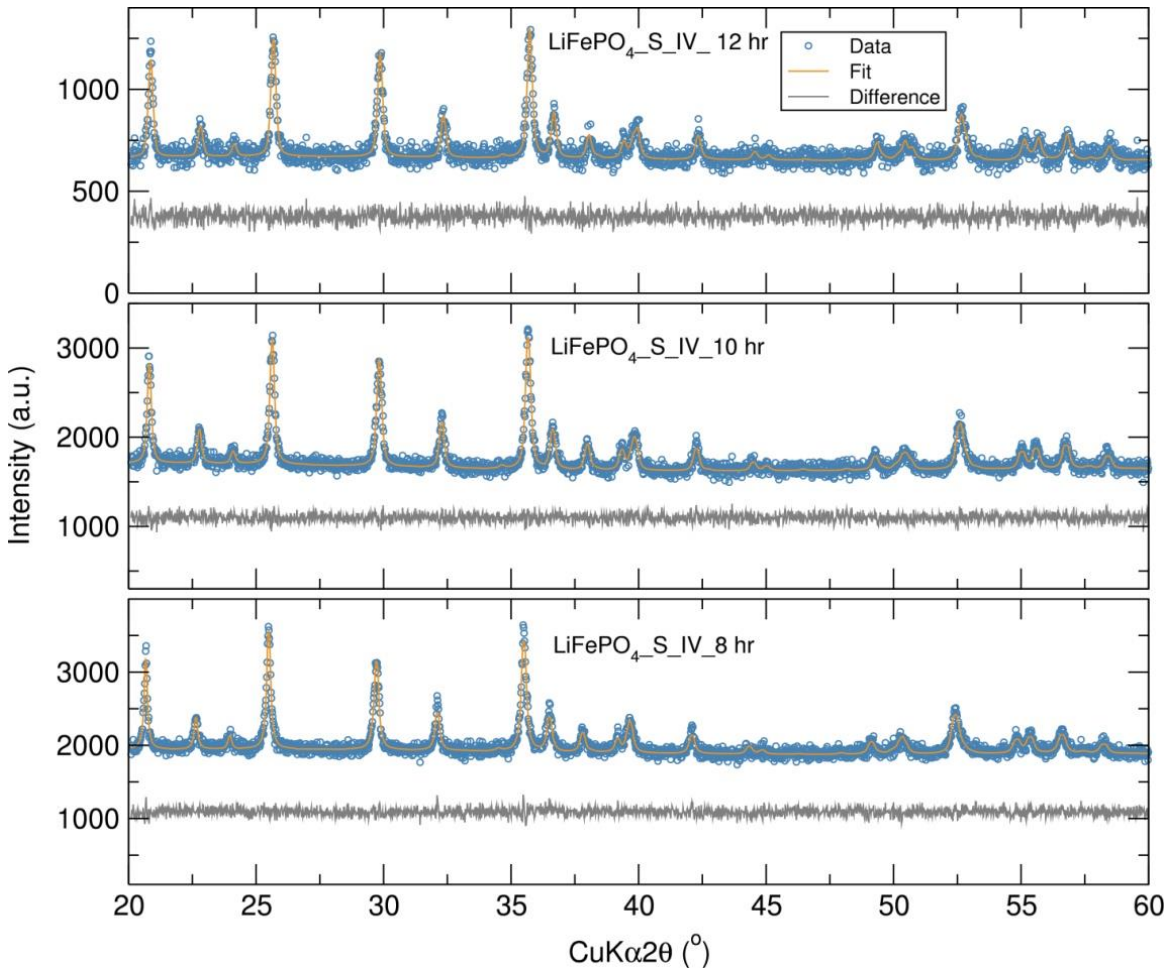

Figure 6.2. Rietveld analysis of PXRD data of $LiFePO_4$ nanostructures prepared at different reaction times (8, 10 and 12 hr) through a solvothermal synthesis at 220 °C using $[FeLi_2Br(O^tBu)_4(THF)_2]_n$ (IV) heterometallic alkoxide precursor.

Table 6.3. Calculated lattice parameters from Rietveld refinements for the different $LiFePO_4$ nanostructures prepared through a solvothermal synthesis at 220 °C using $[FeLi_2Br(O^tBu)_4(THF)_2]_n$ (IV) heterometallic alkoxide precursor at different reaction times.

Sample	$LiFePO_4$_S_IV_12 hr	$LiFePO_4$_S_IV_10 hr	$LiFePO_4$_S_IV_8 hr
pace group	*Pnma*	*Pnma*	*Pnma*
a (Å)	10.310(2)	10.3349(5)	10.3583(6)
b (Å)	5.997(1)	6.0042(3)	6.0051(4)
c (Å)	4.695(1)	4.7067(4)	4.7130(4)
V ($Å^{-3}$)	290.28(9)	292.06(3)	293.16(4)
R_{wp}	36.4 %	25.3 %	27.4 %
R_{exp}	34.41 %	24.01 %	24.44 %
X^2	1.12	1.11	1.25

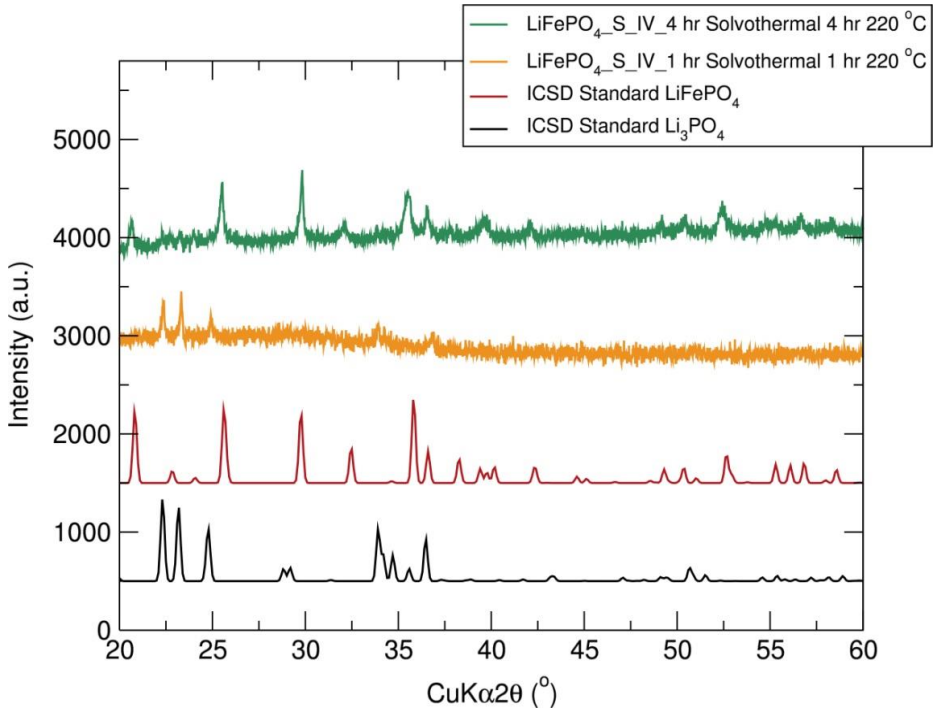

Figure 6.3. PXRD data of $LiFePO_4$ nanostructures prepared at different reaction times (1 and 4 hr) through a solvothermal synthesis at 220 ºC using single source $[FeLi_2Br(O^tBu)_4(THF)_2]_n$ (IV) heterometallic alkoxide precursor.

6.2.1.2 PXRD of $LiFePO_4$ nanostructures prepared from commercial starting materials

In order to compare materials obtained from single source precursors with those obtained from common commercial starting materials, $LiFePO_4$ phases were prepared through a similar solvothermal process under the same reaction conditions (8, 10 and 12 hr at 220 ºC) in an autoclave using $FeSO_4{\cdot}7H_2O$, $LiOH{\cdot}H_2O$ and H_3PO_4 in ethylene glycol. Rietveld analysis of the PXRD data of the $LiFePO_4$_S_Com._8 hr, $LiFePO_4$_S_Com._10 hr and $LiFePO_4$_S_Com._12 hr samples prepared from commercial starting materials at 8, 10 and 12 hr, respectively, confirmed that single phase olivine nanostructured $LiFePO_4$ phases were formed (Figure 6.4). Results from the Rietveld analysis revealed a slight decrease in the lattice parameters of the $LiFePO_4$ phase prepared through the single source precursor route in comparison to the $LiFePO_4$ product from the conventional synthesis employing commercially available starting materials (Table 6.4). This reduction in the lattice parameters could potentially enhance the cycling performance of these olivine nanophases, as the Li^+ hopping process takes place along the *b* axis and shorter Li-Li distances are desirable to facilitate the Li^+ diffusion. The estimated crystallite sizes using the Scherrer equation[208] for the $LiFePO_4$_S_Com._8 hr, $LiFePO_4$_S_Com._10 hr and $LiFePO_4$_S_Com._12 hr nanostructures were calculated to be 44, 43 and 65 nm, respectively. These results suggest that longer reaction times may favour crystal growth affording larger particle sizes. It must also be noted that the presented single source precursor solvothermal route using heterometallic alkoxide precursors yielded smaller

particles than those obtained using conventional starting materials (35 nm for $LiFePO_4$_S_IV_12 hr *vs*. 65 nm for $LiFePO_4$_S_Com._12 hr), suggesting that alkoxide based single source precursor processes are a promising synthetic approach for the generation of nanosized functional materials.

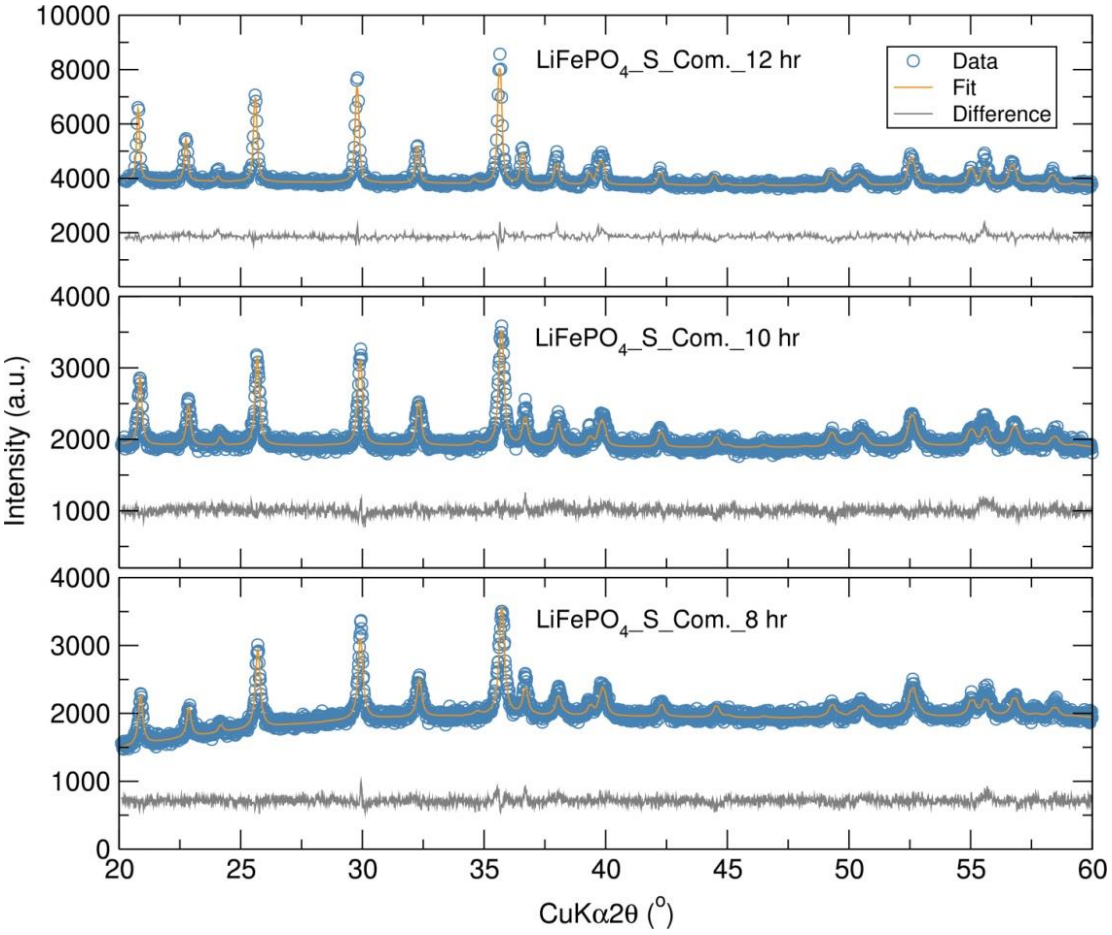

Figure 6.4. Rietveld analysis of PXRD data of $LiFePO_4$ nanostructures prepared through a solvothermal synthesis at 220 °C for different reaction times (8, 10 and 12 hr) using commercial starting materials.

Table 6.4. Calculated lattice parameters from Rietveld refinements for the different $LiFePO_4$ nanostructures prepared through a solvothermal synthesis at 220 °C for different reaction times (8, 10 and 12 hr) using commercial starting materials.

Sample	$LiFePO_4$_S_Com._12 hr	$LiFePO_4$_S_Com._10 hr	$LiFePO_4$_S_Com._8 hr
Space group	*Pnma*	*Pnma*	*Pnma*
a (Å)	10.330(1)	10.345(1)	10.350(1)
b (Å)	6.0078(7)	6.0063(9)	6.010(1)
c (Å)	4.7060(7)	4.717(1)	4.717(1)
V (Å^{-3})	292.05(6)	293.08(9)	293.43(9)
R_{wp}	20.4 %	29.2 %	28.6 %
R_{exp}	15.32 %	24.39 %	24.89 %
X^2	1.78	1.44	1.32

6.2.1.3 Electron microscopy of $LiFe_{1-x}Mn_xPO_4$ nanostructures prepared from "$[MLi_2Br(O^tBu)_4(THF)_2]_n$" (*M*=Fe, Mn)

High resolution SEM images of the $LiFePO_4$_S_IV_12 hr sample revealed non-uniform rectangular platelets with sizes ranging from 40 to 80 nm width (Figure 6.5(a)). Slightly smaller particles (~20-50 nm) with similar shape to the $LiFePO_4$_S_IV_12 hr nanoparticles were obtained for $LiFe_{0.5}Mn_{0.5}PO_4$_S_VII_12 hr powders (Figure 6.5(b)). However, the $LiMnPO_4$_S_VI_12 hr sample was a mixture of bigger platelets of approximately ~400-600 nm in length and 150-200 nm in width, and quasi-spherical nanoparticles of around 20-40 nm (Figure 6.6(c)). This highlights the strong influence of the transition metal on the resulting particle size and morphology. SEM micrographs of the $LiFePO_4$_S_Com._12 hr powders synthesised from commercial starting materials shown in Figure 6.6 (d) were markedly larger spindle-shaped plates with particle sizes of ~1 µm in length and approximately 500 nm in width. These results confirmed the suitability of single source processes employing metal alkoxide precursors for the generation of nanoparticulate materials. Interestingly, the presented solvothermal process for $LiFe_{1-x}Mn_xPO_4$ olivines using heterometallic alkoxide precursors "$[MLi_2Br(O^tBu)_4(THF)_2]_n$" (*M*=Fe, Mn) (IV, VI, VII) [12 hr, 220 °C] also afforded slightly larger particles than the fast microwave treatments (15 min 80 °C and 10 min 240 °C) of a similar reaction mixture. These results could be ascribed to the fact that increased reaction times favours particle growth. Similar rectangular $LiFePO_4$ nanoplates and oval-shaped plates have been observed in solvothermally synthesised $LiFePO_4$ nanoparticles using ethylene glycol. In particular, Huang *et al*. studied the morphology evolution of solvothermally synthesised $LiFePO_4$ powders primarily by varying the $LiOH/H_3PO_4$ molar ratio and consequently the reaction acidity. They reported that predominantly rectangular $LiFePO_4$ particles with (100) exposed faces gradually changed to spindle shaped particles with mainly (010) exposed faces when decreasing solution acidity, as shown in Figure 6.6. This is also in agreement with what is observed here, as a higher pH is possible during the preparation of $LiFePO_4$_S_Com._12 hr due to the utilisation of $LiOH{\cdot}H_2O$ in the synthesis. This afforded oval-shaped particles, while the lower pH when employing the heterometallic alkoxide precursor $[FeLi_2Br(O^tBu)_4(THF)_2]_n$ yielded more rectangular nanoplates.

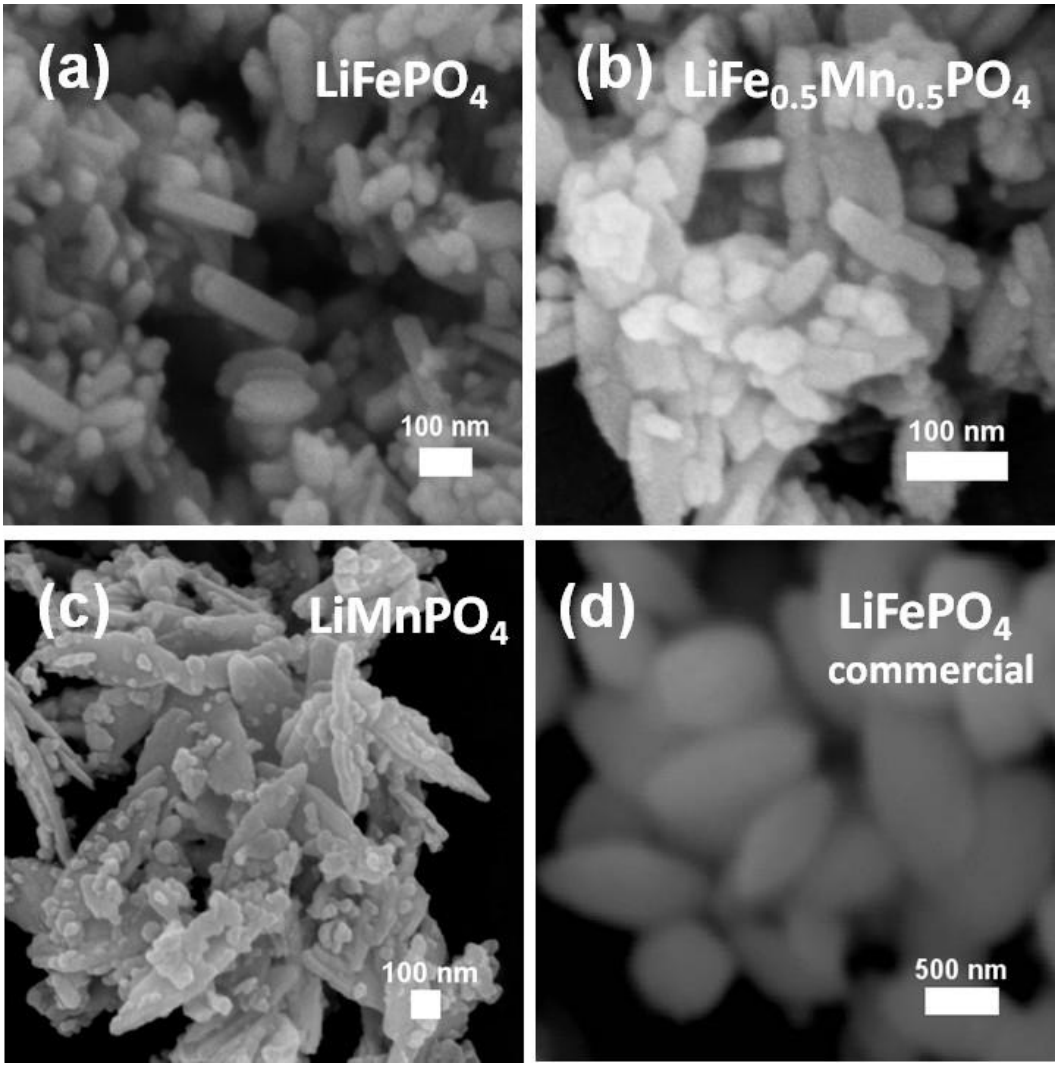

Figure 6.5. High resolution SEM images of **(a)** $LiFePO_4$_S_IV_12 hr, **(b)** $LiFe_{0.5}Mn_{0.5}PO_4$_S_VII_12 hr and **(c)** $LiMnPO_4$_S_VI_12 hr nanostructures prepared through a solvothermal synthesis (12 hr at 220 °C) using heterometallic alkoxide precursors "$[ML_2Br(O^tBu)_4(THF)_2]_n$" (*M*=Fe, Mn) (IV, VI, VII). **(d)** $LiFePO_4$ sample prepared through a solvothermal synthesis (12 hr at 220 °C) using commercial starting materials.

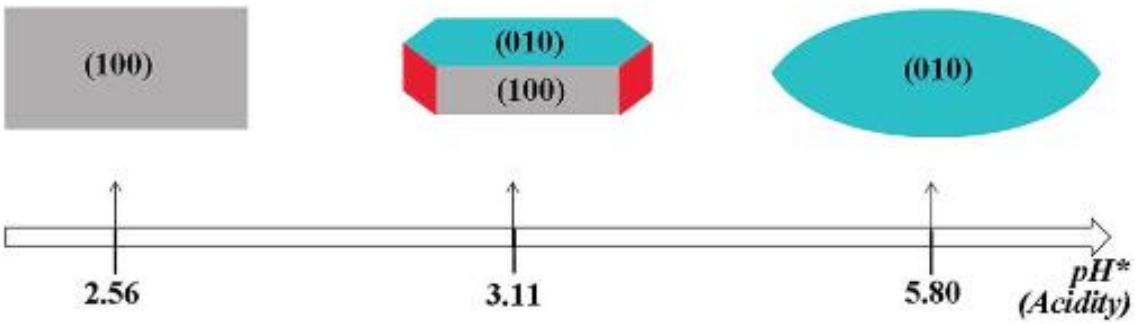

Figure 6.6. Particle morphology evolution of $LiFePO_4$ with the acidity (pH) of the solvothermal synthesis environment. Rectangular nanoplates with main exposed (100) face gradually change to spindle plates predominantly exposed (010) face as pH of mother solutions increases from 2.56 to 5.80.[312]

High resolution TEM images of the $LiFePO_4$_S_IV_12 hr powders confirmed platelet-like particles with a wide range of sizes from 50 to 150 nm in length. The $LiFe_{0.5}Mn_{0.5}PO_4$_S_VII_12 hr particles were slightly smaller platelets. The $LiMnPO_4$_S_VI_12 hr nanostructures adopted an oval shaped morphology with sizes of around 1 μm in length and 200-400 in width (Figure 6.7). The visible lattice fringes in the TEM images confirmed the long range crystallographic nature of these $LiFe_{1-x}Mn_xPO_4$ (x=0, 0.5 and 1) and suggested that uniform crystal structures exist over the imaged areas. The HR TEM fringe spacings for the $LiFePO_4$_S_IV_12 hr, $LiFe_{0.5}Mn_{0.5}PO_4$_S_VII_12 hr and $LiMnPO_4$_S_VI_12 hr nanostructures are 0.46, 0.52 and 1.13 nm, corresponding to the (002), (220) and (101) planes, respectively. SAED over the imaged areas produced a pattern consistent with polycrystalline structures belonging to the *Pnma* space group. The $LiFe_{1-x}Mn_xPO_4$ nanoparticles showed no complete and uniform amorphous coatings over all the paricles. However, where there is an amorphous coating, it is not continuous and is around 2 nm thick.

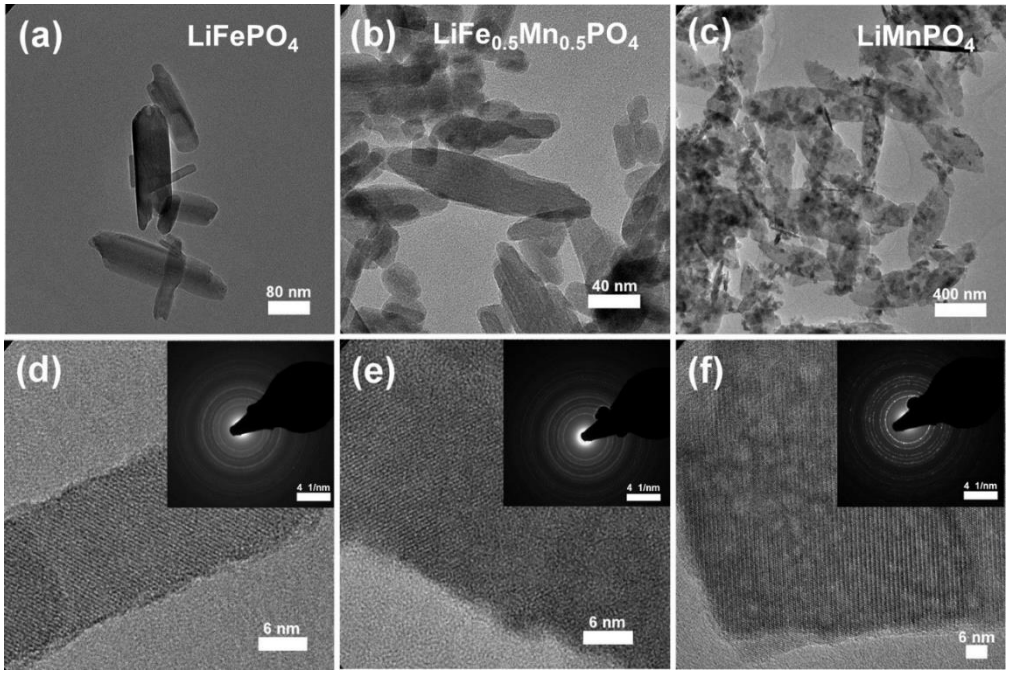

Figure 6.7. High resolution TEM images of **(a, d)** $LiFePO_4$_S_IV_12 hr, **(b, e)** $LiFe_{0.5}Mn_{0.5}PO_4$_S_VII_12 hr, and **(c, f)** $LiMnPO_4$_S_VI_12 hr nanostructures prepared through a solvothermal synthesis (12 hr at 220 °C) using heterometallic alkoxide precursors "$[MLi_2Br(O^tBu)_4(THF)_2]_n$" ($M$=Fe, Mn) (IV, VI, VII).

6.2.1.4 Electrochemical performance of $LiFe_{1-x}Mn_xPO_4$ nanostructures from "$[MLi_2Br(O^tBu)_4(THF)_2]_n$" ($M$=Fe, Mn)

Galvanostatic cycling at room temperature of the C/$LiFe_{1-x}Mn_xPO_4$ (x=0, 0.5 and 1) powders (carbon coated with 15% wt. C from sucrose) were conducted over the voltage range from 2.2 V to 4.0, 4.3 and 4.5 V (depending on the Mn content) and at a C/20 rate. From the galvanostatic cycling test at C/20 rate of the C/$LiFePO_4$_S_IV_12 hr sample in

Figure 6.8 (a) and (b) it can be observed that discharge capacities of approximately 175 $mAh \cdot g^{-1}$ are reached during the cycling process over at least the first 20 cycles with no capacity fading. The slightly higher than theoretical capacity observed for the $C/LiFePO_4$ nanostructures could be attributed to the additional carbon content present in this electrode material, which could be contributing to the reversible intercalation of Li^+ ions. A test battery using only carbon black (no other active material) demonstrated that small amounts on lithium can be reversibly inserted and extracted from the carbon black (see Figure A6.1). Figure 6.8 (c) and (d) depict the voltage-capacity profile of the $C/LiFe_{0.5}Mn_{0.5}PO_4$_S_VII_12 hr sample, indicating that capacities around 140 $mAh \cdot g^{-1}$ were delivered over the first 20 charge/discharge cycles. The discharge curve showed two voltage plateaus at approximately 3.45 V and 4.10 V corresponding to the reduction from Fe^{3+} to Fe^{2+} and from Mn^{3+} to Mn^{2+}, respectively. The relative capacities on the Fe^{3+}/Fe^{2+} and Mn^{3+}/Mn^{2+} plateaus correspond closely with the Fe/Mn ratio of the $LiFe_{0.5}Mn_{0.5}PO_4$ sample. This electrochemical behaviour is in agreement with previous reports for $LiFe_{0.5}Mn_{0.5}PO_4$ nanostructures.[277, 320, 321] Finally, Figure 6.8 (e) and (f) show the electrochemical performance of the $C/LiMnPO_4$_S_VI_12 hr nanostructures at C/20 over a voltage range from 2.2 V to 4.5 V, which exhibited an initial discharge capacity of 160 $mAh \cdot g^{-1}$ which faded to 120 $mAh \cdot g^{-1}$ after the first five charge/discharge cycles. After that, a more moderate decrease of the discharge capacities was observed, reaching 115 $mAh \cdot g^{-1}$ after the 20^{th} cycle. This capacity loss of the $C/LiMnPO_4$_S_VI_12 hr sample during the cycling process is generally attributed to the existence of Mn^{3+} ions in delithiated $MnPO_4$, which triggers a Jahn-Teller distortion and the associated volume and cell distortions leading to a gradual mechanical degradation during cycling. Low coulombic efficiencies can be attributed to electrolyte decomposition under high voltages. This $C/LiMnPO_4$_S_VI_12 hr nanostructure displayed an improved electrochemical performance compared to a $C/LiMnPO_4$ composite synthesised *via* an ion exchange method using citric acid as the carbon source and reducing agent, which only delivered discharge capacities of 70 $mAh \cdot g^{-1}$ at a C/20 rate.[322] Moreover, these $C/LiFe_{1-x}Mn_xPO_4$ nanophases demonstrated superior cycling performance compared to similarly synthesised $C/LiMnPO_4$ and $C/LiFe_{0.5}Mn_{0.5}PO_4$ samples prepared also in ethylene glycol, which delivered 47 $mAh \cdot g^{-1}$ and 65 $mAh \cdot g^{-1}$ at C/10 rate, respectively.[323]

The rate behaviour of the $C/LiFe_{1-x}Mn_xPO_4$ nanophases was also investigated to examine the rate capabilities as a function of Mn content, particle morphology and synthetic methodology. Figure 6.10 shows that the discharge capacities of the $C/LiFe_{1-x}Mn_xPO_4$ nanostructures progressively decrease with increasing C rates, with the most pronounced effect seen for the $C/LiMnPO_4$_S_VI_12 hr sample. High C rates of up to 10 C delivered discharge capacities of 100 $mAh \cdot g^{-1}$, 55 $mAh \cdot g^{-1}$ and 30 $mAh \cdot g^{-1}$ for the $C/LiFePO_4$_S_IV_12 hr, $C/LiFe_{0.5}Mn_{0.5}PO_4$_S_VII_12 hr and $C/LiMnPO_4$_S_VI_12 hr phases, respectively. The

C/$LiFePO_4$_S_IV_12 hr exhibited an outstanding rate capability delivering ~170 mAh·g^{-1} at C/2, ~150 mAh·g^{-1} at 2 C and ~135 mAh·g^{-1} at 5 C. Time-resolved *in situ* PXRD studies conducted by Grey *et al.* revealed the existence of a continuous metastable solid solution phase in nanoparticulate $LiFePO_4$ during rapid Li^+ extraction/insertion, providing a nonequilibrium facile phase transformation route for reaching such high rate performances in this electrode material that operate *via* two phase reactions.[63] The C/$LiFePO_4$_S_IV_12 hr nanostructure presented here exhibited slightly improved rate capabilities compared to the microwave synthesised C/$LiFePO_4$_I sample prepared using the homometallic alkoxide precursor $[Fe(O^tBu)_2(THF)]_2$ (I) (presented in Chapter 4). Comparable rate capabilities have been previously reported in hollow and porous $LiFePO_4$ nanostructures prepared by similar solvothermal processes.[41, 324] A novel microwave-solvothermal process at 300 ºC to $LiFePO_4$ nanorods followed by a carbon coating with a heat treatment with sucrose at 700 ºC for 1 hr similar to the one performed here displayed similar rate capabilities (~100 mAh·g^{-1} at 10 C) to C/$LiFePO_4$_S_IV_12 hr,[325] evidencing the suitability of using single source metal alkoxide precursors for the fabrication of high rate performing olivine $LiFePO_4$ nanophases. On the other hand, the C/$LiMnPO_4$_S_VI_12 hr nanocomposite displayed a poorer rate performance, in which the discharge capacities markedly faded from ~150 mAh·g^{-1} at C/10 to ~90 mAh·g^{-1}, 50 mAh·g^{-1} and 35 mAh g^{-1} at C/2, 2 C and 5 C, respectively. A simple one-pot solvothermal approach to synthesise nanosized $LiMnPO_4$ by using Li_3PO_4 nanorods and $MnSO_4{\cdot}H_2O$ as precursors delivered slightly lower discharge capacities of 147 mAh·g^{-1} at 0.05 C and 46.6 mAh·g^{-1} at C rate.[326] Even more sophisticated $LiMnPO_4$ thin nanoplate/graphene composites synthesised by a solvothermal method in a mixed solvent of water and polyethylene glycol delivered comparable capacities of 149 mAh·g^{-1} at 0.1 C, 90 mAh·g^{-1} at C and 64 mAh·g^{-1} at 5 C charge-discharge rate.[327] These electrochemical studies suggested that introducing Mn in this olivine $LiFePO_4$ nanostructure synthesised from a solvothermal route using a heterometallic alkoxide precursor afforded a noticeable decrease in the rate behaviour of the electrode material C/$LiFe_{0.5}Mn_{0.5}PO_4$. The C/$LiFe_{0.5}Mn_{0.5}PO_4$_S_VII_12 hr phase displayed discharge capacities near 155 mAh·g^{-1} at C/10, C/5 and C/2, after which dropped to ~140 mAh g^{-1}, 115 mAh·g^{-1} and ~75 mAh·g^{-1} at C, 2 C and 5 C, respectively. Similar rate behaviour has previously been observed in $LiFe_{0.5}Mn_{0.5}PO_4$ nanoplates (43 mAh·g^{-1} at 13 C) prepared by a simple solvothermal synthesis in ethylene glycol.[311] The outstanding electrochemical performance delivered by these C/$LiFe_{1-x}Mn_xPO_4$ phases could be mainly attributed to the smaller particle sizes of these olivine structures, which markedly increases the specific surface area in contact with the electrolyte and also decreases the path length for the Li^+ to diffuse. There is also a possibility for residual amorphous carbon from the decomposition of the metal alkoxide precursors during the solvothermal synthesis and post-heat treatment which may enhance the electron

conductivity of these battery materials and consequently lead to improved cycling behaviour. Nevertheless, due to the simplicity of the single source precursor approach presented here using heterometallic alkoxides, there is still a wide range of synthetic strategies that can be applied in order to improve the electrochemical behaviour of these olivine $LiFe_{1-x}Mn_xPO_4$ nanomaterials. For example, slightly improved rate capabilities for $LiFe_{0.5}Mn_{0.5}PO_4$ nanophases have been recently demonstrated in a $LiFe_{0.5}Mn_{0.5}PO_4$/C composite with macro/nano hierarchical porous structure fabricated *via* a more sophisticated spray dry process, which delivered discharge capacities of 161, 160, 157, 146, 137, and 115 $mAh \cdot g^{-1}$ at 0.2, 0.5, 1, 3, 5, and 10 C, respectively.[238] Also, $LiFe_{0.4}Mn_{0.6}PO_4$/C microspheres produced using a double carbon coating process displayed excellent rate capabilities of 132, 103, and 72 mAh g^{-1} at 5, 10, and 20 C, respectively.[328] Furthermore, a cathode material based on C/$LiFe_{0.4}Mn_{0.6}PO_4$ and conducting composite binder poly(3,4-ethylenedioxythiopene):poly(styrenesulfonate)/carboxymethylcellulose (PEDOT:PSS/CMC) showed excellent rate behaviour yielding discharge capacities of 130 $mAh \cdot g^{-1}$ at 5 C and 118 $mAh \cdot g^{-1}$ at 10 C.[329] Improved rate capabilities have also been observed in $LiMn_{0.75}Fe_{0.25}PO_4$ nanorods grown in graphene sheets, which delivered 132 $mAh \cdot g^{-1}$, 107 $mAh \cdot g^{-1}$ and 65 mAh g^{-1} at 30 C, 50 C and 100 C, respectively.[330]

The rate performance of the C/$LiFePO_4$_S_Com._12 hr (15% C from sucrose) sample prepared from commercial starting materials was also investigated for comparison. Results from the galvanostatic cycling tests at different C rates included in Figure 6.9 confirmed the enhanced rate capability of the $LiFePO_4$ olivine material generated through the single source reaction using heterometallic alkoxides. These results clearly evidence the improved electrochemical performance that can be achieved by employing single source precursor processes with thermally labile starting materials such as alkoxide compounds. PXRD analysis of the C/$LiFePO_4$_S_IV_12 hr, C/$LiFe_{0.5}Mn_{0.5}PO_4$_S_VII_12 hr and C/$LiMnPO_4$_S_VI_12 hr cycled materials in the discharge state indicated that the extraction/insertion process did not degrade the olivine structure, confirming the good structural stability of these positive insertion electrodes upon cycling at high charge-discharge rates. Figure 6.10 depicts the Rietveld analysis of the PXRD data from post-cycled C/$LiFe_{1-x}Mn_xPO_4$ nanostructures. The quality of the PXRD patterns is affected by the high amorphous carbon content in the electrode, however, the cell parameters could be refined. Results suggested that no significant variation in the lattice parameters of these olivine nanostructures was observed after the cycling experiments. Furthermore, the increase in the cell parameters with higher Mn content in C/$LiFe_{1-x}Mn_xPO_4$ nanophases was still evident after the cycling process. Table 6.5 shows the crystallographic data of the post-cycled C/$LiFe_{1-x}Mn_xPO_4$ nanostructures determined by Rietveld analysis.

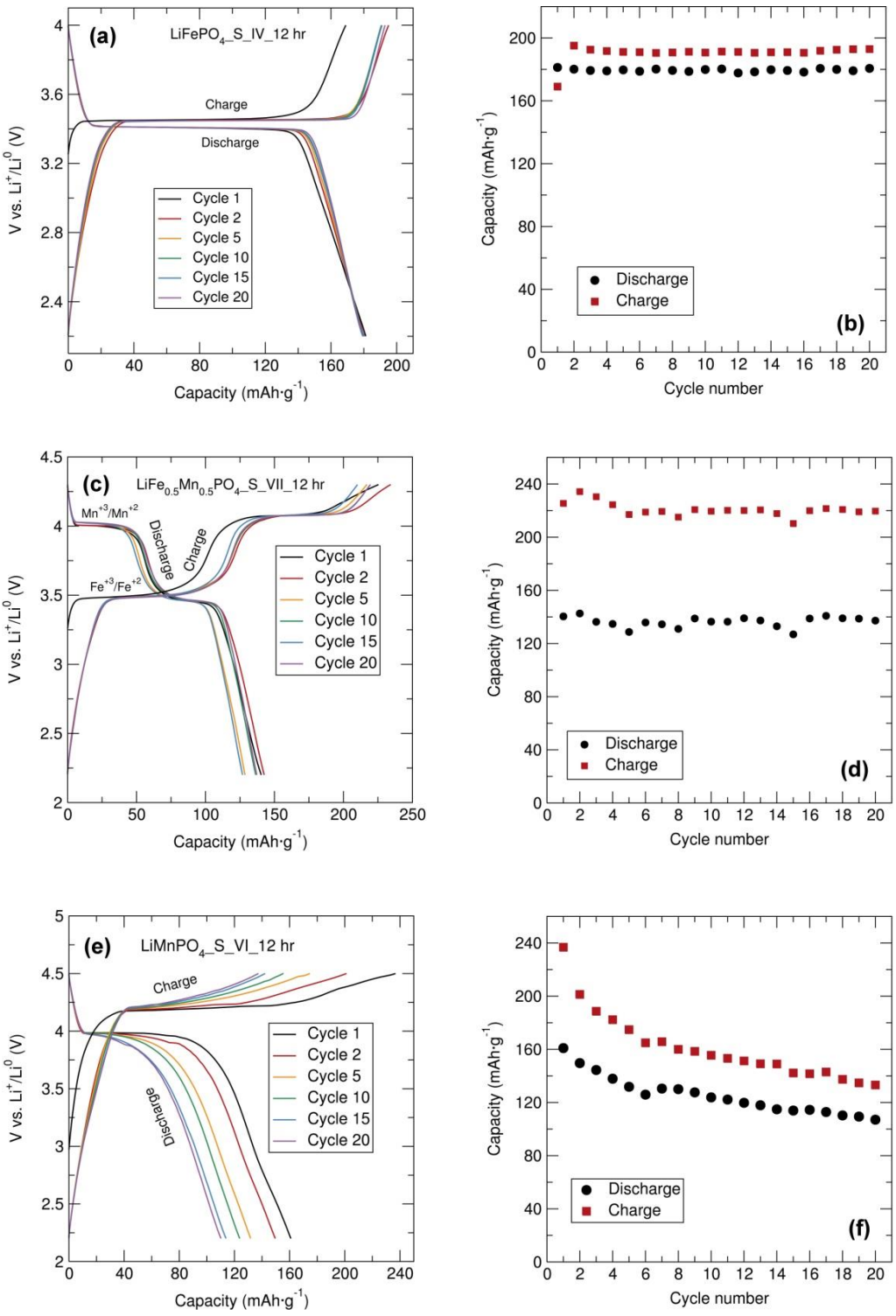

Figure 6.8. Voltage capacity profiles and cycling stability between 2.2 V and 4.0, 4.3 or 4.5 V at C/20 rate of **(a, b)** C/$LiFePO_4$_S_IV_12 hr (15% wt. C from sucrose), **(c, d)** C/$LiFe_{0.5}Mn_{0.5}PO_4$_S_VII_12 hr (15% wt. C from sucrose), and **(e, f)** C/$LiMnPO_4$_S_VI_12 hr (15% wt. C from sucrose). Samples prepared through a solvothermal synthesis for 12 hr at 220 ºC with "$[MLi_2Br(O^tBu)_4(THF)_2]_n$" (*M*=Fe, Mn) (IV, VI, VII) heterometallic alkoxide precursors and mixed with C black and PTFE in 60:30:10 (% wt. ratio).

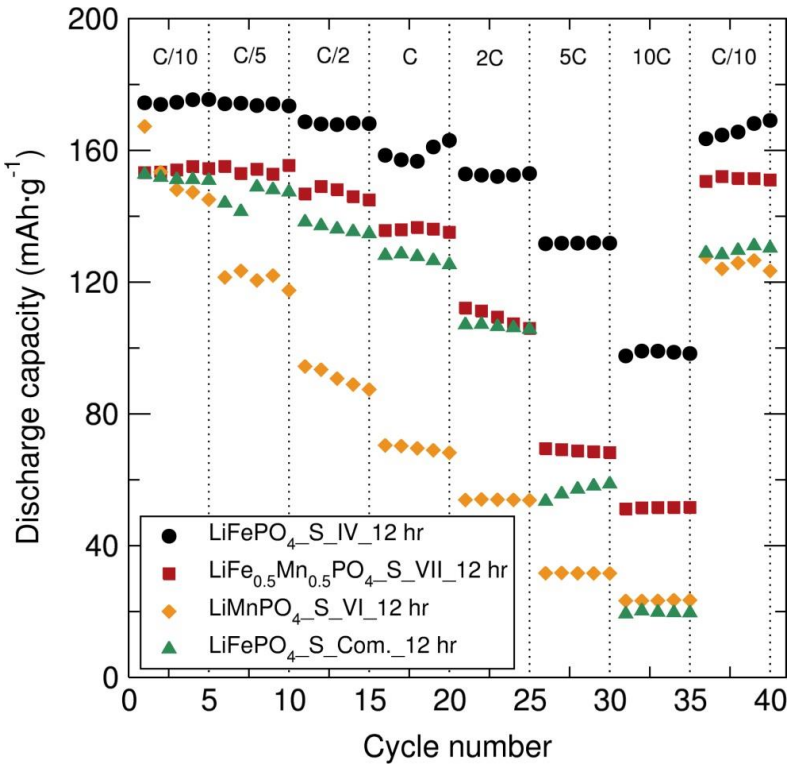

Figure 6.9. Comparative rate performance of C/$LiFe_{1-x}Mn_xPO_4$ (15% wt. C from sucrose) nanostructures prepared with "$[MLi_2Br(O^tBu)_4(THF)_2]_n$" (*M*=Fe, Mn) (IV, VI, VII) heterometallic alkoxide precursors and C/$LiFePO_4$_S_Com._12 hr (15% wt. C from sucrose) sample prepared from commercial starting materials.

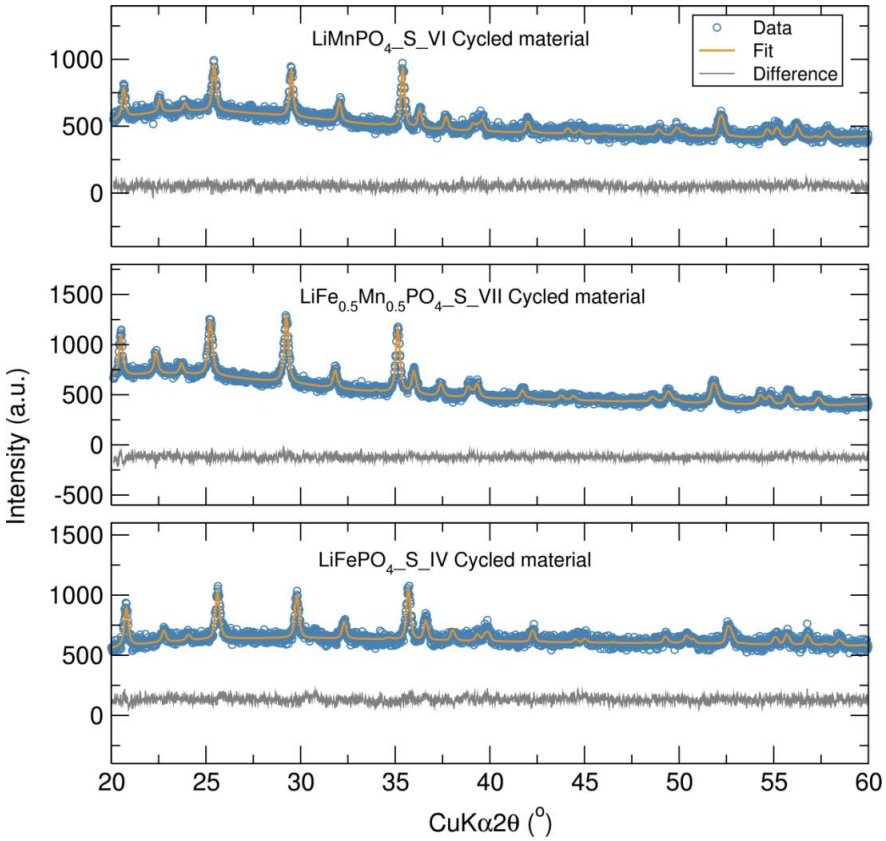

Figure 6.10. Rietveld analysis of PXRD data of post-cycled C/$LiFe_{1-x}Mn_xPO_4$ (*x* = 0, 0.5 and.1) nanostructures prepared through a solvothermal synthesis (12 hr at 220 °C) using single source "$[MLi_2Br(O^tBu)_4(THF)_2]_n$" (*M*=Fe, Mn) (IV, VI, VII) heterometallic alkoxide precursors.

Table 6.5. Calculated lattice parameters from Rietveld analysis of PXRD data for post-cycled $LiFe_{1-x}Mn_xPO_4$ nanostructures prepared through a solvothermal synthesis (12 hr at 220 °C) using single source "$[MLi_2Br(O^tBu)_4(THF)_2]_n$" (*M*=Fe, Mn) (IV, VI, VII) heterometallic alkoxide precursors.

Sample	$LiFePO_4$_S_IV_12 hr	$LiFe_{0.5}Mn_{0.5}PO_4$_S_VI_12 hr	$LiMnPO_4$_S_VII_12 hr
Space group	*Pnma*	*Pnma*	*Pnma*
a (Å)	10.300(2)	10.388(2)	10.447(2)
b (Å)	5.996(1)	6.053(1)	6.101 (1)
c (Å)	4.700(1)	4.723(1)	4.748 (1)
V (Å^{-3})	290.3 (1)	297.0(1)	302.6 (1)
R_{wp}	50.3 %	46.3 %	32.5 %
R_{exp}	45.24 %	43.91 %	30.36 %
X^2	1.24	1.11	1.14

Temperature is known to have a significant impact on the performance, safety and cycle life of LIBs. Therefore, the rate performance of the $LiFePO_4$_S_IV nanostructure was also investigated at 50 °C to study the effect of higher temperatures on the cycling behaviour. Galvanostatic cycling tests at increasingly faster charge-discharge rates indicated that although a poorer rate performance was observed at the slower C rates when cycling at 50 °C compared to room temperature measurements, markedly improved rate capabilities were displayed at the fastest C rates, delivering discharge capacities of 135 mAh g^{-1} at 10 C (Figure 6.11). This improvement is most likely due to the higher ionic conductivity of the electrode at higher temperatures. However, the slightly worse rate performance at the slower C rates (C/10, C/5 and C/2) when cycling at 50 °C could be attributed to the decomposition of the electrolyte at higher temperatures leading to the formation of some HF which can trigger some Fe dissolution from $LiFePO_4$, as previously observed by Amine *et al.*[331] To amend the adverse effect by Fe dissolution Amine *et al.* have shown that the high temperature cycle performance of $LiFePO_4$/graphite cell can be improved by using a lithium bis(oxolato)borate (LiBOB) electrolyte. Wu *et al.* also found that the addition of vinylene carbonate (VC) in the electrolyte solution can greatly improve the higher temperature 55 °C cycling performance of $LiFePO_4$-based LIBs. They reported that the VC additive significantly suppresses Fe dissolution from $LiFePO_4$ and hence, subsequent Fe deposition on the anode side.[332] Also, efficient cycling at 150 °C was found possible when using molten salts electrolyte such as a lithium bis(trifluoromethanesulfonyl)imide (LiTFSI), KTFSI and CsTFSI, demonstrating a large and reversible capacity with an extremely small polarisation.[333] Guerfi *et al.* have used ambient-temperature ILs based on bis(fluorosulfonyl)imide (FSI) as anion and *N*-methyl-*N*-propylpyrrolidinium as cations in $LiFePO_4$ cells with a graphite anode, and observed a reversible capacity of ~150 mAh g^{-1} at 60 °C with negligible capacity fade.[334] The excellent rate performance of the $LiFePO_4$_S_IV nanostructure presented here at elevated temperatures using a standard

EC:DMC electrolyte was significantly better in comparison to a $LiFePO_4$ cell prepared with *N*-methyl-*N*-propyl-pyrrolidinium bis(fluorosulfonyl)imide electrolyte, which yielded specific capacities of 153 and 110 mAh g^{-1} at C/10 and 4 C rates, respectively.[335]

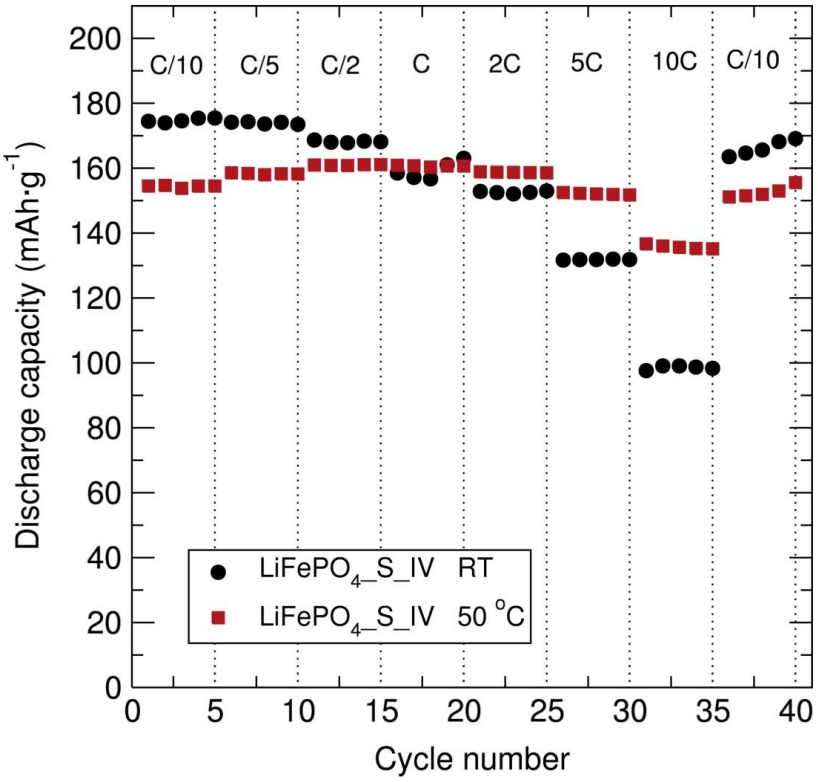

Figure 6.11. Comparative rate performance at room temperature and 50 ºC of C/$LiFePO_4$_S_IV (15% wt. C from sucrose) nanostructure prepared with $[FeLi_2Br(O^tBu)_4(THF)_2]_n$ (IV) heterometallic alkoxide precursors.

CV measurements for the C/$LiFe_{1-x}Mn_xPO_4$ (x=0, 0.5 and 1) nanostructures prepared with the "$[MLi_2Br(O^tBu)_4(THF)_2]_n$" ($M$=Fe, Mn) (IV, VI, VII) heterometallic alkoxide precursors were conducted at a scan rate of 0.1 mV·s^{-1} between 2.5 and 4.5 V. The CV results in Figure 6.12 (a) for the C/$LiFePO_4$_S_IV_12 hr sample showed anodic and cathodic peaks at ~3.529 V and 3.279 V, respectively, due to the Fe^{3+}/Fe^{2+} redox pair. The good superposition of the CV curves after the first cycle confirmed the excellent reversibility of this electrochemical process. CV for the C/$LiFe_{0.5}Mn_{0.5}PO_4$_S_VII_12 hr sample depicted in Figure 6.12 (b) exhibited two oxidation (3.559 V and 4.123 V) and two reduction peaks (3.397 V and 3.892 V) characteristic of the Fe^{3+}/Fe^{2+} and Mn^{2+}/Mn^{3+} redox pairs. These results are in agreement with the two discharge voltage plateaus at about 3.50 V and 4.10 V vs. Li^+/Li^0 corresponding respectively to the redox pairs of Fe^{3+}/Fe^{2+} and Mn^{3+}/Mn^{2+}. Finally, the CV curve of the C/$LiMnPO_4$_S_VI_12 hr nanostructure in Figure 6.12 (c) displayed the expected anodic and cathodic peaks at ~4.314 V and 3.887 V, respectively, due to the Mn^{2+}/Mn^{3+} redox pair. From these CV representations it can also be deduced that the substitution of Mn in the $LiFePO_4$ structure produces a slight shift of the anodic and cathodic peaks towards higher Fe^{3+}/Fe^{2+} potentials. Similar studies by Kobayashi *et*

al. have also revealed a shift in the redox potential of Fe^{3+}/Fe^{2+} and Mn^{3+}/Mn^{2+} as the value of *x* in $LiFe_{1-x}Mn_xPO_4$ is increased. This shift was attributed to the inductive effect in the M–O–P bonding, which acts to increase the ionic character of the transition metal-oxygen bonds. The overall volume expansion upon Mn substitution in the $LiFe_{1-x}Mn_xPO_4$ system may increase the average transition-metal-oxygen bond length and hence the ionicity of each transition metal.[267] This correlates well with the results from the Rietveld analysis of the high resolution PXRD data, which demonstrated an increase in the average transition metal-oxygen bond length with higher Mn contents in $LiFe_{1-x}MnxPO_4$ (3.273(5) Å for $LiFePO_4$_S_IV_12 hr, 3.296(6) Å for $LiFe_{0.5}Mn_{0.5}PO_4$_S_VII_12 and 3.314(9) Å for $LiMnPO_4$_S_VI_12). Similar results have also been previously reported on CV analysis of $LiFe_{1-x}Mn_xPO_4$ materials.[259, 268]

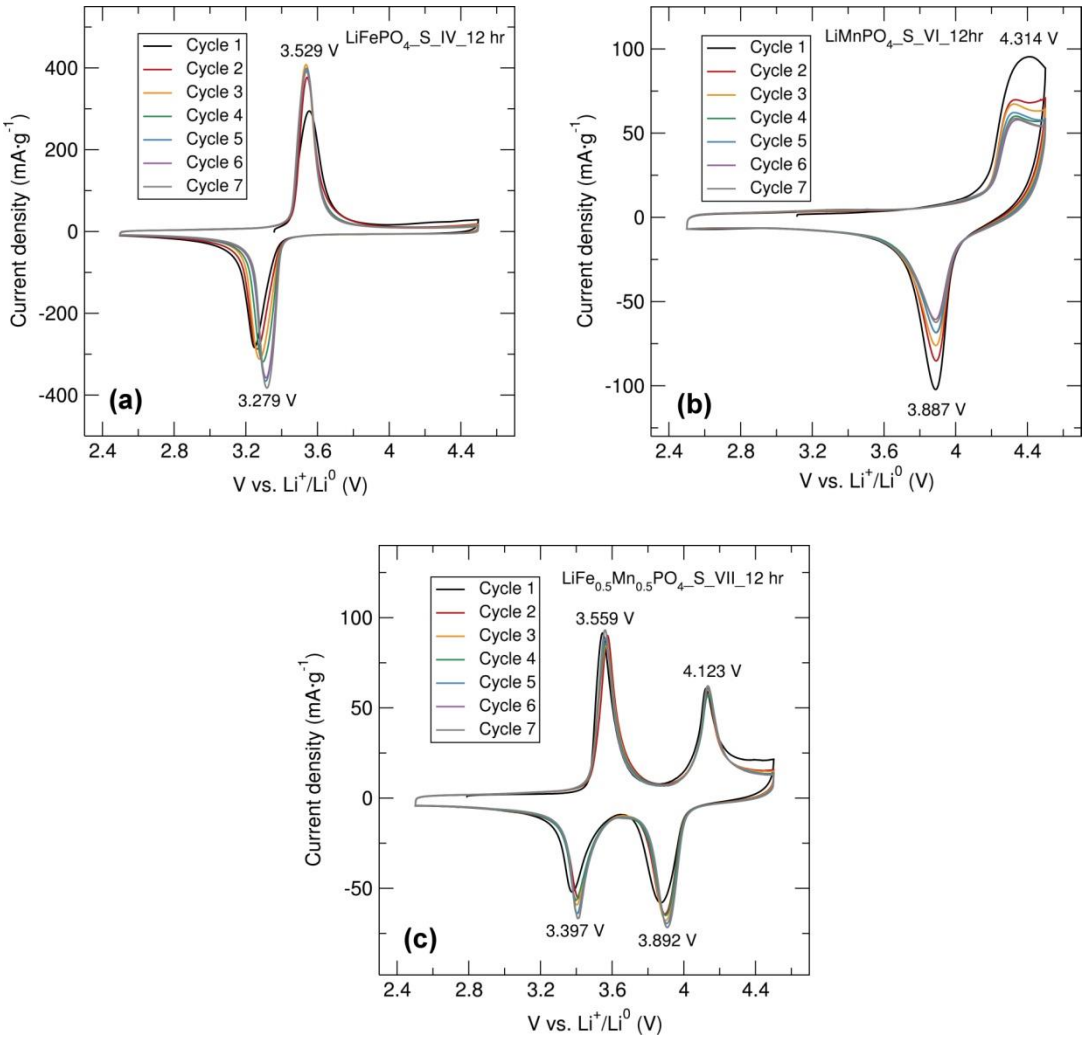

Figure 6.12. CVs at a 0.1 $mV \cdot s^{-1}$ scan rate between 2.5 V and 4.5 V of **(a)** C/$LiFePO_4$_S_IV_12 hr, **(b)** C/$LiMnPO_4$_S_VI_12 hr and **(c)** C/$LiFe_{0.5}Mn_{0.5}PO_4$_S_VII_12 hr nanostructures prepared through a solovothermal synthesis (12 hr 220 °C) with single source "$[MLiBr(O^tBu)_4(THF)_2]_n$" (*M*=Fe, Mn) (IV, VI, VII) heterometallic alkoxide precursors.

6.2.1.5 PXRD and SEM of Fe_3O_4 nanoparticles prepared from hydrolysis of $[FeLi_2Br(O^tBu)_4(THF)_2]_n$

Attempts to prepare Fe_3O_4 magnetite nanoparticles through a room temperature ultrasound-assisted hydrolysis reaction of the $[FeLi_2Br(O^tBu)_4(THF)_2]_n$ (IV) heterometallic alkoxide precursor were pursued, as the hydrolysis of similar metal alkoxides such as $[Fe(O^tBu)_2(THF)]_2$ and $[NaFe(O^tBu)_3(THF)_2]_2$ has already successfully lead to the formation of Fe_3O_4 magnetite nanostructures.[203, 292] The reaction mechanism for the formation of Fe_3O_4 nanoparticles involves ultrasonically generated radical and peroxide species from water or THF contributing to the partial oxidation of Fe^{2+} into Fe^{3+}, as previously reported by Gedanken and co-workers.[336-338] Magnetite has an inverse-spinel structure with space group *Fd-3m* where the O atoms form an approximate cubic close-packed array with one Fe^{3+} per formula unit at the tetrahedrally coordinated position and Fe^{2+} and the remaining Fe^{3+} randomly distributed at the octahedral positions. Magnetite Fe_3O_4 powders synthesised here were characterised by PXRD. Rietveld refinements to a *Fd-3m* space group Fe_3O_4 structure (ICSD No 01-074-0748 19-629)[339] confirmed that Fe_3O_4 magnetite was obtained (Figure 6.13 (a)). The estimated crystallite size of the Fe_3O_4 nanostructure was calculated using the Scherrer equation[208] applied to the (311) diffraction peak and was ~23 nm. SEM images of the magnetite Fe_3O_4 nanophase demonstrated irregular plates with an average particle size of approximately 68 nm (Figure 6.13 (b)). After that, to carbon coat the Fe_3O_4 nanoparticles, the Fe_3O_4 powders were mixed with 15% wt. C from sucrose and thoroughly ground. The mixture was then heat treated in a tube furnace for 3 hr at 500 ºC under Ar atmosphere. PXRD analysis of the heat treated Fe_3O_4 product revealed that mainly Fe_3O_4 was still obtained with some evidence of α-Fe_2O_3 hematite, indicating some degree of oxidation of the Fe^{2+} ions to Fe^{3+} has taken place during the heating process (Figure A6.2). Previous reports have shown that heat treatment of the same $[Fe(O^tBu)_2(THF)]_2$ metal alkoxide precursor to 200 ºC afforded γ-Fe_2O_3 maghemite.[203] In this case, due to the presence of sucrose acting also as a reducing agent, the Fe_3O_4 magnetite phase could still be maintained after the heating process.

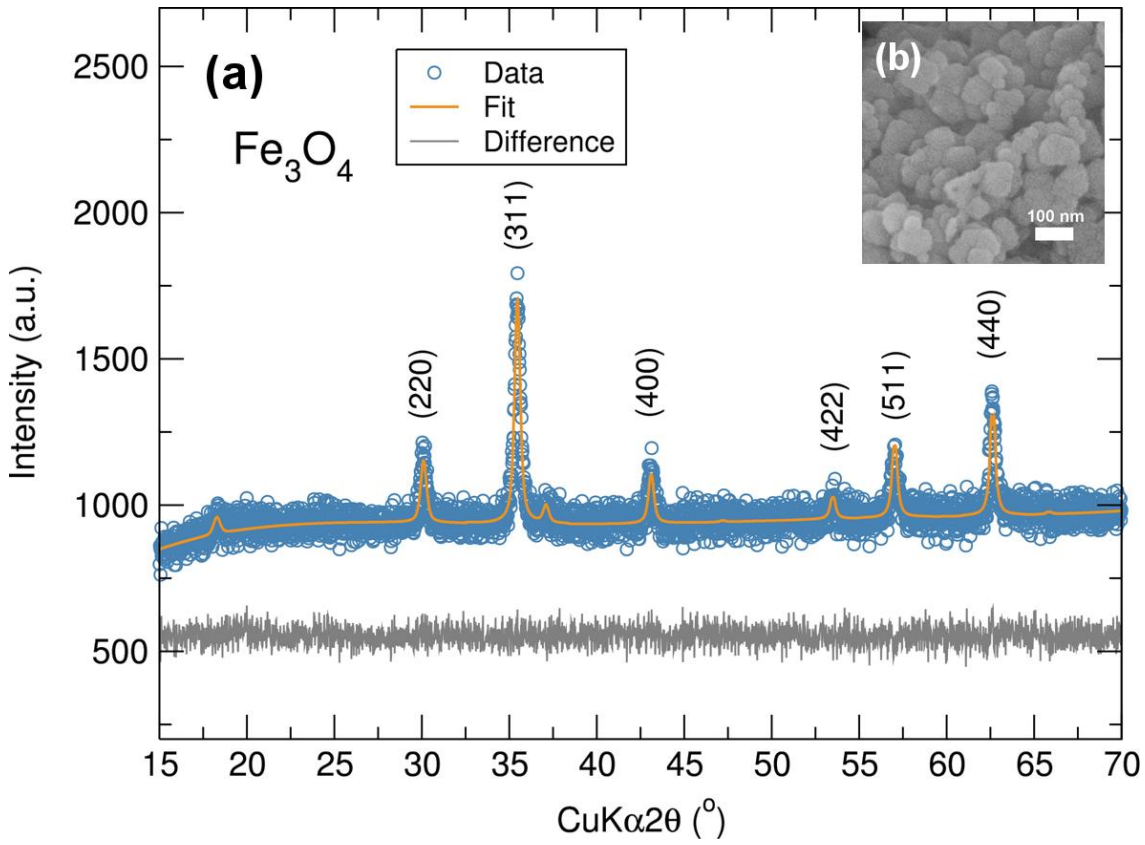

Figure 6.13. (a) Rietveld analysis of PXRD data of magnetite Fe_3O_4 nanostructure. [R_{wp}=50.8 %, R_{exp}=48.14 %, X^2=1.11, *a*=8.388(2) Å, *b*=8.388(2) Å and *c*=8.388(2) Å]. **(b)** SEM image of magnetite Fe_3O_4 nanostructure.

6.2.1.6 Electrochemical performance of Fe_3O_4 nanoparticles prepared from hydrolysis of $[FeLi_2Br(O^tBu)_4(THF)_2]_n$

The electrochemical performance of bare Fe_3O_4 magnetite was examined by galvanostatic cyclicing with potential limitation and CV. The Fe_3O_4 nanostructure was galvanostatically cycled at a current density of 100 mA·g^{-1} over a 0.01-3.00 V range, where the capacity was calculated based on the mass of Fe_3O_4. Galvanostatic cycling results illustrated in Figure A6.3 demonstrated a very high initial discharge capacity of ~3025 mAh·g^{-1} that sharply faded to ~1430 mAh·g^{-1} at the second cycle. Furthermore, a drastic capacity fading over cycling was observed and discharge capacities of approximately 785 mAh·g^{-1} and 340 mAh·g^{-1} were reached after the 10th and 20th cycle, respectively. The galvanostatic discharge and charge profiles show plateaus at approximately 0.9 V and 1.8 V attributed to the conversion reactions of Fe_3O_4 with Li metal into Fe metal and Li_2O. The downward sloping voltage curves below 0.9 V are commonly observed with many transition metal oxide anodes. This effect could be ascribed to combined effects of the formation of SEI layers, the reversible Li^+ storage in the carbon and possibly interfacial lithium storage.[340-342] Comparable electrochemical behavior has been previously observed in a Fe_3O_4 3D composite prepared through a single-heating procedure using a metal-oleate complex.[343] Similar electrochemical performance was found for Fe_3O_4 nanocystals

prepared by a microwave-assisted process, which delivered 201 mAh·g^{-1} after 30 cycles.[344] Composite formation using the Fe_3O_4 magnetite product presented here with carbonaceous matrices could potentially alleviate the capacity loss and improve the capacity retention even at faster charge and discharge rates. For example, enhanced capacity retention was observed on carbon coated Fe_3O_4 nanoparticles homogeneosly anchored to expanded graphite nanosheets prepared by a facile solution-free synthesis, which delivered 728 mAh·g^{-1} after 100 cycles at a current density of 100 mA·g^{-1}.[345] Here, a significant improvement in the capacity retention was observed for the carbon coated C/Fe_3O_4 nanoparticles using 15% wt. C from sucrose, reaching discharge capacities of ~1078 mAh·g^{-1} and 725 mAh·g^{-1} after the 10th and 20th cycle, respectively (Figure 6.14). Comparable electrochemical behavior has been observed in a carbon coated C/Fe_3O_4 composite with ~30 nm Fe_3O_4 nanoparticles as cores and 3-7 nm carbon shells prepared using glucose as a carbon source, which delivered discharge capacities of 718 mAh·g^{-1} after 100 cycles at a 0.1 C rate.[346]

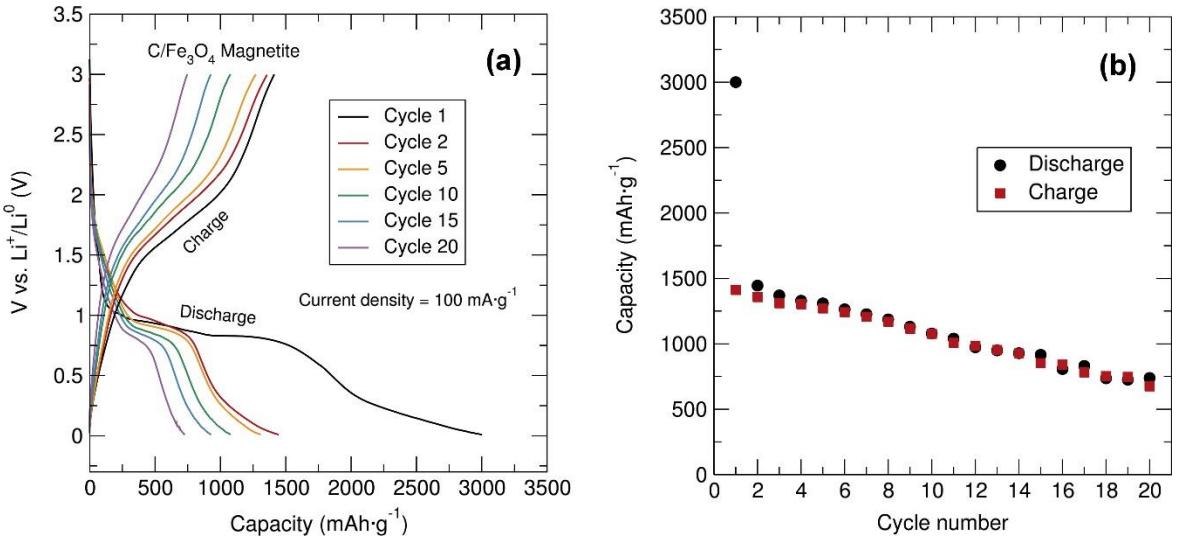

Figure 6.14. (a) Voltage-capacity profileand **(b)** cycling stability of C/Fe_3O_4 magnetite (15% wt. C from sucrose) with C black and PTFE in 60:30:10 % wt. ratio over the potential range of 0.01 V-3.00 V at 100 mA·g^{-1}.

The rate capability of C/Fe_3O_4 nanocomposite was evaluated at various current densities in the range of 200-2000 mA·g^{-1} at the cut-off voltage between 0.01 and 3.00 V. The discharge capacities of ~1350, 1050, 650, 470 and 260 mAh·g^{-1} were retained at current densities of 200, 400, 800, 1200 and 2000 mAh·g^{-1}, respectively (Figure 6.15). When the current was restored to 200 mA·g^{-1}, the C/Fe_3O_4 nanostructures still delivered 930 mAh·g^{-1}, which was about 69% of the initial capacity. This C/Fe_3O_4 nanocomposite displayed slightly enhanced rate performance compared to previous Fe_3O_4 nanocrystals in a mesoporous carbon foam, which delivered approximately 870, 780 and 570 mAh·g^{-1} at current densities of 100, 200 and 500 mA·g^{-1}, respectively.[347] Also, C/Fe_3O_4 nanostructures

fabricated by pyrolysis of a metal-oxide/poly(acrylonitrile) nanocomposite exhibited similar rate capabilities.[348] Carbon-encapsulated Fe_3O_4 nanoparticles homogeneously embedded in two-dimensional porous graphitic carbon nanosheets exhibited very high rate performance and excellent cycling stability, reaching 977 $mAh \cdot g^{-1}$ when cycled at 1 C, 905 $mAh \cdot g^{-1}$ at 2 C, 858 $mAh \cdot g^{-1}$ at 5 C, 587 $mAh \cdot g^{-1}$ at 10 C, 364 $mAh \cdot g^{-1}$ at 15 C, 311 $mAh \cdot g^{-1}$ at 20 C, and finally back to 975 $mAh \cdot g^{-1}$ at 1 C.[104] These results suggested that further improvement in the carbon coating of Fe_3O_4 nanoparticles can significantly enhance the rate capabilities of this material.

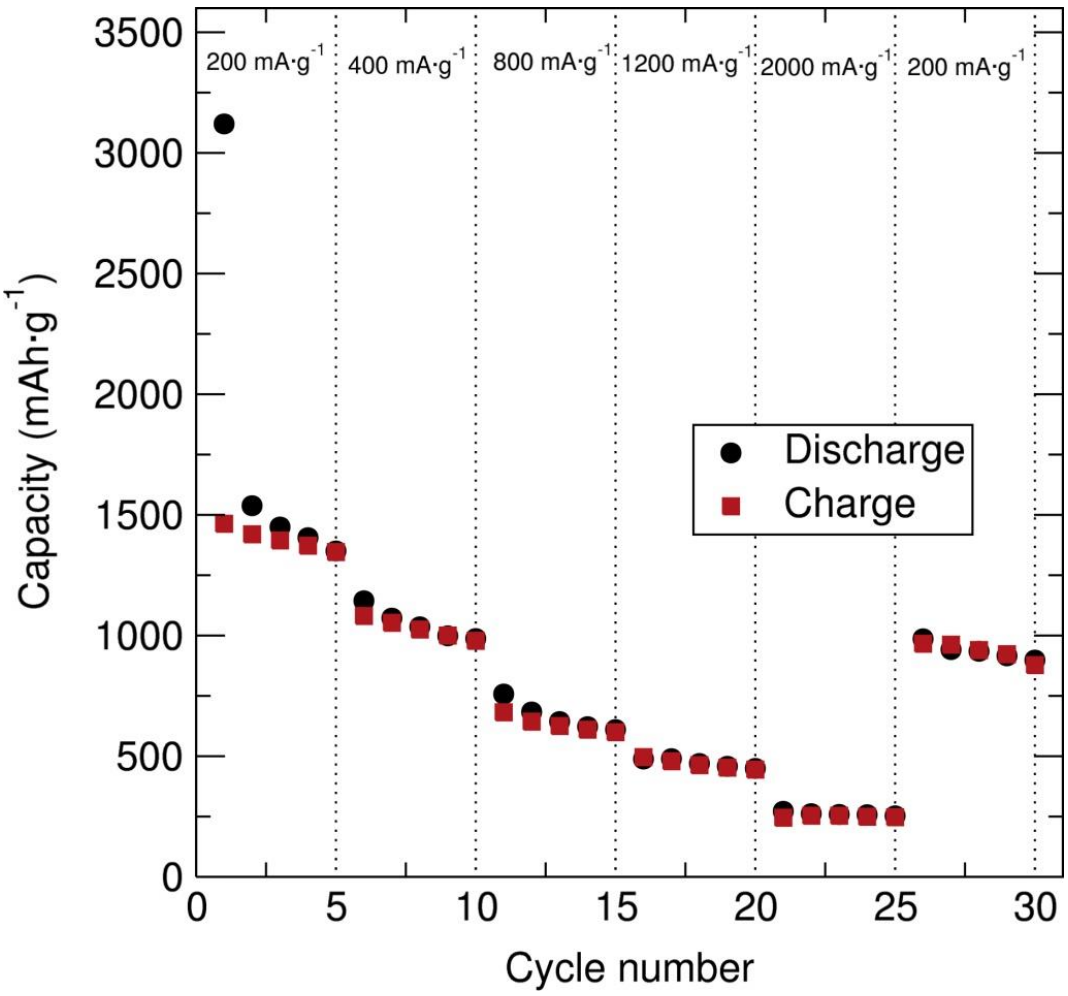

Figure 6.15. Rate performance of C/Fe_3O_4 (15% wt. C from sucrose) mixed with C black and PTFE in 60:30:10 % wt. ratio over the potential range of 0.01 V-3.00 V at at different charge/discharge rates.

The representative CV of Fe_3O_4 magnetite shown in Figure 6.16 demonstrates that the cathodic process is characterised mainly by three reduction peaks. The first weak peak appears at around 1.75 V and could be associated with the initial insertion of the first Li^+ ions into the interstitial octahedral sites in the cubic close-packed Fe_3O_4 structure and the reduction of one electron equivalent of Fe^{3+} to Fe^{2+}. The second small and very broad peak at 1.38-1.45 V could be attributed to the second electron equivalent reduction of

Fe^{3+} to Fe^{2+} and shifting of the Fe ions from the tetrahedral to octahedral sites as additional Li^+ insertion occurs and the material displays a phase transformation from inverse-spinel Fe_3O_4 to a FeO rock-salt structure, as previously discussed by Bock *et al.*[349] The third reduction peak at 0.6 V corresponds to the conversion process of 3 FeO + 6 Li^+ + 6- e^- → 3 Fe^0 + 3 Li_2O, which occurs simultaneously with insertion of the Li^+ into carbon black as well as SEI formation. In the anodic process there are two overlapping peaks centered approximately at 1.75-2.00 V, which can be assigned to the conversion of Fe^0 back to FeO-like structure and delithiation of carbon black. The CV curves after the first cycle were noticeably different from that of the initial cycle. The reduction peaks associated with the initial Li^+ insertion into the Fe_3O_4 host structure and phase change from Fe_3O_4 to FeO are no longer present. Only one intense reduction peak at around 0.80 V is visible and is probably associated with the FeO to Fe^0 metal conversion process and carbon lithiation/SEI formation. Therefore, this CV analysis suggests that after the initial cycle, the reversible electrochemical process is mainly the 3 FeO + 6 Li^+ + 6- e^- ↔ 3 Fe^0 + 3 Li_2O reaction, which is consistent with previous reports.[104, 107, 349-352]

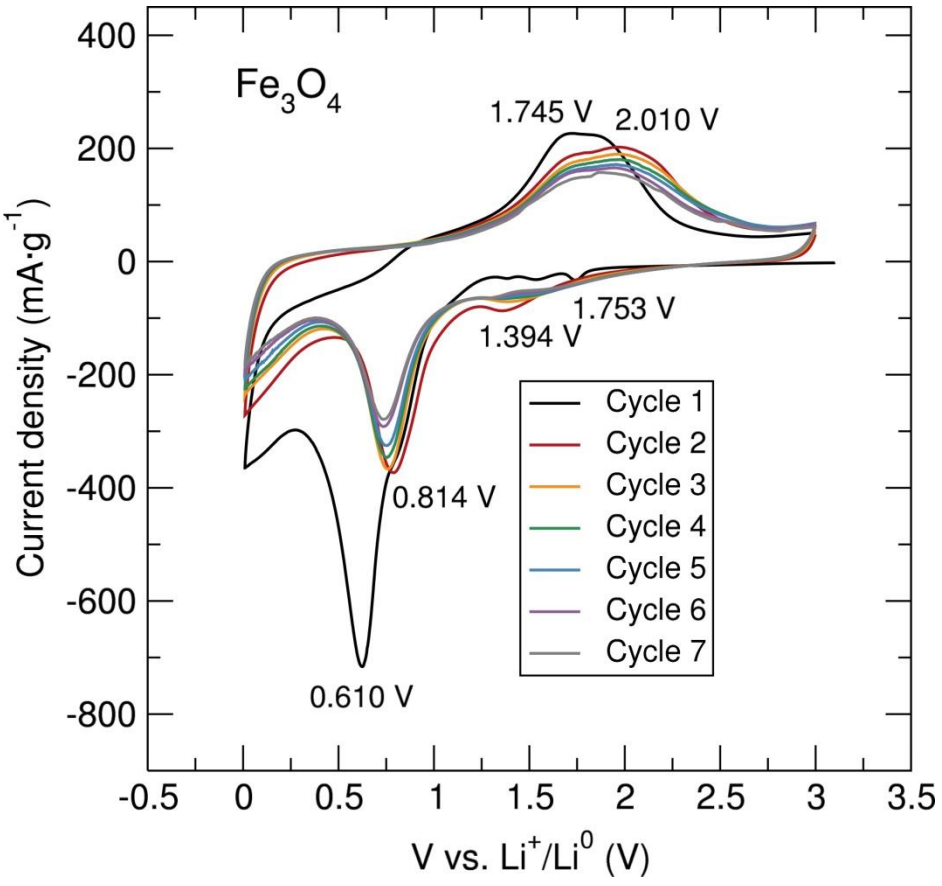

Figure 6.16. CV of Fe_3O_4 magnetite at a 0.1 $mV \cdot s^{-1}$ scan rate between 0.01 V and 3.00 V.

6.3 Conclusions

Facile solvothermal and ultrasound-assisted synthetic approaches using single source heterometallic alkoxide precursors have been presented for the preparation of both high

performing olivine nanostructured $LiFe_{1-x}Mn_xPO_4$ (x=0, 0.5 and 1) cathodes and Fe_3O_4 magnetite nanoparticles as a conversion anode. Investigation of the $LiFePO_4$ synthesis at different reaction times has shown that during the first hour of solvothermal treatment the crystallisation of the Li_3PO_4 intermediate takes place and it is only after 4 hr that the olivine $LiFePO_4$ nanophase is formed. Furthermore, estimation of the crystallite sizes suggests a decrease in the $LiFePO_4$ crystallite with longer reaction times. A strong influence of the transition metal (Fe, Mn) content and precursors used in the resulting particle size and morphology of $LiFe_{1-x}Mn_xPO_4$ nanostructures has also been observed. Electron microscopy analysis has demonstrated smaller $LiFePO_4$ particle size for the material prepared *via* the metal alkoxide based single source precursor route compared to when conventional starting materials are used. Electrochemical testing of these olivine positive insertion electrodes $LiFe_{1-x}Mn_xPO_4$ displayed rate capabilities comparable to the best performing olivine-structured metal phosphates in the literature, suggesting the suitability of the single source heterometallic alkoxide precursor processes presented here in the generation of high performing olivine mixed metal phosphates *via* a straightforward solvothermal routes. Finally, the improved electrochemical performance that can be achieved by employing single source precursor approaches involving heterometallic alkoxides in comparison to conventional reactions employing commercial starting materials has been demonstrated. Moreover, the outstanding rate performance of the $C/LiFePO_4$ nanostructure also at high temperatures of 50 ºC has been presented, yielding discharge capacities of 135 mAh g^{-1} at 10 C. C/Fe_3O_4 magnetite nanoparticles fabricated from the room temperature hydrolysis of the $[FeLi_2Br(O^tBu)_4(THF)_2]_n$ heterometallic alkoxide exhibited a very high initial discharge capacity of 3020 mAh g^{-1} that drastically faded to 725 mAh g^{-1} after 20 cycles. Further investigation of composite formation using this Fe_3O_4 magnetite nanophase presented here with other carbon matrices could afford promising electrochemical performances with a noticeable enhancement of the capacity retention.

7 Single Source Heterometallic Alkoxide precursors to Nickel Olivine and Nickel Oxide electrodes

7.1 Introduction

Selective cationic doping of some electrode materials can result in higher cell voltages, a faster ionic and electronic transport and even some enhancement in the chemical and thermal stability.[167] In particular, Fe-site doping in olivine $LiFePO_4$ cathodes may facilitate the diffusion of Li^+ along the 1D channels and increase both the electronic and ionic conductivity. The enhanced electronic and ionic conductivity may be attributed to the weakening of the Li-O bond in $LiFePO_4$. Previous investigations have revealed that doping $LiFePO_4$ with small amounts of V, Co, Mg, Zn or Cr resulted in improved electrochemical behaviour by enhancing the electronic conductivity.[167] Lu *et al*. reported that $LiFe_{1-x}Ni_xPO_4/C$ composites displayed better electrochemical performance compared to pristine $LiFePO_4/C$ composites because Ni^{2+} doping may stabilise the olivine structure, strengthen the P-O bond and decrease the particle resistance of the $C/LiFe_{1-x}Ni_xPO_4$ composites, leading to improvements in the charge-transfer process during cycling.[322] Amongst several transition metal oxides as conversion anode materials, NiO has attracted substantial interest due to its high capacity, eco-benignity and low cost. Several NiO composites with different nanostructures such as mesoporous nanosheets[353], nanowall[121], nanotube[354], nanofibers and hollow microspheres[355-357] have been successfully fabricated showing highly reversible capacities and long cycling life.

Microwave or ultrasonic-assisted approaches can provide relatively low temperature routes to prepare $LiFe_{1-x}Ni_xPO_4$ and NiO nanostructures offering a significant reduction in reaction times and energy consumption.[151] Niederberger *et al*. have reported a fast microwave-assisted route to $LiFePO_4$ doped with several divalent, trivalent and tetravalent metal ions in varying concentrations. In particular, they showed that 7 mol% Ni doped $LiFePO_4$ nanoparticles delivered a high initial charge capacity of 168 $mAh \cdot g^{-1}$ with a capacity retention of 97% after 300 cycles.[46] In the case of transition metal oxide electrodes, porous NiO hollow microspheres have been fabricated by a facile two-step method involving the ultrasound-assisted synthesis of nickel oxalate precursors and subsequent thermal annealing in air and retained capacities of 380 $mAh \cdot g^{-1}$ after 30 cycles at 200 $mA \cdot g^{-1}$.[357]

Here, non-ionic surfactant polyvinylpyrrolidone (PVP) was selected as both potential capping agent and a carbon source, to prepare nanostructured $C/LiFe_{1-x}Ni_xPO_4$ nanocomposites *via* microwave treatments of single source heterometallic alkoxide precursors. PVP could contribute to the formation of a homogeneous carbon coating and simultaneously control the particle size, morphology and distribution. Recently, $LiFePO_4/C$ nanoparticles prepared by a supercritical hydrothermal method using PVP

displayed higher discharge capacities when comparing to those synthesised by the same synthetic approach with hexadecyl trimethyl ammonium bromide (CTAB) or sucrose, suggesting that the utilisation of PVP affords better-crystallised and smaller-sized $LiFePO_4$/C nanostructures.[358] The preparation of nickel oxide nanoparticles using ultrasonic methods and its cycling performance as conversion anode in LIBs have also been investigated here.

7.2 Results and discussion

7.2.1 Synthesis and characterisation of "$[NiLi_2Cl(O^tBu)_4(THF)_2]_n$" (VIII)

In previous chapters, the preparation of Li and Fe containing heterometallic alkoxides has been presented. Now, the fabrication of a similar heterometallic alkoxide with Ni instead of Fe was attempted. A straightforward room temperature salt elimination reaction using 3 equivalents of LiO^tBu and one equivalent of $NiCl_2$ in dry THF was performed as described in section 2.2.6 for the synthesis of the "$[NiLi_2Cl(O^tBu)_4(THF)_2]_n$" (VIII) metallorganic compound.

The Ni-Li heterometallic alkoxide in THF solution was kept in the freezer for several days and crystals were formed. The obtained single crystals were characterised by single crystal XRD. However, the results obtained demonstrated that the crystals obtained by this route contained no nickel and exhibited a $[Li_4(O^tBu)_3(THF)_3Cl]_2$ THF crystal structure similar to the previously reported by Pauls *et al.*, where two heterocubanes $[Li_4(O^tBu)_3(THF)_3Cl]$ are dimerised by Li-Cl bonds.[294] These results suggest that the $[Li_4(O^tBu)_3(THF)_3Cl]_2$·THF compound will crystallise first out of the THF solvent with the nickel remaining in solution. Pauls *et al.* also attempted the reaction of four equivalents of LiO^tBu with one equivalent of $InCl_3$ in THF and only managed to isolate the $[Li_4(O^tBu)_3(THF)_3Cl]_2$·THF complex,[294] which highlights the difficulty of obtaining pure double metal alkoxides. Efforts were pursued to crystallise the Li and Ni containing alkoxide in other solvents such as toluene or isopropanol, but have so far not been successful. It has been reported that double metal alkoxides with Ni are rare.[269] For this reason, the Ni-Li species is referred to as "$[NiLi_2Cl(O^tBu)_4(THF)_2]_n$" (compound VIII) with the quotation marks denoting that this is purely a suggested nomenclature and not the formula obtained from single crystal XRD. Reactions carried out using this precursor for the preparation of nickel-containing electrodes were done so assuming this speculative formula.

The dry "$[NiLi_2Cl(O^tBu)_4(THF)_2]_n$" (VIII) powder obtained after evaporation of the solvent was characterised by ^1H NMR and FT-IR spectroscopy. The ^1H NMR spectrum of the "$[NiLi_2Cl(O^tBu)_4(THF)_2]_n$" (VIII) dry product conducted in dry C_6D_6 (Figure A7.1) showed two peaks at 0.1 and 0.7 ppm, similar to those previously seen for the μ_2-O^tBu bridging groups in previous alkoxides. The peak at 1.2 ppm can be tentatively assigned to the terminal O^tBu groups. Peaks corresponding to tethered THF groups were found at 1.3 and

2.8 ppm. Although NMR studies can provide valuable information on the terminal and bridging groups, in large number of cases it is difficult to derive meaningful conclusions regarding the structures of metal alkoxides owing to various factors such as intermolecular bridging/terminal site exchange, overlapping resonances, signal broadening due to quadrupolar effects and the oligomeric nature of certain metal alkoxides. A slight shift of the chemical shift towards lower ppm values was observed for "$[NiLi_2Cl(O^tBu)_4(THF)_2]_n$" (VIII) in comparison to $[FeLi_2Br(O^tBu)_4(THF)_2]_n$ (IV), "$[FeLi_2Cl(O^tBu)_4(THF)_2]_n$" (V), "$[MnLi_2Br(O^tBu)_4(THF)_2]_n$" (VI) and "$[Fe_{0.5}Mn_{0.5}Li_2Br(O^tBu)_4(THF)_2]_n$" (VII). However, since the chemical shift is the resultant of several contributing factors, there are generally no obvious correlations with metal oxidation state, atomic radius or co-ordination number.[359]

As previously observed in the FT-IR analysis for the "$[MLi_2X(O^tBu)_4(THF)_2]_n$" (*M*=Fe, Mn; *X*=Br, Cl) (IV, V, VI and VII) heterometallic alkoxides, the FT-IR spectrum in Nujol of the "$[NiLi_2Cl(O^tBu)_2(THF)_2]_n$" (VIII) dry powder exhibited the characteristic Nujol bands at 1460 and 1370 cm^{-1} (Figure A7.2). Vibrations at 726 and 759 cm^{-1} could be assigned to the symmetrical vibration of the *tert*-butyl group, while those at 898 and 832 cm^{-1} are attributed to *tert* butoxy group vibrations. The asymmetric stretch from the C-O-C group in THF appears at 975 cm^{-1}. The band at 1036 cm^{-1} corresponds to a C-C vibration (e.g. from the *tert*-butoxy group), while the 1208 cm^{-1} band could be associated to a C-O stretch vibration characteristic of the *tert*-butyl group.[271, 272] The good agreement of NMR and FTIR between the Ni-Li alkoxide and previous heterometallic alkoxides in preceeding chapters gives some confidence to the general assignment of "$[NiLi_2Cl(O^tBu)_4(THF)_2]_n$" (VIII) to this compound.

7.2.2 Synthesis and characterisation of $LiFe_{1-x}Ni_xPO_4$ and NiO nanostructures prepared from heterometallic alkoxide precursors

$LiFe_{1-x}Ni_xPO_4$ nanostructures were prepared *via* microwave-assisted single source precursor reactions using the "$[FeLi_2Cl(O^tBu)_4(THF)_2]_n$" (V) heterometallic alkoxide as an iron source and either $NiC_2O_4{\cdot}2H_2O$ or "$[NiLi_2Cl(O^tBu)_4(THF)_2]_n$" (VIII) as nickel sources, according to Schematic 7.1 and as described in section 2.2.12. Hydrolysis of the single source precursor "$[NiLi_2Cl(O^tBu)_4(THF)_2]_n$" (VIII) promoted by ultrasound irradiation and a post-heat treatment (3 hr at 500 ºC under air) was followed for the synthesis of C/NiO nanoparticles (see section 2.2.13). Table 7.1 shows the list of C/$LiFe_{1-x}Ni_xPO_4$ and C/NiO nanophases prepared.

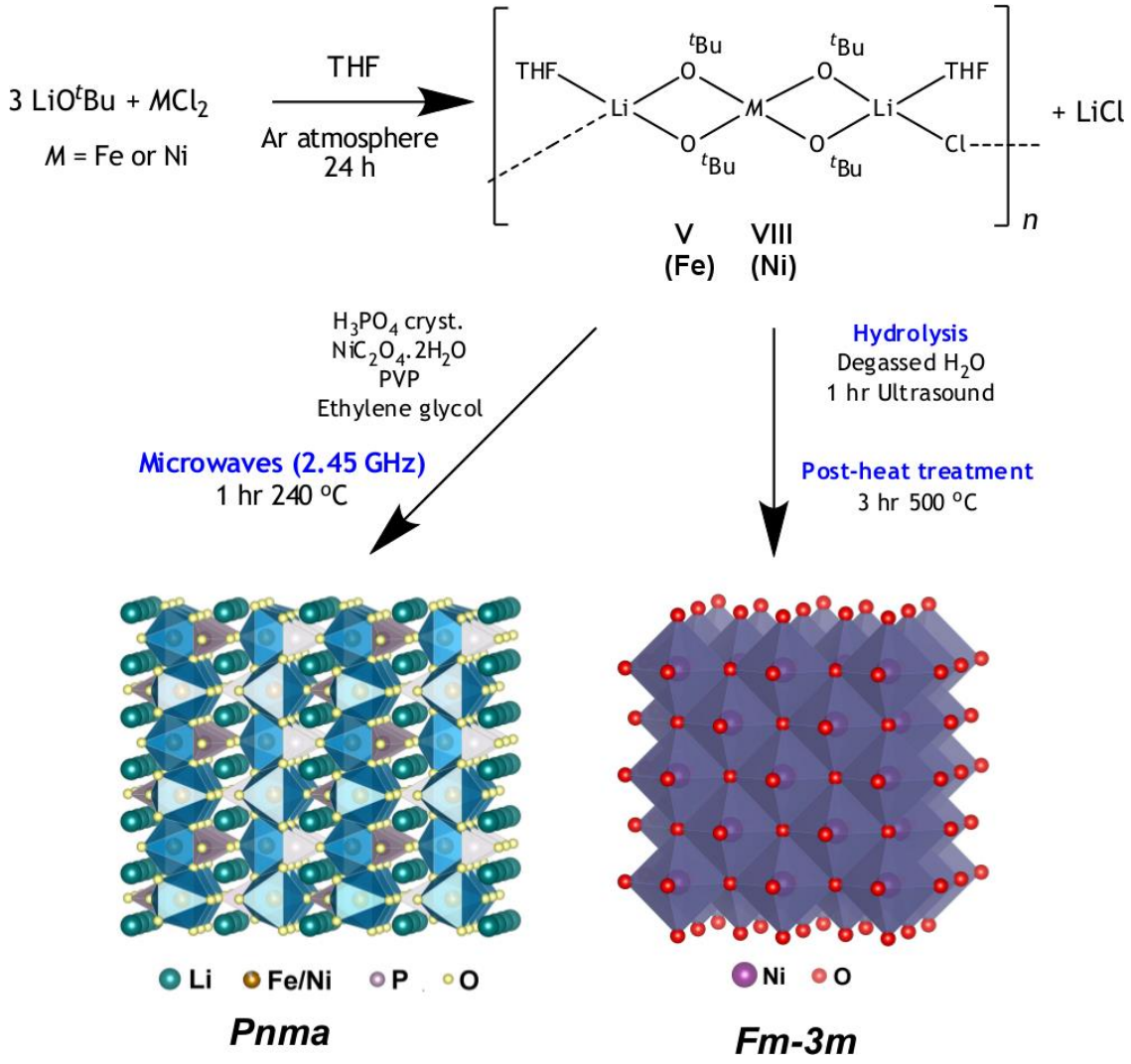

Schematic 7.1. Reaction schematic for the microwave synthesis of $LiFe_{1-x}Ni_xPO_4$ nanostructures and ultrasound synthesis of C/NiO nanoparticles using single source heterometallic alkoxide precursors "$[MLi_2Cl(O^tBu)_4(THF)_2]_n$" ($M$=Fe, Ni) (V, VIII).

Table 7.1. Preparation of olivine $LiFe_{1-x}Ni_xPO_4$ and C/NiO nanostructures from heterometallic alkoxide precursors.

Samples	Reactants	Reaction conditions
"$[NiLi_2Br(O^tBu)_4(THF)_2]_n$" (VIII)	$NiCl_2$ (0.648 g, 5 mmol) + 3 LiO^tBu (1.201 g, 15 mmol) + 40 mL THF	24 hr stirring at RT
$LiFe_{0.95}Ni_{0.05}PO_4$_V	0.95 "$[FeLi_2Cl(O^tBu)_4(THF)_2]_n$" (V) (0.2000 g, 0.370 mmol) + 0.05 $NiC_2O_4{\cdot}2H_2O$ (0.0036 g, 0.019 mmol)+ H_3PO_4 (0.0381 g, 0.389 mmol) + 10 mL EG	Microwave synthesis (2.45 GHz) 1 hr 240 ºC
$LiFePO_4$_V_10PVP	"$[FeLi_2Cl(O^tBu)_4(THF)_2]_n$" (V) (0.2000 g, 0.370 mmol) + H_3PO_4 (0.0362 g, 0.370 mmol) + 10% PVP (0.0026 g) 10 mL EG	Microwave synthesis (2.45 GHz) 1 hr 240 ºC
$LiFe_{0.95}Ni_{0.05}PO_4$_V_10PVP	0.95 "$[FeLi_2Cl(O^tBu)_4(THF)_2]_n$" (V) (0.2000 g, 0.370 mmol) + 0.05 $NiC_2O_4{\cdot}2H_2O$ (0.0036 g, 0.019 mmol)+ H_3PO_4 (0.0381 g, 0.389 mmol) + 10% PVP (0.0026 g) 10 mL EG	Microwave synthesis (2.45 GHz) 1 hr 240 ºC
$LiFe_{0.95}Ni_{0.05}PO_4$_V_15PVP	0.95 "$[FeLi_2Cl(O^tBu)_4(THF)_2]_n$" (V) (0.2000 g, 0.370 mmol) + 0.05 $NiC_2O_4{\cdot}2H_2O$ (0.0036 g, 0.019 mmol)+ H_3PO_4 (0.0381 g, 0.389 mmol) + 15% PVP (0.0035 g) 10 mL EG	Microwave synthesis (2.45 GHz) 1 hr 240 ºC
$LiFe_{0.95}Ni_{0.05}PO_4$_V_20PVP	0.95 "$[FeLi_2Cl(O^tBu)_4(THF)_2]_n$" (V) (0.2000 g, 0.370 mmol) + 0.05 $NiC_2O_4{\cdot}2H_2O$ (0.0036 g, 0.019 mmol)+ H_3PO_4 (0.0381 g, 0.389 mmol) + 20% PVP (0.0046 g) 10 mL EG	Microwave synthesis (2.45 GHz) 1 hr 240 ºC
$LiFe_{0.9}Ni_{0.1}PO_4$_V_10PVP	0.9 "$[FeLi_2Cl(O^tBu)_4(THF)_2]_n$" (V) (0.2000 g, 0.370 mmol) + 0.1 $NiC_2O_4{\cdot}2H_2O$ (0.0072 g, 0.039 mmol)+ H_3PO_4 (0.0401 g, 0.409 mmol) + 10% PVP (0.0026 g) 10 mL EG	Microwave synthesis (2.45 GHz) 1 hr 240 ºC
$LiFe_{0.85}Ni_{0.15}PO_4$_V_10PVP	0.85 "$[FeLi_2Cl(O^tBu)_4(THF)_2]_n$" (V) (0.2000 g, 0.370 mmol) + 0.15 $NiC_2O_4{\cdot}2H_2O$ (0.0072 g, 0.057 mmol)+ H_3PO_4 (0.0418 g, 0.427 mmol) + 10% PVP (0.0026 g) 10 mL EG	Microwave synthesis (2.45 GHz) 1 hr 240 ºC
$LiFe_{0.95}Ni_{0.05}PO_4$_V-VIII	0.95 "$[FeLi_2Cl(O^tBu)_4(THF)_2]_n$" (V) (0.2000 g, 0.370 mmol) + 0.05 "$[NiLi_2Cl(O^tBu)_4(THF)_2]_n$" (0.0110 g, 0.019 mmol) + H_3PO_4 (0.0381 g, 0.389 mmol) 10 mL EG	Microwave synthesis (2.45 GHz) 1 hr 240 ºC
$LiFe_{0.95}Ni_{0.05}PO_4$_V-VIII_15PVP	0.95 "$[FeLi_2Cl(O^tBu)_4(THF)_2]_n$" (V) (0.2000 g, 0.370 mmol) + 0.05 "$[NiLi_2Cl(O^tBu)_4(THF)_2]_n$" (VIII) (0.0110 g, 0.019 mmol) + H_3PO_4 (0.0381 g, 0.389 mmol) + 15% PVP (0.0035 g) 10 mL EG	Microwave synthesis (2.45 GHz) 1 hr 240 ºC
$LiMn_{0.95}Ni_{0.05}PO_4$_VI_15PVP	0.95 "$[MnLi_2Br(O^tBu)_4(THF)_2]_n$" (VI) (0.2000 g, 0.370 mmol) + 0.05 $NiC_2O_4{\cdot}2H_2O$ (0.0036 g, 0.019 mmol)+ H_3PO_4 (0.0381 g, 0.389 mmol) + 15% PVP (0.0035 g) 10 mL EG	Microwave synthesis (2.45 GHz) 1 hr 240 ºC
C/NiO	"$[NiLi_2Cl(O^tBu)_4(THF)_2]_n$" (VIII) + degassed H_2O (2 x 40 mL) + 15% wt. C from sucrose	1 hr Ultrasounds and post-heat treatment for 3 hr at 500 ºC under air

7.2.2.1 PXRD of $LiFe_{1-x}Ni_xPO_4$ nanostructures prepared from "$[FeLi_2Cl(O^tBu)_4(THF)_2]_n$" and $NiC_2O_4 \cdot 2H_2O$ precursors

Doping olivine $LiFePO_4$ with small amounts of Ni has shown to be an effective strategy to enhance the electrochemical performance.[46, 360] Therefore, several microwave-assisted reactions using "$[FeLi_2Cl(O^tBu)_4(THF)_2]_n$" (V), $NiC_2O_4 \cdot 2H_2O$ and H_3PO_4 as starting materials were attempted in order to prepare a family of olivine $LiFe_{1-x}Ni_xPO_4$ nanophases. Initially, the preparation of $LiFe_{0.95}Ni_{0.05}PO_4$ nanostructures was attempted. PXRD analysis of the products obtained after the 10 min microwave treatment at 240 ºC showed an absence of crystalline product, suggesting that longer reaction times may be required for the generation of Ni doped $LiFePO_4$ olivine nanostructures. This may be due to the high insolubility of the $NiC_2O_4 \cdot 2H_2O$ precursor in ethylene glycol. Subsequent reactions were performed for longer duration (1 hr at 240 ºC). Also studied was the effect of adding varying amounts of polyvinylpyrrolidone (PVP) in the reaction mixture, which could act as a capping agent limiting nanoparticle growth and preventing agglomeration. PVP may also be converted into a carbon coating by annealing in order to increase the electron conductivity of the underlying electrode materials. When comparing the PXRD patterns of the $LiFe_{0.95}Ni_{0.05}PO_4$ samples prepared with 10 % PVP ($LiFe_{0.95}Ni_{0.05}PO_4$_V_10PVP) and without PVP ($LiFe_{0.95}Ni_{0.05}PO_4$_V), a noticeable improvement in the crystallisation of the $LiFe_{0.95}Ni_{0.05}PO_4$ product is observed with the addition of PVP, as evidenced by the increased intensity of the diffraction peaks. These results could be explained by the fact that PVP exhibits high polarity which could couple effectively with incoming microwave irradiation, contributing to an improved microwave heating effect. Higher concentrations of Ni in the olivine $LiFePO_4$ structure were also explored (x=0, 0.05, 0.1, 0.15 and 0.2), together with 10 % PVP. PXRD analysis demonstrated that $LiFe_{0.9}Ni_{0.1}PO_4$_V_10PVP powders were obtained after microwave treatment for 1 hr at 240 ºC. Figure 7.2 shows that in the case of $LiFe_{0.85}Ni_{0.15}PO_4$_V_10PVP poorly crystalline product was obtained. When the nickel concentration is above 15%, Ni metal is detected by PXRD. Other Ni-containing starting materials such as $Ni(OH)_2$, $Ni(CH_3CO_2)_2 \cdot 4H_2O$ and $NiSO_4 \cdot 6H_2O$ and less reducing solvents have previously been shown to afford $LiFe_{1-x}Ni_xPO_4$ olivine phases avoiding the reduction of Ni^{2+} ions to Ni metal.[322, 360-362] For example, Qing *et al.* reported a solid state reaction route for the preparation of a series of phase-pure $LiFe_{1-x}Ni_xPO_4$ olivine-type solid solution materials using $Ni(CH_3CO_2)_2 \cdot 4H_2O$.[363] Rietveld analysis of the PXRD data of $LiFePO_4$_V_10PVP, $LiFe_{0.95}Ni_{0.05}PO_4$_V_10PVP and $LiFe_{0.9}Ni_{0.1}PO_4$_V_10PVP shown in Figure 7.2 reveals no evident presence of impurity phases. However, due to the high background in the PXRD patterns obtained, there may be some amorphous components that cannot be assigned. Furthermore, the high noise could also be ascribed to Fe fluorescence, as the

diffractometer employed has a Cu source. These reasons could also explain the elevated R_{wp} and R_{exp} values obtained in the Rietveld refinements. A slight shift of the peaks towards higher 2θ values was observed with increased Ni contents in $LiFe_{1-x}Ni_xPO_4$, as expected by the smaller cation size of Ni^{2+} (69 pm ionic radius) in comparison to Fe^{2+} (78 pm ionic radius) (see Figure A7.3 for a close up PXRD patterns of $LiFePO_4$_V_10PVP, $LiFe_{0.95}Ni_{0.05}PO_4$_V_10PVP and $LiFe_{0.9}Ni_{0.1}PO_4$_V_10PVP).[252] Table 7.2 summarises the calculated lattice parameters from the Rietveld refinements for the $LiFe_{1-x}Ni_xPO_4$ (x=0, 0.05 and 0.1) nanomaterials and show a slight contraction in the a and b lattice parameters with increasing Ni contents while the c lattice parameter remains almost constant (Figure 7.3). This is to be expected due to the smaller cation size of Ni^{2+} in comparison to Fe^{2+}.[252] This suggests incorporation of Ni in the olivine structure. Similar decrease in the unit cell volume of nanosized $LiFe_{1-x}Ni_xPO_4$ (x=0.00-0.20) composites prepared *via* sol-gel-assisted carbothermal reduction method was observed by Örnek *et al.*[176] Furthermore, the lattice parameters and unit cell volume of $LiFe_{0.95}Ni_{0.05}PO_4$_V are in very good agreement with values previously reported by Niederberger *et al.* on a microwave synthesised $LiFe_{0.95}Ni_{0.05}PO_4$ nanostructure (a=10.3179(8) Å, b=5.9903(3) Å, c=4.6950(4) Å and V=290.18(4) Å^3).[46]

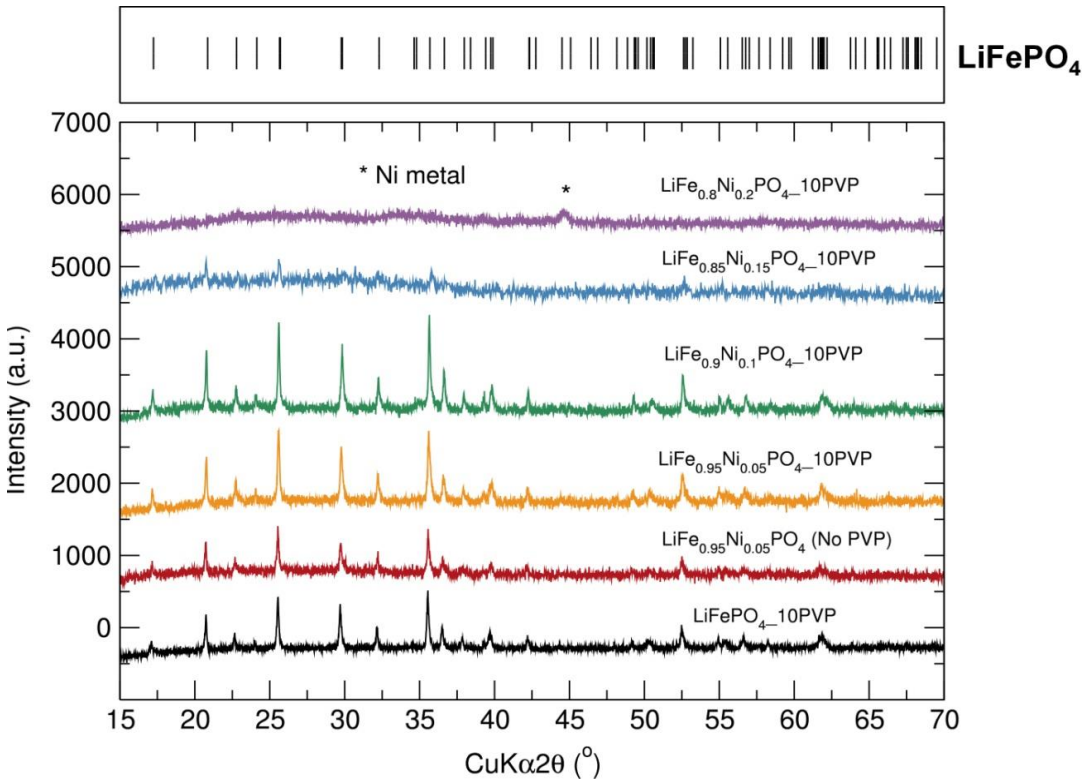

Figure 7.1. Comparative PXRD patterns of $LiFe_{1-x}Ni_xPO_4$ (x=0, 0.05, 0.1, 0.15 and 0.2) nanostructures after microwave synthesis using "$[FeLi_2Cl(O^tBu)_4(THF)_2]_n$," (V) heterometallic alkoxide precursor, $NiC_2O_4{\cdot}2H_2O$, H_3PO_4 and 10% PVP in ethylene glycol. Top graph: Bragg positions $LiFePO_4$.

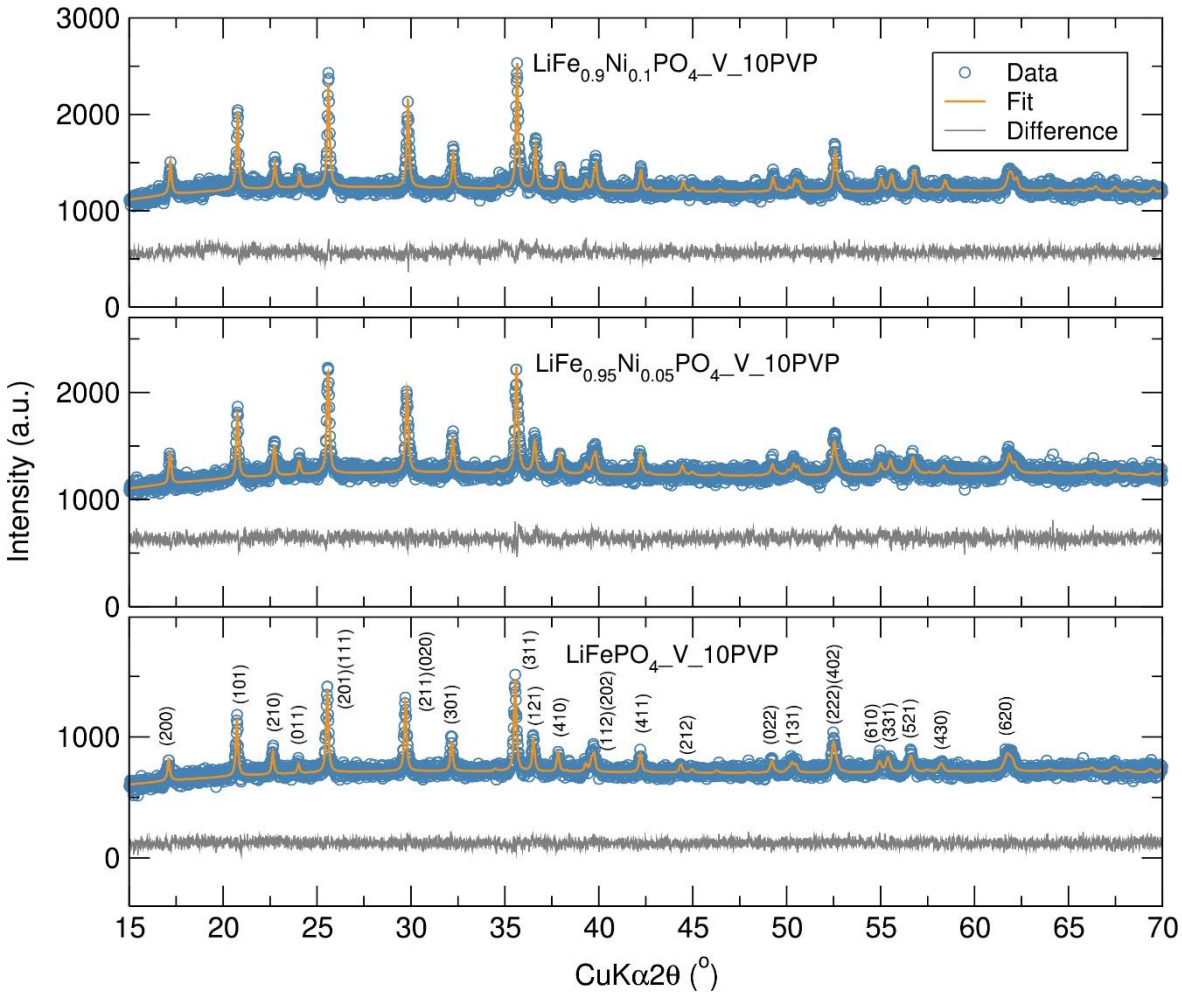

Figure 7.2. Rietveld analysis of PXRD patterns of $LiFe_{1-x}Ni_xPO_4$ (x=0, 0.05 and 0.1) nanostructures after microwave synthesis using "$[FeLi_2Cl(O^tBu)_4(THF)_2]_n$" (V) heterometallic alkoxide precursor, $NiC_2O_4{\cdot}2H_2O$, H_3PO_4 and 10% PVP in ethylene glycol.

Table 7.2. Calculated lattice parameters from Rietveld refinements for $LiFe_{1-x}Ni_xPO_4$ (x=0, 0.05 and 0.1) nanostructures after microwave synthesis using "$[FeLi_2Cl(O^tBu)_4(THF)_2]_n$" (V) heterometallic alkoxide precursor, $NiC_2O_4{\cdot}2H_2O$, H_3PO_4 and 10% PVP in ethylene glycol.

Sample	**$LiFePO_4$_V_10PVP**	**$LiFe_{0.95}Ni_{0.05}PO_4$_V_10PVP**	**$LiFe_{0.9}Ni_{0.1}PO_4$_V_10PVP**
Space group	*Pnma*	*Pnma*	*Pnma*
a (Å)	10.340(1)	10.324(1)	10.315(1)
b (Å)	6.0037(8)	5.996(1)	5.986(1)
c (Å)	4.694(8)	4.697(1)	4.699(1)
V (Å^{-3})	291.38(7)	290.84(8)	290.14(6)
R_{wp}	46.4 %	44.7 %	42.4 %
R_{exp}	43.65 %	40.48 %	37.35 %
X^2	1.13	1.22	1.29

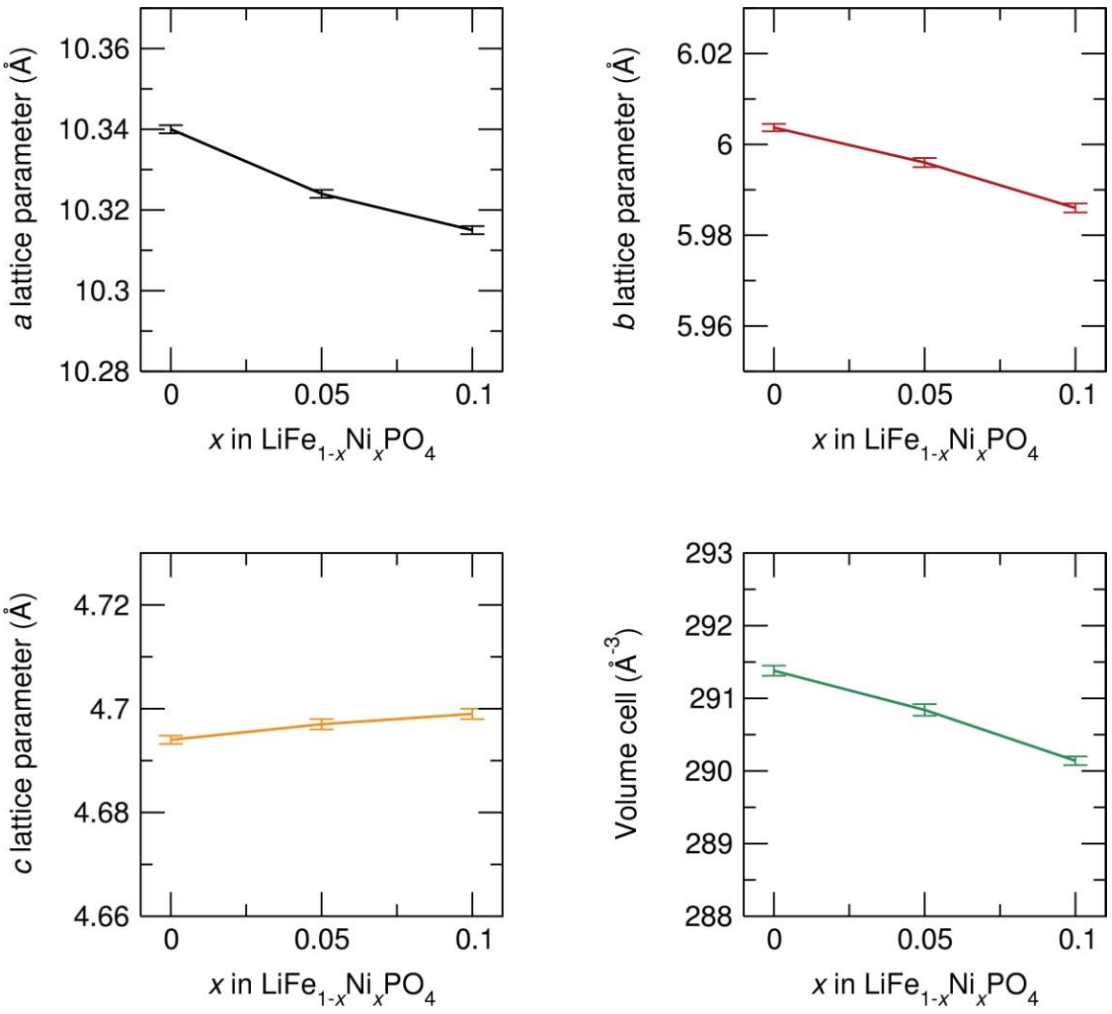

Figure 7.3. Variation of the refined lattice parameters and volume cell values for $LiFe_{1-x}Ni_xPO_4$ (x=0, 0.05 and 0.1) nanostructures after microwave synthesis using "$[FeLi_2Cl(O^tBu)_4(THF)_2]_n$" (V) heterometallic alkoxide precursor, $NiC_2O_4{\cdot}2H_2O$, H_3PO_4 and 10% PVP in ethylene glycol.

To investigate the effect of increased PVP content, a series of $LiFe_{0.95}Ni_{0.05}PO_4$ nanostructures were synthesised employing varying amounts of PVP from 10 to 20 % wt. transition metal content. PXRD analysis of $LiFe_{0.95}Ni_{0.05}PO_4$_V_10PVP, $LiFe_{0.95}Ni_{0.05}PO_4$_V_15PVP and $LiFe_{0.95}Ni_{0.05}PO_4$_V_20PVP nanostructures revealed a slight increase in crystallinity when increasing the PVP content from 10 % to 15 % PVP. Similar results were obtained when using 15 % and 20 % PVP (Figure 7.4). Table 7.3 summarises the results from the Rietveld fits (Figure 7.5) for the $LiFe_{0.95}Ni_{0.05}PO_4$ nanostructures fabricated with different PVP amounts. The structural analysis demonstrated that increasing the PVP up to 15% in the $LiFe_{0.95}Ni_{0.05}PO_4$ materials also lead to a significant reduction in the cell lattice parameters. No substantial changes were noted for 20% PVP. Figure A7.4 illustrates the variation of the refined lattice parameters and volume cell values for the $LiFe_{0.95}Ni_{0.05}PO_4$ nanostructures prepared with different PVP loadings. The $LiFe_{0.95}Ni_{0.05}PO_4$_V_15PVP powders were heated for 1 hr at 700 ºC in Ar atmosphere in an attempt to anneal the surface PVP to provide a carbon coating. Carbon coating was also

attempted by adding sucrose (15% wt. C) to the $LiFe_{0.95}Ni_{0.05}PO_4$_V_15PVP sample under the same heat treatment conditions. Figure 7.6 shows the Rietveld refinements for both samples. Both reveal no obvious secondary phases. Results also indicated that the heat treatment slightly increases the cell volume (Table 7.4).

CHN microanalysis of the $LiFe_{0.95}Ni_{0.05}PO_4$_V_No PVP and $LiFe_{0.95}Ni_{0.05}PO_4$_V_15PVP powders was conducted. Results reveal carbon content of ~3% wt in both cases, suggesting that the addition of PVP does not lead to an increased carbon content in the microwave synthesised $LiFe_{0.95}Ni_{0.05}PO_4$ product (Table 7.5). The carbon may be mainly attributed to some remaining ethylene glycol from the synthesis and to some residual carbon from the decomposition of the metal alkoxide precursors. Therefore, the major effect of the PVP is that of enhanced microwave heating which leads to better crystallinity.

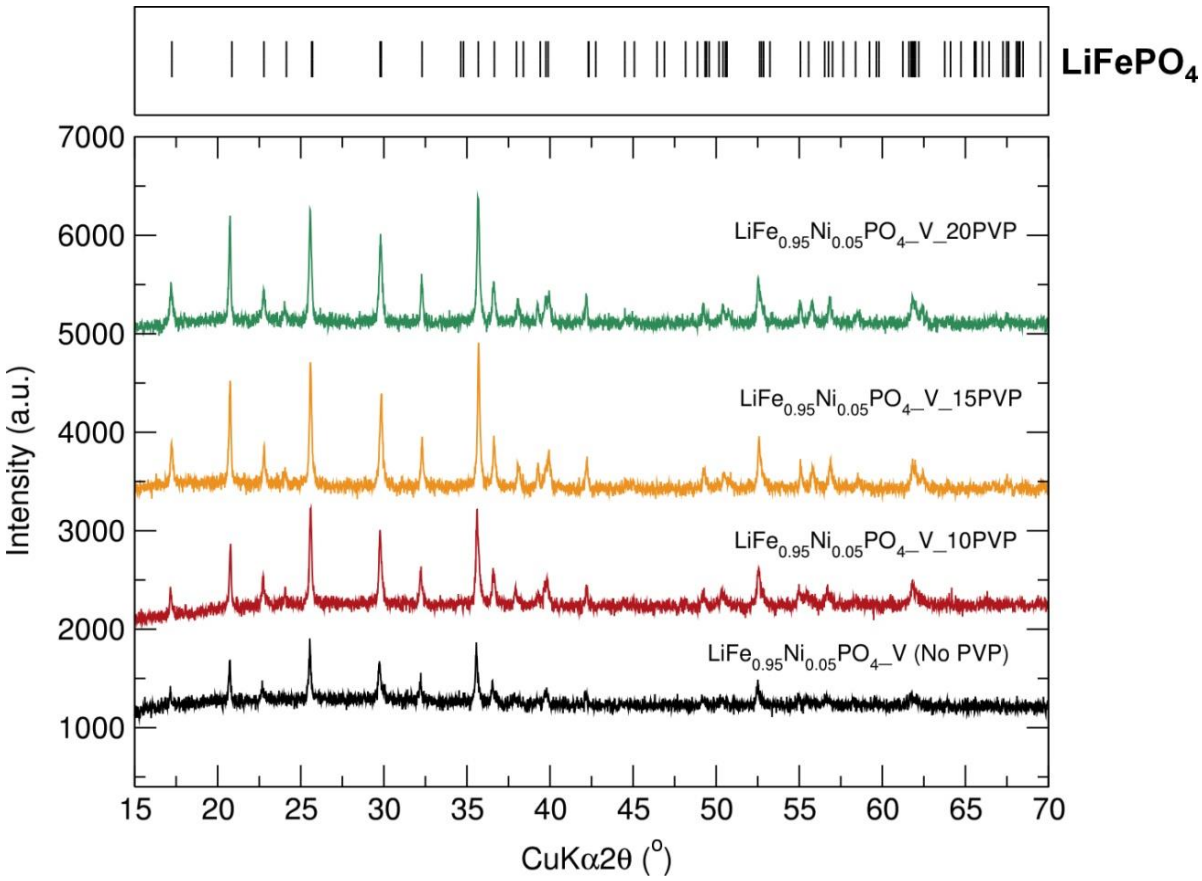

Figure 7.4. Comparative PXRD patterns of $LiFe_{0.95}Ni_{0.05}PO_4$ nanostructures after microwave synthesis using "$[FeLi_2Cl(O^tBu)_4(THF)_2]_n$" (V) heterometallic alkoxide precursor, $NiC_2O_4{\cdot}2H_2O$, H_3PO_4 and different PVP contents in ethylene glycol. Top graph: Bragg positions for $LiFePO_4$.

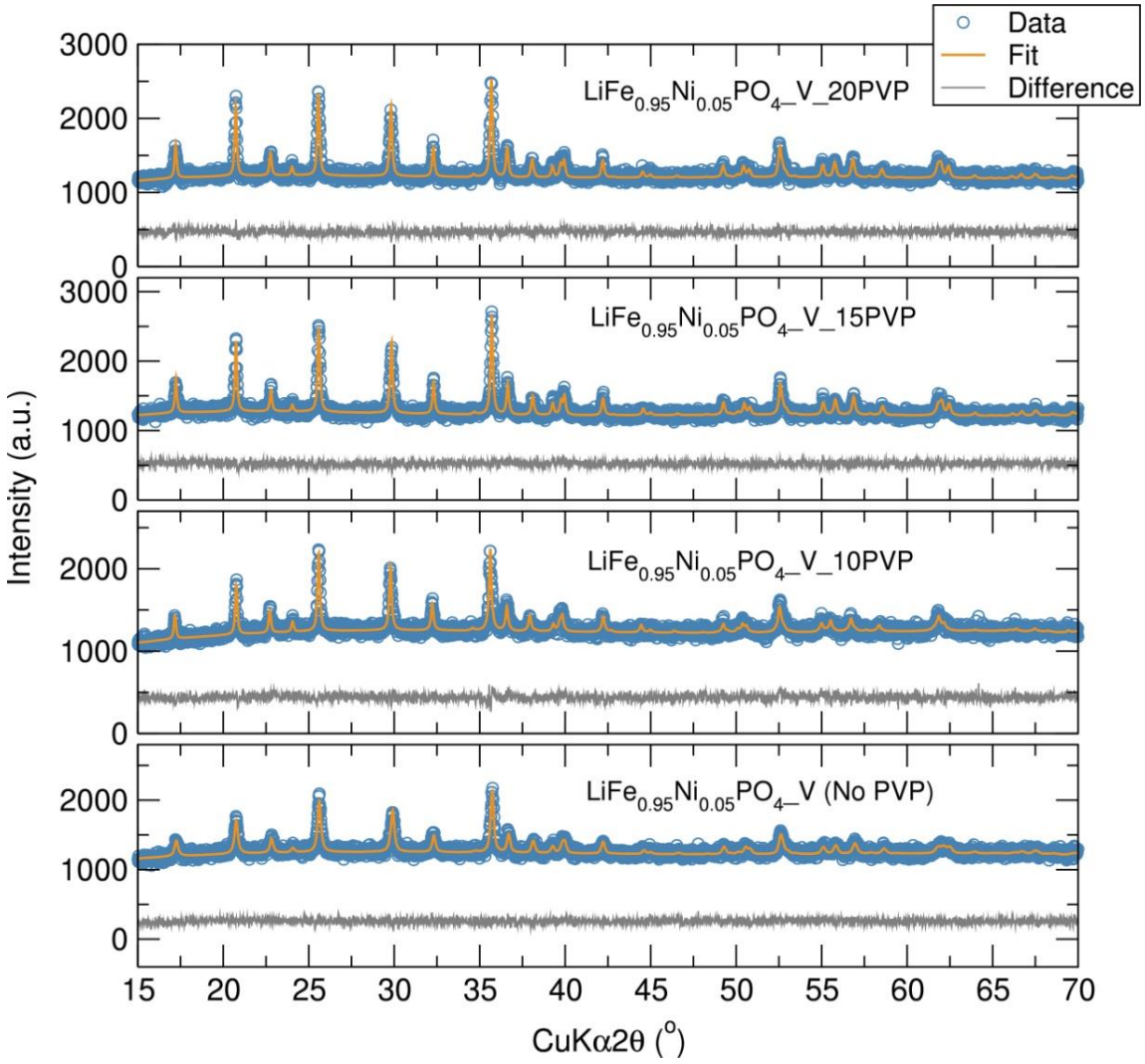

Figure 7.5. Rietveld analysis of PXRD patterns of $LiFe_{0.95}Ni_{0.05}PO_4$ nanostructures after microwave synthesis using "$[FeLi_2Cl(O^tBu)_4(THF)_2]_n$" (V) heterometallic alkoxide precursor, $NiC_2O_4{\cdot}2H_2O$, H_3PO_4 and different PVP contents in ethylene glycol.

Table 7.3. Calculated lattice parameters from Rietveld refinements for $LiFe_{0.95}Ni_{0.05}PO_4$ nanostructures after microwave synthesis using "$[FeLi_2Cl(O^tBu)_4(THF)_2]_n$" (V) heterometallic alkoxide precursor, $NiC_2O_4{\cdot}2H_2O$, H_3PO_4 and different PVP contents in ethylene glycol.

Sample	**$LiFe_{0.95}Ni_{0.05}PO_4$_V**	**$LiFe_{0.95}Ni_{0.05}PO_4$_V_15PVP**	**$LiFe_{0.95}Ni_{0.05}PO_4$_V_20PVP**
Space group	*Pnma*	*Pnma*	*Pnma*
a (Å)	10.336(2)	10.2696(9)	10.2737(9)
b (Å)	6.000(1)	5.9777(5)	5.9815(6)
c (Å)	4.702(1)	4.7005(5)	4.7009(6)
V ($Å^{-3}$)	291.3(1)	288.56(5)	288.88(5)
R_{wp}	65.2 %	35.0 %	36.6 %
R_{exp}	61.71 %	32.75 %	34.04 %
X^2	1.12	1.14	1.16

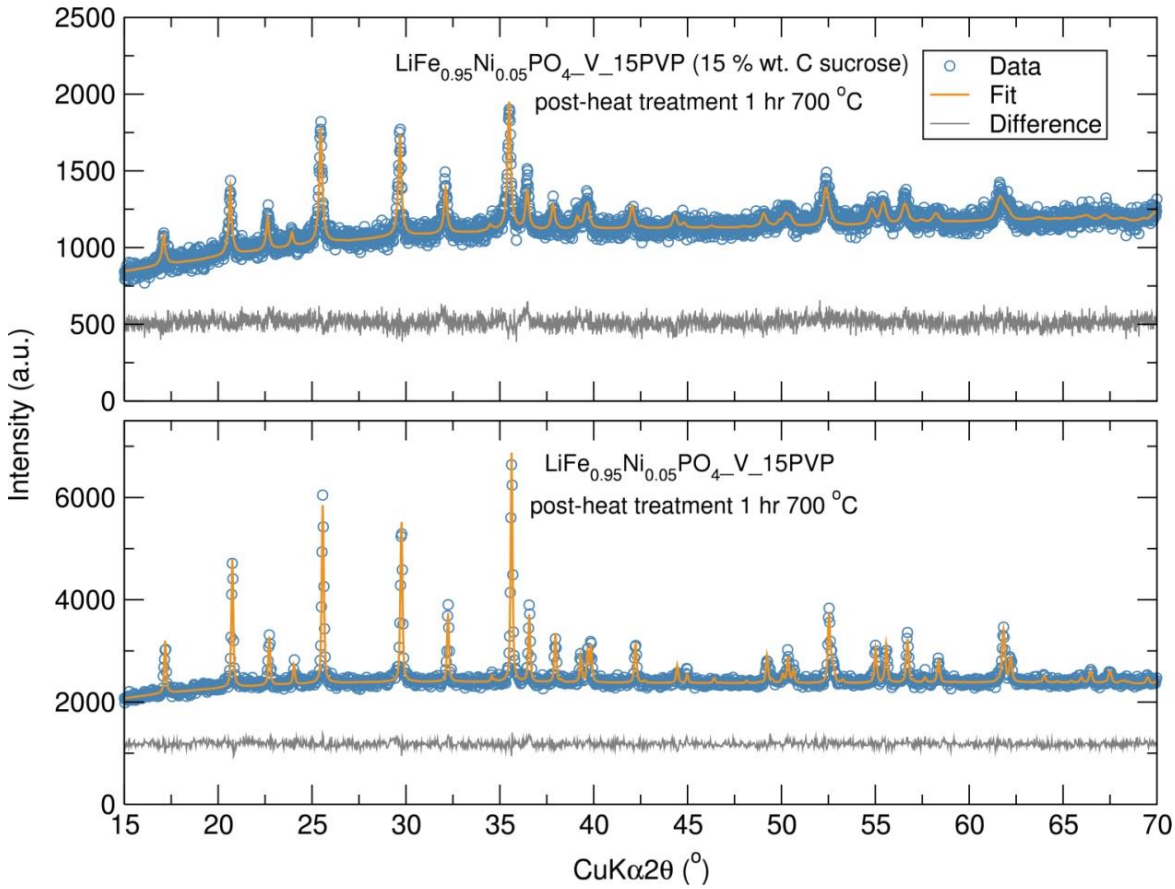

Figure 7.6. Rietveld analysis of PXRD patterns of $LiFe_{0.95}Ni_{0.05}PO_4$_V_15PVP nanostructures after microwave synthesis using 15% PVP and post-heat treatment for 1 hr at 700 ºC under Ar (without and with mixing with 15% wt. C from sucrose). Samples prepared using "$[FeLi_2Cl(O^tBu)_4(THF)_2]_n$" (V) heterometallic alkoxide precursor, $NiC_2O_4{\cdot}2H_2O$, H_3PO_4 and 15% PVP in ethylene glycol.

Table 7.4. Calculated lattice parameters from Rietveld refinements for $LiFe_{0.95}Ni_{0.05}PO_4$_V_15PVP nanostructures after microwave synthesis using 15% PVP and post-heat treatment for 1 hr at 700 ºC under Ar with and without sucrose.

Sample	**$LiFe_{0.95}Ni_{0.05}PO_4$_V_15PVP Post-heat treatment 1 hr 700 ºC**	**$LiFe_{0.95}Ni_{0.05}PO_4$_V_15PVP Post-heat treatment 1 hr 700 ºC 15% wt. C sucrose**
Space group	*Pnma*	*Pnma*
a (Å)	10.3098(5)	10.330(2)
b (Å)	5.99965(3)	6.002(1)
c (Å)	4.6973 (3)	4.712(1)
V (Å^{-3})	290.40(3)	292.2(1)
R_{wp}	21.9 %	45.5 %
R_{exp}	19.85 %	41.12 %
X^2	1.22	1.22

Table 7.5. CHN Microanalysis of $LiFe_{0.95}Ni_{0.05}PO_4$ nanostructures prepared through a microwave-assisted synthesis using "$[FeLi_2Cl(O^tBu)_4(THF)_2]_n$" (V) heterometallic alkoxide precursor with and without PVP.

Sample	C (wt. %)	H (wt.%)
$LiFe_{0.95}Ni_{0.05}PO_4$_V_No PVP	3.33	1.41
$LiFe_{0.95}Ni_{0.05}PO_4$_V_15PVP	2.71	1.35

7.2.2.2 PXRD of $LiMn_{0.95}Ni_{0.05}PO_4$ nanostructure prepared from "$[MnLi_2Br(O^tBu)_4(THF)_2]_n$" and $NiC_2O_4{\cdot}2H_2O$ precursors

As $LiMnPO_4$ has attracted much attention due to its higher operating votage compared to $LiFePO_4$,[66] attempts to prepare Ni doped $LiMnPO_4$ were also pursued. For example, $LiMn_{0.9}Ni_{0.1}PO_4$ nanoparticles have recently been prepared *via* a microwave-assisted hydrothermal process displaying a promising cycling performance with discharge capacities of 136 and 78 $mAh{\cdot}g^{-1}$ at C/20 and 10 C rates, respectively.[364] Here, olivine $LiMn_{0.95}Ni_{0.05}PO_4$ nanostructures were successfully synthesised *via* a 1 hr microwave treatment at 240 ºC using a "$[MnLi_2Br(O^tBu)_4(THF)_2]_n$" (VI) heterometallic alkoxide precursor, $NiC_2O_4{\cdot}2H_2O$, H_3PO_4 and 15% PVP in ethylene glycol. Rietveld analysis of the PXRD patterns of $LiMn_{0.95}Ni_{0.05}PO_4$_VI_15PVP after microwave-assisted synthesis using 15% PVP and post-heat treatment for 1 hr at 700 ºC under Ar flow demonstrated a good fit between the experimental data and the calculated model (Figure 7.7). A broadening of the diffraction peaks was noted, which may indicate a decrease in crystallite size. A noticeable increase in crystallinity and a reduction in peak widths was observed after the heat treatment. Table 7.6 shows the lattice parameters of $LiMn_{0.95}Ni_{0.05}PO_4$_VI_15PVP determined by Rietveld analysis, suggesting that there is no significant variation in the unit cell parameters after heat treatment.

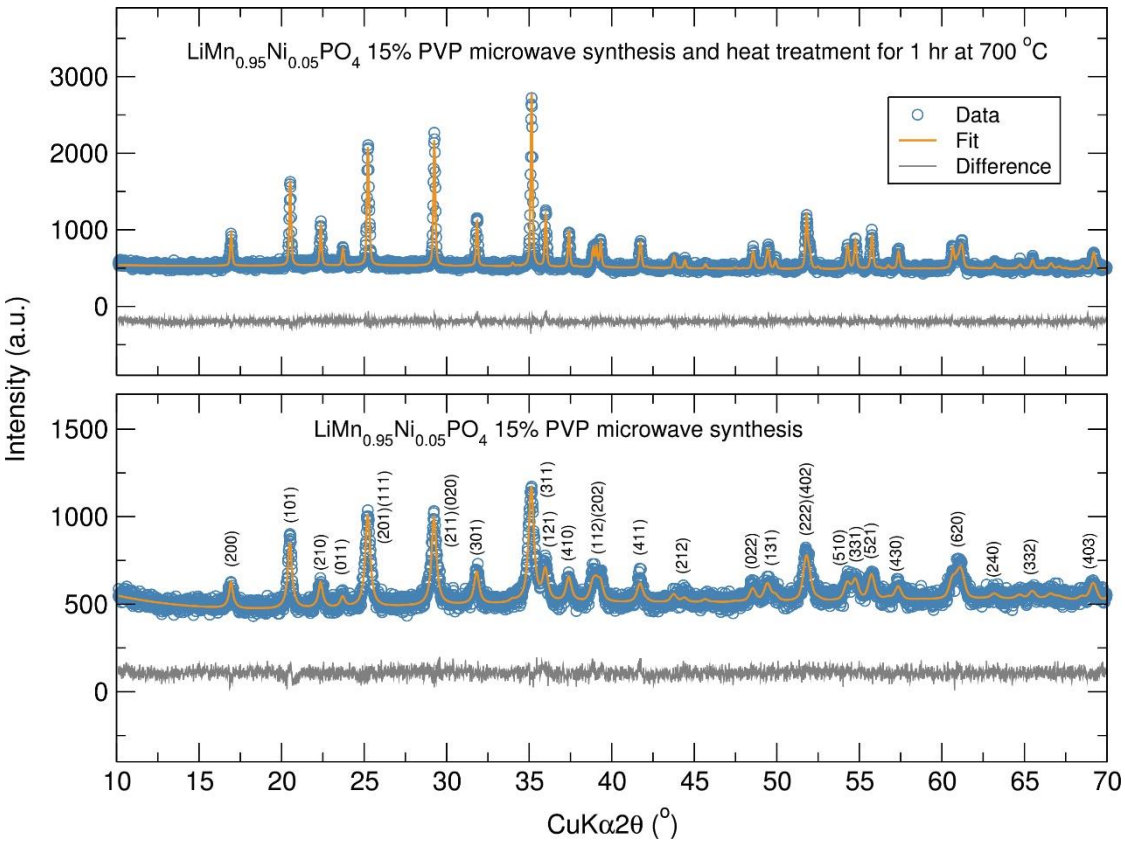

Figure 7.7. Rietveld analysis of PXRD patterns of $LiMn_{0.95}Ni_{0.05}PO_4$ nanostructures after microwave synthesis using 15% PVP and post-heat treatment for 1 hr at 700 ºC under Ar. Samples prepared using "$[MnLi_2Br(O^tBu)_4(THF)_2]_n$" (VI) heterometallic precursor, $NiC_2O_4{\cdot}H_2O$, H_3PO_4 and 15% PVP in ethylene glycol.

Table 7.6. Calculated lattice parameters from Rietveld refinements for $LiMn_{0.95}Ni_{0.05}PO_4$ nanostructures after microwave synthesis using 15% PVP and post-heat treatment for 1 hr at 700 ºC under Ar. Smples prepared with "$[MnLi_2Br(O^tBu)_4(THF)_2]_n$" (VI) heterometallic precursor, $NiC_2O_4{\cdot}H_2O$, H_3PO_4 and 15% PVP in ethylene glycol.

Sample	**$LiMn_{0.95}Ni_{0.05}PO_4$_VI_15PVP**	**$LiMn_{0.95}Ni_{0.05}PO_4$_VI_15PVPPost-heat treatment 1 hr 700 ºC**
Space group	*Pnma*	*Pnma*
a (Å)	10.447(2)	10.4472(5)
b (Å)	6.102(1)	6.0996(3)
c (Å)	4.749(1)	4.7463(2)
V (Å^{-3})	302.7(1)	302.45(2)
R_{wp}	31.5 %	22.4 %
R_{exp}	28.8 %	20.1 %
X^2	1.20	1.24

7.2.2.3 PXRD of $LiFe_{1-x}Ni_xPO_4$ nanostructures prepared from "$[MLi_2Cl(O^tBu)_4(THF)_2]_n$" (*M*=Fe, Ni)

To examine the influence of the Ni precursor, similar reactions (1 hr at 240 °C) using the "$[NiLi_2Cl(O^tBu)_4(THF)_2]_n$" (VIII) precursor instead of $NiC_2O_4.2H_2O$ were carried out to yield $LiFe_{0.95}Ni_{0.05}PO_4$_V-VIII products. PXRD analysis of the $LiFe_{0.95}Ni_{0.05}PO_4$_V-VIII powders revealed that the synthesis route using the Li and Ni containing alkoxide precursor affords slightly better crystallised $LiFe_{0.95}Ni_{0.05}PO_4$ material in comparison to when $NiC_2O_4{\cdot}2H_2O$ is used, as evidenced by the increase in the peak intensities (Figure 7.8). This may be due to an increased solubility of the "$[NiLi_2Cl(O^tBu)_4(THF)_2]_n$" (VIII) precursor in ethylene glycol and its easy decomposition upon heat treatments in comparison to $NiC_2O_4{\cdot}2H_2O$. Similar reactions with 15% added PVP were also carried out. Figure 7.9 depicts the Rietveld fits from the PXRD data of the $LiFe_{0.95}Ni_{0.05}PO_4$_V-VIII sample after microwave-assisted synthesis (1 hr at 240 °C) with and without using 15% PVP, after a post-heat treatment for 1 hr at 700 °C under Ar flow, and after the 5% wt. C from sucrose carbon coating process under the same heating conditions. An increase in the lattice parameters of this $LiFe_{0.95}Ni_{0.05}PO_4$ phase is observed after the heat treatment and carbon coating process (Table 7.7). Again, the addition of PVP also results in a significant reduction of the cell parameters of $LiFe_{0.95}Ni_{0.05}PO_4$_V-VIII.

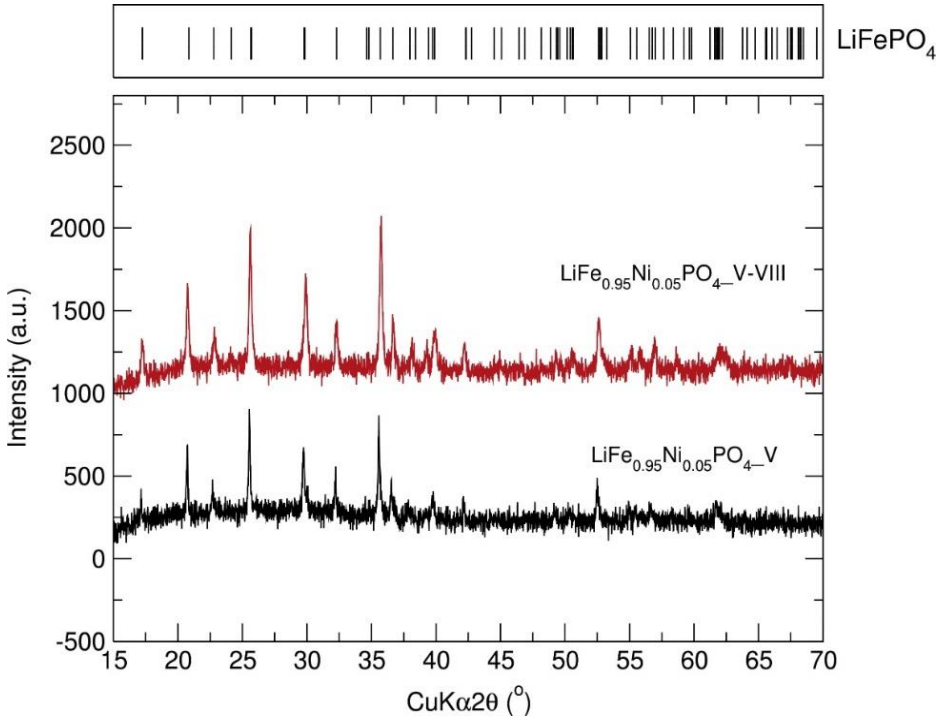

Figure 7.8. Comparative PXRD patterns of $LiFe_{0.95}Ni_{0.05}PO_4$ nanostructures after microwave synthesis using different Ni starting materials. Samples prepared using "$[FeLi_2Cl(O^tBu)_4(THF)_2]_n$" (V) heterometallic alkoxide precursor, $NiC_2O_4{\cdot}2H_2O$ or "$[NiLi_2Cl(O^tBu)_4(THF)_2]_n$" (VIII), and H_3PO_4 in ethylene glycol.

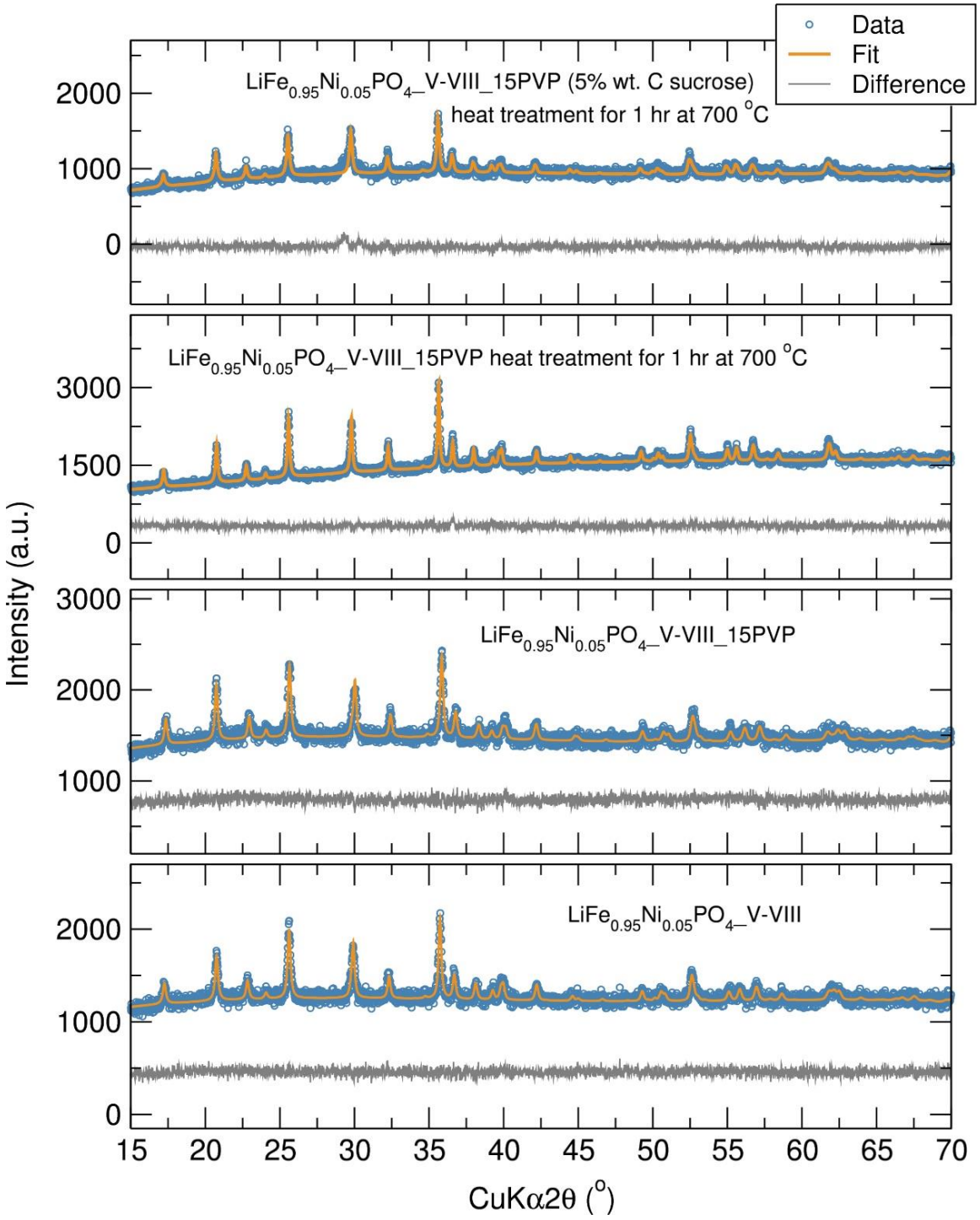

Figure 7.9. Rietveld analysis of PXRD patterns of $LiFe_{0.95}Ni_{0.05}PO_4$_V-VIII nanostructures after microwave synthesis without and with 15% PVP, and post-heat treatment for 1 hr at 700 °C under Ar without and with sucrose carbon coating. Samples prepared using "$[FeLi_2Cl(O^tBu)_4(THF)_2]_n$" (V) and "$[NiLi_2Cl(O^tBu)_4(THF)_2]_n$" (VIII) heterometallic alkoxide precursors, H_3PO_4 and PVP in ethylene glycol.

Table 7.7. Calculated lattice parameters from Rietveld refinements for $LiFe_{0.95}Ni_{0.05}PO_4$_V-VIII nanostructures after microwave synthesis without and with 15% PVP, and post-heat treatment for 1 hr at 700 °C under Ar without and with sucrose carbon coating. Samples prepared using "$[FeLi_2Cl(O^tBu)_4(THF)_2]_n$" (V) and "$[NiLi_2Cl(O^tBu)_4(THF)_2]_n$" (VIII) heterometallic alkoxide precursors, H_3PO_4 and PVP in ethylene glycol.

Sample	$LiFe_{0.95}Ni_{0.05}PO_4$_V-VIII	$LiFe_{0.95}Ni_{0.05}PO_4$_V-VIII_15PVP	$LiFe_{0.95}Ni_{0.05}PO_4$_V-VIII_15PVP Post-heat treatment 1 hr 700 °C	$LiFe_{0.95}Ni_{0.05}PO_4$_V-VIII_15PVP (5% wt. C sucrose) Post-heat treatment 1 hr 700 °C
Space group	*Pnma*	*Pnma*	*Pnma*	*Pnma*
a (Å)	10.271(2)	10.212(2)	10.309(1)	10.318(1)
b (Å)	5.969(1)	5.947(1)	5.9956(6)	6.001(1)
c (Å)	4.704(1)	4.712(1)	4.7041(6)	4.714(1)
V (Å^{-3})	288.4(1)	286.2(1)	290.75(5)	291.9(1)
R_{wp}	44.2 %	44.4 %	36.0 %	48.7 %
R_{exp}	41.31 %	40.28 %	32.85 %	43.73 %
X^2	1.14	1.21	1.20	1.24

Estimation of the crystallite sizes for the Ni doped $LiFePO_4$ nanostructures using the Scherrer equation[208] applied to the (211) diffraction peaks suggested that the addition of PVP slightly decreases the crystallite sizes of the $LiFe_{0.95}Ni_{0.05}PO_4$ nanophases from approximately 56 nm for $LiFe_{0.95}Ni_{0.05}PO_4$_V (No PVP) to ~50 nm for the $LiFe_{0.95}Ni_{0.05}PO_4$_V_10PVP, $LiFe_{0.95}Ni_{0.05}PO_4$_V_15PVP and $LiFe_{0.95}Ni_{0.05}PO_4$_V_20PVP. No significant reduction in the crystallite size of the $LiFe_{0.95}Ni_{0.05}PO_4$ powders was observed when increasing the amount of PVP from 10 to 20 %. A slight increase in crystallite size was observed when increasing the Ni content to $LiFe_{0.9}Ni_{0.1}PO_4$_V_10PVP. Interestingly, a smaller crystallite size (~34 nm) is noted when the Li and Ni containing metal alkoxide precursor is employed with 15% PVP in the preparation of $LiFe_{0.95}Ni_{0.05}PO_4$_V-VIII_15PVP. Heat treatment of samples led to an increase in crystallite size of $LiFe_{0.95}Ni_{0.05}PO_4$_V_15PVP (~71 nm) and $LiFe_{0.95}Ni_{0.05}O_4$_V-VIII_15PVP (~54 nm). Crystallite growth upon heat treatment was not observed for the carbon coated C/$LiFe_{0.95}Ni_{0.05}PO_4$_V_15PVP powders (~48 nm), suggesting that the coating may inhibit the crystallite growth during the heating process. This has been previously similarly noted in the literature.[71, 365] The smallest crystallite sizes were calculated for the $LiMn_{0.95}Ni_{0.05}PO_4$_VI_15PVP sample of ~22 nm. These results are in good agreement with the smaller crystallite size of $LiMnPO_4$_VI compared to $LiFePO_4$_V previously shown in Chapter 5. Table 7.8 summarises the calculated crystallite sizes from Scherrer broadening for Ni doped $LiFePO_4$ and $LiMnPO_4$ nanostructures.

Table 7.8. Calculated crystallite sizes from Scherrer broadening for Ni doped $LiFePO_4$ and $LiMnPO_4$ nanostructures.

Sample	Estimated crystallite size (nm)
$LiFe_{0.95}Ni_{0.05}PO_4$_V	56
$LiFe_{0.95}Ni_{0.05}PO_4$_V_10PVP	49
$LiFe_{0.95}Ni_{0.05}PO_4$_V_15PVP	50
$LiFe_{0.95}Ni_{0.05}PO_4$_V_15PVP post-heat treatment	71
C/$LiFe_{0.95}Ni_{0.05}PO_4$_V_15PVP post-heat treatment (carbon coated)	48
$LiFe_{0.95}Ni_{0.05}PO_4$_V_20PVP	49
$LiFe_{0.9}Ni_{0.1}PO_4$_V_10PVP	63
$LiFe_{0.95}Ni_{0.05}PO_4$_V-VIII	37
$LiFe_{0.95}Ni_{0.05}PO_4$_V-VIII_15PVP	34
$LiFe_{0.95}Ni_{0.05}PO_4$_V-VIII_15PVP-post heat treatment	54
$LiMn_{0.95}Ni_{0.05}PO_4$_VI_15PVP	22

The next aim was to try to reduce the reaction times. A reaction using a mixture of "$[FeLi_2Cl(O^tBu)_4(THF)_2]_n$" (V) and "$[NiLi_2Cl(O^tBu)_4(THF)_2]_n$" (VIII) alkoxide precursors was carried out for 30 min at 240 °C. PXRD analysis of the resulting powder reveals that a mixture of poorly crystalline $LiFe_{0.95}Ni_{0.05}PO_4$ and some oxidised $FePO_4$ product was obtained (Figure 7.10). The formation of $FePO_4$ was also evidenced by the reddish colour of the obtained powder, which indicated that the oxidation from Fe^{2+} and Fe^{3+} had taken place during the synthesis process. These results suggested that longer reaction times were required and a 1 hour microwave treatment instead afforded the target $LiFe_{0.95}Ni_{0.05}PO_4$ product.

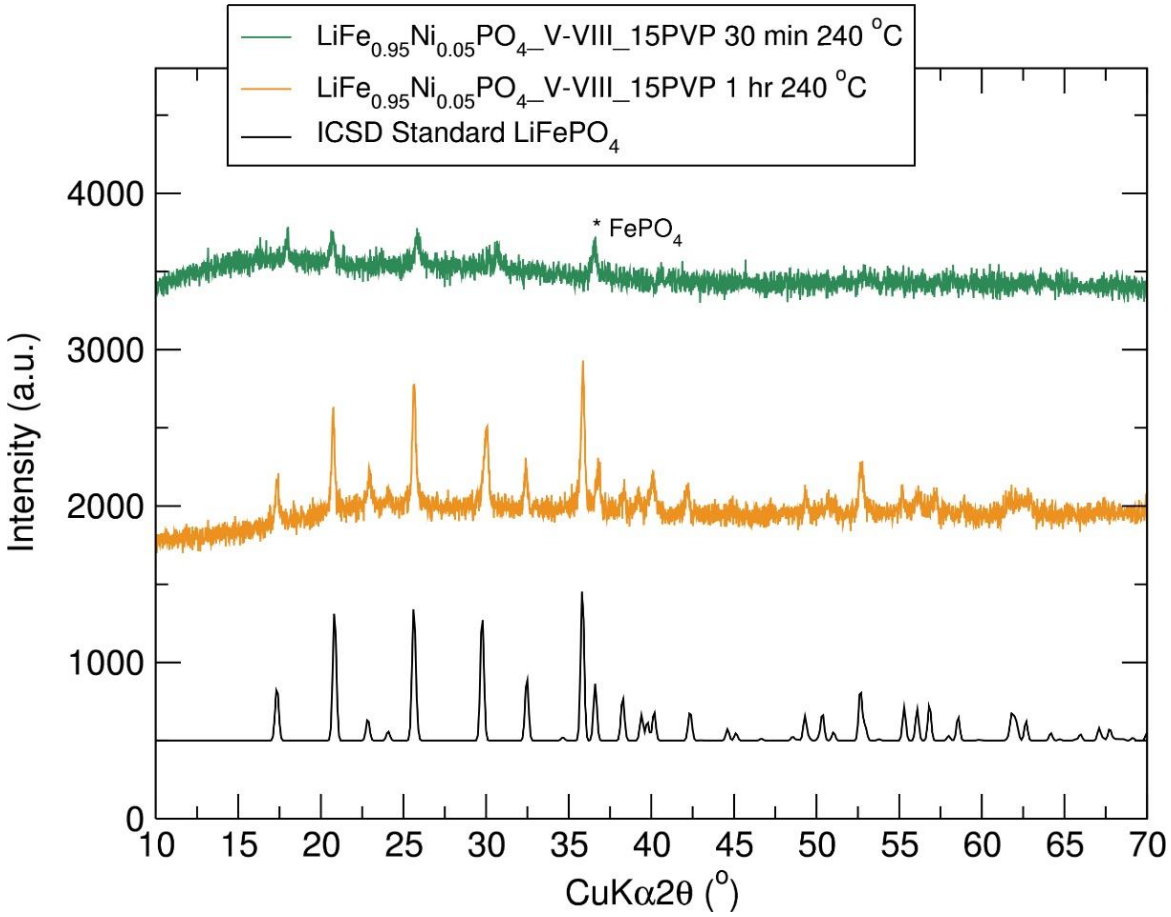

Figure 7.10. Comparative PXRD patterns of $LiFe_{0.95}Ni_{0.05}PO_4$ nanostructures after microwave synthesis at different reaction times using "$[FeLi_2Cl(O^tBu)_4(THF)_2]_n$" (V) and "$[NiLi_2Cl(O^tBu)_4(THF)_2]_n$" (VIII) heterometallic alkoxide precursors, H_3PO_4 and 15% PVP in ethylene glycol.

Finally, the synthesis of single-phase olivine $LiNiPO_4$ *via* a 1 hr microwave treatment at 240 °C of "$[NiLi_2Cl(O^tBu)_4(THF)_2]_n$" (VIII) heterometallic alkoxide precursor and H_3PO_4 in ethylene glycol was attempted ($LiNiPO_4$_VIII product). Unfortunately, as evidenced in the PXRD pattern in Figure 7.12, the reduction of Ni^{2+} to Ni metal took place and a mixture of Ni metal polymorphs belonging to the *Fm-3m* (ICSD No 01-073-6826 4-850)[366] and *P63/mmc* (ICSD No 01-089-7129 45-102)[367] space groups was formed. Further attempts to prepare singe phase $LiNiPO_4$ through a single source precursor route were tried (e.g. using "$[NiLi_2Cl(O^tBu)_4(THF)_2]_n$" (VIII) heterometallic alkoxide and the ionic liquid 1-ethyl-3-methylimidazolium trifluoromethanesulfonate as solvent), but this also afforded Ni metal (see $LiNiPO_4$_VIII_IL in Figure 7.11). Even the less reducing conditions of the 1-ethyl-3-methylimidazolium trifluoromethanesulfonate ionic liquid in comparison to ethylene glycol led to metallic Ni. Other synthetic strategies, the addition of surfactants or the utilisation of different phosphorous sources/solvents may afford phase pure olivine $LiNiPO_4$. For example $LiNiPO_4$ nanorods and nanoplates have been successfully prepared *via* a one-pot synthesis using supercritical fluid process with oleylamine or ascorbic acid

as surfactant and reducing agents.[368] Orthorombic *Pnma* $LiNiPO_4$ has also been synthesised through a citric acid assisted modified sol-gel method using metal acetates and $NH_4H_2PO_4$ as starting materials.[369]

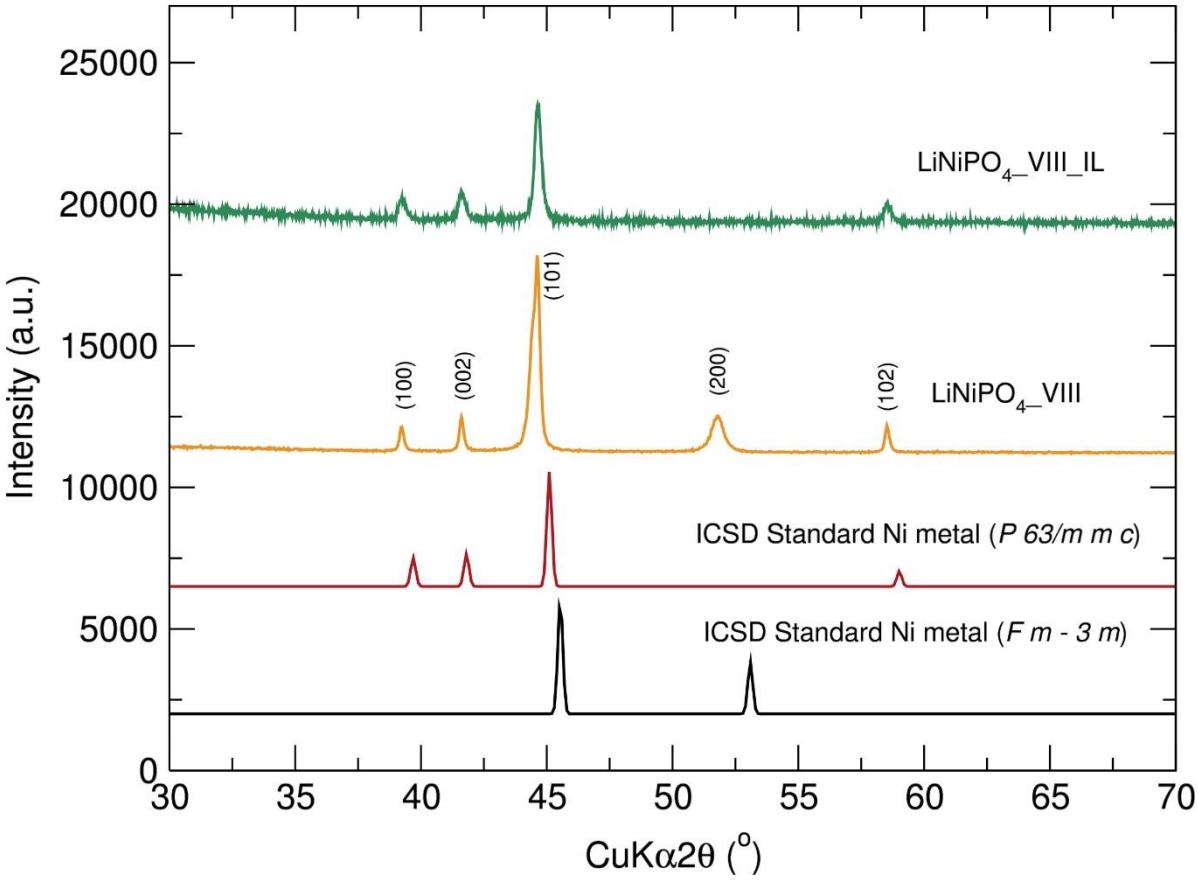

Figure 7.11. PXRD patterns of $LiNiPO_4$ after microwave synthesis using "$[NiLi_2Cl(O^tBu)_4(THF)_2]_n$" (VIII) heterometallic alkoxide precursor and H_3PO_4 in ethylene glycol or EMI-TFMS.

7.2.2.4 SEM and EDS of $LiFe_{0.95}Ni_{0.05}PO_4$ nanostructures

Particle agglomeration can be regarded as a possible cause of deterioration of electrochemical performance in olivine nanomaterials. By avoiding aggregation, larger surface areas are available for the Li (de)insertion and ultimately better electrochemical performance. Here, PVP has been used to control particle size and prevent agglomeration in $LiFe_{0.95}Ni_{0.5}PO_4$ nanoparticles. The viscosity of PVP can limit the aggregation of the precursor particles. Another advantage to this route is the possible carbonisation of the PVP to generate a thin carbon coating on the surface of the formed $LiFe_{0.95}Ni_{0.5}PO_4$, which can impede particle growth and enhance conductivity.[370] PVP has previously been used to control the particle size of nano-$LiFePO_4$/C *via* a simple electrospinning method. The PVP polymer matrix tailors the particle shape and also helps to maintain the connectivity

between nanoparticles as a result of its residual conductive carbon after high-temperature pyrolysis, thereby limiting crystal growth and increasing the conductivity.[371] SEM images of the $LiFe_{0.95}Ni_{0.05}PO_4$_V (No PVP), $LiFe_{0.95}Ni_{0.05}PO_4$_V_15PVP and $LiFe_{0.95}Ni_{0.05}PO_4$_V-VIII_15PVP powders prepared through a microwave synthesis (1 hr at 240 °C) using the heterometallic alkoxide "$[FeLi_2Cl(O^tBu)_4(THF)_2]_n$" (V) and $NiC_2O_4{\cdot}2H_2O$ or "$[NiLi_2Cl(O^tBu)_4(THF)_2]_n$" (VIII) revealed a non-uniform quasi-spherical morphology with particle sizes ranging from 20 to 60 nm (Figure 7.12). Particle morphology was similar in all three $LiFe_{0.95}Ni_{0.05}PO_4$ samples and, unfortunately, particle agglomeration was observed even when using PVP, which indicated that there was no significant dispersion effect for PVP in the established reaction conditions. Similar observations were also reported by Lei *et al*. on solvothermally synthesised $LiFePO_4$-carbon composites.[372] The particle size distributions determined from measuring 70 particles in the SEM images are illustrated in Figure A7.5. From the plots, the mean particle sizes were calculated and results indicate that the particle sizes slightly decreased when using PVP (40.8 ± 9.3 nm for $LiFe_{0.95}Ni_{0.05}PO_4$_V (No PVP) against 35.9 ± 4.4 nm for $LiFe_{0.95}Ni_{0.05}PO_4$_V_15PVP and 33.4 ± 4.0 nm for $LiFe_{0.95}Ni_{0.05}PO_4$_V-VIII_15PVP). These results correlate well with the crystallite size determinations using the Scherrer equation already performed, which showed a decrease in the crystallite in $LiFe_{0.95}Ni_{0.05}PO_4$ size when employing PVP. SEM images of the $LiFe_{0.95}Ni_{0.05}PO_4$_V-VIII_15PVP and $LiMn_{0.95}Ni_{0.05}PO_4$_VI_15PVP nanostructures after the heat treatment for 1 hr at 700 °C under Ar confirmed a clear increase in the particles sizes after the heating process. Particle size analysis of the $LiFe_{0.95}Ni_{0.05}PO_4$_V-VIII_15PVP and $LiMn_{0.95}Ni_{0.05}PO_4$_VI_15PVP samples showed average particle sizes of 67.6 ± 10.1 nm and 71.3 ± 12.0 nm, repectively (Figure 7.13). EDS analysis of the $LiFe_{0.95}Ni_{0.05}PO_4$_V-VIII_15PVP and $LiMn_{0.95}Ni_{0.05}PO_4$_VI_15PVP nanoparticles confirmed the presence of Ni in both samples, indicating that Ni has been successfully introduced in the olivine $LiFePO_4$ and $LiMnPO_4$ structures (Figure 7.14).

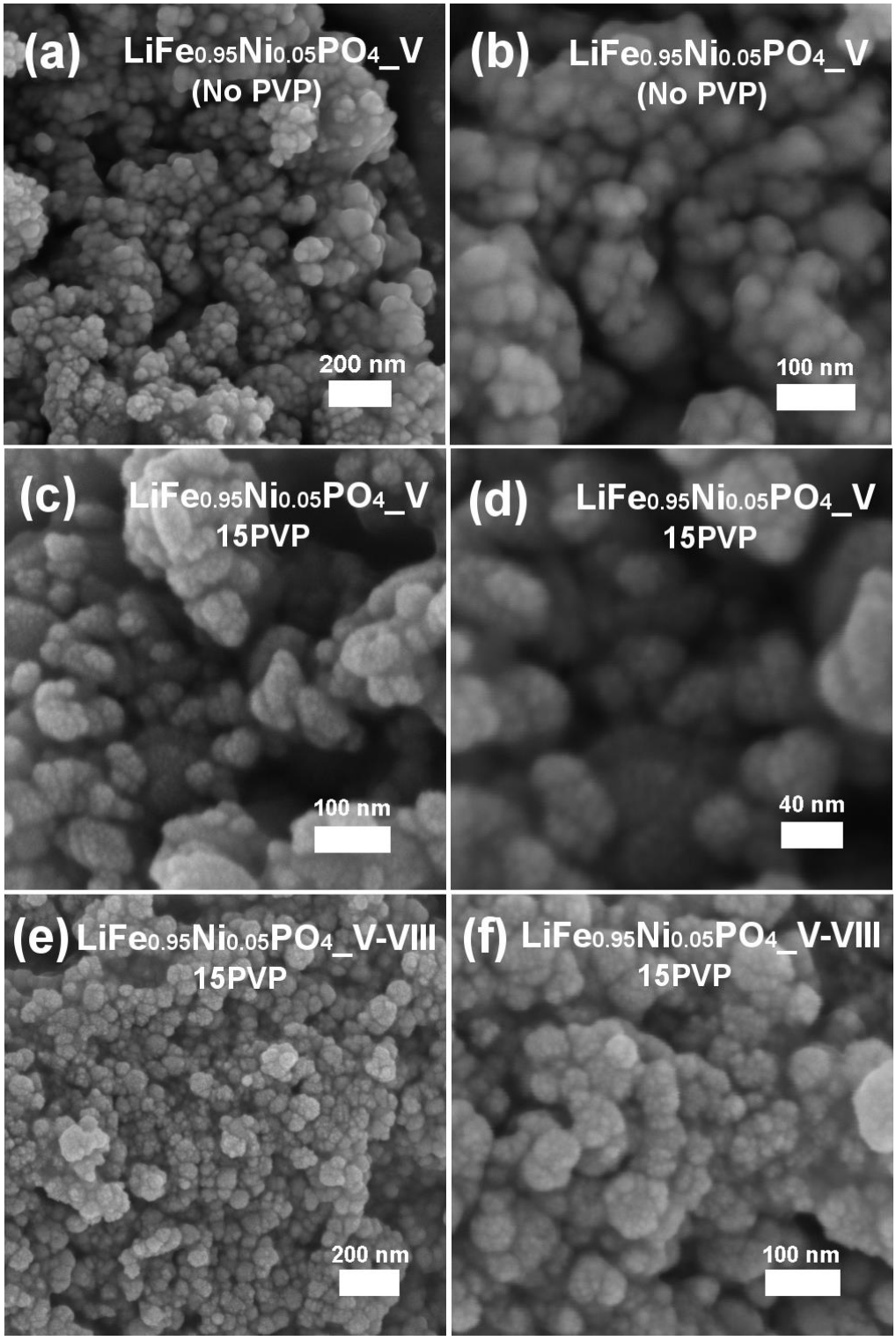

Figure 7.12. SEM images of **(a, b)** $LiFe_{0.95}Ni_{0.05}PO_4$_V (No PVP), **(c, d)** $LiFe_{0.95}Ni_{0.05}PO_4$_V_15PVP nanostructures prepared through a microwave synthesis (1 hr at 240 °C) using heterometallic alkoxide precursor "$[FeLi_2Cl(O^tBu)_4(THF)_2]_n$" (V) and $NiC_2O_4{\cdot}2H_2O$, **(e, f)** $LiFe_{0.95}Ni_{0.05}PO_4$_V-VIII_15PVP nanostructures prepared through a microwave synthesis (1 hr at 240 °C) using heterometallic alkoxide precursors "$[FeLi_2Cl(O^tBu)_4(THF)_2]_n$" (V) and "$[NiLi_2Cl(O^tBu)_4(THF)_2]_n$" (VIII).

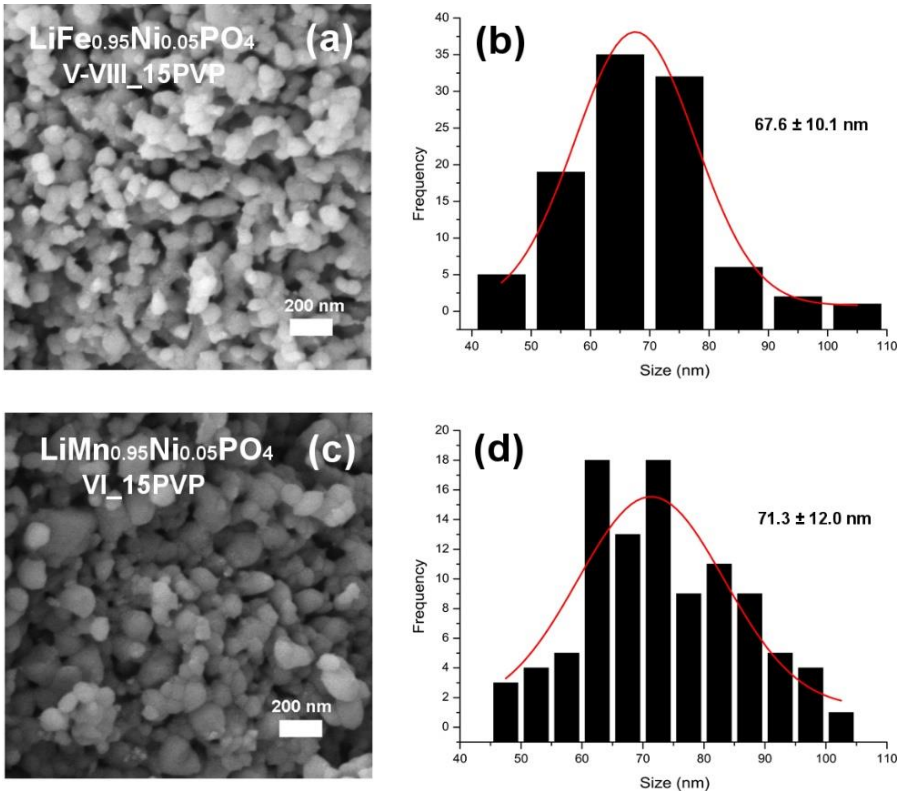

Figure 7.13. SEM images of **(a)** $LiFe_{0.95}Ni_{0.05}PO_4$_V-VIII_15PVP and **(b)** $LiMn_{0.95}Ni_{0.05}PO_4$_VI_15PVP nanostructures after heat treatment for 1 hr at 700 ºC under Ar. Particle size distribution of **(c)** $LiFe_{0.95}Ni_{0.05}PO_4$_V-VIII_15PVP and **(d)** $LiMn_{0.95}Ni_{0.05}PO_4$_VI_15PVP nanostructures.

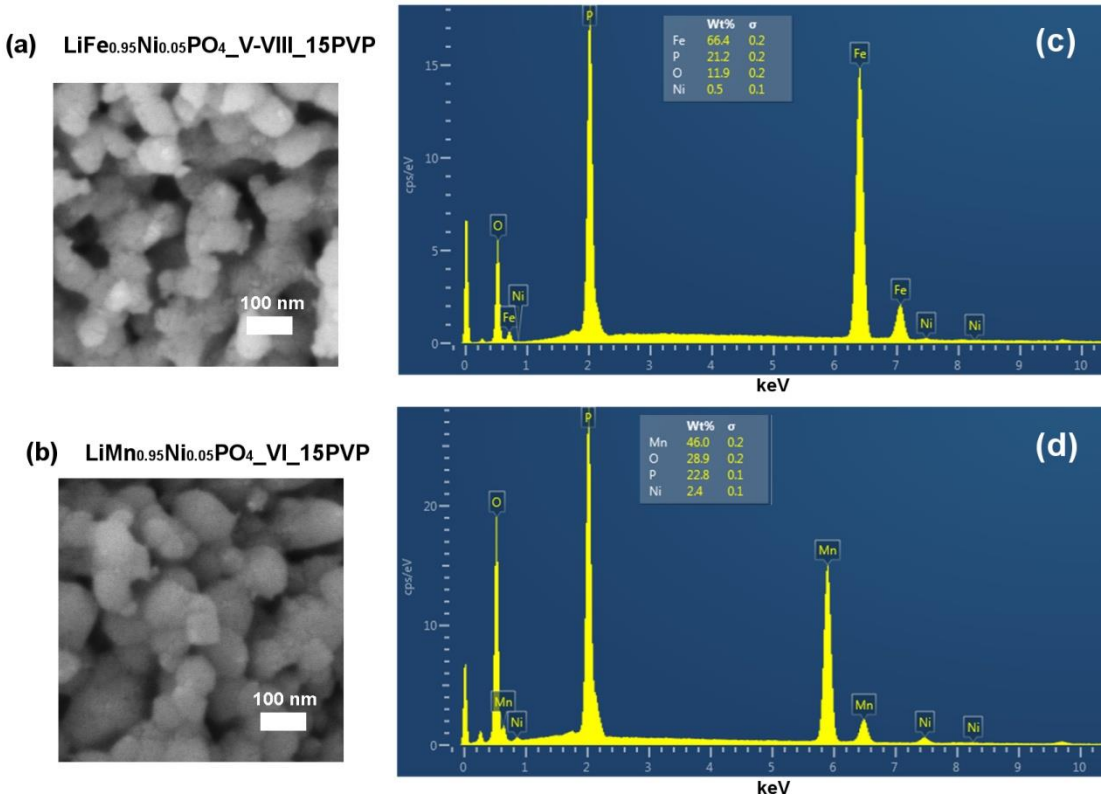

Figure 7.14. SEM images of **(a)** $LiFe_{0.95}Ni_{0.05}PO_4$_V-VIII_15PVP and **(b)** $LiMn_{0.95}Ni_{0.05}PO_4$_VI_15PVP nanostructures. EDS spectra of **(c)** $LiFe_{0.95}Ni_{0.05}PO_4$_V-VIII_15PVP and **(d)** $LiMn_{0.95}Ni_{0.05}PO_4$_VI_15PVP nanostructures.

7.2.2.5 Electrochemical performance of $LiFe_{0.95}Ni_{0.05}PO_4$ nanostructures

The electrochemical behaviour of the C/$LiFe_{0.95}Ni_{0.05}PO_4$ nanostructures prepared with PVP was investigated in an effort to show that a good electrochemical performance can be obtained by only adding PVP in the microwave synthesis without the need for further carbon coating treatments. Galvanostatic cycling at C/20 rate from 2.2 V to 4.2 V of the C/$LiFe_{0.95}Ni_{0.05}PO_4$_V_15PVP and C/$LiFe_{0.95}Ni_{0.05}PO_4$_V-VIII_15PVP nanostructures after post-heat treatment for 1 hr at 700 ºC delivered discharge capacities of approximately ~125 mAh·g^{-1} and 120 mAh·g^{-1}, respectively, over the first 20 cycles. These results indicated that no noticeable differences in the resulting electrochemical behaviour were observed between the $LiFe_{0.95}Ni_{0.05}PO_4$ nanostructures prepared by using $NiC_2O_4{\cdot}2H_2O$ or "$[NiLi_2Cl(O^tBu)_4(THF)_2]_n$" (VIII) as Ni precursors. The progressive improvement of the specific capacity over cycling in $LiFe_{0.95}Ni_{0.05}PO_4$_V-VIII_15PVP could be ascribed to the better wetting of the active material with the electrolyte as the particles develop cracks and pores upon cycling. In order to improve the electronic conductivity and electrochemical performance of the $LiFe_{0.95}Ni_{0.05}PO_4$_V-VIII_15PVP nanoparticles, an additional carbon coating with sucrose was applied. The $LiFe_{0.95}Ni_{0.05}PO_4$_V-VIII_15PVP powders were carbon coated with only 5 % wt. C from sucrose. These samples displayed a slightly enhanced electrochemical performance reaching around 140 mAh·g^{-1} over the first 15 cycles with no evident capacity fading (Figure 7.15 (e) and (f)) and coulombic efficiencies of 98%. However, increasing the carbon coating content up to 15% wt. C did not lead to further enhancement of the electrochemical performance, yielding capacities of only ~80 mAh·g^{-1} (Figure 7.16). This could be attributed to the fact that excessive amorphous carbon in the electrode mixture could hinder the Li^+ extraction insertion process from the $LiFe_{0.95}Ni_{0.05}PO_4$ nanoparticles. Ni et *al*. investigated the effect of different carbon contents in C/$LiFePO_4$ composites coated with carbon layers pyrolysed from sucrose and also reported that too much carbon loading could inhibit the diffusion of Li^+ ions.[193] Previous investigations on microwave synthesised Ni doped $LiFePO_4$ conducted by Niederberger *et al.*[46] demonstrated excellent electrochemical performance exhibiting capacities of 168 mAh·g^{-1} and outstanding capacity retention after 300 cycles when cycling in a slightly wider voltage window between 2.0 V to 4.5 V. Furthermore, they reported that the level of metal doping in $LiFePO_4$ has a strong influence in the capacities delivered and the cycling stability. In the particular case of Ni doping, a concentration of 7 mol% Ni markedly outperformed in comparison to 5 mol% and 2 mol % Ni. These results suggest that other levels of Ni doping in $LiFe_{1-x}Ni_xPO_4$ may lead to enhanced electrochemical performances. On the other hand, the $LiMn_{0.95}Ni_{0.05}PO_4$_VI_15PVP nanostructure (heat treated for 1 hr at 700 ºC under Ar) delivered a poor electrochemical performance reaching capacities of only around 40

mAh·g^{-1} (Figure A7.6). These results indicate that a carbon coating may still be required in order to further enhance the electrochemical performance of $LiMn_{0.95}Ni_{0.05}PO_4$ nanostructures.

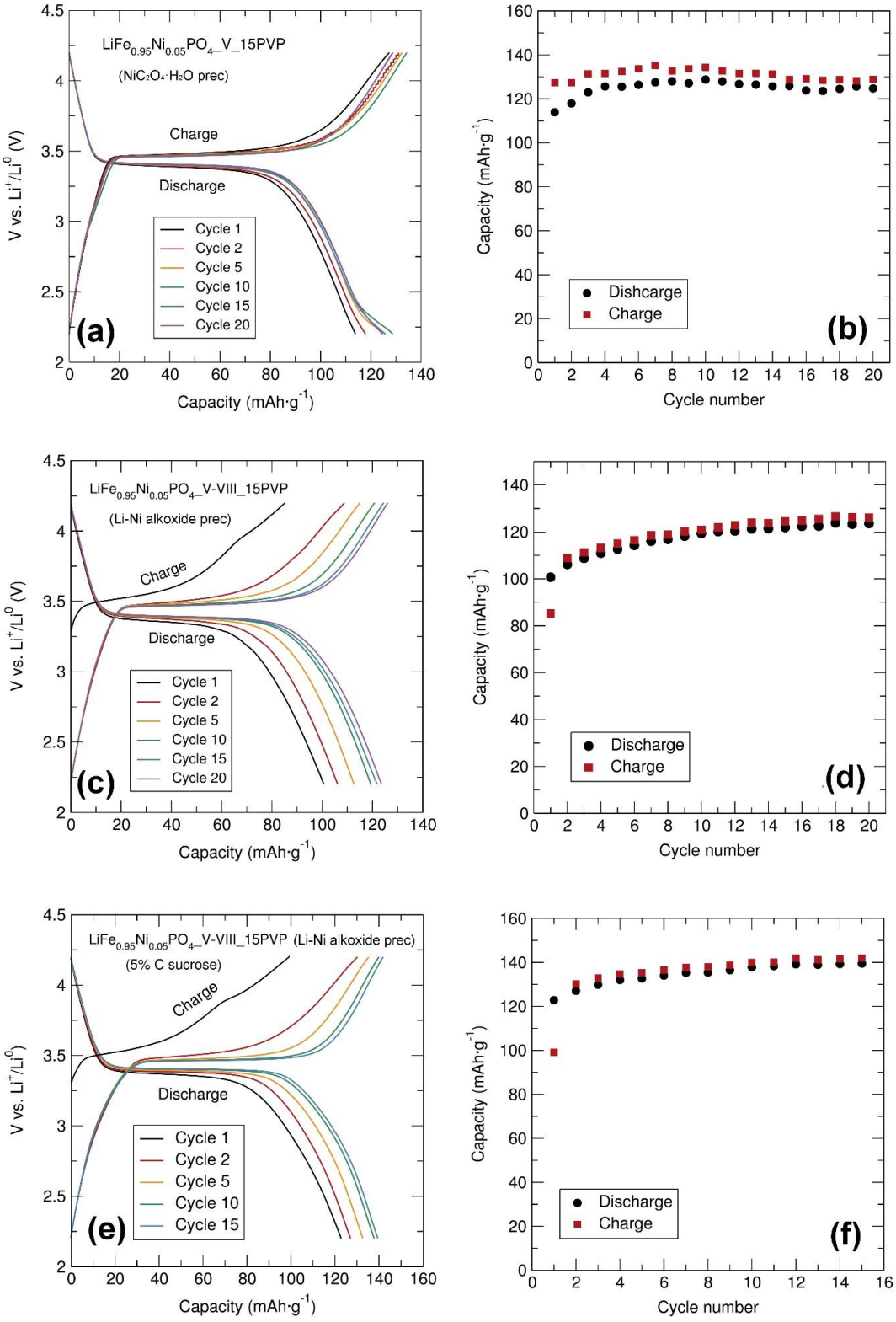

Figure 7.15. (a, c, d) Charge/discharge capacity profiles and **(b, d, f)** cycling stability between 2.2 V and 4.2 V at C/20 rate of $LiFe_{0.95}Ni_{0.05}PO_4$_V_15PVP, $LiFe_{0.95}Ni_{0.05}PO_4$_V-VIII_15PVP and $LiFe_{0.95}Ni_{0.05}PO_4$_V-VIII_15PVP (5% wt. C from sucrose), respectively, mixed with C black and PTFE in 60:30:10 (% wt. ratio).

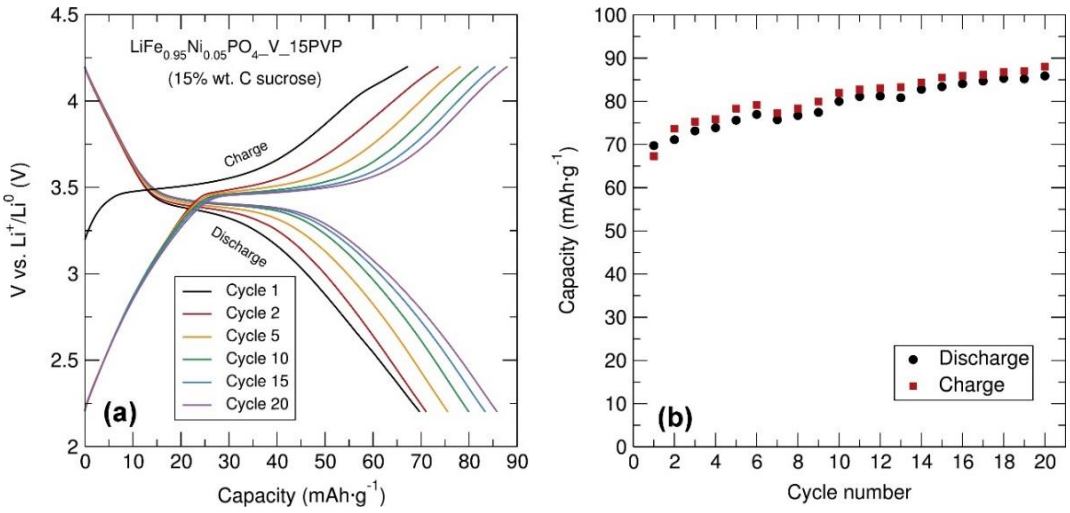

Figure 7.16. (a) Charge/discharge capacities and **(b)** cycling stability of C/$LiFe_{0.95}Ni_{0.05}PO_4$_V (15% wt.C from sucrose) prepared with "$[FeLi_2Cl(O^tBu)_4(THF)_2]_n$" (V) heterometallic alkoxide precursor, $NiC_2O_4{\cdot}2H_2O$ and 15% PVP, and mixed with C black and PTFE in 60:30:10 (% wt. ratio) between 2.2 V and 4.2 V at C/20 rate.

The charge/discharge cycling performance under various discharge rates, ranging from C/10 to 30 C with five cycles at each rate, was tested for the $LiFe_{0.95}Ni_{0.05}PO_4$_V-VIII_15PVP (5% wt. C from sucrose) nanostructures and demonstrated an excellent rate capability (Figure 7.17). The specific capacities generally decreased along with an increase of the charge/discharge rates, delivering discharge capacities of approximately 158, 157, 152, 147.4, 142, 133, 121, 93 and 66 $mAh{\cdot}g^{-1}$ at C/10, C/5, C/2, C, 2 C, 5 C, 10 C, 20 C and 30 C, respectively. This C/$LiFe_{0.95}Ni_{0.05}PO_4$_V-VIII_15PVP (5% wt. C from sucrose) nanostructure demonstrated enhanced rate capabilities compared to previously reported $LiFe_{0.98}Ni_{0.02}PO_4$ composite prepared by a ball-milled assisted solid-state reaction using glucose as a carbon sources, which displayed discharge capacities of 142 and 121 $mAh{\cdot}g^{-1}$ at 0.1 C and 2 C, respectively.[322] On the other hand, a Ni doped $LiFePO_4$/C nanocomposite prepared through a simple solid state reaction using polyvinyl alcohol exhibited a good electrochemical performance delivering discharge capacities of 170 $mAh{\cdot}g^{-1}$ at 0.2 C. That cathode material also demonstrated outstanding rate capability and long-term cycling performance displaying capacities of 150 $mAh{\cdot}g^{-1}$ at 10 C with a capacity retention up to 95% after 5500 cycles. Simultaneous carbon coating and Ni doping led to a great enhancement of electronic conductivity, and the reduced particle size distributed in the range of 20–60 nm improved the Li^+ diffusion process effectively. Consequently, the material exhibited an excellent electrochemical performance, especially the high rate performance.[360] Also, a Ni and Mn co-doped $LiFe_{0.95}Ni_{0.02}Mn_{0.03}PO_4$/C synthesised by a simple solid state route was reported to deliver excellent electrochemical performance with discharge capacities of 154.2 (0.5 C), 146.1 (1 C), 140.9 (2 C) and 128.4 (5 C) $mAh{\cdot}g^{-1}$. Ni and Mn co-doping can stabilise the olivine

crystal structure, lengthen the Li-O bond, decrease the charge transfer resistance, enhance the Li^+ diffusion and thus improve the cycling and high-rate capability of $LiFePO_4$.[178] PXRD analysis of the post-cycled $LiFe_{0.95}Ni_{0.05}PO_4$_V-VIII_15PVP (5% wt. C from sucrose) nanopowders in the discharge state showed weak reflections indexed to the olivine $LiFePO_4$ structure, suggesting that the olivine $LiFe_{0.95}Ni_{0.05}PO_4$ phase may be preserved after the cycling process (Figure 7.18).

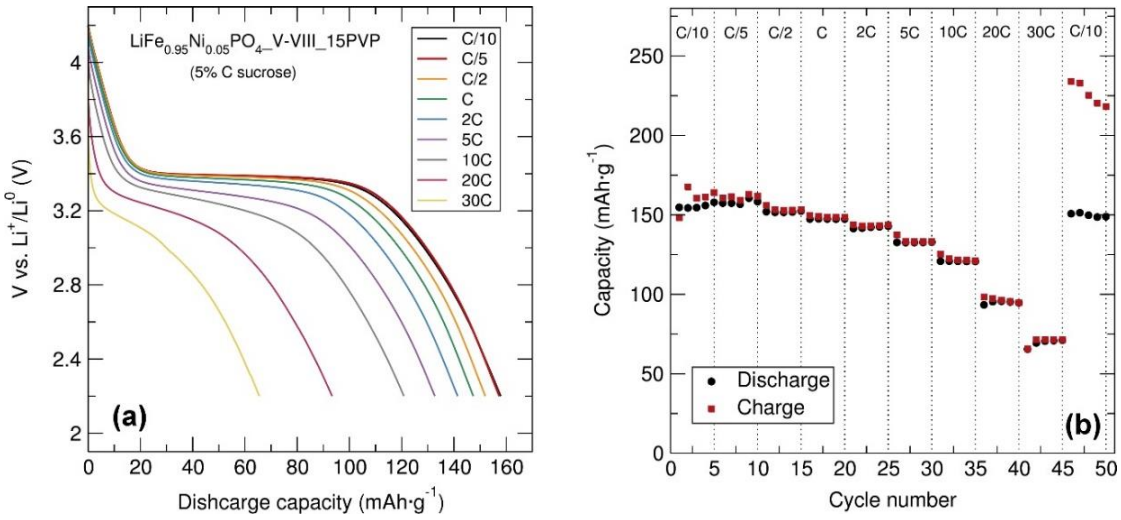

Figure 7.17. (a) Discharge capacity curves and **(b)** cycling stability at different charge-discharge C rates of C/$LiFe_{0.95}Ni_{0.05}PO_4$_V-VII_15PVP (5% wt. C from sucrose) nanostructures prepared with "$[FeLiCl(O^tBu)_4(THF)_2]_n$" (V) and "$[NiLiCl(O^tBu)_4(THF)_2]_n$" (VIII) heterometallic alkoxide precursors and mixed with C black and PTFE in 60:30:10 (% wt. ratio).

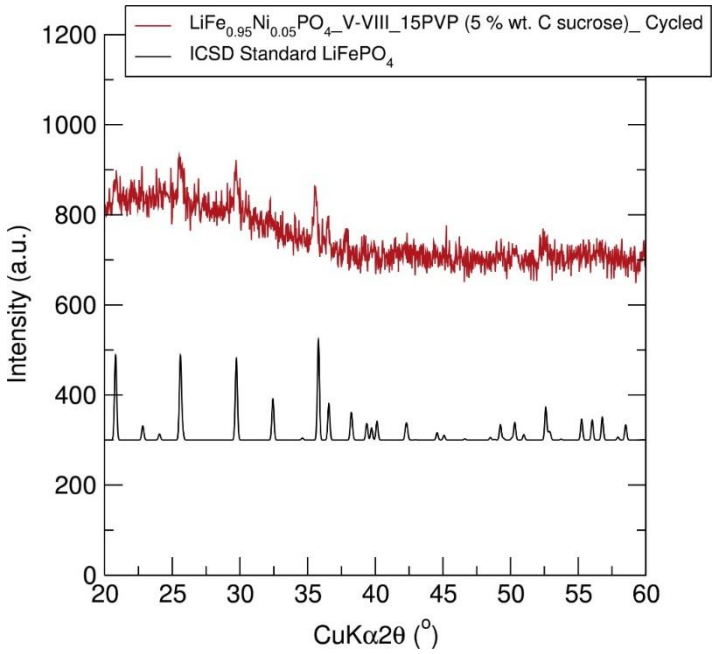

Figure 7.18. PXRD of post-cycled C/$LiFe_{0.95}Ni_{0.05}PO_4$_V and VIII_15PVP (5% wt. C from sucrose) in the discharged state.

The CV for the C/$LiFe_{0.95}Ni_{0.05}PO_4$_V-VIII_15PVP (5% wt. C from sucrose) nanostructure at 0.1 mV·s^{-1} scan rate between 2.5 V and 4.5 V displayed the anodic and cathodic peaks characteristic of the Fe^{3+}/Fe^{2+} redox pair with an excellent overlap of the CV curves over cycling, demonstrating the good reversibility of the material (Figure 7.19 (a)). Figure 7.19 (b) shows the CV for the same material measured at 0.1, 0.2, 0.5 and 1 mV·s^{-1} scan rates. Results showed that the peak separation and the cathodic and anodic peak currents increased with increasing scan rate. At higher scan rates, the polarisation rises, as evidenced by the increase in the oxidation potential and a decrease in the reduction potential for the Fe^{3+}/Fe^{2+} redox couple.

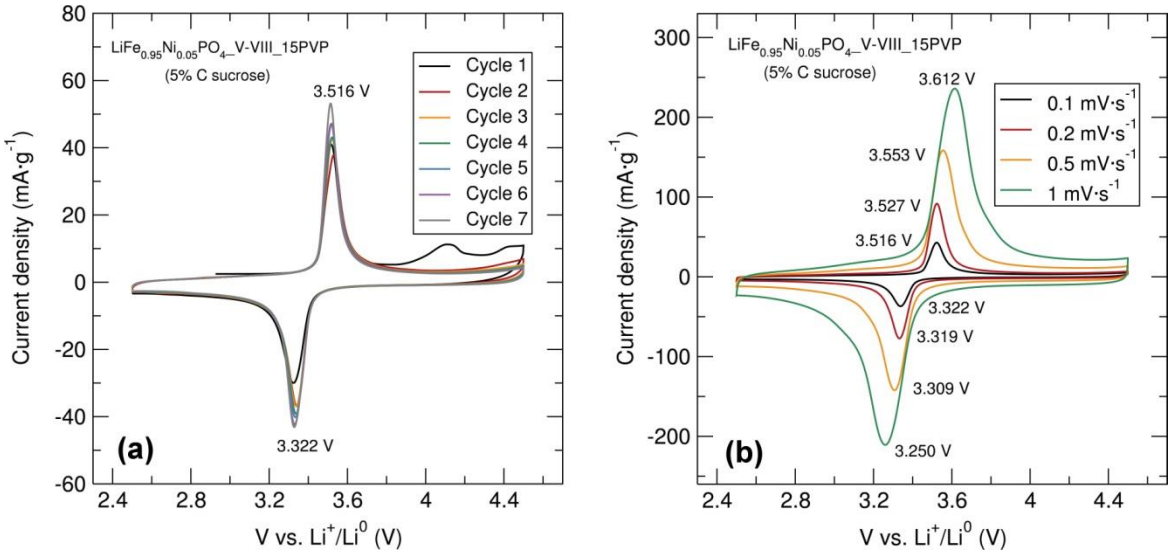

Figure 7.19. (a) CV at a 0.1 mV·s^{-1} scan rate between 2.5 V and 4.5 V of C/$LiFe_{0.95}Ni_{0.05}PO_4$_V-VIII_15PVP (5% wt. C from sucrose) nanostructure prepared through a microwave-assisted synthesis with "$[FeLiCl(O^tBu)_4(THF)_2]_n$" (V) and "$[NiLiCl(O^tBu)_4(THF)_2]_n$" (VIII) heterometallic alkoxide precursors. **(b)** CV profiles of C/$LiFe_{0.95}Ni_{0.05}PO_4$_V-VIII_15PVP (5% wt. C from sucrose) at different scan rates.

The lithium diffusion coefficient for the C/$LiFe_{0.95}Ni_{0.05}PO_4$_V-VIII_15PVP (5 % wt. C from sucrose) nanostructure was estimated from the CV study at different scan rates. For this rough estimation of the lithium diffusion coefficient, it was considered that the pellet of the working electrode was 20 μm thick with a surface area of 0.126 cm^2. Representation of the peak currents against the square root of the scan rates ($v^{0.5}$) shows a linear dependence between the peak current and $v^{0.5}$ (Figure 7.20). Application of Equation 2.10 allows the estimation of the Li^+ diffusion constant. The apparent anodic and cathodic Li^+ diffusion constants of C/$LiFe_{0.95}Ni_{0.05}PO_4$_V-VIII_15PVP (5 % wt. C from sucrose) calculated using equation 2.10 with the slope of the peak current *vs.* $v^{0.5}$ plot were 1.92 x 10^{-9} and 1.55 x 10^{-9} $cm^2 \cdot s^{-1}$, respectively. In the particular case of C/$LiFe_{0.95}Ni_{0.05}PO_4$, the possible presence of Ni-rich and Fe-rich domains may have an effect in the Li^+ transport

characteristics during charge and discharge. The calculated lithium diffusion coefficient for the C/$LiFe_{0.95}Ni_{0.05}PO_4$_V-VIII_15PVP (5 % wt. C from sucrose) nanostructure measured here is significantly higher than the D_{Li} of 4.28 x 10^{-11} $cm^2 \cdot s^{-1}$ for a C/$LiFe_{0.98}Ni_{0.02}PO_4$ composite determined by similar CV analysis.[322]

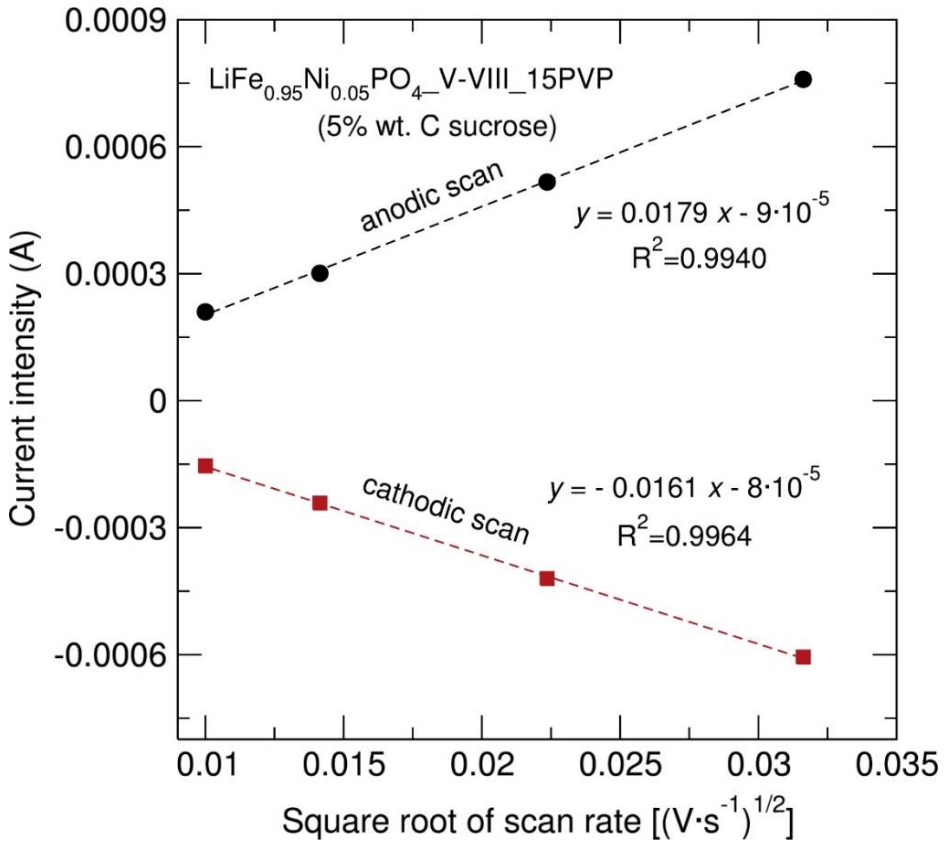

Figure 7.20. Peak current *vs.* square root of the scan rate for the C/$LiFe_{0.95}Ni_{0.05}PO_4$_V-VIII_15PVP (5% wt. C from sucrose) nanostructure prepared through a microwave-assisted synthesis using "$[FeLiCl(O^tBu)_4(THF)_2]_n$" (V) and "$[NiLiCl(O^tBu)_4(THF)_2]_n$" (V) heterometallic alkoxide precursors.

Comparing the CV curves of C/$LiFe_{0.95}Ni_{0.05}PO_4$_V-VIII_15PVP (5% wt. C from sucrose) nanostructures with undoped C/$LiFePO_4$_V (15% wt. C from sucrose) reveals a slight enhancement in the Li^+ kinetics when substituting some Fe^{2+} for Ni^{2+}, as evidenced by the narrower voltage difference between the cathodic and anodic peak in C/$LiFe_{0.95}Ni_{0.05}PO_4$_V-VIII_15PVP (Figure 7.21), which suggests a lower electron transfer resistance. Previous reports have shown that the presence of a small amount of Ni^{2+} such as in the $LiMn_{0.8}Fe_{0.1}Ni_{0.1}PO_4$ olivine provided structural stability accommodating the volume change between the $LiMnPO_4$ and $MnPO_4$ phases, favouring the redox exchange and the reversible extraction−insertion of Li^+ ions. Moreover, relatively longer Li−O bonds with smaller binding energy would lead to an easier migration of Li^+ cations during the charge−discharge processes.[364, 373]

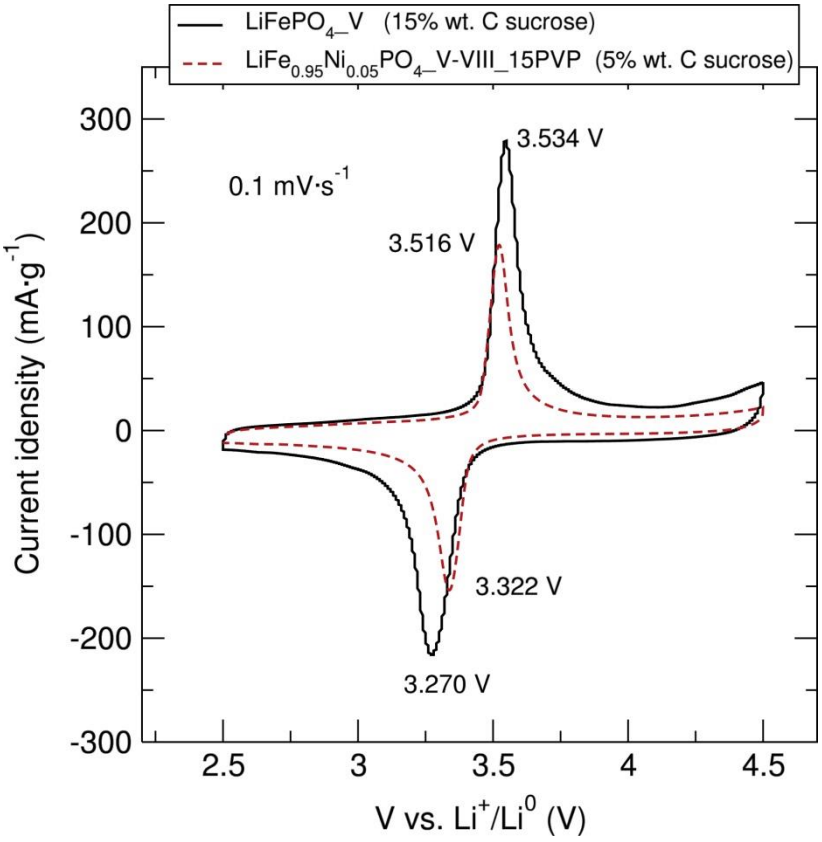

Figure 7.21. CVs at a 0.1 mV·s^{-1} scan rate between 2.5 V and 4.5 V of C/$LiFe_{0.95}Ni_{0.05}PO_4$_V-VIII_15PVP (5% wt. C from sucrose) and C/$LiFePO_4$_V (15% wt. C from sucrose) nanostructures prepared through microwave-assisted synthesis with "$[FeLiCl(O^tBu)_4(THF)_2]_n$" (V) and "$[NiLiCl(O^tBu)_4(THF)_2]_n$" (VIII) heterometallic alkoxide precursors.

7.2.2.6 PXRD and SEM of NiO nanoparticles prepared from hydrolysis of "$[NiLi_2Cl(O^tBu)_4(THF)_2]_n$

The utilisation of the "$[NiLi_2Cl(O^tBu)_4(THF)_2]_n$" (VIII) heterometallic alkoxide precursor for the generation of the transition metal oxide NiO has also been explored. The hydrolysis of "$[NiLi_2Cl(O^tBu)_4(THF)_2]_n$" (VIII) promoted by ultrasound irradiation and a heat treatment with 15% wt. C from sucrose for 3 hr at 500 ºC under air afforded single phase C/NiO nanostructures. Figure 7.22 shows the PXRD patterns of the as-synthesised NiO precursor and the thermally decomposed product after heat treatment for 3 hr at 500 ºC under air. The PXRD pattern of the Ni oxide precursor shows a strong low-angle reflection with an intense peak at around 15º 2θ. Such feature in the PXRD pattern has also been previously found on other precursor materials used for the preparation of NiO. It has been considered a typical feature of the coordination of alkoxides to metal ions.[374-376] The PXRD pattern of the calcined powder matches well with the face-centered cubic NiO phase. Rietveld refinements of the PXRD of the C/NiO powders to a NiO *Fm-3m* structure (ICSD No 01-075-0269 47-1049)[377] (Figure 7.23) revealed a good fit (R_{wp}=13.9 %) between the exerimental data and the calculated model. A weak reflection at 33 2θº

indicates the small precence of an unknown impurity phase. The estimated crystallite size of the NiO nanostructure was calculated using the Scherrer equation[208] applied to the (200) diffraction peak and was ~26 nm. SEM images of the C/NiO powders revealed irregular pebble shaped particles with sizes around 30-50 nm (Figure 7.24).

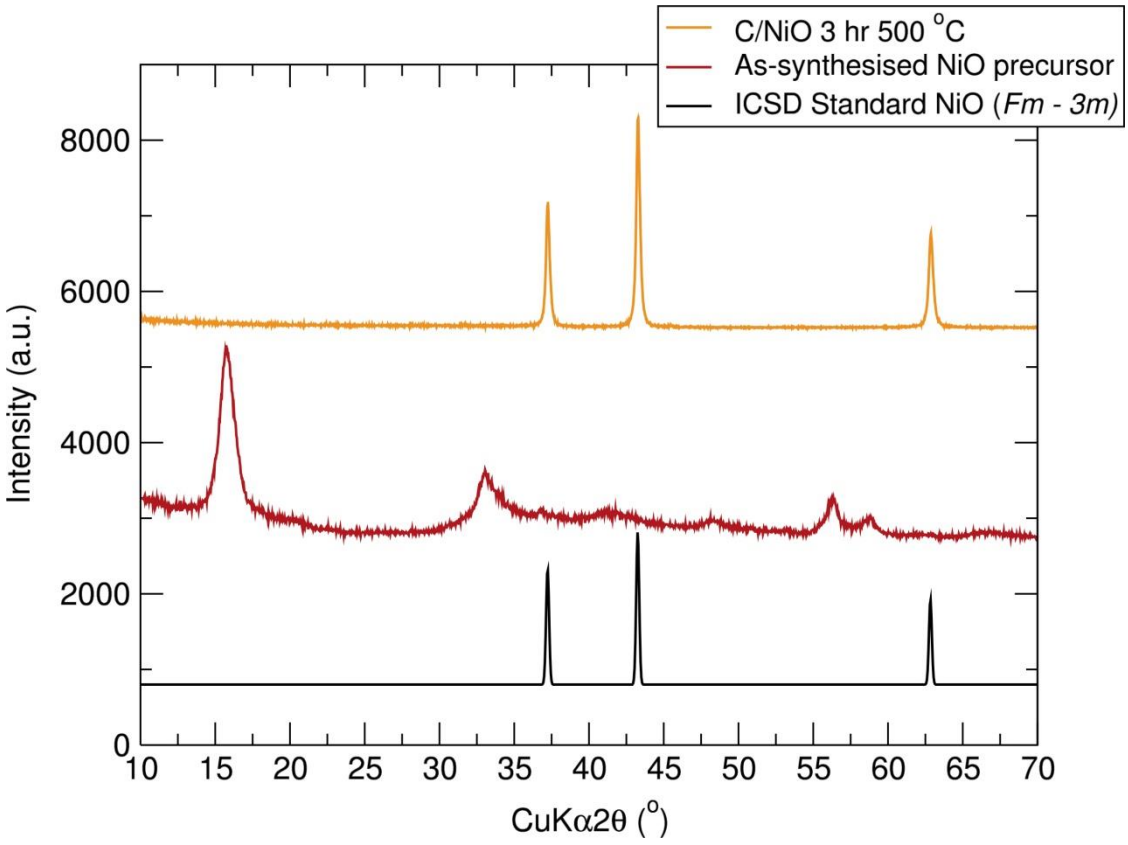

Figure 7.22. PXRD of as-synthesised NiO precursor and C/NiO heat treated for 3 hr at 500 °C under air.

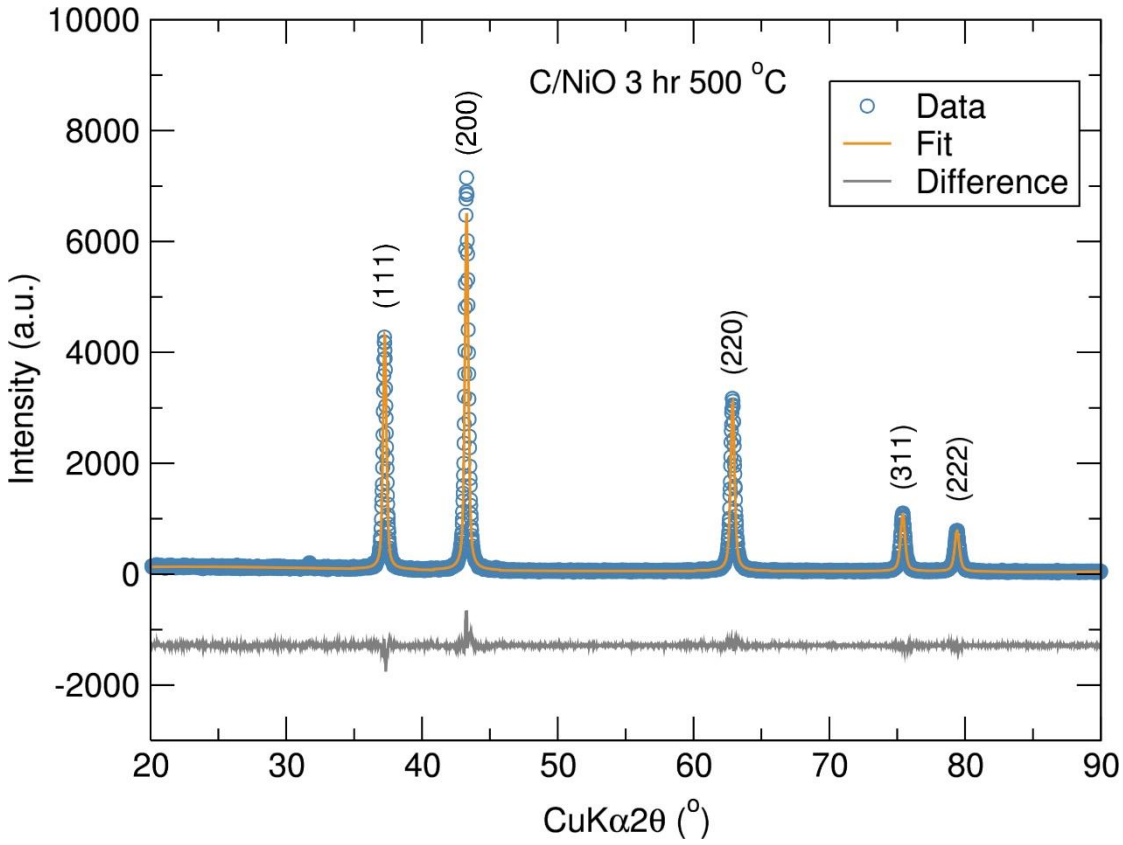

Figure 7.23. Rietveld analysis of PXRD data of C/NiO sample. [R_{wp}=13.9 %, R_{exp}=10.76 %, x^2=1.68, *a*=4.1770(2) Å, *b*=4.1770(2) Å and *c*=4.1770(2) Å].

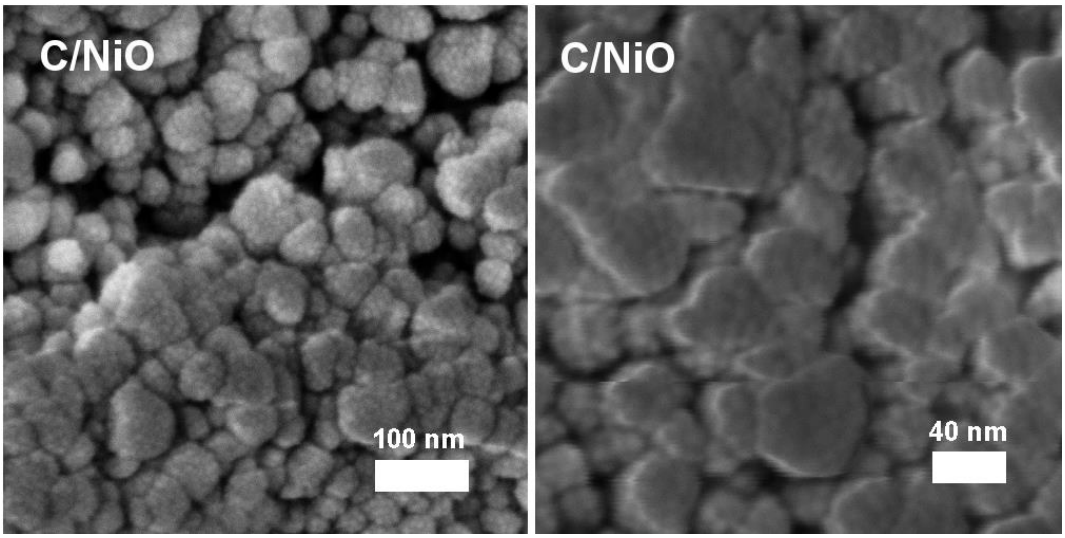

Figure 7.24. SEM images of C/NiO preprared from hydrolysis of "$[NiLi_2Cl(O^tBu)_4(THF)_2]_n$" (VIII) heterometallic alkoxide precursor.

7.2.2.7 Electrochemical performance of NiO nanoparticles prepared from hydrolysis of "$[NiLi_2Cl(O^tBu)_4(THF)_2]_n$"

Galvanostatic cycling of the C/NiO sample (carbon coated with 15% C from sucrose) at a current density of 100 mAh·g^{-1} over a 0.01-3.00 V range displayed a first

discharge capacity of ~3450 mAh·g^{-1} that sharply decreased to approximately 1450 mAh·g^{-1} at the second cycle. This initial discharge capacity of C/NiO is significantly larger than in previous reports.[241, 375, 378, 379] The large capacity drop after the first cycle could be attributed to inevitable irreversible processes such as SEI formation and electrolyte decomposition, and also to incomplete conversion reaction (a mixture of irreversible amorphous Li_2O and Ni metal could be formed during the cycling process). In Figure 7.25 (a) two potential regions can be observed in the discharge profile, one around 0.7 V, which is the result of the reduction of NiO to Ni and the formation of a SEI film, and other at around 0.8 V corresponding to the Li^+ storage in the carbonaceous matrix and also SEI formation. The first charge curve exhibited a "plateau" at around 2.3 V, which could be assigned to the oxidation of Ni nanograins. Furthermore, Figure 7.25 (b) shows a significant decrease in capacity over cycling, but a discharge capacity of 970 mAh·g^{-1} is still retained at the 20th cycle. Similar electrochemical performance has been previously observed in an ultrathin porous NiO nanosheets/graphene hierarchical structure, which displayed a reversible capacity of 982 mAh·g^{-1} at a current density of 100 mA·g^{-1} even after 50 cycles when cycled from 0.01 V to 3.00 V.[375] This metal alkoxide precursor synthetic route even afforded C/NiO nanoparticles that showed slightly improved electrochemical behavior compared to nanostructured NiO electrodes fabricated by a direct thermal oxidation of Ni foams at 400 ºC in air, which exhibited reversible capacities of 746 mAh·g^{-1} at 0.2 C rate after 10 cycles.[241] Comparable electrochemical performance was reported for NiO/multiwalled carbon nanotube composites prepared by direct thermal decomposition, demonstrating a lithium storage capacity of ~800 mAh·g^{-1} after 50 cycles.[378] However, enhanced capacity retention was observed in NiO 2D nanostructures obtained after calcination of the sonocrystallised β-$Ni(OH)_2$ precursor, which delivered ca. 1500 mAh·g^{-1} after 30 cycles.[379]

The high rate electrochemical performance of the C/NiO nanostructure was investigated by multiple-step rate galvanostatic strategy and the results are shown in Figure 7.26. After 20 cycles at 100 mA·g^{-1}, five cycles on each step rate were measured to evaluate the capacity and the capacity retention at different charge/discharge current conditions (from 200 mA·g^{-1} to 2000 mA·g^{-1}). The discharge and charge capacities of the nanostructured C/NiO electrode faded notably even at low current of 100 mA·g^{-1}, going from discharge capacitites of 1450 mAh·g^{-1} at the second cycle to 970 mAh·g^{-1} at the 20th cycle. After that, the charge/discharge capacities exhibited a drastic capacity loss upon cycling at higher C rates, delivering 740 mAh·g^{-1} at 200 mA·g^{-1}, 390 mAh·g^{-1} at 400 mA·g^{-1}, 210 mAh·g^{-1} at 800 mA·g^{-1}, 120 mAh·g^{-1} at 1200 mA·g^{-1} and 80 mAh·g^{-1} at 2000 mA·g^{-1}. After that, discharge capacities of 600 mAh·g^{-1} were still retained when returning to the slower rate of 100 mA·g^{-1}. This C/NiO nanocomposite showed a comparable rate

capabilities to NiO microspheres with waxberry-like structure delivering 597.8 mAh·g^{-1} after 100 cycles at a current density of 500 mA·g^{-1}.[380] Discharge capacities of 712, 656, 607, 582, and 515 mA·g^{-1} have been observed for a mesoporous NiO at 0.1 C, 0.2 C, 0.5 C, C, and 2 C, respectively, demonstrating the benefit of porous electrodes for excellent high rate performance for high power LIBs.[381] It has been demonstrated that porous C/NiO can reach discharge capacities of 864 mAh·g^{-1} after 10 cycles at a current density of 718 mA·g^{-1}. The high reversibility and excellent cycling stability could be explained by the interconnected porous NiO structure, which would be favourable for Li^+ diffusion. The sufficient void volume of the structure can help to accommodate the volume expansion during cycling.[382] PXRD pattern of the cycled C/NiO displayed very broad peaks corresponding to NiO and Ni metal phases (Figure 7.27), suggesting that some crystalline nanoparticulate NiO may still be present after the cycling process.

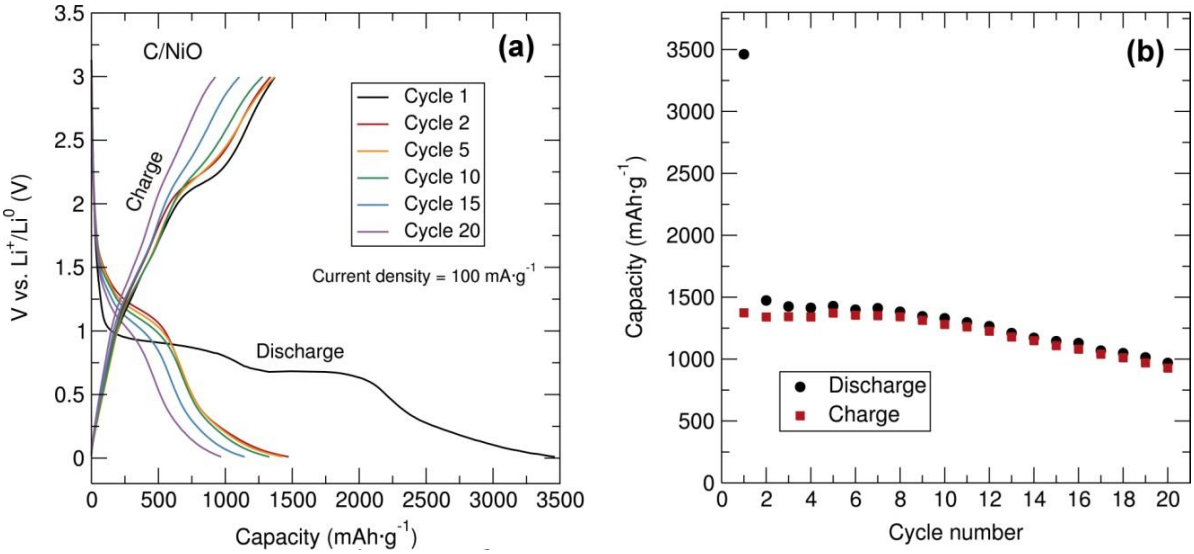

Figure 7.25. Voltage-capacity profile and **(b)** cycling stability of C/NiO (15% wt. C from sucrose) with C black and PTFE in 60:30:10 % weight ratio over the potential range of 0.01 V-3.00 V at 100 mA·g^{-1}.

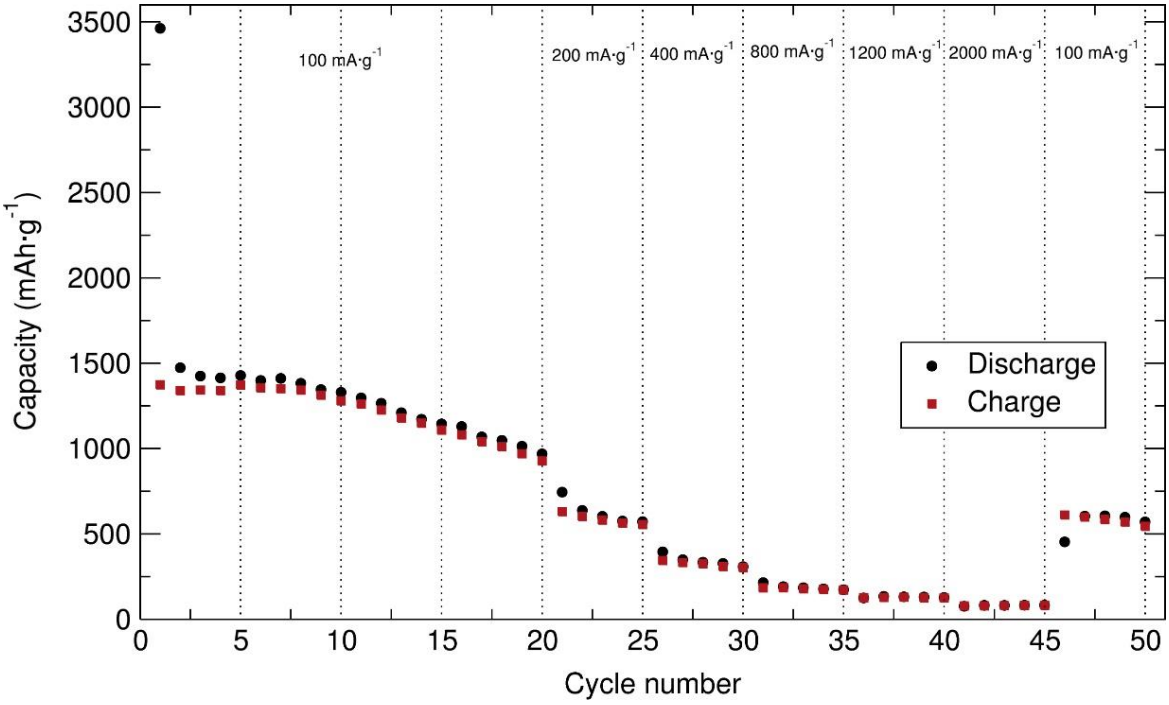

Figure 7.26. Rate performance of C/NiO (15% wt. C from sucrose) mixed with C black and PTFE in 60:30:10 % wt. ratio over the potential range of 0.01 V-3.00 V at different charge/discharge rates.

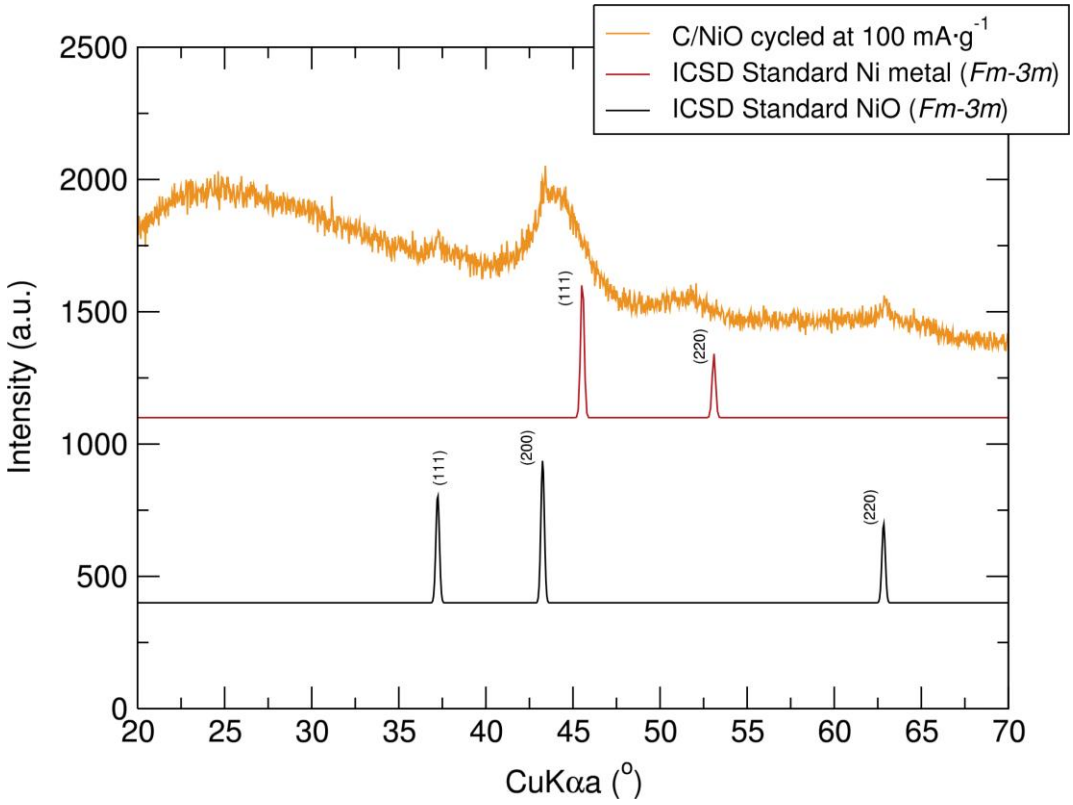

Figure 7.27. PXRD of post-cycled C/NiO in the charged state.

The CV plot at 0.1 mV·s^{-1} scan rate between 0.01 V and 3.20 V of the C/NiO powders shows a reduction peak ranging from 0.3 V to 0.5 V in the first cycle corresponding to the

initial reduction of NiO to metallic Ni (Figure 7.28). In the subsequent cycles, the reduction peak is composed of a main peak at around 1.01 V and a shoulder peak near 1.3 V. In the oxidation scan, a very broad peak at 1.46 V and a more intense peak a ~2.33 V were observed, which could be assigned to the oxidation of the SEI layer and Ni metal nanograins, respectively.[379, 383] The well-known mechanisms for these reactions are the reversible reaction of NiO to Ni metal and Li_2O.[384] The CV analysis suggests that after the initial cycle, the reversible electrochemical process is mainly the NiO + 2 Li^+ + 2- e^- ↔ Ni^0 + Li_2O reaction, which is consistent with previous reports.[121, 241, 379] The good overlap of the CV curves comfirms the good reversibility of this electrochemical process.

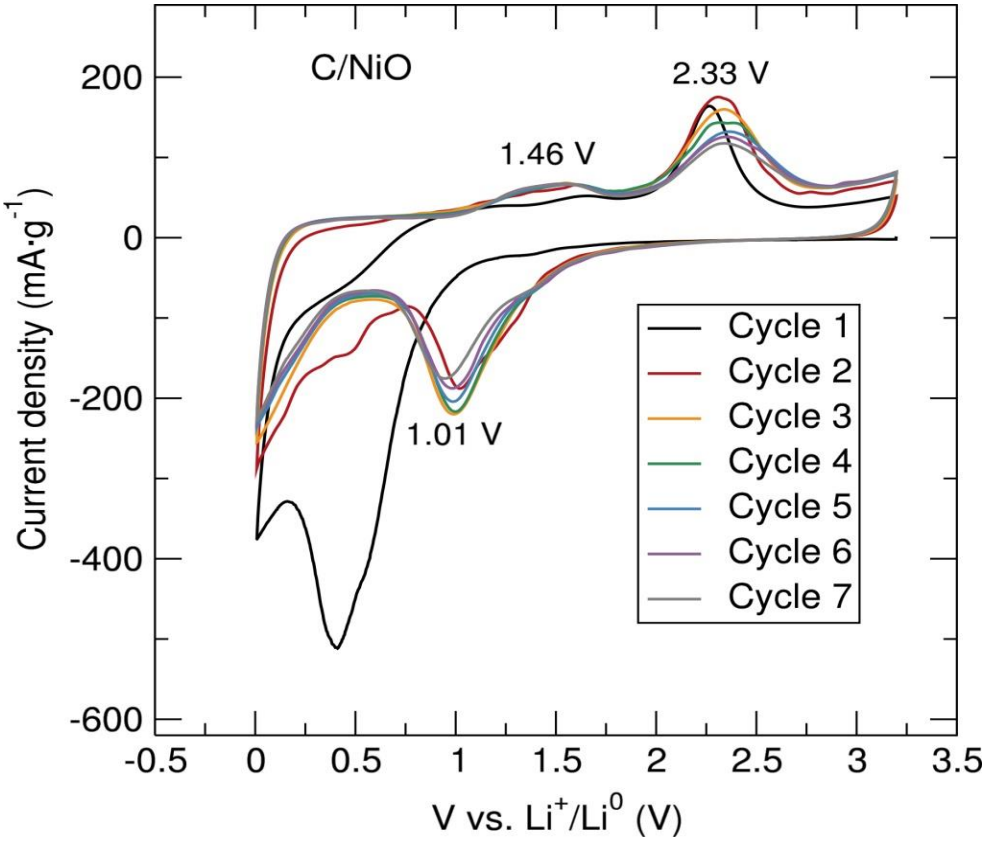

Figure 7.28. CV at a 0.1 mV·s^{-1} scan rate between 0.01 V and 3.20 V of C/NiO nanostructures prepared through a ultrasound-assisted "$[NiLi_2Cl(O^tBu)_4(THF)_2]_n$" (VIII) alkoxide precursor.

7.3 Conclusions

In this chapter, a low cost and green synthetic approach for the preparation of olivine $LiFe_{1-x}Ni_xPO_4$ and C/NiO nanostructures through simple microwave and ultrasound-assisted routes using single source metal alkoxide precursors has been presented. Therefore, the versatility of using single source heterometallic alkoxide precursors for the synthesis of both nanocrystalline olivine cathodes and conversion anode materials for Li-ion batteries has again been demonstrated. Moreover, the effect of the addition of PVP

as a capping agent for the generation of $LiFe_{1-x}Ni_xPO_4$ nanophases has been examined, resulting in better crystallised and smaller sized $LiFe_{1-x}Ni_xPO_4$ nanoparticles. Furthermore, the PVP could also act as a carbon source contributing towards the formation of a conductive carbon coating on the olivine nanostructures. Finally, it has also been suggested that the utilisation of a Li and Ni containing alkoxide precursor instead of $NiC_2O_4 \cdot 2H_2O$ may slightly increase the crystallinity of the $LiFe_{1-x}Ni_xPO_4$ nanophases prepared *via* microwave methods. Electrochemical testing of $LiFe_{0.95}Ni_{0.05}PO_4$ nanostructures prepared with 15% PVP displayed a good cyclability with charge/discharge capacities around 130 $mAh \cdot g^{-1}$ at C/20 rate. An additional carbon coating using only 5% wt. C from sucrose slightly enhanced the electrochemical performance, delivering discharge capacities of 140 $mAh \cdot g^{-1}$ at C/20 and 93 $mAh \cdot g^{-1}$ at 10 C rate. On the other hand, the ultrasound-assisted hydrolysis of the Li and Ni containing alkoxide precursor yielded C/NiO nanoparticles delivering an excellent electrochemical performance, reaching discharge capacities of 970 $mAh \cdot g^{-1}$ after the 20^{th} cycle at 100 $mA \cdot g^{-1}$ current density.

8 Overall Conclusions and Future Work

8.1 Overall conclusions

In this thesis, microwave and ultrasonic treatments of single source metal alkoxide precursors have been proved as facile, rapid and low cost route to both anode and cathode nanomaterials for LIB applications. In particular, the formation of olivine $LiFe_{1-x}M_xPO_4$ (*M*=Mn, Ni) nanostructures and several transition metal oxide nanoparticles (Mn_3O_4 hausmannite, Fe_3O_4 magnetite and NiO) have been investigated, which afforded electrode nanomaterials exhibiting outstanding cycling performances. A significant reduction in processing times and energy consumption during the preparation of nanostructured battery materials when using single source metal alkoxides precursors instead of commercially available starting materials has been demonstrated. Efforts have been directed to co-locate all the required metals in these metallorganic precursors in order to overcome the need of diffusional mixing and allow the reactions to proceed faster and at lower temperatures generating highly crystalline nanomaterials. Furthermore, it has been shown that the presented metal alkoxide compounds are suitable single source precursors for the fabrication of $LiFe_{1-x}Mn_xPO_4$ nanostructures *via* both fast microwave-assisted processes and also in more conventional solvothermal synthesis using autoclaves. Moreover, the composition of the single source precursors can have a strong impact in the resulting polymorph chemistry, as modification of the nature of the metal alkoxide precursor has revealed that obtaining different $LiFePO_4$ polymorphs (*Pnma* and *Cmcm* space groups) is possible. On the other hand, the influence of the solvent (ethylene glycol *vs*. ionic liquid EMI-TFMS) in these fast microwave-assisted processes using single source metal alkoxides has also been examined. PXRD and X-ray PDF analyses in conjunction with cycling tests have demonstrated that better crystallised and electrochemically optimised $LiFePO_4$ can be obtained through the ionothermal microwave approach using EMI-TFMS. Finally, the utilisation of PVP as a capping agent in microwave treatments of single source metal alkoxide precursors for the fabrication of Ni doped $LiFePO_4$ nanoparticles has been explored, revealing that the addition of PVP can afford better crystallised and smaller sized $LiFe_{0.95}Ni_{0.05}PO_4$ nanostructures.

Throughout this thesis, PXRD analysis in combination with Rietveld refinements has confirmed the phase purity of the presented materials. After that, electron microscopy imaging has allowed examination of the particle size, morphology and agglomeration. In the case of $LiFe_{1-x}Mn_xPO_4$ nanostructures, SEM results have confirmed the smaller particle sizes of the olivine products prepared using single source heterometallic alkoxide precursor compared to when homometallic alkoxides or commercial starting materials are used. Therefore, these results suggest that single source metal alkoxides are ideal candidates for the generation of nanosized inorganic functional materials. Control over

morphology and particle size depending on the Mn content and choice of solvent has also been demonstrated. Investigation of the local structure and the presence of defects or amorphous material is crutial to gain a deeper insight into the electrochemical performance of electrode materials. Neutron and X-ray PDF analyses of olivine $LiFe_{1-x}Mn_xPO_4$ nanophases have been conducted to examine the local structure and defect chemistry. Results have shown that microwave processes afford highly crystalline olivine structured nanomaterials. The suitability of single source precursor processes using heterometallic alkoxides in conjunction with microwave-assisted routes for the generation of highly crystalline olivine mixed-metal phosphate nanostructues has been therefore demonstrated. μ^+SR has been applied for the first time as a local probe to investigate the Li^+ diffusion properties in a family of $LiFe_{1-x}Mn_xPO_4$ olivine phases, suggesting that the D_{Li} may slightly decrease with higher Mn contents. Finally, cycling studies of these nanostructured battery materials have been conducted in order to probe the relationship between synthetic route, composition, particle size and morphology, and electrochemical performance.

Galvanostatic cycling tests of the $LiFe_{1-x}M_xPO_4$ (*M*=Mn, Ni) nanostructures prepared from metal alkoxide precursors displayed a significant improvement in the electrochemical performance in comparison to the olivine phases synthesised using commercial starting materials and the rate capabialities exhibited were comparable to the best performing in the literature. Figure 8.1 depicts the rate performance from C/10 to 10 C rates for all the $LiFePO_4$ samples prepared in this thesis and some literature values for microwave synthesised $LiFePO_4$ reported by Niederberger *et al.*[45] When comparing the cycling performance for the $LiFePO_4$ samples prepared using commercial starting materials *via* a microwave-assisted method and a conventional solvothermal process ($LiFePO_4$_MW_Commercial *vs.* $LiFePO_4$_S_Commercial), results indicate that microwave synthesised $LiFePO_4$ displayed a better rate performance at the fastests C rates, confirming the suitability of microwave methods to yield high rate performing electrodes. Fast microwave treatments of metal alkoxides afforded $LiFePO_4$ nanostructures delivering comparable rate behaviour to $LiFePO_4$_MW_Commercial prepared with commercial starting materials. However, the reaction times were reduced from 3 hr to 10 min with the metal alkoxide precursor approach. Furthermore, a slight enhancement of the electrochemical behaviour at high C rates was observed when single source heterometallic alkoxides were used instead of homometallic alkoxides, suggesting that having all of the required metals in a single source precursor may be beneficial to obtain high performing $LiFePO_4$ nanostructures. $LiFePO_4$_S_IV (Heterometallic) nanophase synthesised by conventional solvothermal treatments of single source heterometallic alkoxide precursors displayed an enhanced electrochemical behaviour in comparison to

$LiFePO_4$_S_Commercial, confirming the improvement in the electrochemical performance that can be achieved with single source heterometallic alkoxide precursors. Finally, the fast ionothermal microwave-assisted synthesis of olivine $LiFePO_4$_MW_V_IL employing single source heterometallic alkoxides and the ionic liquid EMI-TFMS afforded the best performing material at the fastest C rate even compared to previous reports on microwave synthesised $LiFePO_4$ by Niederberger *et al*,[45] establishing this synthetic approach as one to yield high performance electrode materials across the olivines.

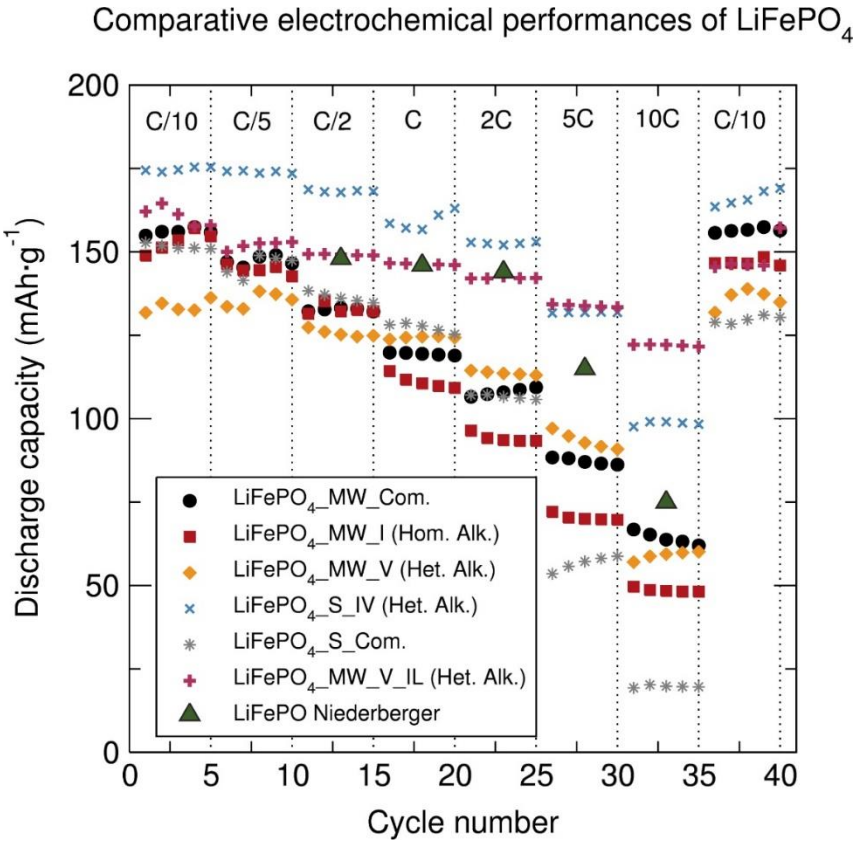

Figure 8.1. Comparative rate performance from 2.2 V to 4.0 V for C/$LiFePO_4$ (15% wt. C from sucrose) samples ($LiFePO_4$_MW_Com., $LiFePO_4$_MW_I (Hom. Alk.), $LiFePO_4$_MW_V (Het. Alk.), $LiFePO_4$_S_V (Het. Alk.), $LiFePO_4$_S_Com. and $LiFePO_4$_MW_V_IL (Het. Alk.)).

Olivine nanostructured $LiMnPO_4$ exhibited a significant improvement of the electrochemical performance when using the metal alkoxide precursors instead of other commercial starting materials (Figure 8.2). A noticeable enhancement of the rate capabilities was also observed when using single source heterometallic alkoxides compared to just homometallic alkoxides. Furthermore, microwave synthesised $LiMnPO_4$_MW_VI (Heterometallic) displayed an improved rate behaviour compared to solvothermally synthesised $LiMnPO_4$_S_VI (Heterometallic), confirming again that microwave methods are promising synthetic routes to high performing nanostructured electrodes. $LiMnPO_4$_MW_VI (Heterometallic) even exhibited improved rate capabilities

at the fastest C rates compared to previous microwaved synthesised $LiMnPO_4$ by Niederberger *et al.*[45]

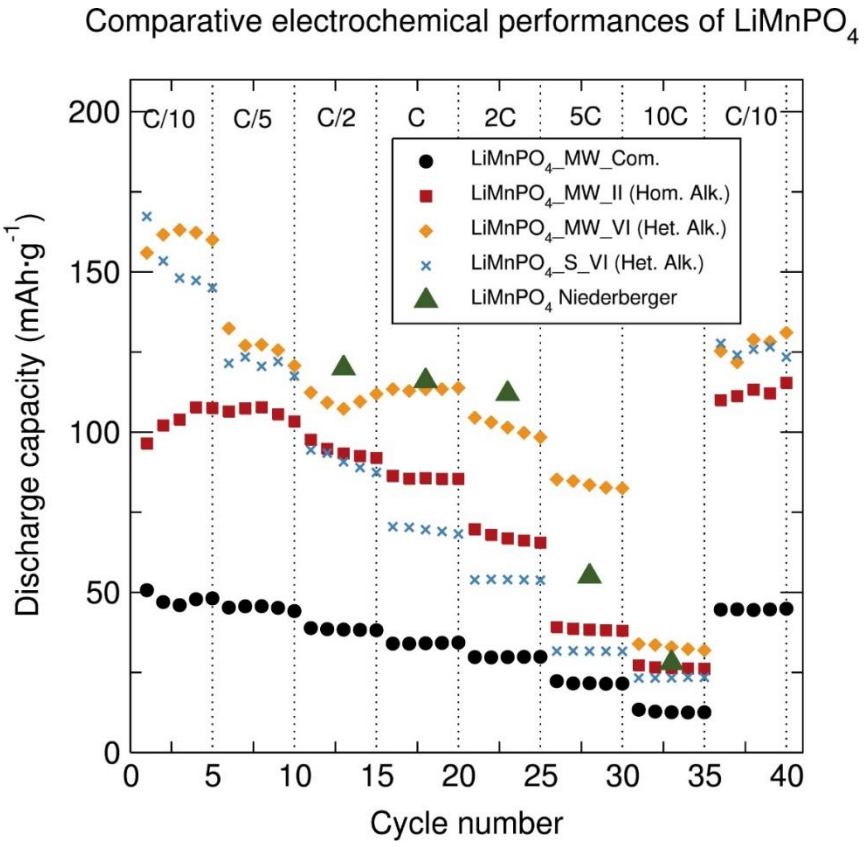

Figure 8.2. Comparison rate performance from 2.2 V to 4.5 V for $LiMnPO_4$ (15% wt. C from sucrose) samples ($LiMnPO_4$_MW_Com., $LiMnPO_4$_MW_II (Hom. Alk.), $LiMnPO_4$_MW_VI (Het. Alk.) and $LiMnPO_4$_S_VI (Het. Alk.)).

A similar trend was observed for the mixed transition metal phosphate $LiFe_{0.5}Mn_{0.5}PO_4$ samples, in which $LiFe_{0.5}Mn_{0.5}PO_4$ nanophases synthesised through the metal alkoxide route demonstrated an enhanced rate performance compared to $LiFe_{0.5}Mn_{0.5}PO_4$_MW_Commercial prepared from commercial starting materials (Figure 8.3). Moreover, a slight improvement in the rate capability of the $LiFe_{0.5}Mn_{0.5}PO_4$_MW_VII (Heterometallic) powders prepared from a trimetallic alkoxide in comparison to $LiFe_{0.5}Mn_{0.5}PO_4$_MW_V-VI (mixture of heterometallic alkoxide precursors) was observed, which suggests that having all the required metals closer together at the atomic level during the synthesis process may slightly improve the electrochemical properties of olivine nanomaterials. Furthermore, microwave synthesised $LiFe_{0.5}Mn_{0.5}PO_4$_MW_VII (Heterometallic) again exhibited improved rate capabilities at the fastests C rates compared to solvothermally synthesised $LiFe_{0.5}Mn_{0.5}PO_4$_S_VII (Heterometallic). These $LiFe_{0.5}Mn_{0.5}PO_4$ nanostructures synthesised using metal alkoxides exhibited comparable rate capabilities to previous $LiFe_{0.5}Mn_{0.5}PO_4$ phases reported in the literature.[238]

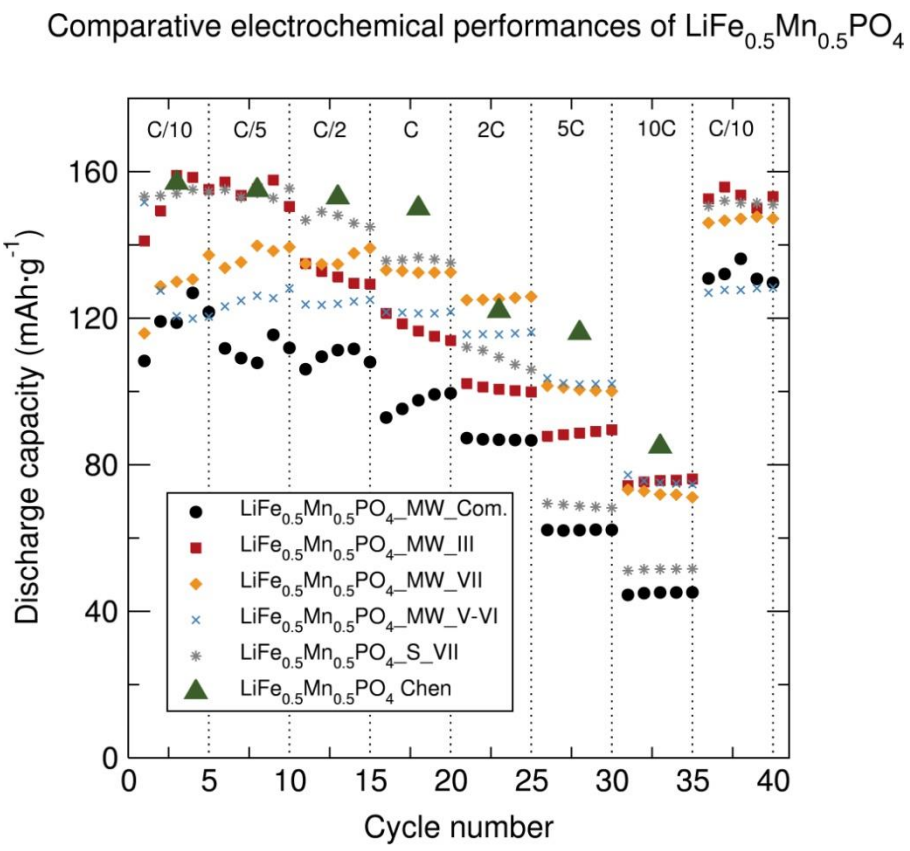

Figure 8.3. Comparative rate performance from 2.2 V to 4.3 V for $LiFe_{0.5}Mn_{0.5}PO_4$ (15% wt. C from sucrose) samples ($LiFe_{0.5}Mn_{0.5}PO_4$_MW_Com., $LiFe_{0.5}Mn_{0.5}PO_4$_MW_III (Hom. Alk.), $LiFe_{0.5}Mn_{0.5}PO_4$_MW_VII (Het. Alk.), $LiFe_{0.5}Mn_{0.5}PO_4$_MW_V-VI (Mix Het. Alk.) and $LiFe_{0.5}Mn_{0.5}PO_4$_S_VII (Het. Alk.)).

8.2 Future work

As ionothermal microwave-assisted methods has shown to afford the best performing $LiFePO_4$ olivine, further investigation on the utilisation of different ionic liquids in these fast microwave treatments of single source metal alkoxide precursors for the preparation of Ni and Mn doped $LiFePO_4$ nanoparticles could afford olivine nanostructures with increased cell voltage exhibiting enhanced rate capabilities. Studies on how to reuse the ionic liquids after the synthesis employing metal alkoxides would be necessary to reduce production costs and make this ionothermal process more environmentally-friendly, low cost and scalable. One pot single source precursor sysnthesis of $LiFe_{1-x}Mn_xPO_4$ nanocomposites with different carbon additives such as reduced graphene oxide or carbon nanotubes could also afford olivine nanostructures with enhanced electrochemical performances. Also, investigating a wider range of $LiFe_{1-x}Mn_xPO_4$ stoichiometries could contribute to find out the optimum Mn doping level leading to the best cycling behaviour and rate capabilities. For example, Ding *et al.* reported that $LiFe_{0.9}Mn_{0.1}PO_4$ displayed the best electrochemical performance among a series of $LiFe_{1-x}Mn_xPO_4$/C composites (x=0, 0.1, 0.3, 0.5, 1).[385] The simple, facile and low cost

synthetic strategy using metal alkoxide precursors explored in this thesis to prepare metal oxide conversion anodes can be extended to fabricate other transition metal oxides C/M_xO_y (*M*=Fe, Co, Ni, Mn...) and mixed metal oxide nanocomposites, which may exhibit promising performances as high capacity LIB converion anodes.

Understanding the fundamental processes of nanoparticle growth and the evolution of their morphology in solution is crucial for the development of synthetic methodologies leading to novel energy storage nanomaterials. The development of advanced *in situ* characterisation techniques for real-time observation of synthesis are then very promising. Determination of the reaction mechanism underlying the formation and growth of the crystalline solid is essential in order to investigate the formation of intermediates between the reactants and product, the crystal's growth rate, and the amount of structural disorder.[137] This information is essential to improve the synthetic procedures and potentially reduce manufacturing costs of functional materials. For example, *in situ* XRD can provide new and valuable insights into the chemical synthesis of electrode materials and greatly benefit Li-ion battery technology for materials synthesis. Moreover, this technique could provide important information in determining procedures and conditions required for preparing new metastable phases that are not easily generated by conventional syntheses. Therefore, *in situ* XRD analysis during the synthesis of $LiFe_{1-x}Mn_xPO_4$ nanostructures using commercial starting materials or single source metal alkoxide precursors would unravel fundamental information regarding the reaction intermediates and mechanisms in these processes. Comparison of *in situ* XRD studies in conventional solvothermal processes and in microwave-assisted solvothermal reactions would also help to understand the differences between the reaction mechanisms under different heating regimes. *In-operando* diffraction studies during battery cycling can also provide valuable insights into the structural changes taking place during the Li^+ extraction-insertion process. Therefore, combining time series PDFs with voltage-current measurements could give key insights into the local structural changes in LIBs during charge-discharge cycles allowing a detailed understanding of the Li^+ extraction/insertion mechanism in nanostructured electrodes, especially in the case of transition metal oxide conversion anodes where a deeper understanding of the conversion reaction process could potentially help to improve their capacity retention. In general, these *in operando* local structure studies can potentially contribute to the achievement of high-performing battery technology.

It would also be interesting to investigate the utilisation of single source heterometallic alkoxide precursors for the preparation of nanotstructured $Li_2Fe_{1-x}Mn_xSiO_4$ cathodes through relatively fast and low temperature processes. Lithium orthosilicates are currently attracting increasing attention as potential high capacity cathode materials for

Li-ion batteries due to the fact that two Li^+ ions (de)insertion per formula unit can take place raising the theoretical capacity of the material to 332 mAh g^{-1}. Furthermore, lithium orthosilicates offer the advantage of the abundance and low cost of silicon, environmental benignity and high safety from strong Si-O bonding.[386]

8.2.1 Microwave synthesis of non-olivine β-$LiFe_{1-x}M_xPO_4$ (*M*=Fe, Co or Ni) nanostructures

Previous experimental studies have demonstrated that β-$LiFePO_4$ exhibits almost no electrochemical activation with very low capacity (10-20 mAh·g^{-1})[50, 295, 387] and, as a consequence, β-$LiFePO_4$ has not been pursued as a cathode material for LIBs. However, it has recently been shown that ball milling β-$LiFePO_4$ with conductive carbon can induce disorder such as $Fe_{Li}Li_{Fe}$ antisite defects, crystal distortion and amorphous domains thus improving the cycling performance.[52] The amorphous structure can facilitate Li^+ ions migration due to redistribution of the FeO_n polyhedron and the PO_4 tetrahedrons resulting in much more space to create new migration passages for the imprisoned Li^+ ions. To date, the effect of transition metal site doping in β-$LiFePO_4$ has not been explored. Therefore, investigations of the electrochemical performances of Ni and Co doped β-$LiFePO_4$ nanostructures are planned, which will help to understand if transition metal doping can lead to enhanced Li^+ storage capabilities in β-$LiFePO_4$. ß-$LiFePO_4$, ß-$LiFe_{0.9}Co_{0.1}PO_4$ and ß-$LiFe_{0.9}Ni_{0.1}PO_4$ nanostructures have already been successfully synthesised by a facile microwave approach (15 min 70 ºC and 30 min 280 ºC) using LiH_2PO_4 and the appropriate transition metal oxalate ($FeC_2O_4{\cdot}2H_2O$, $CoC_2O_4{\cdot}2H_2O$, $NiC_2O_4{\cdot}2H_2O$) precursors in tetraethylene glycol (see Figure A8.1 for PXRD patterns of ß-$LiFe_{0.9}M_{0.1}PO_4$ (*M*=Fe, Co or Ni)). EDS analysis of ß-$LiFe_{0.9}Co_{0.1}PO_4$ and ß-$LiFe_{0.9}Ni_{0.1}PO_4$ have also confirmed the presence of Co and Ni (Figure A8.2). Galvanostatic cycling of the ball milled (15 min) ß-$LiFePO_4$, ß-$LiFe_{0.9}Co_{0.1}PO_4$ and ß-$LiFe_{0.9}Ni_{0.1}PO_4$ powders with conductive carbon black (60:40 wt. ratio) at a C/20 rate demonstrated reversible discharge capacities of 120 mAh·g^{-1}, 145 mAh·g^{-1} and 120 mAh·g^{-1} for the ß-$LiFePO_4$, ß-$LiFe_{0.9}Co_{0.1}PO_4$ and ß-$LiFe_{0.9}Ni_{0.1}PO_4$ materials, respectively (Figure 8.4). No obvious capacity fading was observed over at least 10 cycles, confirming the good cyclability of these materials. These results suggested that Ni doping in ß-$LiFePO_4$ does not lead to any enhancement of the electrochemical performance while ß-$LiFe_{0.9}Co_{0.1}PO_4$ demonstrated that Co doping may be beneficial to increase the reversible specific capacity. Furthermore, the ball milling treatment markedly improved the electrochemical performance from ~60 mAh·g^{-1} for non-ball milled ß-$LiFePO_4$ to 120 mAh·g^{-1} for ß-$LiFePO_4$ ball milled for 15 min. This enhancement can be attributed to the fact that the amorphous domains formed during the ball milling process may benefit the Li^+ diffusion by creating new migration passages for the Li^+ ions.[52] Figure A8.3 shows the voltage-composition profiles of the ß-

$LiFe_{0.9}M_{0.1}PO_4$ (*M*=Fe, Co or Ni) nanostructures confirming the slightly improved Li^+ storage capabilities of ß-$LiFe_{0.9}Co_{0.1}PO_4$ compared to ß-$LiFe_{0.9}Ni_{0.1}PO_4$ and ß-$LiFePO_4$.

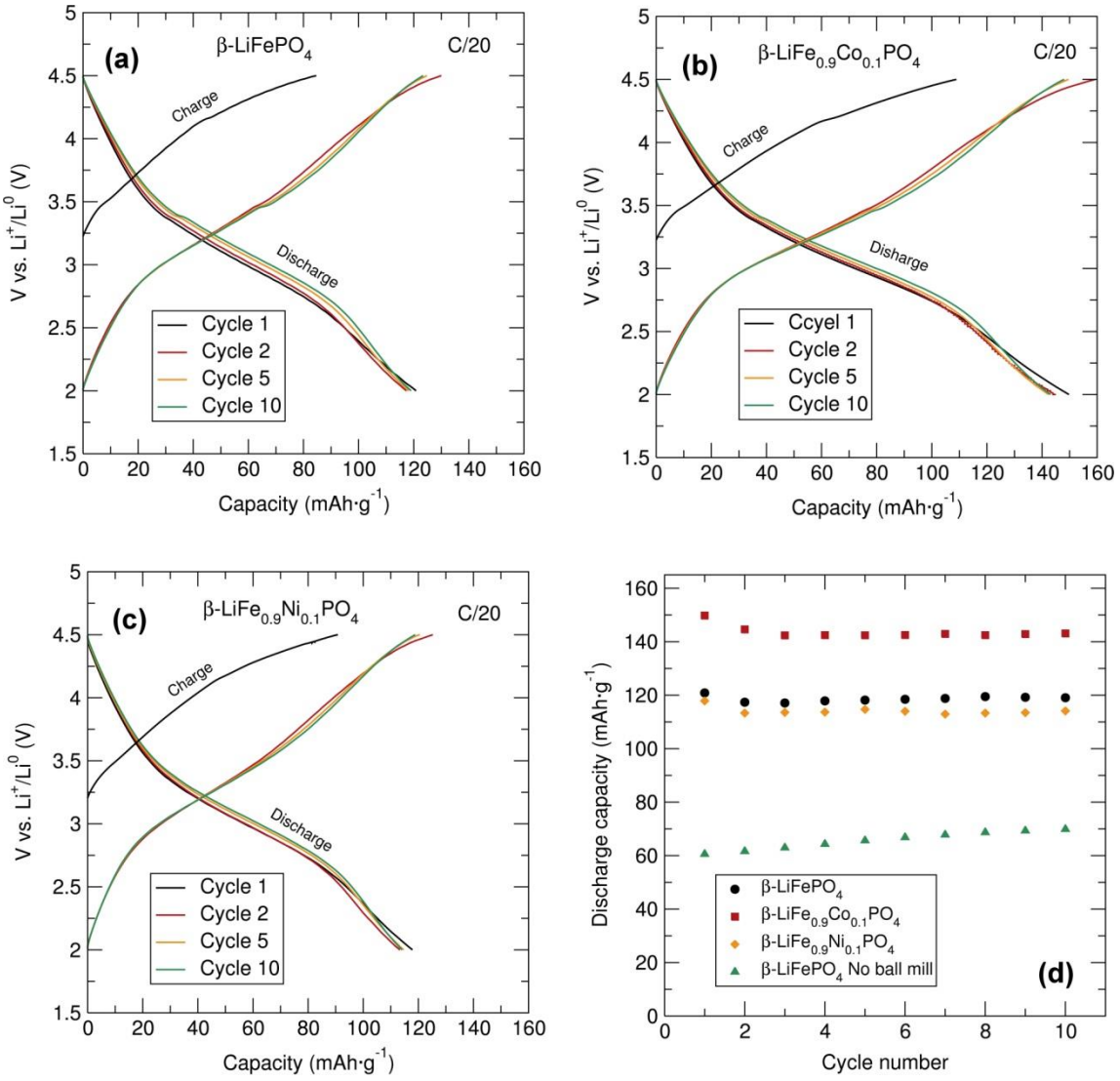

Figure 8.4. Charge-discharge voltage profiles at C/20 of **(a)** ß-$LiFePO_4$, **(b)** ß-$LiFe_{0.9}Co_{0.1}PO_4$, **(c)** ß-$LiFe_{0.9}Ni_{0.1}PO_4$ and **(d)** Comparative cycling performance of ß-$LiFe_{0.9}Co_{0.1}PO_4$, ß-$LiFe_{0.9}Co_{0.1}PO_4$ and ß-$LiFe_{0.9}Co_{0.1}PO_4$.

8.2.2 Microwave treatments of single source heterometallic alkoxide precursors to maricite $NaFe_{1-x}Mn_xPO_4$ nanostructures

The rapidly increasing demand for Li-ion batteries is starting to face nowadays the challenge of shortages in lithium resources.[388] Therefore, the development of new types of energy storage technologies beyond lithium such as Na-ion, Mg-ion and Al-ion batteries using cost-effective and sustainable materials is urgently needed. Among them, Na-ion batteries have been regarded as a promising alternative to Li-ion batteries owing to the similar underlaying electrochemical reaction to Li-ion batteries and to the unlimited sodium resources.[389] In particular, $NaFePO_4$ can be regarded as a promising cathode material for Na-ion batteries due to its low cost, non-toxicity, safety and natural

abundance of Na and Fe. It has been recently demonstrated that hollow amorphous $NaFePO_4$ maricite nanospheres can function as an excellent cathode material for rechargeable Na batteries exhibiting high storage capacity of 152 $mAh \cdot g^{-1}$ at 0.1 C after 300 cycles and also high rate capability.[390] The development of energy-efficient synthetic routes to $NaFePO_4$ and further understanding of the $NaFePO_4$ maricite structure and its correlation to the electrochemical performance is needed to advance this promising cathode material.

In some preliminary work, a single source precursor microwave-assisted synthetic strategy using $[NaM(O^tBu)_3(THF)]_2$ (*M*=Fe, Mn) heterometallic alkoxides has been applied for the preparation of maricite $NaFe_{1-x}Mn_xPO_4$ (*x*=0, 0.5 and 1) nanostructures (see Figure 8.4 for PXRD patterns). SEM images of the maricite $NaFe_{1-x}Mn_xPO_4$ (*x*=0, 0.5 and 1) nanostructures revealed a non-uniform round morphology with particle sizes of approximately 25-35 nm (Figure A8.5). For the first time, the preparation of single-phase maricite $NaFe_{1-x}Mn_xPO_4$ (*x*=0, 0.5 and 1) nanoparticles *via* microwave methods at such low temperatures of 280 ^oC has been presented. With this, the suitability of fast microwave treatments of single source metal alkoxide precursors for the fabrication of nanostructured Na-ion battery electrodes is demonstrated. Preliminary galvanostatic cycling investigations at C/20 rate on the $NaFePO_4$ nanostructure ($NaFePO_4$: C in 80:20 % weight ratio mixture ball milled for 2 hr) revealed that charge and discharge capacities of approximately 110 $mAh \cdot g^{-1}$ were delivered with a slight capacity fading over cycling. More sophisticated synthetic strategies using surfactants or several carbon additives can be applied to the proposed single source precursor approach using metal alkoxides in order to afford electrochemically optimised maricite $NaMPO_4$ (*M*=Fe, Mn) nanoparticles. Moreover, optimisation of the carbon loading and ball milling times may lead to significant improvements in the electrochemical behaviour. Further electrochemical testing of this family of maricite $NaFe_{1-x}Mn_xPO_4$ (*x*=0, 0.5 and 1) nanostructures is under investigation and results will unravel if substituting Mn by Fe in maricite $NaFePO_4$ leads to any enhancement of the cycling performance. Also, *in operando* Mössbauer spectroscopy of maricite $NaFePO_4$ would confirm if the electrochemical activity is attributed to the oxidation/reduction of the Fe^{3+}/Fe^{2+} redox pair.

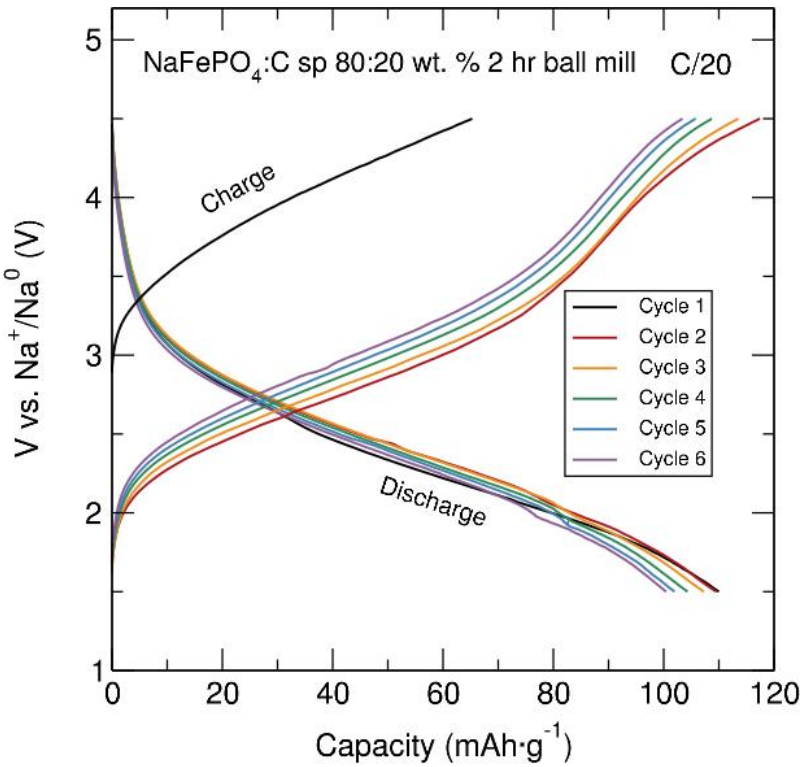

Figure 8.5. Voltage-capacity profile of maricite $NaFePO_4$ between 1.5 V and 4.5 V at C/20 rate. $NaFePO_4$: C sp in 80:20 (% weight ratio) mixture ball milled for 2 hr.

Appendix

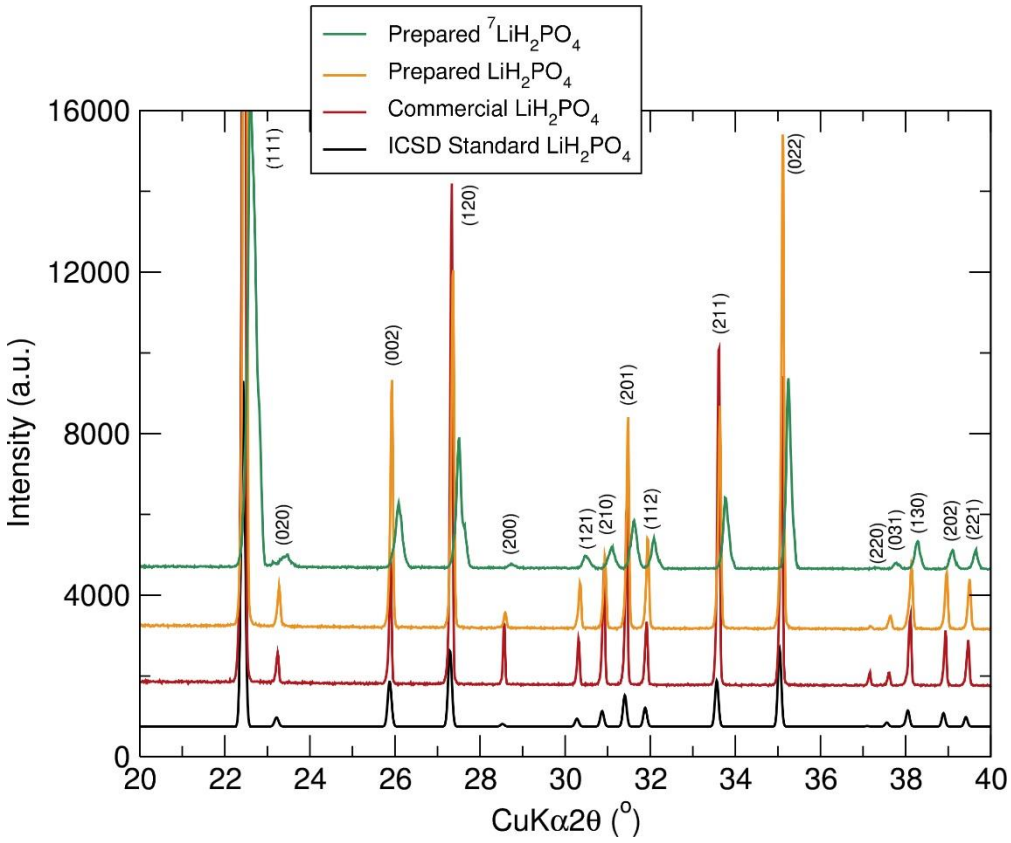

Figure 0A3.1. Comparative PXRD patterns of commercial LiH_2PO_4, LiH_2PO_4 prepared with $LiOH{\cdot}H_2O$ and $^{7}LiH_2PO_4$ prepared with $^{7}LiOH{\cdot}H_2O$.

Table A3.1. Structural parameters of $LiFePO_4$ sample from Rietveld analysis of high resolution PND data at room temperature.

$LiFePO_4$		R_{exp}=0.0193	R_{wp}=0.0153	χ^2=1.879	d=3.564 mg/cm^3
Pnma		a=10.3386(2) Å	b=0.0003(1) Å	c=4.6947(1) Å	V=291.24(1) Å^3
Atom	Site	x	y	z	Uiso (Å^2)	Frac
^{7}Li	4*a*	0.0000	0.0000	0.0000	0.015(1)	0.747(7)
Fe	4*c*	0.2819(1)	0.2500	0.9752(1)	0.0049(1)	1.001(2)
P	4*c*	0.0954(1)	0.2500	0.4182(1)	0.0029(1)	1.000
O	4*c*	0.0977(1)	0.2500	0.7420(2)	0.0068(1)	1.000
O	4*c*	0.4575(1)	0.2500	0.2057(2)	0.0066(1)	1.000
O	8*d*	0.1658(1)	0.0474(1)	0.2854(1)	0.0062(1)	1.000
^{6}Li	4*a*	0.0000	0.0000	0.0000	0.015(1)	0.030

Table A3.2. Structural parameters of $LiFe_{0.75}Mn_{0.25}PO_4$ sample from the Rietveld analysis of high resolution powder neutron diffraction data at room temperature.

$LiFe_{0.75}Mn_{0.25}PO_4$	R_{exp}=0.0174	R_{wp}=0.0144	χ^2=1.879	*d*=3.538 mg/cm^3	
Pnma	*a*=10.3646(2) Å	*b*=6.0222(1) Å	*c*=4.7055(1) Å	*V*=293.71(2) Å^3	
Atom	Site	*x*	*y*	*z*	Uiso (Å^2)	Frac
^{7}Li	4*a*	0.0000	0.0000	0.0000	0.013(1)	0.807(7)
Fe	4*c*	0.2820(1)	0.2500	0.9735(1)	0.0052(1)	0.771(1)
Mn	4*c*	0.2820(1)	0.2500	0.9735(1)	0.0052(1)	0.229(1)
P	4*c*	0.0949(1)	0.2500	0.4158(1)	0.0029(1)	1.000
O	4*c*	0.0975(1)	0.2500	0.7393(2)	0.0067(1)	1.000
O	4*c*	0.4571(1)	0.2500	0.2073(2)	0.0071(1)	1.000
O	8*d*	0.1651(1)	0.0479(1)	0.2839(1)	0.0066(1)	1.000
^{6}Li	4*a*	0.0000	0.0000	0.0000	0.013(1)	0.030

Table A3.3. Structural parameters of $LiFe_{0.5}Mn_{0.5}PO_4$ sample from Rietveld analysis of high resolution PND data at room temperature.

$LiFe_{0.5}Mn_{0.5}PO_4$	R_{exp}=0.0176	R_{wp}=0.0150	χ^2=1.879	*d*=3.511 mg/cm^3	
Pnma	*a*=10.3901(3) Å	*b*=6.0454(2) Å	*c*=4.7167(1) Å	*V*=296.27(2) Å^3	
Atom	Site	*x*	*y*	*z*	Uiso (Å^2)	Frac
^{7}Li	4*a*	0.0000	0.0000	0.0000	0.011(1)	0.858(8)
Fe	4*c*	0.2821(1)	0.2500	0.9714(3)	0.0070(3)	0.521(1)
Mn	4*c*	0.2821(1)	0.2500	0.9714(3)	0.0070(3)	0.479(1)
P	4*c*	0.0945(1)	0.2500	0.4129(2)	0.0025(1)	1.000
O	4*c*	0.0973(1)	0.2500	0.7355(2)	0.0066(1)	1.000
O	4*c*	0.4567(1)	0.2500	0.2091(2)	0.0076(1)	1.000
O	8*d*	0.1640(1)	0.0487(1)	0.2820(1)	0.0068(1)	1.000
^{6}Li	4*a*	0.0000	0.0000	0.0000	0.011(1)	0.030

Table A3.4. Structural parameters of $LiFe_{0.25}Mn_{0.75}PO_4$ sample from Rietveld analysis of high resolution PND data at room temperature.

$LiFe_{0.25}Mn_{0.75}PO_4$		R_{exp}=0.0234	R_{wp}=0.0169	χ^2=1.879	*d*=3.476 mg/cm^3	
Pnma		*a*=10.4168(2) Å	*b*=6.0713(1) Å	*c*=4.7287(1) Å	*V*=299.06(3) Å^3	
Atom	Site	*x*	*y*	*z*	Uiso (Å^2)	Frac
^{7}Li	4*a*	0.0000	0.0000	0.0000	0.010(1)	0.883(8)
Fe	4*c*	0.280(1)	0.2500	0.977(3)	0.007	0.249(1)
Mn	4*c*	0.280(1)	0.2500	0.977(3)	0.007	0.751(1)
P	4*c*	0.0937(1)	0.2500	0.4103(2)	0.0029(1)	1.000
O	4*c*	0.0976(1)	0.2500	0.7317(2)	0.0068(1)	1.000
O	4*c*	0.4561(1)	0.2500	0.2106(2)	0.0066(1)	1.000
O	8*d*	0.1629(1)	0.0497(1)	0.2796(1)	0.0062(1)	1.000
^{6}Li	4*a*	0.0000	0.0000	0.0000	0.010(1)	0.030

Table A3.5. Structural parameters of $LiMnPO_4$ sample from Rietveld analysis of high resolution PND data at room temperature.

$LiMnPO_4$		R_{exp}=0.0287	R_{wp}=0.0205	χ^2=1.879	*d*=3.496 mg/cm^3	
Pnma		*a*=10.4470(5) Å	*b*=6.1012(3) Å	*c*=4.7440(2) Å	*V*=302.38(4) Å^3	
Atom	Site	*x*	*y*	*z*	Uiso (Å^2)	Frac
Li	4*a*	0.0000	0.0000	0.0000	0.0087(8)	0.98(1)
Mn	4*c*	0.2815(2)	0.2500	0.9694(4)	0.0037(3)	1.045(7)
P	4*c*	0.0928(1)	0.2500	0.4080(2)	0.0014(1)	1.000
O	4*c*	0.0988(1)	0.2500	0.7295(2)	0.0072(2)	1.000
O	4*c*	0.4550(1)	0.2500	0.2108(3)	0.0064(2)	1.000
O	8*d*	0.1619(1)	0.0510(1)	0.2768(2)	0.0053(1)	1.000

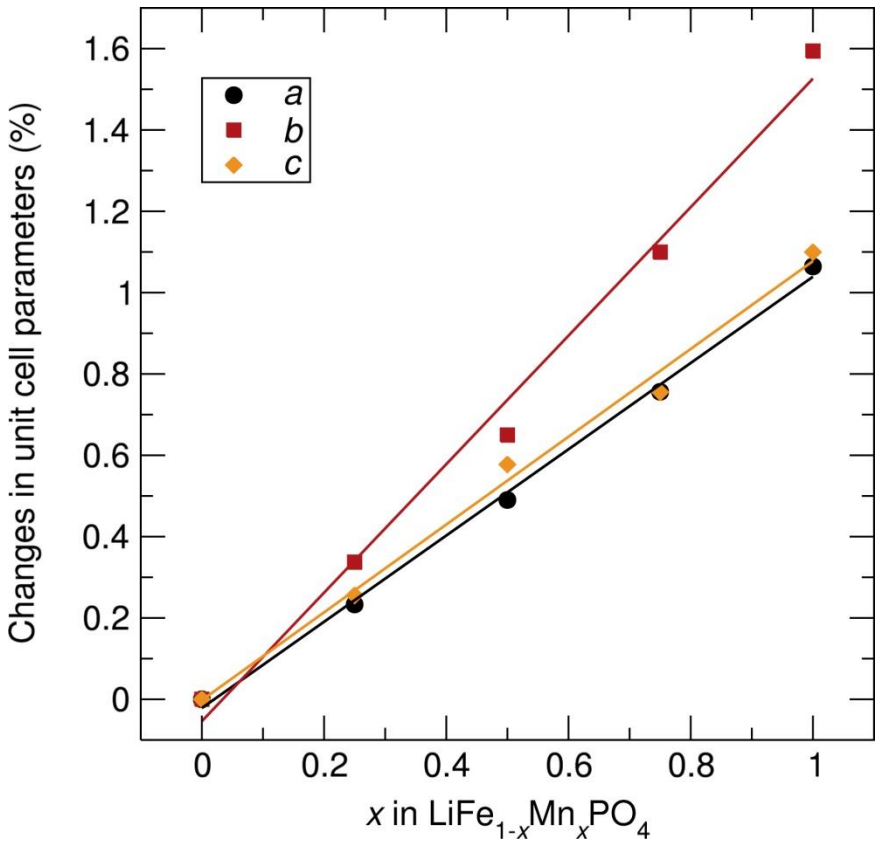

Figure A3.2. Changes in the unit-cell parameters as a function of the Mn content obtained from fitting neutron PDF data of $LiFe_{1-x}Mn_xPO_4$ (x=0, 0.25, 0.50, 0.75, 1) nanostructures.

Table A3.6. Calculated lattice parameters for the $LiFe_{1-x}Mn_xPO_4$ olivine phases obtained from real space Rietveld refinements of neutron PDF data from 1 to 30 Å.

Sample	**$LiFePO_4$**	**$LiFe_{0.75}Mn_{0.25}PO_4$**	**$LiFe_{0.5}Mn_{0.5}PO_4$**	**$LiFe_{0.25}Mn_{0.75}PO_4$**	**$LiMnPO_4$**
Space group	*Pnma*	*Pnma*	*Pnma*	*Pnma*	*Pnma*
a (Å)	10.356(8)	10.386(7)	10.407(3)	10.435(6)	10.468(5)
b (Å)	6.017(6)	6.037(5)	6.056(5)	6.084(4)	6.114(3)
c (Å)	4.701(4)	4.713 (3)	4.726(4)	4.736(3)	4.753(2)
Scale factor	0.69(3)	0.68(3)	0.70(3)	0.73(2)	0.68(2)
R_{wp}	0.1299	0.1331	0.1577	0.1468	0.1849

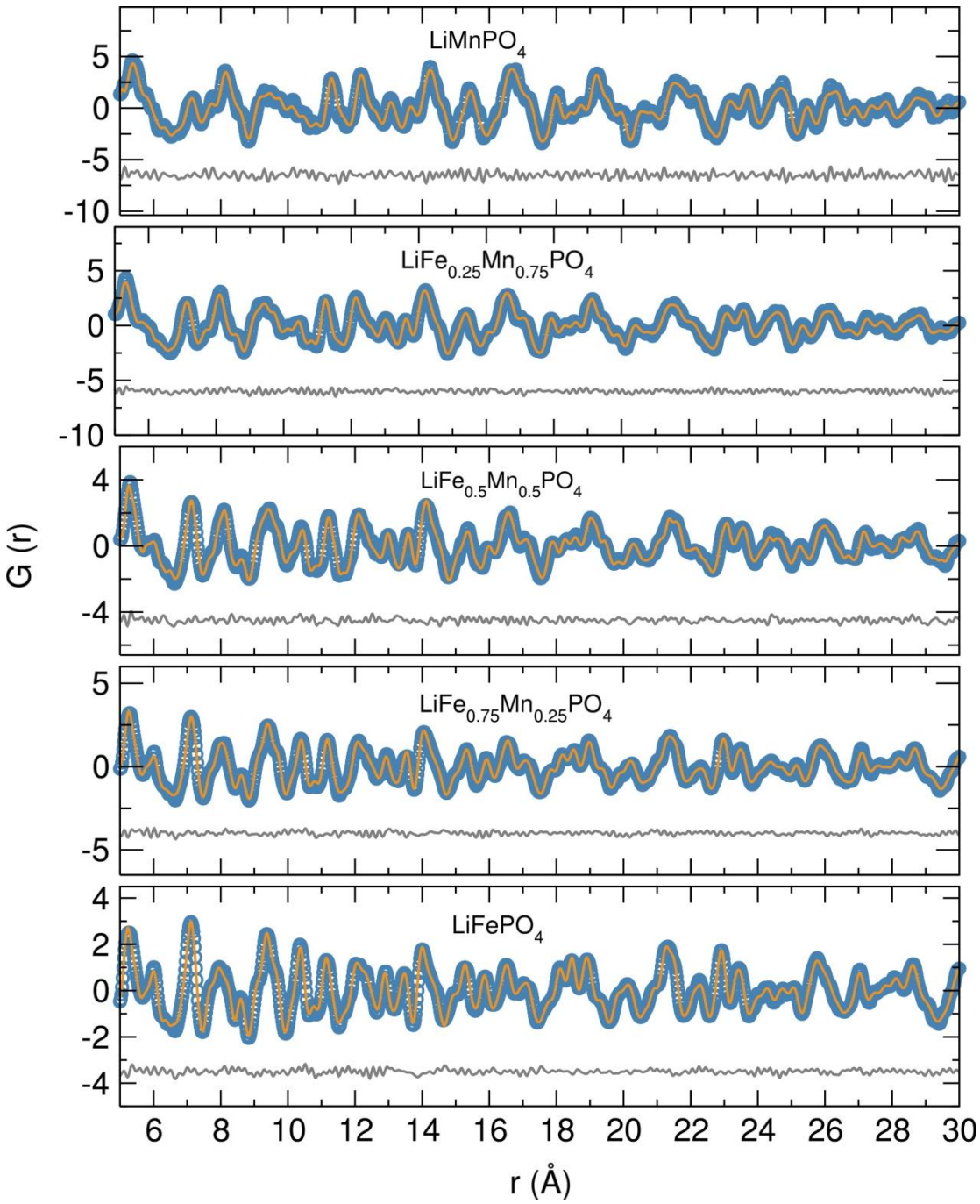

Figure A3.3. Fits of neutron PDF data obtained for single-phase $LiFe_{1-x}Mn_xPO_4$ nanoparticles (x=0, 0.25, 0.5, 0.75 and 1) at room temperature in the r range from 5 Å to 30 Å. Dots represent observed data and solid line the calculated pattern. The lower line is the difference curve.

Table A3.7. Atom-atom distances in $LiFe_{1-x}Mn_xPO_4$ samples determined from fits of neutron PDF data in the *r* range from 1-30 Å.

$LiFePO_4$		**$LiFe_{0.75}Mn_{0.25}PO_4$**		**$LiFe_{0.5}Mn_{0.5}PO_4$**		**$LiFe_{0.25}Mn_{0.75}PO_4$**		**$LiMnPO_4$**	
Atom-Atom distance (Å)		Atom-Atom distance (Å)		Atom-Atom distance (Å)		Atom-Atom distance (Å)		Atom-Atom distance (Å)	
P-O	1.49(3)	P-O	1.50(1)	P-O	1.493(1)	P-O	1.493(7)	P-O	1.4972(2)
	1.55(4)		1.54(2)		1.5476(2)		1.551(9)		1.5596(6)
	1.56(3)		1.57(1)		1.557(1)		1.558(1)		1.5665(6)
Fe-O	2.07(2)	Mn-O	1.847(2)	Mn-O	1.9597(5)	Fe-O	1.76(5)	Li-O	2.1162(7)
	2.10(4)	Fe-O	2.08(1)	Fe-O	2.093(2)	Mn-O	1.794(1)	Mn-O	2.1184(7)
Li-O	2.10(2)	Li-O	2.104(2)	Li-O	2.111(2)	Fe-O	2.09(2)		2.1379(9)
	2.19(2)	Fe-O	2.11(2)	Fe-O	2.1616(5)	Mn-O	2.093(1)	Li-O	2.1620(7)
Fe-O	2.21(4)	Li-O	2.189(2)	Mn-O	2.163(1)	Li-O	2.109(1)		2.2513(8)
O-O	2.44(2)		2.200(2)		2.166(1)		2.170(1)	Mn-O	2.2635(8)
	2.48(3)	Mn-O	2.206(2)	Li-O	2.1859(7)		2.239(1)		2.2749(8)
	2.53(5)	Fe-O	2.22(2)	Fe-O	2.1921(5)	Mn-O	2.419(1)	O-O	2.456(1)
	2.56(4)		2.26(2)	Li-O	2.221(1)	O-O	2.444(2)		2.498(1)
Li-P	2.67(2)	Mn-O	2.301(2)	Fe-O	2.257(1)		2.45(4)		2.5553(6)
Fe-P	2.85(4)	O-O	2.452(2)	Mn-O	2.3981(5)		2.489(1)	Li-P	2.6659(8)
O-O	2.93(4)		2.487(2)	O-O	2.456(2)		2.540(2)	Mn-P	2.8717(8)
	2.94(4)		2.537(2)		2.4885(6)		2.544(2)	O-O	2.9662(6)
	2.98(4)		2.565(2)		2.526(1)	Mn-O	2.585(1)		3.006(1)
	3.01(5)	Li-O	2.67(2)		2.548(2)	Fe-O	2.62(5)	Li-Li	3.057(1)
Li-Li	3.009(3)	Mn-O	2.784(2)	Li-P	2.667(2)	Li-P	2.66(1)	O-O	3.0724(8)
O-O	3.04(3)	Fe-P	2.87(4)	Mn-P	2.712(1)	Fe-P	2.91(5)		3.105(1)
	3.07(1)	O-O	2.935(2)	Fe-P	2.839(1)	Mn-P	2.96(1)		3.126(1)
P-O	3.21(3)		2.959(2)	O-O	2.962(2)	O-O	2.963(2)	P-O	3.2566(5)
Fe-P	3.24(4)		2.996(2)		2.965(2)		2.992(2)	O-O	3.269(1)

$LiFePO_4$		$LiFe_{0.75}Mn_{0.25}PO_4$		$LiFe_{0.5}Mn_{0.5}PO_4$		$LiFe_{0.25}Mn_{0.75}PO_4$		$LiMnPO_4$	
Atom-Atom distance (Å)		Atom-Atom distance (Å)		Atom-Atom distance (Å)		Atom-Atom distance (Å)		Atom-Atom distance (Å)	
Li-P	3.26(2)	Li-Mn	3.001(2)		3.017(2)	Li-Li	3.042(2)	Mn-P	3.301(1)
O-O	3.27(3)	Mn-O	3.002(2)	Li-Li	3.028(2)	Mn-P	3.04(1)	O-O	3.312(1)
Fe-P	3.27(1)	O-O	3.013(2)	O-O	3.047(2)	O-O	3.049(2)	Mn-P	3.3247(8)
O-O	3.28(3)	Li-Li	3.019(3)	Li-Mn	3.0526(7)		3.061(2)	Li-Mn	3.328(1)
Li-Fe	3.29(1)	O-O	3.056(2)	Mn-P	3.066(2)	Fe-P	3.08(6)	Li-P	3.3340(8)
Fe-P	3.29(3)	Mn-P	3.07(2)	O-O	3.075(1)	O-O	3.091(2)	Mn-P	3.338(2)
P-O	3.33(2)	O-O	3.074(3)	Fe-P	3.210(2)		3.107(2)	P-O	3.405(1)
Fe-O	3.43(4)	Mn-P	3.11(2)		3.233(2)	Mn-O	3.128(2)	Mn-O	3.433(1)
	3.48(2)		3.183(8)	Li-Fe	3.2482(7)	Fe-P	3.20(2)	O-O	3.474(1)
Li-O	3.49(2)	P-O	3.21(1)	O-O	3.2634(2)	Mn-P	3.211(6)	Li-O	3.490(1)
P-O	3.49(4)	Fe-P	3.26(4)		3.2995(5)	P-O	3.244(7)	Mn-O	3.519(2)

Table A3.8. Calculated scale factor and amorphous content for the $LiFe_{1-x}Mn_xPO_4$ olivine phases obtained from two isostructural phases refinements of neutron PDF data from 1 to 30 Å.

Sample	**$LiFePO_4$**	**$LiFe_{0.75}Mn_{0.25}PO_4$**	**$LiFe_{0.5}Mn_{0.5}PO_4$**	**$LiFe_{0.25}Mn_{0.75}PO_4$**	**$LiMnPO_4$**
Scale factor Phase 1	0.68(3)	0.66(4)	0.68(3)	0.71(2)	0.66(2)
Scale factor Phase 2	0.05(7)	0.04(6)	0.05(6)	0.06(5)	0.06(3)
Amorphous content (%)	6.7	5.6	6.9	7.7	8.1
Spdiameter (Å)	15	18	14	12	12
R_{wp}	0.1284	0.1321	0.1560	0.1446	0.1825

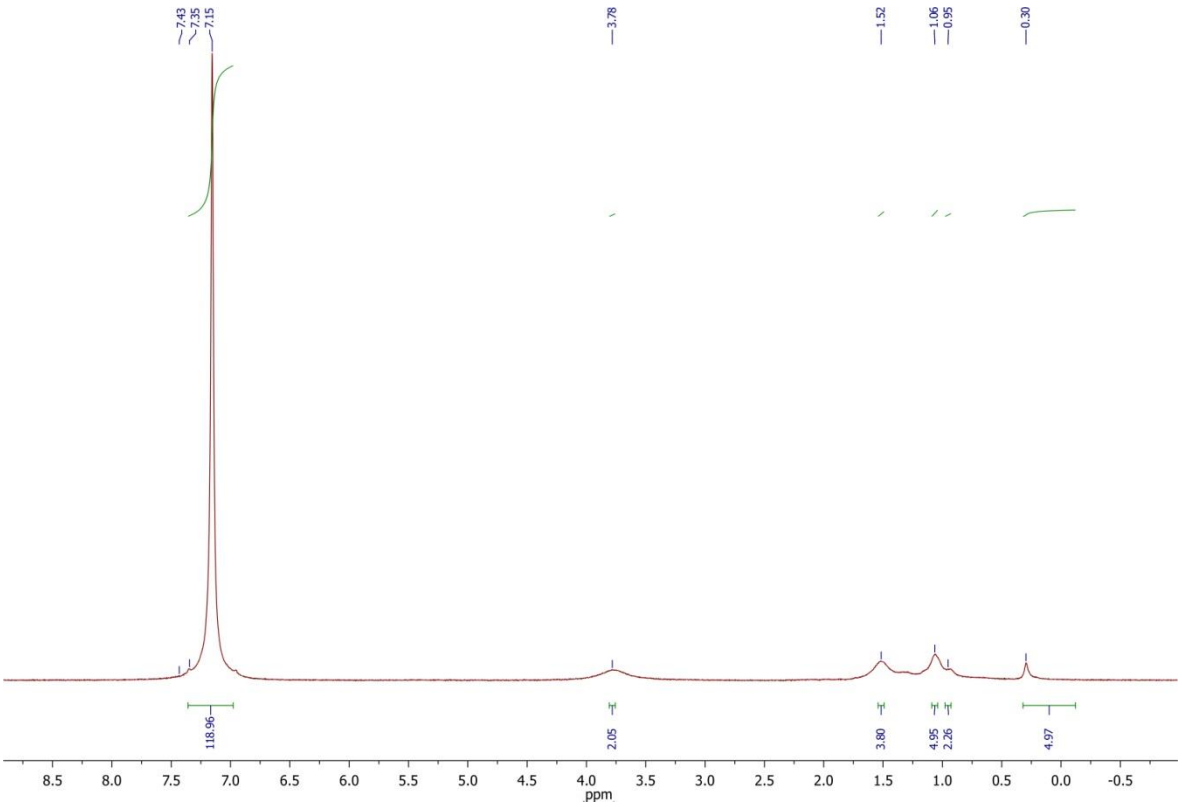

Figure A4.1. ^1H NMR spectrum of $[Fe(O^tBu)_2(THF)]_2$ (I) (400 MHz, C_6D_6, 25 °C): δ=0.3 (s., μ_2-O^tBu), 1.1 (br, teminal-O^tBu), 1.5 (br., THF), 3.8 (br., THF) ppm.

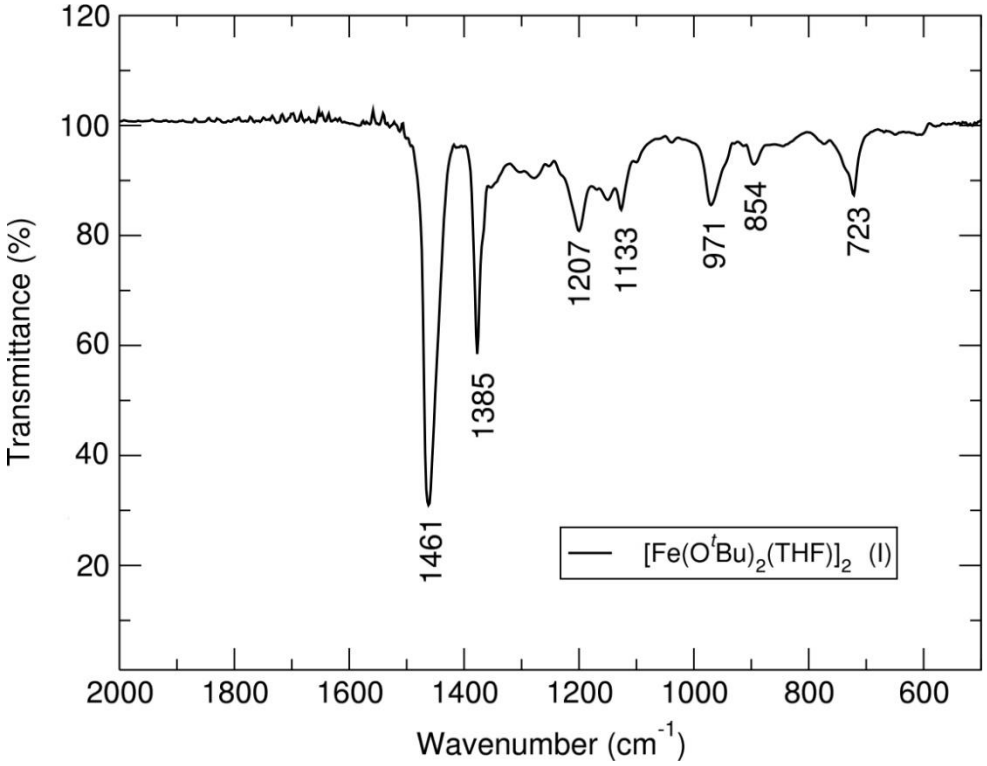

Figure A4.2. FT-IR spectrum of $[Fe(O^tBu)_2(THF)]_2$ (I) metal alkoxide.

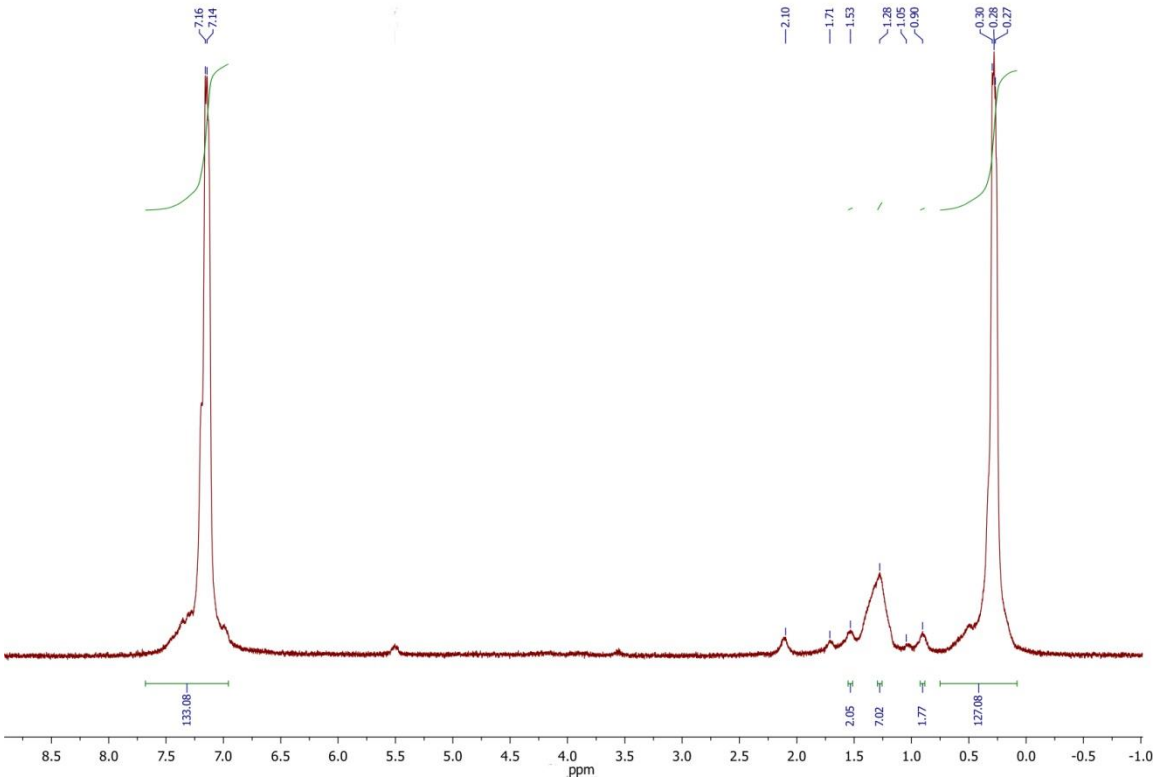

Figure A4.3. ^1H NMR spectrum of "$[Mn(O^tBu)_2(THF)]_2$" (II) (500 MHz, C_6D_6, 25 °C): δ=0.3 (s., μ_2-O^tBu), 0.9 (br, teminal-O^tBu), 1.3 (br., THF) ppm.

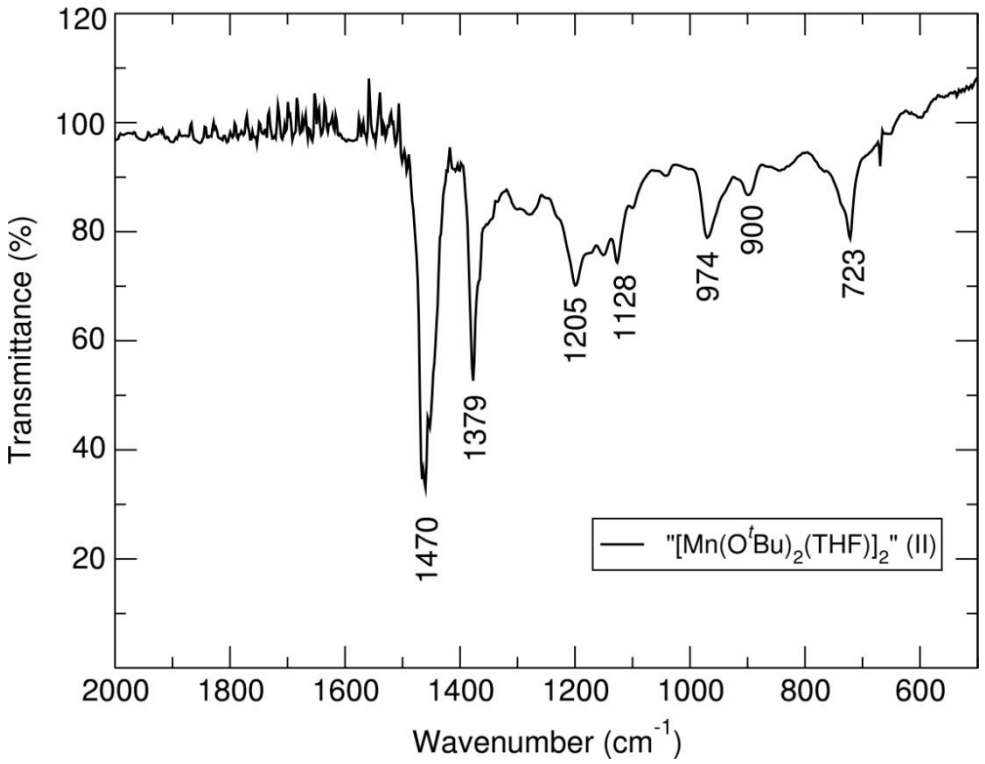

Figure A4.4. FT-IR spectrum of "$[Mn(O^tBu)_2(THF)]_2$"(II) metal alkoxide precursor.

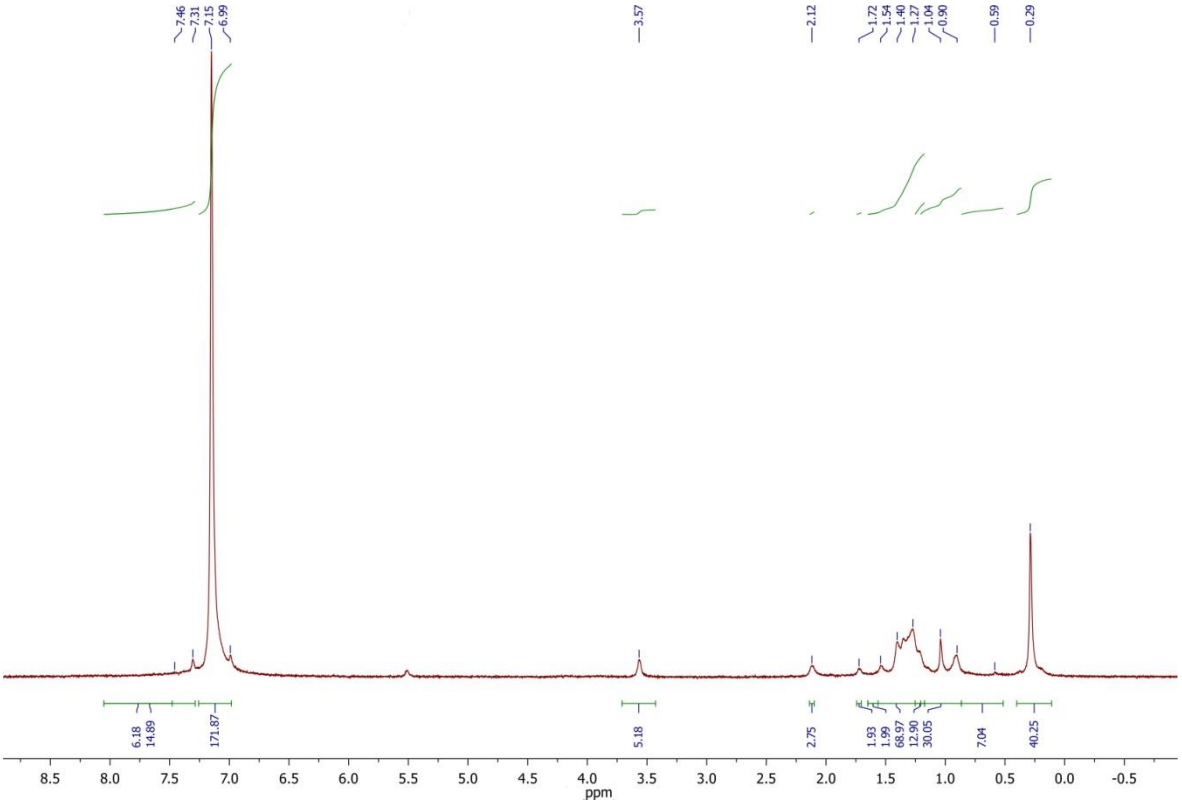

Figure A4.7. ^1H NMR spectrum of "$[Fe_{0.5}Mn_{0.5}(O^tBu)_2(THF)]_2$" (III) (500 MHz, C_6D_6, 25 °C): δ=0.3 (s., μ_2-O^tBu), 0.9 (br, teminal-O^tBu), 1.0 (br, teminal-O^tBu), 1.4 (br., THF), 2.1, 3.6 (br., THF) ppm.

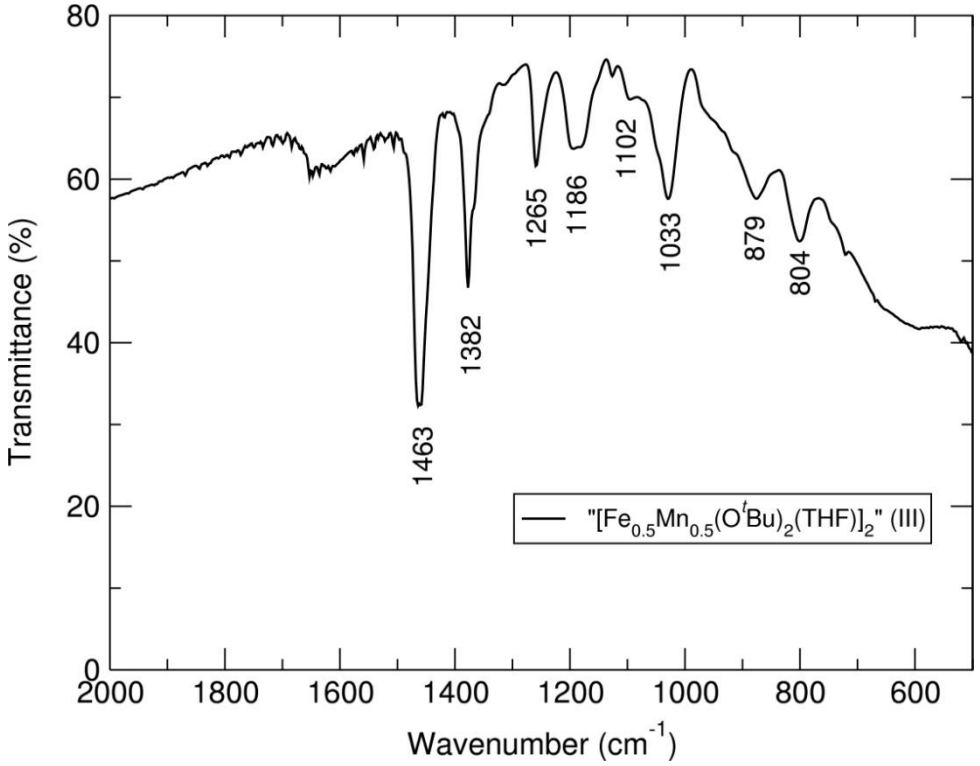

Figure A4.6. FT-IR spectrum of "[$Fe_{0.5}Mn_{0.5}(O^tBu)_2(THF)]_2$" (III) metal alkoxide precursor.

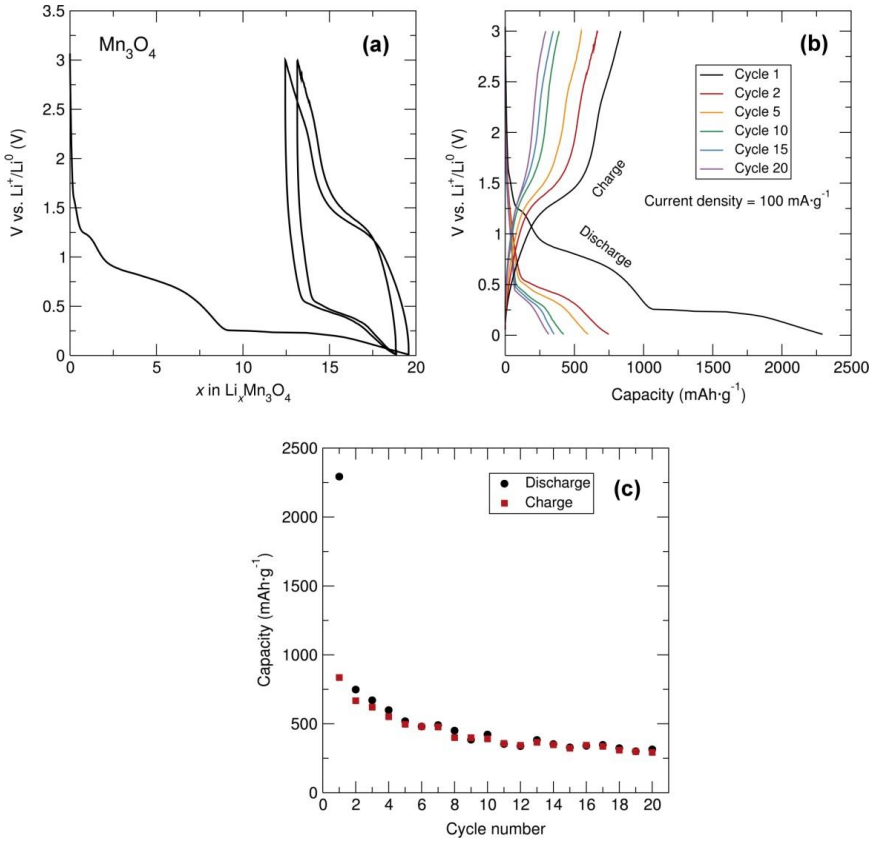

Figure A4.7. (a) Voltage-composition profile, **(b)** voltage-capacity profile and **(c)** cycling stability of Mn_3O_4 with C black and PTFE in 60:30:10 % wt. ratio over the potential range of 0.01 V-3.00 V at 100 mA·g^{-1}.

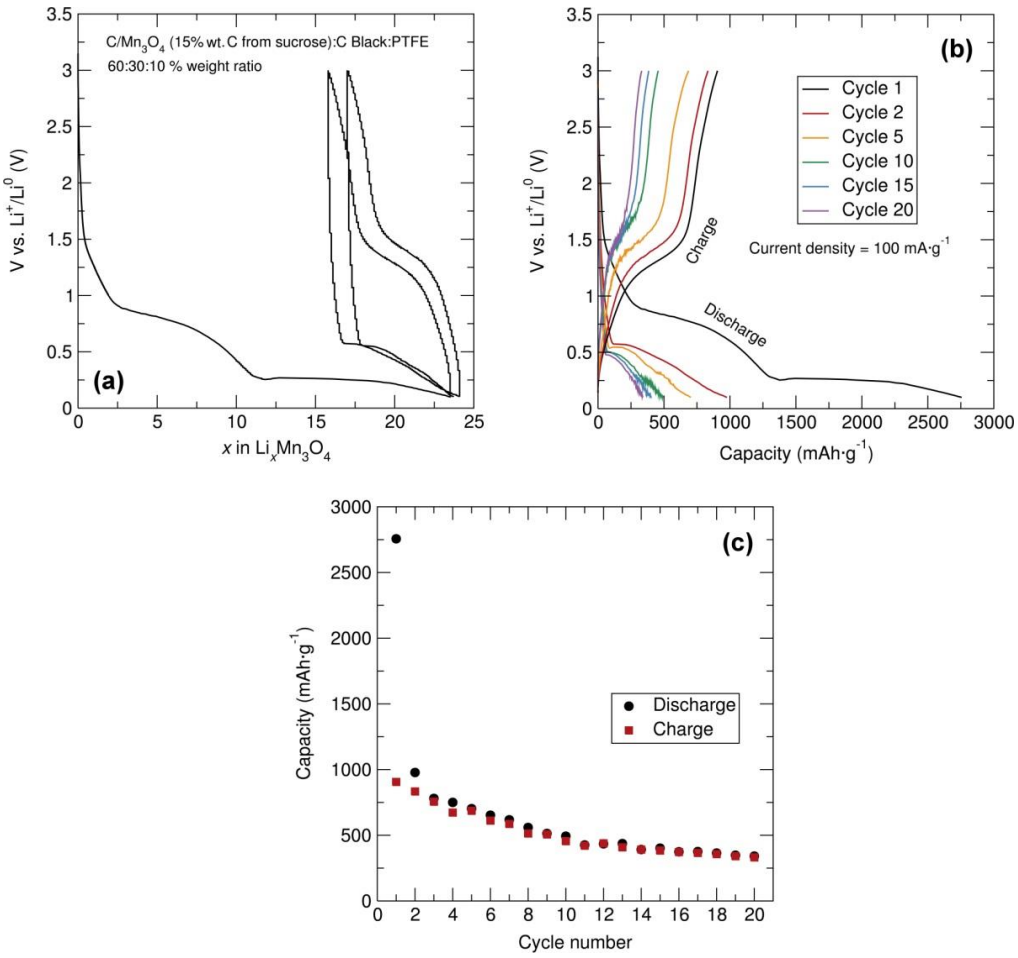

Figure A4.8. (a) Voltage-composition profile, **(b)** voltage-capacity profile, **(c)** cycling stability of C/Mn_3O_4 (15% C from sucrose) with C black and PTFE in 60:30:10 % wt. ratio over the potential range of 0.10 V-3.00 V at 100 $mA \cdot g^{-1}$ current density.

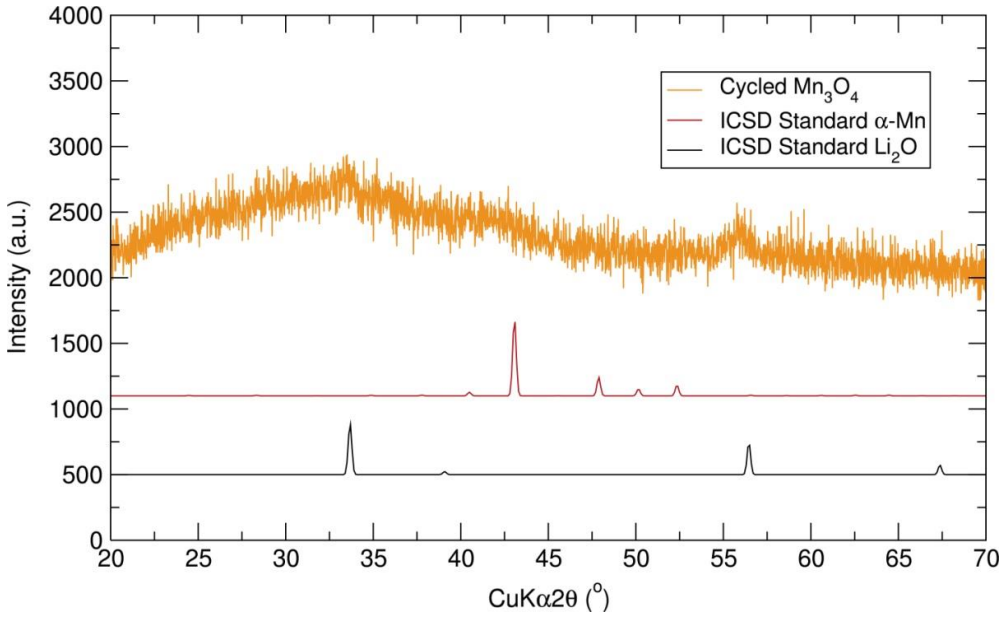

Figure A4.9. Close up of PXRD pattern of C/Mn_3O_4 hausmannite after 20 cycles, showing the possible presence of conversion product Li_2O after repeated cycles.

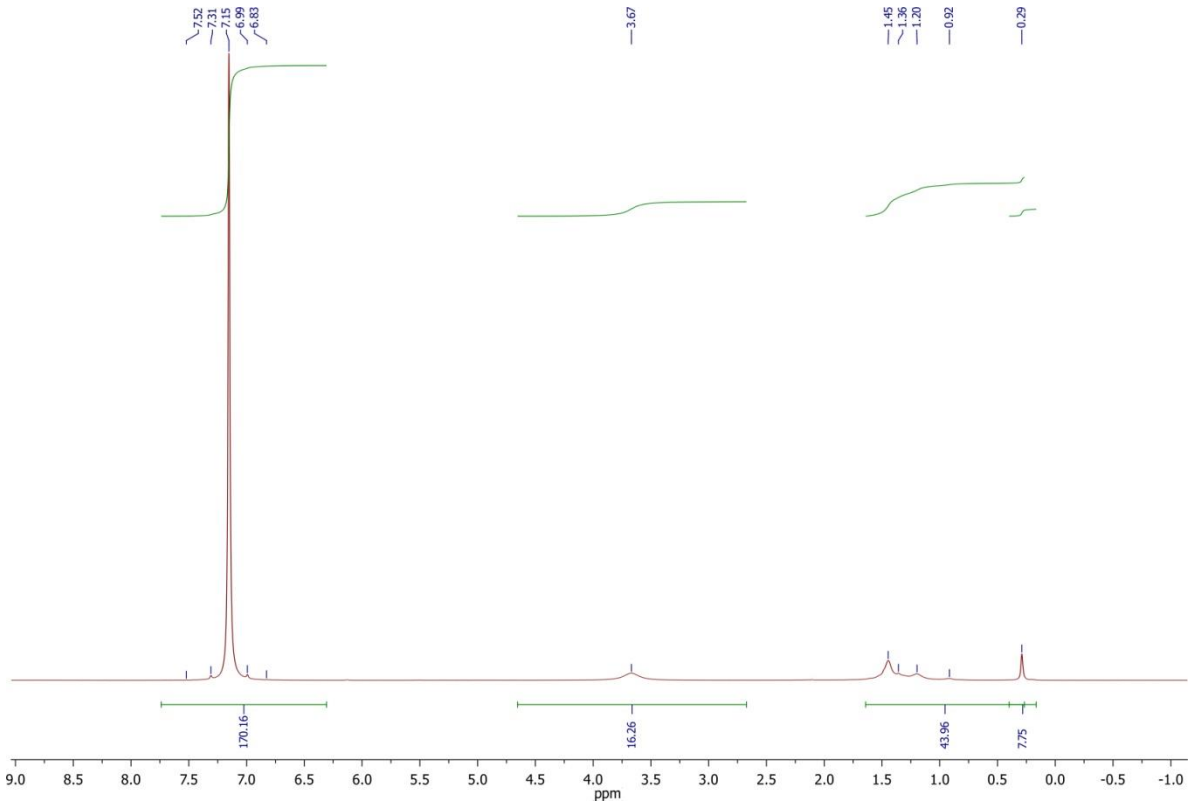

Figure A5.1. ^{1}H NMR spectrum of $[FeLi_2Br(O^tBu)_4(THF)_2]_n$ (IV) (500 MHz, C_6D_6, 25 °C): δ=0.3 (s., μ_2-O^tBu), 1.2 (br, teminal-O^tBu), 1.4 (s., THF), 3.6 (br., THF) ppm.

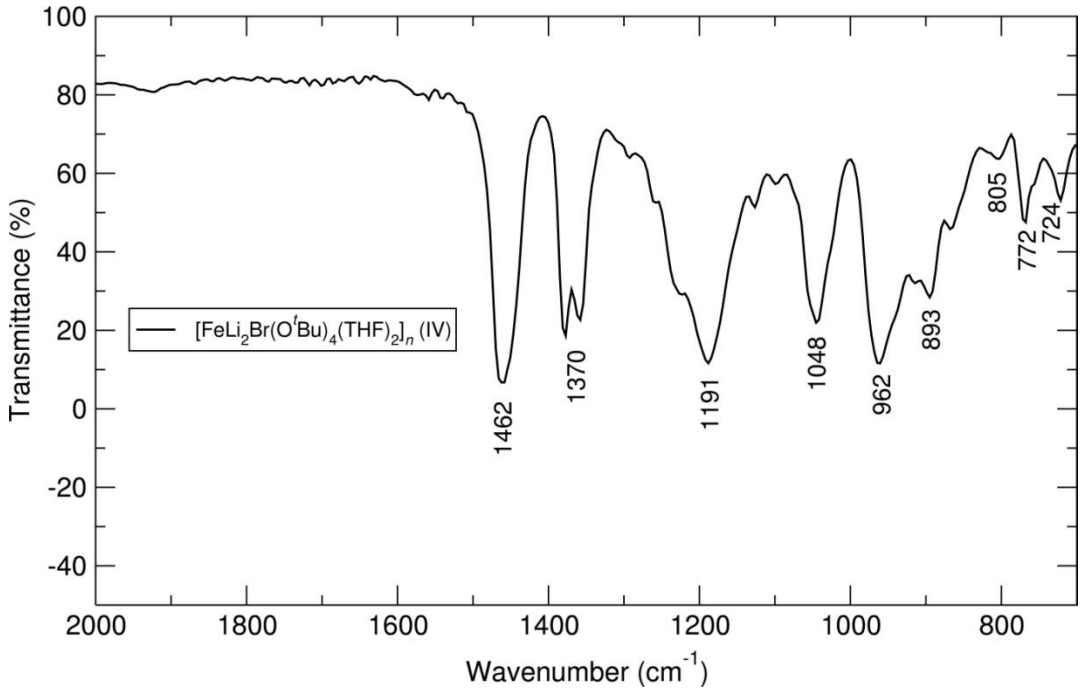

Figure A5.2. FT-IR spectrum of $[FeLi_2Br(O^tBu)_4(THF)_2]_n$ (IV).

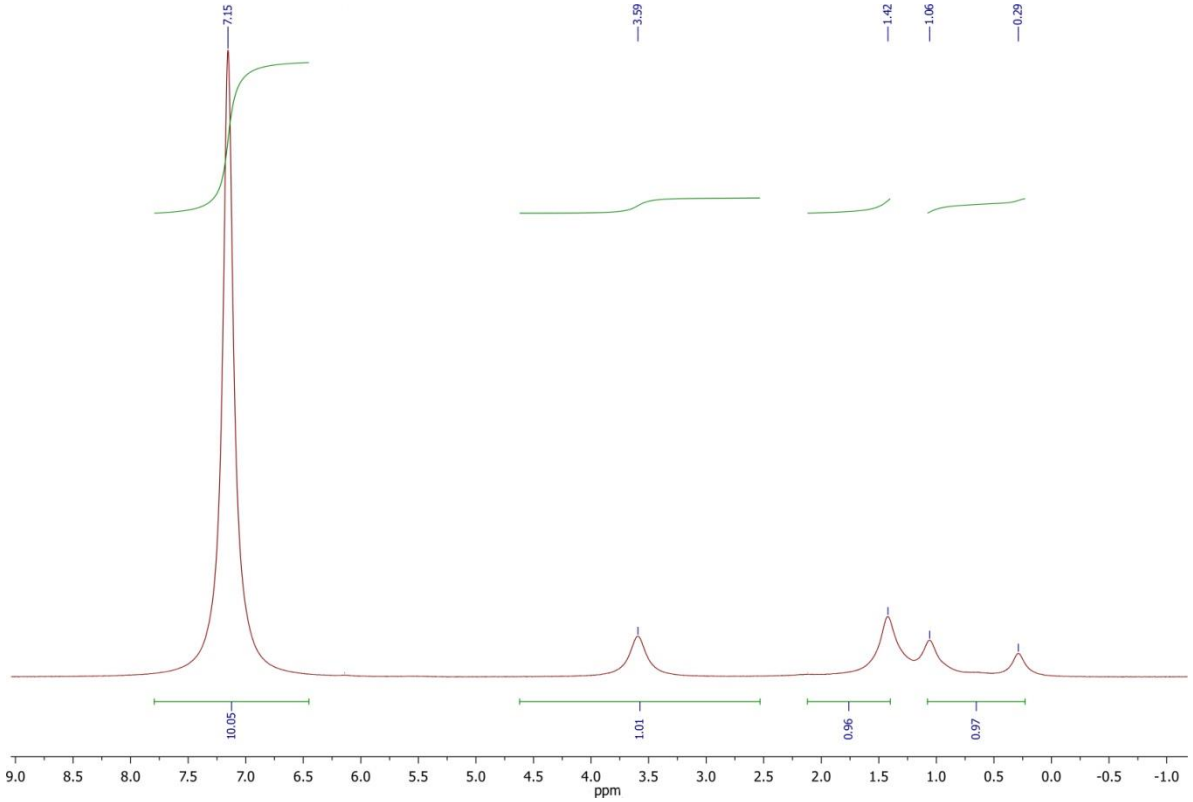

Figure A5.3. ^{1}H NMR spectrum of "$[FeLi_2Cl(O^tBu)_4(THF)_2]_n$ " (V) (500 MHz, C_6D_6, 25 °C): δ=0.3 (br., μ_2-O^{t}Bu), 1.1 (br, teminal-O^{t}Bu), 1.4 (br., THF), 3.6 (br., THF) ppm.

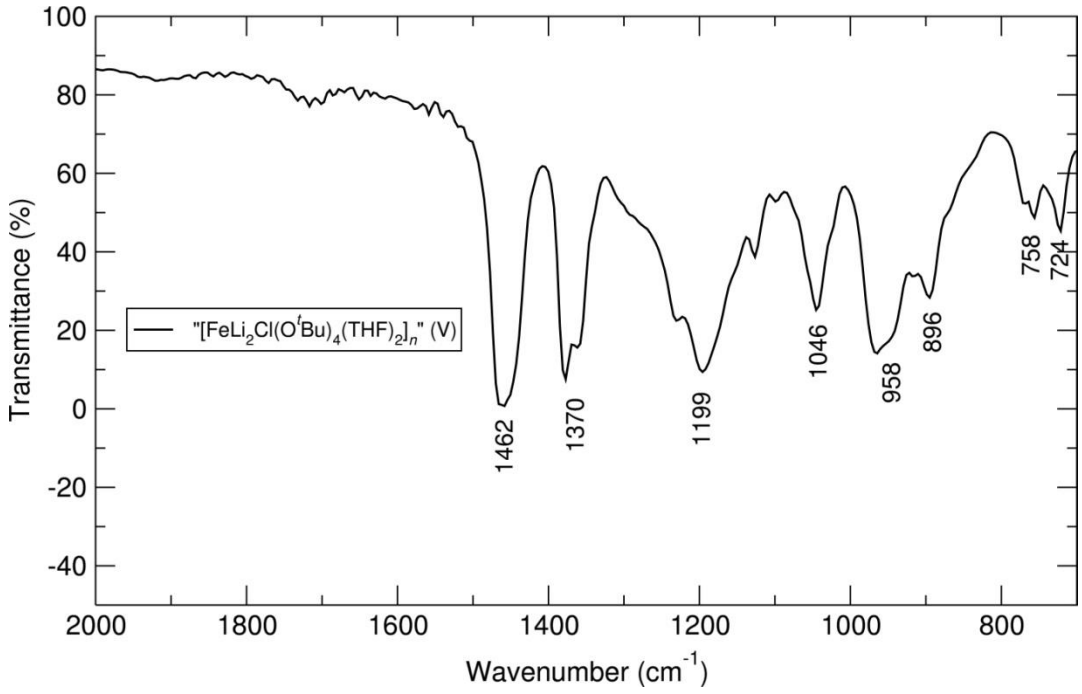

Figure A5.4. FT-IR spectrum of "$[FeLi_2Cl(O^tBu)_4(THF)_2]_n$" (V).

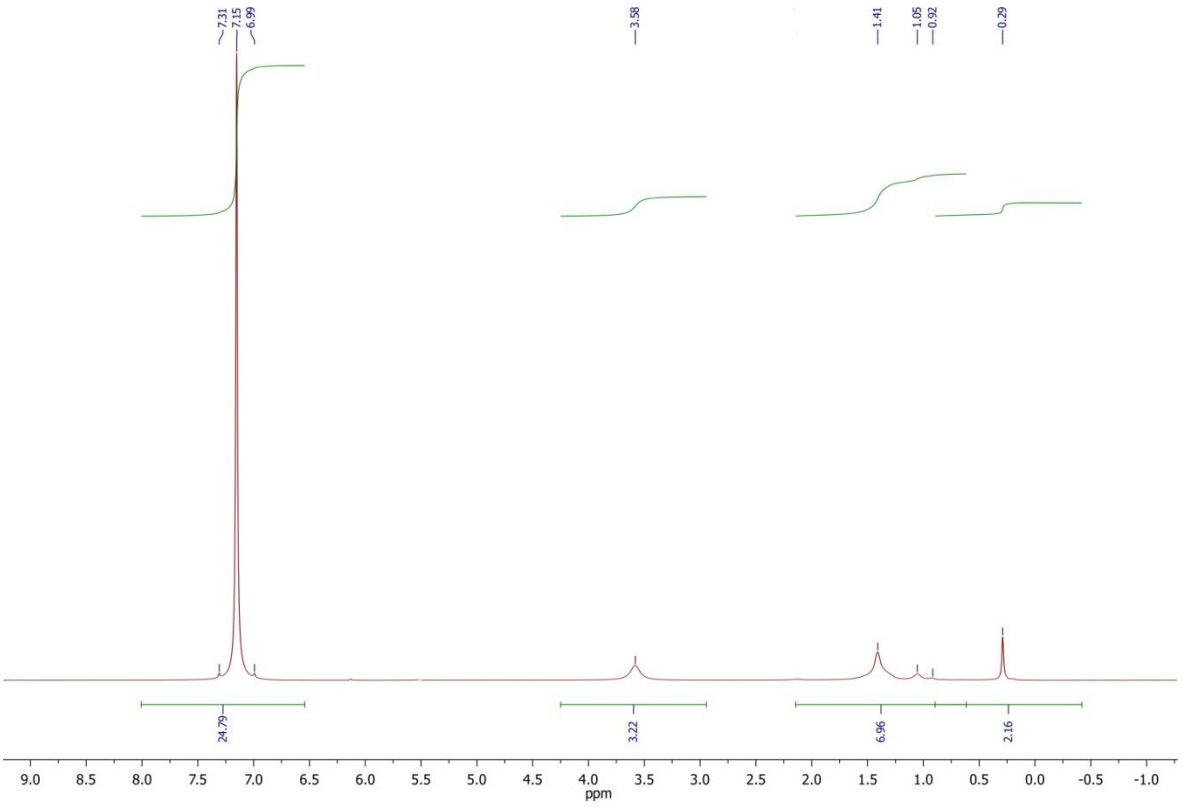

Figure A5.5. ^{1}H NMR spectrum of "$[MnLi_2Br(O^tBu)_4(THF)_2]_n$" (VI) (500 MHz, C_6D_6, 25 °C): δ=0.3 (s., μ_2-O^{t}Bu), 1.2 (br, teminal-O^{t}Bu), 1.4 (s., THF), 3.6 (br., THF) ppm.

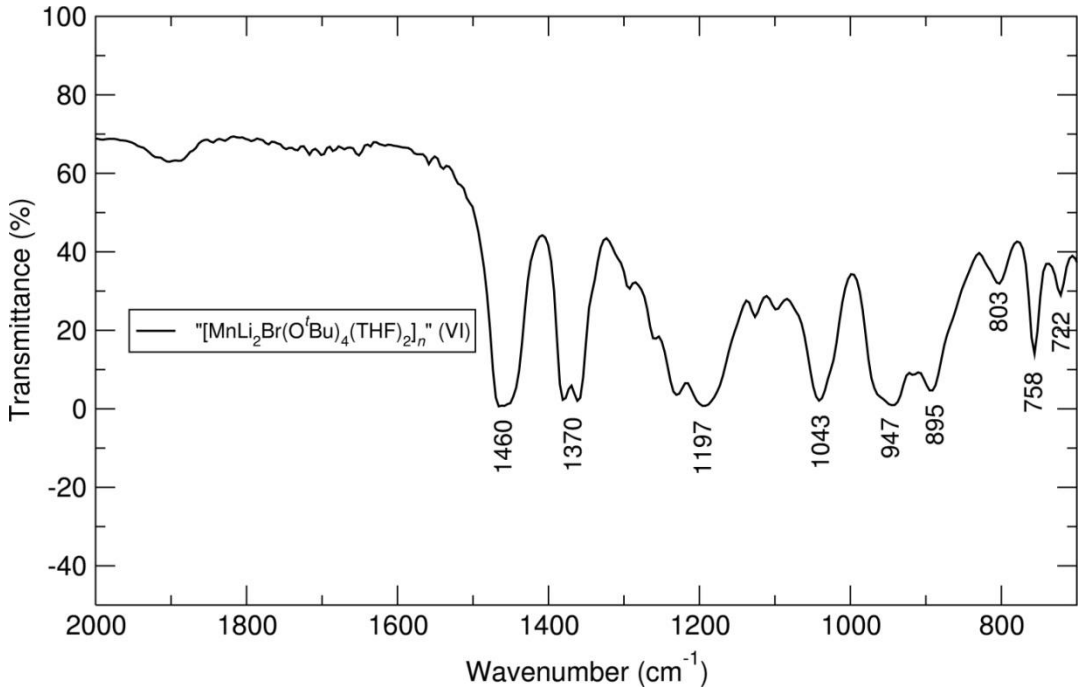

Figure A5.6. FT-IR spectrum of "$[MnLi_2Br(O^tBu)_4(THF)_2]_n$" (VI).

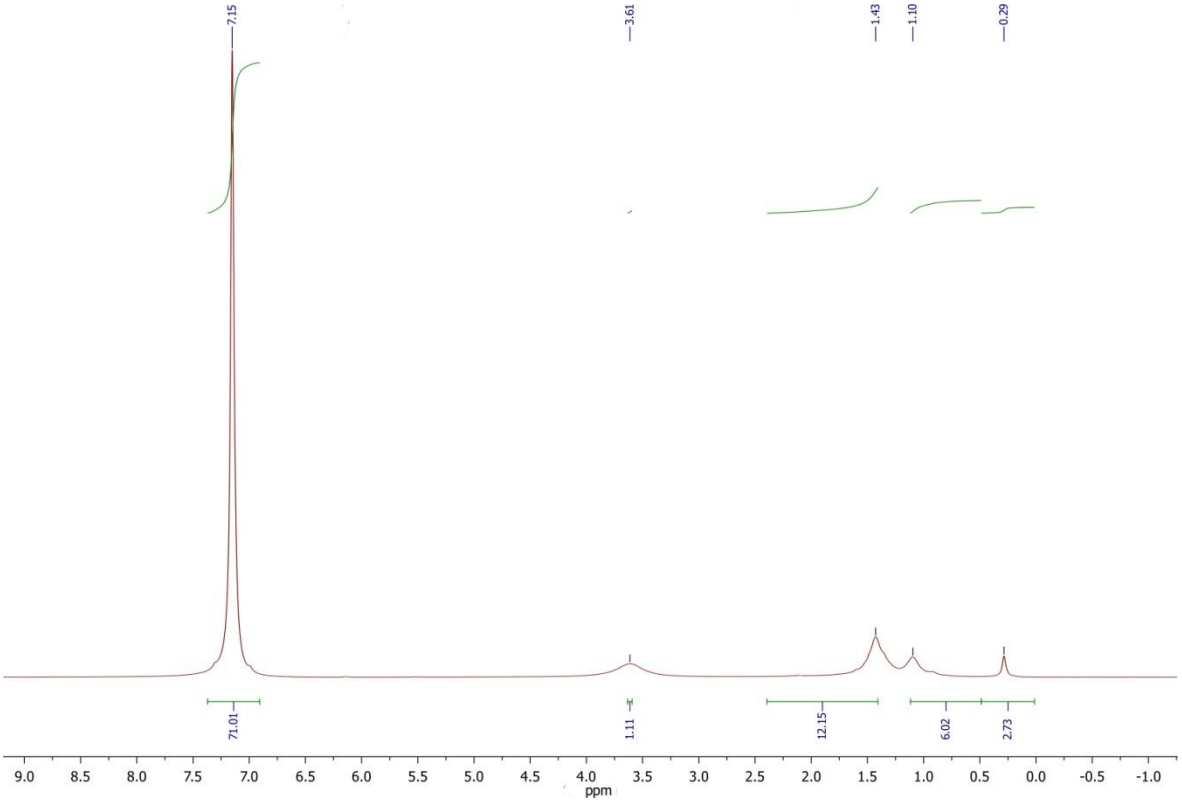

Figure A5.7. ^{1}H NMR spectrum of "$[Fe_{0.5}Mn_{0.5}Li_2Br(O^tBu)_4(THF)_2]_n$" (VII) (500 MHz, C_6D_6, 25 °C): δ=0.3 (s., μ_2-O^{t}Bu), 1.2 (br, teminal-O^{t}Bu), 1.4 (s., THF), 3.6 (br., THF) ppm.

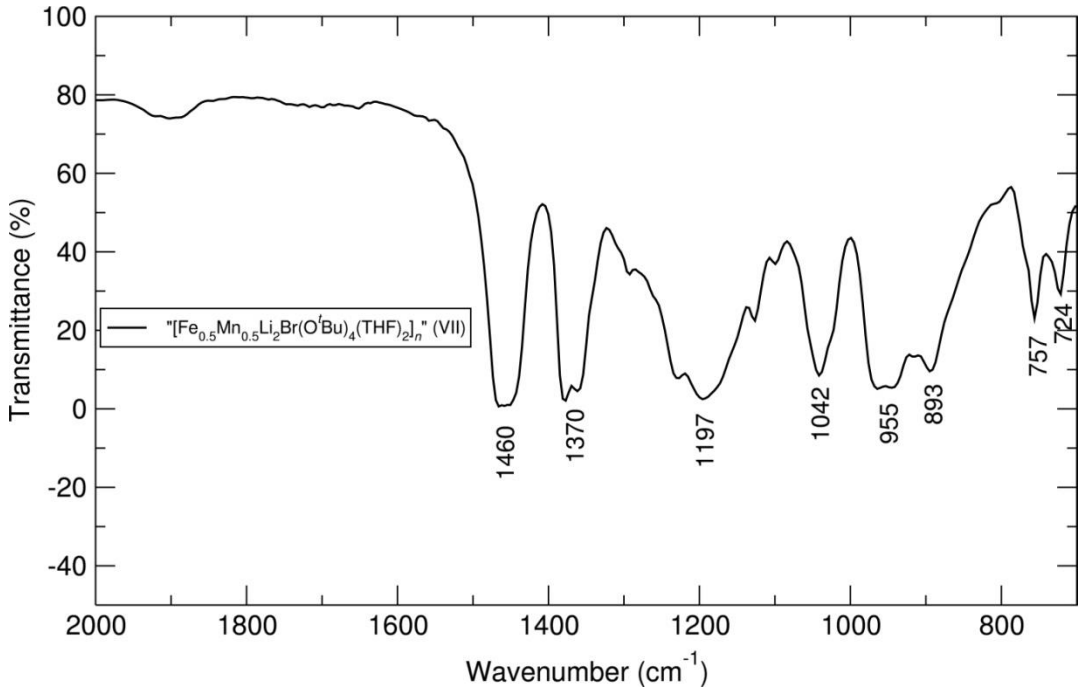

Figure A5.8. FT-IR spectrum of "$[Fe_{0.5}Mn_{0.5}Li_2Br(O^tBu)_4(THF)_2]_n$" (VII).

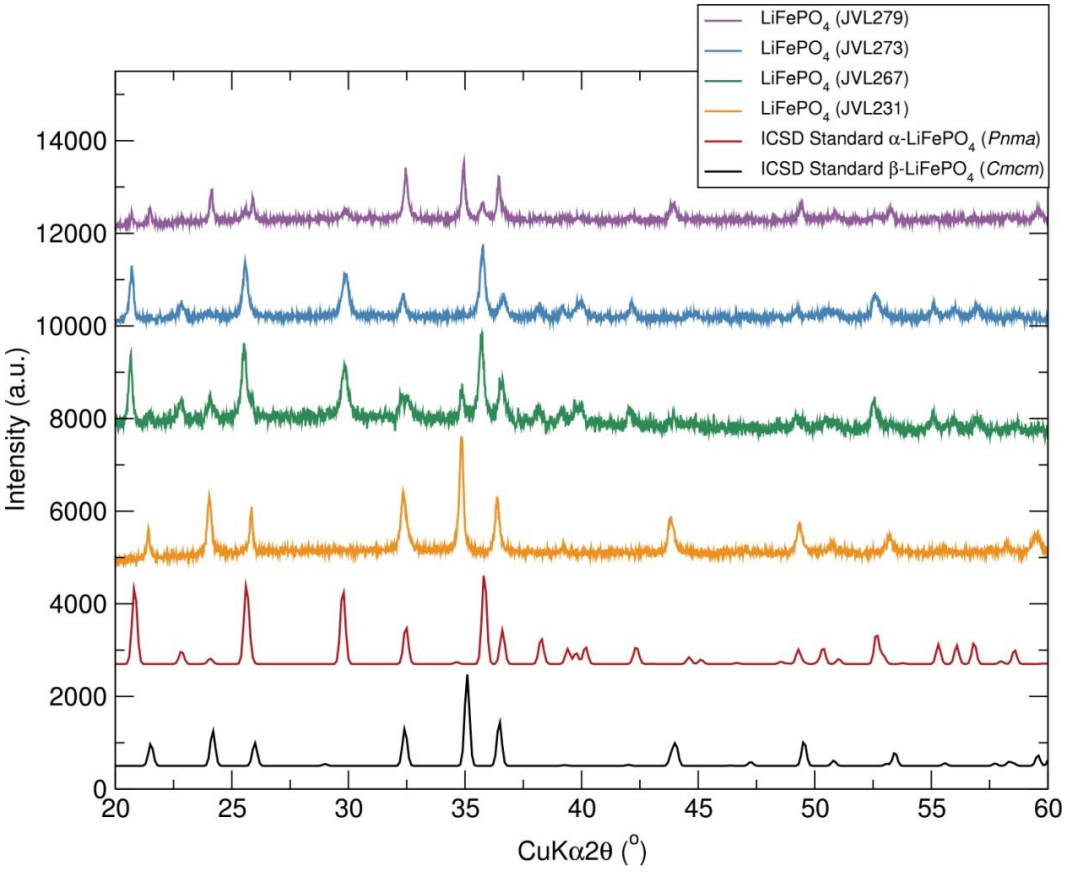

Figure A5.9. PXRD pattern of $LiFePO_4$ samples prepared from different batches of heterometallic alkoxide precursor $[FeLi_2Br(O^tBu)_4(THF)_2]_n$.

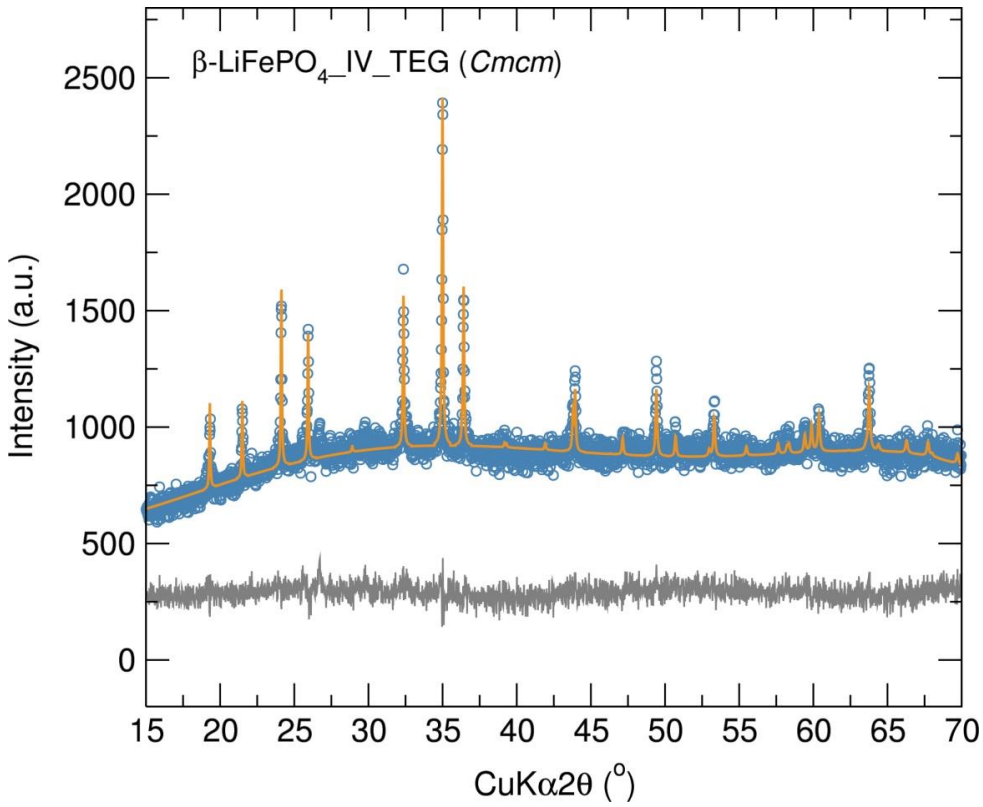

Figure A5.10. PXRD pattern of β-$LiFePO_4$_IV_TEG sample prepared from single source heterometallic alkoxide precursor $[FeLi_2Br(O^tBu)_4(THF)_2]_n$ in tetraethylene glycol.

Table A5.2. Atom-atom distances in $LiFe_{1-x}Mn_xPO_4$ samples determined from fits of X-ray PDF data in the *r* range from 1-5 Å.

$LiFePO_4$_V		**$LiFe_{0.5}Mn_{0.5}PO_4$_VII**		**$LiMnPO_4$_VI**		**$LiFePO_4$_IL**	
Atom-Atom distance (Å)		Atom-Atom distance (Å)		Atom-Atom distance (Å)		Atom-Atom distance (Å)	
P-O	1.56(3)	P-O	1.55(1)	P-O	1.54(1)	P-O	1.48(7)
	1.56(4)		1.58(1)		1.64(1)		1.57(7)
Fe-O	2.04(2)	Fe-O	1.95(1)	**Li-O**	**1.95(1)**	Fe-O	2.06(3)
	2.04(2)	Mn-O	1.96(2)		2.03(1)		2.10(11)
Li-O	**2.05(4)**	Fe-O	2.05(1)		2.15(1)	**Li-O**	**2.13(9)**
	2.05(4)	**Li-O**	**2.05(1)**	Mn-O	2.17(1)		2.13(10)
Fe-O	2.06(5)	Mn-O	2.14(1)		2.22(2)	Fe-O	2.20(2)
Li-O	2.09(4)	Li-O	2.15(1)		2.25(1)		2.21(12)
	2.10(3)	Mn-O	2.16(1)	O-O	2.44(1)	Li-O	2.21(2)
Fe-O	2.11(5)	Li-O	2.19(2)	Mn-O	2.49(1)	O-O	2.41(3)
	2.30(5)	Mn-O	2.21(2)	Li-P	2.59(1)		2.48(8)
O-O	2.45(2)	Fe-O	2.24(2)	O-O	2.65(1)		2.5(2)
Li-P	2.64(4)	O-O	2.46(2)		2.75(1)	Li-P	2.65(9)
O-O	2.72(6)		2.497(1)		2.79(1)	Fe-P	2.83(11)
	2.75(4)	Mn-O	2.66(2)		2.87(2)	O-O	2.84(10)
	2.77(6)	Li-P	2.69(2)	Mn-P	2.89(2)		2.93(12)
Fe-P	2.84(3)	O-O	2.72(2)	O-P	2.92(2)		2.94(3)
O-O	2.88(5)		2.782)	O-O	3.04(2)		2.97(23)
P-O	2.97(1)		2.84(2)		3.15(1)	**Li-Li**	**2.97(4)**
Li-Li	**2.99(3)**	Fe-P	2.86(2)	**Li-Li**	**3.18(1)**	O-O	3.02(10)
O-O	3.05(6)	**Li-Li**	**3.06(1)**	O-O	3.20(1)		3.05(8)

Table A5.1. CHN Microanalysis of $LiFe_{1-x}Mn_xPO_4$ nanostructures preared fom through fast microwave treatments using "$[MLi_2Br(O^tBu)_4(THF)_2]_n$" (*M*=Fe, Mn) heterometallic alkoxide precursors.

Sample	C	H
$LiFePO_4$_IV	1.78 %	0.38 %
$LiFePO_4$_V	1.84 %	0.57 %
$LiFe_{0.5}Mn_{0.5}PO_4$_VII	1.57 %	0.41 %
$LiMnPO_4$_VI	2.76 %	1.11 %

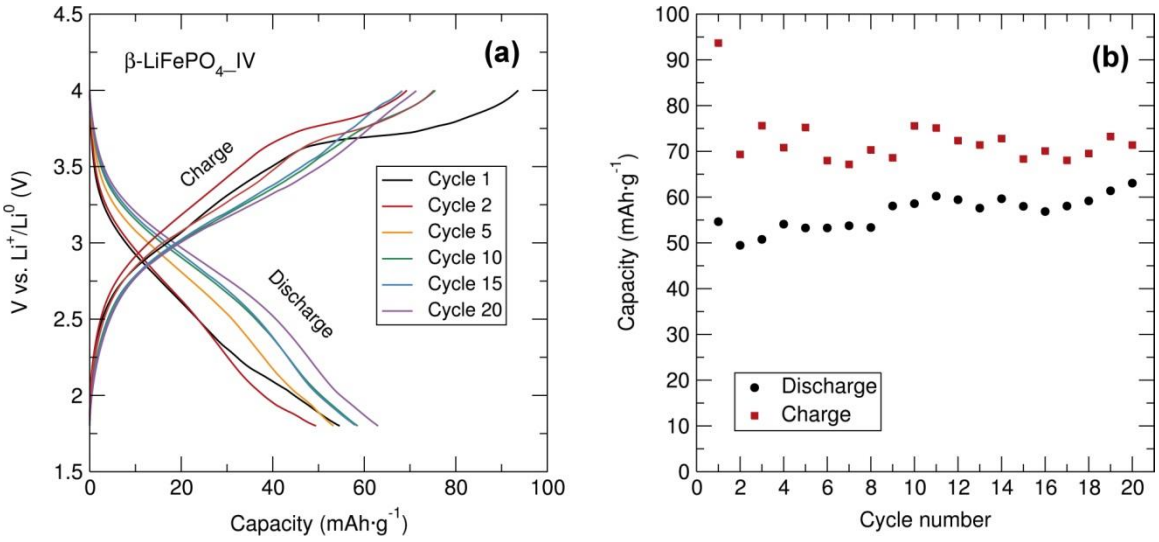

Figure A5.11. (a) Voltage-capacity profile and **(b)** cycling stability of β-$LiFePO_4$_IV with C black in 60:40 % weight ratio (2 hr ball mill) over the potential range of 4.0 V-1.8 V at C/20 rate.

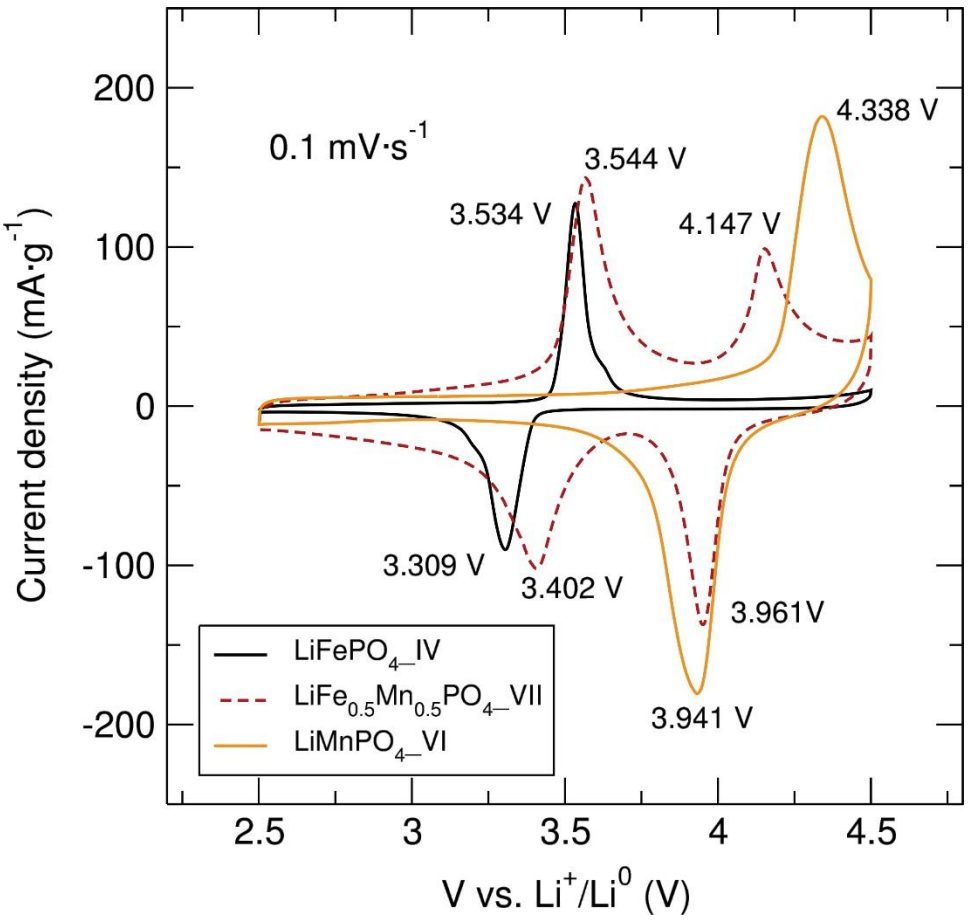

Figure A5.12. Comparative CVs at a 0.1 mV·s^{-1} scan rate of C/$LiFePO_4$_IV, C/$LiMnPO_4$_VI and C/$LiFe_{0.5}Mn_{0.5}PO_4$_VII nanostructures.

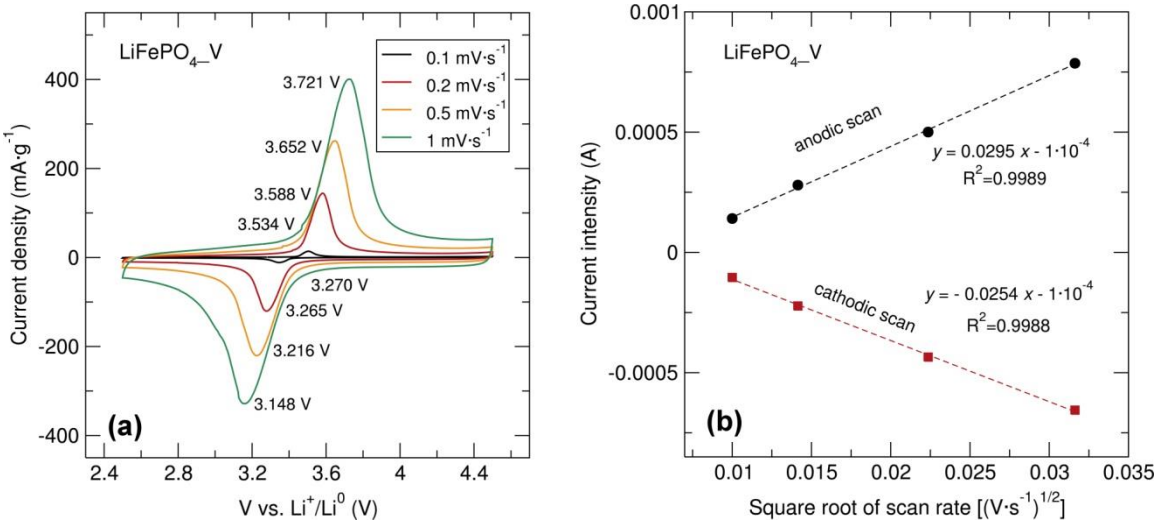

Figure A5.13. (a) CV profiles of C/$LiFePO_4$_V at different scan rates. **(b)** Graph of peak current *vs.* squre root of the scan rate for the C/$LiFePO_4$_V_IL (15% wt. C from sucrose) nanostructure prepared through a microwave-assisted synthesis using "$[FeLiCl(O^tBu)_4(THF)_2]_n$" (V) heterometallic alkoxide precursor.

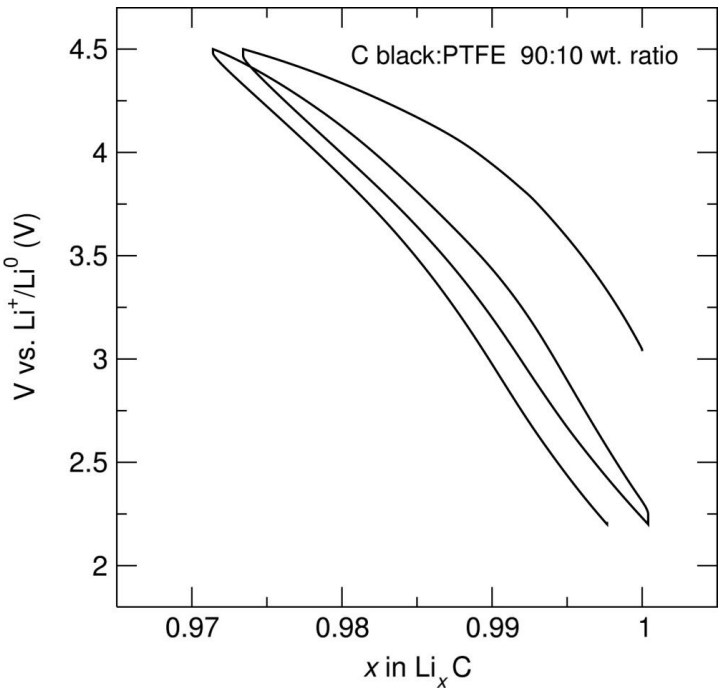

Figure A6.1. Galvanostatic cycling test of carbon black at C/20 rate from 2.2 V to 4.5 V.

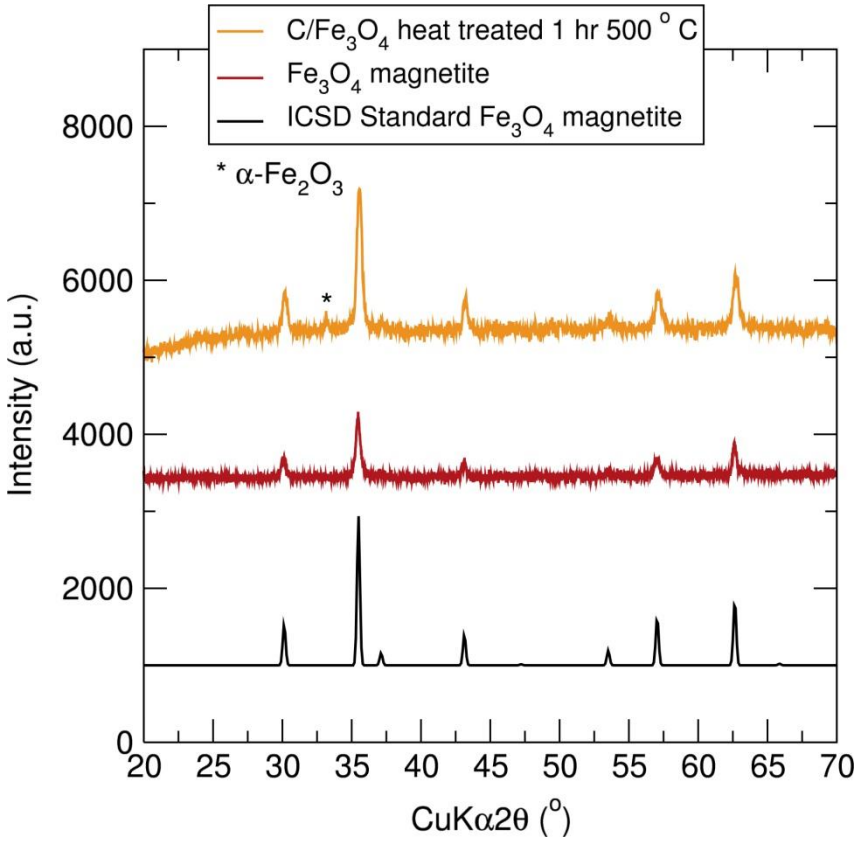

Figure A6.2. PXRD pattern of Fe_3O_4 magnetite nanoparticles prepared from ultrasound-assisted hydrolysis of heterometallic alkoxide precursor $[FeLi_2Br(O^tBu)_4(THF)_2]_n$ and post heat treatment for 3 hr at 500 °C under Ar flow.

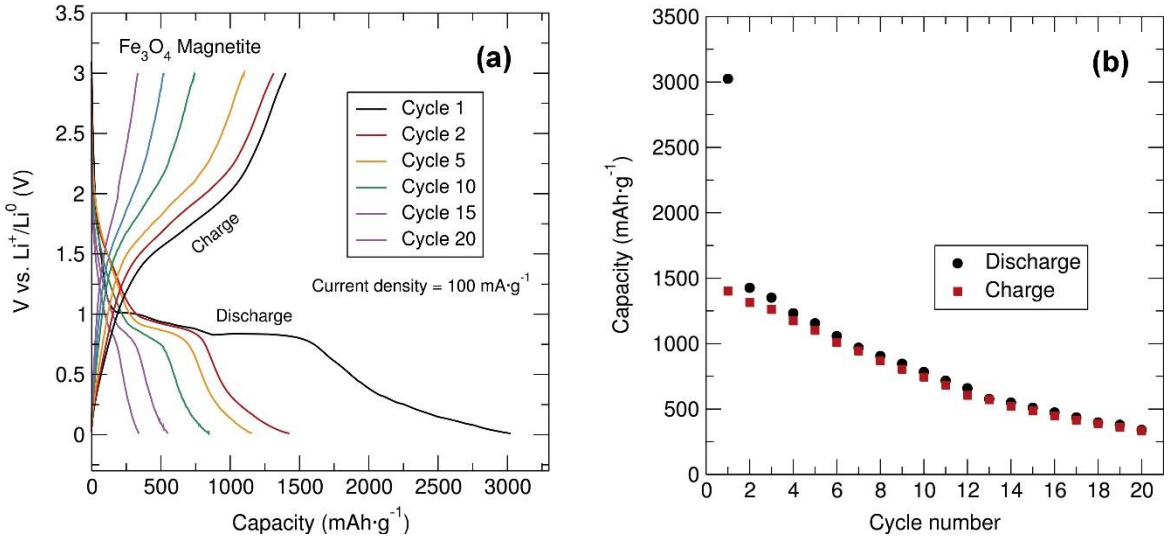

Figure A6.3. (a) Voltage-capacity profileand **(b)** cycling stability of bare Fe_3O_4 magnetite with C black and PTFE in 60:30:10 % wt. ratio over the potential range of 0.01 V-3.00 V at 100 $mA \cdot g^{-1}$.

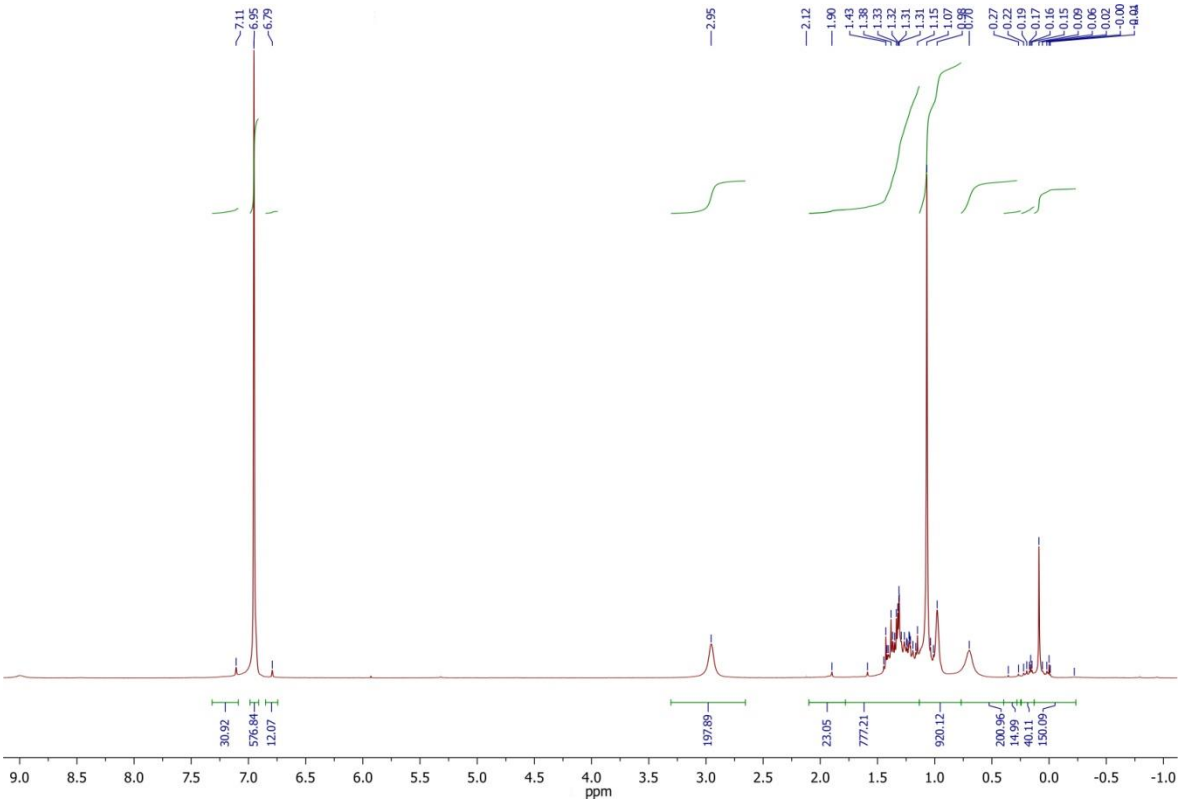

Figure A7.1. ^1H NMR spectrum of "$[NiLi_2Cl(O^tBu)_4(THF)_2]_n$" (VIII) (500 MHz, C_6D_6, 25 °C): δ=0.1 (s., μ_2-O^tBu), 0.7 (br., teminal-O^tBu), 1.2 (s., teminal-O^tBu), 1.3 (br., THF), 2.9 (br., THF) ppm.

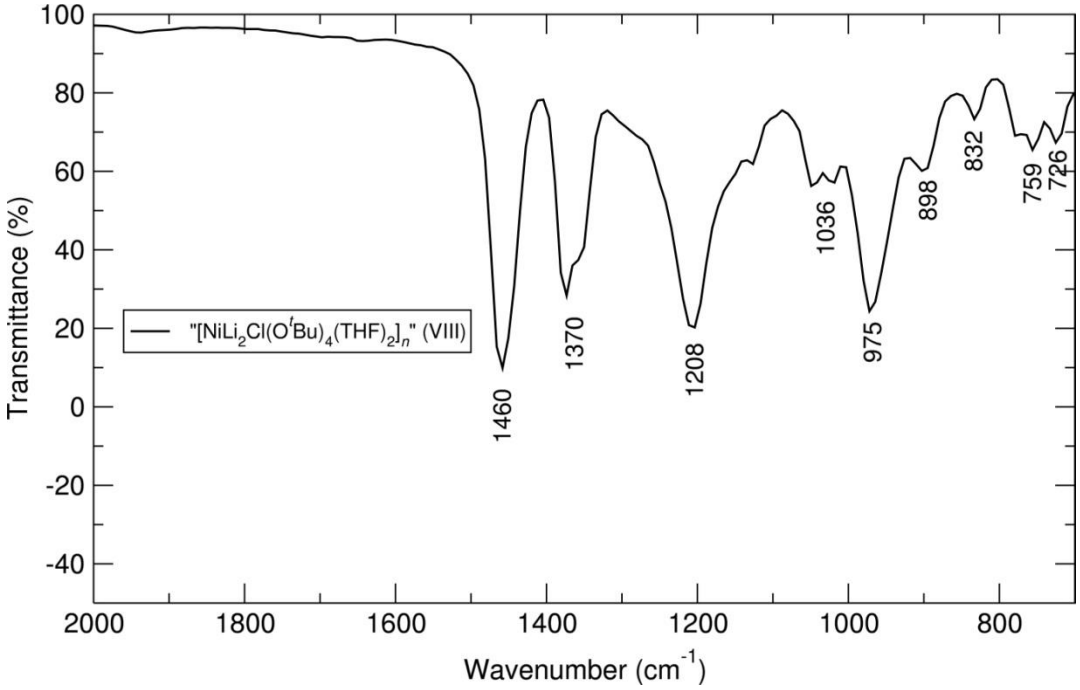

Figure A7.2. FT-IR spectrum of "$[NiLi_2Cl(O^tBu)_4(THF)_2]$" (VIII).

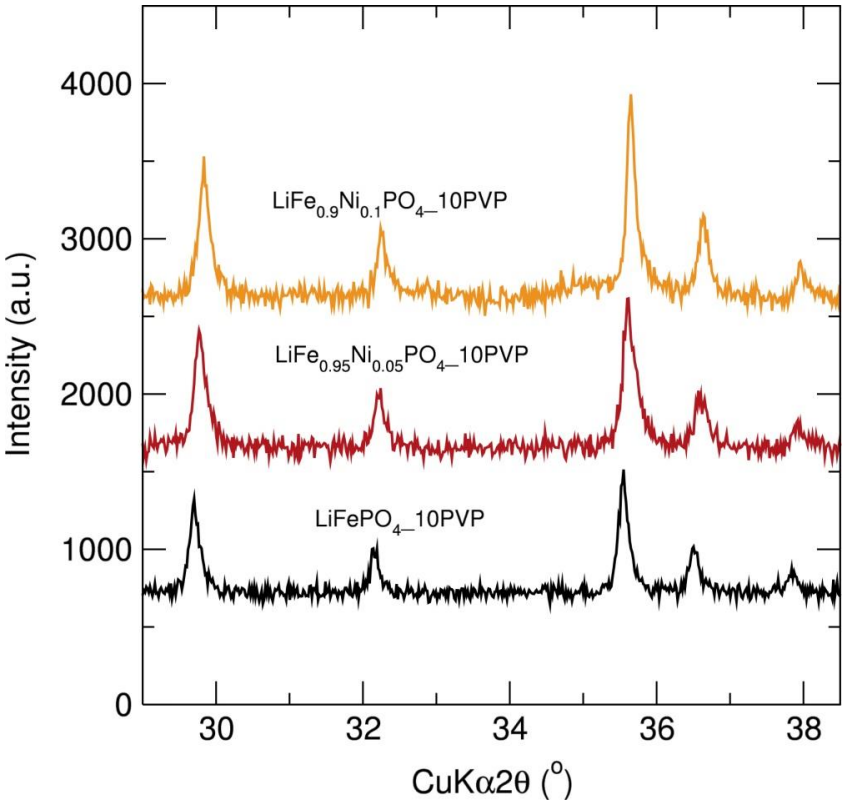

Figure A7.3. Close up of comparative PXRD patterns of $LiFe_{1-x}Ni_xPO_4$ (x=0, 0.05 and 0.1) nanostructures after microwave-assisted synthesis (1 hr at 240 ºC) using "$[FeLi_2Cl(O^tBu)_4(THF)_2]_n$," (V) heterometallic alkoxide precursor, $NiC_2O_4{\cdot}2H_2O$, H_3PO_4 and 10% PVP in ethylene glycol.

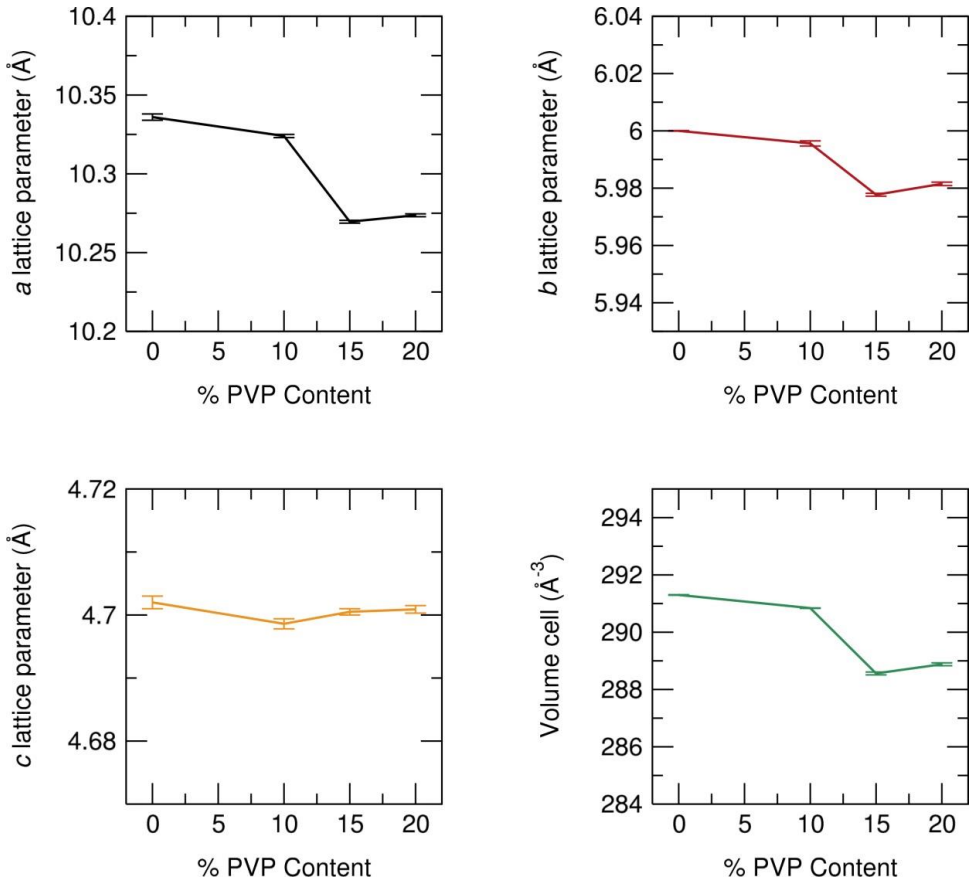

Figure A7.4. Variation of the refined lattice parameters and volume cell values for $LiFe_{0.95}Ni_{0.05}PO_4$ nanostructures after microwave-assisted synthesis using "$[FeLi_2Cl(O^tBu)_4(THF)_2]_n$" (V) heterometallic alkoxide precursor, $NiC_2O_4{\cdot}2H_2O$, H_3PO_4 and different PVP contents in ethylene glycol.

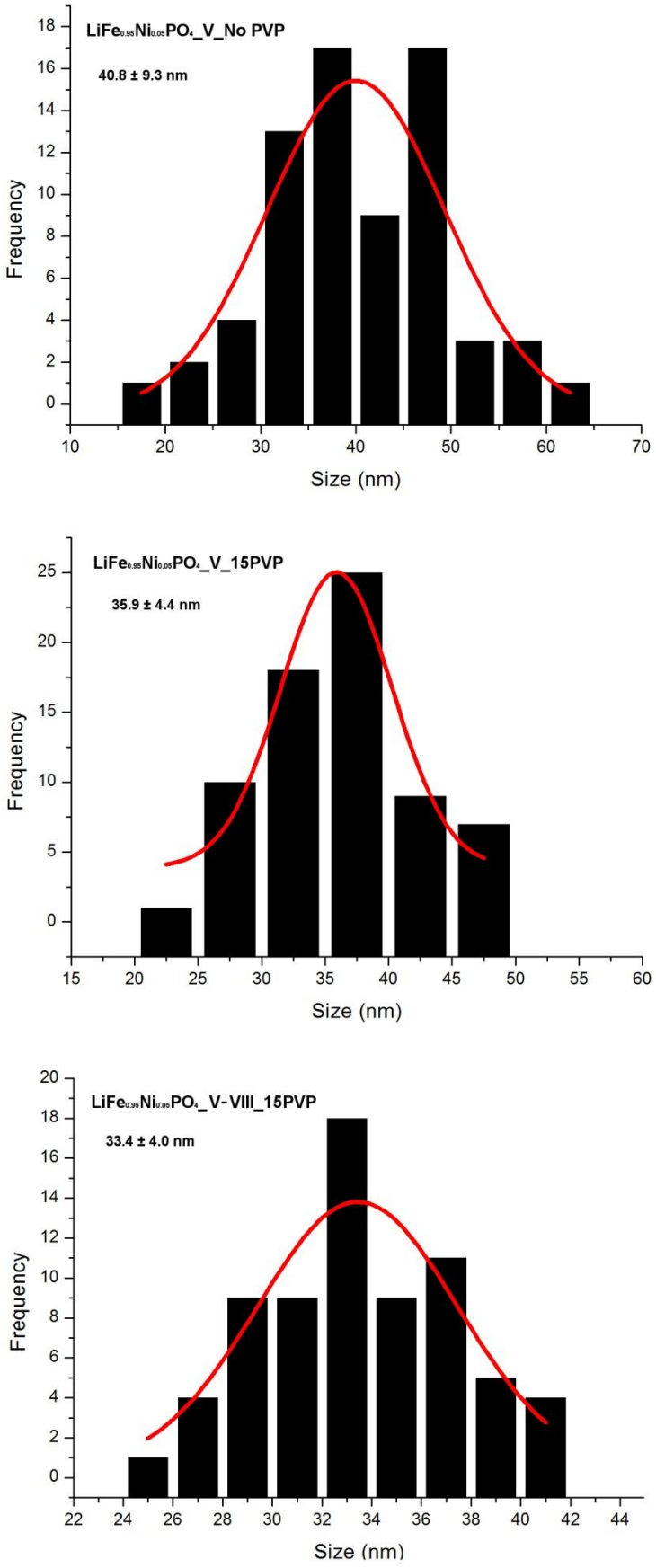

Figure A7.5. Particle size distribution of C/$LiFe_{0.95}Ni_{0.05}PO_4$_V_No PVP, C/$LiFe_{0.95}Ni_{0.05}PO_4$_V_15PVP and C/$LiFe_{0.95}Ni_{0.05}PO_4$_V-VIII_15PVP nanostructures.

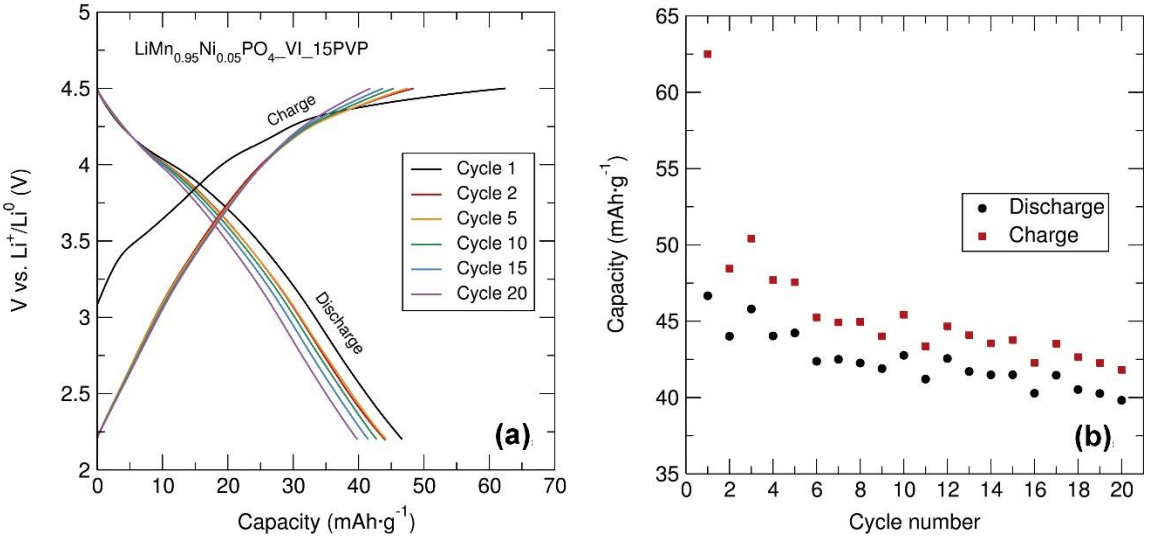

Figure A7.6. (a) Voltage-capacity profile and **(b)** cycling stability of C/$LiMn_{0.95}Ni_{0.05}PO_4$_VI prepared with "$[MnLi_2Br(O^tBu)_4(THF)_2]_n$" (VI) alkoxide precursor, $NiC_2O_4{\cdot}2H_2O$ and 15% PVP, and mixed with C black and PTFE in 60:30:10 (% wt. ratio) between 2.2 V and 4.2 V at C/20 rate.

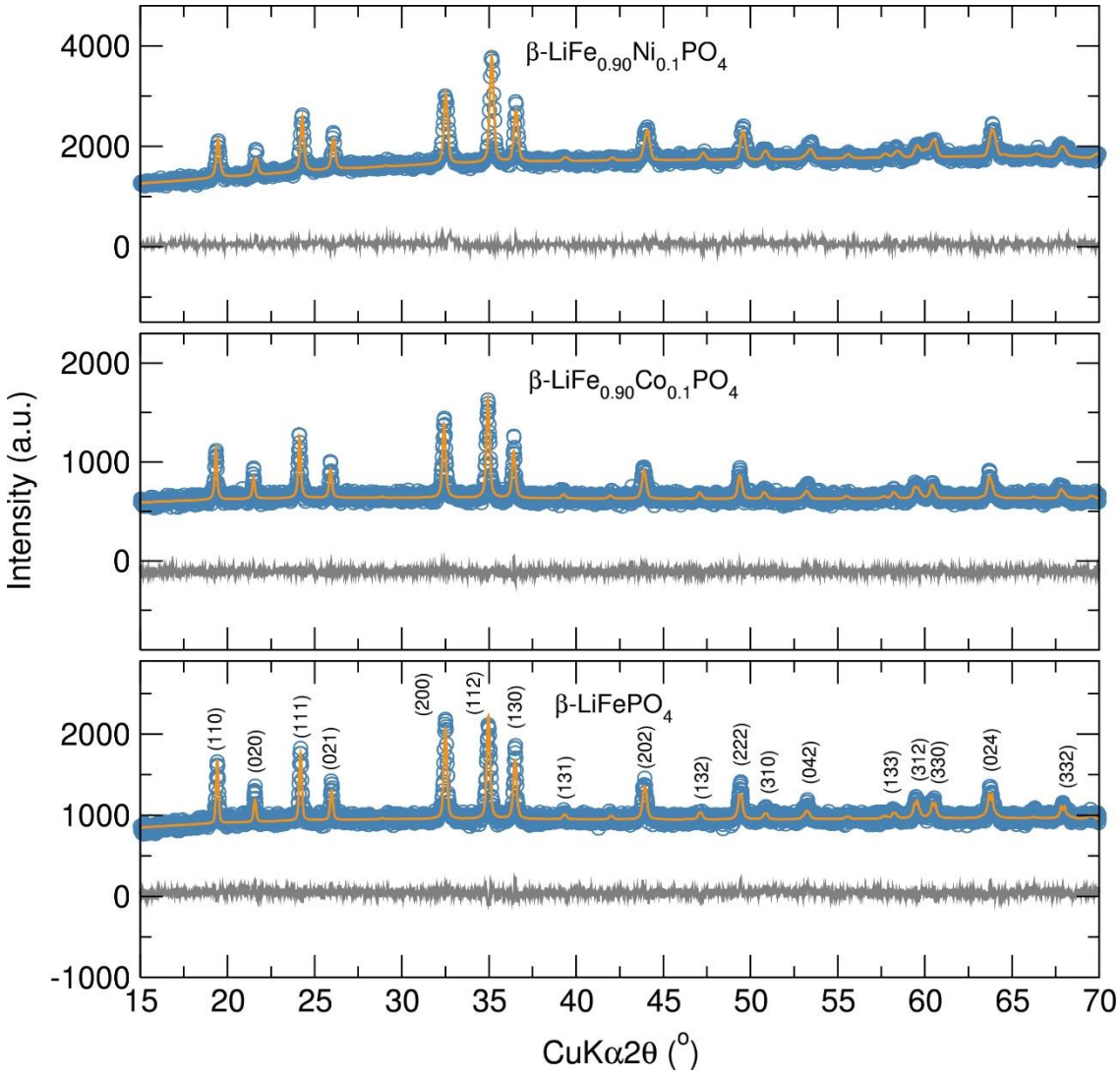

Figure A8.1. Rietveld analysis of PXRD data of non-olivine β-$LiFe_{0.9}M_{0.1}PO_4$ (*M*=Fe, Co or Ni) nanostructures.

β-LiFe$_{0.9}$Co$_{0.1}$PO$_4$

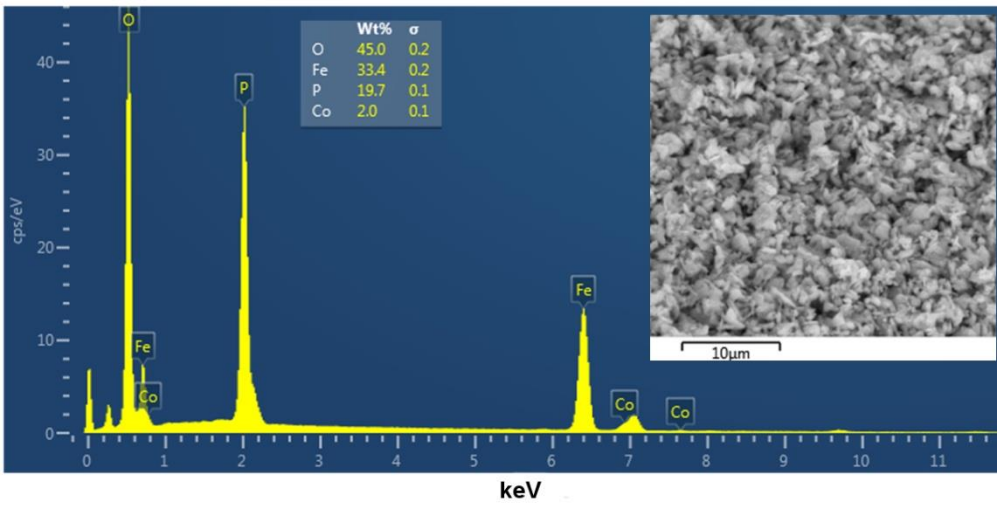

β-LiFe$_{0.9}$Ni$_{0.1}$PO$_4$

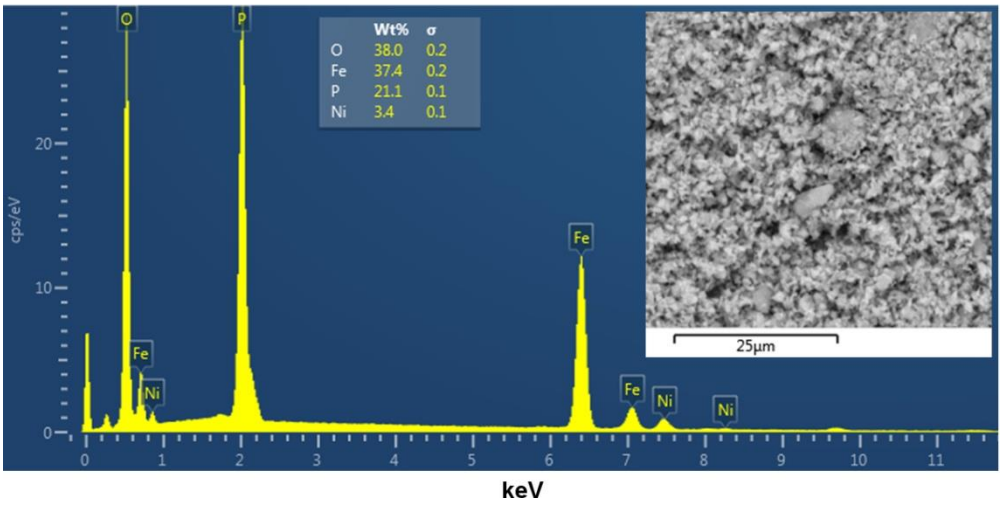

Figure A8.2. EDS spectra of ß-LiFe$_{0.9}$Co$_{0.1}$PO$_4$ and ß-LiFe$_{0.9}$Ni$_{0.1}$PO$_4$ nanostructures.

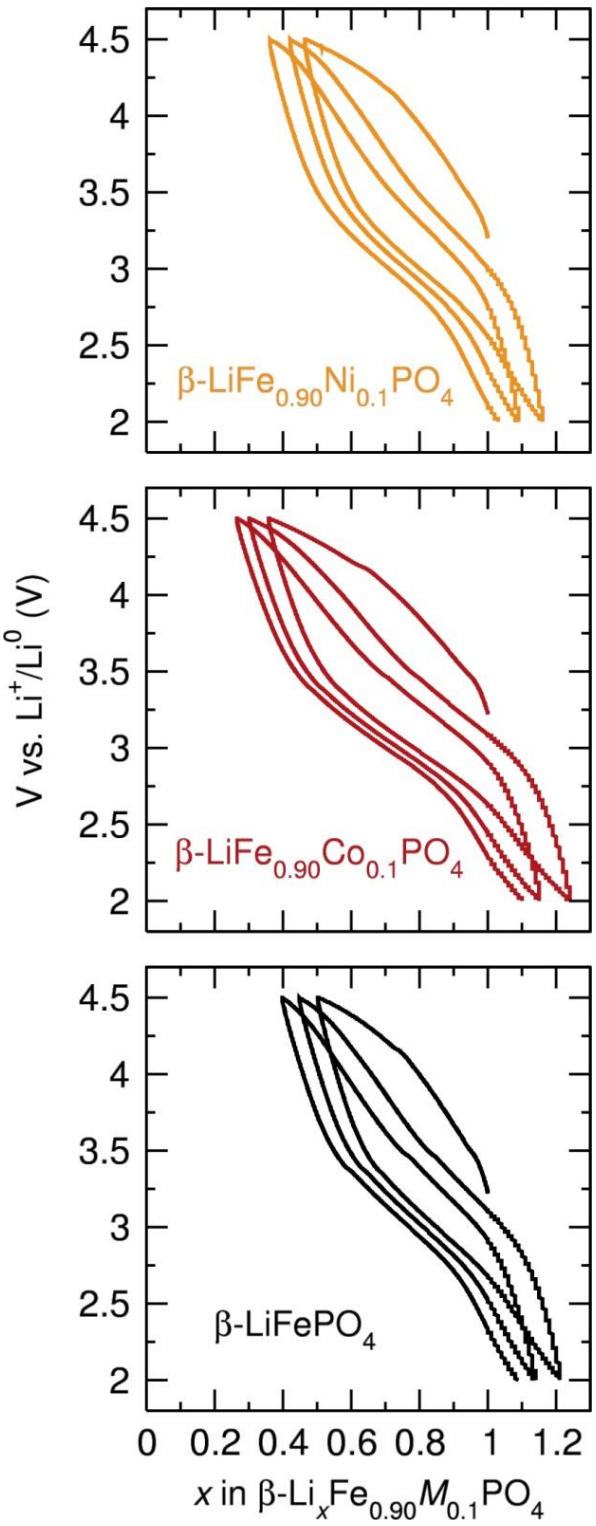

Figure A8.3. Comparison of voltage-compostition profiles at C/20 rate between 2.0 V and 4.5 V of non-olivine ß-$LiFe_{0.9}M_{0.1}PO_4$ (*M*=Fe, Co or Ni) nanostructures.

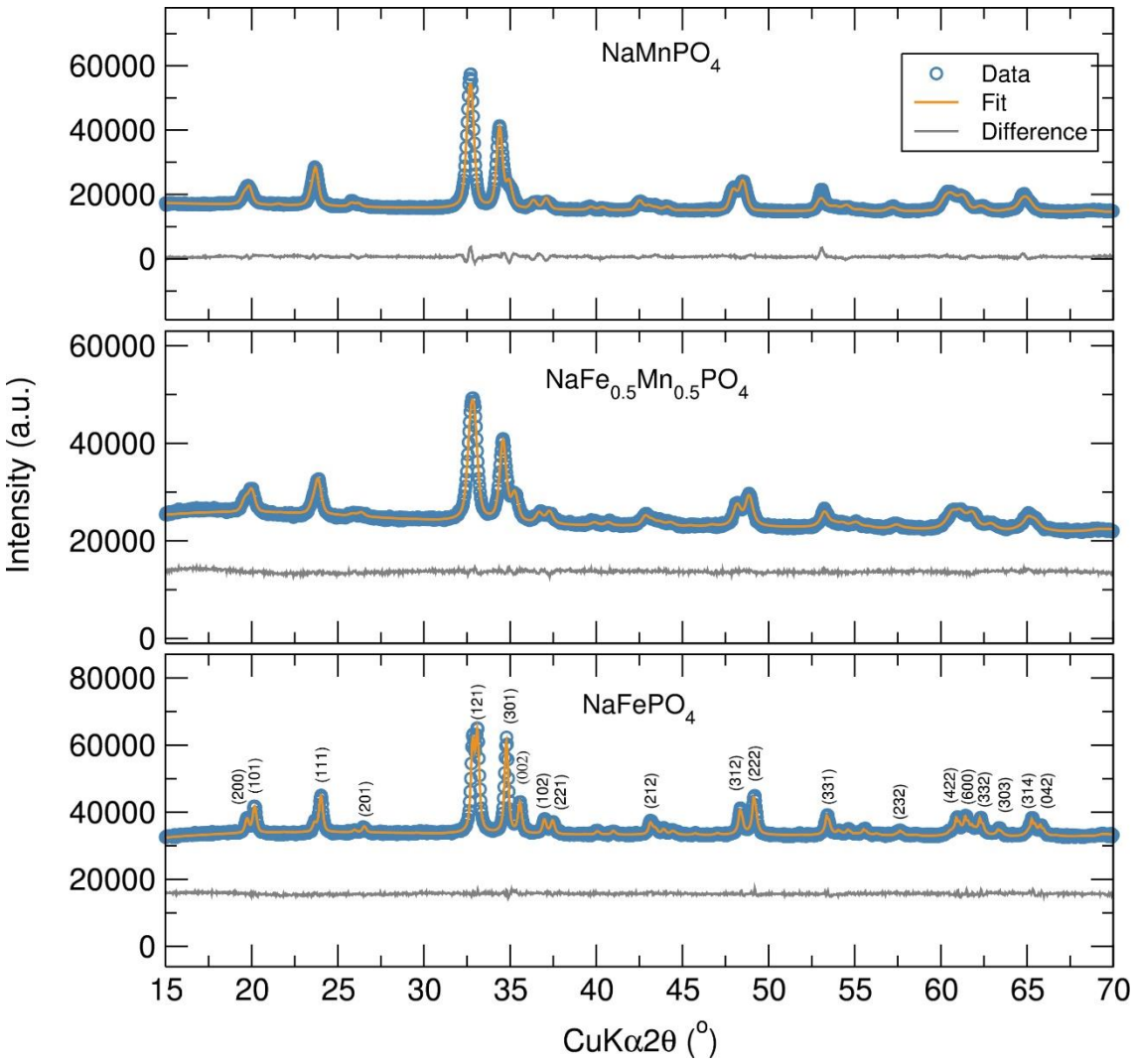

Figure 0A8.4. Rietveld analysis of PXRD data of maricite $NaFe_{1-x}Mn_xPO_4$ (x=0, 0.5 and 1) nanostructures prepared using "$[NaM(O^tBu)_3(THF)]_2$" (M=Fe, Mn) heterometallic alkoxide precursors and H_3PO_4 a 1:2molar ratio in tetraethylene glycol.

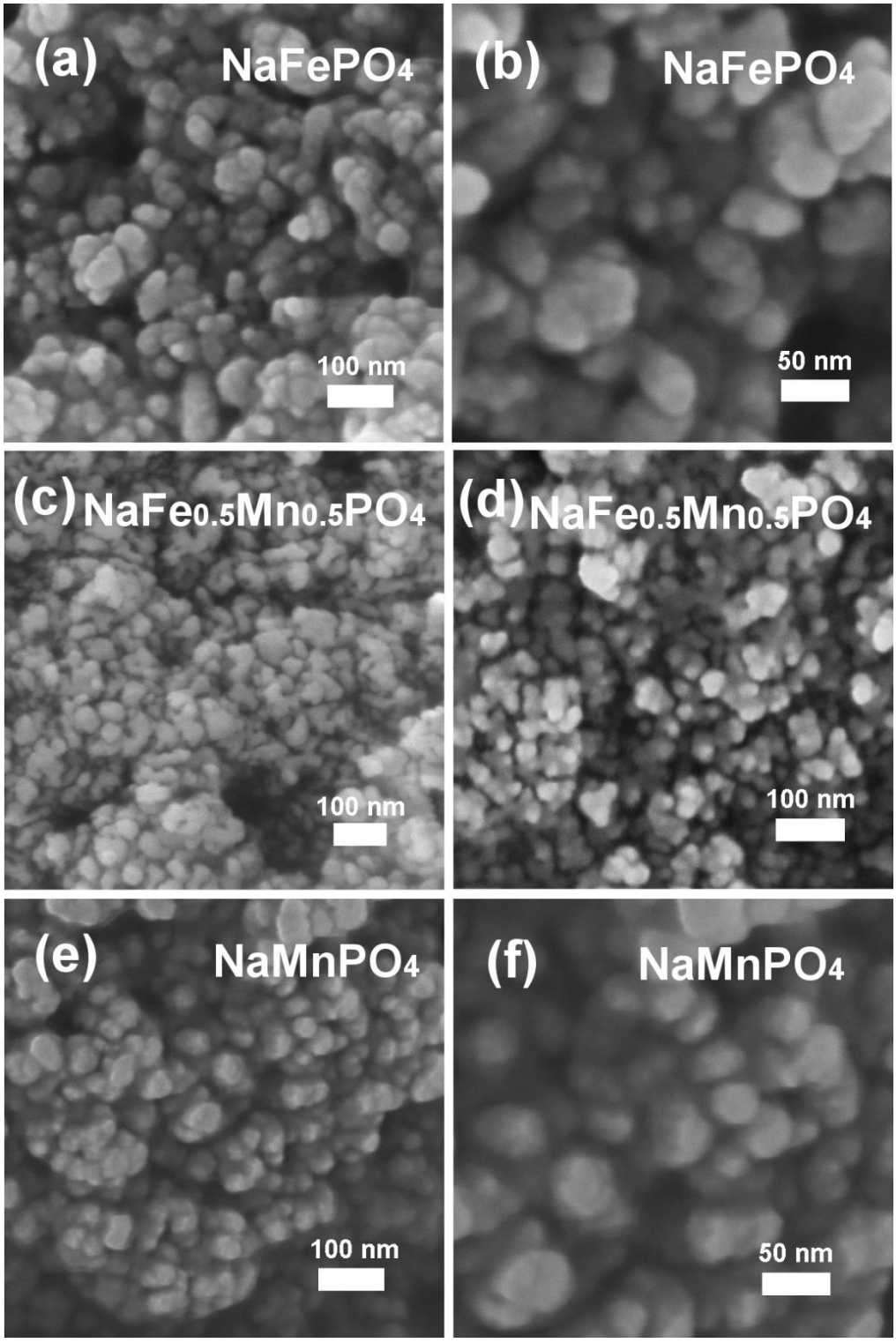

Figure A8.5. SEM images of **(a, b)** $NaFePO_4$, **(c, d)** $NaFe_{0.5}Mn_{0.5}PO_4$ and **(e, f)** $NaMnPO_4$ Nanostructures prepared through a microwave synthesis (30 min at 280 °C) using "$[NaM(O^tBu)_3(THF)]_2$" (*M*=Fe, Mn) heterometallic alkoxide precursors.

References

1. C. F. Liu, Z. G. Neale and G. Z. Cao, *Mater Today*, 2016, **19**, 109-123.
2. T. Nagaura and K. Tozawa, *Prog. Batter. Sol. Cells*, 1990, **9**, 209-217.
3. J. M. Tarascon and M. Armand, *Nature*, 2001, **414**, 359-367.
4. B. Dunn, H. Kamath and J. M. Tarascon, *Science*, 2011, **334**, 928-935.
5. M. V. Reddy, G. V. S. Rao and B. V. R. Chowdari, *Chem Rev*, 2013, **113**, 5364-5457.
6. V. Etacheri, R. Marom, R. Elazari, G. Salitra and D. Aurbach, *Energ Environ Sci*, 2011, **4**, 3243-3262.
7. J. M. Tarascon, *Chemsuschem*, 2008, **1**, 777-779.
8. J. M. Tarascon, *Philos T R Soc A*, 2010, **368**, 3227-3241.
9. D. Larcher and J. M. Tarascon, *Nat Chem*, 2015, **7**, 19-29.
10. M. S. Whittingham, *Chem Rev*, 2004, **104**, 4271-4301.
11. K. Mizushima, P. C. Jones, P. J. Wiseman and J. B. Goodenough, *Mater Res Bull*, 1980, **15**, 783-789.
12. Y. Shao-Horn, L. Croguennec, C. Delmas, E. C. Nelson and M. A. O'Keefe, *Nat Mater*, 2003, **2**, 464-467.
13. Y. H. Rho and K. Kanamura, *J Electrochem Soc*, 2004, **151**, A1406-A1411.
14. J. N. Reimers and J. R. Dahn, *J Electrochem Soc*, 1992, **139**, 2091-2097.
15. S. Venkatraman, Y. Shin and A. Manthiram, *Electrochem Solid St*, 2003, **6**, A9-A12.
16. A. Manthiram, A. V. Murugan, A. Sarkar and T. Muraliganth, *Energ Environ Sci*, 2008, **1**, 621-638.
17. A. Rougier, P. Gravereau and C. Delmas, *J Electrochem Soc*, 1996, **143**, 1168-1175.
18. H. Arai, S. Okada, Y. Sakurai and J. Yamaki, *Solid State Ionics*, 1998, **109**, 295-302.
19. P. G. Bruce, A. R. Armstrong and R. L. Gitzendanner, *J Mater Chem*, 1999, **9**, 193-198.
20. S. Choi and A. Manthiram, *J Electrochem Soc*, 2002, **149**, A1157-A1163.
21. P. He, H. J. Yu, D. Li and H. S. Zhou, *J Mater Chem*, 2012, **22**, 3680-3695.
22. N. Yabuuchi, Y. Makimura and T. Ohzuku, *J Electrochem Soc*, 2007, **154**, A314-A321.
23. X. Y. Cao, Y. Zhao, L. M. Zhu, L. L. Xie, X. L. Cao, S. Y. Xiong and C. W. Wang, *Int J Electrochem Sc*, 2016, **11**, 5267-5278.
24. K. M. Shaju and P. G. Bruce, *Adv Mater*, 2006, **18**, 2330-+.
25. H. Xia, Z. T. Luo and J. P. Xie, *Prog Nat Sci-Mater*, 2012, **22**, 572-584.
26. M. M. Thackeray, P. J. Johnson, L. A. Depicciotto, P. G. Bruce and J. B. Goodenough, *Mater Res Bull*, 1984, **19**, 179-187.
27. M. Molenda, R. Dziembaj, E. Podstawka and L. M. Proniewicz, *J Phys Chem Solids*, 2005, **66**, 1761-1768.
28. R. Dziembaj and M. Molenda, *J Power Sources*, 2003, **119**, 121-124.
29. J. Molenda, J. Marzec, K. Swierczek, W. Ojczyk, M. Ziemnicki, M. Molenda, M. Drozdek and R. Dziembaj, *Solid State Ionics*, 2004, **171**, 215-227.
30. M. Molenda, R. Dziembaj, E. Podstawka, L. M. Proniewicz and Z. Piwowarska, *J Power Sources*, 2007, **174**, 613-618.
31. M. Molenda, R. Dziembaj, E. Podstawka, W. Lasocha and L. M. Proniewicz, *J Phys Chem Solids*, 2006, **67**, 1347-1350.
32. Z. Z. a. S. S. Zhang, *Rechargeable Batteries: Materials, Technologies and New Trends*, Springer, Green Energy and Technology, 2015.
33. N. Nitta, F. X. Wu, J. T. Lee and G. Yushin, *Mater Today*, 2015, **18**, 252-264.
34. A. K. Padhi, K. S. Nanjundaswamy and J. B. Goodenough, *J Electrochem Soc*, 1997, **144**, 1188-1194.
35. Q. Ni, Y. Bai, F. Wu and C. Wu, *Adv. Sci.*, 2017, 1600275.

36. Y. Zhang, Q. Y. Huo, P. P. Du, L. Z. Wang, A. Q. Zhang, Y. H. Song, Y. Lv and G. Y. Li, *Synthetic Met*, 2012, **162**, 1315-1326.
37. W. J. Zhang, *J Power Sources*, 2011, **196**, 2962-2970.
38. L. X. Yuan, Z. H. Wang, W. X. Zhang, X. L. Hu, J. T. Chen, Y. H. Huang and J. B. Goodenough, *Energ Environ Sci*, 2011, **4**, 269-284.
39. J. Gim, J. Song, D. Nguyen, M. H. Alfaruqi, S. Kim, J. Kang, A. K. Rai, V. Mathew and J. Kim, *Ceram Int*, 2014, **40**, 1561-1567.
40. J. Yao, S. Bewlay, K. Konstantionv, V. A. Drozd, R. S. Liu, X. L. Wang, H. K. Liu and G. X. Wang, *J Alloy Compd*, 2006, **425**, 362-366.
41. Z. M. Zheng, W. K. Pang, X. C. Tang, D. Z. Jia, Y. D. Huang and Z. P. Guo, *J Alloy Compd*, 2015, **640**, 95-100.
42. J. M. Bai, J. Hong, H. Y. Chen, J. Graetz and F. Wang, *J Phys Chem C*, 2015, **119**, 2266-2276.
43. L. H. Liao, H. T. Wang, H. Guo, P. Y. Zhu, J. Xie, C. H. Jin, S. C. Zhang, G. S. Cao, T. J. Zhu and X. B. Zhao, *J Mater Chem A*, 2015, **3**, 19368-19375.
44. H. Ghafarian-Zahmatkesh, M. Javanbakht and M. Ghaemi, *J Power Sources*, 2015, **284**, 339-348.
45. I. Bilecka, A. Hintennach, I. Djerdj, P. Novak and M. Niederberger, *J Mater Chem*, 2009, **19**, 5125-5128.
46. I. Bilecka, A. Hintennach, M. D. Rossell, D. Xie, P. Novak and M. Niederberger, *J Mater Chem*, 2011, **21**, 5881-5890.
47. D. Carriazo, M. D. Rossell, G. B. Zeng, I. Bilecka, R. Erni and M. Niederberger, *Small*, 2012, **8**, 2231-2238.
48. J. V. Laveda, V. Chandhok, C. A. Murray, G. W. Paterson and S. A. Corr, *Chem Commun (Camb)*, 2015.
49. O. Garcia-Moreno, M. Alvarez-Vega, F. Garcia-Alvarado, J. Garcia-Jaca, J. M. Gallardo-Amores, M. L. Sanjuan and U. Amador, *Chem Mater*, 2001, **13**, 1570-1576.
50. G. B. Zeng, R. Caputo, D. Carriazo, L. Luo and M. Niederberger, *Chem Mater*, 2013, **25**, 3399-3407.
51. T. E. Ashton, J. V. Laveda, D. A. MacLaren, P. J. Baker, A. Porch, M. O. Jones and S. A. Corr, *J Mater Chem A*, 2014, **2**, 6238-6245.
52. H. Guo, X. H. Song, Z. Q. Zhuo, J. T. Hu, T. C. Liu, Y. D. Duan, J. X. Zheng, Z. H. Chen, W. L. Yang, K. Amine and F. Pan, *Nano Lett*, 2016, **16**, 601-608.
53. S. Y. Chung, S. Y. Choi, S. Lee and Y. Ikuhara, *Phys Rev Lett*, 2012, **108**.
54. M. S. Islam, D. J. Driscoll, C. A. J. Fisher and P. R. Slater, *Chem Mater*, 2005, **17**, 5085-5092.
55. G. R. Gardiner and M. S. Islam, *Chem Mater*, 2010, **22**, 1242-1248.
56. S. Nishimura, G. Kobayashi, K. Ohoyama, R. Kanno, M. Yashima and A. Yamada, *Nat Mater*, 2008, **7**, 707-711.
57. A. S. Andersson, B. Kalska, L. Haggstrom and J. O. Thomas, *Solid State Ionics*, 2000, **130**, 41-52.
58. C. Delmas, M. Maccario, L. Croguennec, F. Le Cras and F. Weill, *Nat Mater*, 2008, **7**, 665-671.
59. V. Srinivasan and J. Newman, *J Electrochem Soc*, 2004, **151**, A1517-A1529.
60. A. S. Andersson and J. O. Thomas, *J Power Sources*, 2001, **97-8**, 498-502.
61. J. J. Wang and X. L. Sun, *Energ Environ Sci*, 2015, **8**, 1110-1138.
62. Y. Orikasa, T. Maeda, Y. Koyama, H. Murayama, K. Fukuda, H. Tanida, H. Arai, E. Matsubara, Y. Uchimoto and Z. Ogumi, *J Am Chem Soc*, 2013, **135**, 5497-5500.
63. H. Liu, F. C. Strobridge, O. J. Borkiewicz, K. M. Wiaderek, K. W. Chapman, P. J. Chupas and C. P. Grey, *Science*, 2014, **344**.
64. A. Gutierrez, N. A. Benedek and A. Manthiram, *Chem Mater*, 2013, **25**, 4010-4016.

65. I. Bezza, M. Kaus, R. Heinzmann, M. Yavuz, M. Knapp, S. Mangold, S. Doyle, C. P. Grey, H. Ehrenberg, S. Indris and I. Saadoune, *J Phys Chem C*, 2015, **119**, 9016-9024.
66. V. Aravindan, J. Gnanaraj, Y. S. Lee and S. Madhavi, *J Mater Chem A*, 2013, **1**, 3518-3539.
67. A. Yamada and S. C. Chung, *J Electrochem Soc*, 2001, **148**, A960-A967.
68. N. Meethong, Y. H. Kao, M. Tang, H. Y. Huang, W. C. Carter and Y. M. Chiang, *Chem Mater*, 2008, **20**, 6189-6198.
69. G. H. Li, H. Azuma and M. Tohda, *Electrochem Solid St*, 2002, **5**, A135-A137.
70. L. F. J. Piper, N. F. Quackenbush, S. Sallis, D. O. Scanlon, G. W. Watson, K. W. Nam, X. Q. Yang, K. E. Smith, F. Omenya, N. A. Chernova and M. S. Whittingham, *J Phys Chem C*, 2013, **117**, 10383-10396.
71. T. Muraliganth and A. Manthiram, *J Phys Chem C*, 2010, **114**, 15530-15540.
72. S. M. Oh, S. T. Myung and Y. K. Sun, *J Mater Chem*, 2012, **22**, 14932-14937.
73. E. Markevich, R. Sharabi, H. Gottlieb, V. Borgel, K. Fridman, G. Salitra, D. Aurbach, G. Semrau, M. A. Schmidt, N. Schall and C. Bruenig, *Electrochem Commun*, 2012, **15**, 22-25.
74. D. Choi, X. Li, W. A. Henderson, Q. Huang, S. K. Nune, J. P. Lemmon and V. L. Sprenkle, *Heliyon*, 2016, **2**.
75. P. R. Kumar, V. Madhusudhanrao, B. Nageswararao, M. Venkateswarlu and N. Satyanarayana, *J Solid State Electr*, 2016, **20**, 1855-1863.
76. A. Ornek and M. Z. Kazancioglu, *Scripta Mater*, 2016, **122**, 45-49.
77. P. J. Zuo, L. G. Wang, W. Zhang, G. P. Yin, Y. L. Ma, C. Y. Du, X. Q. Cheng and Y. Z. Gao, *Nanoscale*, 2015, **7**, 11509-11514.
78. A. Yamada, Y. Kudo and K. Y. Liu, *J Electrochem Soc*, 2001, **148**, A1153-A1158.
79. A. Yamada, Y. Takei, H. Koizumi, N. Sonoyama, R. Kanno, K. Itoh, M. Yonemura and T. Kamiyama, *Chem Mater*, 2006, **18**, 804-813.
80. A. Yamada, Y. Kudo and K. Y. Liu, *J Electrochem Soc*, 2001, **148**, A747-A754.
81. J. Molenda, W. Ojczyk, K. Swierczek, W. Zajac, F. Krok, J. Dygas and R. S. Liu, *Solid State Ionics*, 2006, **177**, 2617-2624.
82. W. F. Huang, S. Tao, J. Zhou, C. Si, X. Chen, W. Huang, C. H. Jin, W. S. Chu, L. Song and Z. Y. Wu, *J Phys Chem C*, 2014, **118**, 796-803.
83. A. Paolella, G. Bertoni, E. Dilena, S. Marras, A. Ansaldo, L. Manna and C. George, *Nano Lett*, 2014, **14**, 1477-1483.
84. J. Kim, K. Y. Park, I. Park, J. K. Yoo, J. Hong and K. Kang, *J Mater Chem*, 2012, **22**, 11964-11970.
85. F. C. Strobridge, H. Liu, M. Leskes, O. J. Borkiewicz, K. M. Wiaderek, P. J. Chupas, K. W. Chapman and C. P. Grey, *Chem Mater*, 2016, **28**, 3676-3690.
86. J. F. Qian, W. A. Henderson, W. Xu, P. Bhattacharya, M. Engelhard, O. Borodin and J. G. Zhang, *Nat Commun*, 2015, **6**.
87. W. Xu, J. L. Wang, F. Ding, X. L. Chen, E. Nasybutin, Y. H. Zhang and J. G. Zhang, *Energ Environ Sci*, 2014, **7**, 513-537.
88. D. Aurbach, M. L. Daroux, P. W. Faguy and E. Yeager, *J Electrochem Soc*, 1987, **134**, 1611-1620.
89. M. Winter, J. O. Besenhard, M. E. Spahr and P. Novak, *Adv Mater*, 1998, **10**, 725-763.
90. K. Persson, V. A. Sethuraman, L. J. Hardwick, Y. Hinuma, Y. S. Meng, A. van der Ven, V. Srinivasan, R. Kostecki and G. Ceder, *J Phys Chem Lett*, 2010, **1**, 1176-1180.
91. S. H. Yu, S. H. Lee, D. J. Lee, Y. E. Sung and T. Hyeon, *Small*, 2016, **12**, 2146-2172.
92. H. Kim, D. H. Seo, H. Kim, I. Park, J. Hong, K. Y. Park and K. Kang, *Chem Mater*, 2012, **24**, 720-725.
93. S. L. P. Poizot, S. Grugeon, L. Dupont and J-M. Tarascon, *Nature*, 2000, **407**.

94. S. Luo, H. C. Wu, Y. Wu, K. L. Jiang, J. P. Wang and S. S. Fan, *J Power Sources*, 2014, **249**, 463-469.
95. Y. Jiang, Z. J. Jiang, L. F. Yang, S. Cheng and M. L. Liu, *J Mater Chem A*, 2015, **3**, 11847-11856.
96. X. Q. Yu, Y. He, J. P. Sun, K. Tang, H. Li, L. Q. Chen and X. J. Huang, *Electrochem Commun*, 2009, **11**, 791-794.
97. J. Morales, L. Sanchez, F. Martin, J. R. Ramos-Barrado and M. Sanchez, *Electrochim Acta*, 2004, **49**, 4589-4597.
98. M. E. Donders, H. C. M. Knoops, W. M. M. Kessels and P. H. L. Notten, *J Power Sources*, 2012, **203**, 72-77.
99. T. Brousse, R. Retoux, U. Herterich and D. M. Schleich, *J Electrochem Soc*, 1998, **145**, 1-4.
100. H. Cheng, Z. G. Lu, R. G. Ma, Y. C. Dong, H. E. Wang, L. J. Xi, L. X. Zheng, C. K. Tsang, H. Li, C. Y. Chung, J. A. Zapien and Y. Y. Li, *J Mater Chem*, 2012, **22**, 22692-22698.
101. L. Taberna, S. Mitra, P. Poizot, P. Simon and J. M. Tarascon, *Nat Mater*, 2006, **5**, 567-573.
102. J. J. Chen, *Recent Pat Nanotech*, 2013, **7**, 2-12.
103. Y. G. Guo, J. S. Hu and L. J. Wan, *Adv Mater*, 2008, **20**, 4384-4384.
104. C. N. He, S. Wu, N. Q. Zhao, C. S. Shi, E. Z. Liu and J. J. Li, *Acs Nano*, 2013, **7**, 4459-4469.
105. G. M. Zhou, D. W. Wang, F. Li, L. L. Zhang, N. Li, Z. S. Wu, L. Wen, G. Q. Lu and H. M. Cheng, *Chem Mater*, 2010, **22**, 5306-5313.
106. Z. P. Zeng, H. L. Zhao, J. Wang, P. P. Lv, T. H. Zhang and Q. Xia, *J Power Sources*, 2014, **248**, 15-21.
107. K. L. Sun, H. B. Zhao, J. Yao, S. Q. Zhang and J. X. Xu, *Ionics*, 2015, **21**, 1901-1908.
108. Q. Lin, J. Wang, Y. J. Zhong, J. Sunarso, M. O. Tade, L. Li and Z. P. Shao, *Electrochim Acta*, 2016, **212**, 179-186.
109. Y. M. Zhong, X. F. Zhou, X. Li, S. S. Zhang, Y. J. Liu, X. Y. Yu, H. Q. Wang, Q. Y. Li, Y. P. Fang and J. Li, *Solid State Sci*, 2016, **57**, 16-23.
110. Y. Chen, B. H. Song, L. Lu and J. M. Xue, *Nanoscale*, 2013, **5**, 6797-6803.
111. J. Cabana, L. Monconduit, D. Larcher and M. R. Palacin, *Adv Mater*, 2010, **22**, E170-E192.
112. Y. F. Deng, L. N. Wan, Y. Xie, X. S. Qin and G. H. Chen, *Rsc Adv*, 2014, **4**, 23914-23935.
113. H. L. Wang, L. F. Cui, Y. A. Yang, H. S. Casalongue, J. T. Robinson, Y. Y. Liang, Y. Cui and H. J. Dai, *J Am Chem Soc*, 2010, **132**, 13978-13980.
114. C. Chen, H. Jian, X. X. Fu, Z. M. Ren, M. Yan, G. D. Qian and Z. Y. Wang, *Rsc Adv*, 2014, **4**, 5367-5370.
115. J. Yue, X. Gu, L. Chen, N. N. Wang, X. L. Jiang, H. Y. Xu, J. Yang and Y. T. Qian, *J Mater Chem A*, 2014, **2**, 17421-17426.
116. Z. C. Bai, X. Y. Zhang, Y. W. Zhang, C. L. Guo and B. Tang, *J Mater Chem A*, 2014, **2**, 16755-16760.
117. J. G. Wang, D. D. Jin, R. Zhou, X. Li, X. R. Liu, C. Shen, K. Y. Xie, B. H. Li, F. Y. Kang and B. Q. Wei, *Acs Nano*, 2016, **10**, 6227-6234.
118. X. Y. Fan, Y. Cui, P. Liu, L. Gou, L. Xu and D. L. Li, *Phys Chem Chem Phys*, 2016, **18**, 22224-22234.
119. A. Kvasha, E. Azaceta, O. Leonet, M. Bengoechea, I. Boyano, R. Tena-Zaera, I. de Meatza, O. Miguel, H. J. Grande and J. A. Blazquez, *Electrochim Acta*, 2015, **180**, 16-21.
120. L. H. Chu, M. C. Li, X. D. Li, Y. Wang, Z. P. Wan, S. Y. Dou, D. D. Song, Y. F. Li and B. Jiang, *Rsc Adv*, 2015, **5**, 49765-49770.

121. B. Varghese, M. V. Reddy, Z. Yanwu, C. S. Lit, T. C. Hoong, G. V. S. Rao, B. V. R. Chowdari, A. T. S. Wee, C. T. Lim and C. H. Sow, *Chem Mater*, 2008, **20**, 3360-3367.
122. A. S. Arico, P. Bruce, B. Scrosati, J. M. Tarascon and W. Van Schalkwijk, *Nat Mater*, 2005, **4**, 366-377.
123. V. P. a. T. Rojo, in *Lithium ion batteries*, ed. D. I. Belharouak, InTech, 2012.
124. A. K. Padhi, K. S. Nanjundaswamy, C. Masquelier, S. Okada and J. B. Goodenough, *J Electrochem Soc*, 1997, **144**, 1609-1613.
125. M. Koltypin, D. Aurbach, L. Nazar and B. Ellis, *J Power Sources*, 2007, **174**, 1241-1250.
126. N. J. Yun, H. W. Ha, K. H. Jeong, H. Y. Park and K. Kim, *J Power Sources*, 2006, **160**, 1361-1368.
127. G. T. K. Fey and T. L. Lu, *J Power Sources*, 2008, **178**, 807-814.
128. C. M. Julien, A. Manger, A. Ait-Salah, M. Massot, F. Gendron and K. Zaghib, *Ionics*, 2007, **13**, 395-411.
129. K. Zaghib, N. Ravet, M. Gauthier, F. Gendron, A. Mauger, J. B. Goodenough and C. M. Julien, *J Power Sources*, 2006, **163**, 560-566.
130. A. Yamada, S. C. Chung and K. Hinokuma, *J Electrochem Soc*, 2001, **148**, A224-A229.
131. X. Y. Li, B. Zhang, Z. G. Zhang, L. H. He, H. Li, X. J. Huang and F. W. Wang, *Powder Diffr*, 2014, **29**, 248-253.
132. J. A. Hong, F. Wang, X. L. Wang and J. Graetz, *J Power Sources*, 2011, **196**, 3659-3663.
133. J. Chen, S. Wang and M. S. Whittingham, *J Power Sources*, 2007, **174**, 442-448.
134. M. K. Devaraju and I. Honma, *Adv Energy Mater*, 2012, **2**, 284-297.
135. S. L. Yang, X. F. Zhou, J. G. Zhang and Z. P. Liu, *J Mater Chem*, 2010, **20**, 8086-8091.
136. S. L. Yang, M. J. Hu, L. J. Xi, R. G. Ma, Y. C. Dong and C. Y. Chung, *Acs Appl Mater Inter*, 2013, **5**, 8961-8967.
137. K. M. O. Jensen, C. Tyrsted, M. Bremholm and B. B. Iversen, *Chemsuschem*, 2014, **7**, 1594-1611.
138. J. J. Chen, J. M. Bai, H. Y. Chen and J. Graetz, *J Phys Chem Lett*, 2011, **2**, 1874-1878.
139. K. S. Suslick, *Science*, 1990, **247**, 1439-1445.
140. J. H. Bang and K. S. Suslick, *Adv Mater*, 2010, **22**, 1039-1059.
141. V. M.-O. M. I. Díez-García, M. Jankulovska, S. Anandan, P. Bonete, R. Gómez and T. Lana-Villarreal, *Physics Procedia*, 2015, **63**, 85-90.
142. R. V. Kumar, Y. Diamant and A. Gedanken, *Chem Mater*, 2000, **12**, 2301-2305.
143. Y. C. Zhu, H. L. Li, Y. Koltypin, Y. R. Hacohen and A. Gedanken, *Chem Commun*, 2001, 2616-2617.
144. R. V. Kumar, Y. Koltypin, X. N. Xu, Y. Yeshurun, A. Gedanken and I. Felner, *J Appl Phys*, 2001, **89**, 6324-6328.
145. P. Jeevanandam, Y. Koltypin and A. Gedanken, *Nano Lett*, 2001, **1**, 263-266.
146. S. Avivi, Y. Mastai, G. Hodes and A. Gedanken, *J Am Chem Soc*, 1999, **121**, 4196-4199.
147. S. Avivi, Y. Mastai and A. Gedanken, *Chem Mater*, 2000, **12**, 1229-1233.
148. K. V. P. M. Shafi, I. Felner, Y. Mastai and A. Gedanken, *J Phys Chem B*, 1999, **103**, 3358-3360.
149. E. Ohayon and A. Gedanken, *Ultrason Sonochem*, 2010, **17**, 173-178.
150. Y. Y. Liu and C. B. Cao, *Electrochim Acta*, 2010, **55**, 4694-4699.
151. I. Bilecka and M. Niederberger, *Nanoscale*, 2010, **2**, 1358-1374.
152. M. A. Herrero, J. M. Kremsner and C. O. Kappe, *J Org Chem*, 2008, **73**, 36-47.
153. D. M. P. Mingos and D. R. Baghurst, *Chem Soc Rev*, 1991, **20**, 1-47.
154. P. Lidstrom, J. Tierney, B. Wathey and J. Westman, *Tetrahedron*, 2001, **57**, 9225-9283.

155. K. L. Harrison, C. A. Bridges, M. P. Paranthaman, C. U. Segre, J. Katsoudas, V. A. Maroni, J. C. Idrobo, J. B. Goodenough and A. Manthiram, *Chem Mater*, 2013, **25**, 768-781.
156. K. L. Harrison and A. Manthiram, *Chem Mater*, 2013, **25**, 1751-1760.
157. C. Jahne, C. Neef, C. Koo, H. P. Meyer and R. Klingeler, *J Mater Chem A*, 2013, **1**, 2856-2862.
158. G. Assat and A. Manthiram, *Inorg Chem*, 2015, **54**, 10015-10022.
159. M. Antonietti, D. B. Kuang, B. Smarsly and Z. Yong, *Angew Chem Int Edit*, 2004, **43**, 4988-4992.
160. Z. J. Lin, Y. Li, A. M. Z. Slawin and R. E. Morris, *Dalton T*, 2008, 3989-3994.
161. E. R. Parnham and R. E. Morris, *Accounts Chem Res*, 2007, **40**, 1005-1013.
162. N. Recham, L. Dupont, M. Courty, K. Djellab, D. Larcher, M. Armand and J. M. Tarascon, *Chem Mater*, 2009, **21**, 1096-1107.
163. P. Barpanda, K. Djellab, N. Recham, M. Armand and J. M. Tarascon, *J Mater Chem*, 2011, **21**, 10143-10152.
164. N. Recham, J. N. Chotard, J. C. Jumas, L. Laffont, M. Armand and J. M. Tarascon, *Chem Mater*, 2010, **22**, 1142-1148.
165. X. L. Li, W. X. He, Z. H. Xiao, F. F. Peng and J. J. Chen, *J Solid State Electr*, 2013, **17**, 1991-2000.
166. N. Leadbeater, *Green Chem*, 2003, **5**, 677-677.
167. S. Y. Chung, J. T. Bloking and Y. M. Chiang, *Nat Mater*, 2002, **1**, 123-128.
168. Z. H. Wang, L. X. Yuan, J. Ma, L. Qie, L. L. Zhang and Y. H. Huang, *Electrochim Acta*, 2012, **62**, 416-423.
169. X. G. Yin, K. L. Huang, S. Q. Liu, H. Y. Wang and H. Wang, *J Power Sources*, 2010, **195**, 4308-4312.
170. X. D. Xin, H. J. Li, Q. Q. Chang and W. L. Wang, *Chinese J Chem Phys*, 2012, **25**, 429-433.
171. C. Delacourt, C. Wurm, L. Laffont, J. B. Leriche and C. Masquelier, *Solid State Ionics*, 2006, **177**, 333-341.
172. Z. P. Ma, G. J. Shao, G. L. Wang, Y. Zhang and J. P. Du, *J Solid State Chem*, 2014, **210**, 232-237.
173. A. Kulka, A. Braun, T. W. Huang, A. Wolska, M. T. Klepka, A. Szewczyk, D. Baster, W. Zajac, K. Swierczek and J. Molenda, *Solid State Ionics*, 2015, **270**, 33-38.
174. N. Ravet, A. Abouimrane and M. Armand, *Nat Mater*, 2003, **2**, 702.
175. P. S. Herle, B. Ellis, N. Coombs and L. F. Nazar, *Nat Mater*, 2004, **3**, 147-152.
176. A. Ornek, E. Bulut, M. Can and M. Ozacar, *J Solid State Electr*, 2013, **17**, 3101-3107.
177. A. Y. Shenouda and H. K. Liu, *J Alloy Compd*, 2009, **477**, 498-503.
178. H. B. Shu, X. Y. Wang, Q. Wu, B. N. Hu, X. K. Yang, Q. L. Wei, Q. Q. Liang, Y. S. Bai, M. Zhou, C. Wu, M. F. Chen, A. W. Wang and L. L. Jiang, *J Power Sources*, 2013, **237**, 149-155.
179. W. M. Liu, Q. Z. Huang and G. R. Hu, *J Alloy Compd*, 2015, **632**, 185-189.
180. Q. L. Liu, W. M. Liu, D. X. Li and Z. X. Wang, *Mater Lett*, 2016, **162**, 87-90.
181. J. Lee, P. Kumar, G. Lee, B. M. Moudgil and R. K. Singh, *Ionics*, 2013, **19**, 371-378.
182. H. W. Lee, P. Muralidharan, R. Ruffo, C. M. Mari, Y. Cui and D. K. Kim, *Nano Lett*, 2010, **10**, 3852-3856.
183. Y. S. Hu, L. Kienle, Y. G. Guo and J. Maier, *Adv Mater*, 2006, **18**, 1421-+.
184. J. Jamnik and J. Maier, *Phys Chem Chem Phys*, 2003, **5**, 5215-5220.
185. P. Balaya, *Energ Environ Sci*, 2008, **1**, 645-654.
186. Q. Wang, H. Li, L. Q. Chen and X. J. Huang, *Carbon*, 2001, **39**, 2211-2214.
187. N. A. Naskhedikar and J. Maier, *Adv Mater*, 2009, **21**, 2664-2680.
188. P. G. Bruce, B. Scrosati and J. M. Tarascon, *Angew Chem Int Edit*, 2008, **47**, 2930-2946.

189. Z. Y. Bi, X. D. Zhang, W. He, D. D. Min and W. S. Zhang, *Rsc Adv*, 2013, **3**, 19744-19751.
190. Y. G. Wang, Y. R. Wang, E. J. Hosono, K. X. Wang and H. S. Zhou, *Angew Chem Int Edit*, 2008, **47**, 7461-7465.
191. L. L. Peng, Y. Zhao, Y. Ding and G. H. Yu, *Chem Commun*, 2014, **50**, 9569-9572.
192. J. J. Wang and X. L. Sun, *Energ Environ Sci*, 2012, **5**, 5163-5185.
193. H. F. Ni, J. K. Liu and L. Z. Fan, *Nanoscale*, 2013, **5**, 2164-2168.
194. P. R. Kumar, M. Venkateswarlu, M. Misra, A. K. Mohanty and N. Satyanarayana, *J Electrochem Soc*, 2011, **158**, A227-A230.
195. J. Liu, S. Z. Qiao, J. S. Chen, X. W. Lou, X. R. Xing and G. Q. Lu, *Chem Commun*, 2011, **47**, 12578-12591.
196. T. Mandal, G. Piburn, V. Stavila, I. Rusakova, T. Ould-Ely, A. C. Colson and K. H. Whitmire, *Chem Mater*, 2011, **23**, 4158-4169.
197. T. Mandal, V. Stavila, I. Rusakova, S. Ghosh and K. H. Whitmire, *Chem Mater*, 2009, **21**, 5617-5626.
198. S. Boulmaaz, R. Papiernik, L. G. HubertPfalzgraf, B. Septe and J. Vaissermann, *J Mater Chem*, 1997, **7**, 2053-2061.
199. A. M. Moneeb, A. M. Alabdulrahman, A. A. Bagabas, C. K. Perkins and A. W. Apblett, *Ceram Int*, 2016, **42**, 1366-1372.
200. X. X. Zou, G. D. Li, M. Y. Guo, X. H. Li, D. P. Liu, J. Su and J. S. Chen, *Chem-Eur J*, 2008, **14**, 11123-11131.
201. Y. F. Deng, S. D. Tang, Q. M. Zhang, Z. C. Shi, L. T. Zhang, S. Z. Zhan and G. H. Chen, *J Mater Chem*, 2011, **21**, 11987-11995.
202. J. Guo, X. Chen, Y. J. Yi, W. Z. Li and C. H. Liang, *Rsc Adv*, 2014, **4**, 16716-16720.
203. G. B. Biddlecombe, Y. K. Gun'ko, J. M. Kelly, S. C. Pillai, J. M. D. Coey, M. Venkatesan and A. P. Douvalis, *J Mater Chem*, 2001, **11**, 2937-2939.
204. S. A. Corr, Y. K. Gun'ko, A. P. Douvalis, M. Venkatesan, R. D. Gunning and P. D. Nellist, *J Phys Chem C*, 2008, **112**, 1008-1018.
205. V. K. P. a. P. Y. Zavalij, *Fundamentals of Powder Diffraction and Structural Characterization of Materials*, Springer, 2005.
206. R. E. D. a. S. J. L. Billinge, *Powder Diffraction: Theory and Practice*, RSCPublishing, 2008.
207. https://icsd.fiz-karlsruhe.de/search/index.xhtml.
208. A. L. Patterson, *Phys Rev*, 1939, **56**, 978-982.
209. H. M. Rietveld, *J Appl Crystallogr*, 1969, **2**, 65-&.
210. B. H. Toby, *Powder Diffr*, 2006, **21**, 67-70.
211. R. A. Young, *The Rietveld method. (IUCr Monogrph on Crystallography, No. 5)*, 1993.
212. G. Will, *Powder Diffraction: The Rietveld Method and the Two Stage to Determine and Refine Crystal Structures from Powder Diffraction Data*, Springer, 2006.
213. R. M. Ibberson and W. I. F. David, in *Neutron powder diffraction*, Oxford University Press, 2002.
214. E. H. K. a. C. J. Howard, *Applications of Neutron Powder Diffraction*, Oxford University Press, 2012.
215. B. T. M. Willis, *Z Kristallogr*, 1994, **209**, 385-389.
216. G. Barone, L. Bartoli, C. M. Belfiore, V. Crupi, F. Longo, D. Majolino, P. Mazzoleni and V. Venuti, *J Anal Atom Spectrom*, 2011, **26**, 1060-1067.
217. S. J. L. Billinge, *J Solid State Chem*, 2008, **181**, 1695-1700.
218. A. Mancini and L. Malavasi, *Chem Commun*, 2015, **51**, 16592-16604.
219. L. Malavasi, *Dalton T*, 2011, **40**, 3777-3788.
220. C. A. Young and A. L. Goodwin, *J Mater Chem*, 2011, **21**, 6464-6476.
221. S. J. L. Billinge and I. Levin, *Science*, 2007, **316**, 1698-1698.

222. T. Proffen, S. J. L. Billinge, T. Egami and D. Louca, *Z Kristallogr*, 2003, **218**, 132-143.
223. T. E. a. S. J. L. Billinge, Pergamon, 2003.
224. S. A. K., Rutherford Appleton Laboratory Technical Report RAL-TR-2011-013, 2011.
225. M. G. Tucker, D. A. Keen, M. T. Dove, A. L. Goodwin and Q. Hui, *J Phys-Condens Mat*, 2007, **19**.
226. P. J. Chupas, X. Y. Qiu, J. C. Hanson, P. L. Lee, C. P. Grey and S. J. L. Billinge, *Journal of Applied Crystallography*, 2003, **36**, 1342-1347.
227. A. P. Hammersley, 1998.
228. P. J. Xiaohao Yang, Christopher L. Farrow and Simon J. L. Billinge, *J Appl Crystallogr*, 2014.
229. C. L. Farrow, P. Juhas, J. W. Liu, D. Bryndin, E. S. Bozin, J. Bloch, T. Proffen and S. J. L. Billinge, *J Phys-Condens Mat*, 2007, **19**.
230. D. W. Bennet, *Understanding Single-Crystal X-Ray Crystallography*, Wiley-VCH, 2010.
231. G. M. Sheldrick, *Acta Crystallographica Section C-Structural Chemistry*, 2015, **71**, 3-8.
232. R. F. Egerton, *Physical Principles of Electron Microscopy*, Springer, 2016.
233. J. Goldstein, *Scanning Electron Microscopy and X-ray Microanalysis*, 2003.
234. D. B. a. C. Williams, C. D., *Transmission Electron Microscopy*, Springer, 2009.
235. D. B. Williams and C. Barry Carter, *Transmission Electron Microscopy*, Springer, 2009.
236. S. J. Blundell, *Contemp Phys*, 1999, **40**, 175-192.
237. F. L. Pratt, *Physica B*, 2000, **289**, 710-714.
238. C. C. Yang and W. H. Chen, *Mater Chem Phys*, 2016, **173**, 482-490.
239. A. K. Cheetham and A. L. Goodwin, *Nat Mater*, 2014, **13**, 760-762.
240. N. Wiberg, A. F. Holleman and E. Wiberg, *Inorganic Chemistry*, Academic Press, 2001.
241. X. H. Wang, X. W. Li, X. L. Sun, F. Li, Q. M. Liu, Q. Wang and D. Y. He, *J Mater Chem*, 2011, **21**, 3571-3573.
242. D. K. Gosser, *Cyclic voltammetry: simulation and analysis of reaction mechanisms*, VCH Publishers, New York, 1994.
243. L. R. F. A. J. Bard, *Electrochemical Methods*, John Wiley & Sons, 1980.
244. D. Y. W. Yu, C. Fietzek, W. Weydanz, K. Donoue, T. Inoue, H. Kurokawa and S. Fujitani, *J Electrochem Soc*, 2007, **154**, A253-A257.
245. S. Brunauer, P. H. Emmett and E. Teller, *J Am Chem Soc*, 1938, **60**, 309-319.
246. K. S. W. Sing, *Adv Colloid Interfac*, 1998, **76**, 3-11.
247. F. Pregl, *Quantitative Micro-Analysis of Organic Substances*, Springer, Berlin, 1917.
248. B. W. a. M. Sperling, *Atomic Absorption Spectrometry*, Wiley-VCH, Weinheim, Germany, 1999.
249. J. D. Roberts, *Nuclear Magnetic Resonance: applications to organic chemistry*, Mc Graw-Hill Book Company, 1959.
250. J. A. P. a. W. G. Schneider, *High-resolution Nuclear Magnetic Resonance*, Mc Graw-Hill Book Company, 1959.
251. B. Stuart, *Infrared Spectroscopy: Fundamentals and Applications*, Wiley, 1996.
252. R. D. Shannon, *Acta Crystallogr A*, 1976, **32**, 751-767.
253. A. C. Larson and R. B. Von Dreele, in *Los Alamos National Laboratory Report LAUR*, 2004, pp. 86-748.
254. B. H. Toby, *J Appl Crystallogr*, 2001, **34**, 210-213.
255. A. R. Denton and N. W. Ashcroft, *Phys Rev A*, 1991, **43**, 3161-3164.
256. V. F. Sears, *Neutron News*, 1992, **3**.
257. K. M. O. Jensen, M. Christensen, H. P. Gunnlaugsson, N. Lock, E. D. Bojesen, T. Proffen and B. B. Iversen, *Chem Mater*, 2013, **25**, 2282-2290.

258. R. S. Hayano, Y. J. Uemura, J. Imazato, N. Nishida, T. Yamazaki and R. Kubo, *Phys Rev B*, 1979, **20**, 850-859.
259. D. Di Lecce and J. Hassoun, *J Phys Chem C*, 2015, **119**, 20855-20863.
260. P. J. Baker, I. Franke, F. L. Pratt, T. Lancaster, D. Prabhakaran, W. Hayes and S. J. Blundell, *Phys Rev B*, 2011, **84**.
261. J. Sugiyama, H. Nozaki, M. Harada, K. Kamazawa, Y. Ikedo, Y. Miyake, O. Ofer, M. Mansson, E. J. Ansaldo, K. H. Chow, G. Kobayashi and R. Kanno, *Phys Rev B*, 2012, **85**.
262. D. H. Kim and J. Kim, *Electrochem Solid St*, 2006, **9**, A439-A442.
263. B. Kang and G. Ceder, *Nature*, 2009, **458**, 190-193.
264. C. Delacourt, L. Laffont, R. Bouchet, C. Wurm, J. B. Leriche, M. Morcrette, J. M. Tarascon and C. Masquelier, *J Electrochem Soc*, 2005, **152**, A913-A921.
265. J. Jiang, W. Liu, J. T. Chen and Y. L. Hou, *Acs Appl Mater Inter*, 2012, **4**, 3062-3068.
266. B. Zhang, X. J. Wang, H. Li and X. J. Huang, *J Power Sources*, 2011, **196**, 6992-6996.
267. G. Kobayashi, A. Yamada, S. Nishimura, R. Kanno, Y. Kobayashi, S. Seki, Y. Ohno and H. Miyashiro, *J Power Sources*, 2009, **189**, 397-401.
268. M. R. Roberts, G. Vitins, G. Denuault and J. R. Owen, *J Electrochem Soc*, 2010, **157**, A381-A386.
269. M. Mantymaki, M. Ritala and M. Leskela, *Coordin Chem Rev*, 2012, **256**, 854-877.
270. S. A. Corr, Y. K. Gun'ko, A. P. Douvalis, M. Venkatesan and R. D. Gunning, *J Mater Chem*, 2004, **14**, 944-946.
271. C. T. Lynch, K. S. Mazdiyasni, W. J. Crawford and J. S. Smith, *Anal Chem*, 1964, **36**, 2332-&.
272. H. A. Ory, *Anal Chem*, 1960, **32**, 509-511.
273. K. L. Taft, A. Caneschi, L. E. Pence, C. D. Delfs, G. C. Papaefthymiou and S. J. Lippard, *J Am Chem Soc*, 1993, **115**, 11753-11766.
274. C. Gabriel, S. Gabriel, E. H. Grant, B. S. J. Halstead and D. M. P. Mingos, *Chem Soc Rev*, 1998, **27**, 213-223.
275. A. Losey, J. Rakovan, J. M. Hughes, C. A. Francis and M. D. Dyar, *Can Mineral*, 2004, **42**, 1105-1115.
276. J. Rodriguez-Carvaja, *ILL (unpublished)*.
277. K. Wang, M. Y. Hou, S. Y. Yuan, H. C. Yu, Y. G. Wang, C. X. Wang and Y. Y. Xia, *Electrochem Commun*, 2015, **55**, 6-9.
278. R. von Hagen, H. Lorrmann, K. C. Moller and S. Mathur, *Adv Energy Mater*, 2012, **2**, 553-559.
279. N. N. Zhao, Y. S. Li, X. X. Zhao, X. K. Zhi and G. C. Liang, *J Alloy Compd*, 2016, **683**, 123-132.
280. C. B. Wang, L. W. Yin, D. Xiang and Y. X. Qi, *Acs Appl Mater Inter*, 2012, **4**, 1636-1642.
281. D. Jarosch, *Miner Petrol*, 1987, **37**, 15-23.
282. H. Huang, L. Y. Zhang, Y. Xia, Y. P. Gan, X. Y. Tao, C. Liang and W. K. Zhang, *New J Chem*, 2014, **38**, 4743-4747.
283. J. Gao, M. A. Lowe and H. D. Abruna, *Chem Mater*, 2011, **23**, 3223-3227.
284. L. J. Hu, B. Qiu, Y. G. Xia, Z. H. Qin, L. F. Qin, X. F. Zhou and Z. P. Liu, *J Power Sources*, 2014, **248**, 246-252.
285. I. Nam, N. D. Kim, G. P. Kim, J. Park and J. Yi, *J Power Sources*, 2013, **244**, 56-62.
286. C. S. Wang, A. J. Appleby and F. E. Little, *J Electroanal Chem*, 2001, **497**, 33-46.
287. Y. Y. Liu, V. I. Artyukhov, M. J. Liu, A. R. Harutyunyan and B. I. Yakobson, *J Phys Chem Lett*, 2013, **4**, 1737-1742.
288. L. F. Wang, C. C. Ou, K. A. Striebel and J. J. S. Chen, *J Electrochem Soc*, 2003, **150**, A905-A911.

289. L. G. Hubertpfalzgraf, *Appl Organomet Chem*, 1992, **6**, 627-643.
290. L. G. Hubertpfalzgraf, R. Papiernik and M. Verdaguer, *Abstr Pap Am Chem S*, 1990, **199**, 33-Inor.
291. D. C. Bradley, *Philos T R Soc A*, 1990, **330**, 167-171.
292. Y. K. Gun'ko, U. Cristmann and V. G. Kessler, *Eur J Inorg Chem*, 2002, 1029-1031.
293. H. R. L. Barley, A. R. Kennedy and R. E. Mulvey, *Acta Crystallogr C*, 2005, **61**, M346-M347.
294. J. P. a. B. Neumüller, *Z Anorg Allg Chem*, 2000, **626**, 270-279.
295. C. Wu, W. Huang, L. Liu, H. T. Wang, Y. Zeng, J. Xie, C. Jin and Z. Zhang, *Cryst Eng Comm*, 2016, **18**, 7707.
296. http://www.dow.com/ethyleneglycol/about/properties.htm.
297. H. S. Fang, Z. Y. Pan, L. P. Li, Y. Yang, G. F. Yan, G. S. Li and S. Q. Wei, *Electrochem Commun*, 2008, **10**, 1071-1073.
298. M. Bini, S. Ferrari, D. Capsoni, P. Mustarelli, G. Spina, F. Del Giallo, M. Lantieri, C. Leonelli, A. Rizzuti and V. Massarotti, *Rsc Adv*, 2012, **2**, 250-258.
299. J. N. Zhu, W. C. Li, F. Cheng and A. H. Lu, *J Mater Chem A*, 2015, **3**, 13920-13925.
300. C. C. Yang, Y. W. Hung and S. J. Lue, *J Power Sources*, 2016, **325**, 565-574.
301. J. Su, Z. Z. Liu, Y. F. Long, H. Yao, X. Y. Lv and Y. X. Wen, *Electrochim Acta*, 2015, **173**, 559-565.
302. H. Guo, C. Y. Wu, J. Xie, S. C. Zhang, G. S. Cao and X. B. Zhao, *J Mater Chem A*, 2014, **2**, 10581-10588.
303. Y. Hong, Z. L. Tang, S. T. Wang, W. Quan and Z. T. Zhang, *J Mater Chem A*, 2015, **3**, 10267-10274.
304. N. Recham, J. Oro-Sole, K. Djellab, M. R. Palacin, C. Masquelier and J. M. Tarascon, *Solid State Ionics*, 2012, **220**, 47-52.
305. F. Teng, M. D. Chen, G. Q. Li, Y. Teng, T. G. Xu, S. I. Mho and X. Hua, *J Power Sources*, 2012, **202**, 384-388.
306. N. Zhou, Y. Y. Liu, J. G. Li, E. Uchaker, S. Q. Liu, K. L. Huang and G. Z. Cao, *J Power Sources*, 2012, **213**, 100-105.
307. A. V. Murugan, T. Muraliganth and A. Manthiram, *Electrochem Commun*, 2008, **10**, 903-906.
308. J. Liu, T. E. Conry, X. Y. Song, M. M. Doeff and T. J. Richardson, *Energ Environ Sci*, 2011, **4**, 885-888.
309. K. M. Jensen, C. Tyrsted, M. Bremholm and B. B. Iversen, *Chemsuschem*, 2014, **7**, 1594-1611.
310. M. Wu, Z. H. Wang, L. X. Yuan, W. X. Zhang, X. L. Hu and Y. H. Huang, *Chinese Sci Bull*, 2012, **57**, 4170-4175.
311. K. Saravanan, V. Ramar, P. Balaya and J. J. Vittal, *J Mater Chem*, 2011, **21**, 14925-14935.
312. X. K. Huang, X. M. He, C. Y. Jiang and G. Y. Tian, *Rsc Adv*, 2014, **4**, 56074-56083.
313. C. Y. Nan, J. Lu, C. Chen, Q. Peng and Y. D. Li, *J Mater Chem*, 2011, **21**, 9994-9996.
314. K. Saravanan, P. Balaya, M. V. Reddy, B. V. R. Chowdari and J. J. Vittal, *Energ Environ Sci*, 2010, **3**, 457-464.
315. M. Talebi-Esfandarani and O. Savadogo, *J Appl Electrochem*, 2015, **45**, 245-251.
316. W. P. Kang, C. H. Zhao, R. Liu, F. F. Xu and Q. Shen, *Crystengcomm*, 2012, **14**, 2245-2250.
317. X. Qin, J. M. Wang, J. Xie, F. Z. Li, L. Wen and X. H. Wang, *Phys Chem Chem Phys*, 2012, **14**, 2669-2677.
318. O. Garcia-Moreno, M. Alvarez-Vega, F. Garcia-Alvarado, J. Garcia-Jaca, J. M. Gallardo-Amores, M. L. Sanjuan and U. Amador, *Chem Mater*, 2001, **13**, 2455-2455.

319. S. P. Badi, M. Wagemaker, B. L. Ellis, D. P. Singh, W. J. H. Borghols, W. H. Kan, D. H. Ryan, F. M. Mulder and L. F. Nazar, *J Mater Chem*, 2011, **21**, 10085-10093.
320. X. Zhou, Y. Xie, Y. F. Deng, X. S. Qin and G. H. Chen, *J Mater Chem A*, 2015, **3**, 996-1004.
321. K. Zaghib, A. Mauger, F. Gendron, M. Massot and C. M. Julien, *Ionics*, 2008, **14**, 371-376.
322. Y. Lu, J. C. Shi, Z. P. Guo, Q. S. Tong, W. J. Huang and B. Y. Li, *J Power Sources*, 2009, **194**, 786-793.
323. K. Saravanan, J. J. Vittal, M. V. Reddy, B. V. R. Chowdari and P. Balaya, *J Solid State Electr*, 2010, **14**, 1755-1760.
324. C. W. Sun, S. Rajasekhara, J. B. Goodenough and F. Zhou, *J Am Chem Soc*, 2011, **133**, 2132-2135.
325. A. V. Murugan, T. Muraliganth and A. Manthiram, *J Phys Chem C*, 2008, **112**, 14665-14671.
326. S. L. Yang, R. G. Ma, M. J. Hu, L. J. Xi, Z. G. Lu and C. Y. Chung, *J Mater Chem*, 2012, **22**, 25402-25408.
327. Z. H. Qin, X. F. Zhou, Y. G. Xia, C. L. Tang and Z. P. Liu, *J Mater Chem*, 2012, **22**, 21144-21153.
328. Y. P. Huang, T. Tao, Z. Chen, W. Han, Y. Wu, C. J. Kuang, S. X. Zhou and Y. Chen, *J Mater Chem A*, 2014, **2**, 18831-18837.
329. R. V. Apraksin, S. N. Eliseeva, E. G. Tolstopjatova, A. M. Rumyantsev, V. V. Zhdanov and V. V. Kondratiev, *Mater Lett*, 2016, **176**, 248-252.
330. H. L. Wang, Y. Yang, Y. Y. Liang, L. F. Cui, H. S. Casalongue, Y. G. Li, G. S. Hong, Y. Cui and H. J. Dai, *Angew Chem Int Edit*, 2011, **50**, 7364-7368.
331. K. Amine, J. Liu and I. Belharouak, *Electrochem Commun*, 2005, **7**, 669-673.
332. H. C. Wu, C. Y. Su, D. T. Shieh, M. H. Yang and N. L. Wu, *Electrochem Solid St*, 2006, **9**, A537-A541.
333. F. Mestre-Aizpurua, S. Hamelet, C. Masquelier and M. R. Palacin, *J Power Sources*, 2010, **195**, 6897-6901.
334. A. Guerfi, S. Duchesne, Y. Kobayashi, A. Vijh and K. Zaghib, *J Power Sources*, 2008, **175**, 866-873.
335. A. P. Lewandowski, A. F. Hollenkamp, S. W. Donne and A. S. Best, *J Power Sources*, 2010, **195**, 2029-2035.
336. R. V. Kumar, Y. Koltypin, Y. S. Cohen, Y. Cohen, D. Aurbach, O. Palchik, I. Felner and A. Gedanken, *J Mater Chem*, 2000, **10**, 1125-1129.
337. R. Vijayakumar, Y. Koltypin, I. Felner and A. Gedanken, *Mat Sci Eng a-Struct*, 2000, **286**, 101-105.
338. X. Cao, Y. Koltypin, G. Katabi and R. Prozorov, *J Mater Chem*, 1997, **7**, 1007-1009.
339. M. E. Fleet, *Acta Crystallogr B*, 1981, **37**, 917-920.
340. P. C. Lian, X. F. Zhu, H. F. Xiang, Z. Li, W. S. Yang and H. H. Wang, *Electrochim Acta*, 2010, **56**, 834-840.
341. X. L. Wu, Y. G. Guo, L. J. Wan and C. W. Hu, *J Phys Chem C*, 2008, **112**, 16824-16829.
342. L. Chun, X. Z. Wu, X. M. Lou and Y. X. Zhang, *Electrochim Acta*, 2010, **55**, 3089-3092.
343. B. Jang, M. Park, O. B. Chae, S. Park, Y. Kim, S. M. Oh, Y. Piao and T. Hyeon, *J Am Chem Soc*, 2012, **134**, 15010-15015.
344. Z. M. Cui, L. Y. Hang, W. G. Song and Y. G. Guo, *Chem Mater*, 2009, **21**, 1162-1166.
345. Y. Zhao, C. L. Ma, C. Ma, J. Shi and J. L. Shi, *Mater Lett*, 2016, **177**, 148-151.
346. H. P. Li, Y. Li, Y. G. Zhang and C. W. Zhang, *J Nanopart Res*, 2015, **17**.
347. T. Yoon, C. Chae, Y. K. Sun, X. Zhao, H. H. Kung and J. K. Lee, *J Mater Chem*, 2011, **21**, 17325-17330.
348. Z. C. Yang, J. G. Shen and L. A. Archer, *J Mater Chem*, 2011, **21**, 11092-11097.

349. D. C. Bock, C. J. Pelliccione, W. Zhang, J. J. Wang, K. W. Knehr, J. Wang, F. Wang, A. C. West, A. C. Marschilok, K. J. Takeuchi and E. S. Takeuchi, *Acs Appl Mater Inter*, 2016, **8**, 11418-11430.
350. F. S. Ke, L. Jamison, L. Huang, B. Zhang, J. T. Li, X. D. Zhou and S. G. Sun, *Solid State Ionics*, 2014, **262**, 18-21.
351. M. Lubke, N. M. Makwana, R. Gruar, C. Tighe, D. Brett, P. Shearing, Z. L. Liu and J. A. Darr, *J Power Sources*, 2015, **291**, 102-107.
352. T. Yoon, J. Kim, J. Kim and J. K. Lee, *Energies*, 2013, **6**, 4830-4840.
353. X. H. Wang, L. Qiao, X. L. Sun, X. W. Li, D. K. Hu, Q. Zhang and D. Y. He, *J Mater Chem A*, 2013, **1**, 4173-4176.
354. S. A. Needham, G. X. Wang and H. K. Liu, *J Power Sources*, 2006, **159**, 254-257.
355. X. H. Huang, J. P. Tu, C. Q. Zhang and F. Zhou, *Electrochim Acta*, 2010, **55**, 8981-8985.
356. S. J. Hao, B. W. Zhang, S. Ball, B. Hu, J. S. Wu and Y. Z. Huang, *Mater Design*, 2016, **92**, 160-165.
357. D. Xie, W. W. Yuan, Z. M. Dong, Q. M. Su, J. Zhang and G. H. Du, *Electrochim Acta*, 2013, **92**, 87-92.
358. X. W. Liu, T. Z. Feng, S. H. Chen and H. Wei, *Int J Electrochem Sc*, 2016, **11**, 2276-2283.
359. R. C. M. D. C. Bradley, I. P. Rothwell and A. Singh, *Alkoxo and Aryloxo Derivatives of Metals*, Academic Press, 2001.
360. Y. C. Ge, X. D. Yan, J. Liu, X. F. Zhang, J. W. Wang, X. G. He, R. S. Wang and H. M. Xie, *Electrochim Acta*, 2010, **55**, 5886-5890.
361. W. K. Zhang, Y. L. Hu, X. Y. Tao, H. Huang, Y. P. Gan and C. T. Wang, *J Phys Chem Solids*, 2010, **71**, 1196-1200.
362. S. M. Zheng, X. Wang, X. Huang and C. H. Liu, *Ceram Int*, 2012, **38**, 4391-4394.
363. R. Qing, M. C. Yang, Y. S. Meng and W. Sigmund, *Electrochim Acta*, 2013, **108**, 827-832.
364. Y. J. Yun, M. Wu, J. K. Kim, J. Y. Ju, S. S. Lee, K. W. Kim, W. I. Park, H. K. Jung, K. H. Kim, J. S. Park and S. Choi, *J Nanomater*, 2015.
365. H. B. Liu, C. Miao, Y. Meng, Y. B. He, Q. Xu, X. H. Zhang and Z. Y. Tang, *Electrochim Acta*, 2014, **130**, 322-328.
366. E. R. Jette and F. Foote, *J Chem Phys*, 1935, **3**, 605-616.
367. H. H. Weik, P., *Bulletin of the American Physical Society*, 1965, **10**, 1140-1140.
368. M. K. Devaraju, Q. D. Truong, H. Hyodo, Y. Sasaki and I. Honma, *Sci Rep-Uk*, 2015, **5**.
369. Gangulibabu, D. Bhuvaneswari, N. Kalaiselvi, N. Jayaprakash and P. Periasamy, *J Sol-Gel Sci Techn*, 2009, **49**, 137-144.
370. G. L. Huang, W. Li, H. Z. Sun, J. W. Wang, J. P. Zhang, H. X. Jiang and F. Zhai, *Electrochim Acta*, 2013, **97**, 92-98.
371. M. J. Li, L. Q. Sun, K. Sun, S. H. Yu, R. S. Wang and H. M. Xie, *J Solid State Electr*, 2012, **16**, 3581-3586.
372. Y. B. Lou, J. J. Zhang, L. Zhu and L. X. Lei, *J Nanomater*, 2013.
373. A. Iturrondobeitia, A. Goni, I. G. de Muro, L. Lezama, C. Kim, M. Doeff, J. Cabana and T. Rojo, *Inorg Chem*, 2015, **54**, 2671-2678.
374. G. H. Zhang, Y. J. Chen, B. H. Qu, L. L. Hu, L. Mei, D. N. Lei, Q. Li, L. B. Chen, Q. H. Li and T. H. Wang, *Electrochim Acta*, 2012, **80**, 140-147.
375. Y. Huang, X. L. Huang, J. S. Lian, D. Xu, L. M. Wang and X. B. Zhang, *J Mater Chem*, 2012, **22**, 2844-2847.
376. L. S. Zhong, J. S. Hu, A. M. Cao, Q. Liu, W. G. Song and L. J. Wan, *Chem Mater*, 2007, **19**, 1648-1655.
377. H. Kedesdy and A. Drukalsky, *J Am Chem Soc*, 1954, **76**, 5941-5946.
378. C. H. Xu, J. Sun and L. A. Gao, *J Power Sources*, 2011, **196**, 5138-5142.
379. A. Caballero, L. Hernan, J. Morales, Z. Gonzalez, A. J. Sanchez-Herencia and B. Ferrari, *Energ Fuel*, 2013, **27**, 5545-5551.

380. Q. Wang, Y. F. Xu, G. L. Xu, H. Su, S. Y. Shen, T. T. Tu, L. Huang, J. T. Li and S. G. Sun, *J Alloy Compd*, 2015, **648**, 59-66.
381. H. Liu, G. X. Wang, J. Liu, S. Z. Qiao and H. J. Ahn, *J Mater Chem*, 2011, **21**, 3046-3052.
382. G. P. Kim, S. Park, I. Nam, J. Park and J. Yi, *J Power Sources*, 2013, **237**, 172-177.
383. P. Poizot, S. Laruelle, S. Grugeon and J. M. Tarascon, *J Electrochem Soc*, 2002, **149**, A1212-A1217.
384. L. Yuan, Z. P. Guo, K. Konstantinov, P. Munroe and H. K. Liu, *Electrochem Solid St*, 2006, **9**, A524-A528.
385. J. Ding, Z. Su and H. L. Tian, *Ceram Int*, 2016, **42**, 12435-12440.
386. S. Ferrari, D. Capsoni, S. Casino, M. Destro, C. Gerbaldi and M. Bini, *Phys Chem Chem Phys*, 2014, **16**, 10353-10366.
387. B. Voss, J. Nordmann, A. Kockmann, J. Piezonka, M. Haase, D. H. Taffa and L. Walder, *Chem Mater*, 2012, **24**, 633-635.
388. S. W. Kim, D. H. Seo, X. H. Ma, G. Ceder and K. Kang, *Adv Energy Mater*, 2012, **2**, 710-721.
389. V. Palomares, P. Serras, I. Villaluenga, K. B. Hueso, J. Carretero-Gonzalez and T. Rojo, *Energ Environ Sci*, 2012, **5**, 5884-5901.
390. C. Li, X. Miao, W. Chu, P. Wu and D. G. Tong, *J Mater Chem A*, 2015, **3**, 8265-8271.